

Nanoscience and Technology

Francesco Marinello  
Daniele Passeri  
Enrico Savio *Editors*

# Acoustic Scanning Probe Microscopy

 Springer

# NanoScience and Technology

## *Series Editors*

Phaedon Avouris  
Bharat Bhushan  
Dieter Bimberg  
Klaus von Klitzing  
Hiroyuki Sakaki  
Roland Wiesendanger

For further volumes:  
<http://www.springer.com/series/3705>

The series NanoScience and Technology is focused on the fascinating nano-world, mesoscopic physics, analysis with atomic resolution, nano and quantum-effect devices, nanomechanics and atomic-scale processes. All the basic aspects and technology-oriented developments in this emerging discipline are covered by comprehensive and timely books. The series constitutes a survey of the relevant special topics, which are presented by leading experts in the field. These books will appeal to researchers, engineers, and advanced students.

Francesco Marinello · Daniele Passeri  
Enrico Savio  
Editors

# Acoustic Scanning Probe Microscopy

*Editors*

Francesco Marinello  
Department of Land, Environment,  
Agriculture and Forestry  
University of Padua  
Legnaro, Padua  
Italy

Enrico Savio  
Department of Industrial Engineering  
University of Padua  
Padua  
Italy

Daniele Passeri  
Department of Basic and Applied Sciences  
for Engineering  
University of Rome Sapienza  
Rome  
Italy

ISSN 1434-4904

ISBN 978-3-642-27493-0

ISBN 978-3-642-27494-7 (eBook)

DOI 10.1007/978-3-642-27494-7

Springer Heidelberg New York Dordrecht London

Library of Congress Control Number: 2012944383

© Springer-Verlag Berlin Heidelberg 2013

This work is subject to copyright. All rights are reserved by the Publisher, whether the whole or part of the material is concerned, specifically the rights of translation, reprinting, reuse of illustrations, recitation, broadcasting, reproduction on microfilms or in any other physical way, and transmission or information storage and retrieval, electronic adaptation, computer software, or by similar or dissimilar methodology now known or hereafter developed. Exempted from this legal reservation are brief excerpts in connection with reviews or scholarly analysis or material supplied specifically for the purpose of being entered and executed on a computer system, for exclusive use by the purchaser of the work. Duplication of this publication or parts thereof is permitted only under the provisions of the Copyright Law of the Publisher's location, in its current version, and permission for use must always be obtained from Springer. Permissions for use may be obtained through RightsLink at the Copyright Clearance Center. Violations are liable to prosecution under the respective Copyright Law.

The use of general descriptive names, registered names, trademarks, service marks, etc. in this publication does not imply, even in the absence of a specific statement, that such names are exempt from the relevant protective laws and regulations and therefore free for general use.

While the advice and information in this book are believed to be true and accurate at the date of publication, neither the authors nor the editors nor the publisher can accept any legal responsibility for any errors or omissions that may be made. The publisher makes no warranty, express or implied, with respect to the material contained herein.

Printed on acid-free paper

Springer is part of Springer Science+Business Media ([www.springer.com](http://www.springer.com))

*Ingenuity without poetry is like poetry without inspiration*

F. Marinello

*To Silvia, Angela and Angelica*

# Foreword

Mechanical properties of materials such as dislocation generation, fatigue, creep, crack propagation, or electrical migration in strip conductors are to a large extent determined by their microstructure. Therefore, the details of the microstructures have a strong impact on the life expectancy of a material in a given component. Materials microstructures are examined by optical microscopy, by scanning electron microscopy, and by transmission electron microscopy, often when loaded in situ mechanically or chemically.

Ultrasonic imaging as used in non-destructive testing is applied for defect detection in a component. Non-destructive materials characterization by ultrasonic imaging can be used to study the microstructure of optically nontransparent solids, in particular, metals employing scattering. In both cases, the acoustic waves penetrate into the materials, enabling one to study the microstructure of materials within the volume, to detect small defects, to study adhesive interfaces, and also to gain information about elasticity as well as absorption (also called internal friction). Ultrasonic waves of frequencies from approximately 20 kHz–2 GHz are used for acoustical imaging and mechanical spectroscopy. In acoustic imaging technologies, the contrast in reflection and transmission provides a map of the spatial distribution of elasticity, density, ultrasonic absorption and scattering, and the occurrence and distribution of defects. These parameters in turn may be used to obtain information on the mechanical properties as defined above, although often only by calibration with test components of known properties because the inter-relatedness of the various parameters is often too complex, so that an appropriate analytical formula does not exist. There are many books, handbooks, and review articles providing a detailed account of acoustical imaging for medical, material science, and non-destructive testing applications.

Acoustical imaging modes can be classified into near-field imaging techniques, focusing techniques, and holographic techniques. Examples of near-field imaging techniques are contact oscillators like the Fokker bond test system for monitoring adhesive bonds in an airplane wing. They are operated in a frequency range covering some kHz to some 100 kHz. Their spatial resolution depends on the

antenna size, i.e., the probe size and not on the frequency and hence on the wavelength employed.

Due to the smaller scale of components, in particular, in microelectronics, there was always the demand to obtain higher and higher spatial and temporal resolutions in acoustical imaging systems. This became possible with (a) the ever-increasing capabilities of computers allowing one to store the huge amount of data which followed; (b) the use of operating frequencies beyond 20 MHz for obtaining higher spatial resolution based on focusing probes, and (c) the increase of the bandwidth of the electronic receiving system to increase the temporal resolution of the imaging system. This led to the development of scanning acoustic microscopy (SAM), sometimes also called high-frequency C-scan imaging. Whereas, the physical principle of SAM was known for a long time, it took some efforts in the 1980s to engineer reliable systems. At room temperature, the highest frequency attainable in SAM is approximately 2 GHz, because the attenuation in the liquid water used as couplant necessary to transmit the ultrasonic signals from the acoustic lens to the material to be examined becomes so high that more than 99 % of the ultrasonic power gets absorbed. Even if one uses liquid metals like gallium or mercury as a couplant serving also for impedance matching, the situation does not improve much. Wavelengths at GHz frequencies are some micrometers, depending on the sound velocity. Hence, in an acoustical imaging system using a focusing transducer or an acoustical lens, the spatial resolution is at most 1  $\mu\text{m}$ . Having this technological barrier in mind, it was logical to exploit the principle of near-field imaging, where the resolution is given by the size of the antenna and less by the frequency. This comes at the cost of being able to image only the surface of a component or a material. Such efforts have been undertaken by various groups parallel to the development of SAM.

A further step toward higher resolution based on the near-field principle became possible with the advent of scanning tunneling microscopy (STM) and later of atomic force microscopy (AFM). There were early attempts to construct a near-field ultrasonic microscope based on an STM which, however, was not much pursued because it could only be used in high vacuum and on metals. The situation changed with the invention of the AFM. In atomic force microscopy, a micro-fabricated elastic beam with a sensor tip at its end is scanned over the sample surface and generates high-resolution images of surfaces. The tip radius is typically from a few nm to 100 nm. The contact radius at the surface is much smaller and even atomic resolution is possible with an AFM. It can be operated in ambient conditions for many applications. Thus, it was natural to combine AFM with ultrasonics in order to exploit its high, resolution capacity for acoustical imaging.

Very early in the development of atomic force microscopy, dynamic modes such as force modulation where the cantilever or the sample surface is vibrated, belonged to the standard equipment of most commercial instruments, allowing one to image the surface of a material, where the contrast depends on the elasticity, the friction, and the adhesion of the tip-sample contact, in particular on compliant materials. The quantitative determination of the Young's modulus of a sample surface with an AFM was a challenge however. Especially when stiff materials



such as metals or ceramics were encountered, the image contrast due to elasticity was very low in force modulation, because the spring constants of common AFM cantilevers, ranging from 0.01 to 70 N/m, are then much lower than the tip-sample contact stiffness. This barrier can be overcome by using the atomic force acoustic microscopy (AFAM) technique, or by ultrasonic atomic force microscopy (UAFM), or similar schemes. One measures the resonances of atomic force cantilevers with the tip contacting the specimen surface, hence often the term contact resonances is used for this class of dynamic atomic force microscopies. From such measurements, one can derive the local contact stiffness  $k^*$  and by using a suitable mechanical model for the contact stiffness, one can invert  $k^*$  data to measure the local indentation modulus  $M$ . The indentation modulus is an elastic constant which accounts for the compressive and the shear deformations in the contact zone between isotropic or anisotropic materials. Similarly, one can gain information on the anelastic part of the indentation modulus, which entails information on the local friction and adhesion within the contact zone and on the material's internal friction within the contact volume. In AFAM, the cantilever with its tip plays the role of the horn in impedance spectroscopy or of the contact oscillators in the Fokker bond tester and the tip-sample contact serves to probe the local mechanical impedance. Due to the small tip radii, the spatial resolution at the surface of the material examined is, however, much smaller and of nanoscale, and resolution much below 10 nm can be obtained if measurement parameters are set right. As it turned out, there is a multitude of factors determining the obtainable spatial resolution, the physical background of the contrast, and the oscillatory behavior of the cantilever when using an AFM tip as acoustical near-field antenna. It stems from the richness of the forces between tip and surface which can be adhesive, elastic, electrical, and magnetic in a linear and nonlinear fashion and because an AFM cantilever can be excited to many vibrational modes.

The authors contributing to this book, perfectly edited by F. Marinello, D. Passeri, and E. Savio, give a first-hand account on the status of the various AFM contact-resonance techniques, the theory of their operation, and the tip-sample contact mechanics. The authors provide many examples of applications and therefore serve the AFM as well as acoustical imaging communities and also those who want to apply these techniques for studying elastic, anelastic, and mechanical properties on the scale of some nanometers, and finally those who want to further develop the techniques.

What might lie ahead? I think that an improved spatial resolution can be achieved by using tips with radii much below 50 nm loaded with static forces of some nN to some 10 nN. This would allow one to examine compliant materials and hence may open the door to image biological samples and to obtain quantitative data as discussed in a chapter of the book. Such improved contact-resonance techniques should allow one to image the nanostructure of materials as well and to shed more light on the local phenomena which are behind adhesion, hardness, yield stress, elastic stresses, closing the circle to conventional acoustical imaging. Then, there is the urgent need to increase the depth sensitivity of the contact-resonance techniques for defect detection which can be achieved by an opposite

approach, using very stiff cantilevers or exploiting the higher cantilever modes with their effective higher stiffness and larger contact radii. This calls for wear-resistant tips. Finally, by using modulated propagating waves in the GHz range demodulated by the nonlinear tip-sample contact, one should be able to exploit ultrasonic scattering to study detailed features of the microstructure, for example, of materials employed in microelectronics, defects buried in wafers deeper than the Hertzian contact stress-field or in biological cells.

Saarbrücken and Göttingen

W. Arnold

# Foreword

Advancements in virtually all areas of science and technology demand materials with improved performance. In the past decades, we have witnessed new materials being continually introduced for commercial use in diverse areas like electronics, construction, transportation, textiles, and in medical devices and implants. Key to these new developments is the ability to engineer materials on the nanoscale by incorporating a multitude of components and geometric features. The resulting heterogeneity and complexity of materials call for novel characterization technologies with nanoscale spatial resolution.

Scanning probe microscopes, in particular, atomic force microscopes have played an important role in visualizing materials with nanoscale features. Owing to their mechanical operation principles, there is now a significant potential for the use of atomic force microscopes in measuring and mapping mechanical properties of nanoscale materials. A variety of techniques has already been introduced and their accuracy and range of applicability are continuously improving with an accelerating pace. Consequently, a vast literature on this subject has emerged. In that regard, Francesco Marinello, Daniele Passeri, and Enrico Savio have put together a great sourcebook on scanning probe microscopy-based nanomechanical characterization. This timely book provides a good introduction to newcomers and a thorough source of references and reviews for those already in the field.

Despite the popularity of atomic force microscopes in imaging nanoscale materials, generating quantitative information about material properties has proven difficult. As contributing author Donna C. Hurley puts it; developments in this field have been successful in generating “pretty pictures” from the nanoscale world, with qualitative contrast mechanisms. Characterization of advanced materials, however, requires reliable quantitative measurements of mechanical properties. Inaccuracies can be introduced to the measurements at various stages of information transduction. The book investigates two of the most critical stages in great depth: the contact mechanics that govern tip–sample interactions and the dynamics of the vibrating cantilever. Both intuitive and rigorous treatments of these subjects merge in the book, allowing readers from various backgrounds to benefit from the material.

Once equipped with the basic understanding of the underlying theories of contact mechanics and cantilever dynamics, the reader finds contributed chapters from leading experts in acoustic AFM and related experimental techniques, reviewing what is possible in the current state of the art. The authors share valuable tips in getting reliable measurements. I find it especially helpful that the book devotes a chapter for an in-depth comparison of the quantitative measurements obtained by scanning probe microscopy with more established techniques like instrumented indentation and surface acoustic wave spectroscopy.

The book includes contributions beyond the more established methods. The rise in demand for research in developing advanced nanomaterials is fueling the expansion of the nanomechanical characterization toolbox. Tools geared toward “soft matter” and tools providing contrast from below the surface of materials are rapidly advancing. By incorporating several examples of new techniques, including the applications of acoustic characterization techniques in biological problems, the book provides a breadth of topics that makes it a valuable source-book for anyone interested in nanomechanical analysis.

Columbia University, New York, USA

Ozgur Sahin

# Preface

The rapid progress of nanotechnologies poses significant challenges in manufacturing and characterization. Scanning Probe Microscopy (SPM) techniques have significantly contributed to such development, allowing characterization of a number of properties at the microscale and nanoscale. Having been invented for the morphological investigation of surfaces, SPM has represented the basis for the development of techniques where the tip is used for probing physical properties and the SPM position control system is used for imaging such properties on the samples surface, simultaneously to their topography.

The combination of scanning probe microscopy, and in particular of Atomic Force Microscopy (AFM) with ultrasound techniques, led to the development of acoustic AFM (A-AFM) and acoustic SPM (A-SPM) opening up to a number of measuring techniques which allow surface mechanical properties imaging.

In A-AFM, piezoelectric transducers are used to set the sample surface or the AFM cantilever into vibration at ultrasonic frequencies that are well above the cutoff frequency of the electronics, so that the oscillations are not compensated by the feedback. As a consequence such oscillation does not influence the standard topographical reconstruction, and on the other hand, the ac component of the deflection signal is not suppressed and thus can be subsequently analyzed. The particular way in which ultrasonics and SPM are combined is different for each specific technique and allows collection of different information.

Readers working in different fields of nanotechnology, material science, and biology will find in this book a comprehensive overview of such A-SPM techniques, presented by evidencing similarities and peculiarities. We proudly say that the most widely recognized scientists and researchers have contributed to the 17 chapters of the present volume, discussing acoustic SPM techniques both from the theoretical and from the practical points of view. The volume is divided into three parts.

The first part includes three chapters on subjects that form the basis of all A-SPM techniques, namely, the contact mechanics describing the tip-sample interaction, the analytical models for the dynamics of the cantilevers interacting

with the sample in the different A-SPM modalities, and numerical methods for their simulation.

The second section describes the most important A-SPM techniques emphasizing recent advances: Atomic Force Acoustic Microscopy (AFAM), Ultrasonic Atomic Force Microscopy (UAFM), Scanning Microdeformation Microscopy (SMM), Ultrasonic Force Microscopies (UFM) and related techniques, Scanning Near-Field Ultrasound Holography (SNFUH), and Torsional Harmonic Atomic Force Microscopy (TH-AFM). Two chapters are dedicated to quantitative data extrapolation, presenting strategies for enhancing the sensitivity of such techniques allowing exploitation of measuring performance and discussing the main points of data post processing, providing hints and strategies for repeatable analysis of surface data sets. The presentation of A-SPM techniques is completed with a comparison between quantitative elastic measurements by A-SPMs and conventional techniques (i.e., nanoindentation and surface acoustic wave spectroscopy).

The third section reviews applications of A-SPM. Two chapters are devoted to quantitative aspects in the characterization of friction and internal friction and in subsurface imaging. Finally, the last two chapters describe some recent results in the quantitative mechanical characterization of polymers and of biological samples.

We gratefully acknowledge the support of all authors. We also wish to thank Springer, and in particular Mr. Claus Ascheron, for his initiative to setup this volume and his organizational work. We sincerely hope that readers will find this volume scientifically stimulating and rewarding.

Padua, Rome

Francesco Marinello  
Daniele Passeri  
Enrico Savio

# Contents

<b>1</b>	<b>Acoustic Scanning Probe Microscopy: An Overview</b> . . . . .	1
1.1	Touching Instead of Seeing . . . . .	1
1.1.1	Facing the Limitations... . . . .	2
1.1.2	... and Converting them into Opportunities . . . . .	3
1.2	Two Points of View . . . . .	4
1.2.1	Modulating the Indentation of the Surface . . . . .	4
1.2.2	Detecting the Near-Field Acoustic Waves . . . . .	5
1.3	An Intimately Nonlinear World . . . . .	6
1.4	Applications. . . . .	10
1.4.1	Quantitative Elastic Modulus Measurement . . . . .	10
1.4.2	Subsurface Imaging . . . . .	14
1.5	Why a Book on Acoustic AFM Techniques? . . . . .	14
1.6	About this Book . . . . .	17
	References . . . . .	17
<b>2</b>	<b>Contact, Interactions, and Dynamics</b> . . . . .	21
2.1	Introduction: Contact and Adhesion . . . . .	21
2.2	Adhesionless Contact: Stiffness . . . . .	22
2.2.1	Hertz: Contact Radius and Loading . . . . .	23
2.2.2	Contact Stiffness . . . . .	25
2.3	Interactions: Adhesion. . . . .	25
2.3.1	Interactions: Derjaguin Approximation . . . . .	26
2.3.2	Nature of the Interactions . . . . .	26
2.3.3	Adhesive Contact with Weak Interactions . . . . .	28
2.3.4	Impact of Adhesion on Dynamic Response in AFM. . . . .	29
2.4	Coupling with Strong Interactions. . . . .	31
2.4.1	JKR Model . . . . .	31
2.4.2	Pull-Out Force . . . . .	32

2.5	AFM Tips: An Intermediate Case? . . . . .	33
2.5.1	Adhesive Interactions Revisited: Contact Problem . . . . .	33
2.5.2	Which Model: Does Adhesion Induce Deformation? . . . . .	35
2.5.3	Small Tips . . . . .	36
2.6	Films . . . . .	36
2.6.1	Stiffness . . . . .	36
2.6.2	Adhesion . . . . .	37
2.7	Roughness . . . . .	38
2.8	Dynamics . . . . .	39
2.8.1	Sphere Impact . . . . .	40
2.8.2	Inertial Effects . . . . .	41
2.8.3	Material Dissipation: Contact Area . . . . .	41
2.8.4	Adhesion Hysteresis: Elastic Instability . . . . .	42
2.8.5	Material Dissipation: Contact Edges . . . . .	43
2.9	Conclusion. . . . .	44
	References . . . . .	44
<b>3</b>	<b>Cantilever Dynamics: Theoretical Modeling . . . . .</b>	<b>47</b>
3.1	Introduction . . . . .	48
3.2	General Dynamical Equations and Eigenmodes of Cantilever Motion. . . . .	51
3.3	Single System Model of Cantilever Dynamics . . . . .	54
3.3.1	Polynomial Expansions of the Interaction Force. . . . .	55
3.3.2	Dynamical Effects of the Expansion Coefficients . . . . .	58
3.3.3	Image Contrast in Dynamic Atomic Force Microscopy. . . . .	58
3.3.4	Harmonic Generation . . . . .	61
3.3.5	Connection Between Model Parameters and Material Properties . . . . .	64
3.4	Coupled Independent Systems Model of Cantilever-Sample Dynamics . . . . .	65
3.4.1	Variations in Signal Amplitude and Phase from Subsurface Features . . . . .	66
3.4.2	Solution to the Coupled Dynamical Equations . . . . .	68
3.4.3	Signal Generation for Various d-AFM Modalities in the CIS Model . . . . .	73
3.4.4	Image Contrast in the CIS Model. . . . .	80
3.5	Conclusion. . . . .	82
	References . . . . .	97
<b>4</b>	<b>One-Dimensional Finite Element Modeling of AFM Cantilevers . . . . .</b>	<b>101</b>
4.1	Introduction . . . . .	101



4.2	Finite Element Model for a Beam . . . . .	103
4.2.1	Kinematic Parameters . . . . .	103
4.2.2	Matricial Form of Kinetic Energy: Mass Matrix. . . . .	105
4.2.3	Matricial Form of Elastic Potential Energy: Stiffness Matrix . . . . .	106
4.2.4	Mesh with N Elements: Global Matrix Construction . . . . .	107
4.2.5	Free and Forced Vibration Analysis . . . . .	109
4.3	Model for the Tip. . . . .	110
4.4	Solutions of the Finite Element Model . . . . .	111
4.4.1	Effect of the Excitation Mode . . . . .	113
4.4.2	Concepts of Apparent and Real Force. . . . .	117
4.4.3	Effect of the Beam Shape . . . . .	117
4.4.4	Effect of Normal and Tangential Stiffness. . . . .	119
4.5	Conclusion. . . . .	121
	References . . . . .	121
<b>5</b>	<b>Atomic Force Acoustic Microscopy . . . . .</b>	<b>123</b>
5.1	Introduction . . . . .	123
5.2	Analytical and Finite-Element Models for AFAM . . . . .	125
5.2.1	Analytical Model of the Cantilever Vibrating in Air . . . . .	126
5.2.2	Contact-Resonance Models . . . . .	129
5.2.3	Finite-Element Models (FEM) . . . . .	133
5.3	Experimental Methods for Quantitative AFAM . . . . .	135
5.3.1	Experimental Setup. . . . .	135
5.3.2	Single Point Measurements . . . . .	136
5.3.3	Grid Measurements. . . . .	138
5.3.4	Contact-Resonance Frequency Images. . . . .	139
5.4	Contact Mechanics and Calibration Methods . . . . .	139
5.4.1	Single Reference Method . . . . .	141
5.4.2	Dual Reference Method. . . . .	142
5.4.3	AFAM Image Calibration . . . . .	144
5.5	Nonlinear AFAM . . . . .	144
5.5.1	Evaluation of the Full Force Curve. . . . .	145
5.6	Conclusions . . . . .	150
	References . . . . .	151
<b>6</b>	<b>Ultrasonic Atomic Force Microscopy UAFM . . . . .</b>	<b>155</b>
6.1	Conceptual Design . . . . .	155
6.1.1	Forced Vibration of Cantilever from the Base . . . . .	155
6.1.2	Tracking Quantitative Information, Directional Control, and Resonance Frequency. . . . .	156

- 6.2 Analysis . . . . . 157
  - 6.2.1 Effective Enhancement of Cantilever Stiffness . . . . . 157
  - 6.2.2 Stiffness, Q Factor, and Nonlinear Parameter  
in Resonance Spectra . . . . . 157
  - 6.2.3 Quantitative Evaluation of Elasticity . . . . . 169
  - 6.2.4 Frequency-Stiffness Relation Depending  
on the Type of Differential Equation . . . . . 171
- 6.3 Instrumentation . . . . . 174
  - 6.3.1 Possibility of Large Sample Stage . . . . . 174
  - 6.3.2 Suppression of Spurious Vibration . . . . . 175
  - 6.3.3 Electronics for Resonance Frequency Tracking  
and Q Factor Mapping . . . . . 177
- 6.4 Illustrative Examples . . . . . 178
  - 6.4.1 Heat Treatment of Advanced Carbon Fiber  
for Reinforced Plastics . . . . . 178
  - 6.4.2 Extremely Soft Domain Boundary of Efficient  
Ferroelectric Materials . . . . . 179
  - 6.4.3 Friction and Shear Elasticity on Surface Layer  
by Lateral Force Modulation . . . . . 183
- 6.5 Conclusion . . . . . 185
- References . . . . . 186

- 7 Enhanced Sensitivity of AFAM and UAFM  
by Concentrated-Mass Cantilevers . . . . . 189**
  - 7.1 Introduction . . . . . 189
  - 7.2 Theory of Concentrated-Mass Cantilevers . . . . . 192
    - 7.2.1 Forced Vibration . . . . . 192
    - 7.2.2 Effects of Lateral Stiffness . . . . . 206
  - 7.3 Experimental Demonstrations with CM Cantilevers . . . . . 211
    - 7.3.1 Contact Spectra and Elasticity Mapping . . . . . 211
    - 7.3.2 Quantitative Evaluation for Elastic Modulus . . . . . 216
- References . . . . . 225

- 8 Scanning Microdeformation Microscopy: Advances  
in Quantitative Micro- and Nanometrology . . . . . 227**
  - 8.1 Introduction . . . . . 227
  - 8.2 The Scanning Microdeformation Microscope . . . . . 229
    - 8.2.1 The Experimental Setup . . . . . 229
    - 8.2.2 The Basic Model . . . . . 231
  - 8.3 Optimization of the SMM . . . . . 236
    - 8.3.1 The Theoretical Study . . . . . 236
    - 8.3.2 Experimental Validation . . . . . 239
    - 8.3.3 New Cantilever Geometries . . . . . 241

8.4	Applications on Polymers . . . . .	246
8.4.1	Materials and Experimental Procedures . . . . .	247
8.4.2	Experimental Results . . . . .	251
8.5	Conclusion. . . . .	257
	References . . . . .	258
<b>9</b>	<b>Ultrasonic Force Microscopies . . . . .</b>	<b>261</b>
9.1	Introduction . . . . .	262
9.2	Nanoscale “Mechanical Diode”: Force–Distance Nonlinearity and Detection of Ultrasonic Vibrations . . . . .	263
9.3	How UFM Works: Experimental Setup and Theoretical Analysis . . . . .	264
9.3.1	UFM Fundamentals . . . . .	264
9.3.2	Selection of UFM Operating Parameters . . . . .	265
9.3.3	Experimental Setup. . . . .	267
9.4	Examples of UFM Output . . . . .	268
9.4.1	Imaging of Elastic Properties with UFM: From Semiconductors to Biopolymers. . . . .	273
9.4.2	“Director’s Cut” of UFM Imaging: Artifacts (and ways to avoid them) and Unique Benefits of UFM. . . . .	276
9.4.3	Subsurface Imaging in UFM: From Delaminations to Subsurface Elasticity Mapping . . . . .	280
9.4.4	“Mechanical Diode” Versus “Mechanical Heterodyne”: Sensing Nanosecond Time Scale Dynamic Phenomena in Nanostructures . . . . .	285
9.5	In Lieu of Conclusion: Ultrasound in SPM—Expanding the Alliance . . . . .	289
	References . . . . .	289
<b>10</b>	<b>Scanning Near-Field Ultrasound Holography . . . . .</b>	<b>293</b>
10.1	History of Development of Acoustic Methods for Imaging. . . . .	294
10.2	Introduction to Acoustic Methods Developed on SPM Platform . . . . .	294
10.3	Challenges and Difficulties with SPM Acoustic Methods . . . . .	297
10.4	Introduction to Scanning Near-Field Ultrasound Holography (SNFUH) . . . . .	298
10.4.1	Description of the SNFUH Method. . . . .	298
10.4.2	Applications of SNFUH . . . . .	300
10.4.3	Non-Invasive Nanomechanics of Subcellular Structures . . . . .	306
10.4.4	Future Development . . . . .	309
10.5	Conclusions . . . . .	310
	References . . . . .	311

**11 Mapping of the Surface’s Mechanical Properties Through Analysis of Torsional Cantilever Bending in Dynamic Force Microscopy . . . . . 315**

11.1 Introduction . . . . . 316

11.2 Time-Resolved Tapping Mode in Mapping of the Mechanical Properties of the Surface. . . . . 318

11.2.1 Modeling of Tip–Sample Interaction Forces in Intermittent Contact AFM . . . . . 318

11.2.2 Extraction of the High Bandwidth Oscillation of the Cantilever. . . . . 322

11.2.3 Recovering the Time-Varying Interaction Signal of the Tip–Sample Forces . . . . . 324

11.2.4 Mapping of the Mechanical Properties Basing on Advanced Signal Processing . . . . . 331

11.2.5 The Principles of the Measurement Setup . . . . . 335

11.2.6 Signal Acquisition and Processing Issues in Terms of the Algorithm’s Efficiency Demands . . . . . 336

11.2.7 Utilization of High-Order Harmonics of the Cantilever’s Oscillations for the Surface’s Stiffness Mapping. . . . . 338

11.3 Application Examples . . . . . 343

11.4 Outlook and Conclusions. . . . . 347

References . . . . . 348

**12 Quantitative Measurements of Elastic Properties with Ultrasonic-Based AFM and Conventional Techniques. . . . . 351**

12.1 Introduction . . . . . 351

12.2 Overview of Measurement Methods . . . . . 353

12.2.1 Contact Resonance Spectroscopy . . . . . 353

12.2.2 Instrumented (Nano-) Indentation . . . . . 356

12.2.3 Surface Acoustic Wave (SAW) Spectroscopy . . . . . 359

12.2.4 Other Techniques . . . . . 362

12.3 Relative Merits of Individual Methods . . . . . 363

12.4 Results of Measurement Comparisons. . . . . 366

12.5 Summary and Outlook . . . . . 369

References . . . . . 371

**13 Data Processing for Acoustic Probe Microscopy Techniques . . . . . 375**

13.1 Introduction . . . . . 375

13.2 Basic Terminology . . . . . 376

13.3 Distortions and Artifacts . . . . . 377

13.4 Drift and Leveling . . . . . 378

13.5 Bow Effect and Installation Slope . . . . . 381

13.6	Tip Geometry . . . . .	382
13.6.1	Geometrical Dilation . . . . .	382
13.6.2	Geometrical Dilation . . . . .	386
13.7	Conclusions . . . . .	387
	References . . . . .	388
<b>14</b>	<b>Friction and Internal Friction Measurements</b>	
	<b>by Atomic Force Acoustic Microscopy . . . . .</b>	<b>391</b>
14.1	Introduction . . . . .	391
14.2	Atomic Force Acoustic Microscopy and Elasticity Measurements at the Nanoscale . . . . .	392
14.3	Contact Damping . . . . .	401
14.4	Observation of Internal Friction Due to Dislocations in Nanocrystalline Nickel . . . . .	403
14.5	Friction Measurements at the Nanoscale . . . . .	408
14.6	Conclusions . . . . .	413
	References . . . . .	413
<b>15</b>	<b>Quantitative Subsurface Imaging by Acoustic AFM Techniques . . . . .</b>	<b>417</b>
15.1	Introduction . . . . .	417
15.2	Ultrasonic AFM for Contact Stiffness Imaging . . . . .	418
15.3	Contact Stiffness Models of Samples with Subsurface Structures . . . . .	422
15.4	Penetration Depth and Subsurface Resolution in Acoustic AFM . . . . .	429
15.5	Conclusion . . . . .	434
	References . . . . .	434
<b>16</b>	<b>Polymer Material Characterization by Acoustic Force Microscopy . . . . .</b>	<b>437</b>
16.1	Introduction . . . . .	437
16.2	Characterization of Electrospun Polymer Fibers . . . . .	439
16.3	Characterization of Bicomponent Polymer Fibers . . . . .	442
16.4	Characterization of Fiber-Reinforced Epoxy Composites . . . . .	443
16.5	Polymer Nanocomposite Imaging and Characterization . . . . .	449
16.6	Characterization of Polymer Films and Surfaces . . . . .	452
16.7	Tip-Shape Models for Epoxy Characterization . . . . .	454
16.8	Conclusions . . . . .	458
	References . . . . .	458
<b>17</b>	<b>Application of Acoustic Techniques for Characterization of Biological Samples . . . . .</b>	<b>461</b>
17.1	Survey of State of the Art . . . . .	462

- 17.2 Basic Background of Technical Approach . . . . . 463
  - 17.2.1 Resonant Dipping Mode . . . . . 464
  - 17.2.2 Hardware Configuration . . . . . 465
  - 17.2.3 AFAM Imaging Technique . . . . . 466
- 17.3 Analyzes, Modeling, and Simulation . . . . . 467
- 17.4 Sample Preparation . . . . . 472
  - 17.4.1 Sample Characterization . . . . . 472
  - 17.4.2 BHK Cell Viability Under Conditions of Drying . . . . . 473
- 17.5 Results . . . . . 475
  - 17.5.1 Force–Distance Measurements . . . . . 475
  - 17.5.2 Imaging Results . . . . . 477
  - 17.5.3 Interpretation . . . . . 479
- 17.6 Discussion and Summary . . . . . 480
- References . . . . . 482
  
- Index . . . . . 485**

# Symbols

$\alpha_0$	
$A$	Cantilever cross-section area
$a_c$	Contact radius
$b$	Cantilever thickness
$E$	Young modulus of the cantilever
$E^*$	Reduced modulus of the contact
$E'$	Storage modulus
$E''$	Loss modulus
$E_t, E_s$	Young's moduli of the tip and of the sample
$f$	Frequency
$f_0$	Free resonance frequency
$F_{\perp}$	Is the static load, i.e. the normal component of instantaneous force interacting between the tip and the surface, in the coordinate system of the sample surface
$F_{//}$	Lateral load, i.e. the normal component of force interacting between the tip and the surface in the coordinate system of the sample surface
$F_m$	Time-averaged force between tip and sample
$\varphi$	Tilt of the cantilever relatively to the surface
$G^*$	Reduced shear modulus of the contact
$\gamma$	Adhesion energy
$\Phi$	Phase
$\gamma$	Normal damping constant
$\gamma_{\text{lat}}$	Lateral damping constant
$h$	Tip height
$h_1$	Initial sample indentation
$h_{\text{eq}}$	Equilibrium indentation
$k^*$	Normal contact stiffness
$k_{\text{lat}}^*$	Lateral contact stiffness
$k_c$	Static spring constant of the cantilever
$k_n \{n = 1, 2, \dots\}$	Wave numbers of the $n$ th eigenmode

$k_s$	Linear contact stiffness
$L$	Total length of the cantilever
$L_1$	Actual distance between the tip and the chip
$L_{\text{eff}}$	Effective length of the cantilever
$\lambda$	Wavelength
$\chi_s$	Quadratic contact stiffness
$M$	Indentation modulus
$m^*$	Effective mass of the cantilever
$m_c$	Additional or concentrated mass
ns	Nanosecond ( $10^{-9}$ ) s
$R$	Tip radius of curvature
$r_c$	Radius of contact area
$S_{\text{eff}}$	Differential contact stiffness
$\rho$	Density of the cantilever
$t$	Film thickness
$\tau$	Relaxation time
$\nu_b, \nu_s$	The Poisson's ratios of the tip and of the sample
$w$	Cantilever width
$z_{\text{eq}}$	Equilibrium cantilever deflection



# Acronyms

AFAM	Atomic Force Acoustic Microscopy
AFFM	Acoustic Friction Force Microscopy
AFM	Atomic Force Microscopy
AM-AFM	Amplitude Modulation AFM
CM	Concentrated Mass
DOF	Degree of Freedom
FEA	Finite Elements Analysis
FFM	Friction Force Microscopy
FM-AFM	Friction Modulation AFM
FMM	Force Modulation Microscopy
FRF	Frequency Response Function
HFM	Heterodyne Force Microscopy
NC-AFM	Non Contact AFM
NI	Instrumented (nano-) Indentation
SAFM	Scanning Acoustic Force Microscopy
SAM	Scanning Acoustic Microscopy
SAWS	Surface Acoustic Wave Spectroscopy
SLAM	Scanning Local Acceleration Microscopy
SMM	Scanning Microdeformation Microscopy
TM	Tapping Mode
UAFM	Ultrasonic Atomic Force Microscopy
UFM	Ultrasonic Force Microscopy
W-UFM	Waveguide Ultrasonic Force Microscopy

# Chapter 1

## Acoustic Scanning Probe Microscopy: An Overview

D. Passeri and F. Marinello

**Abstract** In this chapter, which serves as an introduction to the entire book, an overview is given of techniques resulting from the synergy between ultrasonic methods and scanning probe microscopy (SPM). Although other acoustic SPMs have been developed, those reviewed in this book are either the earliest proposed techniques, which are most widespread, extensively used, and continuously improved, or have been recently developed, but have been proved to be extremely promising. The techniques are briefly introduced, emphasizing what they have in common, their differences, their capabilities, and limitations.

### 1.1 Touching Instead of Seeing

The invention in the 1980s of the two main scanning probe microscopy (SPM) techniques, namely atomic force microscopy (AFM) [1] and scanning tunneling microscopy (STM) [2–5], extended the significance of microscopy, giving it a wider acceptance beyond its mere etymological significance. Deriving from the Greek *μικρόν* (transliterated as ‘mikron’, meaning ‘small’) and *σκοπέω* (transliterated as ‘skopeo’, meaning ‘I see’ or ‘I look’), the word ‘microscopy’ recalls the idea of seeing ‘by eyes’ and thus by instruments where the visualization of objects is based on the collection of the light diffracted by them by means of suitable lenses. The observability of small objects is thus limited by the wavelength  $\lambda$  of the particular electromagnetic radiation used for illuminating them: the lower the  $\lambda$  the higher the

---

D. Passeri (✉)

Department of Basic and Applied Sciences for Engineering (BASE),  
University of Rome Sapienza, Via A. Scarpa 16, 00161 Roma, Italy  
e-mail: daniele.passeri@uniroma1.it

F. Marinello

Department of Land, Environment, Agriculture and Forestry (TeSAF),  
University of Padua, Viale dell’Università 16, 35020 Legnaro (Padua), Italy

resolution, where the latter can be evaluated for instance by the Abbe's criterion as  $\lambda/2NA$ , where  $NA$  is the numerical aperture of the optical lens. To increase the resolution,  $\lambda$  must be reduced. Such a requirement suggested the use of radiation more energetic than visible light, leading to the invention of X-ray and electron microscopy.

SPM techniques are based on a completely different idea. A tip is brought in close proximity to the sample surface and then is moved across it in two directions (namely, the  $x$  and  $y$  axes). At each point of the surface, which is divided into a homogeneous array of points, a physical parameter is monitored. In the case of STM, such a parameter is the tunneling current flowing between the (conductive) sample and the (conductive) tip. In the case of AFM, such a parameter is the deflection of the cantilever at the extremity of which the tip is mounted. More precisely, the monitored parameter is the cantilever static deflection in AFM contact mode, while it is the amplitude of the oscillating cantilever in AFM semi-contact mode. These parameters can be collected at each point of the scanned area and reported in maps that qualitatively reflect the sample morphology (the open feedback loop mode). In practice, this operation mode exposes the tip to the risk of abrupt damage and thus is scarcely used except in case of very flat sample surfaces (e.g., when atomic resolution is required). Alternatively, the acquired parameter is used as the input signal of a feedback loop that maintains a constant value over the scanned surface by acting on a piezoelectric transducer in the vertical direction, namely, the  $z$  axis (the closed feedback loop mode). This modifies the cantilever-to-sample distance by an amount  $\Delta z$  that is equal to the local height variation of the surface. The value of  $\Delta z$  at each point of the scanned area is reported in a map that quantitatively reflects the sample topography. It is worth noting that in the case of AFM operation in contact mode, the closed feedback loop ensures that the surface is scanned at constant value of the cantilever deflection and thus of the force exerted between tip and sample, which is an important requirement in contact mode acoustic AFM techniques, as described below.

As discussed in the following, imaging performed by *touching* (in the sense of a tip coming into close interaction with the surface), rather than *seeing*, the surface has its own disadvantages, but on the other hand offers the possibility of going beyond topography by developing unique tools for the qualitative and/or quantitative characterization of several physical properties of the sample surface.

### ***1.1.1 Facing the Limitations...***

The reconstruction of a sample morphology by touching and scanning its surface has its own disadvantages. As a direct consequence of touching the surface, collected images are the convolution of both surface features and tip shape, resulting in artifacts that can seriously compromise the quality of the image (e.g., nanoparticles on flat surfaces may lead to images where the apex of the tip is reproduced inverted in correspondence with each nanoparticle) unless a proper deconvolution is performed

[6]. Moreover, in the case of soft samples like polymers or biological specimens, the interaction between tip and sample may contaminate the former and/or damage the latter [7]. These drawbacks can be prevented or reduced by operating in semi- or non-contact mode instead of contact AFM mode.

As a consequence of scanning, movement limitations are introduced by both the  $z$  direction (vertical) piezoelectric actuator and the  $x$  and  $y$  direction (in-plane) scanners. The limitation of the vertical range implies a sufficient flatness of the surface to be analyzed: when such a requirement is not met, only restricted portions of the surface can be imaged, thus reducing the statistical meaning of the SPM investigation. The limitation of the in-plane scanners does not allow the visualization of large areas even for perfectly flat samples, thus not permitting overall visualization of surfaces, fast selection and positioning on specific sample regions, or characterization of features with widely different magnifications, all characteristics that, conversely, allow electron microscopy to collect images that in some cases are admittedly astonishing.

### ***1.1.2 ... and Converting them into Opportunities***

Despite such disadvantages, imaging by touching and scanning the sample surface turned out to represent a key feature that determined the success of SPM techniques as the basis for the development of a wide number of tools to image, measure, and map several physical properties simultaneously with samples' topography. Touching surfaces allows one to probe mechanical, electric, and/or magnetic (e.g., by using AFM cantilevers coated with conductive and/or magnetic films) properties. Scanning surfaces allows one to repeat such measurements at each point and thus to map the measured physical properties over the surface simultaneously with the morphological reconstruction. In some cases new techniques have been developed based on standard SPM setups, while in other cases researchers have reproduced at micro- and nanoscales techniques already available at macroscales. For example, the tip is used from time to time as an indenter, as the probe of a multimeter, etc. Such an approach enables measurements with nanometrical lateral resolution and the collection of qualitative maps of properties beyond the topography, although they are generally affected by artifacts induced by topography itself. Gathering accurate quantitative data is nevertheless limited by the nonideal instrumental parameters such as the real shape of the tip. Theoretical models are thus needed to analyze data that are based on, but generally more complex than, those used by more conventional instruments. A comprehensive review of such techniques far exceeds the aims of this book. In the following we limit our attention to some of the techniques that combine ultrasonic methods with AFM tools for the surface and subsurface mechanical characterization of samples.

## 1.2 Two Points of View

Acoustic or ultrasonic SPM (A-SPM) refers to a class of several different techniques that are characterized by the use of almost standard SPM setups, integrated with some modified electronics and/or mounting specifically functionalized tips. Both AFM and STM setups have been used for developing A-SPM techniques (A-AFM and A-STM, respectively). Nevertheless, in the following we refer only to the AFM-based ones, which are undoubtedly more widespread and versatile. In A-AFMs, piezoelectric transducers are used to set the sample surface and/or the AFM cantilever into vibration at ultrasonic frequencies that are well above the cutoff frequency of the electronics, so that the oscillations are not compensated by the feedback. This ensures that such oscillation does not influence the standard topographical reconstruction, as well as that the ac component of the deflection signal is not suppressed and thus can be subsequently analyzed. These two represent the key points for the simultaneous acquisition of topography and acoustic signal images. The particular way in which ultrasonics and SPM are combined is different for each specific technique and will be described in detail through the chapters of the book. Here, the interest is focused on the common features of these techniques. The enrichment produced by the combination of ultrasonics and SPM can be fully understood by looking at such a combination from two different and complementary points of view. From the first viewpoint, A-SPM techniques can be regarded as nanoscale versions of dynamic indentation tests: the SPM tip replaces standard indenters and the effect of ultrasounds is to modulate the indentation of the sample surface. From the second viewpoint, A-SPMs can be regarded as nanoscale versions of scanning acoustic microscopy techniques: the tip is used for probing the acoustic wave field with high spatial resolution, far beyond the limitation imposed by other methods such as the use of piezoelectric transducers, light wave diffraction, X-ray scattering, or electron reflection. These two points of view are characterized by different approaches, models, and mathematical instruments for rationalizing the results of the experiments. Such grouping can be somewhat limiting, since each technique can be described in terms of each of the two approaches; however, it can be useful to understand the role of ultrasonics in SPM-based techniques.

### *1.2.1 Modulating the Indentation of the Surface*

Used for setting into vibration the sample surface and/or the cantilever, acoustic waves produce a modulation in the cantilever-sample distance. In case of infinitely stiff sample and tip, such a modulation is entirely observed as the modulation of the cantilever deflection. In the case of a sample much more compliant than the cantilever, the modulation results partially in the modulation of the cantilever deflection and partially in a variation of the penetration depth of the tip into the sample surface: the softer the sample, the higher the modulation amplitude of the indentation and the

lower than that of the cantilever deflection. Therefore, the oscillating component of the cantilever deflection can be acquired at each point of the scanned area, thus obtaining an image which is related to the surface elastic modulus. This idea forms the basis of the force modulation microscopy (FMM) technique [8, 9], which has been proved to allow qualitative elastic imaging of soft samples like polymers. Implementation of FMM on materials with higher elastic modulus is indeed limited by the availability of standard cantilevers with sufficiently high spring constant values. In this sense, the merit of ultrasonics is the stiffening of AFM cantilevers at high frequencies: in other words, the cantilever dynamic spring constant values are far higher than the static ones. Therefore, ultrasonics enables dynamic indentation measurements by AFM on relatively stiff samples, especially when combined with ad hoc designed cantilevers having higher static spring constants [10, 11] and/or tips harder than the standard Si or Si<sub>3</sub>N<sub>4</sub> ones [12].

### *1.2.2 Detecting the Near-Field Acoustic Waves*

Widely used for nondestructive testing, ultrasonic waves are employed in the so-called scanning acoustic microscopy (SAM) technique [13–15], which enables the imaging of sample surface elastic properties at submicrometer scale with resolution that highly depends on the ultrasonic wavelength in the investigated material. In a reflection acoustic microscope in the linear regime, the resolution is slightly better than that established by the Rayleigh criterion for a conventional microscope and is  $0.51\lambda_0/NA$ , where  $\lambda_0$  is the ultrasonic wavelength and  $NA$  the numerical aperture of the acoustic lens [16]. Acoustic microscopy takes advantage of the use of surface acoustic waves (SAWs) (also known as Rayleigh waves), whose amplitude exponentially decays into the material as the distance from the surface increases. In other words, SAW energy is confined in a volume of material underneath the surface down to a depth of a few times the wavelength. Therefore, acoustic microscopy is sensitive to the mechanical properties of the material in a volume included from the sample surface to a depth of a few times the wavelength into its interior. The contrast in SAM images is therefore produced by the variation of elastic modulus, as well as by the presence of subsurface defects, voids, and delamination [15]. The acoustic field diffracted by an object is generally composed of both propagating and evanescent waves [17]. The former can be collected by SAM, while the latter—whose amplitude exponentially decays as a function of the distance from the object—cannot propagate up to the piezoelectric transducer acting as the receiver. As the spatial Fourier transform of the diffracting object is involved, the smaller its dimension the more predominant is the evanescent component with respect to the propagating one [17]. The spectrum emerging from nanosized objects that are easily detectable by AFM is generally only composed of evanescent waves, and thus such objects are invisible to SAM. Nevertheless, if the diffracting features are at the interface or under but in proximity to the surface investigated by AFM, the tip can be used as a mechanical probe to collect the evanescent—but not yet extinguished—diffracted waves. In practice, the unique

lateral resolution enabled by SPM techniques suggested to employ both AFM [18, 19] and STM [20–22] for studying SAWs propagation and related phenomena (reflection, mode conversion, diffraction, scattering, interaction with elastic inhomogeneities at nanoscale) [23]. Use of SPM probes for detecting evanescent acoustic waves is the same idea that led to scanning near-field optic microscopy (SNOM) [17, 24–26], where AFM is used for collecting diffracted evanescent electromagnetic waves from nanometrical objects. Thus, the combination of ultrasonics and SPM results in the realization of a class of near-field acoustic microscopy techniques that allow us to extend to the nanometer scale some of the imaging capabilities of SAM. In particular, acoustic SPM techniques enable the visualization of subsurface mechanical discontinuity, variations in the elastic modulus, presence of buried nanostructures, voids, lack of adhesion, delamination, and dislocations.

### 1.3 An Intimately Nonlinear World

A-SPM techniques are based on the tip–sample interaction, which is modulated by the excitation of acoustic oscillations. Limiting our discussion to A-AFM techniques, these can be based either on AFM semi-contact or contact mode. In A-AFMs based on AFM semi-contact mode, the tip–sample force and indentation increase from zero to a peak value and then decrease again during a period of the cantilever oscillation which is the reciprocal of one of the cantilever free resonances (generally the first). In techniques based on AFM contact mode, the tip–sample force and indentation oscillate at ultrasonic frequencies around their static setpoint values. Each A-AFM technique has an intimate nonlinear nature. This can be clearly recognized by considering that the tip–sample interaction, described by the Lennard-Jones potential, derives from intermolecular forces that dramatically vary as a function of the distance and thus on the time when the tip–sample separation is modulated [27]. From the point of view of continuum mechanics, the tip–sample interaction can be described as a spring whose elastic constant is the tip–sample contact stiffness  $k^*$ . Even neglecting more complex effects (adhesion, capillarity...) and limiting to the simple elastic contact between a sphere (the tip) and a plane (the sample), the spring is nonlinear as  $k^*$  varies with the normal load exerted between tip and sample [28]. Thus, even in absence of second order effects, the mechanics of the contact between the tip and sample is an intrinsically nonlinear phenomenon. Therefore, A-SPM techniques force the user to cope with nonlinearities. This may represent a difficulty, since it may force one to use complicated models or to perform experiments in a range where the linear approximation is valid. Nevertheless, it can turn out to be an advantage [29–32], as nonlinear effect can be used as the basis for the development of new A-SPM techniques as well as to extend the characterization capabilities of ‘linear’ A-SPM methods. In the following, we give a short overview of A-SPM techniques—limiting our discussion to those described in this book—illustrating how they deal with nonlinearity.

*Atomic Force Acoustic Microscopy* In atomic force acoustic microscopy (AFAM) [33–36], the tip scans in contact mode the surface of the sample whose back side is coupled to an ultrasonic piezoelectric transducer. The transducer excites out-of-plane oscillation of the surface, resulting in the modulation of both the cantilever deflection and the tip–surface indentation. The resonance frequencies of the sample–tip–cantilever system depend on the tip–sample contact stiffness  $k^*$ , which in turn depends on the local elastic modulus of the sample surface. The stiffer the sample, the higher the  $k^*$ , the higher the resonance frequencies. Collecting the oscillation amplitude at fixed ultrasonic frequency gives images qualitatively reflecting the surface elastic properties [37], while acquiring the local contact resonance frequencies allows the quantitative mapping of the elastic modulus [38–41]. Being based on frequency detection, accurate elastic modulus measurements require linear AFAM resonance curves.

*Ultrasonic Atomic Force Microscopy* In ultrasonic atomic force microscopy (UAFM) [42, 43], the piezoelectric transducer is bonded to the cantilever chip instead of to the sample. This avoids the contamination of the sample and allows the analysis of highly irregular samples for which a proper coupling of the back side with the transducer is difficult to realize. A secondary advantage is that UAFM is somewhat more familiar to standard AFM users who are well aware of the possibility of coupling a transducer to the cantilever chip, as it is used for making the cantilever oscillating when operating in AFM semi-contact mode. Conversely, UAFM spectra often exhibit spurious resonances [44] that must be suppressed by proper clamping of the cantilever [45, 46] or—as recently proposed—by using specially designed cantilevers excited directly instead of through their holder [47]. UAFM uses an approach similar to the AFAM one for the imaging and the measurement of the elastic properties of the sample by acquiring resonance frequency and quality factor of the cantilever whose tip is in contact with the surface [48]. Therefore, accurate modulus measurements with UAFM also require the acquisition of linear spectra. In the case of stiff samples, both AFAM and UAFM experience the sensitivity reduction as the contact resonance frequencies reach their saturation values which correspond to the resonance frequencies of the pinned-end cantilever [49]. In this case, higher flexural modes can be used. Alternatively, a smart solution to such a limitation consists in using concentrated mass cantilevers that are obtained by depositing a particle of hundreds of nanograms on the cantilever backside in proximity to the tip [50].

*Scanning Microdeformation Microscopy* Scanning microdeformation microscopy (SMM) [10, 51] has a similar approach, taking advantage of AFM  $xyz$  scanners and tracking hardware in combination with specifically designed and fabricated cantilevers with increased spring constant stiffness, which oscillate in contact with the sample surface at frequencies ranging from a few to tens of kilohertz. The SMM sensor is larger than standard AFM ones. In particular, the tip is made of materials harder than standard Si or  $\text{Si}_3\text{N}_4$  (typically diamond or sapphire) and it has a radius of curvature at the apex which is one or two orders of magnitude larger than for standard probes [52, 53]. This reduces the possibility of imaging at nanoscale



but increases the reliability of quantitative elastic modulus measurements: because it operates at mesoscales, it is less sensitive to variations in the contact area not induced by the elastic modulus but by the topography. The contact resonance frequency shift is measured (and thus linear spectra have to be acquired) to evaluate the sample elastic modulus using the same models of AFAM and UAFM, with the further simplification that the use of hard and stable tips allows to neglect their deformations during indentation.

Although relying on the acquisition of linear spectra for the quantitative evaluation of elastic modulus, interesting applications have been proposed for AFAM, UAFM, and SMM operating in nonlinear regime. Relying on the high frequency stiffening of the cantilever, nonlinearities in AFAM have been used for reconstructing the force–distance curve on stiff samples [54], where the cantilever static spring constant prevents the acquisition of the same curves by quasi-static AFM indentation which conversely finds application on compliant materials like polymers [55–57] or biological samples [58–61]. Nonlinear spectra collected by UAFM that showed either softening or stiffening typical of nonlinear oscillators have been used for detecting and imaging subsurface dislocations and lattice defects in high oriented pyrolytic graphite (HOPG) [62, 63] as well as delamination and voids at thin films/substrates buried interfaces [45]. Finally, SMM allows acquisition of the characteristic ‘non-linear signature’ of materials, which is obtained by studying the evolution of the amplitude of higher harmonics of the fundamental contact resonance frequency as a function of the excitation signal amplitude for a fixed value of the normal load [64]. Such a ‘nonlinear signature’ has been suggested for the elastic characterization of materials, the characterization of mechanical inhomogeneity, and the detection of subsurface defects [64].

*Ultrasonic Force Microscopy* In contrast to the aforementioned techniques that require oscillation in the linear regime for the reliable evaluation of the sample elastic modulus, ultrasonic force microscopy (UFM) [65–67] purposely exploits the nonlinear region of the tip–sample interaction for the qualitative and quantitative imaging and measurement of sample elastic modulus. In UFM, the tip is in contact with the surface of a sample whose back side is coupled to a piezoelectric transducer. The latter is driven by a signal, oscillating at ultrasonic frequency and whose amplitude is modulated by a ramp, thus setting into out-of-plane vibration the sample surface with the consequent oscillation of the tip–sample indentation. When the maximum variation of the indentation equals the static indentation and thus the pull-off point is reached, a periodic discontinuity in the cantilever static deflection occurs. The cantilever deflection signal can be visualized by an oscilloscope and analyzed by a lock-in amplifier in order to estimate the tip–sample contact stiffness, which is inversely proportional to the amplitude of the driving signal at which the pull-off occurs [65, 67]. Therefore, UFM is a nonlinear A-SPM technique because the signal for the elastic imaging and measurement is obtained from the discontinuity between the in-contact and out-of-contact region of the force–distance curve.

*Scanning Near-Field Ultrasound Holography* The intrinsic nonlinearity of the tip–sample contact is exploited by scanning near-field ultrasound holography (SNFUH) [68, 69], where the tip is in contact with the surface of a sample bonded to a piezoelectric transducer. Here, the sample surface and the cantilever oscillate at two ultrasonic frequencies whose difference is the contact resonance frequency of the system. As a result of the nonlinearity of tip–sample interaction, a signal at the frequency difference is generated whose phase is collected and mapped simultaneously to the topographic characterization. On the same principle is based the so-called resonant difference frequency atomic force ultrasonic microscopy (RDF-AFUM) [70]. In contrast to the previously mentioned techniques, where the development of a suitable model allows the quantitative evaluation of the sample elastic modulus, the contrast in the SNFUH phase image may be related only qualitatively to the elastic properties of the sample. Notwithstanding this limitation, SNFUH has been demonstrated to be a versatile tool for the characterization of nanoscale subsurface features of samples. SNFUH has been used to detect defects at buried interfaces in interconnect architectures [71] and for the subsurface imaging of cells, revealing the intracellular structures [68] as well as the presence of internalized submicrometrical and nanometrical objects either biological (malaria parasites) [69] or synthetic (nanoparticles) [72, 73].

*Torsional Harmonic Atomic Force Microscopy* Quite outside the classification based on linear/nonlinear tip–sample interaction and more in general the group of A-SPM techniques as no oscillations at ultrasonic frequencies are directly excited by the cantilever nor by the sample, torsional harmonic atomic force microscopy (TH-AFM) [74, 75] is a tapping-mode based AFM technique that takes advantage of the use of T-shaped cantilevers with the tip offset from the cantilever long axis. During tapping (at frequencies of tens of kilohertz), the intermittent tip–sample interaction generates a torque around the long axis exciting the torsional modes (at ultrasonic frequencies) of the cantilever which are enhanced by its shape. While the cantilever vertical deflection signal is used for the morphological reconstruction as in standard AFM tapping mode, its torsional signal is acquired and analyzed to extract the tip–sample force waveform. From such a curve, the force-separation curve is reconstructed and the tip–sample contact stiffness is evaluated, thus allowing the quantitative sample elastic modulus measurement provided a suitable contact mechanics model is assumed (as in AFAM, UAFM, SMM, and UFM). TH-AFM has been demonstrated to allow accurate quantitative elastic modulus measurements and mapping on several polymeric samples with elastic modulus varying between 1 MPa and 10 GPa [75].

## 1.4 Applications

As evidenced by the above discussion, classical A-SPM applications fall into two categories, namely the quantitative measurement and imaging of elastic modulus and the detection of subsurface features, which are associated to both similar and different problems to be addressed. Obviously, each technique requires suitable electronics for the acquisition of the specific signal needed for the subsequent analysis. Moreover, the electronics have to fulfill specifications regarding the acquisition rate when imaging is to be performed. The reason for this is to avoid too slow scan rates and thus too long image acquisition times that may compromise the reliability of the measurement due to drift and variations in the experimental parameters.

### 1.4.1 *Quantitative Elastic Modulus Measurement*

#### 1.4.1.1 Cantilever Model

Accurate quantitative measurements of sample elastic modulus require realistic models of the cantilever and/or the tip-sample contact. Efforts have been made to take into account as many experimental parameters as possible when describing the cantilever [76, 77]. From the simplest model where the tip-sample contact is modeled as an elastic spring of constant  $k^*$  and the cantilever mass is assumed to be concentrated in a single point, subsequent improvements have introduced the description of the cantilever as a beam with distributed mass, the tip not placed at the very end of the beam, nonzero tip height, cantilever and tip inclination, normal damping at the contact by a dashpot  $\gamma^*$  in parallel with  $k^*$  [78, 79], and the effect of lateral forces by a parallel lateral contact stiffness  $k_{\text{lat}}$  and lateral dashpot  $\gamma_{\text{lat}}$  [76, 77]. Finally, a nonuniform cantilever cross section along the axis can be taken into account [80–83]. Such improvement in the models is fundamental in particular for AFAM and UAFM, which use standard AFM setups, while it is a less pressing requirement for SMM, which uses ad hoc designed probes. The simpler models permit analytical solution, while the more comprehensive ones may require approximate solution or finite element methods (FEM) [80–85].

#### 1.4.1.2 Contact Mechanics

The simplest model for describing the tip-sample contact is assuming a spherical tip normally indenting an ideally flat surface, with the only forces acting being the elastic ones generated by the stress field neglecting adhesion (namely, the Hertz model [28]). Nevertheless, van der Waals, capillary, and adhesive forces have to be considered for a more realistic description of the contact depending on the specific experimental conditions. These forces, characterized by different distances where the

interaction is experienced (being identified as ‘long-range’ and ‘short-range’ forces), can act either outside or inside the contact area and are described by different models, namely the Derjaguin-Muller-Toporov (DMT) [86] and the Johnson-Kendall-Roberts (JKR) [87], respectively. Therefore, for a correct interpretation of experimental data it is essential to understand the nature of the forces acting between tip and sample, which consequently is a mandatory issue in all the A-SPM techniques aiming at the quantitative measurement of sample elastic modulus.

### 1.4.1.3 Tip Wear

Probably the most intriguing issue to deal with in quantitative A-SPM techniques is the uncertainty in the geometry and in the mechanical properties of the tip. As for the former, commercial brand new AFM tips are assured by the supplier to have a fixed maximum apex curvature radius (generally 10 nm for standard cantilevers), whose actual value is therefore unknown. Moreover, during a measurement session the tip geometry may experience both gradual and abrupt modifications [43, 88–90]. The former is produced by continuous wear. The latter can be produced by sudden crashes with surface asperities, detachment of the layer possibly coating the tip, or by plastic deformation occurring when the pressure in the contact area is comparable with the tip yield strength [90].

Tip wear more seriously affects measurements on stiff samples than on soft ones, where nevertheless contamination of the tip by material from the sample is more likely to occur. Moreover, tip wear is more severe in contact mode than in tapping mode as the interaction time in tapping mode is limited to a fraction of the period of the cantilever oscillation, also considering that normal loads between tip and sample in contact A-SPM techniques are generally some orders of magnitude higher than those used in standard AFM imaging. On this basis, TH-AFM is expected to be the least affected by tip wear among the techniques described in this book, as it operates in tapping mode on soft samples, while such an effect has to be carefully considered when using contact mode A-SPM methods. To limit the abrasion of the tip, the tip-sample interaction has to be reduced. Lower values of static load can be used, but this could increase the effect of adhesion and capillarity forces. To reduce interaction time, acquisition time at a single point has to be reduced. Increasing the images scan rate would be desirable for reducing the time needed for a single image acquisition, thus reducing drift between two subsequent images, which for instance is detrimental when two frequency maps have to be acquired on the same area as for the elastic modulus maps reconstruction by AFAM [38–40]. Nevertheless, the increase in scan rate has been demonstrated to increase the wear rate [91]. Abrupt contacts with surface asperities can be limited by reducing vibration of the system and properly selecting the feedback parameters. Finally, tip wear can be reduced by using tips entirely made or coated by materials harder than standard Si. The former strategy is that used in SMM, where sapphire or diamond tips are mounted. Tips coated with hard materials such as diamond-like carbon (DLC) have been demonstrated to ensure superior stability under continuous wear during measurements [12], but may incur

in sudden detachment from the tip itself. Moreover, the mechanical properties of the coatings are generally unknown, thus undermining the reliability of the measurements unless they are contextually characterized in the A-SPM experiment as described below. Finally, a strategy going in the opposite direction and applicable when high lateral resolution is not needed consists in intentionally flattening standard tips or tips coated with materials that easily undergo plastic deformations, which increases the stability during measurements as the relatively wide contact area ensures low stress at the tip–sample interface [50, 90].

#### 1.4.1.4 Calibrations

Quantitative elastic modulus evaluation from the measurement of  $k^*$  requires knowledge of the tip–sample contact area and of the tip elastic modulus, which can be evaluated by calibration measurements on reference samples. Supposing a spherical apex with known elastic modulus, its curvature radius and thus the contact area can be retrieved by a single measurement on a single reference sample. In this case, the radius of the tip and that of the contact area are independent and dependent on the applied load, respectively. Similarly, supposing a flat punch tip, a single measurement on a single reference sample allows calculation of the radius of the contact area, which is independent on the exerted load. When performing mechanical imaging of the surface, the calibration of the contact area radius enables conversion of the whole  $k^*$  map into one of the elastic modulus. To this aim, an ‘external’ sample can be used as in reference [92] or a ‘self-calibration’ can be performed using a portion of the  $k^*$  map corresponding to a material with known elastic properties [38, 41, 93, 94]. Moreover, the assumption of a spherical or flat shape of the tip can be removed, and the real geometry of the apex can be evaluated by contact stiffness measurements as a function of the applied load [43, 88, 90, 95]. Such curves allow one to identify the most suitable model for the apex, which is generally intermediate between the two ideal cases of spherical and flat tip [88, 95]. Finally, performing the tip calibration before and after the measurement session allows the effect of wear to be monitored [12]. Reliable measurements of elastic modulus of the sample require knowledge of the modulus of the tip, unless the latter is much higher than the former, allowing one to neglect the deformation of the tip during periodical indentation of the sample. The elastic modulus of standard Si tips can differ from that of monocrystalline Si in the tip crystallographic direction due to the presence of both the oxide layer and the amorphous material at the apex [96]. The mechanical properties of coated tips are generally unknown: this is due to the difference between the elastic properties of thin films and of the corresponding bulk materials. Moreover, the effect of the mechanical properties of the tip itself is generally not negligible, since it acts as a substrate for the few nanometer to few tens of nanometer thick coatings. To measure the elastic modulus of the tip, the aforementioned calibration procedures have to be performed using at least a second reference sample [95, 96].

### 1.4.1.5 Measurable Mechanical Parameters

Almost all the quantitative A-SPM techniques rely on the evaluation of the tip sample contact stiffness  $k^*$ . This allows estimation of the sample indentation modulus  $M$  that is related to both the Young's modulus  $E$  and the Poisson ratio  $\nu$  by the relation  $M = E / (1 - \nu^2)$ . The evaluation of  $E$  requires an independent knowledge of or an assumption about the value of  $\nu$ . In a recent development of AFAM, shear wave piezoelectric transducers have been used in AFAM setup to excite in-plane oscillation of the sample surface at ultrasonic frequencies. This enabled the acquisition of both the flexural and torsional contact resonance frequencies from which  $E$  and  $\nu$  were independently measured [97]. The indentation modulus (or the combination of Young's modulus and Poisson ratio) describes the response to quasi-static or dynamic indentation of an elastic material, when the viscoelastic effect is negligible, i.e., no delay is observed between the applied force and the resulting penetration. On the contrary, in case of viscoelastic materials such as polymers, the response to dynamical indentation is described by a complex modulus or alternatively by two parameters, the storage modulus  $E'$  and the loss modulus  $E''$ . These are respectively the in-phase and quadrature component of the sample mechanical response, i.e., the real and imaginary part of the viscoelastic complex modulus of the sample. A well-established macroscopic technique enabling the measurement of  $E'$  and  $E''$  is dynamic indentation or dynamical mechanical analysis (DMA) [98, 99], while at submicrometer scale a tool has been developed that combines nanoindentation and force modulation and takes advantage of SPM scanners to produce significant results [100–102]. A-SPM techniques have been also employed for mechanical characterization of viscoelastic materials. AFAM has been recently extended to the study of such materials by developing suitable models for the analysis of experimental resonance curves to extract storage and loss moduli [103, 104]. The capability of SMM of allowing the evaluation of  $E'$  and  $E''$  of polymeric samples has been recently demonstrated by comparison with standard DMA measurements [53, 105]. Finally, the quantitative measurement of contact stiffness, quality factor, and damping and their dependence on the applied load enable the investigation of friction [106, 107].

### 1.4.1.6 Artifacts

The last issue to note when interpreting maps of stiffness or elastic modulus is the possibility of topography induced artifacts. The measured contact stiffness is related to the elastic modulus via the contact area. In the aforementioned models, the sample surface is considered ideally flat due to the nanometer scale of the tip radius of curvature. Actually, in the case of surfaces with nanoscale features, such an assumption cannot be verified. In this case, any change in the contact area due to a change in the topography produces a variation in contact stiffness that could be misinterpreted as a variation of the elastic modulus. For asperities on the surface smaller than the contact area, e.g., on the top of nanostructures, the effective contact area is reduced and thus the contact stiffness. Conversely, at the grain boundaries

on granular films, contact can be established between the side of the tip and several grains in the so-called ‘multi-asperities contact’ [108]. In this case, the effective contact area is increased with respect to the ‘true’ contact area at the top of the grain, and the apparent result can ensue of grain boundaries stiffer than the core, which is nonphysical according to general experience [108].

### ***1.4.2 Subsurface Imaging***

During the periodical indentation of the surface, a stress field is generated into the sample. Depending on the amount of stress, the material underneath the surface at a certain depth contributes to the sample mechanical response [109]. As a rule of thumb, the volume of material contributing to the contact stiffness has the dimensions of a few times the contact radius [110]. Therefore, A-SPM techniques can probe the sample down to a depth of few contact radii and thus have to be considered near-surface instead of surface characterization techniques. Mechanical inhomogeneities in this volume, such as buried nanostructures and interfaces, voids, delamination, and lack of adhesion at buried interfaces, produce a contrast in the acoustic image. This is expected to be more pronounced when the buried features are near the surface. Similarly, due to diffraction of the near-field acoustic waves, deeply buried nanostructures are expected to appear more enlarged with respect to their real dimension than nanostructures near the surface. A-SPM techniques have indisputably demonstrated their capability for imaging subsurface features using ad hoc prepared samples [69, 111–114]. In particular, A-SPM quantitative measurements of contact stiffness have shown good agreement with theoretical calculations of reduced adhesion at buried interfaces [111, 115] and of subsurface voids [112]. Apart from the admittedly amazing results attained on test samples, more theoretical and/or experimental efforts are required for the interpretation of subsurface imaging of real samples. To explain some features in the contact stiffness versus load dependence and in the nonlinear spectra, the modeling of cracks and voids as sources of acoustic nonlinearities was performed [43, 45, 116]. Alternatively, electronic interconnect architectures have been cut to demonstrate the capability of A-SPM techniques for imaging subsurface voids [71]. Finally, in some cases, as in the subsurface imaging of cells exposed to nanoparticles, the comparison with blank control samples allowed a better interpretation of A-SPM images [72, 73].

## **1.5 Why a Book on Acoustic AFM Techniques?**

Since the first pioneering works, where inventors of A-SPM techniques reported their use in single experiments mainly for validating and demonstrating their potential for application on different kinds of samples, the community of A-SPM users has continuously increased. To get an idea of the increasing diffusion of A-SPM tech-

niques, Fig. 1.1 reports the results of a bibliographic research performed at the beginning of July 2011 using a scientific search engine (SciVerse Scopus). Figure 1.1a shows the cumulative number of publications from 1986 (first description of AFM [1]) to each year (partial data are available for 2011) retrieved by inserting the full name of FMM, AFAM, UAFM, SMM, UFM, SNFUH, RDF-AFUM, and heterodyne force microscopy (HFM) [117] in Title, Abstract, and Keyword fields. TH-AFM has been purposely excluded in the research since the technique is not yet a well established and accepted name, although it is rapidly emerging and has been used very recently in several works [118–121]. Note also that some recent publications do not report the complete name of the techniques in any of the mentioned above searching fields and, thus, the number of A-SPM publications is expected to be underestimated. Therefore, the following statistics can give only a partial and underestimated indication of the spreading of A-SPMs. Figure 1.1a indicates an almost constant increasing rate in the number of scientific works since 1993. Figure 1.1b shows the cumulative list of authors deduced by the same bibliographic research, which in turn demonstrates that such an increase is ascribable not only to the continuous scientific production of the original proposers of A-SPMs but primarily to the constant increase of researchers involved in such techniques. While continuing the research for improving the existing techniques and developing new ones, some A-SPM techniques are now standardized and are available as tools in commercial SPM setups. Therefore, a new community of A-SPM users-only researchers is developing besides that of inventors and improvers. Nevertheless, our personal experience indicates that A-SPMs are still considered to be niche or at least ‘exotic’ techniques by the scanning probe and atomic force microscopy community. To ‘quantify’ our feeling, a similar bibliographic research has been performed using the names of:

- the principal electric AFM (E-AFM) techniques—electric force microscopy (EFM), spreading resistance microscopy (SRM), scanning capacitance microscopy (SCM), and scanning Kelvin probe microscopy (SKPM)
- magnetic force microscopy (MFM).

The research was done again in Title, Abstract, and Keyword fields. Figure 1.1c compares the absolute number of publications for each year on A-SPM, E-AFM, and MFM. The diffusion of A-SPMs is limited, being two or three times lower than that of E-AFM techniques and about ten times lower than that of MFM. Note that a contribution to the higher diffusion of MFM is that it was proposed earlier [122–124]. Finally, Fig. 1.1d reports the same data of Fig. 1.1c divided by the number of publications each year retrieved by inserting only AFM in Title, Abstract, and Keyword fields. Data for A-SPM and E-AFM are approximately constant, indicating that the diffusion rate of such techniques is the same for AFM, whose primary use is obviously the topographical characterization. Figure 1.1d gives the impression that the diffusion MFM does not keep pace with that of AFM. The increasing interest in acoustic SPM techniques for surface and subsurface mechanical imaging stimulated the idea of a volume collecting advances in early techniques and describing some of the most promising recent developments. Some of the techniques described in this book have been already included in books among other not acoustic SPM techniques



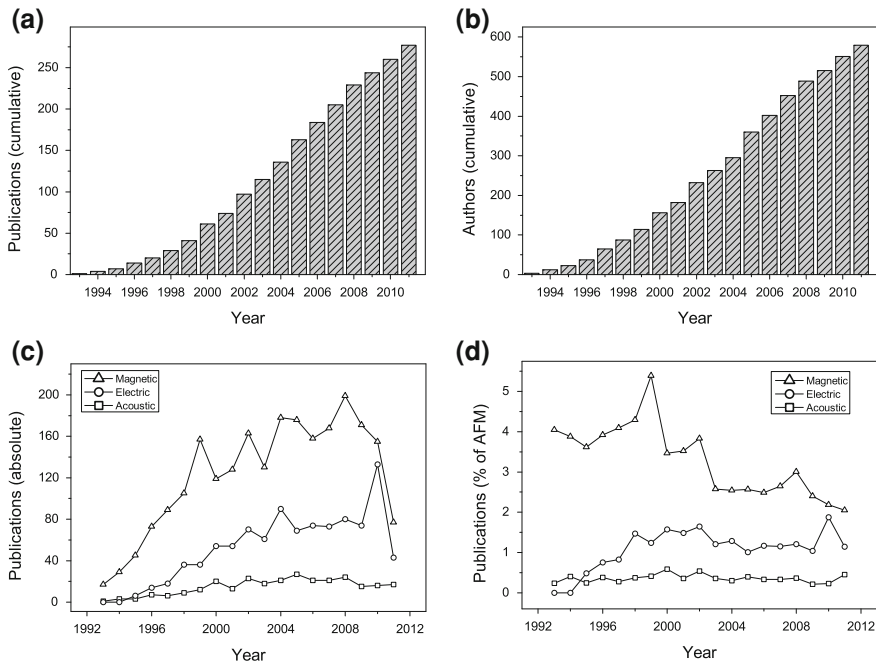


**Fig. 1.1** Evolution as a function of the year of: **a** Cumulative number of publications in A-SPM field; **b** Cumulative number of authors publishing in A-SPM field; **c** Absolute number of publications on A-SPMs (*open squares*) compared to that on electric (*open circles*) and magnetic AFM (*open triangles*); **d** Relative number of publications (i.e., the absolute number of publications divided by the number of publications on AFM) on A-SPMs (*open squares*) compared to that on electric (*open circles*) and magnetic AFM (*open triangles*). Partial data (till July) are available for 2011

[125–128]. The primary reason for a book devoted to A-SPM techniques is that it could be useful both for researchers already expert in one or more A-SPMs, who would be stimulated to explore and improve new techniques, and for standard SPM users, who could find among the described techniques the most suitable for their particular field of interest. To this aim, besides some explanatory examples of application reported contextually to the description of the techniques, a few chapters have been added dealing with the comparison of the potentialities of A-SPM techniques for particular applications which represent present and future challenges of A-SPMs (friction, subsurface imaging, polymers, and biological samples), even if this has led to some overlap.

## 1.6 About this Book

The book is divided into three parts. The first part includes three chapters on subjects that form the basis of all A-SPM techniques, namely, the contact mechanics describing the tip–sample interaction (Chap. 2), the analytical models for the dynamics of the cantilevers interacting with the sample in the different A-SPM modalities (Chap. 3), and numerical methods for their simulation (Chap. 4). The second section describes the most important A-SPM techniques emphasizing their recent advances: AFAM (Chap. 5), UAFM (Chap. 6), SMM (Chap. 8), UFM and related techniques (Chap. 9), SNFUH (Chap. 10), and TH-AFM (Chap. 11). Chapter 7 deals with a strategy for enhancing the sensitivity in AFAM and UAFM by using cantilevers with a concentrated mass added at their end. The presentation of A-SPM techniques is completed with a comparison between quantitative elastic measurements by A-SPMs and conventional techniques (i.e., nanoindentation and surface acoustic wave spectroscopy) which is the subject of Chap. 12. Finally, Chap. 13 discusses the main points of data post processing, providing hints and strategies for repeatable analysis of surface data sets. The third section reviews some particular applications of A-SPMs. Two chapters are devoted to quantitative aspects in the characterization of friction/internal friction (Chap. 14) and subsurface imaging (Chap. 15) by A-SPM techniques. Finally, Chap. 16 describes some recent results in the quantitative mechanical characterization of polymers and Chap. 17 the quantitative mechanical imaging of biological samples.

**Acknowledgments** Donna C. Hurley is kindly acknowledged for the detailed critical revision of the chapter. Andrea Bettucci and Marco Rossi are acknowledged for useful discussions and suggestions.

## References

1. G. Binnig, C.F. Quate, C. Gerber, *Phys. Rev. Lett.* **56**, 930–933 (1986)
2. G. Binnig, H. Rohrer, *Surf. Sci.* **126**, 236–244 (1983)
3. G. Binnig, H. Rohrer, *Ultramicroscopy* **11**, 157–160 (1983)
4. G. Binnig, H. Rohrer, *Rev. Mod. Phys.* **71**, S324–S330 (1999)
5. G. Binnig, H. Rohrer, *IBM J. Res. Develop.* **44**, 279–293 (2000)
6. J.S. Villarrubia, *J. Res. Natl. Inst. Stand. Technol.* **102**, 425–454 (1997)
7. F. Marinello, S. Carmignato, A. Voltan, E. Savio, L. De Chiffre, *J. Manuf. Sci. E. T. ASME* **132**, 031003 (2010)
8. P. Maivald, H.J. Butt, S.A. Gould, C.B. Prater, B. Drake, J.A. Gurley, V.B. Elings, P.K. Hansma, *Nanotechnology* **2**, 103–106 (1991)
9. H.Y. Nie, M. Motomatsu, W. Mizutani, H. Tokumoto, *Thin Solid Films* **273**, 143–148 (1996)
10. B. Cretin, F. Sthal, *Appl. Phys. Lett.* **62**, 829–831 (1996)
11. J. Le Rouzic, B. Cretin, P. Vairac, B. Cavallier, in *IEEE, International Frequency Control Symposium, 2009 Joint with the 22nd European Frequency and Time forum* (2009)
12. S. Amelio, A.V. Goldade, U. Rabe, V. Scherer, B. Bhushan, W. Arnold, *Thin Solid Films* **392**, 75–84 (2001)
13. C.F. Quate, *Phys. Today* **34**, 34–42 (1985)

14. G.A.D. Briggs, O.V. Kolosov, *Acoustic Microscopy* (Oxford University Press, New York, 2010)
15. R.G. Maev, *Acoustic Microscopy—Fundamentals and Applications* (Wiley, Germany, 2008)
16. G. Kino, *Acoustic Waves: Devices, Imaging and Analog Signal Processing* (Prentice-Hall, Englewood Cliffs, 1987)
17. C. Girard, C. Joachim, S. Gauthier, Rep. Prog. Phys. **63**, 893–938 (2000)
18. E. Chilla, W. Rohrbeck, H.-J. Fröhlich, R. Koch, H.K. Rieder, Appl. Phys. Lett. **61**, 69–71 (1992)
19. W. Rohrbeck, E. Chilla, Phys. Status Solidi A **131**, 69–71 (1992)
20. W. Rohrbeck, E. Chilla, H.-J. Fröhlich, J. Riedel, Appl. Phys. A - Mater. **52**, 344–347 (1991)
21. T. Hesjedal, E. Chilla, H.-J. Fröhlich, Thin Solid Films **264**, 226–229 (1995)
22. T. Hesjedal, E. Chilla, H.-J. Fröhlich, J. Vac. Sci. Technol. B **15**, 1569–1572 (1997)
23. T. Hesjedal, Rep. Prog. Phys. **73**, 016102 (2010)
24. D.W. Pohl, W. Denk, M. Lanz, Appl. Phys. Lett. **44**, 651–653 (1984)
25. U. Durig, D.W. Pohl, F. Rohner, J. Appl. Phys. **59**, 3318–3327 (1986)
26. D. Courjon, K. Sarayeddine, M. Spajer, Opt. Commun. **71**, 23–28 (1989)
27. J.N. Israelachvili, *Intermolecular and Surface Forces* (Academic Press, London, 1985)
28. K.L. Johnson, *Contact Mechanics* (Cambridge University Press, Cambridge, 2003)
29. M. Muraoka, W. Arnold, JSME Int. J. A **44**, 396–404 (2001)
30. N.A. Burnham, A.J. Kulik, G. Gremaud, G.A.D. Briggs, Phys. Rev. Lett. **74**, 5092–5095 (1995)
31. S.I. Lee, S.W. Howell, A. Raman, R. Reifengerger, Ultramicroscopy **97**, 185–198 (2003)
32. E.M. Abdel-Rahman, A.H. Nayfeh, Nanotechnology **16**, 199–207 (2005)
33. U. Rabe, W. Arnold, Appl. Phys. Lett. **64**, 1493–1495 (1994)
34. U. Rabe, V. Scherer, S. Hirsekorn, W. Arnold, J. Vac. Sci. Technol. B **15**, 1506–1511 (1997)
35. U. Rabe, S. Amelio, M. Kopycinska, S. Hirsekorn, M. Kempf, M. Göken, W. Arnold, Surf. Interface Anal. **33**, 65–70 (2002)
36. U. Rabe, S. Amelio, E. Kester, V. Scherer, S. Hirsekorn, W. Arnold, Ultrasonics **38**, 430–437 (2000)
37. U. Rabe, M. Kopycinska, S. Hirsekorn, J. Muñoz Saldaña, G.A. Schneider, W. Arnold, J. Phys. D **35**, 2621–2635 (2002)
38. D.C. Hurley, M. Kopycinska-Müller, A.B. Kos, R.H. Geiss, Adv. Eng. Mater. **7**, 713–718 (2005)
39. D.C. Hurley, M. Kopycinska-Müller, A.B. Kos, R.H. Geiss, Meas. Sci. Technol. **16**, 2167–2172 (2005)
40. D. Passeri, A. Bettucci, M. Germano, M. Rossi, A. Alippi, V. Sessa, A. Fiori, E. Tamburri, M.L. Terranova, Appl. Phys. Lett. **88**, 121910 (2006)
41. A. Kumar, U. Rabe, S. Hirsekorn, W. Arnold, Appl. Phys. Lett. **92**, 183106 (2008)
42. K. Yamanaka, S. Nakano, Jpn. J. Appl. Phys. Part **1**(35), 3787–3792 (1996)
43. K. Yamanaka, A. Noguchi, T. Tsuji, T. Koike, T. Goto, Surf. Interface Anal. **27**, 600–606 (1999)
44. S. Banerjee, N. Gayathri, S. Dash, A.K. Tyagi, B. Raj, Appl. Phys. Lett. **86**, 211913 (2005)
45. K. Yamanaka, K. Kobari, T. Tsuji, Jpn. J. Appl. Phys. **47**, 6070–6076 (2008)
46. U. Rabe, S. Hirsekorn, M. Reinstädler, T. Sulzbach, C. Lehrer, W. Arnold, Nanotechnology **18**, 044008 (2007)
47. K. Schwarz, U. Rabe, S. Hirsekorn, W. Arnold, Appl. Phys. Lett. **92**, 183105 (2008)
48. K. Yamanaka, Y. Maruyama, T. Tsuji, K. Nakamoto, Appl. Phys. Lett. **78**, 1939–1941 (2001)
49. U. Rabe, J. Janser, W. Arnold, Rev. Sci. Instrum. **67**, 3281–3293 (1996)
50. M. Muraoka, Nanotechnology **16**, 542–550 (2005)
51. P. Vairac, B. Cretin, Surf. Interface Anal. **27**, 588–591 (1999)
52. L. Robert, B. Cretin, Surf. Interface Anal. **27**, 568–571 (1999)
53. J. Le Rouzic, P. Vairac, B. Cretin, P. Delobelle, Rev. Sci. Instrum. **79**, 033707 (2008)
54. D. Rupp, U. Rabe, S. Hirsekorn, W. Arnold, J. Phys. D: Appl. Phys. **40**, 7136–7145 (2007)
55. B. Cappella, G. Dietler, Surf. Sci. Rep. **34**, 1–104 (1999)

56. H.J. Butt, B. Cappella, M. Kappl, *Surf. Sci. Rep.* **59**, 1–152 (2005)
57. C.A. Clifford, M.P. Seah, *Appl. Surf. Sci.* **252**, 1915–1933 (2005)
58. A. Vinckier, G. Semenza, *FEBS Lett.* **430**, 12–16 (1998)
59. M. Radmacher, in *Atomic Force Microscopy in Cell Biology*, ed. by B.P. Jena, J.K.H. Hober (Academic Press, San Diego, 2002) pp. 67–90
60. D.M. Ebenstein, L.A. Pruitt, *Nanotoday* **1**, 26–33 (2006)
61. A. Ebert, B. Tittmann, J. Du, W. Scheuchenzuber, *Ultrasound Med. Biol.* **32**(11), 1687–1702 (2006)
62. T. Tsuji, K. Yamanaka, *Nanotechnology* **12**, 301–307 (2001)
63. K. Yamanaka, *Thin Solid Films* **273**, 116–121 (1996)
64. P. Vairac, R. Boucenna, J. Le Rouzic, B. Cretin, *J. Phys. D: Appl. Phys.* **41**, 155503 (2008)
65. O. Kolosov, K. Yamanaka, *Jpn. J. Appl. Phys. Part 2* **32**, L1095–L1098 (1993)
66. F. Dinelli, H.E. Assender, N. Takeda, G.A.D. Briggs, O.V. Kolosov, *Surf. Interface Anal.* **27**, 562–567 (1999)
67. F. Dinelli, S.K. Biswas, G.A.D. Briggs, O.V. Kolosov, *Phys. Rev. B* **61**, 13995–14006 (2000)
68. A.C. Diebold, *Science* **310**, 61–62 (2005)
69. G.S. Shekhawat, V.P. Dravid, *Science* **310**, 89–92 (2005)
70. S.A. Cantrell, J.H. Cantrell, P.T. Lillehei, *J. Appl. Phys.* **101**, 114324 (2007)
71. G. Shekhawat, A. Srivastava, S. Avasthy, V.P. Dravid, *Appl. Phys. Lett.* **95**, 263101 (2009)
72. L. Tetard, A. Passian, K.T. Venmar, R.M. Lynch, B.H. Voy, G. Shekhawat, V. Dravid, T. Thundat, *Nat. Nanotechnol.* **3**, 501–505 (2008)
73. L. Tetard, A. Passian, R.M. Lynch, B.H. Voy, G. Shekhawat, V. Dravid, T. Thundat, *Appl. Phys. Lett.* **93**, 133113 (2008)
74. O. Sahin, S. Magonov, C. Su, C.F. Quate, O. Solgaard, *Nat. Nanotechnol.* **2**, 507–514 (2007)
75. O. Sahin, N. Erina, *Nanotechnology* **19**, 445717 (2008)
76. J.H. Cantrell, S.A. Cantrell, *Phys. Rev. B* **77**, 165409 (2008)
77. M.H. Mahdavi, A. Farshidianfar, M. Tahani, S. Mahdavi, H. Dalir, *Ultramicroscopy* **109**, 54–60 (2008)
78. D.C. Hurley, J.A. Turner, *J. Appl. Phys.* **95**, 2403–2407 (2004)
79. D.C. Hurley, M. Kopycinska-Müller, D. Julthongpipit, M.J. Fasolka, *Appl. Surf. Sci.* **253**, 1274–1281 (2006)
80. D.C. Hurley, K. Shen, N.M. Jennett, J.A. Turner, *J. Appl. Phys.* **94**, 2347–2354 (2003)
81. K. Shen, D.C. Hurley, J.A. Turner, *Nanotechnology* **15**, 1582–1589 (2004)
82. R. Arinero, G. Lévêque, *Rev. Sci. Instrum.* **74**, 104–111 (2003)
83. F.J. Espinoza Beltrán, J. Muñoz-Saldaña, D. Torres-Torres, R. Torres-Martínez, G.A. Schneider, *J. Mater. Res.* **21**, 3072–3079 (2006)
84. H.L. Lee, Y.C. Yang, W.J. Chang, S.S. Chu, *Jpn. J. Appl. Phys.* **45**, 6017–6021 (2006)
85. J.A. Turner, J.S. Wiehn, *Nanotechnology* **12**, 322–330 (2001)
86. B.V. Derjaguin, V.M. Muller, Y.P. Toporov, *J. Colloid Interface Sci.* **53**, 314–326 (1975)
87. K.L. Johnson, K. Kendall, A.D. Roberts, *Proc. R. Soc. A* **324**, 301–313 (1971)
88. K. Yamanaka, T. Tsuji, A. Noguchi, T. Koike, T. Mihara, *Rev. Sci. Instrum.* **71**, 2403–2408 (2000)
89. M. Kopycinska-Müller, R.H. Geiss, D.C. Hurley, *Ultramicroscopy* **106**, 466–474 (2006)
90. D. Passeri, A. Bettucci, M. Germano, M. Rossi, A. Alippi, S. Orlanducci, M.L. Terranova, M. Ciavarella, *Rev. Sci. Instrum.* **76**, 093904 (2005)
91. B. Bhushan, K.J. Kwak, *Appl. Phys. Lett.* **91**, 163113 (2007)
92. D. Passeri, A. Bettucci, M. Germano, M. Rossi, A. Alippi, A. Fiori, E. Tamburri, M.L. Terranova, J.J. Vlassak, *Microelectr. Eng.* **84**, 490–494 (2007)
93. Y. Zheng, R.E. Geer, K. Dovidenko, M. Kopycinska-Müller, D.C. Hurley, *J. Appl. Phys.* **100**, 124308 (2006)
94. A. Kumar, U. Rabe, W. Arnold, *Jpn. J. Appl. Phys.* **47**, 6077–6080 (2008)
95. M. Kopycinska-Müller, A. Caron, S. Hirsekorn, U. Rabe, H. Natter, R. Hempelmann, R. Birringer, W. Arnold, *Z. Phys. Chem.* **222**, 471–498 (2008)
96. G. Stan, W. Price, *Rev. Sci. Instrum.* **77**, 103707 (2006)

97. D.C. Hurley, J.A. Turner, *J. Appl. Phys.* **102**, 033509 (2007)
98. C.C. White, M.R. Vanlandingham, P.L. Drzal, N.K. Chang, S.H. Chang, *J. Polym. Sci. B Pol. Phys.* **43**, 1794–1811 (2005)
99. C.C. White, M.R. Vanlandingham, P.L. Drzal, N.K. Chang, S.H. Chang, *J. Polym. Sci. B Pol. Phys.* **43**, 1812–1824 (2005)
100. S.A. Syed Asif, K.J. Wahl, R.J. Colton, *Rev. Sci. Instrum.* **70**, 2408–2413 (1999)
101. S.A. Syed Asif, K.J. Wahl, R.J. Colton, O.L. Warren, *J. Appl. Phys.* **90**, 1192–1200 (2001)
102. Y. Ganor, D. Shilo, *Appl. Phys. Lett.* **88**, 233122 (2006)
103. P.A. Yuya, D.C. Hurley, J.A. Turner, *J. Appl. Phys.* **104**, 074916 (2008)
104. P.A. Yuya, D.C. Hurley, J.A. Turner, *J. Appl. Phys.* **109**, 113528 (2011)
105. J. Le Rouzic, P. Delobelle, P. Vairac, B. Cretin, *Eur. Phys. J. Appl. Phys.* **48**, 11201 (2009)
106. A. Caron, W. Arnold, *Acta Mater.* **57**, 4353–4363 (2009)
107. A. Caron, W. Arnold, H.-J. Fecht, *J. J. Appl. Phys.* **49**, 120204 (2010)
108. G. Stan, R.F. Cook, *Nanotechnology* **19**, 235701 (2008)
109. M. Kopycinska-Müller, R.H. Geiss, J. Müller, D.C. Hurley, *Nanotechnology* **16**, 703–709 (2005)
110. E. Kester, U. Rabe, L. Presmanes, P. Tailhades, W. Arnold, *J. Phys. Chem. Solids* **61**, 1275–1284 (2000)
111. D.C. Hurley, M. Kopycinska-Müller, E.D. Langlois, N. Barbosa III, *Appl. Phys. Lett.* **89**, 021911 (2006)
112. Z. Parlak, F.L. Degertekin, *J. Appl. Phys.* **103**, 114910 (2008)
113. G. Shekhawat, S. Avasthy, A. Srivastava, S.-H. Tark, V. Dravid, *IEEE T. Nanotechnol.* **9**, 501–505 (2010)
114. P. Vairac, B. Cretin, *Appl. Phys. Lett.* **68**, 461–463 (1996)
115. A.F. Sarioglu, A. Atalar, F.L. Degertekin, *Appl. Phys. Lett.* **84**, 5368–5370 (2004)
116. I.Y. Solodov, N. Krohn, G. Busse, *Ultrasonics* **40**, 621–625 (2002)
117. M.T. Cuberes, H.E. Alexander, G.A.D. Briggs, O.V. Kolosov, *J. Phys. D: Appl. Phys.* **33**, 2347–2355 (2000)
118. K.M. Leung, G. Wanger, Q. Guo, Y. Gorby, G. Southam, W.M. Laue, *J. Yang, Soft Matter* **7**, 6617–6621 (2011)
119. P. Ihalainen, J. Järnström, A. Määttänen, J. Peltonen, *Colloid. Surf. A* **373**, 138–144 (2011)
120. P. Schön, K. Bagdi, K. Molnár, P. Markus, B. Pukánszky, G. Julius Vancso, *Eur. Polym. J.* **47**, 692–698 (2011)
121. P. Schön, S. Dutta, M. Shirazi, J. Noordermeer, G. Julius Vancso, *J. Mater. Sci.* **46**, 3507–3516 (2011)
122. Y. Martin, H.K. Wickramasinghe, *Appl. Phys. Lett.* **50**, 1455–1457 (1987)
123. J.J. Sáenz, N. García, P. Grütter, E. Meyer, H. Heinzelmann, R. Wiesendanger, L. Rosenthaler, H.R. Hidber, H.J. Güntherodt, *J. Appl. Phys.* **62**, 4293–4295 (1987)
124. J.J. Sáenz, N. García, J.C. Sloczewski, *Appl. Phys. Lett.* **53**, 1449–1451 (1988)
125. U. Rabe, in *Applied Scanning Probe Methods II*, ed. by B. Bhushan, H. Fuchs (Springer, Berlin, 2006), pp. 37–90
126. D.C. Hurley, in *Applied Scanning Probe Methods XI*, ed. by B. Bhushan, H. Fuchs (Springer, Berlin Heidelberg 2006) pp. 97–138
127. O. Sahin, C.F. Quate, O. Solgaard, F.J. Giessibl, in *Springer Handbook of Nanotechnology*, ed. by B. Bhushan, (Springer, Berlin Heidelberg 2010) pp. 711–729
128. S. Avasthy, G. Shekhawat, V. Dravid, in *Encyclopedia of Analytical Chemistry: Supplementary Volumes S1–S3: Applications, Theory and Instrumentation*, ed. by R.A. Meyers (Wiley Hoboken, 2006) pp. a9146:1–a9146:9

# Chapter 2

## Contact, Interactions, and Dynamics

E. Barthel

**Abstract** In this short introduction to tip–surface interaction, we focus on the impact of adhesion on the elastic contact of small spherical bodies. Standard notions are first reviewed but more complex contact conditions involving coatings or roughness are also considered. Special attention is devoted to dynamic response and ensuing dissipation.

### 2.1 Introduction: Contact and Adhesion

As the denomination suggests, in *force* microscopies, such as atomic force microscopy (AFM), ultrasonic force microscopy (UFM), etc. the interaction between the tip and the substrate lies at the core of the technique. Despite the A(tomic) in AFM, several atoms usually participate in the interaction, so that continuum scale approaches are relevant. The aim of this chapter is to explain some of the basic ideas underlying the adhesive contact of small objects like tips.

A distinctive feature here is the presence of curvature: one of the surfaces, the tip, is axisymmetric and curved, with radius of curvature  $R$ , so that the tip shape  $f(r)$  is approximately

$$f(r) = \frac{r^2}{2R} \quad (2.1)$$

where  $r$  is the radial coordinate. Within the limitations of the following developments, this shape is also a good approximation to the local shape of a sphere, and for historical reasons we will often refer to the tip as the *sphere*. The other surface, the substrate, is flat.

---

E. Barthel (✉)  
Surface du Verre et Interfaces, CNRS/Saint-Gobain,  
UMR 125, 93330 Aubervilliers Cedex, France  
e-mail: etienne.barthel@saint-gobain.com

In a basic view of the tip coming to the surface, the two surfaces initially sit at a separation distance  $d$  (Fig. 2.1a) along the symmetry axis and the gap between the surfaces is  $d + f(r)$ . When the surfaces are brought together, they come into contact as *point contact* and subsequently develop a *contact area* with finite size as the load increases (Fig. 2.1b). In terms of interactions, more or less long-range attractive interactions result in adhesion while short-range Born repulsion will provide for the contact side of the problem. It is the coupling of these interactions with continuum scale mechanical response which we consider here.

Sections 2.2, 2.3, 2.4 and 2.5 consist in an exposition of standard results for sphere contact mechanics while Sects. 2.6, 2.7 and 2.8 contain developments on the impact of more advanced features: coatings, roughness, and dissipation, keeping in mind some dynamic issues relevant for AFM.

The chapter has been designed for a reasonably straightforward reading. Beyond a mere enumeration of results, we also want to provide some hints as to the physical origin of the results. These details, and also more advanced ideas, which we believe would obstruct linear reading, appear in boxes. A first reading could omit all the frames while more advanced understanding should be obtained by their later perusal.

## 2.2 Adhesionless Contact: Stiffness

In this section we assume no interaction between the surfaces and investigate elastic contact. We bring the surfaces from “far away” (Fig. 2.1a) into contact (Fig. 2.1b). Without loss of generality (see frame 1) we assume that it is the tip which is elastic. The reduced modulus is  $E^* = E/(1 - \nu^2)$ , where  $E$  is Young’s modulus and  $\nu$  the Poisson ratio. The flat is rigid.

### Frame 1: Contact—response and boundary conditions

The results presented here are exact under a number of hypotheses, including absence of friction and small deformations. However, they are quite robust. A good example of deviations with large deformation and the resulting breakdown of the sphere/flat symmetry can be found in [1].

Within linear elasticity, if both surfaces are curved, the curvatures  $R_i^{-1}$  add up to provide the overall curvature  $R^{-1}$ . If both tip and substrate feature significant compliances, the compliances add up as

$$E^{*-1} = \left( E_t / (1 - \nu_t^2) \right)^{-1} + \left( E_s / (1 - \nu_s^2) \right)^{-1} \quad (2.2)$$

Moduli are in the 100 GPa range for stiff materials, but can drop considerably for polymers, down to 2 GPa for vitreous polymers or 10 MPa for elastomers. Contact radii in the present context are of the order of 10 nm.

### 2.2.1 Hertz: Contact Radius and Loading

We consider quasi-static response at contact. Due to the elastic deformation of the sphere, contact develops when increasing the *load*  $F$ . Actually, by ‘contact’ we mean: inside the contact zone the normal displacement at the surface is specified so as to cancel the initial shape  $f(r)$ . In this way the *contact zone* is the area in which the normal surface displacement (imposed by the contact boundary conditions) are prescribed for the elastic problem. The short-range repulsion has actually been turned into displacement boundary conditions [2].

In addition to the load  $F$ , another characteristic of the contact is the *penetration*  $\delta$ . It is the rigid body displacement incurred by the undeformed parts of the sphere, far away from the contact. This rigid body displacement is made possible by the local deformation close to the contact area. Note that positive  $\delta$  means penetration while positive  $F$  means compression. For adhesionless contact the geometry is such that if the sphere were to rigidly interpenetrate the flat by the same penetration  $\delta_H(a)$ , then the undeformed sphere would intersect the  $r$  axis at a radius equal to  $\sqrt{2}a$  (Fig. 2.1b). From force and penetration, we can calculate the work expended by the *remote loading* to form the contact (frame 2), and also the work recovered when the contact breaks. A difference between these two means hysteresis and dissipation.

Coming closer to the contact itself, the geometry of the contact zone is defined by the *contact radius*  $a$ . To accommodate the deformation and especially the flattening of the parabolic profile (Eq. 2.1) of the elastic sphere inside the contact zone, a distribution of normal surface stresses arises at the interface. Hertz [3] demonstrated that the solution takes the form of an ellipsoidal distribution of *contact stresses*

$$\frac{\sigma(r)}{p_m} = \frac{3}{2} \sqrt{1 - (r/a)^2} \quad (2.3)$$

where  $p_m$  is the mean contact pressure.

The force as a function of contact radius is found from the integration of the contact stress distribution Eq. 2.3: in the Hertzian theory the (compressive) contact force is

$$F_H(a) = \frac{4E^*a^3}{3R} \quad (2.4)$$

and the mean pressure is

$$p_m \equiv \frac{F_H(a)}{\pi a^2} = \frac{4E^*}{3\pi} \frac{a}{R} \quad (2.5)$$

Finally the relation between penetration and contact radius results from the condition of zero stress at the contact edge and is

$$\delta_H(a) = \frac{a^2}{R} \quad (2.6)$$



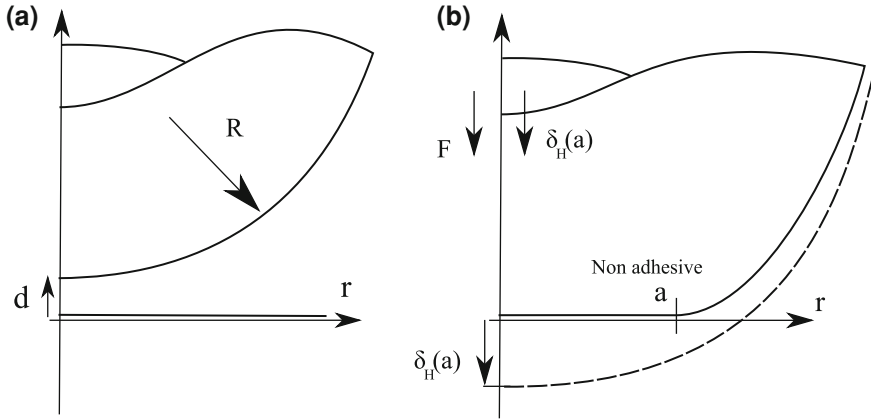


**Fig. 2.1** Adhesionless contact: **a** sphere of radius  $R$  approaching a plane at a distance  $\delta$ ; **b** after contact, when there is no adhesion: the contact radius is  $a$  and the penetration is  $\delta_H$ . The undeformed sphere shape (*dashed line*) intersects the  $r$  axis at  $\sqrt{2}a$

Appearances to the contrary this relation is highly non trivial and results from the calculation of the deformation *outside* the contact zone due to the stress distribution Eq. 2.3 inside.

Equations 2.4 and 2.6 are the contact equations for the adhesionless contact of an elastic sphere on a rigid plane as a function of contact radius  $a$ .

**Frame 2: Hertz model—Approximate derivation**

If we observe the deformation of the elastic body, the surface displacements are of the order of the penetration  $\delta$ . By a very approximate geometrical argument, we estimate

$$\delta R = a^2 \tag{2.7}$$

By Saint-Venant’s principle, we know that these displacements penetrate into the body over a typical distance equal to the contact radius  $a$ . As a result, the typical deformation is  $\delta/a$  and the elastic energy for the penetration  $\delta$  can be calculated as:

$$\varepsilon = \frac{1}{2} E \left( \frac{\delta}{a} \right)^2 a^3 \tag{2.8}$$

from which the relation for the force Eq. 2.4 results:

$$F(a) = \frac{d\varepsilon}{d\delta} \simeq \frac{E^*}{R} a^3 \tag{2.9}$$

and the stiffness defined by Eq. 2.11

$$S(a) \simeq E^* a \quad (2.10)$$

This last result is much more general than the specific case of sphere contact. Indeed it applies for all axisymmetric geometries (flat punch, cone) and depends only on the contact radius. The reason for this invariance is the absence of adhesion. The variation of the *contact radius* with penetration does depend on shape, but does not contribute to the stiffness because the stresses at the edge of the contact are zero. We will see in a later section that this result is significantly modified with adhesion, in which case these stresses are finite.

### 2.2.2 Contact Stiffness

For dynamic problems such as those of interest in this book, the quantity which is directly relevant is the contact stiffness defined by

$$S(a) \equiv \frac{dF}{d\delta} \quad (2.11)$$

In the Hertzian theory, the contact stiffness is given by the equation:

$$S(a) = 2aE^* \quad (2.12)$$

The most interesting feature is that the stiffness depends only on the contact radius  $a$ . This means that for different punch shapes and different loads, the same stiffness will be obtained if the contact radius is the same.

Since the contact radius  $a$  varies with load as Eq. 2.4, it is clear that the sphere contact—unlike a simple spring—does not have a constant stiffness, but that *stiffness increases as the load increases*. The consequences of this intrinsic nonlinearity will be emphasized in Sect. 2.8.1.

This result is remarkable because it was obtained in the framework of *linear* elasticity. The intimate reason is that the area over which the contact boundary conditions apply (specified by the contact radius  $a$ ) change as a function of loading. In this sense, contact is a typical example of geometrical nonlinearity.

## 2.3 Interactions: Adhesion

Adhesive interactions will modify this picture significantly. Let us consider again the case where the two surfaces face each other at some distance, as in Fig. 2.1a. We will briefly discuss these interactions, the force they produce on the tip and finally their impact when they couple with elastic deformation.

### 2.3.1 Interactions: Derjaguin Approximation

When surfaces are brought together within some distance  $d$ , they start to experience “long-range” interactions. The nature of the interactions involved is best investigated from the interaction *force* they produce, which can be measured by AFM or other devices such as Surface Forces Apparatus (SFA) [4]. Here, we consider the case where this interaction is attractive, eventually leading to adhesion.

We can quantify this attraction by an interaction potential  $V(h)$ .  $V$  is defined for two unit surface areas facing each other with a gap  $h$ . The reference state is for infinite separation so that  $V(\infty) = 0$ . In fact infinity is reached rapidly since the range of the interactions  $\delta_{\text{int}}$  is of the order of a few 10 nm or less. For a curved surface facing a flat at a distance  $d$ , there is a simple relation between the interaction force  $F(d)$  and the interaction potential  $V$ . This relation, called the Derjaguin approximation [5] (frame 3), which neglects all deformation induced by the interaction stresses, states that

$$F(d) = 2\pi R V(d) \quad (2.13)$$

Note that  $V$  must be negative for the attractive interactions to result in an attractive (*i.e.* negative) force.

#### Frame 3: Derjaguin approximation

Given the interaction potential, the normal surface stress distribution is obtained by Eq. 2.18. The surface integral of this stress distribution gives the total force

$$F(d) = 2\pi \int_0^{\infty} dr r \sigma(r) \quad (2.14)$$

Taking into account the parabolic shape Eq. 2.1, the surface integral can be turned into an integral over the gap  $h$  resulting into

$$F(d) = -2\pi \int_d^{\infty} R dh(r) \frac{dV}{dh} \quad (2.15)$$

from which Eq. 2.13 results.

### 2.3.2 Nature of the Interactions

A large variety of interactions has been identified, collectively known as surface forces. A full gamut of such interactions is to be found in polar liquids, especially

water, but this is less relevant to the present topic. In vacuum, electrostatic interactions give rise to complex problems due to their long-range nature, whereby simple calculations such as frame 3 do not apply.

### 2.3.2.1 Van der Waals Interaction

Van der Waals interactions are often quoted as the typical surface interactions. It is true that due to material polarisability, van der Waals interactions are always present. Moreover, they lend themselves to a degree of mathematical sophistication verging on fine art [6]. Finally, at longer distances they are well approximated by the simple analytic form:

$$V(h) = -\frac{A}{12\pi h^2} \quad (2.16)$$

where  $A$  is the *Hamaker constant*, of the order of  $1 \times 10^{-20}$  J. For all these reasons, van der Waals forces have become the archetype of surface forces.

Inserting Eq. 2.16 into Eq. 2.13 we obtain the van der Waals force between tip and substrate,

$$F(d) = -\frac{AR}{6d^2} \quad (2.17)$$

an expression which is often used in the literature (see Sect. 2.3.4).

We now turn to the *interaction stresses*  $\sigma_0$ . The normal stress at the surface resulting from the interactions is given by the derivative of the interaction potential:

$$\sigma(h) = -\frac{dV}{dh} \quad (2.18)$$

Typical values for interaction stresses resulting from van der Waals forces can be calculated using Eq. 2.18 with a cutoff distance of about 0.1 nm. A stress in the range of  $\sigma_0 \simeq 1$  GPa appears.

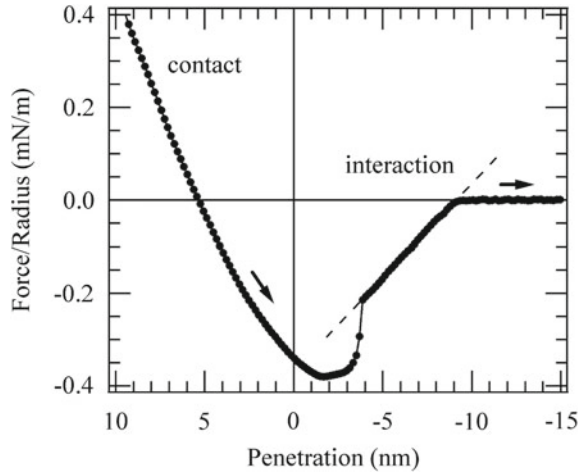
### 2.3.2.2 Liquid Meniscus

In ambient atmosphere, for hydrophilic surfaces, the interaction will be primarily mediated by a thin layer of adsorbed water, which forms a capillary bridge between the surfaces. This example has also been studied in great detail because it is both very frequent and relatively simple [7].

In this case the interaction stresses are a constant  $\sigma_0$  which is given by the hydrostatic pressure inside the liquid meniscus. If the liquid in the meniscus is at equilibrium, the chemical potential in the liquid is constant and so is the pressure. Then

$$\sigma_0 = \gamma/r_0 \quad (2.19)$$

**Fig. 2.2** Adhesive contact between sphere–plane silica surfaces. The interaction is mediated by a meniscus of liquid, with a linear force distance plot typical for an equilibrium state of the meniscus. After [8]



where the surface tension of the liquid  $\gamma$  lies around  $0.1 \text{ J/m}^2$  while the radius of curvature  $r_0$  of the liquid meniscus is, for ordinary vapor pressures, in the nanometer range. As a result the order of magnitude of the interaction stresses is significantly smaller for liquid meniscus than for van der Waals interactions, about  $100 \text{ MPa}$  at most.

In this case Eqs. 2.13 and 2.18 show that the interaction potential is linear, so that the force is:

$$F(d) = -2\pi R2\gamma \left(1 - \frac{d}{2r_0}\right) \quad (2.20)$$

for  $0 < d < 2r_0$ . The radius of curvature of the meniscus  $r_0$  is therefore also the range of the adhesive interactions. This linear behavior is clearly evidenced in some SFA experiments (Fig. 2.2).

### 2.3.3 Adhesive Contact with Weak Interactions

We now bring the surfaces into contact in the presence of adhesive interactions. The logical extension of the Derjaguin approximation is the Derjaguin Muller Toporov (DMT) model [9], which assumes that contact occurs exactly as with the Hertzian model (Sect. 2.2.1). Here, it is considered that the interaction stresses do not bring about significant deformation of the elastic bodies, and the force resulting from this interaction  $F_{\text{stress}}$  can be calculated as if acting on a body deformed by the contact stress distribution only. Put otherwise, we assume that the magnitude of the contact stresses largely exceed the interaction stresses. If calculated strictly, the details of this model are rather tedious [10] but a good approximation has been provided by Maugis [11]. He has suggested a Hertzian model plus a constant force offset

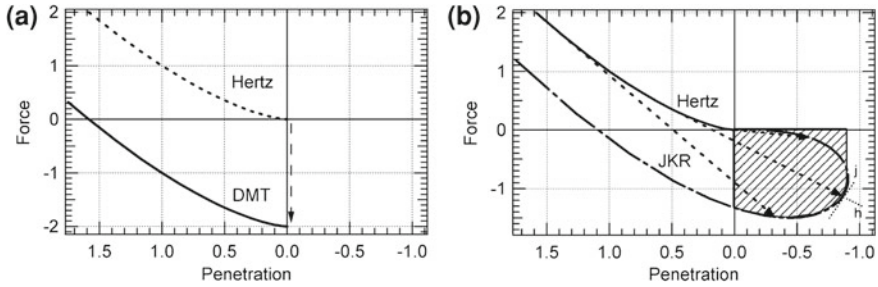


**Fig. 2.3** **a** Hertz versus DMT model in normalized units. The DMT model results from a simple force offset. **b** Hertz versus JKR model. The JKR is obtained by point by point translation along the tangent to the Hertz model by a displacement equal to the neck height  $\delta_{\text{adh}}$ . The shaded area is the energy expended in the stretching of the neck. Also shown as *small dashed lines* are the contact stiffnesses for fixed contact radius (Hertzian stiffness, marked ‘j’) and for free contact radius (JKR stiffness, marked ‘h’) (see Sect. 2.8.5). Note that in the extreme case selected here, these two stiffnesses actually have opposite signs

$$F_{\text{stress}} = -2\pi w R \quad (2.21)$$

resulting in a remote loading (Fig. 2.3a)

$$F(a) = F_H(a) - 2\pi w R \quad (2.22)$$

Continuity with Eq. 2.13 is ensured because the adhesion energy  $w > 0$  obeys

$$w = -V(d = 0) \quad (2.23)$$

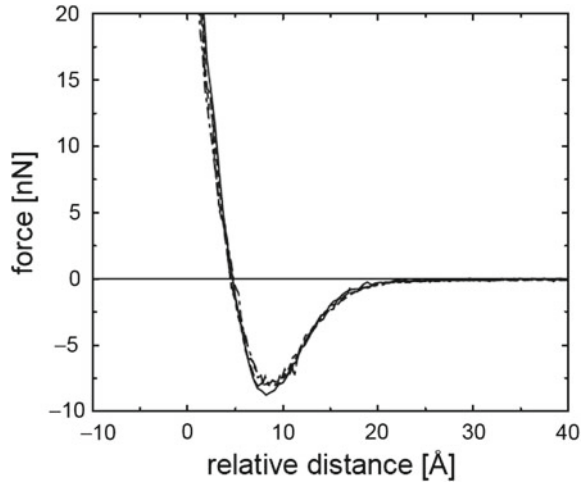
From Eq. 2.22, it becomes clear that the main effect of adhesion is to increase the contact radius for a same external load, since the load acting on the contact  $F_H(a)$  is the remote loading  $F(a)$  plus the adhesive contribution  $2\pi w R$ . Energy is gained from the adhesive interactions but balanced by the increased elastic energy stored due to larger contact area.

In the DMT model however, the contact stiffness is not affected by the interaction. For the same contact radius it is still given by the Hertzian expression Eq. 2.12.

### 2.3.4 Impact of Adhesion on Dynamic Response in AFM

Direct evidence for such long-range interactions has been found in various types of AFM measurements. Here, we illustrate the concept in an experimental configuration where oscillation amplitudes much larger than the interaction range are used. The oscillatory motion of the tip can be fully reconstructed, duly taking into account the small part of the trajectory where interaction of the tip with the surface occurs [12].

**Fig. 2.4** Reconstruction of the interaction potential from the large amplitude oscillatory response of an AFM tip-cantilever. Beyond 10 Å a van der Waals attractive potential is evidenced while the contact compliance sets in at smaller relative distances. From [12]. Copyright (1999) by the American Physical Society



Long-range interactions and contact have been taken into account using Eqs. 2.17 and 2.22 respectively. Profiles of such interactions between a tungsten tip and a silicon substrate has being inferred from the measured frequency and phase shifts (Fig. 2.4) and found to agree well with van der Waals forces.

#### **Frame 4: Adhesive contact—Approximate derivation**

The true nature of the adhesive contact of a curved body is a competition between a gain in adhesion and the ensuing elastic energy penalty (Hertzian term). In the DMT model, the energy gain is obtained from the integral of the interaction potential over the gap as in the calculation of the Derjaguin approximation (frame 3).

In another approach [5], the adhesive energy gain is estimated from the adhesion energy  $w$  and the contact area so that the total energy is

$$\varepsilon \simeq \frac{1}{2} E \left( \frac{\delta}{a} \right)^2 a^3 - \pi w a^2 \quad (2.24)$$

The relation for the force is

$$F(a) = \frac{d\varepsilon}{d\delta} \simeq \frac{E^*}{R} a^3 - \pi R w \quad (2.25)$$

showing that the adhesive contribution is of the order of  $\pi R w$ .

Although this rough estimate is useful for a preliminary discussion, the derivation we have used is actually flawed. In writing the adhesive term  $\pi w a^2$  we implicitly assumed that for an infinitesimal variation of the contact radius  $a$ , the variation in adhesion energy is proportional to the variation of contact area. This implies that the gap shape around the contact edge is sharp enough to exhaust the interaction range. However such a sharp gap shape has an elastic energy penalty which must be taken into account as in Sect. 2.4.

## 2.4 Coupling with Strong Interactions

So far, the coupling was quite simple since elastic deformation results from the contact stresses only (Eq. 2.3). Further difficulties arise when the adhesive stresses themselves are large enough to induce significant deformation of the surface, bringing more than a simple additional load (frame 4).

### 2.4.1 JKR Model

Taking this additional surface deformation into account is a more complex problem. Fortunately, the limit case where considerable deformation occurs can be treated relatively simply.

#### Frame 5: The JKR model

The flat punch elastic energy is

$$\varepsilon = \frac{1}{2} E \left( \frac{\delta}{a} \right)^2 a^3 \quad (2.26)$$

so that the energy release rate is

$$\mathcal{G} = \frac{1}{2\pi a} \frac{d\varepsilon}{da} \simeq E^* \frac{\delta^2}{a} \quad (2.27)$$

Equilibrium results from

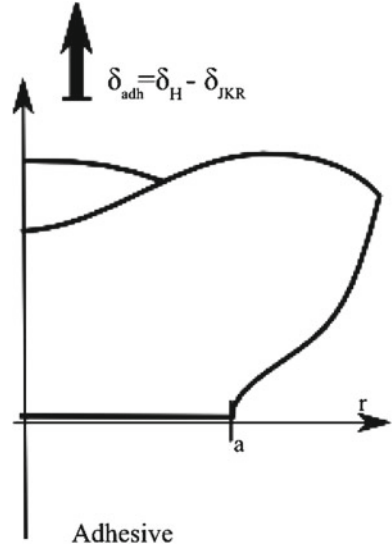
$$\mathcal{G} = w \quad (2.28)$$

so that

$$\delta_{\text{adh}} \simeq \sqrt{\frac{aw}{E^*}} \quad (2.29)$$



**Fig. 2.5** Adhesive contact: cusp at the contact edge in the JKR model, demonstrating the typical JKR flat punch displacement



Johnson, Kendall and Roberts (JKR) have shown that the deformation induced by the interactions amounts to an additional flat punch deformation (Fig. 2.5). The resulting flat punch displacement (see frame 5) is central to the JKR theory [13]:

$$\delta_{adh} = \sqrt{\frac{2\pi aw}{E^*}} \quad (2.30)$$

Here, we take  $\delta_{adh}$  positive but in fact adhesion induces a reduction of the penetration (for a given contact radius) so that a minus sign appears in the contact equations:

$$\delta_{JKR}(a) = \delta_H(a) - \delta_{adh}(a) \quad (2.31)$$

$$F_{JKR}(a) = F_H(a) - S(a)\delta_{adh}(a) \quad (2.32)$$

The force has been derived using the flat punch displacement and stiffness according to Eq. 2.12. This adhesive contribution in Eqs. 2.31 and 2.32 amounts to a translation along the tangent to the Hertzian curve, which is schematized in Fig. 2.3b. The set of Eqs. 2.30, 2.31 and 2.32 together forms the JKR theory. Note that these equations are often presented spelled out, which may be less illuminating.

## 2.4.2 Pull-Out Force

The *pull-out force* is the maximum tensile force which needs to be applied to break the adhesive contact and rip the sphere off the surface. Somewhat by accident, and

for the sphere only, the pull-out force is nearly independent of the type of adhesive contact model

$$F = -\alpha\pi wR \quad (2.33)$$

It is clear that  $\alpha = 2$  in the DMT limit. From Eq. 2.32 and looking for the minimum, we can calculate that  $\alpha = 3/2$  in the JKR case. This value results from the balance of the two energy terms: around pull off, both (compressive) contact load and (tensile) interaction load are of the order of  $\pi wR$ .

#### Frame 6: Is adhesion relevant ?

Equation 2.33 is specific to the sphere geometry. Most if not all other cases (tip shapes or symmetry) do not offer the same simplicity. Under the assumption of sphere geometry, a question in order is: under which type of loading is adhesion relevant? To answer this question we balance interaction load (of the order of  $\pi wR$ ) and contact load. From 2.24 we deduce that adhesion steps in when

$$a \simeq \left( \frac{\pi R^2 w}{E^*} \right)^{1/3} \quad (2.34)$$

The contact load turns out to be dominant above these values of contact radius. In our case, for a comparatively rigid solid, this contact radius is of the order of 1 nm and the load is of the order of 10 nN.

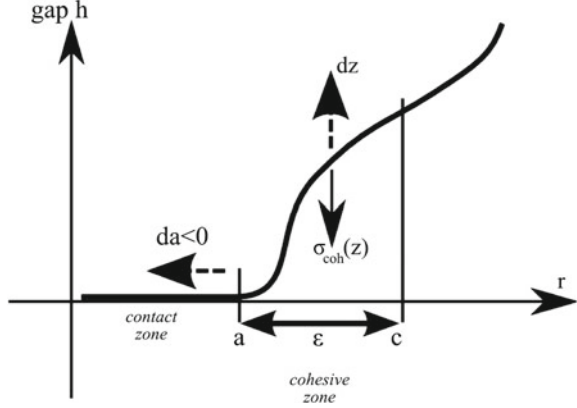
If the pull-out force is barely dependent upon the model, a question may arise: is the choice of contact model of limited consequences and somewhat arbitrary or is there a good reason to pay attention to which contact model to use? If the pull-out force is not very revealing itself, these contact models involve *very different stress distributions*: beyond the mere pull-out force, model-dependent responses are to be expected. This is the case for example in Sects. 2.7 and 2.8. For this reason a more general picture is needed and we now consider how the adhesive interactions are coupled with the contact problem in more detail.

## 2.5 AFM Tips: An Intermediate Case?

### 2.5.1 Adhesive Interactions Revisited: Contact Problem

In fact in both the DMT and the JKR models, the details of the interactions do not appear. We are dealing with limit cases and in the end the adhesion energy  $w$  remains as the only relevant parameter for the description of the physical process of adhesion. In the more general case, the adhesive interactions induce tensile stresses over some area around the contact zone: this area is called the *cohesive zone* (Fig. 2.6). Due to the finite range of the interactions the cohesive zone extends over a distance

**Fig. 2.6** Adhesive contact: schematics of the impact of adhesive interactions on the local deformation around the contact zone (cohesive zone model).  $c$  is the outer limit of the region over which interaction stresses act. Finite range of the interactions result in a lateral extension  $\epsilon = c - a$  of the area over which the interaction stresses operate



$\epsilon = c - a$ . This distance will come out useful when the dynamics of the contact edge is calculated (Sect. 2.8).

In the general case, calculation of the impact of the interaction stresses on the deformation is not an easy task. For recent attempts see [14, 15]. None of these models lends itself to simple explanations however. Let us only mention that the calculation proceeds as in frame 3, but this time taking into account the deformation directly due to the interaction stresses. The contact equations are then

$$\delta_{\text{JKR}}(a) = \delta_H(a) - \delta_{\text{adh}}(a) \quad (2.35)$$

$$F_{\text{JKR}}(a) = F_H(a) - S(a)\delta_{\text{adh}}(a) - F_{\text{stress}} \quad (2.36)$$

revealing the mixed JKR–DMT character of the solution. However, neither  $\delta_{\text{adh}}(a)$  nor  $F_{\text{stress}}$  is given by the JKR (Eq. 2.30) or DMT (Eq. 2.21) model but rather by one of the more general expressions available in the literature, such as [2, 11, 16].

In these models the interaction stresses are defined by Eq. 2.18 where  $h$  is the gap between the surfaces. They form the boundary conditions outside the contact area. There is a difficulty: due to elastic response the gap itself is affected by the interaction stresses. As a result a self-consistent treatment is called for. It has been shown that the finer details of the interaction potential (or the surface stress distribution) are not relevant and play a role only to higher order [2]. Therefore, in most cases, for the coupling between the interactions and the contact mechanics, only two entities must be considered: adhesion energy  $w$  and the interaction stresses with magnitude  $\sigma_0$ . In this context, following Eqs. 2.18 and 2.23, it appears that the range of the interactions  $\delta_{\text{int}}$  obeys

$$\delta_{\text{int}}\sigma_0 \simeq w \quad (2.37)$$

For numerical simplicity, the interaction stresses are often considered constant throughout the cohesive zone [11]. This is the so-called Dugdale-Barrenblat model. In the case of the Dugdale-Barrenblat model, in Eq. 2.37 equality applies.

### 2.5.2 Which Model: Does Adhesion Induce Deformation?

We now discuss the general features of the adhesive contact depending upon interaction, loading, and geometry, in the spirit of the “adhesive map” by Greenwood and Johnson [17]. The relevance of the adhesive contribution is examined in frame 6. Here, we consider whether adhesion affects deformation or not, i.e., whether we are close to the DMT or to the JKR model or in some intermediate case. Based on our earlier considerations on interaction stresses, a characteristic parameter emerges when comparing interaction stresses and contact stresses. We introduce the Tabor parameter [18]

$$\lambda \simeq \frac{\sigma_0}{\sigma} \quad (2.38)$$

where  $\sigma$  stands for the contact stresses.

In the absence of adhesion  $\sigma = p_m$  (Sect. 2.2.1). In the range where adhesion is significant (frame 6), the load  $F$  is of the order of  $\pi w R$  and the contact stresses are

$$\sigma = \frac{F}{\pi a^2} \simeq \left( \frac{w E^* a^2}{\pi^2 R} \right)^{1/3} \quad (2.39)$$

An interesting consideration arises if the Tabor parameter  $\lambda$  is expressed in terms of penetration: then it is found that

$$\lambda \simeq \frac{\delta_{\text{adh}}}{\delta_{\text{int}}} \quad (2.40)$$

If the flat punch displacement  $\delta_{\text{adh}}$  is large compared to the range of the interactions  $\delta_{\text{int}}$ , then the cohesive zone size is small, and adhesion energy is transferred between the interface and the tip by large elastic deformations located close to the contact edge as embodied by the flat punch displacement, resulting in the neck at the contact edge (Fig. 2.5). This is a fracture-like process, central to the JKR limit.

Note however that the neck has to be stretched out upon rupture. However when the sphere comes to the surface, contact forms at a penetration equal to zero since the interaction is short ranged. As a result, hysteresis appears, as illustrated by the shaded area in Fig. 2.5b.

On the contrary, if the flat punch displacement is comparatively small ( $\lambda \ll 1$ ), adhesion energy transfer operates directly through the work done by the interaction stresses in the displacement of the sphere surface. This is the DMT limit where the cohesive zone size is large. Since the interaction range is large the contribution of the interaction to the stiffness is zero, and the stiffness is the Hertzian stiffness as already mentioned.

Intermediate cases appear for  $\lambda \simeq 1$ .

### 2.5.3 Small Tips

Given the typical values for interactions and the typical contact radii of AFM tips, we find that for comparatively rigid surfaces  $\delta_{\text{adh}}$  is of the order of 0.1 nm. It is quite clear that the pure JKR theory is unlikely to apply in our case.

This means that the tip has to be considered as comparatively rigid compared to the attractive interactions. The deformation incurred during the adhesive contact is primarily the deformation of the Hertzian adhesionless contact but for the stiffer types of adhesive interactions, with small decay lengths,  $\lambda$  may range around 1 and the adhesive contact acquires partial JKR character. This is typically the case for ultra-high vacuum measurements. An example of such a case is shown in Fig. 2.7. In contrast, under ambient conditions a longer ranged interaction dominates, which is due to the presence of adsorbed water. The resulting meniscus induces an interaction shown in Fig. 2.2 with a range of several nanometers, and the contact will be in a typical DMT state. One of the rare cases where a contact close to a true JKR case could be obtained is polymeric surfaces where low modulus and high effective adhesion energies are expected to result in large  $\lambda$  through Eqs. 2.30 and 2.40.

For small tips, in the intermediate range, the cohesive zone size is of the order of the adhesive contact radius and the typical contact stresses upon pull-off are in the range of  $\sigma_0$ . This is similar to fiber problems: the average stress at the surface of the tip, or rupture stress increases dramatically and eventually reaches the theoretical interface stress when the size of the contact area decreases [19, 20].

## 2.6 Films

Thin films and coatings are ubiquitous in technological applications. Here, we consider the case of contact to coated substrates.

### 2.6.1 Stiffness

As mentioned earlier (frame 2), the deformation field affects the elastic body to a typical depth of the order of the contact radius  $a$ . It is important to note that this depth is only indirectly related to the penetration  $\delta$ , through Eq. 2.6 for example. In the case of an elastic property mismatch between the coating and the substrate, the macroscopic response will be affected by the presence of the substrate beneath the film if the film thickness is less than several times the contact radius. To estimate the impact of the film, one can suggest to use Eq. 2.6 with film values to infer the contact radius. It will be necessary to consider the full solution if this contact radius is not significantly smaller than the film thickness. If this is the case, exact solutions have been calculated [23–25] which can be used fairly easily.

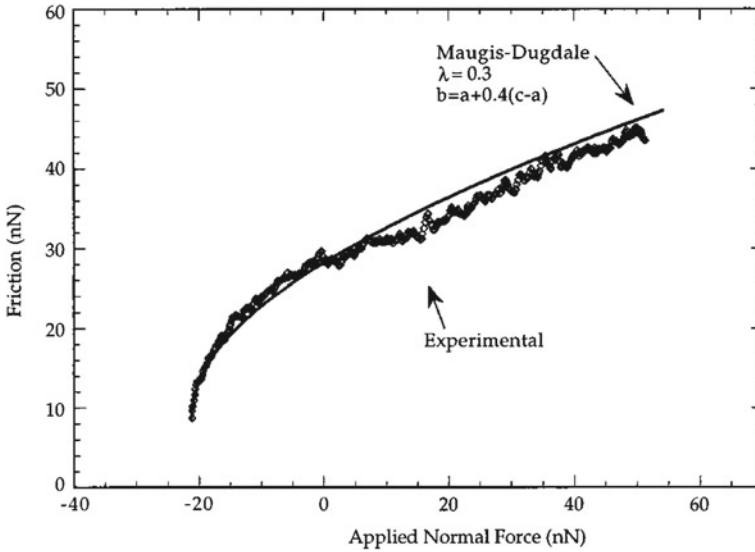


**Fig. 2.7** Friction force (assumed to be proportional to contact area) and model for the adhesive contact area as a function of load. The data are best fitted with an intermediate adhesive contact model where neither pure JKR nor pure DMT models apply. From [21]. Copyright (1997) by the American Physical Society

Note that the problem is especially significant in the case of an elastomeric film, which is somewhat liquid-like and therefore incompressible. Due to the suppression of shear deformation because of confinement, the effective response of the film (Fig. 2.8) is driven by the bulk modulus which is considerably larger than the shear modulus because of incompressibility.

### 2.6.2 Adhesion

For adhesive contacts, the film may have two very different types of impacts. On the one hand, the film is likely to change the interactions between the tip and the surface, and thus the values of the adhesion energy  $w$  and the interaction stresses  $\sigma_0$ . On the other if the film thickness is not large enough according to the criterion outlined above, then the substrate effect will affect the contact response. The contact equations should then take adhesion into account [26]. In the more elaborate case where contact zone radius, film thickness, and cohesive zone size become comparable, recent calculations could become useful although they are by no means numerically simple [27].

Note however that a most salient feature in this case is that, for identical adhesion energy  $w$ , the pull-out force is barely affected by the presence of the coating. This idea

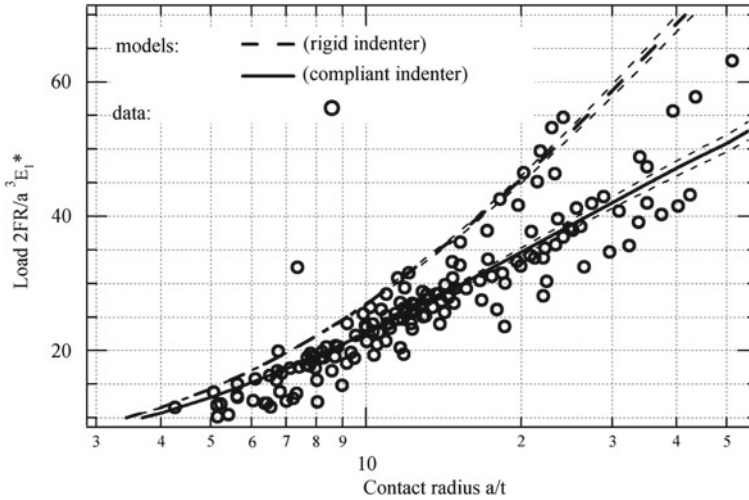


**Fig. 2.8** Load as a function of normalized contact radius for sphere–plane contacts on acrylate films. Confinement results in an increase of the film modulus so that the glass sphere compliance must be taken into account. Adapted from [22] with permission from Springer

must be brought in relation to our previous remark in Sect. 2.4.2: the pull-out force results from a balance between contact and adhesion energies. The result turns out to be independent from the mechanical properties of the half-space if it is homogeneous. In fact, this dependence is only barely reintroduced if homogeneity is lost as when a coating is present.

## 2.7 Roughness

Generally speaking, surface roughness impacts contact problems strongly. However, the real complexity arises from the statistical nature of the roughness coupled to the nonlinear nature of even the most basic contact, namely Hertzian contact [28]. In this sense roughness is likely to alter the qualitative response of a contact. The simplest possible example is an exponential distribution  $n \propto \exp(-z/\tau)$  of summit heights with identical curvatures  $R^{-1}$ . Here,  $\tau$  is the standard deviation of the roughness. Then the density  $d_c$  of summits in contact with a flat surface obeys

$$d_c \propto \exp(-d/\tau) \quad (2.41)$$

where  $d$  is counted from the mid-plane of summit heights. Summing individual summit areas and forces over this exponential distribution we obtain that both total area and total force are also proportional to  $d_c$ . As a result, and in contrast to the

results of Sect. 2.2.1, force and true contact area are now proportional, an idea which is central to our understanding of the laws of friction [29].

In addition, roughness will compete with attractive interactions. It is this issue for which more insight can be provided. In terms of adhesive contact, it is well known in practice that for rather rigid materials, a very limited amount of roughness suppresses the adhesion of a sphere brought to a surface. For weak interaction stresses as in the DMT contact model, the typical lengthscale involved is the interaction range  $\delta_{\text{int}}$ . It is clear that for a roughness  $\tau$  small compared to this interaction range the attractive interactions can still be accounted for as in Sect. 2.3.3. In the other limit where the deformation incurred through attractive interactions are sizeable, the characteristic distance which emerges is the JKR flat punch displacement  $\delta_{\text{adh}}$ . This idea has been elegantly demonstrated by Fuller and Tabor [30]. A handwaving argument goes as follows: the (tensile) contribution of each asperity to the adhesion force is a constant of the order of  $\pi w R$ ; on the other end, the (compressive) contact force generated by each asperity grows faster than linearly with penetration  $\delta$ , following Eq. 2.4. For a roughness distribution with standard deviation  $\tau$ , the sum of the repulsive contributions will far exceed the attractive contributions if the roughness distribution obeys

$$\tau \gtrsim \delta_{\text{adh}} \quad (2.42)$$

For the case of interest here, it is possible that the tip will interact with a limited number of asperities. In this case the statistical approaches are of a somewhat limited relevance and one must rely on the more demanding and less general calculation of distributions of local configurations [31].

## 2.8 Dynamics

We now consider a tip impinging on a surface. In keeping with the rest of this chapter, the viewpoint is the mechanics of a sphere touching a surface. The sphere is considered as free, with initial velocity  $v_0$ , and the rest of the system, and especially the cantilever and its mechanics, is not taken into account. Our aim is to understand dissipation during contact. However, this part of the question is much less advanced than the quasistatic part.

In agreement with the views developed here, friction is not considered, although in some cases it could account for a significant part of dissipation during dynamic contacts. In this restricted frame, the dissipated energy is all the energy which is not fed back to the remote loading when the surfaces have ceased to interact. There are many processes active in this area. For the adhesionless contact, two processes fail to restore all the energy injected in the contact: (1) acoustic emission and (2) material dissipation, which may occur through delayed elastic response (viscoelasticity) or non-elastic response (plastic deformation). If adhesion is present, several additional processes must be mentioned: (3) the physics of adhesion may be partly irreversible (the adhesion energy is different for a growing and a receding interface); and if



adhesion induces additional deformation, as in cases close to the JKR limit: (4) the rupture may occur by instability and part of the energy involved is not restored to the remote loading; (5) material dissipation (as in 2) may result from deformations specific to the adhesive process.

In this area, the number of in-depth studies is quite restricted. Here, we will only hint at a few directions. We will start from the (reversible) elastic rebound of an adhesionless sphere. Then we will qualitatively consider the impact of dissipative mechanisms (1), (2), (4), and (5).

### 2.8.1 Sphere Impact

If we assume a free sphere of mass  $m$  impinging on an elastic adhesionless surface, contact leads to rebound. Taking into account the non-constant stiffness at contact (Sect. 2.2.2), conservation of energy during rebound implies

$$\frac{1}{2}m \left( \frac{d\delta}{dt} \right)^2 + \frac{8}{15}E^*\sqrt{R}\delta^{5/2} = \frac{1}{2}mv_0^2 \quad (2.43)$$

where  $v_0$  is the sphere velocity at impact. Maximum penetration occurs when  $\frac{d\delta}{dt} = 0$  so that

$$\delta_{\max} = \left( \frac{mv_0^2}{\frac{16}{15}E^*\sqrt{R}} \right)^{\frac{2}{5}} \quad (2.44)$$

$$a_{\max} = \left( \frac{mv_0^2 R^2}{\frac{16}{15}E^*} \right)^{\frac{1}{5}} \quad (2.45)$$

To evaluate the rebound,  $d\delta/dt$  can be integrated numerically from Eq. 2.43. In fact a linear approximation

$$\frac{\delta}{\delta_{\max}} = \sin \left( \pi \frac{t}{T_c} \right) \quad (2.46)$$

has been shown to perform well [32], where the typical contact time is

$$T_c = \alpha \frac{\delta_{\max}}{v_0} \simeq 3 \left( \frac{m^2}{E^{*2} R v_0} \right)^{\frac{1}{5}} \quad (2.47)$$

### 2.8.2 Inertial Effects

Dealing with acoustic frequency excitations, it is useful to estimate whether inertial effects are significant, that is to say whether acoustic waves will be generated during such a contact. An estimate can be obtained as follows: an acoustic mode obeys

$$\rho \frac{dv}{dt} = -\text{div}\sigma \quad (2.48)$$

where  $v$  is the velocity field,  $\rho$  the density, and  $\sigma$  the stress field. Order of magnitude estimates from frame 2 show that we remain in the quasistatic limit as long as

$$\rho \frac{\delta}{T_c^2} \ll E \frac{\delta}{a^2} \quad (2.49)$$

or

$$\frac{a_{\max}}{T_c} \ll \sqrt{E/\rho} \quad (2.50)$$

which is the sound velocity. For a free sphere with incident velocity  $v_0$  and mass  $m$ , the criterion is

$$\left( \frac{E^* v_0^3 R^3}{m} \right)^{\frac{1}{5}} \ll \sqrt{E/\rho} \quad (2.51)$$

which is consistent with standard estimates of the dissipation induced by acoustic waves during contacts (Eqs. 11 and 12 in [32]). For a free sphere of mass  $m$ , the criterion becomes independent upon radius since  $m \propto \rho R^3$ . For an incident velocity of about  $1 \times 10^{-2} \text{ ms}^{-1}$ , a high value for a tip touching a surface, it appears that acoustic emission is negligible.

### 2.8.3 Material Dissipation: Contact Area

To account for dissipation during contact, we couple contact zone deformation with out-of-phase material response. This case has been considered in a classical paper [33] with a viscous type of dissipation. The viscous constant  $\eta$  relates dissipative stress to deformation rate. If  $v_1$  is the velocity of the sphere after contact (see frame 7)

$$\frac{v_1}{v_0} = 1 - g v_0^{1/5} \quad (2.52)$$

where

$$g \simeq \frac{\eta}{E^*} \left( \frac{E^* \sqrt{R}}{m} \right)^{\frac{2}{5}} \quad (2.53)$$

To relate the viscous parameter  $\eta$  with materials properties, it should be noted that the characteristic frequency is

$$\omega \simeq \frac{1}{T_c} \quad (2.54)$$

For elastomers the estimate seems consistent with the observed dissipation parameter  $v/v_0 \simeq 0.65$  [34].

### Frame 7: Contact—Dissipation

In the spirit of frame 2, we assume the elastic solution is perturbed by a first order dissipative term.

$$\sigma_{\text{visc}} \simeq \eta \dot{\epsilon} \quad (2.55)$$

where strain is

$$\epsilon \simeq \frac{\delta}{a} \quad (2.56)$$

and strain rate

$$\dot{\epsilon} \simeq \frac{\delta}{a T_c} \quad (2.57)$$

The elastic and the dissipative terms are in parallel. Then the energy dissipated during one contact is

$$\mathcal{E}_{\text{diss}} \simeq \eta \dot{\epsilon} \epsilon a^3 \simeq \eta \delta_{\text{max}} a_{\text{max}} v_0 \quad (2.58)$$

From energy balance

$$\frac{1}{2} m v_1^2 + \mathcal{E}_{\text{diss}} = \frac{1}{2} m v_0^2 \quad (2.59)$$

so that for small velocity variations

$$\frac{v_1}{v_0} \simeq \frac{\mathcal{E}_{\text{diss}}}{\frac{1}{2} m v_0^2} \quad (2.60)$$

from which Eq. 2.52 results.

## 2.8.4 Adhesion Hysteresis: Elastic Instability

If the contact is in a JKR type of limit, then the neck formed upon contact needs to extend up to  $\delta_{\text{adh}}$  before rupture occurs. Using Eqs. 2.30 and 2.34 this stretching energy is about

$$\mathcal{E} \simeq \left( \frac{\pi^2 R^4 w^5}{E^2} \right)^{\frac{1}{3}} \quad (2.61)$$

This energy is spent by the remote loading to stretch the neck but is not gained upon coming-in since the interaction range  $\delta_{\text{int}} \ll \delta_{\text{adh}}$  is small and the neck does not form during surface approach. In short, this is the amount of energy lost in one contact cycle. This elastic instability is a common mechanism for adhesive energy dissipation [35, 36]. Of course, if  $\lambda$  is of the order of one (i.e. we are not in a full JKR case) only a *fraction* of this energy will be dissipated by instability.

### 2.8.5 Material Dissipation: Contact Edges

In the same regime, dissipation induced by material response may occur due to high rate deformation close to the contact edge. This is often the case for polymeric materials. The additional dissipation incurred can be phenomenologically modeled as an effective adhesion which depends upon contact edge velocity  $da/dt$  [37] as

$$G(da/dt) = w(1 + \phi(da/dt)) \quad (2.62)$$

where power laws are often used for the dissipative function  $\phi$ . Relation between  $\phi$  and the dynamic response of the polymer involved has been demonstrated experimentally [37] but theoretical justifications involving contact edge deformation processes are only partly successful to date [38–41].

Nonetheless, the phenomenological relation Eq. 2.62 is very useful. As an example we consider again the rebound dynamics for macroscopic balls [34]. During rebound, the characteristic velocity is

$$\frac{da}{dt} \simeq \frac{a_{\text{max}}}{T_c} \quad (2.63)$$

and the characteristic angular frequency is

$$\omega \simeq \frac{1}{\epsilon} \frac{da}{dt} \simeq \frac{a_{\text{max}}}{\epsilon} \frac{1}{T_c} \quad (2.64)$$

where  $\epsilon$  is the cohesive zone size. Note that for a macroscopic sphere, this frequency is much higher than for contact zone dissipation (Eq. 2.54), due to the typical small size of the cohesive zone. The additional dissipated energy is

$$\mathcal{E}_{\text{diss}} \simeq \pi a_{\text{max}}^2 G(da/dt) \quad (2.65)$$

The results fit rebound experiments on elastomers extremely well [34].

Another remarkable result is that in an oscillatory experiment the stiffness of a JKR contact depends upon frequency in a non-trivial manner. Indeed, for dissipative materials, the high frequency motion of the contact edge may be hindered by large dissipation at high strain rates. Then the stiffness must be calculated *at constant contact radius*: it is the Hertzian stiffness. On the other hand, at comparatively low frequencies, the contact edge is free to move during oscillations and the contact stiffness must be calculated from Eq. 2.32 *at constant adhesion energy*. These two cases have been shown in Fig. 2.3b) as two straight lines marked  $h$  (Hertzian stiffness) and  $j$  (JKR stiffness). This transition has been very clearly observed for polydimethylsiloxane (PDMS) elastomers by oscillatory nanoindentation experiments with a micron-sized sphere [42].

## 2.9 Conclusion

We have outlined a few results on the adhesive contact of tips to surfaces. We have drawn on the body of theories devoted to spheres to discuss contact and the resulting contact stiffness.

We have emphasized the fact that in the presence of attractive interactions, leading to adhesion, the results are impacted in a non-trivial way. We have briefly discussed typical interactions which can be met with during AFM operation. We have shown in which way these interactions couple with elastic deformation. If the surface compliance is low enough, the adhesive interactions induce additional local deformation which alter the physics of the contact. Due to their small radius, AFM tips were shown to lie in the stiff to intermediate regime. Pure JKR case is not expected.

The impact is not directly perceptible from the bare pull-out force. Even when homogeneity breaks down, such as with a coating, the pull-out force is still only very moderately affected. More contrast appears when dealing with rough surfaces. However, it is when the dynamics of the response is considered that the strong impact of the low surface compliance really appears in full light, resulting in additional, specific dissipation mechanisms.

## References

1. Y.Y. Lin, H.Y. Chen, Effect of large deformation and material nonlinearity on the JKR (Johnson-Kendall-Roberts) test of soft elastic materials. *J. Polym. Sci. B: Polym. Phys.* **44**, 2912–2922 (2006)
2. E. Barthel, On the description of the adhesive contact of spheres with arbitrary interaction potentials. *J. Colloid Interface Sci.* **200**, 7–18 (1998)
3. H. Hertz, Ueber die Berührung fester elastischer Körper. *J. Reine Angew. Math.* **92**, 156–171 (1881)
4. J.N. Israelachvili, *Intermolecular and Surface Forces* (Academic Press, San Diego, 1992)
5. B.V. Derjaguin, Untersuchungen über Die Reibung und Adhäsion. *Kolloid Zeitschrift* **69**, 55–164 (1934)

6. V.A. Parsegian, *Van der Waals Forces* (CUP, New York, 2006)
7. E. Charlaix, M. Ciccotti, Capillary condensation in confined media, in *Handbook of Nanophysics: Principles and Methods*, ed. by K. Sattler (CRC Press, Boca Raton, 2010)
8. E. Barthel, X.Y. Lin, J.L. Loubet, Adhesion energy measurements in the presence of adsorbed liquid using a rigid surface force apparatus. *J. Colloid Interface Sci.* **177**, 401–406 (1996)
9. B.V. Derjaguin, V.M. Muller, YuP Toporov, Effect of contact deformation on the adhesion. *J. Colloid Interface Sci.* **53**, 314 (1975)
10. R.M. Pashley, P.M. McGuiggan, B.W. Ninham, J. Brady, D.F. Evans, Direct measurements of surface forces between bilayers of double-chained quaternary ammonium acetate and bromide surfactants. *J. Phys. Chem.* **90**, 1637–1642 (1986)
11. D. Maugis, Adhesion of spheres: the JKR-DMT transition using a Dugdale model. *J. Colloid Interface Sci.* **150**, 243–269 (1992)
12. H. Hölscher, W. Allers, U.D. Schwarz, A. Schwarz, R. Wiesendanger, Determination of tip-sample interaction potentials by dynamic force spectroscopy. *Phys. Rev. Lett.* **83**(23), 4780–4783 (1999)
13. K.L. Johnson, K. Kendall, A.D. Roberts, Surface energy and the contact of elastic solids. *Proc. Roy. Soc. A* **324**, 301–313 (1971)
14. J.A. Greenwood, The theory of viscoelastic crack propagation and healing. *J. Phys. D: Appl. Phys.* **37**, 2557–2569 (2004)
15. E. Barthel, A. Perriot, Adhesive contact to a coated elastic substrate. *J. Phys. D: Appl. Phys.* **40**, 1059–1067 (2007)
16. J.A. Greenwood, K.L. Johnson, An alternative to the Maugis model of adhesion between elastic spheres. *J. Phys. D: Appl. Phys.* **31**, 3279–3290 (1998)
17. K.L. Johnson, Contact mechanics and adhesion of viscoelastic solids, in *Microstructure and Microtribology of Polymer Surfaces*, ed. by K.J. Wahl, V.V. Tsukruk (ACS, Washington, 2000), p. 24
18. D. Tabor, Surface forces and surface interactions. *J. Colloid Interface Sci.* **58**, 2 (1977)
19. C.-Y. Hui, N.J. Glassmaker, T. Tang, A. Jagota, Design of biomimetic fibrillar interfaces: 2 mechanics of enhanced adhesion. *J. R. Soc. Interface* **1**, 35–48 (2004)
20. H. Gao, H. Yao, Shape insensitive optimal adhesion of nanoscale fibrillar structures. *PNAS* **101**(21), 7851–6 (2004)
21. M.A. Lantz, S.J. O’Shea, M.E. Welland, Atomic-force microscope study. *Phys. Rev. B* **55**, 10776 (1997)
22. E. Gacoin, A. Chateauinois, C. Frétygny, A. Perriot, E. Barthel, Measurement of the mechanical properties of thin films mechanically confined within contacts. *Tribol. Lett.* **21**, 245–52 (2006)
23. H.J. Gao, C.H. Chiu, J. Lee, Elastic contact versus indentation modeling of multi-layered materials. *Int. J. Solids Struct.* **29**, 2471–2492 (1992)
24. A. Perriot, E. Barthel, Elastic contact to a coated half-space: effective elastic modulus and real penetration. *J. Mater. Res.* **19**, 600–608 (2004)
25. D. Reedy, Thin-coating contact mechanics with adhesion. *J. Mater. Res.* **21**, 2660–2668 (2006)
26. E. Barthel, Elastic adhesive contact—JKR and more. *J. Phys. D: Appl. Phys.* **41**, 163001 (2008)
27. A. Onur Sergici, G.G. Adams, S. Muftu, Adhesion in the contact of a spherical indenter with a layered elastic half-space. *J. Mech. Phys. Sol.* **54**, 1843–1861 (2006)
28. S. Hyun, L. Pei, J.F. Molinari, M.O. Robbins, Finite-element analysis of contact between elastic self-affine surfaces. *Phys. Rev. E* **70**(2), 26117 (2004)
29. J.A. Greenwood, J.B.P. Williamson, Contact of nominally flat Surf. *Proc. Roy. Soc. A* **295**(1442), 300–319 (1966)
30. K. Fuller, D. Tabor, The effect of surface roughness on the adhesion of elastic solids. *Proc. Roy. Soc. A* **345**, 327–342 (1975)
31. M.C. Audry, S. Ramos, E. Charlaix, Adhesion between highly rough alumina surfaces: an atomic force microscope study. *J. Colloid Interface Sci.* **331**(2), 371–378 (2009)
32. J. Reed, Energy losses due to elastic wave propagation during an elastic impact. *J. Phys. D: Appl. Phys.* **18**, 2329 (1985)

33. G. Kuwabara, K. Kono, Restitution coefficient in a collision between two spheres. *Jpn. J. Appl. Phys.* **26**(8), 1230–1233 (1987)
34. M. Barquins, J.-C. Charmet, Influence of surface properties on the rebound of a rigid ball on a rubber surface. *J. Adh.* **57**, 5–19 (1996)
35. G.J. Lake, A.G. Thomas, The strength of highly elastic materials. *Proc. Roy. Soc. Lond. Ser. A* **300**, 108–119 (1967)
36. A. Jagota, S.J. Bennison, Mechanics of adhesion through a fibrillar microstructure. *Integr. Comp. Biol.* **42**(6), 1140 (2002)
37. A.N. Gent, Adhesion and strength of viscoelastic solids. Is there a relationship between adhesion and bulk properties? *Langmuir* **12**(19), 4492–4496 (1996)
38. R.A. Schapery, A theory of crack initiation and growth in viscoelastic media II. Approximate methods of analysis. *Int. J. Fract.* **11**(1), 369–388 (1975)
39. J.A. Greenwood, K.L. Johnson, The mechanics of adhesion of viscoelastic solids. *Philos. Mag. A* **43**(3), 697–711 (1981)
40. P.G. de Gennes, Soft adhesives. *Langmuir* **12**(19), 4497–4500 (1996)
41. E. Barthel, C. Frétiigny, Adhesive contact of elastomers: effective adhesion energy and creep function. *J. Phys. D: Appl. Phys.* **42**(19), 195302 (2009)
42. K.J. Wahl, S.A.S. Asif, J.A. Greenwood, K.L. Johnson, Oscillating adhesive contacts between micron-scale tips and compliant polymers. *J. Colloid Interface Sci.* **296**, 178–188 (2006)

# Chapter 3

## Cantilever Dynamics: Theoretical Modeling

John H. Cantrell and Sean A. Cantrell

**Abstract** To provide a measure of flexibility and symmetry regarding the description of tip-sample interactions, a dynamical model is presented for which the cantilever tip and the sample surface are treated as independently damped simple harmonic oscillators passively coupled via the nonlinear tip-sample interaction forces. The sample oscillations are assumed to occur in the coupling from a small element of surface mass (active mass) attached to the remainder of the sample for which the spring constant is the sample stiffness constant. The analytical model reduces to a pair of coupled nonlinear differential equations, the general solutions of which are obtained using a matrix iteration procedure. The general solutions are applied to the quantitative assessment of signal generation and contrast mechanisms in atomic force acoustic microscopy (AFAM), force modulation microscopy (FMM), ultrasonic force microscopy (UFM), ultrasonic atomic force microscopy (UAFM), amplitude modulation atomic force microscopy (AM-AFM), and scanning near-field ultrasonic holography (SNFUH) including the related heterodyne force atomic force microscopy (HF-AFM) and resonant difference-frequency atomic force ultrasonic microscopy (RDF-AFUM). In addition to obtaining quantitative expressions for surface contrast mechanisms, contrast mechanisms from subsurface features are accounted in the model for AFAM, FMM, UFM, and SNFUH.

---

J. H. Cantrell (✉)  
NASA Langley Research Center, Hampton, VA 23681, USA  
e-mail: john.h.cantrell@nasa.gov

S. A. Cantrell  
Johns Hopkins University, Baltimore, MD 21218, USA

S. A. Cantrell  
NanoSonix, Skokie, IL 60077, USA



### 3.1 Introduction

Atomic force microscopy (AFM) [1] has rapidly developed from a quasi-static detection technology into a fully dynamic nanoscale characterization tool. The development of new materials and devices produced from nanostructural constituents has placed increasing demands on the development of new measurement methods to assess physical properties at the nanoscale. Dynamic implementations of the AFM, collectively called dynamic atomic force microscopy (*d*-AFM) (known also as acoustic-atomic force microscopy and scanning probe acoustic microscopy), utilize the interaction force between the cantilever tip and the sample surface to extract information about sample physical properties. Such properties include elastic moduli, adhesion, viscoelasticity, embedded particle distributions, device integrity, and topography. The most commonly used *d*-AFM modalities include amplitude modulation-atomic force microscopy (AM-AFM) (including intermittent contact mode or tapping mode) [2], ultrasonic atomic force microscopy (UAFM) [3], force modulation microscopy (FMM) [4], atomic force acoustic microscopy (AFAM) [5, 6], ultrasonic force microscopy (UFM) [7, 8], heterodyne force microscopy (HFM) [9] scanning near-field ultrasonic holography (SNFUH) [10], resonant difference-frequency atomic force ultrasonic microscopy (RDF-AFUM) [11], and variations of these techniques [12–19].

To model properly the various *d*-AFM modalities, it is necessary to reduce the modalities to their basic operational characteristics. Central to all *d*-AFM modalities is the AFM. The basic AFM consists of a scan head, an FM controller, and an image processor. The typical scan head consists of a cantilever with a sharp tip, a piezoelement stack attached to the cantilever for cantilever control, and a light beam from a laser source that reflects off the cantilever surface to a photo-diode detector used to monitor the motion of the cantilever as the scan head moves over the sample surface. The output from the photo-diode is used in the image processor to generate the micrograph.

The *d*-AFM output signal is derived from the interaction between the cantilever tip and the sample surface. The interaction occurs via an interaction force  $F$  that is highly dependent on the tip-sample separation distance  $z$ . A typical force-separation curve is illustrated in Fig. 3.1. Above the separation distance  $z_A$  the interaction force is negative, hence attractive, and below  $z_A$  the interaction force is positive, hence repulsive. The separation distance  $z_B$  is the point on the curve at which the maximum rate of change of the slope of the curve occurs and is thus the point of maximum nonlinearity on the curve (the maximum nonlinearity regime).

Modalities such as AFM, AM-AFM, and UAFM are available for surface and near-surface characterization, while UFM, AFAM, FMM, HFM, SNFUH, and RDF-AFUM are generally used to assess deeper (subsurface) features at the nanoscale. A schematic of the basic equipment arrangement for various *d*-AFM modalities is shown in Fig. 3.2. The arrangement used for AFAM and FMM is shown in Fig. 3.2 where switch  $A$  is closed and switch  $B$  is open. AFAM and FMM utilize ultrasonic waves transmitted into the material by a transducer attached to the bottom of the

**Fig. 3.1** Interaction force plotted as a function of the separation distance  $z$  between cantilever tip and sample surface

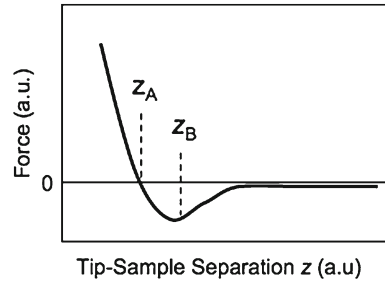
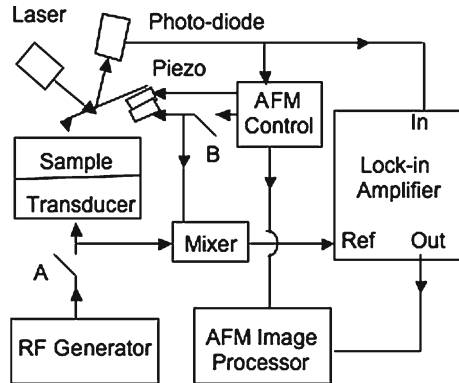


**Fig. 3.2** Equipment configuration for various dynamic atomic force microscopies. Switch A is closed and switch B is open for AFAM, FMM, and UFM. Switch A is open and switch B is closed for AM-AFM and UAFM. Both switches are closed for HFM, SNFUH, and RDF-AFUM



sample. After propagating through the bulk of the sample, the wave impinges on the sample top surface where it excites the engaged cantilever. The basic equipment arrangement used for UFM is the same as that for AFAM and FMM. However, the cantilever tip for UFM is set to assure tip-sample engagement near the maximum nonlinearity regime of the force-separation curve. The UFM output signal is a static or “dc” signal resulting from the interaction nonlinearity.

The equipment arrangement for HFM, SNFUH, and RDF-AFUM is shown in Fig. 3.2 where the indicated switches are in the closed positions. Similar to the AFAM, FMM, and UFM modalities, HFM, SNFUH, and RDF-AFUM employ ultrasonic waves launched from the bottom of the sample. However, in contrast to the AFAM, FMM, and UFM modalities, the cantilever in HFM, SNFUH, and RDF-AFUM is also driven into oscillation. HFM, SNFUH, and RDF-AFUM operate in the maximum nonlinearity regime of the force-separation curve, so the nonlinear interaction of the surface and cantilever oscillations produces a strong difference-frequency output signal. For the AM-AFM modality only the cantilever is driven into oscillation and the rest or quiescent tip-sample separation distance may be set to any position on the force-separation curve, even for operation where the quiescent separation distance lies well beyond the region of strong tip-sample interaction, i.e., where the quiescent separation  $z_0 \gg z_B$ . For UAFM the cantilever is set in constant forced contact with

the sample surface, while the cantilever is driven at ultrasonic frequencies with small oscillation amplitudes.

Various approaches to assessing cantilever probe dynamics have been published [7, 8, 20–35]. We present here a general, yet detailed, analytical treatment of the cantilever and the sample as independent systems in which the nonlinear interaction force provides a coupling between the cantilever tip and the volume element of sample surface involved in the coupling [coupled independent systems (CIS) model]. The general equations of cantilever dynamics are reduced to a set of local, phase-correlated, damped harmonic oscillator equations corresponding to the temporal components in the solution space of the governing dynamical equation. The set collectively defines the eigenmodes of cantilever motion.

A polynomial expansion is developed to represent the tip-sample interaction force that accounts for cantilever-to-sample energy transfer. The polynomial expansion is first applied in obtaining solutions to the commonly used single system model of cantilever dynamics where the cantilever, as a single dynamical system, is subjected to external forces and boundary conditions. Analytical expressions for the image contrast mechanisms are obtained with particular emphasis on the contributions of conservative and non-conservative forces to the contrast. Finite drive amplitudes are shown to generate harmonics of the drive frequency resulting from the nonlinearities in the tip-sample interaction forces. The finite drive amplitudes are shown in Appendix B also to generate fractional harmonics (including subharmonics) resulting from the nonlinearities in the tip-sample interaction forces. The stability of the subharmonic solutions is discussed analytically and routes to chaotic cantilever motion are addressed. The higher order expansion coefficients in the polynomial expansion are shown in Appendices A and C to be responsible for the occurrence of both amplitude bifurcation and resonance bifurcation, respectively, which are often observed upon cantilever-sample contact.

Also addressed in Appendix C is the concern, sometimes cited in the literature, that conventional spring models (i.e., spring models with fixed spring constants) fail to describe cantilever dynamics adequately, particularly at drive frequencies much larger than the fundamental cantilever resonance frequency. It is shown from group renormalization methods (often used in high energy physics and in descriptions of critical phase transitions in condensed matter) that over a small range of frequencies near the arbitrarily chosen renormalization scale (reference frequency), cantilever dynamics can be treated quite accurately as that of a conventional spring with a point mass. Outside this frequency range, the cantilever dynamics is modeled accurately by the renormalization method as spring dynamics with frequency-dependent stiffness and damping parameters.

Limitations of the single system model are discussed that beg consideration of the CIS model of cantilever-sample dynamics wherein the cantilever and sample are treated as fully symmetric, independent, oscillatory systems coupled by a mutual interaction force. The symmetry of the governing dynamical equations in the CIS model allows direct application of the model to the various *d*-AFM modalities cited above. General solutions of the CIS model are found to first order in the nonlinearity

and applied to the assessment of signal generation for each of the  $d$ -AFM modalities cited. Contrast mechanisms in the CIS model are addressed.

### 3.2 General Dynamical Equations and Eigenmodes of Cantilever Motion

The cantilever of the AFM is able to vibrate in a number of different modes in free space corresponding to various displacement types or modes (flexural, torsional, longitudinal, shear, etc.) with corresponding resonant frequencies and effective stiffness constants. Although any cantilever shape or displacement type of cantilever oscillation can in principle be used in the analysis to follow, for definiteness and expediency we consider only the flexural modes of a cantilever modeled as a rectangular, elastic beam of length  $L$ , width  $a$ , and height  $b$ . We assume the beam to be clamped at the position  $x = 0$  and unclamped at the position  $x = L$ , as indicated in Fig. 3.3. We consider the flexural displacement  $y(x, t)$  of the beam to be subjected to some general force per unit length  $H(x, t)$ , where  $x$  is the position along the beam and  $t$  is time. The dynamical equation for such a beam is [36]

$$E_B I \frac{\partial^4 y(x, t)}{\partial x^4} + \rho_B A_B \frac{\partial^2 y(x, t)}{\partial t^2} = H(x, t) \quad (3.1)$$

where  $E_B$  is the elastic modulus of the beam,  $I = ab^3/12$  is the bending moment of inertia,  $\rho_B$  is the beam mass density, and  $A_B = ab$  is the cross-sectional area of the beam.

The solution to Eq. (3.1) can be obtained as a superposition of the natural vibrational modes of the unforced cantilever as

$$y(x, t) = \sum_{n=1}^{\infty} Y_n(x) \eta_{cn}(t) \quad (3.2)$$

where  $\eta_{cn}$  is the  $n$ th mode cantilever displacement ( $n = 1, 2, 3, \dots$ ) and the spatial eigenfunctions  $Y_n(x)$  form an orthogonal basis set given by [36]

$$Y_n(x) = \left( \frac{\sin q_n x - \sinh q_n x}{\cos q_n x + \cosh q_n x} \right) (\sin q_n x - \sinh q_n x) + (\cos q_n x - \cosh q_n x). \quad (3.3)$$

The flexural wave numbers  $q_n$  in Eq. (3.3) are determined from the boundary conditions as  $\cos(q_n L) \cosh(q_n L) = -1$  and are related to the corresponding modal angular frequencies  $\omega_n$  via the dispersion relation  $q_n^4 = \omega_n^2 \rho_B A_B / E_B I$ . The general force per unit length  $H(x, t)$  can also be expanded in terms of the spatial eigenfunctions as [37]

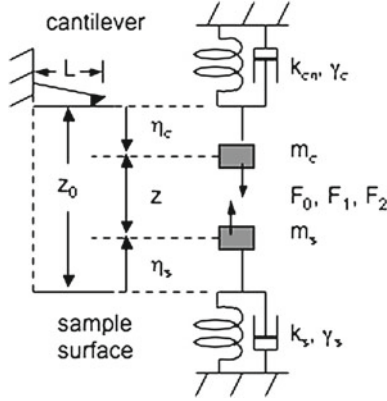


**Fig. 3.3** Schematic of cantilever tip-sample surface interaction:  $z_0$  is the quiescent (rest) tip-surface separation distance (setpoint),  $z$  the oscillating tip-surface separation distance,  $\eta_c$  the displacement of the cantilever tip (positive up),  $\eta_s$  the displacement of the sample surface (positive down),  $k_{cn}$  is the  $n$ th mode cantilever stiffness constant (represented as an  $n$ th mode spring),  $m_c$  the cantilever mass,  $k_s$  the sample stiffness constant (represented as a spring),  $m_s$  the active sample mass, and  $F_0$ ,  $F_1$ , and  $F_2$  are the first three interaction force ‘conservative’ expansion coefficients

$$H(x, t) = \sum_{n=1}^{\infty} B_n(t) Y_n(x). \quad (3.4)$$

Applying the orthogonality condition

$$\int_0^L Y_m(x) Y_n(x) dx = L \delta_{mn} \quad (3.5)$$

( $\delta_{mn}$  are the Kronecker deltas) to Eq. (3.4), we obtain

$$B_n(t) = \int_0^L H(\xi, t) Y_n(\xi) d\xi. \quad (3.6)$$

We now assume that the general force per unit length acting on the cantilever is composed of a cantilever driving force per unit length  $H_C(x, t)$ , an interaction force per unit length  $H_T(x, t)$  between the cantilever tip and the sample surface, and a dissipative force per unit length  $H_d(x, t)$  [35]. Thus, the general force per unit length  $H(x, t) = H_C(x, t) + H_T(x, t) + H_d(x, t)$ . We assume that the driving force per unit length is a purely sinusoidal oscillation of angular frequency  $\omega_c$  and magnitude  $P_c$ . We also assume the driving force to result from a drive element (e.g., a piezo-transducer) applied at the point  $x_c$  along the cantilever length. We thus write  $H_C(x, t) = P_c (\cos \omega_c t) \delta(x - x_c)$  where  $\delta(x - x_c)$  is the Dirac delta function. The

interaction force per unit length  $H_T(x, t)$  of magnitude  $P_T$  is applied to the cantilever tip at  $x = x_T$  and is not a direct function of time, since it serves as a passive coupling between the independent cantilever and sample systems. We thus write the interaction force per unit length as  $H_T(x, t) = P_T \delta(x - x_T)$ . We assume the modal dissipation force per unit length  $H_d(x, t)$  to be a product of the spatial eigenfunction and the cantilever displacement velocity given as  $H_d(x, t) = -P_d Y_n(x)(d\eta_{cn}/dt)$ . The coefficient  $B_n(t)$  is then obtained from Eq. (3.6) as

$$B_n(t) = P_c Y_n(x_c)(\cos \omega_c t) + P_T Y_n(x_T) - [P_d \int Y_n(x) dx](d\eta_{cn}/dt) \quad (3.7)$$

where the integration in the last term is taken over the range  $x = 0$  to  $x = L$ . Substituting Eqs. (3.2) and (3.4) in (3.1) and collecting terms, we find that the dynamics for each mode  $n$  must independently satisfy the relation

$$\begin{aligned} \rho_B A_B Y_n(x) \frac{d^2 \eta_{cn}(t)}{dt^2} + E_B I \frac{d^4 Y_n(x)}{dx^4} \eta_{cn} = P_c Y_n(x_c) Y_n(x) \cos \omega_c t \\ + P_T Y_n(x_T) Y_n(x) + [P_d \int_0^L Y_n(x) dx] \frac{d\eta_{cn}}{dt}. \end{aligned} \quad (3.8)$$

From Eq. (3.3) we write  $d^4 Y_n(x)/dx^4 = q_n^4 Y_n$ . Using this relation and the dispersion relation between  $q_n$  and  $\omega_n$ , we obtain that the coefficient of  $\eta_{cn}$  in Eq. (3.8) is given by  $E_B I (d^4 Y_n(x)/dx^4) = \omega_n^2 \rho_B A_B$ . Multiplying Eq. (3.8) by  $Y_m(x)$  and integrating from  $x = 0$  to  $x = L$ , we obtain

$$m_c \ddot{\eta}_{cn} + \gamma_{cn} \dot{\eta}_{cn} + k_{cn} \eta_{cn} = F_c \cos \omega_c t + F \quad (3.9)$$

where the overdot denotes the time derivative operator  $d/dt$ ,  $m_c = \rho_B A_B L$  is the total mass of the cantilever and  $F_c = P_B L Y_n(x_c)$ . The tip-sample interaction force  $F$  is defined by  $F = P_T L Y_n(x_T)$  and the cantilever stiffness constant  $k_{cn}$  is defined by  $k_{cn} = m_c \omega_n^2$ . The damping coefficient  $\gamma_{cn}$  of the cantilever is defined as  $\gamma_{cn} = P_d L \int Y_n(x) dx$ . Note that for a given mode  $n$  the effective magnitudes of the driving term  $F_c$  and the interaction force  $F$  are dependent via  $Y_n(x_c)$  and  $Y_n(x_T)$ , respectively, on the positions  $x_c$  and  $x_T$  at which the forces are applied. The damping factor, in contrast, results from a more general dependence on  $x$  via the integral of  $Y_n(x)$  over the range zero to  $L$ . If the excitation force per unit length is a distributed force over the cantilever surface rather than applied at a point, then the resulting calculation for  $F_c$  would involve an integral over  $Y_n(x)$  as obtained for the damping coefficient.

The interaction force  $F$  in Eq. (3.9) is derived without regard to the cantilever tip-sample surface separation distance  $z$ . Realistically, the magnitude of  $F$  is quite-dependent on the separation distance. In particular, various parameters derived from the force-separation curve play essential roles in the response of the cantilever to all driving forces. We consider that the interaction force not only involves the cantilever at the tip position  $x_T$  but also some elemental volume of material at the sample

surface. To maintain equilibrium it is appropriate to view the elemental volume of sample surface as a mass element  $m_s$  (active mass) that, in addition to the interaction force, is subjected to a restoring force from material in the remainder of the sample. We assume that the restoring force per unit displacement of  $m_s$  is quantified by the sample stiffness constant  $k_s$ .

The interaction force  $F$  is in general a nonlinear function of the cantilever tip-sample surface separation distance  $z$ , as shown in Fig. 3.1. The interaction force results from a number of possible fundamental mechanisms including electrostatic forces [38], van der Waals forces [39], interatomic repulsive (e.g., Born-Mayer) potentials [40], Casimir forces [41], chemical bonding forces [42], and hydroxyl groups formed from atmospheric moisture accumulation on the cantilever tip and sample surface [43].

Since the force  $F(z)$  is common to the cantilever tip and the sample surface element, the cantilever and the sample form a coupled dynamical system. Figure 3.3 shows a schematic representation of the various elements of the coupled system. The dynamical equations expressing the responses of the cantilever and the sample surface to all driving and damping forces may be written for each mode  $n$  of the coupled system as

$$m_c \ddot{\eta}_{cn} + \gamma_{cn} \dot{\eta}_{cn} + k_{cn} \eta_{cn} = F_c \cos \omega_c t + F(z) \quad (3.10)$$

$$m_s \ddot{\eta}_s + \gamma_s \dot{\eta}_s + k_s \eta_s = F_s \cos(\omega_s t + \theta) + F(z) \quad (3.11)$$

where  $\eta_{cn}$  (positive up) is the cantilever tip displacement for mode  $n$ ,  $\eta_s$  (positive down) is the sample surface displacement from its equilibrium position,  $\omega_c$  is the angular frequency of the cantilever oscillations,  $\omega_s$  is the angular frequency of the sample surface vibrations,  $\gamma_c$  is the damping coefficient for the cantilever,  $\gamma_s$  is the damping coefficient for the sample surface,  $F_c$  is the magnitude of the cantilever driving force,  $F_s$  is the magnitude of the sample driving force that we assume here to result from an incident ultrasonic wave generated at the opposite surface of the sample.  $F(z)$  is the nonlinear tip-sample interaction force and  $z$  is the instantaneous distance between the cantilever tip and the sample surface. We assume, as shown in Fig. 3.3, that  $z - z_0 = (\eta_c + \eta_s)$  where  $z_0$  is the quiescent separation distance between the cantilever tip and sample surface. The factor  $\theta$  in Eq. (3.11) is a phase contribution resulting from the propagation of the ultrasonic wave through the sample material and is considered in more detail in Sect. 3.4.1.

### 3.3 Single System Model of Cantilever Dynamics

In most treatments of cantilever dynamics the cantilever is considered to be a single dynamical system subjected to external forces and constraints, including the cantilever tip-sample surface interaction forces. As shown by the solution to the beam equation given in Sect. 3.2, the cantilever dynamics at a given point on the

cantilever can be represented by a set of oscillators with each oscillator being modeled as a mass attached to a damped spring. Each spring has a stiffness constant and damping coefficient appropriate to the mode under consideration and is subjected to external forces. The model is often referred to as the spring model and the cantilever dynamics is assessed from the modal solutions of Eq. (3.10) alone. In other single system approaches the dynamics is obtained by absorbing the driving and damping forces in the boundary conditions for the elastic beam equation. The sample surface displacement  $\eta_s$  is not generally considered directly in single system models of cantilever dynamics in part because the focus has been on the dynamics of the cantilever only. The influence of  $\eta_s$  on the cantilever dynamics is usually considered only indirectly by assuming such influences to be manifested in the interaction force or in the boundary conditions. Strictly, neglecting  $\eta_s$  completely would correspond to assuming the sample stiffness constant  $k_s$  to be infinitely large in Eq. (3.11). Before developing the CIS model, it is useful to consider the implications of the single system approach as represented by the spring model.

### 3.3.1 Polynomial Expansions of the Interaction Force

To explore the features of the single system model, we ignore  $\eta_s$  directly [and thus Eq. (3.11)] and consider an appropriate expansion of the interaction force  $F$  that accounts for the relevant influences of the cantilever-sample interactions. Although the dependence of the interaction force  $F$  on  $z$  alone accounts for effects associated with the instantaneous separation between the cantilever tip and sample surface, it does not account for the dynamic transfer of energy from the cantilever to the sample surface without specifically solving for the effects of surface dynamics. Such an accounting can be obtained indirectly in the single system spring model by absorbing the effects of the surface dynamics in the interaction force. We absorb the surface dynamics by assuming a dependence of the interaction force on the time derivative of the cantilever sample separation distance  $dz/dt = \dot{z} = \sum_n (d\eta_{cn}/dt) = \sum_n \dot{\eta}_{cn}$  in addition to  $z - z_0 = \sum_n \eta_{cn}$  such that  $F = F(z, \dot{z})$ . We thus seek solutions to Eq. (3.10) by expanding  $F = F(z, \dot{z})$  in a polynomial series which we write as [44] (note: We have taken  $F_{i0} \rightarrow F_i$ ,  $F_{0i} \rightarrow S_i$ , and  $F_{i,j} (i, j \neq 0) \rightarrow R_{i,j} (i, j \neq 0)$  in reference [44])

$$\begin{aligned}
 F(z, \dot{z}) &= [F_0 + F_1(z - z_0) + F_2(z - z_0)^2 + \cdots] \\
 &\quad + [S_1\dot{z} + S_2\dot{z}^2 + \cdots] + [R_{11}(z - z_0)(\dot{z}) + \cdots] \\
 &= [F_0 + F_1\eta_{cn} + F_2\eta_{cn}^2 + \cdots] + [S_1\dot{\eta}_{cn} + S_2\dot{\eta}_{cn}^2 + \cdots] \\
 &\quad + [R_{11}\eta_{cn}\dot{\eta}_{cn} + \cdots]
 \end{aligned} \tag{3.12}$$

where the  $F_i$ ,  $S_i$ , and  $R_{ij}$  are expansion coefficients ( $i$  and  $j$  are nonnegative integers). In the last equality of Eq. (3.12) mode coupling has been ignored, resulting in a



suppression of the sum over the various modes (i.e., we assume that  $z - z_0 = \eta_{cn}$  and  $\dot{z} = \dot{\eta}_{cn}$  for each mode  $n$ ). The mode decoupling is justified on the grounds that to a reasonable approximation only the mode whose resonance is closest to the driving frequency dominates the interaction. The cantilever response from the inclusion of all modes is the focus of Appendix C where group renormalization methods are used to obtain the cantilever dynamics from the coupling of the modes via interaction force nonlinearities.

The expansion coefficient  $F_1$  is the interaction force gradient and plays a role in the interaction force similar to that of the cantilever spring constant. The  $S_i$  ( $i = 1, 2, 3, \dots$ ) coefficients in Eq. (3.12) account for the transfer of energy from the cantilever to the sample during tip-sample interactions and are thus ‘dissipation’ coefficients in the expansion. This is easily seen by substituting Eq. (3.12) in (3.10) and comparing terms on each side of the resulting equation. It is apparent that the  $S_1$  coefficient plays a role in the interaction force similar to that of the cantilever damping term  $\gamma_c$ . The remaining  $S_i$  coefficients are higher order dissipative terms. Zero values of the dissipative terms thus imply that no cantilever-to-sample energy transfer occurs and that the sample surface is infinitely stiff (i.e., no sample surface oscillations occur). We also note the appearance of cross terms in Eq. (3.12) with expansion coefficients  $R_{ij}$  ( $i, j \neq 0$ ) that make a contribution to both conservative and dissipative forces and also vanish in the limit of an infinitely stiff surface.

We point out that if Eq. (3.12) were a Taylor series, the coefficients in the expansion would be evaluated as derivatives of the interaction force function at a given cantilever tip-sample separation. Although the agreement between the function and a truncated polynomial series of the function in this case would be optimized in the immediate vicinity of a given tip-sample separation  $z$  and time derivative  $\dot{z}$ , the truncation could result in a sharp divergence from that of the actual function over the range of cantilever oscillation as the result of a complicated dependence of the interaction force on  $z$  and  $\dot{z}$ . In such case the cantilever dynamics may not be accurately predicted by a truncated Taylor series expansion. This is particularly true if the cantilever oscillations span a range of tip-sample separation between the nearly free-space and highly nonlinear interactive regimes such that the period of cantilever oscillation spends a non-trivial amount of time in regions for which the divergence is pronounced. Increasingly more terms in the expansion are needed to properly represent the cantilever oscillations as the amplitude of the drive force  $F_c$  increases. Even for small oscillation amplitudes more terms in the expansion are needed, if the quiescent separation between the cantilever and sample surface is near the highly nonlinear portion of the force-separation curve.

An alternative and improved evaluation of the expansion coefficients of Eq. (3.12) that accounts for the functional behavior of the interaction force over the entire range of cantilever oscillations can be obtained from considerations of linear algebra and inner product spaces. Assuming symmetry of the oscillations about the cantilever quiescent position, we place the interaction force function in the space of smooth functions over the relevant ranges of cantilever displacements,  $\eta \in [-\eta_{\max}, \eta_{\max}]$ , and displacement rates,  $\dot{\eta} \in [-\dot{\eta}_{\max}, \dot{\eta}_{\max}]$ , and equip the space with an inner product

$$\langle g, h \rangle = \int_{-\eta_{\max}}^{\eta_{\max}} \int_{-\dot{\eta}_{\max}}^{\dot{\eta}_{\max}} g(\eta, \dot{\eta}) h(\eta, \dot{\eta}) d\eta d\dot{\eta}. \quad (3.13)$$

where  $g$  and  $h$  are elements of the inner product space. (If the oscillations are not symmetric, the inner product can be modified phenomenologically to account for the deviation from symmetry.) In this scheme, we minimize the square of the norm of the difference between the actual function and its projection onto the span of the second-order truncation of the polynomial series. The square of the norm of a function is the inner product of the function with itself. We thus write the second order truncation of the series in Eq.(3.12) as  $f(\eta, \dot{\eta}) = [F_0 + F_1\eta_{cn} + F_2\eta_{cn}^2] + [S_1\dot{\eta}_{cn} + S_2\dot{\eta}_{cn}^2] + [R_{11}\eta_{cn}\dot{\eta}_{cn}]$ , let  $g = h = (F-f)$  and from Eq.(3.13) minimize

$$\langle (F - f), (F - f) \rangle = \int_{-\eta_{\max}}^{\eta_{\max}} \int_{-\dot{\eta}_{\max}}^{\dot{\eta}_{\max}} [F(\eta, \dot{\eta}) - f(\eta, \dot{\eta})]^2 d\eta d\dot{\eta} \quad (3.14)$$

with respect to  $F_i$ ,  $S_i$ , and  $R_{ij}$ .

The expansion coefficients are obtained by substituting  $f(\eta, \dot{\eta})$  in Eq.(3.14), taking derivatives with respect to each of the coefficients  $F_i$ ,  $S_i$ , and  $R_{ij}$  in  $f(\eta, \dot{\eta})$ , setting each derivative to zero, and solving the resulting system of linear equations. Performing this procedure, we find that the first few expansion coefficients are given as

$$F_0 = \frac{1}{16\eta_{\max}^3 \dot{\eta}_{\max}^3} \left[ 14\eta_{\max}^2 \dot{\eta}_{\max}^2 \langle F, 1 \rangle - 15\eta_{\max}^2 \langle F, \dot{\eta}^2 \rangle - 15\dot{\eta}_{\max}^2 \langle F, \eta^2 \rangle \right], \quad (3.15)$$

$$F_1 = \frac{3}{4\eta_{\max}^3 \dot{\eta}_{\max}} [\langle F, \eta \rangle], \quad (3.16)$$

$$F_2 = \frac{15}{16\eta_{\max}^5 \dot{\eta}_{\max}} \left[ 3\langle F, \eta^2 \rangle - \eta_{\max}^2 \langle F, 1 \rangle \right], \quad (3.17)$$

$$S_1 = \frac{3}{4\eta_{\max} \dot{\eta}_{\max}^3} [\langle F, \dot{\eta} \rangle], \quad (3.18)$$

$$S_2 = \frac{15}{16\eta_{\max} \dot{\eta}_{\max}^5} \left[ 3\langle F, \dot{\eta}^2 \rangle - \dot{\eta}_{\max}^2 \langle F, 1 \rangle \right], \quad (3.19)$$

and

$$R_{11} = \frac{9}{4\eta_{\max}^3 \dot{\eta}_{\max}^3} [\langle F, \eta \dot{\eta} \rangle]. \quad (3.20)$$

We note that the series in Eq.(3.12) is quite different from that of the Taylor series. The coefficients of the Taylor series are evaluated at a single point, while the

coefficients in Eq. (3.12) are determined by appropriate averages of the interaction force  $F(\eta, \dot{\eta})$  over the entire range of oscillatory motion as obtained in Eqs. (3.15)–(3.20). Such averaging provides a more robust accounting of the interaction force over the entire range of oscillatory motion and leads to requiring fewer terms in the expansion than would be needed in a Taylor series to cover the same range of oscillation amplitude.

### 3.3.2 Dynamical Effects of the Expansion Coefficients

Substituting Eq. (3.12) in (3.10), we obtain [44]

$$m_c \ddot{\eta}_{cn} + (\gamma_{cn} - S_1) \dot{\eta}_{cn} + (k_{cn} - F_1) \eta_{cn} = F_c \cos \omega_c t + F_0 + F_2 \eta_{cn}^2 + F_3 \eta_{cn}^3 + \dots \quad (3.21)$$

It is apparent from Eq. (3.21) that  $F_1$  leads to a change in the effective spring stiffness constant of the cantilever as the result of cantilever-sample contact and thus plays the role of an effective interaction force gradient. We point out that ‘contact’ is defined as that period of time, however briefly, that the cantilever is under the influence of the tip-sample interaction force  $F[z(t), \dot{z}(t)]$ . Similarly, it is seen from Eq. (3.21) that  $S_1$  plays the role of a damping coefficient resulting from the interaction force that occurs in addition to the damping coefficient  $\gamma_{cn}$  provided by the cantilever. A negative value of  $S_1$  means that energy is transferred from the cantilever to the sample via the interaction force coupling [44].

Since the transfer of energy is a dynamic process in  $d$ -AFM, the sample surface must necessarily oscillate during the energy transfer. If the interaction force were dependent only on  $z(t)$ , there would be no accounting for surface oscillations, since from Eqs. (3.18)–(3.20) the dissipative  $S_n$  (and  $R_{mn}$ ) terms are then zero. This implies that the sample surface is infinitely stiff (no energy transfer). However, the inclusion of an independent dissipative (time derivative) term  $\dot{z}$  in the interaction force leads to nonzero  $S_n$  (and  $R_{mn}$ ) terms and allows for the possibility of surface oscillations [44]. For  $S_n$  to be nonzero it is thus essential that contributions from sample surface oscillations appear via  $\dot{z}$  in the interaction force  $F$ .

The various expansion coefficients,  $F_0, F_1, F_2$ , etc., play significant, sometimes surprising, roles in the  $d$ -AFM output signals. For example, amplitude bifurcation is well-documented in the literature and is a significant source of image “streaking” [34, 45, 46]. The role that the expansion coefficients play in the solution to Eq. (3.21) leading to amplitude bifurcation is shown in Appendix A.

### 3.3.3 Image Contrast in Dynamic Atomic Force Microscopy

Any change affecting the oscillatory characteristics of the cantilever in  $d$ -AFM can lead to a change in the amplitude and phase of the cantilever output signal. Variations in material physical properties, such as the elastic moduli, viscosity, or even surface topography can lead to such changes. If the change results from signals acquired

at two different points in a line scan, the difference in the cantilever output signal from the two points defines the ‘contrast’ between the two points. Image contrast can be generated either from changes in the amplitude or phase signal from the cantilever. The choice depends on the  $d$ -AFM modality being used and the information needed for the sample material. In UFM only the amplitude signal is available for image contrast. In AM-AFM, HFM, SNFUH, and RDF-AFUM, however, contrast is usually generated from the phase signal using constant amplitude control, since it allows simultaneous images to be acquired from both variations in sample material properties and topographies. The operation of AM-AFM in constant amplitude control is commonly called frequency modulation AFM or FM-AFM, since the output signal is derived from shifts in the resonance frequency during scanning.

It is often assumed that image contrast for relevant  $d$ -AFM modalities operating in constant amplitude control results only from dissipative forces acting in the cantilever tip-sample surface interaction region of the AFM. The assumption is based on a misinterpretation of the findings of several papers published in the late 1990s pertaining to AM-AFM [47–49]. For example, Cleveland et al. [48] show that “phase imaging is performed with the amplitude held constant by a feedback loop, so it is only when the tip–sample interaction losses vary that phase contrast will be observed.” Although their finding is certainly true, it is often interpreted to mean that variations in the dissipative forces alone generate the image contrast using constant amplitude control.

More recently, Schröter et al. [50] argue that for images generated at constant amplitude the variation in the ‘dissipative’ forces are not the result of a variation in a true material property but are driven by the variation in the conservative forces. They conclude that the only directly measurable true material property that drives phase contrast in constant amplitude control are the variations in the conservative forces. We show analytically that both conservative and dissipative forces must be considered in constant amplitude  $d$ -AFM operation but that phase contrast can be assessed either from conservative or dissipative force parameters alone when operating near cantilever resonance.

We consider the assessment of contrast mechanisms within the context of the single system spring model using the polynomial expression given in Eqs. (3.12) and (3.21) to characterize the interaction force  $F(z, \dot{z})$  [44]. The salient features of phase contrast can be obtained from a consideration of the linear terms alone in the expansion. We assume a solution of the form  $\eta_{cn} = \text{Re}\eta_{cn0} \exp(i\omega_{ct})$ , and substitute the expression in Eq. (3.21), neglecting the static and nonlinear terms. We obtain the solution  $\eta_{cn} = \eta_{cn0} \cos(\omega t + \phi)$  where the amplitude  $\eta_{cn0}$  of the cantilever output signal is given by

$$\eta_{cn0} = \frac{F_c}{[(k_{\text{eff}} - m_c \omega^2)^2 + \gamma_{\text{eff}}^2 \omega^2]^{1/2}}, \quad (3.22)$$

the output phase  $\phi$  by

$$\phi = -\tan^{-1} \frac{\gamma_{\text{eff}} \omega}{k_{\text{eff}} - m_c \omega^2}, \quad (3.23)$$

the effective stiffness constant  $k_{\text{eff}}$  by

$$k_{\text{eff}} = k_{cn} - F_1, \quad (3.24)$$

and the effective damping coefficient  $\gamma_{\text{eff}}$  by

$$\gamma_{\text{eff}} = \gamma_{cn} - S_1. \quad (3.25)$$

Resonance occurs at a frequency  $\omega_c = \omega_1$  such that  $d\eta_{cn0}/d\omega_c^2 = 0$ . From Eq. (3.22) we obtain that at resonance

$$k_{\text{eff}} - m_c\omega_1^2 = \frac{\gamma_{\text{eff}}^2}{2m_c}. \quad (3.26)$$

During scanning the only variables in the spring model are  $k_{\text{eff}}$  and  $\gamma_{\text{eff}}$ . For constant amplitude control,  $\Delta\eta_{cn0} = 0$  and we obtain from Eq. (3.22) that the variation  $\Delta k_{\text{eff}}$  is related to the variation  $\Delta\gamma_{\text{eff}}$  as

$$\Delta k_{\text{eff}} = -\frac{\gamma_{\text{eff}}\omega_c^2}{k_{\text{eff}} - m_c\omega_1^2} \Delta\gamma_{\text{eff}}. \quad (3.27)$$

For operation near resonance, we substitute the resonance condition Eq. (3.26) in (3.27) to obtain

$$\Delta k_{\text{eff}} = -\frac{2m_c\omega_1^2}{\gamma_{\text{eff}}} \Delta\gamma_{\text{eff}} = -\frac{\omega_1\sqrt{2m_c\omega_1^2(k_{\text{eff}} - m_c\omega_1^2)}}{k_{\text{eff}} - m_c\omega_1^2} \Delta\gamma_{\text{eff}}. \quad (3.28)$$

The phase variation  $\Delta\phi$  (phase contrast) that occurs during constant amplitude scanning is obtained from Eq. (3.23) as

$$\Delta\phi = \frac{\gamma_{\text{eff}}\omega_c}{(k_{\text{eff}} - m_c\omega_1^2)^2 + \gamma_{\text{eff}}^2\omega_c^2} \Delta k_{\text{eff}} - \frac{(k_{\text{eff}} - m_c\omega_c^2)\omega_c}{(k_{\text{eff}} - m_c\omega_c^2)^2 + \gamma_{\text{eff}}^2\omega_c^2} \Delta\gamma_{\text{eff}} \quad (3.29)$$

where the first and second terms in the equality represent the conservative and dissipative contributions, respectively. Equation (3.29) can be written in terms of a relationship between  $\Delta\phi$  and conservative force parameters alone by employing Eqs. (3.26) and (3.28) to obtain

$$\Delta\phi = \left\{ \frac{\sqrt{2m_c\omega_1^2(k_{\text{eff}} - m_c\omega_1^2)}}{(k_{\text{eff}} - m_c\omega_1^2)^2 + 2m_c\omega_1^2(k_{\text{eff}} - m_c\omega_1^2)} + \frac{(2m_c\omega_1^2)^{-1/2}(k_{\text{eff}} - m_c\omega_1^2)^{3/2}}{(k_{\text{eff}} - m_c\omega_1^2)^2 + 2m_c\omega_1^2(k_{\text{eff}} - m_c\omega_1^2)} \right\} \Delta k_{\text{eff}} \quad (3.30)$$

when operating in constant amplitude control near the cantilever resonance. Note that  $\Delta k_{\text{eff}} = \Delta(k_{cn} - F_1) = -\Delta F_1$ . A similar equation can be written for  $\Delta\phi$  in terms of dissipative force parameters  $\gamma_{\text{eff}}$  and  $\Delta\gamma_{\text{eff}} = \Delta(\gamma_{cn} - S_1) = -\Delta S_1$  as

$$\Delta\phi = - \left\{ \frac{8m_c^3\omega_1^3}{\gamma_{\text{eff}}^4 + 4m_c^2\gamma_{\text{eff}}^2\omega_1^2} + \frac{2m_c\gamma_{\text{eff}}^2\omega_1}{\gamma_{\text{eff}}^4 + 4m_c^2\gamma_{\text{eff}}^2\omega_1^2} \right\} \Delta\gamma_{\text{eff}}. \quad (3.31)$$

Although both terms in the brackets of Eqs. (3.30) and (3.31) are written in terms of either conservative or dissipative force parameters alone, the first term in the brackets of each equation is the contribution associated with conservative forces and the second term is that associated with dissipative forces. It is interesting to note that the ratio of the dissipative to the conservative contributions in Eq. (3.30) is  $(k_{\text{eff}} - m_c\omega_1^2)/2m_c\omega_1^2$ , while from Eq. (3.31) the ratio is given as  $\gamma_{\text{eff}}^2/4m_c^2\omega_1^2$ . Although the equations hold strictly for operation at the contact resonance frequency  $\omega_1$ , the expressions yield a useful approximation for *d*-AFM operation in constant amplitude control when operating near the free-space resonance. Under such conditions the ratio  $(k_{\text{eff}} - m_c\omega_c^2)/2m_c\omega_c^2 \approx -F_1/2m_c\omega_c^2$ . Assuming a typical value  $m_c \approx 10^{-10}$  kg,  $F_1$  of order  $1 \text{ N m}^{-1}$ , and operating frequencies  $\omega_c$  in the range 0.05–1.0 MHz, we obtain that the magnitude of  $(-F_1/2m_c\omega_c^2)$  ranges from roughly 2.0 at  $\omega_c = 0.05$  MHz to roughly 0.005 at  $\omega_c = 1.0$  MHz. Thus, the relative dissipative and conservative force contributions to the phase contrast are highly sensitive to the oscillation drive frequency. At low drive frequencies dissipative forces dominate phase contrast, while at high drive frequencies conservative forces dominate phase contrast. It is important to remember that both  $F_1$  and  $S_1$  are coefficients in the polynomial expansion of the interaction force  $F(z, \dot{z})$ .

The above derivation is based on the assumption of operation in the linear regime of the force-separation curve for the relevant *d*-AFM modalities. For the nonlinear regime of operation the inclusion of nonlinear terms in Eq. (3.21) leads to more complicated expressions for the cantilever output amplitude and phase signals, as shown in Sect. 3.3.4. However, the conclusion that both conservative and dissipative forces contribute to the phase image contrast remains true, even for constant amplitude control. It is, of course, apparent that both conservative and dissipative forces contribute to amplitude contrast.

### 3.3.4 Harmonic Generation

We consider in more detail the effects on the cantilever dynamics of the static and nonlinear terms in the polynomial expansion of the interaction force by including the terms in the dynamical equation for the cantilever given by Eq. (3.21). We solve the equation using a perturbative procedure [35, 44, 51] whereby we re-write Eq. (3.21) as

$$m_c \ddot{\eta}_{cn} + \gamma_{\text{eff}} \dot{\eta}_{cn} + k_{\text{eff}} \eta_{cn} = F_c \cos \omega_c t + F_0 + \varepsilon_s F_2 \eta_{cn}^2 + \dots \quad (3.32)$$

and let

$$\eta_{cn} = \eta_{cn}^{(0)} + \varepsilon_s \eta_{cn}^{(1)} + \varepsilon_s^2 \eta_{cn}^{(2)} + \dots \quad (3.33)$$

where  $\eta_{cn}^{(0)}$  is the zeroth-order solution to Eq. (3.32),  $\eta_{cn}^{(1)}$  is the first-order solution,  $\eta_{cn}^{(2)}$  is the second-order solution, etc. The parameter  $\varepsilon_s$  in Eqs. (3.32) and (3.33) is a scaling factor used to track the order of the approximation being considered. When  $\varepsilon_s$  is set to unity, we recover the solution to the original Eq. (3.21). We consider only solutions to first order, which is also first order in the nonlinearity. Substituting Eq. (3.33) in (3.32) and equating terms of the same degree in  $\varepsilon_s$ , we obtain the zeroth-order equation

$$m_c \ddot{\eta}_{cn}^{(0)} + \gamma_{\text{eff}} \dot{\eta}_{cn}^{(0)} + k_{\text{eff}} \eta_{cn}^{(0)} = F_c \cos \omega_c t + F_0 \quad (3.34)$$

and the first-order equation

$$m_c \ddot{\eta}_{cn}^{(1)} + \gamma_{\text{eff}} \dot{\eta}_{cn}^{(1)} + k_{\text{eff}} \eta_{cn}^{(1)} = F_2 (\eta_{cn}^{(0)})^2. \quad (3.35)$$

The solution to Eq. (3.34) is

$$\eta_{cn}^{(0)} = \varepsilon + \xi_0 \cos(\omega_c t + \phi) \quad (3.36)$$

where

$$\varepsilon = \frac{F_0}{k_{\text{eff}}}, \quad (3.37)$$

$$\xi_0 = \frac{F_c}{\sqrt{(k_{\text{eff}} - m_c \omega_c^2)^2 + \gamma_{\text{eff}}^2 \omega_c^2}}, \quad (3.38)$$

and

$$\phi = -\tan^{-1} \frac{\gamma_{\text{eff}} \omega_c}{k_{\text{eff}} - m_c \omega_c^2}. \quad (3.39)$$

We substitute the solution  $\eta_{cn}^{(0)}$  given by Eq. (3.36) in (3.35) and solve the resulting expression to obtain the first order solution

$$\eta_{cn}^{(1)} = \zeta_0 + \zeta_1 \cos(\omega t + 2\phi) + \zeta_2 \cos(2\omega t + 2\phi + \alpha) \quad (3.40)$$

where

$$\zeta_0 = \frac{F_2(\varepsilon^2 + \frac{1}{2}\xi_0^2)}{k_{\text{eff}}}, \quad (3.41)$$

$$\zeta_1 = \frac{2F_2\varepsilon\xi_0}{\sqrt{(k_{\text{eff}} - m_c\omega_c^2)^2 + \gamma_{\text{eff}}^2\omega_c^2}}, \quad (3.42)$$

$$\zeta_2 = \frac{F_2\xi_0^2}{\sqrt{(k_{\text{eff}} - 4m_c\omega_c^2) + 4\gamma_{\text{eff}}^2\omega_c^2}}, \quad (3.43)$$

and

$$\alpha = -\tan^{-1} \frac{2\gamma_{\text{eff}}\omega_c}{k_{\text{eff}} - 4m_c\omega_c^2}. \quad (3.44)$$

The solution to Eq.(3.21) to first order in the nonlinearity is obtained from Eqs.(3.33), (3.36), and (3.40) after setting the scaling parameter  $\varepsilon_s = 1$ . We get

$$\eta_{cn} = \eta_{cn}^{(0)} + \eta_{cn}^{(1)} = Q_0 + Q_1 \cos(\omega t + \beta) + Q_2 \cos(2\omega t + 2\phi + \alpha) \quad (3.45)$$

where

$$Q_0 = (\varepsilon + \zeta_0), \quad (3.46)$$

$$Q_1 = (\xi_0^2 + \zeta_1^2 + 2\xi_0\zeta_1 \cos \phi)^{1/2}, \quad (3.47)$$

$$Q_2 = \zeta_2, \quad (3.48)$$

and

$$\beta = \tan^{-1} \frac{\xi_0 \sin \phi + \zeta_1 \sin 2\phi}{\xi_0 \cos \phi + \zeta_1 \cos 2\phi}. \quad (3.49)$$

We see from Eq.(3.45) that the solution of Eq.(3.21) to first order has static, linear oscillatory, and nonlinear oscillatory components resulting from the first-order nonlinear term  $F_2\eta_{cn}^2$  in the polynomial expansion of  $F(z)$ . Further iterations in the perturbation procedure corresponding to higher order in the scaling factor  $\varepsilon_s$  lead to the inclusion of higher order harmonics in the solution to Eq.(3.21).

For an appropriate range of values of the dynamical parameters, including drive frequency, the interaction force nonlinearities that lead to the generation of harmonics are known to stimulate the generation of subharmonics [51]. The nonlinearities also lead to modal interactions that result in the resonance bifurcations reported in the literature [52, 53] whereby a cantilever resonance mode is split into multiple modes upon cantilever-sample ‘contact.’ An analytical discussion of subharmonic generation and routes to chaos in  $d$ -AFM is given in Appendix B. Resonance bifurcations in  $d$ -AFM are shown in Appendix C to be predicted from an application of the group renormalization method to the nonlinear coupling of cantilever modes.



### 3.3.5 Connection Between Model Parameters and Material Properties

The results so far obtained are derived from the single system model where the effects of the sample surface displacements  $\eta_s$  are absorbed in the interaction force in the spring model representation (or for equivalent representations where the effects of  $\eta_s$  are absorbed in the boundary conditions). One of the critical connections, explicitly or implicitly stated, between the cantilever oscillations and the sample physical properties occurs in the spring model through the relation  $k^* = F_1$ , where  $k^*$  is an effective spring constant of the interaction force. The connection occurs via the shift in the cantilever resonance frequency. The only other possible link between cantilever oscillations and the sample physical properties in the spring model is via the interaction-force damping coefficient  $S_1$ . Indeed, as pointed out in Sect. 3.3.2,  $S_1$  accounts for the transfer of energy from the cantilever to the sample via the interaction force. Although the parameters  $F_1$  and  $S_1$  collectively account for the effects of the sample physical properties in the spring model, the de-convolution of specific sample physical properties from an assessment of  $F_1$  and  $S_1$  is not at all straightforward.

The transfer of energy from an oscillating cantilever through  $S_1$  in the spring model implies that the sample surface receiving the energy must itself oscillate. To maintain equilibrium the amplitude of surface oscillations for a given energy input is necessarily determined by a sample restoring force that, like the restoring force for cantilever dynamics, can be modeled as a surface spring with an effective stiffness constant  $k_s$ . The magnitude of  $k_s$  is often assessed by the Hertzian contact method that provides a static measurement of  $k_s$ . The transfer of energy from the cantilever, however, does not occur statically but rather at cantilever oscillation frequencies. The energy transfer is dynamic and must be accounted dynamically, just as the effective  $n$ th mode cantilever stiffness constant  $k_{cn}$  ( $n = 1, 2, 3, \dots$ ) is a dynamic quantity whose magnitude is assessed in free-space by its dependence on the modal oscillation frequency  $\omega_{cn}$ . Evidence for the necessity of a dynamic modulus is apparent in certain applications of  $d$ -AFM. For example, the use of an effective dynamic modulus or equivalently of the surface acoustic impedance is central to the assessment of delaminations and voids in layered materials using UAFM [16].

From physical and symmetry considerations it is advantageous and appropriate to view the vibrating sample as a system independent of the cantilever and to assess  $k_s$  in free-space, just as  $k_c$  is evaluated in free space. It is reasonable to expect that  $k_s$  depends on the various free-space vibration modes of the sample in a way similar to that of  $k_{cn}$  for the cantilever. For present considerations, however, we assume that the value of  $k_s$  is adequately approximated by the value obtained from the Hertzian contact method. It is important to note that just as the cantilever stiffness constant  $k_{cn}$  is independent of the interaction force, so  $k_s$  must be independent of the interaction force.

### 3.4 Coupled Independent Systems Model of Cantilever-Sample Dynamics

The occurrence of independent stiffness constants  $k_{cn}$  and  $k_s$  for the cantilever and sample, respectively, begs direct consideration of the surface displacement  $\eta_s$  in tip-sample dynamics. The inclusion of the variable  $\eta_s$  in addition to the cantilever displacement  $\eta_{cn}$  in the expansion of the interaction force  $F(z)$  means from Fig. 3.3 that we must write  $(z - z_0) = (\eta_{cn} + \eta_s)$ . The inclusion of  $\eta_s$  in the expansion necessitates two dynamical equations for solution. One dynamical equation is Eq. (3.10). The second dynamical equation is Eq. (3.11) describing damped oscillatory displacements  $\eta_s$  of the sample surface that is subject to the same cantilever tip-sample surface interaction force  $F(z)$  as that of the cantilever. We thus consider that the cantilever and sample can be treated analytically as two independent, damped, oscillatory systems coupled by a mutual interaction force. We shall call this model the coupled independent systems (CIS) model.

From Eqs. (3.10), (3.11), and (3.16) we accordingly write the governing temporal equations as

$$m_c \ddot{\eta}_{cn} + \gamma_c \dot{\eta}_{cn} + (k_c - F_1) \eta_{cn} - F_1 \eta_s = F_c \cos \omega_c t + F_0 + F_2 (\eta_{cn} + \eta_s)^2 + \dots \quad (3.50)$$

$$m_s \ddot{\eta}_s + \gamma_s \dot{\eta}_s + (k_s - F_1) \eta_s - F_1 \eta_{cn} = F_s \cos(\omega_s t + \theta) + F_0 + F_2 (\eta_{cn} + \eta_s)^2 + \dots \quad (3.51)$$

where  $m_s$  is the “active” mass of the sample participating in the surface oscillations. We note that it is no longer necessary to include the time derivative  $\dot{z}$  in the interaction force  $F(z)$ , since the transfer of energy from the cantilever to the sample is accounted directly in the CIS model by the mutual coupling defined by  $F(z)$ . Thus, the interaction force damping (energy transfer) coefficient  $S_1$  is eliminated in Eqs. (3.50) and (3.51). The sample damping coefficient, in analogy to the cantilever damping coefficient, is denoted by  $\gamma_s$ .

We point out that Eqs. (3.50) and (3.51) are obtained assuming that the cantilever is a rectangular beam of constant cross-section. Such a restriction is not necessary, since the mathematical procedure leading to Eqs. (3.10) and (3.11), hence to Eqs. (3.50) and (3.51), is based on the assumption that the general displacement of the cantilever can be expanded in terms of a set of eigenfunctions that form an orthogonal basis set for the problem. For the rectangular beam cantilever the eigenfunctions are shown in Sect. 3.2 to be  $Y_n(x)$  defined by Eq. (3.3). For some other cantilever shape a different orthogonal basis set of eigenfunctions would be appropriate. However, the mathematical procedure followed in Sect. 3.2 would lead again to Eqs. (3.50) and (3.51) with values of the coefficients appropriate to the different cantilever geometry.

The phase factor  $\theta$  in the driving term of Eq. (3.51) results from the difference in phase between the ultrasonic wave launched at the sample surface opposite to that of cantilever contact and the oscillations resulting from the ultrasonic wave incident on the cantilever side of the sample. Variations in  $\theta$  result from features embedded in the sample that produce changes in the ultrasonic velocity and wave amplitude, hence

cantilever output signal. Before obtaining solutions to Eqs. (3.50) and (3.51) for the various  $d$ -AFM modalities cited in the introduction, we consider an assessment of  $\theta$ .

### 3.4.1 Variations in Signal Amplitude and Phase from Subsurface Features

Following the “propagating wave” approach for assessing continuous waves [54], we consider a traveling stress wave of unit amplitude of the form  $e^{-\alpha x} \cos(\omega_s t - kx) = \text{Re}[e^{-\alpha x} e^{i(\omega_s t - kx)}]$ , where  $\alpha$  is the attenuation coefficient,  $x$  is the propagation distance,  $\omega_s$  is the angular frequency,  $t$  is time,  $k = \omega_s/c$ , and  $c$  is the ultrasonic phase velocity, propagating through a sample of thickness  $a/2$ . We assume that the wave is generated at the bottom surface of the sample by an ultrasonic transducer attached at the position  $x = 0$  and that the wave is reflected between the top and bottom surfaces of the sample. We assume that the most important effect of the reflections is simply to change the direction of wave propagation. Phase changes from transducer bonding and compound transducer-sample resonances are not included. The following results are thus most applicable for measurements using non-contacting ultrasonic excitation sources such as capacitive transducers, electromagnetic acoustic transducers, and optical excitation sources, since compound resonator effects are avoided.

For continuous waves the complex waveform at a point  $x$  in the material consists of the sum of all contributions resulting from waves which had been generated at the point  $x = 0$  and have propagated to the point  $x$  after multiple reflections from the sample boundaries. We thus write the complex wave  $\bar{A}(t)$  as

$$\begin{aligned} \bar{A}(t) &= e^{-\alpha x} e^{i(\omega_s t - kx)} [1 + e^{-(\alpha a + ika)} + \dots + e^{-n(\alpha a + ika)} + \dots] \\ &= e^{-\alpha x} e^{i(\omega_s t - kx)} \sum_{n=0}^{\infty} [e^{-(\alpha a + ika)}]^n = e^{-\alpha x} e^{i(\omega_s t - kx)} \frac{1}{1 - e^{-(\alpha a + ika)}} \quad (3.52) \end{aligned}$$

where the last equality follows from the geometric series generated by the infinite sum. The real waveform  $A(t)$  is obtained from Eq. (3.52) as

$$A(t) = \text{Re}[\bar{A}(t)] = e^{-\alpha x} (A_1^2 + A_2^2)^{1/2} \cos(\omega_s t - kx - \phi) = e^{-\alpha x} B \cos(\omega_s t - kx - \phi) \quad (3.53)$$

where

$$A_1 = \frac{e^{\alpha a} - \cos ka}{2(\cosh \alpha a - \cos ka)}, \quad (3.54)$$

$$A_2 = -\frac{\sin ka}{2(\cosh \alpha a - \cos ka)}, \quad (3.55)$$

$$\phi = \tan^{-1} \frac{\sin ka}{e^{\alpha a} - \cos ka}, \quad (3.56)$$

and

$$B = (A_1^2 + A_2^2)^{1/2} = (1 + e^{-2\alpha a} - 2e^{-\alpha a} \cos ka)^{-1/2}. \quad (3.57)$$

The evaluation (detection) of a continuous wave at the end of the sample opposite to that of the source is obtained by setting  $x = a/2$  in the above equations. It is at  $x = a/2$  that the AFM cantilever engages the sample surface. In the following equations we set  $x = a/2$ .

The above results are derived for a homogeneous specimen. Consider now that the specimen of thickness  $a/2$  having phase velocity  $c$  contains embedded material of thickness  $d/2$  having phase velocity  $c_d$ . The phase factor  $ka = \omega_s a/c$  in Eqs. (3.53)–(3.57) must then be replaced by  $ka - \psi$  where

$$\psi = \omega_s d \left( \frac{1}{c} - \frac{1}{c_d} \right) = \omega_s d \frac{\Delta c}{c_d c} = kd \frac{\Delta c}{c_d}, \quad (3.58)$$

and  $\Delta c = c_d - c$ . We thus set  $x = a/2$  and re-write Eqs. (3.53), (3.56), and (3.57) as

$$\hat{A}(t) = e^{-\alpha a/2} \hat{B} \cos \left[ \omega_s t - \frac{(ka - \psi)}{2} - \hat{\phi} \right] \quad (3.59)$$

where

$$\hat{\phi} = \tan^{-1} \frac{\sin(ka - \psi)}{e^{\alpha a} - \cos(ka - \psi)}, \quad (3.60)$$

and

$$\hat{B} = [1 + e^{-2\alpha a} - 2e^{-\alpha a} \cos(ka - \psi)]^{-1/2}. \quad (3.61)$$

We have assumed in obtaining the above equations that the change in the attenuation coefficient resulting from the embedded material is negligible.

For small  $\psi$  we may expand Eq. (3.59) in a power series about  $\psi = 0$ . Keeping only terms to first order, we obtain

$$\hat{\phi} = \phi + \Delta\phi \quad (3.62)$$

where

$$\Delta\phi = -\psi \left[ \frac{e^{\alpha a} \cos ka - 1}{(e^{\alpha a} - \cos ka)^2 + \sin^2 ka} \right]. \quad (3.63)$$

Equation (3.59) is thus approximated as

$$\hat{A}(t) = e^{-\alpha a/2} \hat{B} \cos \left( \omega_s t - \frac{ka}{2} - \phi + \frac{\psi}{2} - \Delta\phi \right) = e^{-\alpha a/2} \hat{B} \cos(\omega_s t + \theta) \quad (3.64)$$

where

$$\theta = -(\chi + \Delta\chi) = -\left( \frac{ka}{2} + \phi - \frac{\psi}{2} + \Delta\phi \right), \quad (3.65)$$

$$\chi = \frac{ka}{2} + \phi, \quad (3.66)$$

and

$$\Delta\chi = -\frac{\psi}{2} + \Delta\phi = -\psi \left[ \frac{1}{2} + \frac{e^{\alpha a} \cos ka - 1}{(e^{\alpha a} - \cos ka)^2 + \sin^2 ka} \right]. \quad (3.67)$$

Equation (3.67) reveals that the total phase contribution at  $x = a/2$  is  $\theta$  and, from Eqs. (3.65) and (3.67), that the phase variation resulting from embedded material is  $-\Delta\chi$ .

The fractional change in the Young modulus  $\Delta E/E$  is approximately related to the fractional change in the ultrasonic longitudinal velocity  $\Delta c/c$  as  $\Delta E/E \approx \Delta C_{11}/C_{11} = (2\Delta c/c) + (\Delta\rho/\rho)$  where  $\rho$  is the mass density of the sample and  $C_{11}$  is the Brugger longitudinal elastic constant. If the fractional change in the mass density is small compared to the fractional change in the wave velocity, we estimate the relationship between  $\Delta E/E$  and  $\Delta c/c$  as  $\Delta E/E \approx 2\Delta c/c$ . This relationship may be used to express  $\psi$ , given in Eq. (3.58) in terms of  $\Delta c/c_d = (c/c_d)(\Delta c/c)$ , in terms of  $\Delta E/E$ .

### 3.4.2 Solution to the Coupled Dynamical Equations

We solve the coupled nonlinear Eqs. (3.50) and (3.51) for the steady-state (particular) solution by first writing the coupled equations in matrix form as [35]

$$M\ddot{\eta} + \gamma\dot{\eta} + k\eta - F_1\eta = F_d T + F_0 + F_2\eta_{cs} + \dots \quad (3.68)$$

where

$$\begin{aligned} M &= \begin{pmatrix} m_c & 0 \\ 0 & m_s \end{pmatrix}, \quad \eta = \begin{pmatrix} \eta_{cn} \\ \eta_s \end{pmatrix}, \quad \gamma = \begin{pmatrix} \gamma_c & 0 \\ 0 & \gamma_s \end{pmatrix}, \quad k = \begin{pmatrix} k_{cn} - F_1 & 0 \\ 0 & k_s - F_1 \end{pmatrix}, \\ F_d &= \begin{pmatrix} F_c & 0 \\ 0 & F_s \end{pmatrix}, \quad T = \begin{pmatrix} \cos \omega_c t \\ \cos(\omega_s t + \theta) \end{pmatrix}, \quad F_0 = \begin{pmatrix} F_0 \\ F_0 \end{pmatrix}, \quad F_1 = \begin{pmatrix} 0 & F_1 \\ F_1 & 0 \end{pmatrix}, \\ F_2 &= \begin{pmatrix} F_2 & 0 \\ 0 & F_2 \end{pmatrix}, \quad \text{and } \eta_{cs} = \begin{pmatrix} (\eta_{cn} + \eta_s)^2 \\ (\eta_{cn} + \eta_s)^2 \end{pmatrix}. \end{aligned}$$

We solve Eq. (3.68) using the perturbative procedure given in Sect. 3.3.4 where the zeroth-order solution is obtained by neglecting the nonlinear expansion terms in Eq. (3.68) and solving the resulting expression. The first-order solution is obtained by substituting the zeroth-order solution in the nonlinear terms of Eq. (3.68) and solving the resulting expression. It is important to recognize that the procedure provides solutions for both the cantilever tip and the sample surface displacements—a result stemming from the symmetry of the governing dynamical equations, Eqs. (3.50) and (3.51). The procedure is much too lengthy to reproduce here in full detail. Thus, only the salient features of the procedure leading to the steady state solution for the

cantilever displacements  $\eta_{cn}$  are given. The solutions for the sample displacements  $\eta_s$  mostly correspond to an interchange of cantilever and sample parameters in the solution set for  $\eta_{cn}$ .

We begin by writing

$$\eta_{cn} = \eta_{cn}^{(0)} + \eta_{cn}^{(1)} = \varepsilon_{cn} + \xi_{cn} + \zeta_{cn}, \quad (3.69)$$

and

$$\eta_s = \eta_s^{(0)} + \eta_s^{(1)} = \varepsilon_s + \xi_s + \zeta_s \quad (3.70)$$

where  $\eta_{cn}^{(0)} = \varepsilon_{cn} + \xi_{cn}$  with  $\varepsilon_{cn}$  and  $\xi_{cn}$  representing the zeroth-order (i.e. linear) static and oscillatory solutions, respectively, for the  $n$ th mode cantilever displacement. The term  $\eta_{cn}^{(1)} = \zeta_{cn}$  is the first-order (i.e., nonlinear) solution for the  $n$ th mode cantilever displacement. The terms  $\eta_s^{(0)} = \varepsilon_s + \xi_s$  and  $\eta_s^{(1)} = \zeta_s$  are the corresponding zeroth-order and first-order displacements for the sample surface.

### 3.4.2.1 Zeroth-Order Solution

The zeroth-order solution is obtained by neglecting the nonlinear terms in the matrix Eq.(3.68) to obtain a static solution  $\varepsilon_{cn}$  and an oscillatory solution  $\xi_{cn}$  for the cantilever. The static solution is given by

$$\varepsilon_{cn} = \frac{k_s F_0}{k_{cn} k_s - F_1(k_{cn} + k_s)}. \quad (3.71)$$

The oscillatory solution is given by

$$\xi_{cn} = Q_{cc} \cos(\omega_c t + \alpha_{cc} - \phi_{cc}) + Q_{cs} \cos(\omega_s t - \phi_{ss} + \theta) \quad (3.72)$$

where

$$\phi_{cc} = \tan^{-1} \frac{\omega_c(\gamma_s k_{cn} + \gamma_c k_s) - \omega_c^3(\gamma_s m_c + \gamma_c m_s) - F_1 \omega_c(\gamma_s + \gamma_c)}{k_{cn} k_s + m_s m_c \omega_c^4 - \omega_c^2(m_s k_{cn} + m_c k_s + \gamma_c \gamma_s) - F_1(k_{cn} + k_s - m_s \omega_c^2 - m_c \omega_c^2)}, \quad (3.73)$$

$$\phi_{ss} = \tan^{-1} \frac{\omega_s(\gamma_s k_{cn} + \gamma_c k_s) - \omega_s^3(\gamma_s m_c + \gamma_c m_s) - F_1 \omega_s(\gamma_s + \gamma_c)}{k_{cn} k_s + m_s m_c \omega_s^4 - \omega_s^2(m_s k_{cn} + m_c k_s + \gamma_c \gamma_s) - F_1(k_{cn} + k_s - m_s \omega_s^2 - m_c \omega_s^2)}, \quad (3.74)$$

$$\begin{aligned}
Q_{cc} = & F_c \{ [k_s - F_1 - m_s \omega_c^2]^2 + \gamma_s^2 \omega_c^2 \}^{1/2} \{ [k_{cn} k_s + m_s m_c \omega_c^4 \\
& - \omega_c^2 (m_s k_{cn} + m_c k_s + \gamma_c \gamma_s) - F_1 (k_{cn} + k_s - m_s \omega_c^2 - m_c \omega_c^2)]^2 \\
& + [\omega_c (\gamma_s k_{cn} + \gamma_c k_s) - \omega_c^3 (\gamma_s m_c + \gamma_c m_s) - F_1 \omega_c (\gamma_s + \gamma_c)]^2 \}^{-1/2},
\end{aligned} \tag{3.75}$$

and

$$\begin{aligned}
Q_{cs} = & F_s F_1 \{ [k_{cn} k_s + m_s m_c \omega_s^4 - \omega_s^2 (m_s k_{cn} + m_c k_s + \gamma_c \gamma_s) \\
& - F_1 (k_{cn} + k_s - m_s \omega_s^2 - m_c \omega_s^2)]^2 \\
& + [\omega_s (\gamma_s k_{cn} + \gamma_c k_s) - \omega_s^3 (\gamma_s m_c + \gamma_c m_s) - F_1 \omega_s (\gamma_s + \gamma_c)]^2 \}^{-1/2}.
\end{aligned} \tag{3.76}$$

### 3.4.2.2 First-Order (Nonlinear) Solution

The first-order (nonlinear) solution  $\eta_{cn}^{(1)} = \zeta_{cn}$  for each mode  $n$  of the cantilever is considerably more complicated, since it contains sum-frequency, difference-frequency, and generated harmonic-frequency components in addition to linear and static components. The solution  $\eta_{cn}^{(1)} = \zeta_{cn}$  is thus written as

$$\eta_{cn}^{(1)} = \zeta_{cn} = \zeta_{cn, \text{stat}} + \zeta_{cn, \text{lin}} + \zeta_{cn, \text{diff}} + \zeta_{cn, \text{sum}} + \zeta_{cn, \text{harm}} \tag{3.77}$$

where  $\zeta_{cn, \text{stat}}$  is the static or “dc” contribution generated by the nonlinear tip-surface interaction,  $\zeta_{cn, \text{lin}}$  is the generated linear oscillatory contribution,  $\zeta_{cn, \text{diff}}$  is the generated difference-frequency contribution resulting from the nonlinear mixing of the cantilever and sample oscillations,  $\zeta_{cn, \text{sum}}$  is the generated sum-frequency contribution resulting from the nonlinear mixing of the cantilever and sample oscillations, and  $\zeta_{cn, \text{harm}}$  are generated harmonic contributions.

Generally, the cantilever responds with decreasing displacement amplitudes as the drive frequency is increased above the fundamental resonance, even when driven at higher modal frequencies (Note: for some cantilevers the second resonance mode has the largest amplitude). Dynamic AFM methods do not generally utilize harmonic or sum-frequency signals. For expediency, such signals from the first-order solution will not be considered here. Only the static, linear, and difference-frequency terms from the first-order solution are relevant to the most commonly used  $d$ -AFM modalities.

The static contribution generated by the nonlinear interaction force is obtained to be

$$\begin{aligned}
\zeta_{cn, \text{stat}} = & \frac{1}{2} \frac{k_s F_2}{[k_{cn} k_s - F_1 (k_{cn} + k_s)]} [2\varepsilon_o^2 + Q_{cc}^2 + Q_{cs}^2 + Q_{sc}^2 + Q_{ss}^2 \\
& + 2Q_{cc} Q_{sc} \cos(\alpha_{cc} - 2\phi_{cc}) + 2Q_{cs} Q_{ss} \cos \alpha_{ss}]
\end{aligned} \tag{3.78}$$

where

$$\varepsilon_o = \frac{(k_{cn} + k_s)F_0}{k_{cn}k_s - F_1(k_{cn} + k_s)}, \quad (3.79)$$

$$\begin{aligned} Q_{sc} = & F_c F_1 \{ [k_{cn}k_s + m_s m_c \omega_c^4 - \omega_c^2(m_s k_{cn} + m_c k_s + \gamma_c \gamma_s) \\ & - F_1(k_{cn} + k_s - m_s \omega_c^2 - m_c \omega_c^2)]^2 \\ & + [\omega_c(\gamma_s k_{cn} + \gamma_c k_s) - \omega_c^3(\gamma_s m_c + \gamma_c m_s) - F_1 \omega_c(\gamma_s + \gamma_c)]^2 \}^{-1/2}, \end{aligned} \quad (3.80)$$

$$\begin{aligned} Q_{ss} = & F_s \{ [k_{cn} - F_1 - m_c \omega_s^2]^2 + \gamma_c^2 \omega_s^2 \}^{1/2} \{ [k_{cn}k_s + m_s m_c \omega_s^4 \\ & - \omega_s^2(m_s k_{cn} + m_c k_s + \gamma_c \gamma_s) - F_1(k_{cn} + k_s - m_s \omega_s^2 - m_c \omega_s^2)]^2 \\ & + [\omega_s(\gamma_s k_{cn} + \gamma_c k_s) - \omega_s^3(\gamma_s m_c + \gamma_c m_s) - F_1 \omega_s(\gamma_s + \gamma_c)]^2 \}^{-1/2}, \end{aligned} \quad (3.81)$$

$$\alpha_{cc} = \tan^{-1} \frac{\gamma_s \omega_c}{k_s - F_1 - m_s \omega_c^2}, \quad (3.82)$$

$$\alpha_{ss} = \tan^{-1} \frac{\gamma_c \omega_s}{k_{cn} - F_1 - m_c \omega_s^2} \quad (3.83)$$

and  $\phi_{cc}$  is given by Eq. (3.73),  $Q_{cc}$  by Eq. (3.75) and  $Q_{cs}$  by Eq. (3.76).

The linear oscillatory contribution  $\zeta_{cn,lin}$  generated by the nonlinear interaction force in the first order solution is obtained to be

$$\begin{aligned} \zeta_{cn,lin} = & 2 \frac{D_c}{R_{cc}} \varepsilon_o F_2 [Q_{cc}^2 + Q_{sc}^2 + 2Q_{cc}Q_{sc} \cos \alpha_{cc}]^{1/2} \cos(\omega_c t - 2\phi_{cc} + \beta_c + \mu_{cc}) \\ & + 2 \frac{D_s}{R_{ss}} \varepsilon_o F_2 [Q_{ss}^2 + Q_{cs}^2 + 2Q_{ss}Q_{cs} \cos \alpha_{ss}]^{1/2} \\ & \cos(\omega_s t - 2\phi_{ss} + \beta_s + \mu_{ss} + \theta) \end{aligned} \quad (3.84)$$

where

$$\mu_{cc} = \tan^{-1} \frac{Q_{cc} \sin \alpha_{cc}}{Q_{cc} \cos \alpha_{cc} + Q_{sc}}, \quad (3.85)$$

$$\mu_{ss} = \tan^{-1} \frac{Q_{ss} \sin \alpha_{ss}}{Q_{ss} \cos \alpha_{ss} + Q_{cs}}, \quad (3.86)$$

$$\beta_c = \tan^{-1} \frac{\gamma_s \omega_c}{k_s - m_s \omega_c^2}, \quad (3.87)$$

$$\beta_s = \tan^{-1} \frac{\gamma_c \omega_s}{k_{cn} - m_c \omega_s^2}, \quad (3.88)$$



$$D_c = [(k_s - m_s \omega_c^2)^2 + \gamma_s^2 \omega_c^2]^{1/2}, \quad (3.89)$$

$$D_s = [(k_s - m_s \omega_s^2)^2 + \gamma_s^2 \omega_s^2]^{1/2}, \quad (3.90)$$

$$\begin{aligned} R_{ss} = & \{ [k_{cn} k_s + m_s m_c \omega_s^4 - \omega_s^2 (m_s k_{cn} + m_c k_s + \gamma_c \gamma_s) \\ & - F_1 (k_{cn} + k_s - m_s \omega_s^2 - m_c \omega_s^2)]^2 + [\omega_s (\gamma_s k_{cn} + \gamma_c k_s) \\ & - \omega_s^3 (\gamma_s m_c + \gamma_c m_s) - F_1 \omega_s (\gamma_s + \gamma_c)]^2 \}^{1/2}, \end{aligned} \quad (3.91)$$

and

$$\begin{aligned} R_{cc} = & \{ [k_{cn} k_s + m_s m_c \omega_c^4 - \omega_c^2 (m_s k_{cn} + m_c k_s + \gamma_c \gamma_s) \\ & - F_1 (k_{cn} + k_s - m_s \omega_c^2 - m_c \omega_c^2)]^2 + [\omega_c (\gamma_s k_{cn} + \gamma_c k_s) \\ & - \omega_c^3 (\gamma_s m_c + \gamma_c m_s) - F_1 \omega_c (\gamma_s + \gamma_c)]^2 \}^{1/2}. \end{aligned} \quad (3.92)$$

The difference-frequency contribution  $\zeta_{cn,diff}$  generated by the nonlinear interaction force in the first-order solution is obtained to be

$$\zeta_{cn,diff} = G_n \cos[(\omega_c - \omega_s)t - \phi_{cc} + \phi_{ss} + \beta_{cs} - \phi_{cs} + \Gamma - \theta] \quad (3.93)$$

where

$$\begin{aligned} G_n = & \frac{D_{cs}}{R_{cs}} F_2 \{ Q_{cc}^2 Q_{cs}^2 + Q_{sc}^2 Q_{ss}^2 + Q_{cc}^2 Q_{ss}^2 + Q_{cs}^2 Q_{sc}^2 \\ & + 2 Q_{cc} Q_{cs} Q_{sc} Q_{ss} \cos(\alpha_{cc} + \alpha_{ss}) + 2 Q_{cc}^2 Q_{cs} Q_{ss} \cos \alpha_{ss} \\ & + 2 Q_{cc} Q_{cs}^2 Q_{sc} \cos \alpha_{cc} + 2 Q_{sc}^2 Q_{ss} Q_{cs} \cos \alpha_{ss} \\ & + 2 Q_{cc} Q_{ss} Q_{cs} Q_{sc} \cos(\alpha_{cc} - \alpha_{ss}) \}^{1/2}, \end{aligned} \quad (3.94)$$

$$D_{cs} = \sqrt{[k_s - m_s (\omega_c - \omega_s)]^2 + \gamma_s^2 (\omega_c - \omega_s)^2}, \quad (3.95)$$

$$R_{cs} = \sqrt{R_{cs1}^2 + R_{cs2}^2}, \quad (3.96)$$

$$\begin{aligned} R_{cs1} = & k_{cn} k_s - m_s k_{cn} (\omega_c - \omega_s)^2 - m_c k_s (\omega_c - \omega_s)^2 + m_s m_c (\omega_c - \omega_s)^4 \\ & - \gamma_c \gamma_s (\omega_c - \omega_s)^2 - F_1 [k_{cn} + k_s - m_s (\omega_c - \omega_s)^2 - m_c (\omega_c - \omega_s)^2], \end{aligned} \quad (3.97)$$

$$\begin{aligned} R_{cs2} = & (\omega_c - \omega_s) (\gamma_s k_c + \gamma_c k_s) - (\omega_c - \omega_s)^3 (\gamma_s m_c + \gamma_c m_s) \\ & - F_1 (\omega_c - \omega_s) (\gamma_s + \gamma_c), \end{aligned} \quad (3.98)$$

$$\phi_{cs} = \tan^{-1} \frac{R_{cs2}}{R_{cs1}}, \quad (3.99)$$

$$\beta_{cs} = \tan^{-1} \frac{\gamma_s(\omega_c - \omega_s)}{k_s - m_s(\omega_c - \omega_s)^2}, \quad (3.100)$$

and

$$\Gamma = \tan^{-1} \frac{Q_{cc}Q_{cs} \sin \alpha_{cc} - Q_{sc}Q_{ss} \sin \alpha_{ss} + Q_{cc}Q_{ss} \sin(\alpha_{cc} - \alpha_{ss})}{Q_{cc}Q_{cs} \cos \alpha_{cc} + Q_{sc}Q_{ss} \cos \alpha_{ss} + Q_{cc}Q_{ss} \cos(\alpha_{cc} - \alpha_{ss}) + \frac{Q_{cs}Q_{sc}}{(3.101)}}.$$

### 3.4.3 Signal Generation for Various *d*-AFM Modalities in the CIS Model

The treatment in the CIS model of the cantilever and sample as coupled independent systems introduces a high degree of symmetry in the mathematical analysis. The symmetry allows considerable flexibility in quantifying the cantilever-sample dynamics for a variety of *d*-AFM modalities. We apply the CIS model to the assessment of the cantilever output signal for the most frequently used *d*-AFM modalities including heterodyne force microscopy, scanning near-field ultrasonic holography, resonant difference-frequency atomic force ultrasonic microscopy, ultrasonic force microscopy, atomic force acoustic microscopy, force modulation microscopy, amplitude modulation atomic force microscopy, and ultrasonic atomic force microscopy.

We note that for the range of frequencies generally employed in *d*-AFM the contribution from terms in the solution set involving the mass of the sample element  $m_s$  is small compared to the remaining terms and may to an excellent approximation be neglected in the following applications of the CIS model.

#### 3.4.3.1 Heterodyne Force Microscopy, Scanning Near-Field Ultrasonic Holography, and Resonant Difference-Frequency Atomic Force Ultrasonic Microscopy

Heterodyne force microscopy [9], scanning near-field ultrasonic holography [10], and resonant difference-frequency atomic force ultrasonic microscope [11] employ an ultrasonic wave launched from the bottom of a sample, while the AFM cantilever tip engages the sample top surface. The cantilever in RDF-AFUM is driven at a frequency differing from the ultrasonic frequency by one of the contact resonance frequencies of the engaged cantilever. As pointed out in the introduction the tip-sample interaction force varies nonlinearly with the tip-surface separation distance (see Fig. 3.1). During the mixing of the forced cantilever and sample oscillations the nonlinearity of the mutual interaction force generates a difference-frequency output signal from the cantilever. The maximum difference-frequency signal amplitude occurs when the

cantilever oscillation amplitude and tip-sample quiescent separation distance are optimized to produce the maximum magnitude of the nonlinearity parameter  $F_2$  in the polynomial expansion of Eq. (3.16). Maximum nonlinearity occurs near the bottom of the force curve as shown in Fig. 3.1. There the maximum change in the slope of the force versus separation curve (hence maximum interaction force nonlinearity) occurs. We shall call this region of operation the maximum nonlinearity regime.

Variations in the amplitude and phase of the bulk wave due to the presence of subsurface nano/microstructures and features as well as variations in near-surface material parameters produce variations in the amplitude and phase of the difference-frequency signal. The variations in the difference-frequency signal are used to generate spatial mappings (micrographs) of the subsurface and near-surface structures. Most commonly, the micrographs are obtained from variations in phase (phase imaging) using constant amplitude control.

The dominant term or terms for the cantilever difference-frequency displacement in Eqs. (3.2) and (3.69) depend on the values of  $k_{cn}$  for the free-space modes of cantilever oscillation,  $\Delta\omega = (\omega_c - \omega_s)$ , and the value of the nonlinearity coefficient  $F_2$  obtained for an appropriate oscillation amplitude and quiescent separation distance  $z_0$  for which the maximum difference-frequency signal occurs. The maximum difference-frequency signal occurs when the tip-sample separation during oscillation encompasses the region near  $z_B$  in Fig. 3.1. We designate the free-space mode  $n$  corresponding to the difference-frequency contact resonance occurs as  $n = p$ . The dominant difference-frequency component in Eqs. (3.2) and (3.69) is thus  $\eta_{cp} = \eta_{cp,\text{diff}} = \zeta_{cp,\text{diff}}$  and is given by Eq. (3.93) for  $n = p$  as

$$\zeta_{cp,\text{diff}} = G_p \cos[(\omega_c - \omega_s)t - \phi_{cc} + \phi_{ss} + \beta_{cs} - \phi_{cs} + \Gamma - \theta] \quad (3.102)$$

where  $G_p$ , given by Eq. (3.94), and the phase terms in Eq. (3.102) are obtained from Eqs. (3.65), (3.73), (3.74), (3.82), (3.83), (3.99)–(3.101). Since Eqs. (3.99) and (3.100) only involve factors pertaining to the difference-frequency  $\Delta\omega$ , the appropriate cantilever stiffness constant to use in the equations is  $k_{cp}$ . Equations (3.73) and (3.82), however, only involve factors pertaining to the cantilever drive frequency  $\omega_c$ , while Eqs. (3.74) and (3.83) only involve factors pertaining to the sample drive (ultrasonic) frequency  $\omega_s$ . The cantilever drive frequency  $\omega_c$  and ultrasonic frequency  $\omega_s$  are usually set near (but not necessary equal to) higher resonance modes  $n = q$  and  $n = r$ , respectively, of the engaged cantilever. In such case the appropriate cantilever stiffness constant is  $k_{cq}$  for  $n = q$  and  $k_{cr}$  for  $n = r$ . For relatively small difference-frequencies, it may occur that  $q = r$ . If  $\omega_c$  and  $\omega_s$  are not set at or near a resonance modal frequency of the engaged cantilever, then it may be necessary to include several terms in Eqs. (3.2) and (3.69) corresponding to multiple values of  $q$  and  $r$ .

The equations for  $G_p$  and the phase terms in Eq. (3.102) may be obtained from Eqs. (3.80), (3.81), (3.94)–(3.98) where the terms involving the sample mass  $m_s$  may be dropped to an excellent approximation. For ultrasonic wave and cantilever drive frequencies in the low megahertz range we obtain, setting  $\Delta\omega = (\omega_c - \omega_s)$ , that

$$\beta_{cs} \approx \tan^{-1} \frac{\gamma_s(\Delta\omega)}{k_s}, \quad (3.103)$$

$$\phi_{cs} \approx \tan^{-1} \frac{(\gamma_c k_s + \gamma_s k_{cp})(\Delta\omega) - \gamma_s m_c (\Delta\omega)^3 - F_1(\gamma_c + \gamma_s)(\Delta\omega)}{k_{cp} k_s - (m_c k_s + \gamma_c \gamma_s)(\Delta\omega)^2 - F_1[k_{cp} + k_s - m_c(\Delta\omega)^2]}, \quad (3.104)$$

$$\phi_{cc} \approx \tan^{-1} \frac{(\gamma_c k_s + \gamma_s k_{cq})\omega_c - \gamma_s m_c \omega_c^3 - F_1(\gamma_c + \gamma_s)\omega_c}{k_{cq} k_s - (m_c k_s + \gamma_c \gamma_s)\omega_c^2 - F_1(k_{cq} + k_s - m_c \omega_c^2)}, \quad (3.105)$$

$$\phi_{ss} \approx \tan^{-1} \frac{(\gamma_c k_s + \gamma_s k_{cr})\omega_s - \gamma_s m_c \omega_s^3 - F_1(\gamma_c + \gamma_s)\omega_s}{k_{cr} k_s - (m_c k_s + \gamma_c \gamma_s)\omega_s^2 - F_1(k_{cr} + k_s - m_c \omega_s^2)}, \quad (3.106)$$

and  $G_p$  is given by Eq. (3.94) where

$$\begin{aligned} \frac{D_{cs}}{R_{cs}} &\approx \{k_s^2 + \gamma_s^2(\Delta\omega)^2\}^{1/2} \{ [k_{cp} k_s - (\Delta\omega)^2(m_c k_s + \gamma_c \gamma_s) \\ &\quad - F_1(k_{cp} + k_s - m_c(\Delta\omega)^2)]^2 \\ &\quad + [(\Delta\omega)(\gamma_s k_{cp} + \gamma_c k_s) - (\Delta\omega)^3 \gamma_s m_c - F_1 \omega_c(\gamma_s + \gamma_c)]^2 \} - 1/2, \end{aligned} \quad (3.107)$$

$$\begin{aligned} Q_{cc} &\approx F_c \{ [k_s - F_1]^2 + \gamma_s^2 \omega_c^2 \}^{1/2} [k_{cq} k_s \\ &\quad - \omega_c^2(m_c k_s + \gamma_c \gamma_s) - F_1(k_{cq} + k_s - m_c \omega_c^2)]^2 \\ &\quad + [\omega_c(\gamma_s k_{cq} + \gamma_c k_s) - \omega_c^3 \gamma_s m_c - F_1 \omega_c(\gamma_s + \gamma_c)]^2 - \frac{1}{2}, \end{aligned} \quad (3.108)$$

$$\begin{aligned} Q_{ss} &\approx F_s \{ [k_s - F_1]^2 + \gamma_s^2 \omega_s^2 \}^{1/2} [k_{cr} k_s \\ &\quad - \omega_s^2(m_c k_s + \gamma_c \gamma_s) - F_1(k_{cr} + k_s - m_c \omega_s^2)]^2 \\ &\quad + [\omega_s(\gamma_s k_{cr} + \gamma_c k_s) - \omega_s^3 \gamma_s m_c - F_1 \omega_c(\gamma_s + \gamma_c)]^2 - \frac{1}{2}, \end{aligned} \quad (3.109)$$

$$\begin{aligned} Q_{cs} &\approx F_s F_1 [k_{cr} k_s - \omega_s^2(m_c k_s + \gamma_c \gamma_s) - F_1(k_{cr} + k_s - m_c \omega_s^2)]^2 \\ &\quad + [\omega_s(\gamma_s k_{cr} + \gamma_c k_s) - \omega_s^3 \gamma_s m_c - F_2 \omega_s(\gamma_s + \gamma_c)]^2 - \frac{1}{2}, \end{aligned} \quad (3.110)$$

and

$$\begin{aligned} Q_{sc} &\approx F_c F_1 [k_{cq} k_s - \omega_c^2(m_c k_s + \gamma_c \gamma_s) - F_1(k_{cq} + k_s - m_c \omega_c^2)]^2 \\ &\quad + [\omega_c(\gamma_s k_{cq} + \gamma_c k_s) - \omega_c^3 \gamma_s m_c - F_1 \omega_c(\gamma_s + \gamma_c)]^2 - \frac{1}{2} \end{aligned} \quad (3.111)$$

The phase term  $\Gamma$  in Eq. (3.102) is given by Eq. (3.101) and is quite complicated. However, advantage can be taken of the fact that  $k_s$  is generally large compared to other terms in the numerators of  $Q_{cc}$ ,  $Q_{ss}$ ,  $Q_{cs}$ , and  $Q_{sc}$ ; the denominators of these terms are very roughly all equal. Hence, the magnitudes of  $Q_{cc}$  and  $Q_{ss}$  are usually large compared to those of  $Q_{cs}$  and  $Q_{sc}$ . The  $Q_{cc}Q_{ss}$  term thus dominates in Eq. (3.101) and we may approximate  $\Gamma$  as

$$\Gamma \approx \alpha_{cc} - \alpha_{ss} = \tan^{-1} \frac{\gamma_s \omega_c}{k_s - F_1} - \tan^{-1} \frac{\gamma_c \omega_s}{k_{cr} - F_1 - m_c \omega_s^2}. \quad (3.112)$$

To the extent that  $\Gamma$  may be approximated by Eq. (3.112) we may approximate  $G_p$  as

$$G_p \approx F_2 \frac{D_{cs}}{R_{cs}} Q_{cc} Q_{ss}. \quad (3.113)$$

RDF-AFM operation requires that the difference-frequency correspond to a contact resonance mode of the cantilever. No such requirement is imposed on HFM or SNFUH. However, it is important to be aware that if the difference-frequency is larger than the lowest contact resonance but not near a higher contact resonance, a single difference-frequency mode  $p$  does not generally dominate the signal output. For such cases a sum of the largest modal contributions must be used to assess the signal output. If the difference-frequency is set well below the lowest modal frequency of the engaged cantilever, the appropriate equations are those with  $p$  equal to the lowest modal frequency of the engaged cantilever but the magnitude of the output signal would not be optimized.

### 3.4.3.2 Ultrasonic Force Microscopy

In ultrasonic force microscopy [7, 8] the cantilever drive frequency  $\omega_c$  and drive amplitude  $F_c$  are zero, while the surface drive amplitude  $F_s$  and the drive frequency  $\omega_s$  of the wave generated by the transducer at the bottom of the sample are nonzero. UFM can be operated at very large frequencies, even in the gigahertz range. Although the vibration response of the cantilever is certainly quite small at such frequencies, operation at a quiescent separation distance  $z_0$  corresponding to the nonlinear regime of the force-separation curve, such that  $F_2$  is maximum, will produce a detectable static or “dc” signal from the interaction nonlinearity. The generated static signal is called the ultrasonic force.

The nonlinear force-separation interaction in the CIS model results in a static displacement of the cantilever  $\eta_{c,\text{stat}}$  given as

$$\eta_{c,\text{stat}} = \sum_n Y_n(x_L) \eta_{cn,\text{stat}} \quad (3.114)$$

where  $\eta_{cn,\text{stat}}$  is the contribution from mode  $n$  given by

$$\eta_{cn,stat} = \varepsilon_{cn} + \zeta_{cn,stat}, \quad (3.115)$$

and the zeroth-order contribution  $\varepsilon_{cn}$  and the first-order contribution  $\zeta_{cn,stat}$  are given by Eqs. (3.71) and (3.78), respectively. Terms in Eq. (3.78) involving  $Q_{cc}$  and  $Q_{sc}$  are zero, since  $F_c$  is zero for UFM. We assume operation of the UFM in the nonlinear regime of the force curve where  $F_2$  is maximized. We approximate the nonzero terms  $Q_{ss}$  and  $Q_{cs}$  in Eq. (3.78) by (3.109) and (3.110), respectively. We obtain

$$\begin{aligned} \eta_{cn,stat} = & \frac{k_s}{k_{cn}k_s - F_1(k_{cn} + k_s)} \{F_0 \\ & + \frac{F_2}{2} [2\varepsilon_o^2 + Q_{cs}^2 + Q_{ss}^2 + 2Q_{cs}Q_{ss} \cos \alpha_{ss}]\} \end{aligned} \quad (3.116)$$

where  $\varepsilon_o$  is given by Eq. (3.79) and  $\alpha_{ss}$  is given by Eq. (3.83). To the extent that  $Q_{ss}$  is much larger than  $Q_{cs}$  because of the occurrence of  $k_s$  and  $\gamma_s \omega_s$  in the numerator of  $Q_{ss}$ , Eq. (3.116) may be simplified by dropping the terms involving  $Q_{cs}$ .

It is interesting to note that the  $\varepsilon_{cn}$  and  $\varepsilon_o$  terms in Eqs. (3.115) and (3.116) do not explicitly involve the sample surface drive amplitude  $F_s$  and frequency  $\omega_s$ . These terms predict that a static signal exists even without the presence of an ultrasonic wave propagating through the sample and results directly from the interaction of the cantilever with the sample surface via the static term  $F_0$  in the polynomial expansion of the interaction force. The  $\zeta_{cn,stat}$  terms in Eqs. (3.115) and (3.116) involving the  $Q$  factors depend directly on the magnitude of  $F_2$  and strongly on the surface drive amplitude  $F_s$  and frequency  $\omega_s$ . This means that only the contributions stemming from the nonlinearity in the cantilever tip-sample surface interaction force respond directly to variations in the surface drive amplitude and thus to surface and subsurface physical features of the material giving rise to variations in  $F_s$ . The magnitude of the contribution  $\zeta_{cn,stat}$  is strongly dependent on the surface oscillation amplitude and the cantilever tip-sample surface quiescent separation  $z_o$ , since the value of the nonlinear stiffness constant  $F_2$  that dominates these contributions is highly sensitive to the oscillation amplitude and  $z_o$ . Indeed,  $F_2$  attains a maximum value for oscillations near the bottom of the force-separation curve of Fig. 3.1.

Since  $\eta_{cn,stat}$  is dependent on both  $F_s$  and  $k_s$ , amplitude scans of the sample contain information about the elastic stiffness of the sample through  $k_s$  as well as information about subsurface features via the dependence of the amplitude on  $F_s$ . The dependence on  $\gamma_s$  means that UFM is sensitive to viscous properties of the sample as well.

### 3.4.3.3 Atomic Force Acoustic Microscopy and Force Modulation Microscopy

For both atomic force acoustic microscopy [5, 6] and force modulation microscopy [4] the cantilever drive amplitude  $F_c$  and frequency  $\omega_c$  are zero. As in UFM, the

surface drive amplitude  $F_s$  and the frequency  $\omega_s$  are nonzero. However, unlike UFM, the surface drive frequency is limited to a range of frequencies that produce measurable displacement amplitudes of cantilever oscillation. The cantilever displacement amplitude  $\eta_{cn,\text{lin}}$  corresponding to the  $n$ th mode is obtained as  $\eta_{cn,\text{lin}} = \xi_{cn} + \zeta_{cn,\text{lin}}$ , where the zeroth-order contribution  $\xi_{cn}$  is given by Eq. (3.72) with the term involving  $Q_{cc}$  set equal to zero and the first-order contribution  $\zeta_{cn,\text{lin}}$  is given by Eq. (3.85) with all terms involving  $Q_{sc}$  and  $Q_{cc}$  set equal to zero. We obtain

$$\eta_{cn,\text{lin}} = H_1 \cos(\omega_s t - \phi_{ss} + \theta + \Lambda_1) \quad (3.117)$$

where

$$H_1 = [Q_{cs}^2 + W_1^2 + 2Q_{cs} W_1 \cos(\beta_s + \mu_{ss} - \phi_{ss})]^{1/2}, \quad (3.118)$$

$$W_1 = 2 \frac{D_s}{R_{ss}} \varepsilon_0 F_2 [Q_{ss}^2 + Q_{cs}^2 + 2Q_{ss} Q_{cs} \cos \alpha_{ss}]^{1/2}, \quad (3.119)$$

and

$$\Lambda_1 = \tan^{-1} \frac{\sin(\beta_s + \mu_{ss} - \phi_{ss})}{\cos(\beta_s + \mu_{ss} - \phi_{ss}) + (Q_{cs}/W_1)}. \quad (3.120)$$

If the oscillation amplitude and quiescent distance  $z_0$  are set for AFAM operation well away from the highly nonlinear region of the force-separation curve where  $F_2$  is sufficiently small, then we may approximate  $\eta_{cn}$  from the zeroth contribution alone as

$$\eta_{cn,\text{lin}} \approx \xi_{cn} \approx Q_{cs} \cos(\omega_s t - \phi_{ss} + \theta) \quad (3.121)$$

where  $Q_{cs}$  is given by Eq. (3.110),  $\phi_{ss}$  by Eq. (3.106), and  $\theta$  by Eq. (3.65). Small values of  $F_2$  can be achieved when operating in the region of the force-separation curve well above  $z_B$  or well below  $z_B$  (see Fig. 3.1). Usually, the AFAM is operated in hard contact where the tip-sample interaction force is repulsive over at least a portion of the oscillation cycle. If the oscillation amplitude and quiescent distance  $z_0$  are sufficiently small,  $F_1$  is large and negative, and  $F_2$  is negligible. The harmonically generated signals resulting from the interaction force nonlinearity are then negligible and the AFAM may be said to operate in the “linear detection regime.”

### 3.4.3.4 Amplitude Modulation-Atomic Force Microscopy

The amplitude modulation-atomic force microscope modality (also called intermittent contact mode or tapping mode) [2] is a standard feature on many atomic force microscopes for which the cantilever is driven in oscillation ( $F_c$  and  $\omega_c$  are nonzero), but no surface oscillations resulting from bulk ultrasonic waves are generated (i.e.,  $F_s$  and  $\omega_s$  are zero). The cantilever is driven at ultrasonic frequencies. As with AFAM and FMM, the general equation for the cantilever output  $\eta_{cn}$  is given as  $\eta_{cn,\text{lin}} = \xi_{cn} + \zeta_{cn,\text{lin}}$ , where for AM-AFM  $\xi_{cn}$  is given by Eq. (3.72) with the term

involving  $Q_{cs}$  set equal to zero and  $\zeta_{cn,lin}$  is given by Eq. (3.74) with all terms involving  $Q_{cs}$  and  $Q_{ss}$  set equal to zero.

The expression for  $\eta_{cn,lin}$  is

$$\eta_{cn,lin} = H_2 \cos(\omega_c t - \phi_{cc} + \Lambda_2) \quad (3.122)$$

where

$$\Lambda_2 = \tan^{-1} \frac{\sin(\beta_c + \mu_{cc} - \phi_{cc} - \alpha_{cc})}{\cos(\beta_c + \mu_{cc} - \phi_{cc} - \alpha_{cc}) + (Q_{cc}/W)}, \quad (3.123)$$

$$H_2 = [Q_{cc}^2 + W_2^2 + 2Q_{cc}W_2 \cos(\beta_c + \mu_{cc} - \phi_{cc} - \alpha_{cc})]^{1/2}, \quad (3.124)$$

and

$$W_2 = 2 \frac{D_c}{R_{cc}} \varepsilon_0 F_2 (Q_{cc}^2 + Q_{sc}^2 + 2Q_{cc}Q_{sc} \cos \alpha_{cc})^{1/2} \quad (3.125)$$

where  $Q_{cc}$  is given by Eq. (3.108),  $Q_{sc}$  by Eq. (3.111),  $\phi_{cc}$  by Eq. (3.105),  $\mu_{cc}$  by Eq. (3.85),  $\varepsilon_0$  by Eq. (3.79);  $a_{cc}$ ,  $\beta_c$ ,  $D_c$ , and  $R_{cc}$ , are given by Eqs. (3.82), (3.87), (3.89), and (3.92), respectively, with the terms involving  $m_s$  set equal to zero.

The complexity of the cantilever response  $\eta_{cn,lin}$  is greatly reduced, if, as for AFAM and FMM, the oscillation amplitude and quiescent distance  $z_0$  are set for AM-AFM operation well away from the highly nonlinear region of the force-separation curve where  $F_2$  is sufficiently small. As for AFAM and FMM, small values of  $F_2$  can be achieved when operating in the region of the force-separation curve well above  $z_B$  or well below  $z_B$  (see Fig. 3.1). Usually, AM-AFM is operated such that  $z_0$  is well above  $z_B$ . If the oscillation amplitude is such that the tip-sample separation also remains well above  $z_B$ , then  $F_2$  is relatively small and the AM-AFM is said to operate in the soft contact (also called non-contact) regime of operation. Otherwise, the operation is considered to occur in the hard contact regime, especially if intermittent contact is made with the sample surface. For the non-contact regime of AM-AFM operation, we obtain to a reasonable approximation

$$\eta_{cn,lin} \approx Q_{cc} \cos(\omega_c t - \phi_{cc}). \quad (3.126)$$

### 3.4.3.5 Ultrasonic Atomic Force Microscopy

UAFM [3] utilizes a cantilever tip in permanent forced contact with the sample surface. Ultrasonic oscillations are usually induced in the cantilever either through the cantilever base or directly through the cantilever. The oscillation amplitude is usually kept small, so that  $F_2$  is sufficiently small that harmonic oscillations are not generated. The operational characteristics of UAFM usually falls in the linear range of the force-separation curve where Eq. (3.126) for AM-AFM applies. It is clear from Eqs. (3.126), (3.105), and (3.108) that the output signal from the cantilever is dependent on  $k_s$ ,  $\gamma_s$ , and  $F_1$ , and is thus sensitive to both conservative and dissipative



forces. The polynomial coefficient  $F_1$  is an independent parameter in the CIS model, but can be related to  $k_s$  and  $\gamma_s$  by invoking the resonance condition  $\partial\eta_{cn,\text{lin}}/\partial\omega^2 = 0$ . We emphasize, as pointed out in Sect. 3.3.5, that  $k_s$  is a dynamic modulus and is thus dependent on the frequency of the drive oscillation, as in the case for the cantilever stiffness constant  $k_{cn}$ . The use of an effective dynamic modulus [3], or equivalently of the surface acoustic impedance [16], is central to the detection of delaminations and voids in the assessment of layered materials using UAFM. The success of UAFM in detecting subsurface features serves to validate the view that  $k_s$  in the CIS model is a dynamic modulus.

For sufficiently hard contact and sufficiently small oscillation amplitude,  $F_1$  is large and negative. We approximate  $\phi_{cc}$  and  $Q_{cc}$  in such case as

$$\phi_{cc} \approx \tan^{-1} \frac{(\gamma_s + \gamma_c)\omega_c}{k_{cn} + k_s - m_c\omega_c^2}, \quad (3.127)$$

and

$$Q_{cc} \approx \frac{F_c}{[(k_{cn} + k_s - m_c\omega_c^2)^2 + (\gamma_s + \gamma_c)^2\omega_c^2]^{1/2}}. \quad (3.128)$$

### 3.4.4 Image Contrast in the CIS Model

The equations for cantilever signal generation are derived in the CIS model in terms of the sample stiffness constant  $k_s$ , the sample damping coefficient  $\gamma_s$ , and the interaction force polynomial expansion coefficients  $F_0$ ,  $F_1$ , and  $F_2$ . If, in an area scan of the sample, these parameters remain constant from point-to-point, the image generated from the scan would be flat and featureless. However, the parameters generally vary from point to point on the sample surface and lead to variations in the cantilever output signal that is interpreted as material contrast. Indeed, variations in the sample stiffness constant  $k_s$ , for example, can lead to an assessment of variations in the Young modulus, since  $k_s$  is dependent on the Young modulus, and when combined with variations in the damping coefficient  $\gamma_s$  can lead to an assessment of material viscoelasticity.

The variations in the material and interaction force expansion parameters produce changes in both the amplitude and phase of the cantilever output signal for HFM, SNFUH, RDF-AFUM, FMM, AFAM, AM-AFM, and UAFM but only changes in the amplitude are relevant to UFM. In the single system model the material and interaction force parameters are  $k_{\text{eff}}$  and  $\gamma_{\text{eff}}$  and lead to the variations  $\Delta k_{\text{eff}} = \Delta(k_c - F_1) = -\Delta F_1$  ( $k_c$  is constant) and  $\Delta\gamma_{\text{eff}} = \Delta(\gamma_c - S_1) = -\Delta S_1$  ( $\gamma_c$  is constant) in the expressions for phase image contrast. Phase image contrast in the linear approximation for AM-AFM operation in constant amplitude control is specifically addressed in Sect. 3.3.3 for the single system model where it is shown that the equations for phase contrast are simplified considerably when operating in cantilever resonance with constant amplitude control.

In the CIS model the independent material and interaction force parameters are  $k_s$ ,  $F_1$ , and  $\gamma_s$ . The occurrence of three independent parameters leads to more complicated expressions for image contrast, even in the linear approximation. For example, phase contrast for AM-AFM operation in the non-contact regime is obtained in the CIS model from Eq. (3.105) as the variation in  $\phi_{cc}$ . We get from Eq. (3.105) that

$$\Delta\phi_{cc} = \frac{-[(\gamma_c + \gamma_s)\omega_c F_1 + \gamma_c^2 \omega_c^3 \gamma_s] \Delta k_s + [\gamma_c \omega_c k_s^2 + (\gamma_c + \gamma_s) \gamma_c \gamma_s \omega_c^3] \Delta F_1 + [\gamma_c^2 \omega_c^3 k_s + \omega_c k_s F_1^2] \Delta \gamma_s}{\{\gamma_c^2 \omega_c^2 k_s^2 + [(\gamma_c + \gamma_s)^2 \omega_c^2 + k_s^2] F_1^2 - 2\gamma_c^2 \omega_c^2 k_s F_1 + \gamma_c^2 \gamma_s^2 \omega_c^4\}} \quad (3.129)$$

We note from Eq. (3.129) that phase contrast in the CIS model depends not only on variations in the parameters  $k_s$ ,  $F_1$ , and  $\gamma_s$ , but on the initial values of  $k_s$ ,  $F_1$ , and  $\gamma_s$  as well. For operation near the resonant frequency, however, one of the parameters can be expressed in terms of the other two parameters via the solution to the resonance relation  $\partial Q_{cc}/\partial \omega_c^2 = 0$ . If also operating in constant amplitude control, the solution to the relation  $\Delta Q_{cc} = 0$  allows the expression of one of the parameter variations in terms of variations in the other two parameters. Thus, when operating in constant amplitude control near resonance, the solutions to  $\partial Q_{cc}/\partial \omega_c^2 = 0$  and  $\Delta Q_{cc} = 0$  can be used to reduce Eq. (3.129) to an expression involving only two of the variables  $k_s$ ,  $F_1$ , and  $\gamma_s$ , and two of the variations  $\Delta k_s$ ,  $\Delta F_1$ , and  $\Delta \gamma_s$ . The procedure does not lead to the degree of simplification for Eq. (3.129) that occurs for the corresponding equation in the single system model (see Sect. 3.3.3), but the reduction to two independent variables is nonetheless helpful in assessing the phase contrast analytically and experimentally.

Expressions for both amplitude and phase image contrast, similar to that of Eq. (3.129) for phase contrast, can be obtained for each of the other  $d$ -AFM modalities, but page limitations prevent such an assessment here. The reader can obtain the contrast equations for a particular regime of operation for a given  $d$ -AFM modality straightforwardly from the signal generation equations for the modality of interest. For example, phase contrast in the nonlinear regime of operation for AFAM can be obtained from the variations  $\Delta\phi = (-\Delta\phi_{ss} + \Delta\theta + \Delta\Lambda_1)$  in Eq. (3.117) or for amplitude contrast from the variation  $\Delta H_1$  where  $H_1$  is given by Eq. (3.118).

Notwithstanding the more complicated expressions for image contrast, the advantage of the CIS model is that all material and interaction force parameters appear directly in the signal generation and contrast equations; and that each model parameter is unambiguously linked to a specific material property. The material properties are thus in principle assessable utilizing a particular  $d$ -AFM modality or a combination of  $d$ -AFM modalities. Further, the sample stiffness constant  $k_s$  is decoupled from  $F_1$  and the symmetry of the governing dynamical equations places the analysis of cantilever and sample oscillations on equal footing. The physical and mathematical symmetry of the cantilever and sample dynamics enables the direct evaluation of the various  $d$ -AFM modalities presented here.

### 3.5 Conclusion

The various dynamical implementations of the atomic force microscope have become important nanoscale characterization tools for the development of novel materials and devices. To understand the operational characteristics, signal generation, and image contrast from the various *d*-AFM modalities we have presented a general, yet detailed, mathematical model of cantilever dynamics as an oscillating cantilever coupled to a sample through a mutual interaction force. For definiteness we assume that the cantilever is a rectangular beam of constant cross-section, the dynamics of which are characterized by a set of eigenfunctions that form an orthogonal basis for the solution set. The general equations of cantilever dynamics are reduced to a set of local, phase-correlated, damped harmonic oscillator equations. The set reflects the geometrical space defined by the cantilever shape and collectively defines the eigenmodes of cantilever motion. The equations account for the positions on the cantilever of drive forces, damping forces, tip contact with the sample, and boundary conditions. For some other cantilever shape a different orthogonal basis set of eigenfunctions would be appropriate. However, the mathematical procedure used here would lead again to a set of local, phase-correlated, damped harmonic oscillator equations with values of the coefficients appropriate to the different cantilever geometry. Practicably, this means that the shape of the cantilever is not as important in the solution set as knowing the cantilever modal resonant frequencies, obtained experimentally. An advantage of the approach is that the solution set can be expanded to include nonlinear modes generated by the nonlinearity of interaction forces for large cantilever or sample drive amplitudes.

One of the most significant factors affecting the cantilever dynamics is the cantilever tip-sample surface interaction force. The analytical solution to the dynamical equations usually entails a series expansion of the interaction force. Even for small oscillation amplitudes, more terms in the expansion are needed, if the quiescent separation between the cantilever and sample surface is near the highly nonlinear portion of the force-separation curve. Although using more expansion terms leads to increasingly better approximations to the solution, the task becomes ever more daunting algebraically as the number of terms increases. A polynomial expansion based on linear algebra and inner product spaces is developed to represent the tip-sample interaction force that somewhat reduces the number of terms needed in the iterative approximation procedure for solving the dynamical equations. The coefficients in the polynomial expansion are responsible for significant features of the cantilever dynamics. For example, the higher order coefficients in the expansion explain the occurrence of amplitude bifurcation (see Appendix A) as well as the generation of both harmonic and subharmonic modes of oscillation (see Appendix B). The coupling of the cantilever oscillation modes by the interaction force nonlinearity leads via the group renormalization method to an explanation of often observed resonance bifurcation upon cantilever-sample contact (see Appendix C). The general validity of the spring model is also addressed in Appendix C.

The cantilever dynamics are first treated using the single system model for which the effects of sample surface oscillations are absorbed within the interaction force itself. The model leads to expressions of image contrast involving, in the linear approximation, only variations in the  $F_1$  and  $S_1$  interaction-force expansion coefficients. The connection between the cantilever oscillations and the sample physical properties occurs implicitly in the single system model through the relation  $k^* = F_1$ , where  $k^*$  is an effective spring constant of the interaction force. The connection occurs via the measured shift in the cantilever resonance frequency determined by  $F_1$ . Another link between the cantilever oscillations and the sample physical properties in the single system model is via the interaction-force damping coefficient  $S_1$ . Although the parameters  $F_1$  and  $S_1$  collectively account for the effects of the sample physical properties in the single system model in the linear approximation, the de-convolution of specific sample physical properties from an assessment of  $F_1$  and  $S_1$  is not at all straightforward and has sometimes led to confusion and controversy.

To provide a greater measure of flexibility and symmetry regarding the description of tip-sample interactions, a dynamical model is presented for which the cantilever tip and the sample surface are treated as independently damped simple harmonic oscillators passively coupled via the nonlinear tip-sample interaction forces. The analytical model, called the CIS model, reduces to a pair of coupled nonlinear differential equations. The general solutions, obtained using a matrix perturbation procedure, are applied to the quantitative assessment of signal generation for the most commonly used  $d$ -AFM modalities. A notable feature of the CIS model is the treatment of the sample stiffness constant  $k_s$  similarly to that of the cantilever stiffness constant  $k_{cn}$ . No effective spring constant  $k^*$  is necessary to connect to sample physical properties as for the single system model. The sample physical properties in the CIS model are ascertained in the linear approximation through  $k_s$ , the sample damping coefficient  $\gamma_c$ , and the expansion coefficient  $F_1$ . Although the occurrence of the three independent parameters  $k_s$ ,  $\gamma_c$ , and  $F_1$  leads to more complicated expressions for signal generation and image contrast, notable advantage is gained in having a more direct link between the cantilever output signal and the sample physical properties. For  $d$ -AFM operation in the highly nonlinear regime of the force-separation curve (as is always the case for HFM, SNFUH, RDF-AFUM, and UFM) the analytical expressions for the amplitude must also include higher order expansion terms such as  $F_2$ . The nonlinearity also results in phase terms that appear in both the output amplitude and phase signal in addition to that obtained in the linear approximation.

**Acknowledgments** SAC thanks the US Department of Energy, Washington, DC, for support under Prime Award DE-SC0001764.

## Appendix A: Amplitude Bifurcations

A general assessment of the effects of the various expansion coefficients  $F_0$ ,  $F_1$ ,  $F_2$ , etc., on the frequency and amplitude in the solution to Eq. (3.21) can be achieved

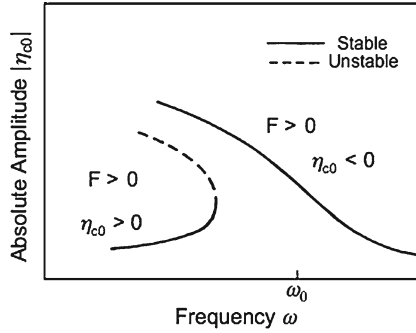


**Fig. 3.4** Amplitude bifurcation resulting from the creation of a fold in the amplitude versus frequency curve. The left-oriented fold for the case depicted in the figure gives rise to stable upper ( $\eta_c < 0$ ) and lower ( $\eta_c < 0$ ) oscillation amplitudes (amplitude bi-stability) represented by the solid portion of the curves for drive frequencies below the free-space resonance frequency  $\omega_0$ . The dashed portion of the lower curve is an unstable region of the curve that produces a third oscillation amplitude not observed experimentally

most expediently by taking  $\eta_{cn} \rightarrow \eta_c$ ,  $\gamma_{cn} \rightarrow \gamma_c$ , and  $k_{cn} \rightarrow k_c$  in Eq. (3.21), and assuming that in first-order approximation  $\eta_c = c + \eta_{c0} \cos \omega_c t$  where  $c$  is a constant. Substituting the expression in Eq. (3.21), neglecting harmonic frequency terms in the resulting expression, and solving the resulting equation, we obtain

$$\omega_c \approx \left\{ \left[ \left( \omega_0^2 - \frac{F_1}{m_c} \right)^2 - \frac{4F_0F_2}{m_c^2} - \frac{2F_2^2}{m_c^2} \eta_{c0}^2 \right]^{1/2} - \frac{F_c}{m_c \eta_{c0}} \right\}^{1/2} \quad (\text{A.1})$$

where  $\omega_0$  is the free-space resonance frequency of the cantilever. It is seen directly from Eq. (A.1) that  $F_1$  leads to a shift in  $\omega_0$  that is dependent via Eqs. (3.14) and (3.16) on the amplitude of cantilever oscillation, the quiescent separation distance  $z_0$ , and the sign of  $F_1$ .

The product term  $F_0F_2$  in Eq. (A.1), where  $F_0$  is the static term and  $F_2$  is the first nonlinear term in the polynomial expansion of the interaction force, also leads to a shift in  $\omega_0$ , the shift direction being dependent on the signs of  $F_0$  and  $F_2$ . However, the  $F_2$  term alone in Eq. (A.1) leads to a bifurcation in the cantilever oscillation amplitude that produces upper and lower amplitude versus frequency curves over specific ranges of drive frequency. The bifurcation results from the left-oriented fold shown in Fig. 3.4 where from Eq. (A.1) the absolute oscillation amplitude  $|\eta_c|$  is plotted as a function of the drive frequency  $\omega_c$ . We point out that since Eq. (A.1) does not include the effects of damping, the resonance “peak” in the figure is not closed. The factor  $(2F_2^2\eta_{c0}^2/m_c^2)$  in Eq. (A.1) is responsible for the frequency shift in the “peak” of the resonance curve that increases with an increase in the oscillation amplitude  $\eta_{c0}$ . The increasing shift in the resonance peak with increasing amplitude produces the fold shown in Fig. 3.4.

Since  $F_2$  is squared in Eq. (A.1), the frequency of the resonance “peak” decreases with increasing amplitude irrespective of the sign of  $F_2$ , and results in the left-oriented fold shown in the figure. It is apparent from the figure that three possible oscillation amplitudes  $\eta_{c0}$  are possible when the drive frequency  $\omega_c$  lies within the fold. Only the upper and lower amplitudes are stable and lead to the experimentally observed amplitude bi-stability; the middle amplitude is unstable and not seen in experiments. It is emphasized that the curve folding (peak frequency shifting) from  $F_2$  is quite independent of the frequency shift produced by  $F_1$  and the product  $F_0F_2$ .  $F_1$  and  $F_0F_2$  shift the entire resonance curve to larger or smaller frequencies – not a portion of the curve leading to folding, as is the case for  $F_2$ .

To more clearly delineate the role of  $F_3$  in the frequency-amplitude relation, we repeat the derivation leading to Eq. (A.1) using only the terms  $F_1$  and  $F_3$  in the polynomial expansion. We now assume that in first-order approximation  $\eta_c = \eta_{c0}\cos\omega_c t$  and substitute the expression in Eq. (3.21). Again neglecting harmonic frequency terms in solving the resulting expression, we obtain

$$\omega_c = \left( \omega_0^2 - \frac{F_1}{m_c} - \frac{3}{4} \frac{F_3}{m_c} \eta_{c0}^2 - \frac{F_c}{m_c \eta_{c0}} \right)^{1/2}. \quad (\text{A.2})$$

Equation (A.2) shows that  $F_3$  plays a role similar to that of  $F_2$  in the frequency-amplitude relationship. However, unlike  $F_2$  in Eq. (A.1),  $F_3$  appears to the first power in Eq. (A.2). This means that the frequency of the resonance “peak” increases or decreases in accordance with the sign of  $F_3$ , producing either a right-oriented or left-oriented fold, respectively.

Amplitude bifurcation is well-documented in the literature [34, 45, 46] and is often attributed to the occurrence of attractive and repulsive components in the force-separation curve. Equations (A.1) and (A.2) show, however, that amplitude bi-stability is a consequence only of the nonlinearity in  $F(z)$  (represented in Eq. (A.1) by the term  $F_2$  and in Eq. (A.2) by  $F_3$ ). The attractive and repulsive components in the interaction force affect only the magnitude and sign of the expansion coefficients. The upper amplitude curve in Fig. 3.4 corresponds to the case where the cantilever oscillations are 180 degrees out of phase with the drive force ( $F_c/\eta_{c0} < 0$ ), while the lower amplitude curve corresponds to the case where the cantilever oscillations and drive force are in phase ( $F_c/\eta_{c0} > 0$ ).

## Appendix B: Subharmonic Generation and Routes to Chaos

We show in Sect. 3.3.2 that nonlinearity in the interaction force leads to a shift in the resonance frequency with increasing drive amplitude. In Sect. 3.3.4 we find that the nonlinearity also generates harmonics of the driving force frequency. For an appropriate range of values of the dynamical parameters, including drive frequency, the interaction force nonlinearities that lead to the generation of harmonics is known

to stimulate the generation of subharmonics [51]. This is seen, for example, from a consideration of the forced Duffing equation  $\ddot{x} + \alpha x + \varepsilon x^3 = \Gamma \cos \omega t$ .

Let  $\tau = \omega t$  and re-write the Duffing equation as [51]

$$\omega^2 x'' + \alpha x + \varepsilon x^3 = \Gamma \cos \tau \quad (\text{B.1})$$

where the prime symbol in Eq. (B.1) denotes the operator  $d/d\tau$ . We look for solutions of Eq. (B.1) having period  $6\pi$  (corresponding to frequency  $\omega/3$ ). Letting  $\omega = \omega_0 + \varepsilon_s \omega_1$ , substituting in Eq. (B.1), and using the perturbation procedure given Sect. 3.3.4 where  $\varepsilon = \varepsilon_s$ , we obtain the zeroth- and first-order perturbation equations, respectively, as

$$\omega_0^2 x''_0 + \alpha x_0 = \Gamma \cos \tau \quad (\text{B.2})$$

and

$$\omega_0^2 x''_1 + \alpha x_1 = -2\omega_0 \omega_1 x'_0 - x_0^3. \quad (\text{B.3})$$

The periodicity condition,  $6\pi$ , applied to Eq. (B.2) means that  $\omega_0 = 3\sqrt{\alpha}$ . The solution to Eq. (B.2) [zeroth-order solution to Eq. (B.1)] is thus

$$x_0(\tau) = a_{1/3} \cos \frac{1}{3}\tau + b_{1/3} \sin \frac{1}{3}\tau - \frac{\Gamma}{8\alpha} \cos \tau. \quad (\text{B.4})$$

Although Eq. (B.4) suggests the possibility of a period-3 solution, it does not guarantee the solution. The second-order perturbation equation, Eq. (B.3), is used to determine the conditions on the coefficients  $a_{1/3}$  and  $b_{1/3}$  that allows the generation of a subharmonic. Such a determination is not straightforward and shall not be presented here (for details see Jordan and Smith [51]). We simply point out that the conditions allow the generation of the  $1/3$  subharmonic for Eq. (B.1), but a similar solution for the  $1/2$  subharmonic is not allowed when  $\varepsilon$  is small. Even when the conditions permit a given subharmonic, the subharmonic may not be observed experimentally. Whether a given subharmonic is observed experimentally depends on the stability of the subharmonic.

We now consider the cantilever dynamical equation. Subharmonic stability for the cantilever dynamical equation (3.21) is more conveniently addressed by re-writing Eq. (3.21) in dimensionless form as

$$x'' + \Gamma_c x' + \Omega^2 x = f_c \cos \tau + f_0 + f_2 x^2 + \dots \quad (\text{B.5})$$

where

$$\begin{aligned} x &= \eta_{cn}, \quad \tau = \omega t, \quad \Gamma_c = \frac{\gamma_{\text{eff}}}{m_c \omega^2}, \quad \Omega^2 = \frac{k_{\text{eff}}}{m_c \omega^2} = \frac{\omega_0^2}{\omega^2}, \\ f_c &= \frac{F_c}{m_c \omega^2}, \quad f_0 = \frac{F_0}{m_c \omega^2}, \quad f_2 = \frac{F_2}{m_c \omega^2}. \end{aligned} \quad (\text{B.6})$$

Equation (B.5) is an example of a second-order nonlinear ordinary differential equation of general form

$$x'' = f(x, x', \tau). \quad (\text{B.7})$$

The stability of any solution to Eq. (B.7) can be assessed by first reducing Eq. (B.7) to a system of first-order equations as

$$x' = g_1(x, y, \tau), \quad y' = g_2(x, y, \tau) \quad (\text{B.8})$$

or in matrix form as

$$X' = G(X, \tau) \quad (\text{B.9})$$

where

$$X = \begin{pmatrix} x \\ y \end{pmatrix}, \quad X' = \begin{pmatrix} x' \\ y' \end{pmatrix}, \quad G(X, \tau) = \begin{pmatrix} g_1(x, y, \tau) \\ g_2(x, y, \tau) \end{pmatrix}. \quad (\text{B.10})$$

Let  $X_s$  be a solution to Eq. (B.9) and  $\Xi$  be a small perturbation to the solution such that

$$X = X_s + \Xi \quad (\text{B.11})$$

where

$$X_s = \begin{pmatrix} x_s \\ y_s \end{pmatrix}, \quad \Xi = \begin{pmatrix} \xi \\ \eta \end{pmatrix}. \quad (\text{B.12})$$

Substituting Eq. (B.11) in Eq. (B.9), we obtain

$$X'_s + \Xi' = G(X_s + \Xi, \tau). \quad (\text{B.13})$$

If  $\Xi$  is sufficiently small, we may reduce Eq. (B.13) to the linear matrix equation

$$\Xi' = G(X_s + \Xi, \tau) - G(X_s, \tau) \approx A(\tau)\Xi \quad (\text{B.14})$$

where  $\mathbf{A}$  is a  $2 \times 2$  linear matrix. Equation (B.13), known as the first variational equation, implies that the stability of the solution  $x_s$  to Eq. (B.5) is the same as the stability of solutions  $\Xi$  to Eq. (B.9) and, hence, to Eq. (B.7) [51].

We apply the above results to Eq. (B.5) by re-writing Eq. (B.5) as a pair of first order differential equations given in matrix form by

$$X' = \begin{pmatrix} x' \\ y' \end{pmatrix} = \begin{pmatrix} y \\ -\Gamma_c y - \Omega^2 x + f_0 + f_2 x^2 + f_c \cos \tau \end{pmatrix} = \begin{pmatrix} g_1(x, y, \tau) \\ g_2(x, y, \tau) \end{pmatrix} = G(X, \tau). \quad (\text{B.15})$$

It is straightforward to show that Eq. (B.15) is identical to Eq. (B.5) by differentiating the top element on both sides of the second equality and substituting the bottom elements in the resulting expression. We now write



$$X = \begin{pmatrix} x \\ y \end{pmatrix} = \begin{pmatrix} x_s + \xi \\ y_s + \eta \end{pmatrix} = X_s + \Xi \quad (\text{B.16})$$

and substitute Eq. (B.16) in (B.14) to get

$$\begin{pmatrix} x' \\ y' \end{pmatrix} = \begin{pmatrix} x'_s + \xi' \\ y'_s + \eta' \end{pmatrix} = \begin{pmatrix} y_s + \eta \\ -\Gamma_c(y_s + \eta) - \Omega^2(x_s + \xi) + f_0 + f_2(x_s + \xi)^2 + f_c \cos \tau \end{pmatrix}. \quad (\text{B.17})$$

Expanding the quadratic term in Eq. (B.17), retaining only the first power of  $\xi$ , and subtracting  $X'_s = G(X_s, \tau)$  from the resulting expression, we obtain

$$\begin{pmatrix} \xi' \\ \eta' \end{pmatrix} = \begin{pmatrix} \eta \\ -\Gamma_c \eta - \Omega^2 \xi + 2f_2 x_s \xi \end{pmatrix}. \quad (\text{B.18})$$

Differentiating the top elements on both sides of the equality in Eq. (B.18) and substituting the bottom elements in the resulting expression, we obtain the second order linear differential equation

$$\xi'' + \Gamma_c \xi' + (\Omega_c^2 - 2f_2 x_s) \xi = 0. \quad (\text{B.19})$$

The factor  $x_s$  in Eq. (B.19) is a solution to Eq. (B.5) which, from Sect. 3.3.4, we approximate to first order as  $x_s \approx (f_0/\Omega^2) + A \cos \tau$ . Writing

$$\xi(\tau) = e^{-(1/2)\Gamma_c \tau} \zeta(\tau) \quad (\text{B.20})$$

and substituting both  $x_s$  and Eq. (B.20) in (B.19), we obtain Mathieu's equation (in standard form) [55]

$$\zeta'' + (\alpha + \beta \cos \tau) \zeta = 0 \quad (\text{B.21})$$

where in the present case

$$\alpha = \Omega_c^2 - \frac{1}{4}\Gamma_c^2 - 2\frac{f_0 f_2}{\Omega_c^2} = \frac{\omega_0^2}{\omega} - \frac{1}{4} \left( \frac{\gamma_{\text{eff}}}{m_c \omega^2} \right)^2 - 2\frac{F_0 F_2 \omega^2}{\omega_0^2}, \quad (\text{B.22})$$

and

$$\beta = -2f_2 A = -2\frac{F_2 A}{m_c \omega^2}. \quad (\text{B.23})$$

The solutions to Mathieu's equation for a given value of  $\alpha$  occur in alternating regions or bands of stability and instability as the magnitude of  $\beta$  increases [note from Eq. (B.23) that  $\beta$  increases with oscillation amplitude  $A$ ]. The Mathieu equation belongs to the class of linear differential equations with periodic coefficients. The general solutions to such equations, known as Floquet solutions, are of the form [51]

$$\zeta(\tau) = c e^{\rho \tau} P(\tau) \quad (\text{B.24})$$

where  $P(\tau)$  is a periodic function with minimum period  $T$ ,  $\rho$  is the Floquet index, and  $c$  is a constant. The Floquet indices for Eq. (B.21) are obtained from solutions to the expression

$$e^{2\rho T} - \phi(\alpha, \beta)e^{\rho T} + 1 = 0. \quad (\text{B.25})$$

The factor  $\phi(\alpha, \beta)$  is not known explicitly. However, writing  $\mu = \exp(\rho T)$  and substituting in Eq. (B.25) yields a quadratic equation that can be solved for  $\mu$ , hence for  $\rho$ , as a function of  $\phi(\alpha, \beta)$ . Thus, the solution  $\rho$  to Eq. (B.25) in terms of  $\phi(\alpha, \beta)$  determines the stability or instability of the solution to the Mathieu equation, Eq. (B.21), for a range of values of  $\phi(\alpha, \beta)$ . The ranges of values of  $\phi(\alpha, \beta)$  lead to a plot of  $\alpha$  versus  $\beta$  showing alternating regions of stability and instability.

The solutions to Eq. (B.25) corresponding to regions of stability lead to solutions of the Mathieu equation of the form [56]

$$\zeta(\tau) = e^{i\nu\tau} \sum_{n=-\infty}^{\infty} c_n e^{in\tau} = e^{i\nu\omega t} \sum_{n=-\infty}^{\infty} c_n e^{in\omega t} \quad (\text{B.26})$$

where the Floquet index takes the value  $\rho = i\nu$  ( $\nu$  real) and  $c_n$  are constants. A fractional value of  $\nu$  leads to fractional harmonics (including subharmonics). In the unstable regions of the  $\alpha$ - $\beta$  plot the solutions are given as [56]

$$\zeta(\tau) = c_1 e^{\sigma\tau} P_1(\tau) + c_2 e^{-\sigma\tau} P_2(\tau) \quad (\text{B.27})$$

where  $\rho = \sigma$  ( $\sigma$  real),  $c_1$  and  $c_2$  are constants, and  $P_1(\tau)$  and  $P_2(\tau)$  are periodic functions. It is clear from Eq. (B.25) that in the regions of instability at least one solution is unbounded as the result of exponential growth and is, in fact, the origin of the instability.

Numerical solutions of the Mathieu equation reveal that not all solutions in the regions of instability are unbounded. Kim and Hu [57] show from numerical calculations that upon entering regions of instability from a region of stability the fundamental oscillation undergoes a cascade of period-doubling or pitchfork bifurcations that culminates in the establishment of bounded, chaotic motion. They also found that upon encountering the region of stability from a region of instability, the instability becomes stable through a reverse pitchfork or period-doubling bifurcation. However, the occurrence of a stable oscillation does not necessarily mean re-establishment of the fundamental oscillation frequency. For example, numerical solutions of the damped Duffing equation with  $\alpha = -1$  and  $\varepsilon = 1$  reveal the appearance of a period-five stable solution upon entering the second stable region from the preceding unstable region [51]. Such a solution is allowed by Eq. (B.26). Experimental AM-AFM measurements show that the stable oscillation frequency upon entering a second stability region is highly dependent on the initial conditions [58].

It is important to note from Eqs. (B.22) and (B.23) that both  $\alpha$  and  $\beta$  are dependent on  $F_2$  and  $\omega$ , while  $\alpha$  depends additionally on  $\gamma_{\text{eff}}$  and  $\omega_0$ . From Eqs. (3.19) and (3.20)  $F_2$  and  $\gamma_{\text{eff}} = \gamma_c - S_1$  vary with the amplitude of oscillation. When the amplitude

of oscillation is such that the tip-sample separation distance enters the strong force region (near the sample surface) of the force-separation curve, the variation in  $F_2$  and  $S_1$  can be substantial. Such changes affect  $\alpha$  and  $\beta$  and thus the solutions of the Mathieu equation with an increase in drive amplitude.

## Appendix C: Renormalization Methods

As indicated in Sect. 3.2 the general cantilever dynamics is quite properly described in terms of an infinite set of superimposed, damped, harmonic oscillators (modes), each with an associated free-space resonance frequency. Typically, the mode with the largest contribution to the cantilever displacement amplitude is chosen for consideration, the others ignored, and the cantilever modeled as a set of decoupled oscillators as given by Eqs. (3.21). However, the nonlinearity of the tip-sample interaction force leads to the possibility of interactions among the modes that produce significant effects in the cantilever dynamics. Such possibilities are affirmed in amplitude versus frequency spectra taken from AFAM experiments [52, 53]. The spectra very often reveal the bifurcation of a single free-space resonance into multiple resonances upon cantilever-sample contact.

We show that resonance bifurcation is analytically predictable and occurs as the result of nonlinear modal interactions [44]. Our analytical approach is quite similar to that of group renormalization used in quantum field theory and in the description of critical phase transitions in materials. In the present application of renormalization, deviations of the cantilever displacements  $\eta_{cn}$  from that expected for the spring model at frequencies well away from some initially chosen renormalization reference frequency are formally absorbed into the model by allowing the parameters in the model to vary with frequency. Since the mathematical machinery is analogous to that of the renormalization group, we adopt the language used in the mathematical formalism for renormalization: in the present model the chosen reference frequency is the ‘renormalization scale,’ the model parameters are said to ‘run’ with the scale, and the theory is said to be ‘renormalized.’

To obtain the appropriate equations of motion that couple the separate modes, we take  $\eta_{cn} \rightarrow \eta_n$ ,  $\gamma_{cn} \rightarrow \gamma_n$ , and  $k_{cn} \rightarrow k_n$  on the left-hand side of Eq. (3.21), and  $\omega_c \rightarrow \omega$  and  $\eta_{cn} \rightarrow \sum_{m \in Z^+} \eta_m$  (where  $Z^+ = \{1, 2, \dots\}$ ) on the right-hand side of Eq. (3.21). For present purposes it is expedient to ignore the dissipative terms in the expansion of Eq. (3.12) involving the coefficients  $S_n$ . The implications of nonzero  $S_n$  will be considered following the renormalization. We thus obtain the dynamical equations that account for mode coupling as [44]

$$L_n \eta_n = F_c \cos \omega t + F_{00} + F_{10} \sum_{m \in Z^+} \eta_m + F_{20} \left( \sum_{m \in Z^+} \eta_m \right)^2 + \dots \quad (\text{C.1})$$

where the operator  $L_n = \left( m_c \frac{d^2}{dt^2} + \gamma_n \frac{d}{dt} + k_n \right)$ . The greater difficulty in accounting for mode coupling is apparent: a single, nonlinear differential equation, Eq. (3.21), has been traded for an infinite number of coupled ones, Eq. (C.1). The renormalization method is quite appropriate to handle such a situation.

$L_n$  can be inverted outside its nullspace to obtain the particular solution [44]

$$\begin{aligned} \eta_n &= 2\pi \tilde{G}_n^0(0) F_{00} + \frac{1}{2} F_c \left( 2\pi \tilde{G}_n^0(\omega) e^{i\omega t} + 2\pi \tilde{G}_n^0(-\omega) e^{-i\omega t} \right) \\ &+ F_{10} \int dt' G_n^0(t-t') \left( \sum_{m \in Z^+} \eta_m(t') \right) \\ &+ F_{20} \int dt' G_n^0(t-t') \left( \sum_{m \in Z^+} \eta_m(t') \right)^2 + \dots \end{aligned} \quad (\text{C.2})$$

(Note: the 0 superscript is a label, not an exponent) where  $G_n^0(t-t')$  is the Green function for  $L_n$ ,  $L_n G_n^0 = \delta(t-t')$ :

$$G_n^0(t-t') = \int d\omega' \tilde{G}_n^0(\omega') e^{i\omega'(t-t')}, \quad (\text{C.3})$$

$$\tilde{G}_n^0(\omega') = \frac{-1}{2\pi m_c \left( \omega'^2 - \frac{k_n}{m_c} - i \frac{\gamma_n}{m_c} \omega' \right)}. \quad (\text{C.4})$$

We sum over all modes to obtain the total cantilever deflection  $\eta_c$  and define the function

$$G^0 \equiv \sum_{n \in Z^+} G_n^0 \quad (\text{C.5})$$

along with the corresponding Fourier transform  $\tilde{G}^0 \equiv \sum_{n \in Z^+} \tilde{G}_n^0$ . We obtain from Eq. (C.2) an integral equation for the total cantilever deflection  $\eta_c$  (the exact parameter of interest) as [44]

$$\begin{aligned} \eta_c(t) &= \sum_{n \in Z^+} \eta_n = 2\pi \tilde{G}^0(0) F_{00} + \frac{1}{2} F_c \left( 2\pi \tilde{G}^0(\omega) e^{i\omega t} + 2\pi \tilde{G}^0(-\omega) e^{-i\omega t} \right) \\ &+ F_{10} \int dt' G^0(t-t') [\eta_c(t')] + F_{20} \int dt' G^0(t-t') [\eta_c(t')]^2 + \dots \end{aligned} \quad (\text{C.6})$$

For a given driving frequency  $\omega$ , the nonlinearity of the tip-sample interaction force is known to generate harmonic terms  $I\omega$  ( $I \in Z^+$ ) as shown in Sect. 3.3.4. In solving Eq. (C.6) the generation of harmonics leads us to consider the ansatz [44]

$$\eta_c(t) = \sum_{I \in \mathbb{Z}} a_I e^{iI\omega t} \Rightarrow \quad (\text{C.7})$$

$$\begin{aligned} \sum_{I \in \mathbb{Z}} a_I e^{iI\omega t} &= 2\pi \tilde{G}^0(0) F_{00} + \frac{1}{2} F_c \left( 2\pi \tilde{G}^0(\omega) e^{i\omega t} + 2\pi \tilde{G}^0(-\omega) e^{-i\omega t} \right) \\ &+ F_{10} \sum_{J \in \mathbb{Z}} \tilde{G}^0(J\omega) a_J e^{iJ\omega t} \\ &+ F_{20} \sum_{(J,K) \in \mathbb{Z}^2} \tilde{G}^0[(J+K)\omega] a_J a_K e^{i(J+K)\omega t} + \dots \end{aligned} \quad (\text{C.8})$$

where  $\mathbb{Z}$  is the set of integers. The Fourier coefficients  $a_{\pm I}$  determine the cantilever amplitude that is experimentally observed at the frequency  $|I|\omega$ . Explicitly, the amplitude is given as  $A(I\omega) = 2|a_I|$ , which follows from the reality condition  $\eta_c = \eta_c^*$ , where the star denotes complex conjugation. The non-triviality of the coefficients  $a_I$  ( $|I| > 1$ ) reflects the nonlinearity of the interaction force.

Using the orthogonality of the Fourier basis, we obtain from Eq. (C.8) the recursion relation [44]

$$a_I = 2\pi \tilde{G}^0(I\omega) \left[ \frac{1}{2} F_c (\delta_{I,1} + \delta_{I,-1}) + F_{00} \delta_{I,0} + F_{10} a_I + F_{20} \sum_{J \in \mathbb{Z}} a_J a_{I-J} + \dots \right] \quad (\text{C.9})$$

We note that if  $\tilde{G}^0(I\omega)$  were the Fourier-space Green function  $\tilde{G}_n^0(I\omega)$  for a single harmonic oscillator mode  $n$ , Eq. (C.9) would have the same form as that for the typical solution found for a decoupled mode  $n$ . In such case the exact solution for the total cantilever displacement would look identical to that of a linear spring subjected to nonlinear forces—a more immediately tractable problem mathematically than the one at hand. This suggests that, in analogy to Eq. (C.4) for  $\tilde{G}_n^0(I\omega)$ ,  $\tilde{G}^0$  should be expressed as

$$\tilde{G}^0(\omega) = \frac{-1}{2\pi m_c \left( \omega^2 - \frac{K(\omega)}{m_c} - i \frac{G(\omega)}{m_c} \omega \right)} \quad (\text{C.10})$$

where  $K$  and  $G$  are the renormalized cantilever spring and damping coefficients, respectively.

When transforming Eq. (C.10) to ‘time’-space, the Green function is completely characterized for purposes of integration by its poles and residues. Poles must necessarily occur in Eq. (C.10) at

$$\Omega_n = i \frac{\gamma_n}{2m_c} + \sqrt{\frac{4k_n m_c - \gamma_n^2}{4m_c^2}} \quad (\text{C.11})$$

where the real part of  $\Omega_n$  is the free-space resonance of the cantilever corresponding to the  $n$ th mode.  $K$  and  $G$  must be real-valued functions that, due to constraints on the location of the poles, must satisfy

$$K(\Omega_n) = k_n \quad (\text{C.12})$$

$$G(\Omega_n) = \gamma_n. \quad (\text{C.13})$$

With these constraints the poles of  $\tilde{G}^0$  are  $\{\Omega_n\}$  and  $\text{Re } s[\tilde{G}^0(\Omega_n)] = \text{Re } s[\tilde{G}_n^0(\Omega_n)] = -\left(2\pi\sqrt{4m_c k_n - \gamma_n^2}\right)^{-1}$ . Equations (C.10)–(C.13) lead to the explicit functional forms

$$K(\omega) = \frac{\text{Im}(\omega)}{\text{Re}(\omega)} \text{Im} \left[ m_c \omega^2 + \frac{1}{2\pi \tilde{G}^0(\omega)} \right] + \text{Re} \left[ m_c \omega^2 + \frac{1}{2\pi \tilde{G}^0(\omega)} \right] \quad (\text{C.14})$$

$$G(\omega) = \frac{1}{\text{Re}(\omega)} \text{Im} \left[ m_c \omega^2 + \frac{1}{2\pi \tilde{G}^0(\omega)} \right] \quad (\text{C.15})$$

where  $\tilde{G}^0$  in Eqs. (C.14) and (C.15) is calculated from the infinite sum given by Eqs. (C.4) and (C.5).

From Eqs. (C.9) and (C.10) we re-write the recursive solution as

$$a_I = 2\pi \tilde{G}(I\omega) \left[ F_{00} \delta_{I,0} + \frac{1}{2} F_c (\delta_{I,1} + \delta_{I,-1}) + F_{20} \sum_{J \in \mathbb{Z} \setminus \{0, I\}} a_J a_{I-J} + \dots \right] \quad (\text{C.16})$$

where the interaction force-modified Green function  $\tilde{G}$  is given by

$$\begin{aligned} \tilde{G}(\omega) &\equiv \left[ 1 - 2\pi \sigma \tilde{G}^0(\omega) \right]^{-1} \tilde{G}^0(\omega) \\ &= \frac{-1}{2\pi m_c \left( \omega^2 - \frac{(K(\omega) + \text{Re}(\sigma))}{m_c} - i \frac{(\omega G(\omega) + \text{Im}(\sigma))}{m_c} \right)} \end{aligned} \quad (\text{C.17})$$

$$\sigma = (F_{10} + 2F_{20}a_0 + \dots). \quad (\text{C.18})$$

We note that for nonzero dissipation terms  $S_n$  and  $R_{mn}$  the expansion in Eq. (C.1) would pick up  $S_n$  and  $R_{mn}$  terms that lead to additional sigma-like terms, similar to that of Eq. (C.18), in the denominator of Eq. (C.17).

We now consider a particular application of the renormalized model that demonstrates resonance bifurcation. Since the running of the renormalized parameters with frequency necessarily results in the appropriate multi-peak, free-space resonance spectrum, it is reasonable to suspect that the nonlinear interactions, smoothly introduced to the cantilever system as the cantilever engages the sample surface, would

mix the peaks and bifurcate the resonances. For example, the running of the parameters in the vicinity of a given resonance peak from one parameter value to a second value should result in two contact resonance peaks in place of the given free-space resonance peak. To demonstrate resonance bifurcation, we wish to plot the cantilever amplitude as a function of its driving frequency and observe a splitting in the local maxima of the curve.

We begin by assuming that the cantilever output signal is passed through a lock-in amplifier such that all frequencies except the drive frequency are filtered out. Thus, only the amplitudes corresponding to  $I = \pm 1$  are of interest and the amplitude is  $A = 2|a_I|$ . In such case the nonlinear components of the interaction force vanish from the recursion relation given by Eq. (C.16), if Eq. (C.16) is solved iteratively for  $a_{\pm 1}$  by recursively substituting the relation in Eq. (C.16) into the  $a_I$  on the right-hand side. The resulting expression is

$$a_{\pm 1} = \pi \tilde{G}(\pm\omega) F_c. \quad (\text{C.19})$$

It is emphasized that for an infinitely stiff sample surface Eq. (C.19) is exact and is numerically equivalent to results obtained by starting with the beam equation and applying a nonlinear interaction force at the tip-sample boundary. In most cases the sums defining  $\tilde{G}^0$  and  $\sigma$  converge quite rapidly, so practicably the sums can be truncated with accurate results. The extension of the model to include the more realistic case of an elastic sample surface is more complicated and is the subject of current research. The present model, nonetheless, predicts the resonance bifurcation observed in AFAM experiments quite well.

To calculate the right-hand side of Eq. (C.19), we must determine  $\tilde{G}^0(\pm\omega)$  and  $\sigma$ , and use the relationship given by Eq. (C.17) to obtain  $\tilde{G}(\pm\omega)$ . To determine  $\tilde{G}^0(\pm\omega)$ , we use the rough approximations  $k_n \approx k_1 n^4$  and  $\gamma_n \approx \gamma_1 n^2$  in Eqs. (3.14) and (3.15) for the cantilever modal stiffness constants and damping coefficients, respectively [44]. The exact relationships depend, of course, on the cantilever shape and the experimental environment. If the driving frequency is close to the free-space cantilever resonance frequency, then large  $n$  terms contribute minimally to the calculation of  $\tilde{G}^0$ .  $a_0$ , used in Eq. (C.18) to obtain  $\sigma$ , is calculated recursively from Eq. (C.16) to order  $(F_c)^2 F_2$  as

$$a_0 \approx 2\pi \tilde{G}^0(0) \left[ F_{00} + (2\pi \tilde{G}^0(\omega))^2 (F_c)^2 F_{20} \right]. \quad (\text{C.20})$$

We assume a damping coefficient  $\gamma_1 = 10^{-6} \text{ N s m}^{-1}$ , cantilever mass  $m_c = 10^{-9} \text{ kg}$ , fundamental resonance frequency  $\omega_1 = 22 \text{ kHz}$ , and cantilever stiffness constant  $k_1 = 0.484 \text{ N m}^{-1}$ . We assume typical force parameters  $F_c = 10^{-7} \text{ N}$ ,  $F_{00} = -10^{-6} \text{ N}$ ,  $F_{10} = -1 \text{ N m}^{-1}$ , and  $F_{20} = 10^6 \text{ N m}^{-2}$ . We point out that not all values of the force and damping parameters are found experimentally to give rise to resonance bifurcations. The same is true for the present renormalization model. The values chosen above are all within the range of parameter values typically found for AFAM operation. The specific values given above are found to generate the triple

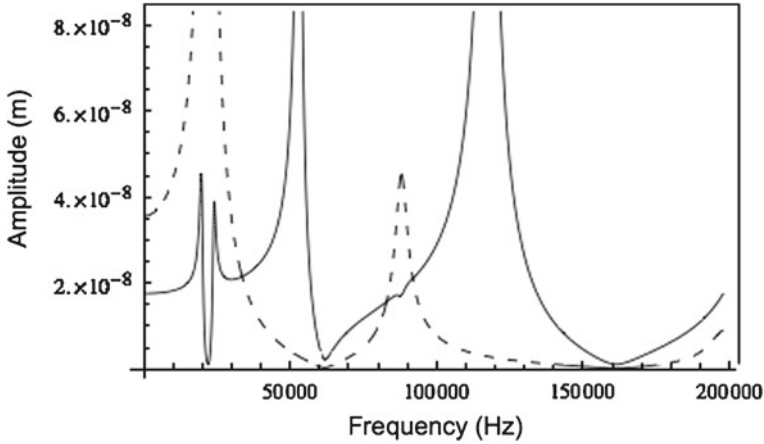


**Fig. 3.5** Cantilever displacement amplitude plotted as a function of drive frequency for free-space cantilever oscillations (*dashed curve*) and for cantilever engagement with the sample surface (*solid curve*) [44]

bifurcation resonance bifurcation given in Fig. 3.5, while many other parameters values do not generate resonance bifurcations in the model at all.

The calculated amplitude of the cantilever as a function of the driving frequency  $\omega$  is plotted in Fig 3.5 for both the free-space and surface-engaged cantilever using the renormalized model. The multiple free-space resonance modal peaks (dashed line) are clearly shown. Resonance bifurcation and frequency shifting is apparent in the curve for the engaged cantilever (solid line). The free-space resonance at angular frequency 22 kHz is shown to bifurcate into three resonances: at angular frequencies 19, 22, and 51 kHz. We point out that the number of bifurcation resonances predicted in the present model is quite sensitive to the values of the cantilever parameters used in the calculation. This is in agreement with the findings of Arnold et al. [52] who report both double and triple bifurcation resonances in the frequency spectra for various materials and cantilevers. Zhao et al. [53] report experimental data showing the bifurcation of a 22 kHz free-space resonance ( $\omega/2\pi$ ) into resonances at roughly 19, 31, and 60 kHz.

Renormalization can also be used to address the concern that conventional spring models (for which the cantilever has fixed cantilever spring and damping constants) fail to describe cantilever dynamics adequately, particularly at drive frequencies much larger than the fundamental cantilever resonance frequency. We begin by noting that although the form of the Fourier-space Green function in Eq. (C.10) is similar to that of the harmonic oscillator, the differential operator associated with the Green function  $G^0(t - t') = - \int [2\pi(m_c\omega^2 - K(\omega) - iG(\omega)\omega)]^{-1} \exp[i\omega(t - t')]d\omega$  does not actually correspond to that of a conventional harmonic oscillator due to the running of the renormalized stiffness and damping parameters with frequency. Rather, it corresponds, as shown above, to that of a superposition of harmonic oscillators



due to the structure of the poles. However, Eq.(C.9) reveals that the amplitude of the cantilever at the excited frequencies ( $\omega$  and its harmonics) depends solely on the Fourier-space Green function at those frequencies. Thus, if the renormalization scale  $\omega_0$  is chosen to be sufficiently close to an integral multiple of the driving frequency of interest, we can use the renormalized values  $K(\omega_0)$  and  $G(\omega_0)$  in  $\tilde{G}^0$  to recover approximately harmonic behavior in a neighborhood of frequencies around the renormalization scale.

To better illustrate why this is so, consider a function  $f(x)$  in a neighborhood of some point  $x_0$ . One can obtain a good approximation to  $f(x)$  in a given neighborhood by expanding  $f(x)$  about  $x_0$  in a Taylor series and keeping only the zeroth order term provided the neighborhood is sufficiently small. As one moves the neighborhood by changing  $x_0$ , the parameter  $f(x_0)$  also changes. In the case of the renormalized cantilever parameters, if one intends to measure cantilever behavior at a frequency  $I\omega$ , it is necessary to determine experimentally  $K(\omega_0)$  and  $G(\omega_0)$  for a renormalization scale  $\omega_o$  near  $I\omega$  before the theoretical spring model gains predictive power. Once the parameters at the renormalization scale are determined,  $\omega$  can be changed slightly without necessarily needing to determine new values.

There may be situations where the frequency at which cantilever dynamics of interest are probed is not an integral multiple of the driving frequency. In such cases, the procedure generalizes naturally to choosing a renormalization scale in the neighborhood of this probed frequency. In application, this is similar to the previously established practice of throwing away the least excited modes in the modal sum that determines the total cantilever deflection amplitude and keeping only the mode with resonance closest to the probed frequency. However, in this former practice, it would become awkward to choose a ‘most excited’ mode if the probed frequency were between two resonance frequencies. Moreover, throwing away an infinite number of modes could underestimate the total cantilever deflection even if the mode contributions are individually small.

Quantitatively, the above amounts to the following. Eq.(C.6) demonstrates that the cantilever deflection can be expressed as

$$\eta_c(t) = \int dt' G^0(t-t') N[\eta_c(t'), t'] \quad (\text{C.21})$$

where  $N$  is some function that characterizes the interactions governing cantilever dynamics. Writing  $N[\eta_c(t), t] = \frac{1}{2\pi} \int d\omega \tilde{N}(\omega) e^{i\omega t}$  and using Eqs. (C.3), (C.5), and (C.10), we obtain

$$\eta_c(t) = \int d\omega \tilde{G}^0(\omega) \tilde{N}(\omega) e^{i\omega t} = \int d\omega \frac{-1}{2\pi m_c \left( \omega^2 - \frac{K(\omega)}{m_c} - i \frac{G(\omega)}{m_c} \omega \right)} \tilde{N}(\omega) e^{i\omega t}. \quad (\text{C.22})$$

If  $\tilde{N}(\omega)$  is sharply peaked in the range  $[\omega_1, \omega_2]$  or if the signal is probed in a frequency range  $[\omega_1, \omega_2]$ , then we have

$$\begin{aligned}
\eta_c(t) &= \int_{\omega_1}^{\omega_2} d\omega \frac{-1}{2\pi m_c \left( \omega^2 - \frac{K(\omega)}{m_c} - i \frac{G(\omega)}{m_c} \omega \right)} \tilde{N}(\omega) e^{i\omega t} \\
&\approx \int_{\omega_1}^{\omega_2} d\omega \frac{-1}{2\pi m_c \left( \omega^2 - \frac{K(\omega_0)}{m_c} - i \frac{G(\omega_0)}{m_c} \omega \right)} \tilde{N}(\omega) e^{i\omega t} \quad (\text{C.23})
\end{aligned}$$

for some  $\omega_0 \in [\omega_1 - \varepsilon_1, \omega_2 + \varepsilon_2]$ ,  $0 < \varepsilon_i \ll \omega_i$ .

Remarkably, Eq. (C.23) shows that the (observed) cantilever behavior is very nearly identical to that of a conventional spring. We note that in most cases, the integral bounds should symmetrically include  $[-\omega_2, -\omega_1]$ , but, due to the reality conditions imposed on the integrand, the bounds  $[-\omega_2, -\omega_1]$  can be accounted for by keeping the original bounds and adding a term in the integrand that differs trivially from the integrand already considered. Consequently, the above result is quite general.

If the probed frequency deviates significantly from  $\omega_0$  (that is, if in the above  $\omega_0 \notin [\omega_1 - \varepsilon_1, \omega_2 + \varepsilon_2]$ ), it becomes necessary to calculate  $K(\omega)$  and  $G(\omega)$ , or  $\tilde{G}^0$ , explicitly, or to measure a new set of renormalized parameters at a new renormalization scale. Exact precision requires calculating  $\tilde{G}^0$  using an infinite sum of terms, each term being given by Eq. (C.4). However, calculations to any desired accuracy can be obtained by truncating the sum and measuring a finite number of parameters  $k_n$  and  $\gamma_n$  corresponding to modes  $\{n\}$  closest to  $\omega_0$  and  $\omega$ .

Although renormalization methods are initially applied here as a means to explain resonance bifurcation, the utility of renormalization in AFM modeling cannot be over-stated. Since  $d$ -AFM modalities are controlled completely by the cantilever driving frequency, the application of the renormalization method allows for the *accurate* interpretation and modeling of cantilever dynamics as conventional spring and point-mass dynamics with fixed cantilever parameters for driving frequencies sufficiently close to the renormalization scale regardless of the value of scale. This suggests that although quantitative, conventional spring models of cantilever dynamics are insufficient over a large range of frequencies, they can be ‘tuned’ to any frequency such that over a given, sufficiently smaller range they, indeed, yield accurate predictions. Over wider ranges, cantilever dynamics can be understood qualitatively as spring dynamics with frequency-dependent stiffness and damping parameters.

## References

1. G. Binnig, C.F. Quate, Ch. Gerber, Atomic force microscope. *Phys. Rev. Lett.* **56**, 930–933 (1986)
2. Q. Zhong, D. Inniss, K. Kjoller, V.B. Elings, Fractured polymer/silica fiber surface studied by tapping mode atomic force microscopy. *Surf. Sci. Lett.* **290**, L688–L692 (1993)
3. K. Yamanaka, A. Noguchi, T. Tsuji, T. Koike, T. Goto, Quantitative material characterization by ultrasonic atomic force microscopy. *Surf. Interface Anal.* **27**, 600–606 (1999)

4. P. Maivald, H.J. Butt, S.A. Gould, C.B. Prater, B. Drake, J.A. Gurley, V.B. Elings, P.K. Hansma, Using force modulation to image surface elasticities with the atomic force microscope. *Nanotechnology* **2**, 103–106 (1991)
5. U. Rabe, W. Arnold, Acoustic microscopy by atomic force microscopy. *Appl. Phys. Lett.* **64**, 1493–1495 (1994)
6. U. Rabe, S. Amelio, M. Kopychinska, S. Hirsekorn, M. Kempf, M. Goken, W. Arnold, Imaging and measurement of local mechanical properties by atomic force microscopy. *Surf. Interface Anal.* **33**, 65–70 (2002)
7. O. Kolosov, K. Yamanaka, Nonlinear detection of ultrasonic vibrations in an atomic force microscope. *Jpn. J. Appl. Phys.* **32**, L1095–L1098 (1993)
8. K. Yamanaka, H. Ogiso, O. Kolosov, Ultrasonic force microscopy for nanometer resolution subsurface imaging. *Appl. Phys. Lett.* **64**, 178–180 (1994)
9. M.T. Cuberes, H.E. Alexander, G.A.D. Briggs, O.V. Kolosov, Heterodyne force microscopy of PMMA/rubber nanocomposites: nanomapping of viscoelastic response at ultrasonic frequencies. *J. Phys. D Appl. Phys.* **33**, 2347–2355 (2000)
10. G.S. Shekhawat, V.P. Dravid, Nanoscale imaging of buried structures via scanning near-field ultrasonic holography. *Science* **310**, 89–92 (2005)
11. S.A. Cantrell, J.H. Cantrell, P.T. Lillehei, Nanoscale subsurface imaging via resonant difference-frequency atomic force ultrasonic microscopy. *J. Appl. Phys.* **101**, 114324 (2007)
12. L. Muthuswami, R.E. Geer, Nanomechanical defect imaging in premetal dielectrics for integrating circuits. *Appl. Phys. Lett.* **84**, 5082–5084 (2004)
13. D.C. Hurley, K. Shen, N.M. Jennett, J.A. Turner, Atomic force acoustic microscopy methods to determine thin-film elastic properties. *J. Appl. Phys.* **94**, 2347–2354 (2003)
14. R.E. Geer, O.V. Kolosov, G.A.D. Briggs, G.S. Shekhawat, Nanometer-scale mechanical imaging of aluminum damascene interconnect structures in a low-dielectric-constant polymer. *J. Appl. Phys.* **91**, 9549–4555 (2002)
15. O.V. Kolosov, M.R. Castell, C.D. Marsh, G.A.D. Briggs, T.I. Kamins, R.S. Williams, Imaging the elastic nanostructure of Ge islands by ultrasonic force microscopy. *Phys. Rev. Lett.* **81**, 1046–1049 (1998)
16. G.G. Yaralioglu, F.L. Degertekin, K.B. Crozier, C.F. Quate, Contact stiffness of layered materials for ultrasonic atomic force microscopy. *J. Appl. Phys.* **87**, 7491–7496 (2000)
17. Y. Zheng, R.E. Geer, K. Dovidenko, M. Kopycinska-Müller, D.C. Hurley, Quantitative nanoscale modulus measurements and elastic imaging of SnO<sub>2</sub> nanobelts. *J. Appl. Phys.* **100**, 124308 (2006)
18. M. Kopycinska-Müller, R.H. Geiss, D.C. Hurley, Contact mechanics and tip shape in AFM-based nanomechanical measurements. *Ultramicroscopy* **106**, 466–474 (2006)
19. M.T. Cuberes, Intermittent-contact heterodyne force microscopy. *J. Nanomater.* **2009**, 762016 (2009)
20. S. Hirsekorn, U. Rabe, W. Arnold, Theoretical description of the transfer of vibrations from a sample to the cantilever of an atomic force microscope. *Nanotechnology* **8**, 57–66 (1997)
21. L. Nony, R. Boisgard, J.P. Aime, Nonlinear dynamical properties of an oscillating tip-cantilever system in the tapping mode. *J. Chem. Phys.* **111**, 1615–1627 (1999)
22. K. Yagasaki, Nonlinear dynamics of vibrating microcantilevers in tapping-mode atomic force microscopy. *Phys. Rev. B* **70**, 245419 (2004)
23. H.-L. Lee, Y.-C. Yang, W.-J. Chang, S.-S. Chu, Effect of interactive damping on vibration sensitivities of V-shaped atomic force microscope cantilevers. *Jpn. J. Appl. Phys.* **45**, 6017–6021 (2006)
24. J. Kokavecz, O. Marti, P. Heszler, A. Mechler, Imaging bandwidth of the tapping mode atomic force microscope probe. *Phys. Rev. B* **73**, 155403 (2006)
25. K. Wolf, O. Gottlieb, Nonlinear dynamics of a noncontacting atomic force microscope cantilever actuated by a piezoelectric layer. *J. Appl. Phys.* **91**, 4701–4709 (2002)
26. U. Rabe, K. Janser, W. Arnold, Vibrations of free and surface-coupled atomic force microscope cantilevers: theory and experiment. *Rev. Sci. Instrum.* **67**, 3281–3293 (1996)

27. U. Rabe, S. Amelio, E. Kester, V. Scherer, S. Hirsekorn, W. Arnold, Quantitative determination of contact stiffness using atomic force acoustic microscopy. *Ultrasonics* **38**, 430–437 (2000)
28. J.A. Turner, S. Hirsekorn, U. Rabe, W. Arnold, High-frequency response of atomic-force microscope cantilevers. *J. Appl. Phys.* **82**, 966–978 (1997)
29. J.A. Turner, Nonlinear vibrations of a beam with cantilever-Hertzian contact boundary conditions. *J. Sound Vib.* **275**, 177–191 (2004)
30. A. San Paulo, R. Garcia, Unifying theory of tapping-mode atomic force microscopy. *Phys. Rev. B* **66**, 041406(R) (2002)
31. R.W. Stark, W.M. Heckl, Higher harmonics imaging in tapping-mode atomic-force microscopy. *Rev. Sci. Instrum.* **74**, 5111–5114 (2003)
32. R.W. Stark, G. Schitter, M. Stark, R. Guckenberger, A. Stemmer, State-space model of freely vibrating surface-coupled cantilever dynamics in atomic force microscopy. *Phys. Rev. B* **69**, 085412 (2004)
33. H. Hölscher, U.D. Schwarz, R. Wiesendanger, Calculation of the frequency shift in dynamic force microscopy. *Appl. Surf. Sci.* **140**, 344–351 (1999)
34. R. Garcia, R. Perez, Dynamic atomic force microscopy methods. *Surf. Sci. Rep.* **47**, 1–79 (2002)
35. J.H. Cantrell, S.A. Cantrell, Analytical model of the nonlinear dynamics of cantilever tip-sample surface interactions for various acoustic atomic force microscopies. *Phys. Rev. B* **77**, 165409 (2008)
36. L. Meirovitch, *Analytical Methods in Vibrations* (Macmillan, New York, 1967)
37. I.S. Sokolnikoff, R.M. Redheffer, *Mathematics of Physics and Modern Engineering* (McGraw-Hill, New York, 1958)
38. B.M. Law, F. Rieutord, Electrostatic forces in atomic force microscopy. *Phys. Rev. B* **66**, 035402 (2002)
39. M. Saint Jean, S. Hudlet, C. Guthmann, J. Berger, Van der Waals and capacitive forces in atomic force microscopies. *J. Appl. Phys.* **86**, 5245–5248 (1994)
40. T. Eguchi, Y. Hasegawa, High resolution atomic force microscopic imaging of the Si(111)-(7x7) surface: contribution of short-range force to the images. *Phys. Rev. Lett.* **89**, 266105 (2002)
41. H.B. Chan, V.A. Aksyuk, R.N. Kleiman, D.J. Bishop, F. Capasso, Nonlinear micromechanical Casimir oscillator. *Phys. Rev. Lett.* **97**, 211801 (2001)
42. M.A. Lantz, H.J. Hug, R. Hoffmann, P.J.A. van Schendel, P. Kappenberger, S. Martin, A. Baratoff, H.-J. Güntherodt, Quantitative measurement of short-range chemical bonding forces. *Science* **291**, 2580–2583 (2001)
43. J.H. Cantrell, Determination of absolute bond strength from hydroxyl groups at oxidized aluminum-epoxy interfaces by angle beam ultrasonic spectroscopy. *J. Appl. Phys.* **96**, 3775–3781 (2004)
44. S.A. Cantrell, J.H. Cantrell, Renormalization, resonance bifurcation, and phase contrast in dynamic atomic force microscopy. *J. Appl. Phys.* **110**, 094314 (2011)
45. R. Garcia, A. San Paulo, Attractive and repulsive tip-sample interaction regimes in tapping-mode atomic force microscopy. *Phys. Rev. B* **60**, 4961–4967 (1999)
46. R. Garcia, A. San Paulo, Dynamics of a vibrating tip near or in intermittent contact with a surface. *Phys. Rev. B* **61**, R13381 (2000)
47. J. Tamayo, R. Garcia, Effects of elastic and inelastic interactions on phase contrast images in tapping-mode scanning force microscopy. *Appl. Phys. Lett.* **71**, 2394–2396 (1997)
48. J.P. Cleveland, B. Anczykowski, A.E. Schmid, V.B. Elings, Energy dissipation in tapping-mode atomic force microscopy. *Appl. Phys. Lett.* **72**, 2613–2615 (1998)
49. B. Anczykowski, B. Gotsmann, H. Fuchs, J.P. Cleveland, V.B. Elings, How to measure energy dissipation in dynamic mode atomic force microscopy. *Appl. Surf. Sci.* **140**, 376–382 (1999)
50. K. Schröter, A. Petzold, T. Henze, T. Thurn-Albrecht, Quantitative analysis of scanning force microscopy data using harmonic models. *Macromolecules* **42**, 1114–1124 (2009)
51. D.W. Jordan, P. Smith, *Nonlinear Ordinary Differential Equations: An Introduction for Scientists and Engineers* (Oxford, New York, 2007)

52. W. Arnold, A. Caron, S. Hirsekorn, M. Kopycinska-Müller, U. Rabe, M. Reinstädler, in *Atomic Force Microscopy at Ultrasonic Frequencies*, ed. by R.C. Bradt, D. Munz, M. Sakai, K.W. White Fracture Mechanics of Ceramics (Springer, New York, 2005), pp. 1–11
53. Y.-J. Zhao, Q. Cheng, M.-L. Qian, Frequency response of the sample vibration mode in scanning probe acoustic microscope. *Chin. Phys. Lett.* **27**, 56201–56204 (2010)
54. D.I. Bolef, J.G. Miller, in *High-Frequency Continuous Wave Ultrasonics*, ed. by W.P. Mason, R.N. Thurston, Physical Acoustics, vol. VIII (Academic, New York, 1971), pp. 95–201
55. J. Mathews, R.L. Walker, *Mathematical Methods of Physics* (Benjamin, New York, 1964)
56. G. Blanch, Mathieu functions, in *Handbook of mathematical functions with formulas, graphs, and tables*, ed. by A. Abramowitz, I.A. Stegun (US Department of Commerce, Washington, 1970)
57. S.-Y. Kim, B. Hu, Bifurcations and transitions to chaos in an inverted pendulum. *Phys. Rev. E* **58**, 3028–3035 (1998)
58. S. Hu, A. Raman, Chaos in atomic force microscopy. *Phys. Rev. Lett.* **96**, 036107 (2006)

# Chapter 4

## One-Dimensional Finite Element Modeling of AFM Cantilevers

Richard Arinero and Gérard Lévêque

**Abstract** In order to account for realistic cantilever geometries and tip–sample interactions, finite element methods (FEM) can be powerful alternatives. In this chapter, we opted to use a one-dimensional (1D) FEM model for the cantilever beam, which permits to treat the exact vibration of the beam in the contact mode, regardless of its shape (rectangular as well as triangular beams) and excitation mode (by the beam holder, by the sample, by a localized, or distributed force). Based on a classic finite element scheme, it is easy to program for a non-specialist user and as rapid as the usual analytical models. We demonstrate that the mode of excitation of the beam strongly influences the cantilever’s frequency response in the contact mode. This chapter is therefore an attempt to propose in a simple numerical model, a tool allowing a deeper understanding of the dynamic mechanical response of the AFM probe in contact with a viscoelastic sample.

### 4.1 Introduction

All methods consisting of making vibrate the AFM cantilever in contact mode and recording the parameters of the vibration are generally identified as “acoustic methods”. Some methods are often based on the analysis of amplitude (and phase) after a periodic excitation (either at low or high frequency), whereas some others focus on contact resonance frequency measurements. All these methods concern not only flexural vibrations, but also torsional vibrations. The major problem encountered is related to the observed contrast which is not always precisely quantified. Indeed, many factors like adhesion and friction are involved in the tip–sample interaction and play a role in image formation. Other constraints come from cantilever-tip-sample

---

R. Arinero (✉) · G. Lévêque  
Institut d’Electronique du Sud (IES), UMR CNRS 5214, Université, Montpellier 2,  
CC083, Place Eugène Bataillon 34095, Montpellier, France  
e-mail: Richard.arinero@ies.univ-montp2.fr

models which are often over-simplified. For instance, it is admitted that spring-mass models [1, 2] are only valid under certain conditions and do not predict the true frequency response. The best approximation is the cantilever beam model [3–7] where an inclined beam and tip are coupled with a sample represented by vertical and horizontal springs. But only rectangular beams are modeled and always in a linear regime. Moreover, for large amplitudes, nonlinear effects may occur [5–8] (diode effect) but have not been introduced yet in the beam equations. In order to account for realistic cantilever geometries and tip–sample interactions, finite element methods (FEM) can be powerful alternatives. Several authors have already followed this option. In most cases, they used commercial software [9–13]. These tools are easy to implement but are not very adaptable to all the situations encountered during AFM operations. They can be considered as black boxes to which it is not possible to access and to perform some specific task. Mendels et al. [9] used Ansys<sup>TM</sup> FEM codes for evaluating the spring constant of AFM cantilevers. They introduced a hybrid method based on the minimization of the difference between the modeled and experimentally full-field displacement maps of the cantilever’s surface at different resonant frequencies. A similar approach was adopted by Espinoza-Beltran et al. [10]. They followed a specific procedure in which they considered the main geometrical features of commercial cantilevers, as well as the elastic anisotropy of silicon single crystals. The data were fitted in a two-step procedure using the free and contact resonances of the first and third bending mode. Muller et al. [11] have investigated the 3D mechanical deformations of V-shaped cantilevers. They were able to calculate force constants and detection angles for tip displacement in the three spatial directions. Caron et al. in Ref. [12] carried out FEM calculations to identify lateral cantilever modes. They have shown that in AFM experiments in-plane deflection of standard cantilevers is not negligible and can also be used for imaging shear elastic properties of a sample surface. Finally, we can also mention the work of Parlak et al. [13] who described a 3D FEM analysis of the contact between the AFM tip and a substrate with finite subsurface structures. They were able to simulate the contact stiffness measured by the AFM tip on the surface of a sample with buried nanoscale structures. This 3D model was destined to be applied to electromigration defects detection.

Homemade FEM models exist and are much more versatile. A 3D FEM model of tip-cantilevers systems was proposed by Song et al. [14, 15]. This versatile model was adapted to tapping-mode simulations, as well as torsional resonance and lateral excitation mode, but has not been applied to model contact resonance and flexural amplitude as studied in the frame of acoustics methods.

In this chapter, we preferred to use a 1D FEM model for the cantilever beam, which permits to treat the exact vibration of the beam in the contact mode, disregarding its shape (rectangular as well as triangular beams) and excitation mode (by the beam holder, by the sample, by a localized, or distributed force). Based on a classic finite element scheme, it is easy to program for a non-specialist user and as rapid as the usual analytical models. We demonstrate that the mode of excitation of the beam strongly influences the cantilever’s frequency response in the contact mode. This chapter is therefore an attempt to propose in a simple numerical model a tool allowing a deeper understanding of the mechanical response of the AFM microscope.

We begin by describing in detail the 1D FEM model. The kinematic parameters involved in the discretization of the beam are first identified and the construction of the mass and stiffness matrix associated with each element is then explained, as well as the steps leading to the global system matrix. Then, we describe how the tip and the contact with the sample are introduced in the model. Finally, in the last part, we analyze the solutions obtained from the FEM model. The effect of the excitation mode is studied, as well as the effects of both normal and tangential contact stiffness. The concepts of apparent and real force, providing a complete description of the tip-sample interaction, are finally discussed.

## 4.2 Finite Element Model for a Beam

The cantilever geometry is described in a transverse plane in Fig. 4.1, in the same way as in Refs. [4] and [5]. The beam is tilted by an angle  $\alpha$  relative to the sample. It is defined by the length  $L$ , the width  $b$  (depending on  $x$  in the case of a triangular cantilever), the thickness  $e$ , the tip height  $h$  (supposed of conical shape), the tip mass  $M$ , and the mechanical properties of the beam material (Silicon oriented in the  $\langle 110 \rangle$  crystallographic direction). The tip-sample interaction is described in the linear regime by two complex constants, the normal stiffness  $k_N$  and the tangential stiffness  $k_T$ , which include all forces and damping at the working frequency. We chose a finite element model for the beam vibration, because all the above features can be included easily.

### 4.2.1 Kinematic Parameters

We used a classic FEM, as described in Ref. [16], limited to the pure flexion case (there is no extension of the beam). The beam is decomposed in  $N$  thin slices (or elements) perpendicular to the  $(Ox)$  axis, and a “1D” description of the beam flexure is adopted, as detailed below. Each element  $AB$  is taken with the same length  $\Delta$  ( $\Delta = 2 \mu\text{m}$ ) and has four degrees of liberty, also called kinematic parameters, which are the transverse displacements  $z_A$  et  $z_B$ , and the corresponding slopes  $\theta_A$  et  $\theta_B$  at the extremities nodes  $A$  and  $B$  (Fig. 4.2).

We define  $\{q\}$  the vector composed of the kinematic parameters:

$$\{q\} = \{q_{i=1,4}\} = \{z_A \quad \theta_A \quad z_B \quad \theta_B\} \quad (4.1)$$

We make the assumption that at each instant  $t$ , the deformation of the element  $AB$  (which will be an element of the cantilever) can be expressed by a third-order polynomial function of the form:

$$Z(y) = a_1 + a_2y + a_3y^2 + a_4y^3 \quad (4.2)$$

where  $a_1$ ,  $a_2$ ,  $a_3$  and  $a_4$  are adjustable constants.



**Fig. 4.1** On Scale scheme of the vibrating cantilever beam in contact with a sample, for the two extreme positions. The shape of the cantilever is deduced from the model, with a tip supposed to slide on a hard sample. Amplitude is amplified by a factor 1,000, in order to make the deformation visible. Reproduced with permission from [21]. Copyright 2003, American Institute of Physics

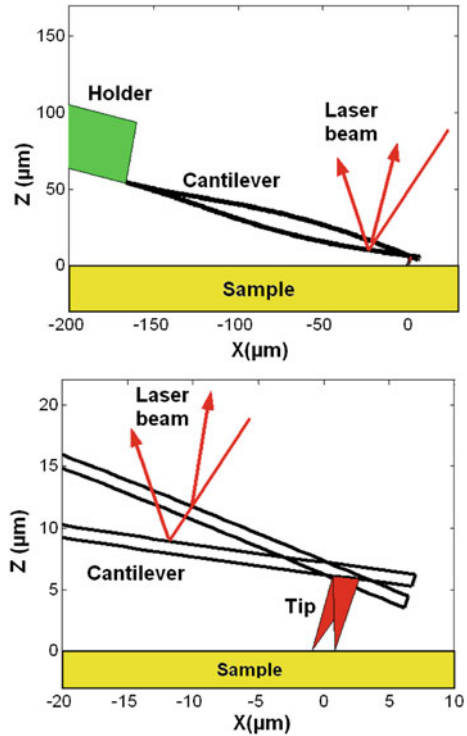
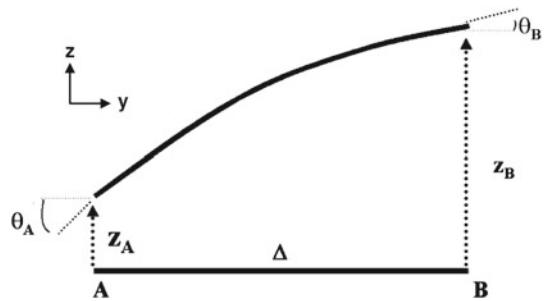


**Fig. 4.2** Beam element defined 4 kinematic parameters



Introducing particular values of  $Z$  at points  $A$  and  $B$ , we can write:

$$Z(y) = z_A \Phi_1(y) + \theta_A \Phi_2(y) + z_B \Phi_3(y) + \theta_B \Phi_4(y) \tag{4.3}$$

where  $\Phi_i(y)$  are also third-order polynomial functions obtained by identification with Eq. (4.3). These functions are called interpolation functions of the element  $AB$ .

A classical calculation [14] yields the following expression:

$$\begin{aligned}
Z(y) = & \left[ 1 - \frac{3y^2}{\Delta^2} + \frac{2y^3}{\Delta^3} \right] z_A + \left[ y - \frac{2y^2}{\Delta} + \frac{y^3}{\Delta^2} \right] \theta_A \\
& + \left[ \frac{3y^2}{\Delta^2} - \frac{2y^3}{\Delta^3} \right] z_B + \left[ -\frac{y^2}{\Delta} + \frac{y^3}{\Delta^2} \right] \theta_B
\end{aligned} \quad (4.4)$$

which can be written under a matricial form:

$$Z(y) = \sum_{i=1}^4 \Phi_i(y) q_i \quad (4.5)$$

$q_i$  are sinusoidal functions of the pulsation  $\omega$ , in such way that:

$$\frac{\partial q_i}{\partial t} = j\omega q_i \quad (4.6)$$

### 4.2.2 Matricial Form of Kinetic Energy: Mass Matrix

The kinetic energy of an element  $AB$  expresses as:

$$T_{AB} = \frac{1}{2} \int_0^{\Delta} \rho e b \left( \frac{\partial Z}{\partial t} \right)^2 dy \quad (4.7)$$

where  $\rho$  is density of silicon.

By derivating expression (4.5) with respect to time, we obtain:

$$\left( \frac{\partial Z}{\partial t} \right)^2 = -\omega^2 \sum_{i=1}^4 \sum_{j=1}^4 \Phi_i(y) \Phi_j(y) q_i q_j \quad (4.8)$$

Thus, it comes:

$$\begin{aligned}
T_{AB} &= \frac{-\omega^2}{2} \sum_i \sum_j m_{ij} q_i q_j = \frac{-\omega^2}{2} \{q\}^T [M_{AB}] \{q\} \\
&= \frac{\omega^2}{2} \{z_A \theta_A z_B \theta_B\}^T [M_{AB}] \{z_A \theta_A z_B \theta_B\}
\end{aligned} \quad (4.9)$$

The coefficients  $m_{ij}$  are relative to the (symmetrical) mass matrix  $[M_{AB}]$  of the element  $AB$ . They are defined by:

$$m_{ij} = \int_0^{\Delta} \rho e b \Phi_i(y) \Phi_j(y) dy = m_{ji} \quad (4.10)$$

Integer calculations in expression (4.10) lead to the following form of  $[M_{AB}]$ :

$$[M_{AB}] = \frac{\rho e b \Delta}{420} \begin{bmatrix} 156 & 22\Delta & 54 & -13\Delta \\ 22\Delta & 4\Delta^2 & 13\Delta & -3\Delta^2 \\ 54 & -13\Delta & 156 & -22\Delta \\ 13\Delta & -3\Delta^2 & -22\Delta & 4\Delta^2 \end{bmatrix} \quad (4.11)$$

### 4.2.3 Matricial Form of Elastic Potential Energy: Stiffness Matrix

The elastic potential energy of an element  $AB$  expresses as:

$$W_{AB} = \frac{1}{2} \int_0^{\Delta} EI \left( \frac{\partial^2 Z}{\partial y^2} \right)^2 dy \quad (4.12)$$

where  $I = e^3 b / 12$  is the moment of inertia of the beam section and  $E$  is the Young's modulus of silicon in the  $\langle 110 \rangle$  direction (169 GPa).

By derivating expression (4.5) with respect to  $y$ , we obtain:

$$\frac{\partial^2 Z}{\partial y^2} = \sum_i \frac{\partial^2 \Phi_i(y)}{\partial y^2} q_i \quad (4.13)$$

Thus, it comes:

$$\left( \frac{\partial^2 Z}{\partial y^2} \right)^2 = \sum_i \sum_j q_i q_j \left[ \frac{\partial^2 \Phi_i}{\partial y^2} \cdot \frac{\partial^2 \Phi_j}{\partial y^2} \right] \quad (4.14)$$

Finally, we have:

$$\begin{aligned} W_{AB} &= \frac{1}{2} \sum_i \sum_j k_{ij} q_i q_j = \frac{1}{2} \{q\}^T [K_{AB}] \{q\} \\ W_{AB} &= \frac{1}{2} \{z_A \theta_A z_B \theta_B\}^T [K_{AB}] \{z_A \theta_A z_B \theta_B\} \end{aligned} \quad (4.15)$$

The coefficients  $k_{ij}$  are relative to the (symmetrical) stiffness matrix  $[K_{AB}]$  of the element  $AB$ . They are defined by:

$$k_{ij} = \int_0^l EI \frac{\partial^2 \Phi_i}{\partial y^2} \cdot \frac{\partial^2 \Phi_j}{\partial y^2} \cdot dy = k_{ji} \quad (4.16)$$

Integer calculations in expression (4.16) lead to the following form of  $[K_{AB}]$ :

$$[K_{AB}] = \frac{Ee^3b}{12\Delta^3} \begin{bmatrix} 12 & 6\Delta & -12 & 6\Delta \\ 6\Delta & 4\Delta^2 & -6\Delta & 2\Delta^2 \\ -12 & 6\Delta & 12 & -6\Delta \\ 6\Delta & 2\Delta^2 & -6\Delta & 4\Delta^2 \end{bmatrix} \quad (4.17)$$

#### 4.2.4 Mesh with $N$ Elements: Global Matrix Construction

Let us consider a cantilever beam of length  $L$  discretized in  $N$  elements of matricial indexes  $n$  ( $n = 1, N$ ) and of width  $\Delta = L/N$  as shown in Fig. 4.3. Both extremities of each element are called «nodes». There are thus  $N + 1$  nodes for the whole beam. An element of index  $n$  is localized between nodes of index  $n' = n$  and  $n' = n + 1$ ; it possesses four degrees of freedom ( $z_{n'=n}$ ,  $\theta_{n'=n}$ ,  $z_{n'=n+1}$  et  $\theta_{n'=n+1}$ ).

Finally, the whole beam is well defined by  $2N + 2$  parameters, included in the vector  $\{q\}$ :

$$\{q\} = \{z_1 \quad \theta_1 \quad z_2 \quad \theta_2 \quad \cdots \quad \cdots \quad z_{n'} \quad \theta_{n'} \quad \cdots \quad \cdots\} \quad (n' = 1, N + 1) \quad (4.18)$$

The mass matrix  $[M_n]$  and the stiffness matrix  $[K_n]$  relative to elements of index  $n$  are given by expressions (4.11) and (4.17), respectively. It is possible to introduce a particular value of the width  $b$  ( $n$ ) and the thickness  $e$  ( $n$ ) for each element. This is how we take into account the specific geometry of cantilever, rectangular or triangular.

The coefficients of the matrix  $[M_n]$  et  $[K_n]$  are noted  $m_{ij}^{(n)}$  et  $k_{ij}^{(n)}$  with  $i = 1, 4$  and  $j = 1, 4$ . Then, we can build the global mass matrix  $[M_{\text{tot}}]$  and the global stiffness matrix  $[K_{\text{tot}}]$ , which are matrix of dimension  $2N + 2$ , according to the method of assembly described in Fig. 4.4. On the diagonal, the terms correspond to the sum of the matrix coefficients of two consecutive beam elements. Finally, we obtain the

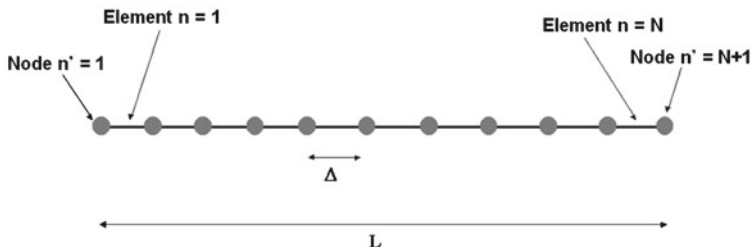


**Fig. 4.3** Discretization of the cantilever beam in  $N$  elements of length  $\Delta$ . The extremities of each element are called “nodes”

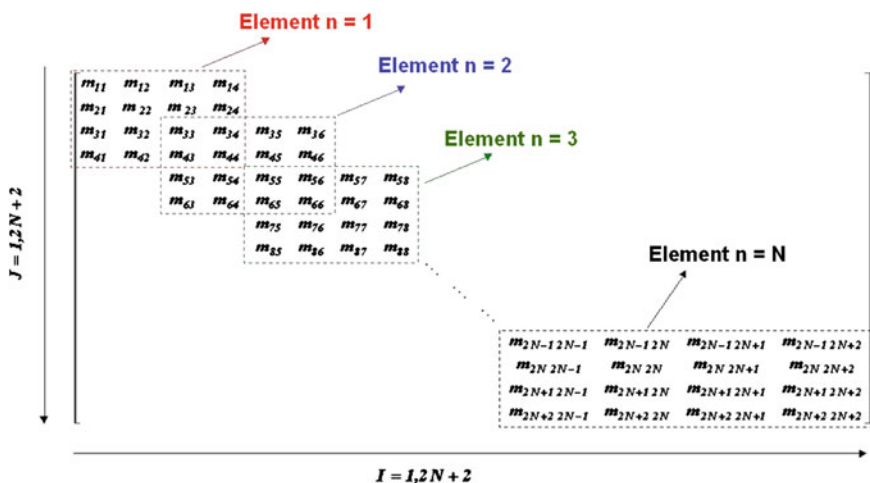


**Fig. 4.4** Construction of the global mass matrix by assembly of the matrix relative to each beam element. On the diagonal, the terms correspond to the sum of the matrix coefficients of two consecutive beam elements. The global stiffness matrix is built in an identical way

global matrix  $[M_{tot}]$  and  $[K_{tot}]$  of coefficients  $m_{IJ}$  and  $k_{IJ}$  where  $I = 1, 2N + 2$  and  $J = 1, 2N + 2$ , in such way that:

$$\begin{aligned}
 m_{2n+1 \ 2n+1} &= m_{11}^{(n+1)} + m_{33}^{(n)} \\
 m_{2n+2 \ 2n+2} &= m_{22}^{(n+1)} + m_{44}^{(n)} \\
 m_{2n+2 \ 2n+1} &= m_{2n+1 \ 2n+2} = m_{12}^{(n+1)} + m_{34}^{(n)}
 \end{aligned}
 \tag{4.19}$$

The other coefficients are equal to zero.

The coefficients  $k_{IJ}$  of the global stiffness matrix are obtained in an identical way.

### 4.2.5 Free and Forced Vibration Analysis

Let us consider the matrix  $[S]$ :

$$[S] = [K_{\text{tot}}] - \omega^2 [M_{\text{tot}}] \quad (4.20)$$

The coefficients of  $[S]$  are given by  $S_{IJ} = k_{IJ} - \omega^2 m_{IJ}$  where  $I = 1, 2N + 2$  and  $J = 1, 2N + 2$ .

By analogy with classical point mechanics, free vibrations (natural frequencies and mode shapes) are calculated by solving the following linear system:

$$[S] \{q\} = 0 \quad (4.21)$$

The system is homogeneous and to obtain nontrivial solutions, we need to solve the following equation:

$$\det [S] = 0 \quad (4.22)$$

To study the forced vibrations response, the Lagrange equation of the system has to be solved:

$$[S] \{q\} = \{F\} \quad (4.23)$$

The vector  $\{q\}$  [expression (4.18)] is the solution of the system at the angular frequency  $\omega$  and  $\{F\}$  is a vector formed by forces  $F_{n'}$  et moments  $\Gamma_{n'}$  applied at each node.

To take into account the air damping, one can introduce a force at each node  $F_{\text{damping}} = i\omega az$  proportional to the velocity. The damping coefficients  $a$  can be calculated theoretically according to the laws of aerodynamics applied to thin plates, but one can rather find them by an empirical adjustment of experimental free resonance curves.

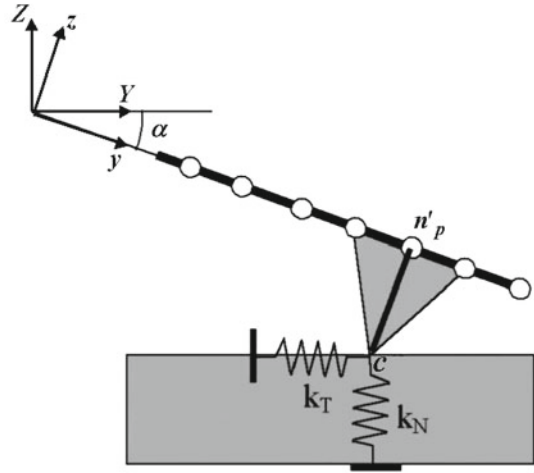
The air damping matrix  $[A]$  for the whole beam can be written as:

$$[A] = \begin{bmatrix} a & 0 & 0 & & & \\ 0 & 0 & 0 & & 0 & \\ 0 & 0 & a & & & \\ 0 & 0 & 0 & 0 & & \\ 0 & 0 & & & \ddots & \\ 0 & 0 & & & & \ddots \end{bmatrix} \quad (4.24)$$

Finally,  $[S]$  expresses as:

$$[S] = [K_{\text{tot}}] - \omega^2 [M_{\text{tot}}] + i\omega [A] \quad (4.25)$$

**Fig. 4.5** Schema of the tip attached to the cantilever at a node  $n'_p$  and the contact with the sample occurs at point  $c$ . The tip is supposed to be rigid and to interact with only one beam node. The contact interaction is modeled by two springs with stiffness  $k_N$  and  $k_T$ . Reproduced with permission from [21]. Copyright 2003, American Institute of Physics



### 4.3 Model for the Tip

The presence of the tip at the extremity of the cantilever is schematized on Fig. 4.5. The tip is supposed of conical shape and indeformable. It is attached to the beam at a node  $n'_p$  and the contact with the sample at point  $c$  is modeled by the normal contact stiffness  $k_N$  and the tangential contact stiffness  $k_T$ . The tip mass  $m_t$  and inertia moment  $I_G$  with respect to the center of mass  $G$ , are given by:

$$m_t = \frac{\pi r^2 h \rho}{3} \quad \text{and} \quad I_G = m_t \left( \frac{3h^2}{80} + \frac{3r^2}{20} \right) \quad (4.26)$$

where  $h$  is the tip height,  $r$  the radius of the cone's base and  $\rho$  the density of silicon.

In the coordinate system  $(Oyz)$ , the velocity of the center of mass  $G$  is:

$$\vec{V}_G = i\omega \left( z_{n'_p} \mathbf{k} + \frac{h}{4} \theta_{n'_p} \mathbf{i} \right) \quad (4.27)$$

Then, the kinetic energy of the tip can be written as:

$$T_{\text{Tip}} = \frac{1}{2} m_p V_G^2 + \frac{1}{2} I_G \left( \frac{\partial \theta_{n'_p}}{\partial t} \right)^2 = \frac{1}{2} m_p \omega^2 \left[ z_{n'_p}^2 + \left( \frac{h^2}{10} + \frac{3r^2}{20} \right) \theta_{n'_p}^2 \right] \quad (4.28)$$

An additional mass matrix  $\Delta M_{n'_p}$  relative to the node  $n'_p$  is deduced from expression (4.28). It can be expressed as:

$$\Delta M_{n'_p} = -\omega^2 m_p \begin{bmatrix} 1 & 0 \\ 0 & \frac{h^2}{10} + \frac{3r^2}{20} \end{bmatrix} \quad (4.29)$$

The coefficients of  $\Delta M_{n'_p}$  are summed with the other coefficients  $m_{2n'_p-1}$   $2n'_p-1$  and  $m_{2n'_p}$   $2n'_p$  of the global mass matrix  $[M_{\text{tot}}]$ .

The potential elastic energy of the contact expresses as (The elastic energy of the tip is supposed to be null):

$$W_{\text{contact}} = \frac{1}{2} \left( k_N Z_c^2 + k_T Y_c^2 \right) \quad (4.30)$$

$Y_c$  and  $Z_c$  are the coordinates of the contact point  $c$  in the coordinate system  $(OYZ)$ . They verify the relations:

$$Y_d = h\theta_{n'_p} \cos \alpha + z_{n'_p} \sin \alpha \text{ and } Z_d = -h\theta_{n'_p} \sin \alpha + z_{n'_p} \cos \alpha \quad (4.31)$$

An additional stiffness matrix  $\Delta K_{n'_p}$  relative to the node  $n'_p$  is deduced from expression (4.30). It can be expressed as:

$$\Delta K_{n'_p} = \begin{bmatrix} k_T \sin^2 \alpha + k_N \cos^2 \alpha & h \sin \alpha \cos \alpha (k_T - k_N) \\ h \sin \alpha \cos \alpha (k_T - k_N) & h^2 (k_T \cos^2 \alpha + k_N \sin^2 \alpha) \end{bmatrix} \quad (4.32)$$

The coefficients of  $\Delta K_{n'_p}$  are summed with the other coefficients  $k_{2n'_p-1}$   $2n'_p-1$ ,  $k_{2n'_p}$   $2n'_p$ ,  $k_{2n'_p-1}$   $2n'_p-1$  of the global stiffness matrix  $[K_{\text{tot}}]$ .

The values of  $k_N$  and  $k_T$  depend on the contact mechanical properties and will be detailed further.

## 4.4 Solutions of the Finite Element Model

The solution of the forced vibration analysis (4.23) gives the deformation of the beam as a complex transverse amplitude  $z(y)$ , for each frequency. The photodetector signal recorded by the microscope (in the case of a laser detection), and analyzed by a lock-in amplifier, is proportional to the flexion slope  $z'(y_l)$  at the abscissa  $y_l$  of the laser impact on the beam. Assuming small-amplitude oscillations  $z'(y_l)$  is nearly equal to the flexion angle  $\theta_{n'_l}$  calculated at the corresponding node  $n'_l$ . The photodetector signal is usually calibrated, using static force-distance mode, to directly give the tip vertical displacement. In vibrating mode, however, the flexure of the beam is different than in static mode, then the measured signal amplitude is not equal to the true amplitude of vibration of the tip. Then we introduce the notions of: true normal (vertical) and true tangential (horizontal) amplitudes,  $A_N$  and  $A_T$  respectively, corresponding to the amplitude of the beam at the node  $n'_p$  where the tip apex is located, and apparent amplitude  $A_A$  measured directly from the lock-in amplifier. This allows a complete study of cantilevers vibrating in contact with a sample.  $A_A$ ,



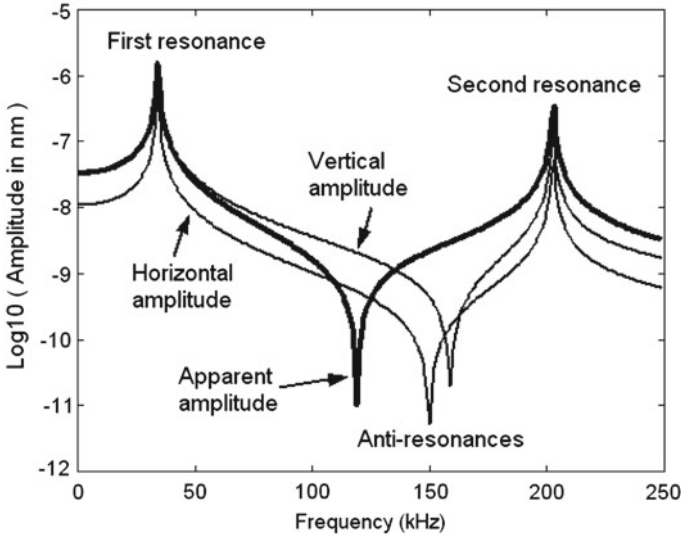


**Fig. 4.6** Amplitude of oscillation of a free cantilever beam (Cantilever A in Table 4.1), with an electrostatic excitation. The true vertical amplitude of the tip apex ( $A_N$  normal), the true horizontal amplitude ( $A_T$  tangential), and the apparent amplitude ( $A_A$ ), as measured by the lock-in amplifier are reported. Reproduced with permission from [21]. Copyright 2003, American Institute of Physics

$A_N$  and  $A_T$  are defined by:

$$A_A = s\theta_{n'_l} \quad (4.33)$$

$$A_N = Z_c = -h\theta_{n'_p} \sin \alpha + z_{n'_p} \cos \alpha \quad (4.34)$$

$$A_T = Y_c = h\theta_{n'_p} \cos \alpha + z_{n'_p} \sin \alpha \quad (4.35)$$

where  $s$  is the coefficient of proportionality between the apparent amplitude  $A_A$  and the flexion angle  $\theta_{n'_l}$ .

Figure 4.6 represents the amplitude of vibration of a free cantilever (Cantilever A in Table 4.1), excited by a distributed electrostatic force. In this example the relative position of tip  $y_{n'_p}$  and the laser  $y_l$  are considered to be the same, i.e., 95 % of the total cantilever length. We have  $A_A = A_N$  at low frequencies as expected, and large differences elsewhere in the curves. The free resonance frequency appears at 34 kHz and the second harmonic resonance occurs at 202 kHz, where  $A_A$ ,  $A_N$  and  $A_T$  present simultaneous maxima. This is not the case for anti-resonance, for instance an anti-resonance in the apparent amplitude is obtained near 119 kHz, indicating that the beam at the abscissa  $y_l$  (laser impact) vibrates in pure translation (without slope variation), at this frequency. We also observe anti-resonance on the true amplitude  $A_N$  and  $A_T$  curves (150 and 159 kHz), indicating that the tip apex moves either horizontally or vertically at these frequencies.

**Table 4.1** Dimensions of the cantilever and of the tip

Type	A	B	C	D
Cantilever shape	Triangle	Rectangle	Rectangle	Triangle
Beam length $L$	180	180	180	265
Beam width $b$	50	50	50	85
Beam thickness $e$	0.8	0.8	0.8	0.8
Tip length $h$	5	5	20	17
Tip base radius $r$	1	1	4	4
Tip apex radius $R$	.050	.050	.050	.100
Free first frequency $f_1$	34.19	27.37	25.30	17.82
Free second frequency $f_2$	202.5	171.6	161.8	98.5
Sliding contact frequency $f_1'$	128.7	129.1	134.8	74.5
Nonsliding contact frequency $f_1''$	161.1	184.5	184.5	92.8
Ratio $f_2/f_1$	5.92	6.27	6.40	5.52
Ratio $f_1'/f_1$	3.77	4.72	5.33	4.18
Ratio $f_1''/f_1$	3.84	6.74	7.29	5.21

The dimensions are in  $\mu\text{m}$ , and the frequencies in kHz. Resonance frequencies are obtained by finite elements analysis. Reproduced with permission from [21]. Copyright 2003, American Institute of Physics

Using the proposed 1D finite element model, it is now tried to appreciate the importance of various specific factors to each experiment, such as the excitation mode, the shape of the cantilever, or normal and tangential contact stiffness effects.

#### 4.4.1 Effect of the Excitation Mode

It is pointed out that different methods are employed to excite the cantilever, either by using the bimorph actuator fixed near the clamped extremity of the beam [17, 18] or by using a piezoelectric element located under the sample holder [19, 20]. Other methods consist of applying external forces, distributed along the cantilever by means of an electrostatic pressure [21, 22] or localized on one single part via a magnetic element [23–25]. The excitation mode is taken into account in the finite element model by introducing, in each case, the corresponding external force vector  $\{F\}$ .

##### 4.4.1.1 Excitation by the Cantilever Holder

If the beam holder is moved in sinusoidal translation, with an amplitude  $a$ , then  $z_1 = a$  and  $\theta_1 = 0$ , and system (4.23) is modified as follows:

$$\begin{bmatrix} 1 & 0 & 0 & 0 \\ 0 & 1 & 0 & 0 \\ 0 & 0 & S_{33} & S_{34} & S_{35} & S_{36} \\ 0 & 0 & S_{43} & S_{44} & S_{45} & S_{46} \\ & & S_{53} & S_{54} & S_{55} & S_{56} & S_{57} & S_{58} \\ & & S_{63} & S_{64} & S_{65} & S_{66} & S_{67} & S_{68} \\ & & \dots & \dots & \dots & \dots & \dots & \dots \end{bmatrix} \times \begin{Bmatrix} z_1 \\ \theta_1 \\ z_2 \\ \theta_2 \\ z_3 \\ \theta_3 \\ \dots \end{Bmatrix} = \begin{Bmatrix} a \\ 0 \\ 0 \\ 0 \\ 0 \\ 0 \\ \dots \end{Bmatrix} \tag{4.36}$$

**4.4.1.2 Excitation via the Sample Holder**

If the sample is moved in sinusoidal translation, with an amplitude  $a$ , then a normal force  $F_N = ak_N$  is applied at point  $c$ . The resulting action on the node  $n'_p$  is composed of a force and a moment:  $F_{n'_p} = ak_N \cos \alpha$  and  $\Gamma_{n'_p} = -ahk_N \sin \alpha$ . The clamped end condition (appearing in cases 4.4.1.2–4.4.1.4) expresses as  $z_1 = 0$  and  $\theta_1 = 0$ . Then, the two first lines of the system are ignored and will not be reported in the following cases. The resulting system is:

$$\begin{bmatrix} S_{33} & S_{34} & S_{35} & S_{36} \\ S_{43} & S_{44} & S_{45} & S_{46} \\ S_{53} & S_{54} & S_{55} & S_{56} & S_{57} & S_{58} \\ S_{63} & S_{64} & S_{65} & S_{66} & S_{67} & S_{68} \\ & & \dots & & & \\ & & & \dots & & \\ & & & & \dots & \\ & & & & & \dots \end{bmatrix} \times \begin{Bmatrix} z_2 \\ \theta_2 \\ z_3 \\ \theta_3 \\ \dots \\ z_{n'_p} \\ \theta_{n'_p} \\ \dots \end{Bmatrix} = \begin{Bmatrix} 0 \\ 0 \\ 0 \\ 0 \\ \dots \\ F_{n'_p} \\ \Gamma_{n'_p} \\ \dots \end{Bmatrix} \tag{4.37}$$

**4.4.1.3 Excitation by a Localized Magnetic Force**

If a force of magnitude  $F_{mag}$  is applied via a magnetic element supposed punctual and situated on the node  $n'$  (not necessarily identical to node  $n'_p$ , the resulting system is:

$$\begin{bmatrix} S_{33} & S_{34} & S_{35} & S_{36} \\ S_{43} & S_{44} & S_{45} & S_{46} \\ S_{53} & S_{54} & S_{55} & S_{56} & S_{57} & S_{58} \\ S_{63} & S_{64} & S_{65} & S_{66} & S_{67} & S_{68} \\ & & \dots & & & \\ & & & \dots & & \\ & & & & \dots & \\ & & & & & \dots \end{bmatrix} \times \begin{Bmatrix} z_2 \\ \theta_2 \\ z_3 \\ \theta_3 \\ \dots \\ z_{n'} \\ \theta_{n'} \\ \dots \end{Bmatrix} = \begin{Bmatrix} 0 \\ 0 \\ 0 \\ 0 \\ \dots \\ F_{mag} \\ 0 \\ \dots \end{Bmatrix} \tag{4.38}$$

#### 4.4.1.4 Excitation by a Distributed Electrostatic Force

If an electrostatic force is applied on the beam, a force is applied on each node. The expression of the elemental forces depends on the geometry of the capacitor formed by the beam and the sample holder. For an insulating sample, electrostatic charges at the sample surface must also be taken into account. Generally, the exact electrostatic pressure on the beam is difficult to estimate and an approximate value  $P_{\text{elec}} = 1/2\epsilon_0 V^2/d^2$  is taken, depending on the variable beam-sample distance  $d$  (the expression is exact for a plane parallel metallic capacitor). Then,  $F_{\text{elec}} = \Delta b P_{\text{elec}}$  is estimated on each node and noted  $F_2, F_3, \dots$

The system becomes:

$$\begin{bmatrix} S_{33} & S_{34} & S_{35} & S_{35} & & & & \\ S_{43} & S_{44} & S_{45} & S_{46} & & & & \\ S_{53} & S_{54} & S_{55} & S_{56} & S_{57} & S_{58} & & \\ S_{63} & S_{64} & S_{65} & S_{66} & S_{67} & S_{68} & & \\ & & & & \ddots & & & \\ & & & & & & \ddots & \\ & & & & & & & \ddots & \\ & & & & & & & & \ddots & \end{bmatrix} \times \begin{bmatrix} z_2 \\ \theta_2 \\ z_3 \\ \theta_3 \\ \dots \\ z_{n'} \\ \theta_{n'} \\ \dots \end{bmatrix} = \begin{bmatrix} F_2 \\ 0 \\ F_3 \\ 0 \\ \dots \\ F_{n'} \\ 0 \\ \dots \end{bmatrix} \quad (4.39)$$

#### 4.4.1.5 Comparison of Excitation Modes

The results obtained for cases presented in Sects. 4.4.1.2–4.4.1.4 (Cantilever A in Table 4.1), introducing a typical value for the contact stiffness of a polymer are reported on Fig. 4.7.

The conclusions are obvious:

- The resonance frequency is the same for any excitation mode. This first remark is evident, if we consider that the resonance frequency, in absence of damping, is given by  $\det([K_{\text{tot}}] - \omega^2 [M_{\text{tot}}]) = 0$  [Eq. (4.22)], which is independent of the force distribution;
- The true amplitude  $A_N$  is very different to the measured  $A_A$ ;
- The true amplitudes are very sensitive to the excitation modes, and may exhibit anti-resonance for some frequencies;
- The ratio  $A_N/A_A$  and  $A_T/A_A$  are given by the numerical model, which can serve to estimate the true amplitudes in any case. At the resonance, they are only determined by the proper vectors of Eq. (4.22), and are also independent of the force distribution.

To resume, the finite element model allows a complete description of the vibration of the beam, in any excitation case. Moreover, the model predicts the true vibration amplitude and the apparent amplitude as recorded by the lock-in amplifier. It is

**Fig. 4.7** Amplitude of oscillation of a cantilever beam, in contact with a sample characterized by arbitrary stiffness values  $k_N = 100 \text{ N/m}$  and  $k_T = 67 \text{ N/m}$ , for the types of excitation mentioned in Sect. 4.4.1. *Solid thick line* apparent amplitude ( $A_A$  normalized to 1 nm at zero frequency). *Thin line* vertical amplitude ( $A_N$ ). *Dotted line* horizontal amplitude ( $A_T$ ). Reproduced with permission from [21]. Copyright 2003, American Institute of Physics

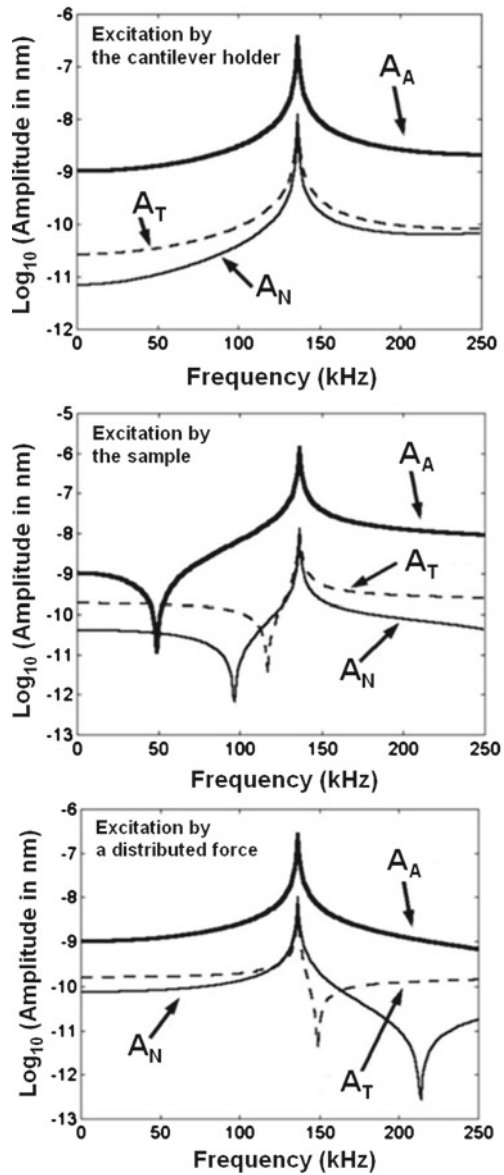
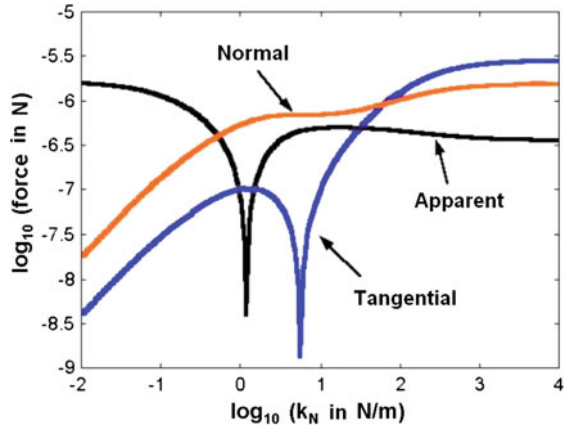


**Fig. 4.8** Forces between the sample and the tip in function on the normal stiffness  $k_N$  calculated at the first resonance frequency and in absence of viscous damping. The tangential stiffness is supposed equal to  $k_T = 2/3k_N$  for a nonsliding contact. The excitation force is taken constant. Reproduced with permission from [21]. Copyright 2003, American Institute of Physics



evident in Fig. 4.7, that in the used frequency range, the apparent vibration amplitude is very different to the true amplitude, which can now be estimated.

### 4.4.2 Concepts of Apparent and Real Force

The same results like in previous section can be presented in the form of apparent force  $F_A = k_l A_A$ , real normal force  $F_N = k_N A_N$  and real tangential force  $F_T = k_T A_T$  applied on the sample. The case of cantilever A in Table 4.1 is represented in Fig. 4.8. Forces have been calculated at first contact resonance frequency. The curves indicate that normal and tangential forces very strongly and differently depending on the sample stiffness. For soft samples, the sinusoidal part of the normal force is greater than the tangential force, whereas the opposite occurs for hard samples. This point also has repercussions in the analysis of nonlinearity effects due to large vibration amplitude, because the larger force will be the first to reach the nonlinear threshold, which is not always the normal force, as assumed in the “diode effect” [5, 8] analysis. Another possible interpretation of Fig. 4.8 is that when the sample is soft (low values of  $k_N$ ), the normal force being superior to the tangential force, the conditions are optimized for a nonsliding contact, whereas for rigid samples (high values of  $k_N$ ), a sliding contact may occur. This hypothesis will be verified in Sect. 4.4.4.

### 4.4.3 Effect of the Beam Shape

The beam shape can be taken into consideration by introducing in the model a variable width along the cantilever as presented in Fig. 4.9. The function  $b(n)$  represents the value of the width attributed at each element  $n$ . It is shown that a triangular shape is equivalent to a rectangular one of which the width would be the double of each arm

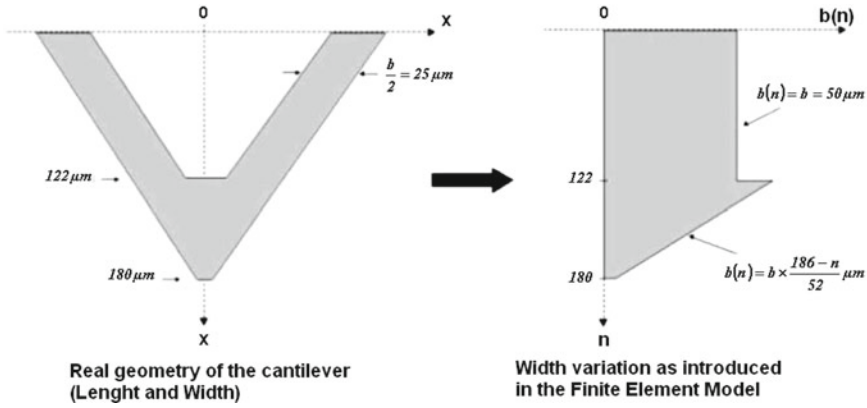


**Fig. 4.9** Top view of the real geometry of a triangular cantilever as taken into account in the Finite Element Model (Cantilever A in Table 4.1). A variable value of the width is attributed to each element (180 elements in that case)

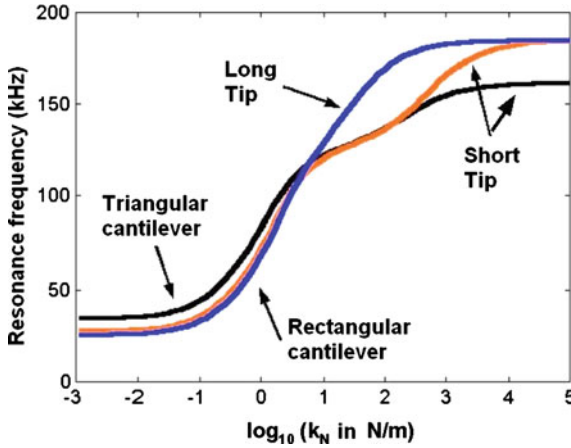
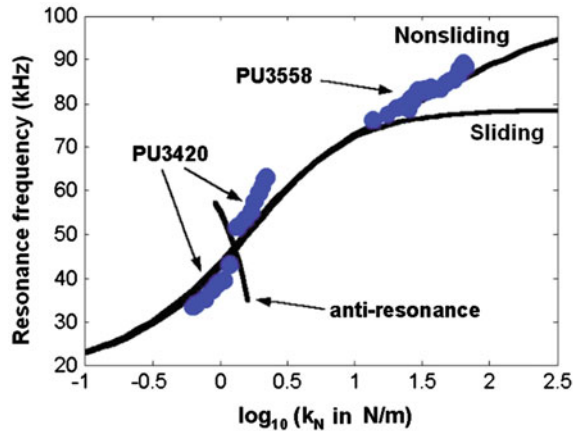


**Fig. 4.10** Resonance frequency of the cantilever, the tip being in contact with a sample, characterized by its normal stiffness  $k_N$ . The tangential stiffness is assumed to be  $k_T = 2/3k_N$ . Triangular cantilever A (Black line) and rectangular cantilevers B and C (Red and Blue lines respectively) are compared, as well as the effect of tip height (short tip  $5 \mu\text{m}$ , long tip  $20 \mu\text{m}$ ). Cantilever and tip dimensions (for A, B and C) are given in Table 4.1. Reproduced with permission from [21]. Copyright 2003, American Institute of Physics

and would be terminated by a function reproducing the diminution of the total width at the extremity.  $b(n)$  can be estimated from optical observations.

Resonance frequency versus the normal stiffness is plotted in Fig. 4.10 for two classic cantilever shapes (A and B in Table 4.1), rectangular or triangular (all dimensions of the cantilever and tip are taken equal). The tangential stiffness is supposed equal to  $k_T = 2/3k_N$ .

**Fig. 4.11** Resonance frequency (Cantilever D) in Table 4.1, in two cases: the sliding contact case  $k_T = 0$  and the nonsliding contact  $k_T = 2/3k_N$ . The anti-resonance frequency is indicated by the small segment of curve. *Dots* experimental points corresponding to two polyurethane samples. Reproduced with permission from [21]. Copyright 2003, American Institute of Physics



The effect of the beam shape is mainly to modify the frequencies of the two extreme cases, the free ( $k_N = 0$ ) and the clamped cases ( $k_N \rightarrow \infty$ ). For hard samples ( $k_N$  in the 1,000 N/m range), the rectangular beam appears superior to the triangular one, because of the greater slope  $df_1/dk_N$ , indicating a better sensitivity to the sample stiffness.

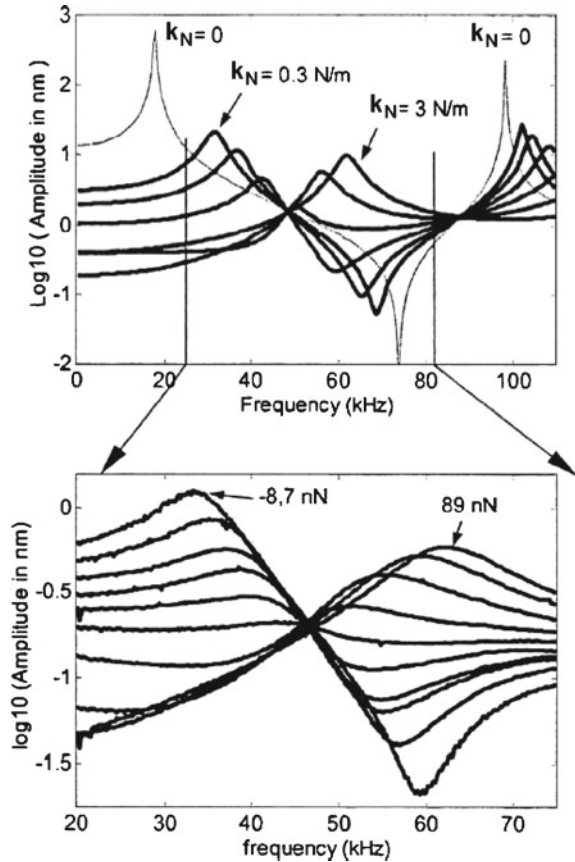
We reported also on Fig. 4.10 the effect of the tip height  $h$  for the rectangular beam ( $B$  and  $C$  in Table 4.1). We observe that the free resonance frequency and the hinged frequency are only slightly modified. The main effect lies in the 10–100 N/m range, where the curve for the long tip presents much higher slope than the curve corresponding to the short tip. The long tip induces a strong bending moment on the beam, resulting in a greater sensitivity to the sample properties. For quantitative experiments, it is desirable to count on a precise frequency–stiffness curve, which can be used as a reference function. The curve then allows us to deduce from the measured frequency, the stiffness, and the elastic constant of the sample. The curve obtained by taking the beam and tip dimensions as given by the constructors is generally approximate, and it is preferable to adjust the dimensions in order to obtain a good fit of the free frequencies (first and second modes) and of some contact frequencies on known standard samples.

#### 4.4.4 Effect of Normal and Tangential Stiffness

Figure 4.11 presents the calculated resonance frequency of the beam (Cantilever D in Table 4.1) in function of the normal stiffness. Two cases for the tangential stiffness are introduced ( $k_T = 0$  for a sliding contact and  $k_T = 2/3k_N$  for a nonsliding contact), which gives different calculated resonance frequencies. We observe that the tangential stiffness has little influence on the resonance frequency of the beam, up to a certain  $k_N$  value (around 10 N/m in Fig. 4.11), and diverges strongly for superior values. This means that experiments in the lower part of the curve is not sensitive to



**Fig. 4.12** *Top* apparent amplitude versus excitation frequency (Cantilever D in Table 4.1) calculated for a different contact stiffness. The tangential stiffness is taken as  $k_T = 2/3k_N$ . All curves include a damping effect, obtained by multiplying the stiffness real values by the arbitrary complex number:  $1 + i/5$ , in order to be more similar to the experimental curves below. *Bottom* apparent amplitude measured on a polyurethane sample (PU 3420) for an applied force increasing from  $-8.7$  nN (closed to the pull-off force) to  $89$  nN. Reproduced with permission from [21]. Copyright 2003, American Institute of Physics



the tangential forces, the opposite behavior occurs in the upper part. The origin of this behavior is probably related to the remark made above relative to the amplitude of the forces in Fig. 4.8.

This discussion cannot be made without an experimental illustration, then experimental results for two known polyurethane samples are also presented in Fig. 4.11. One sample (PU3420) has a low stiffness, and lies in the part of the calculated curve independent on  $k_T$ . The other sample (PU3558) is stiffer and agrees well with the nonsliding curve. We conclude that, at the frequency of the experiments, the tip and the sample can be considered as “stuck together,” and that a strong tangential force is acting on the tip.

The dots in Fig. 4.11 report the experimental data for different applied normal forces. Changing the normal force induces a change in the contact area and contact stiffness. The contact stiffness in Fig. 4.11 is calculated according to the DMT model, and line up correctly on the calculated curves. The JKR model gives a slightly inferior fit for these samples. We also observe that the points for the PU3420 sample seems to arrange in two groups, with a gap near 46 kHz. This strange behavior is

interpreted here by the presence of an anti-resonance in that frequency range. This anti-resonance induces a dissymmetry in the resonance curve (Fig. 4.12), which shifts the measured resonance frequencies. Theoretically, the frequencies for resonance and anti-resonance are equal for  $k_N \approx 1.2nN$ , and for this value the resonance disappears. This corresponds to a range of bad experimental conditions, for this particular cantilever.

The calculated and experimental curves reported in Fig. 4.12 are very similar, indicating that the numerical model fits the reality well. A constant damping has been introduced in the calculated curves, in order to be more similar to the experimental curves, by taking the stiffness complex value proportional to  $(1 + i/5)$ . The experimental widths of the resonance still appear larger than the calculated ones, indicating that a larger imaginary part is needed to fit the observed width.

## 4.5 Conclusion

In this chapter, a 1D finite element model of AFM cantilevers is described. The discretization process is detailed and the matricial form of kinetic and elastic potential energy of each element is defined. These steps allow building the system to solve, composed of global mass and stiffness matrixes. It is explained how both free and forced vibration analysis can be carried out. The proposed model made possible to analyze the exact vibration in the contact mode, whatever the shape and the excitation mode. Moreover, it is simple to program and as rapid as the usual analytical methods. It was shown that excitation mode strongly influences the frequency response of the cantilever. Anti-resonances were observed on the frequency response. Those can sometimes disturb measurement on certain samples. We analyzed the real amplitudes, normal and tangential, as well as the real forces. We established assumptions concerning the nature of tip-sample contact during experiments. For the samples of low rigidity, the presence of a nonsliding contact is highlighted, and the threshold of nonlinearity can be reached under the effect of the normal force. For more rigid samples, this is the opposite assumption that can be made.

## References

1. M. Radmacher, R. Tillman, H. Gaub, *Biophys. J.* **64**, 735–742 (1993)
2. N.A. Burnham, G. Gremaud, A.J. Kulik, P.J. Gallo, F. Oulerey, *J. Vac. Sci. Technol. B* **14**, 1308–1312 (1996)
3. O. Wright, N. Nishigushi, *Appl. Phys. Lett.* **71**, 626–628 (1997)
4. U. Rabe, J. Turner, W. Arnold, *Appl. Phys. A Mater. Sci. Process.* **66**, S277–S282 (1998)
5. K. Yamanaka, A. Noguchi, T. Tsuji, T. Koike, T. Goto, *Surf. Interface Anal.* **27**, 600–606 (1999)
6. O. Pietrement, M. Troyon, *Tribol. Lett.* **9**, 77–87 (2000)
7. E. Dupas, G. Gremaud, A. Kulik, J.L. Loubet, *Rev. Sci. Instrum.* **72**, 3891–3897 (2001)
8. M. Muraoka, W. Arnold, *JSME Int. J.* **44**, 396–405 (2001)

9. D.A. Mendels, M. Lowe, A. Cuenat, M.G. Cain, E. Vallejo, D. Ellis, F. Mendels, J. Micromech. Microeng. **16**, 1720–1733 (2006)
10. F.J. Espinoza-Beltran, K. Geng, J. Munoz Saldana, U. Rabe, S. Hirsekorn, W. Arnold, New J. Phys. **11**, 083034 (2009)
11. M. Müller, T. Schimmel, P. Häussler, H. Fettig, O. Müller, A. Albers, Surf. Interface Anal. **38**, 1090–1095 (2006)
12. A. Caron, U. Rabe, M. Reinstadtler, J.A. Turner, W. Arnold, App. Phys. Lett. **85**, 26 (2004)
13. Z. Parlak, F. Levent Degertekin, J. App. Phys. **103**, 114910 (2008)
14. Y. Song, B. Bhushan, Ultramicroscopy **106**, 847–873 (2006)
15. Y. Song, B. Bhushan, J. Phys, Condens. Matter **20**, 225012 (2008)
16. B. Drouin, J. Senicourt, F. Lavaste, G. Fezans, *De la mécanique vibratoire classique à la méthode des éléments finis* (AFNOR, Paris, 1993), p. 405
17. U. Rabe, E. Kester, W. Arnold, Surf. Interface Anal. **27**, 386 (1999)
18. K. Yamanaka, S. Nakano, Jpn. J. Appl. Phys. **35**, 3787 (1996)
19. N.A. burnham, A.J. Kulik, G. Gremaud, P.J. Gallo, F. Oulevey, Jpn. J. Vac. Sci. Technol. B **14**, 794 (1996)
20. U. Rabe, K. Janser, W. Arnold, Rev. Sci. Instrum. **67**, 3281 (1996)
21. R. Arinéro, G. Lévêque, Rev. Sci. Instrum. **74**, 104 (2003)
22. S. Cuénot, C. Frétigny, S. Demoustier-Champagne, B. Nysten, J. App. Phys. **93**, 5650 (2003)
23. P.E. Mazeran, J.L. Loubet, Tribol. Lett. **3**, 125 (1997)
24. E.L. Florin, M. Radmacher, B. Fleck, H.E. Gaub, Rev. Sci. Instrum. **65**, 639 (1994)
25. O. Piètrement, M. Troyon, Tribol. Lett. **9**, 77 (2000)

# Chapter 5

## Atomic Force Acoustic Microscopy

U. Rabe, M. Kopycinska-Müller and S. Hirsekorn

**Abstract** This chapter shortly reviews the scientific background of Atomic Force Acoustic Microscopy (AFAM), the basic theoretical models, the experimental techniques to obtain quantitative values of local elastic constants, and non-linear AFAM. Analytical and finite element models describing transverse flexural vibrations of AFM cantilevers with and without tip-surface contact are recapitulated. The models are suitable for micro fabricated silicon cantilevers of approximately rectangular cross section which are typically used in AFAM. Experimental methods to obtain single-point as well as array measurements and full spectroscopy images are discussed in combination with the respective reference methods for calibration. In a non-linear AFAM experiment, the vibration amplitudes of the sample surface and the cantilever are measured quantitatively with an interferometer at different excitation amplitudes, and the full tip-sample interaction force curve is reconstructed using a frequency dependent transfer function.

### 5.1 Introduction

In the beginning of the 1990s, atomic force microscopy (AFM) [1] became increasingly well known, commercial instruments were available and relatively easy to handle, and images demonstrating nanometer scale and even “atomic resolution” were published. On the other hand, the emerging progress in nanotechnology pro-

---

U. Rabe (✉) · S. Hirsekorn  
Fraunhofer Institute for Non-Destructive Testing (IZFP), Campus E3.1,  
66123 Saarbrücken, Germany  
e-mail: ute.rabe@izfp.fraunhofer.de

M. Kopycinska-Müller  
Fraunhofer Institute for Non-Destructive Testing (IZFP), Maria-Reiche-Strasse 2,  
01069 Dresden, Germany  
e-mail: malgorzata.kopycinska-mueller@izfp-d.fraunhofer.de

vided a need to examine materials non-destructively at nanometer scale. A common non-destructive inspection method is ultrasonic microscopy [2], which is used to reveal flaws and inhomogeneities inside components and materials and to measure elastic properties with high precision. However, as implied by Abbe's principle, a conventional acoustic microscopy can hardly reach nanometer local resolution. Therefore, a variety of combinations of AFM with acoustic microscopy were developed with the aim to make atomic or nanometer local resolution available to ultrasonic probing. Examples for such inventions are atomic force acoustic microscopy (AFAM) [3], Ultrasonic Force Microscopy (UFM) [4], ultrasonic atomic force microscopy (UAFM) [5], scanning acoustic force microscopy (SAFM) [6], and scanning microdeformation microscopy (SMM) [7]. The main difference to conventional microscopy is that—instead of using a focusing lens or transducer—the ultrasonic waves are detected or excited locally with the tip of a scanning force microscope. In this case, the local resolution is determined by the tip-sample contact radius of a few nanometers, and not by the acoustic wavelength, which can be orders of magnitude larger. One general limitation of such near-field microscopes is that the high local resolution is only attained in the near field, i.e., in close proximity to the tip. This means that AFAM and related techniques provide mainly information on the sample surface or sample regions in close proximity to the surface—in contrast to conventional ultrasonic techniques using propagating waves. Ongoing research on subsurface contrast using mixing and heterodyning techniques is currently extending these limits (Chap. 10).

Different strategies are possible to detect ultrasonic vibration with an AFM. In techniques like UFM (Chap. 9) and SAFM the AFM sensor is treated as an oscillator having a resonant frequency that is considerably lower than the ultrasonic frequency. The nonlinearity of the tip-sample interaction forces is exploited to down-convert the high-frequency ultrasonic signal into a frequency range, which is detectable by the AFM cantilever. In techniques like AFAM, UAFM (Chap. 6), or SMM (Chap. 8) ultrasonic sample surface vibration is directly detected by exciting vibration modes of the cantilever beams with frequencies equal to the excitation frequencies. A variety of other dynamic operation modes of the AFM are known, in which the cantilever is vibrated while the sample surface is scanned, and the amplitude, phase, or resonant frequency is recorded. In AFAM and related modes, the sensor tip of the AFM is constantly in contact with the sample surface while the cantilever vibrates (Fig. 5.1). The flexural and torsional resonance frequencies of commercial cantilevers with lengths of a few hundreds micron are predominantly higher than 20 kHz, and hence in the ultrasonic frequency range. The tip-sample forces in the contact area influence the mechanical boundary conditions of the cantilever, and therefore its frequencies increase considerably compared to the frequencies in air. The shift of the resonance frequencies is evaluated to measure lateral and normal sample surface stiffness and elasticity, and the width of the resonance peaks is used to measure viscoelasticity [8] and internal friction [9] (Chap. 14) in the sample. If the amplitude of vibration is increased above a critical threshold, the resonance curves develop plateaus or asymmetries, which are typical for nonlinear oscillators (Sect. 5.5).

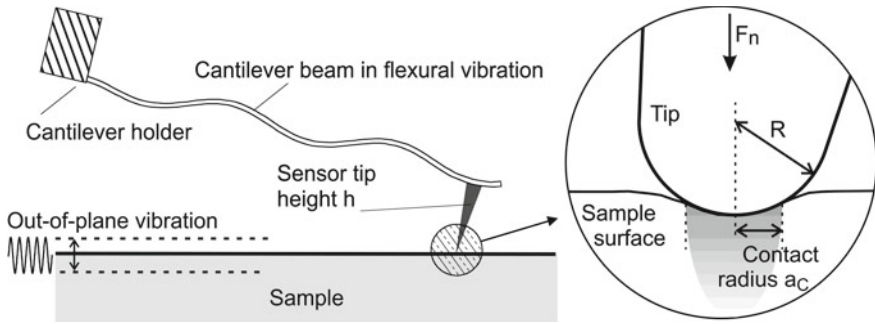


**Fig. 5.1** AFM cantilever vibrating in contact with a sample surface. The vibration of the cantilever is excited by an out-of-plane sample surface vibration. The mechanical forces of the tip-sample contact area influence the resonance frequencies of the system. The repulsive tip-sample contact is visualized on the right hand side

In the AFAM-mode, an ultrasonic wave is excited inside the sample by a conventional transducer (a piezoelectric element) attached to one side of the sample. The ensuing out-of-plane or in-plane sample surface vibration transfers to the tip of the AFM and excites a forced flexural (Fig. 5.1), lateral bending, or torsional vibration of the cantilever, respectively. Wave phenomena in the sample such as reflection and interference are not exploited in AFAM, in contrast, multiple reflections in the sample should be avoided because interference patterns at the sample surface can lead to sample surface areas with low vibration amplitudes. A sample surface amplitude as homogeneous as possible in the scanned area is favorable. AFAM is a contact-resonance technique, which probes the local elastic properties of the sample. In the last years, the term contact-resonance AFM (CR-AFM) [10, 11] has been introduced as a generic term comprehending all methods, in which the contact-resonance frequencies of the cantilevers are measured as a function of position and evaluated to obtain elastic and inelastic sample surface properties. Some authors understand CR-AFM as an extension of force modulation microscopy [12] to higher frequencies [13, 14]. Contact resonances can not only be used to measure mechanical properties of the sample surface, but they are also proved to be useful for signal enhancement in other contact techniques such as piezo-mode AFM [15, 16].

## 5.2 Analytical and Finite-Element Models for AFAM

AFM cantilevers are small flexible beams, which are suspended at one end and free at the other end that carries the sensor tip (Fig. 5.2). As a response to dynamic excitation, AFM cantilevers exhibit different sets of vibration modes, such as transverse and lateral flexural and torsional modes. All types of modes show an infinite set of resonance frequencies, which depend on the shape, the geometrical dimensions,

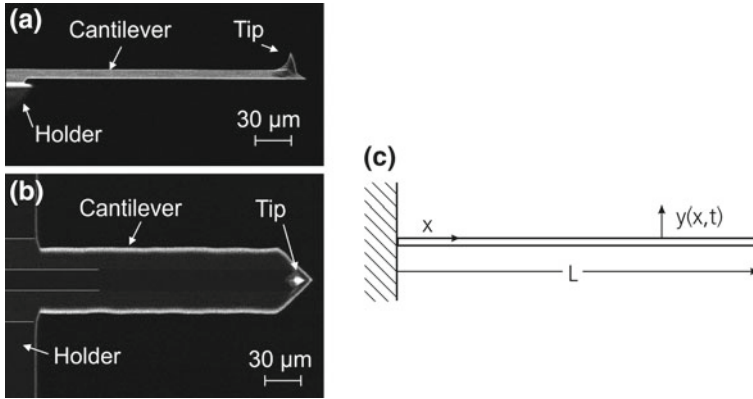


**Fig. 5.2** Scanning electron micrographs showing **a** a side-view of an AFM cantilever made of single crystal silicon, **b** a view from the bottom side where the tip is mounted, and **c** the mechanical model of an AFM cantilever with constant cross-section (clamped-free beam)

the material of the cantilever, and on its mechanical boundary conditions. A variety of microfabricated cantilevers are available. Cantilevers with triangular shape (V-shape) were used for contact-resonance spectroscopy [17], and their vibration modes were studied with analytical and finite-element models [18, 19]. In the following, only cantilevers with approximately rectangular shape will be treated, because their vibration can be described with relatively simple analytical models. Lateral contact-modes of rectangular cantilevers with bending vibration in width direction [20] and torsional modes can be used to measure in-plane elastic tip-sample forces and friction [21, 22]. If torsional contact-resonances are evaluated quantitatively in addition to flexural modes, a second elastic constant of the sample, the Poisson's ratio, can be obtained [10]. However, this chapter will restrict to transverse flexural modes, i.e., flexural modes with deflections in thickness direction of the cantilever.

### 5.2.1 Analytical Model of the Cantilever Vibrating in Air

The Euler–Bernoulli equation describes transverse flexural vibration of a straight beam with constant cross-section [23]:

$$EI \frac{\partial^4 y}{\partial x^4} + \eta \rho A \frac{\partial y}{\partial t} + \rho A \frac{\partial^2 y}{\partial t^2} = 0. \quad (5.1)$$

Here,  $x$  is the coordinate in length direction of the beam (Fig. 5.2c),  $E$  is the Young's modulus of the cantilever,  $\rho$  is its mass density,  $A$  is the area of its cross-section,  $I$  is the area moment of inertia, and  $\eta$  is a damping constant expressing the internal friction in the cantilever and dissipation caused by air. In case of a rectangular cross-

section of the cantilever with width  $w$  and thickness  $b$ , the area moment of inertia is  $I = wb^3/12$ . A harmonic solution in time with angular frequency  $\omega = 2\pi f$  is searched for the local deflection  $y(x, t)$  at position  $x$ :

$$y(x, t) = y(x) \cdot y(t) = (a_1 e^{\alpha x} + a_2 e^{-\alpha x} + a_3 e^{i\alpha x} + a_4 e^{-i\alpha x}) e^{i\omega t}, \quad (5.2)$$

where  $a_1, a_2, a_3$ , and  $a_4$  are constants and  $i$  is the imaginary unit. By substituting the general solution Eq. 5.2 into the equation of motion Eq. 5.1, one obtains the dispersion relation for a flexural wave with complex wave number  $\alpha$ :

$$EI\alpha^4 + i\rho A\eta\omega - \rho A\omega^2 = 0 \Rightarrow \alpha_{\pm} = \pm \sqrt[4]{\frac{\rho A}{EI}(\omega^2 \mp i\eta\omega)}. \quad (5.3)$$

If the second term in the partial differential Eq. 5.1, which contains the damping is omitted, the wave number  $k = 2\pi/\lambda$  is real, and the dispersion equation simplifies to:

$$EI k^4 - \rho A \omega^2 = 0 \Rightarrow k = \sqrt[4]{\frac{\rho A}{EI} \omega^2} \Rightarrow f = \frac{(kL)^2}{2\pi} \frac{1}{L^2} \sqrt{\frac{EI}{\rho A}}. \quad (5.4)$$

The boundary conditions of the beam of finite length  $L$  depend on its suspension and on the tip-sample forces. Without surface contact a cantilever can be considered as a clamped-free beam Fig. 5.2c, the small mass of the sensor tip is neglected. In this case, the mechanical boundary condition at the clamped end ( $x = 0$ ) and at the free end ( $x = L$ ) are as follows:

$$x = 0 : \begin{cases} y(x) = 0 \\ \frac{\partial y(x)}{\partial x} = 0 \end{cases} \quad x = L : \begin{cases} \frac{\partial^2 y(x)}{\partial x^2} = 0 \\ \frac{\partial^3 y(x)}{\partial x^3} = 0 \end{cases}. \quad (5.5)$$

By substituting the general solution 5.2 into the boundary conditions, a characteristic equation is found, which defines the discrete wave numbers  $k_n, n = \{1, 2, 3, \dots\}$  of the resonant modes of the system:

$$\cos k_n L \cosh k_n L + 1 = 0. \quad (5.6)$$

The first seven roots of Eq. 5.6 are listed in Table 5.1.

The resonance frequencies of the clamped-free beam are obtained by using the normalized wave numbers in Table 5.1 and the dispersion Eq. 5.4. For a beam with rectangular cross-section ( $A = wb$ ) the result is:

$$f_n = \frac{(k_n L)^2}{2\pi} \frac{b}{L^2} \sqrt{\frac{E}{12\rho}} = \frac{(k_n L)^2}{c_C^2}. \quad (5.7)$$



**Table 5.1** The first seven normalized wave numbers  $k_n L$  of the clamped-free beam and the corresponding resonance frequency ratio  $f_n/f_1$ 

$n$	1	2	3	4	5	6	7
$k_n L$	1.875	4.694	7.855	10.996	14.137	17.279	20.420
$f_n/f_1$	1	6.27	17.55	34.39	56.84	84.91	118.60

The geometrical and material data of the cantilever can be combined in a constant  $c_C$  defined as:

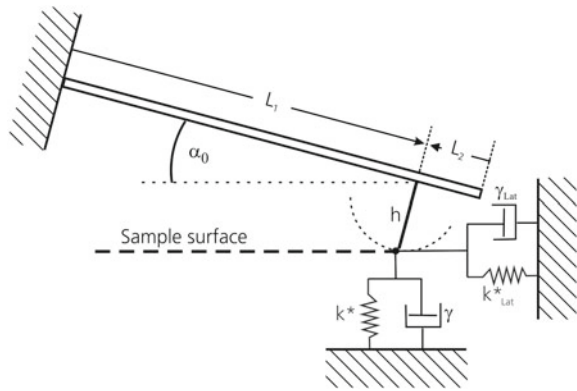
$$c_C = L \sqrt{2\pi \sqrt{\frac{12\rho}{b^2 E}}}. \quad (5.8)$$

The resonance frequencies  $f_n$  are proportional to the square of the wave numbers, which means that the phase velocity of the flexural modes is not constant, i.e., the modes are dispersive and not equidistant. However, equation 5.7 shows that the frequency ratio of the flexural modes is independent of the material and geometry data of the cantilever. The ratio of the higher resonance frequencies to the first flexural frequency is shown in the third row of Table 5.1.

The resonance frequencies of the clamped-free cantilever play an important role in quantitative AFAM. The geometrical data of the commercial cantilevers made of single crystal silicon are subject to unavoidable deviations caused by the batch fabrication process. These geometrical variations cause wide frequency and spring-stiffness ranges for the same type of cantilever (up to 100% variation is possible depending on the beam type). It is time consuming to measure the geometrical dimensions of individual beams by optical or electron microscopy. Furthermore, the errors in the obtained geometry data are so high that the resonance frequencies calculated with these data are not precise enough. It is relatively easy to measure the first few flexural resonance frequencies of a cantilever in air either using forced vibration excited at the cantilever holder or just by observing the noise spectrum. In spite of the air damping the  $Q$ -values of the lower modes are generally much higher than 50 [24], therefore the free resonance frequencies can be measured with high precision, and they can be used to calculate the cantilever constant  $c_C$ . Some authors suggest to retrieve the geometrical cantilever dimensions from the frequencies of their higher modes and use these data for calibration of the spring constants [25–27].

A comparison of the experimental frequency ratio to the theoretical one shows how well commercial rectangular cantilevers fit the model [24, 28]. The Euler–Bernoulli beam equation does not take into account shear deformation and rotary inertia, which is only a good assumption if thickness  $b$  and width  $w$  are much smaller than the length  $L$ . Thin, long, and soft cantilevers like the ones used for contact and lateral force mode obey much better this requirement than the thicker, shorter, and stiffer cantilevers with static spring constants of 20 N/m and more that are used for intermittent contact and non-contact techniques. Furthermore, the geometry of real cantilevers differs from the model, for example the cross-section is not exactly constant and of

**Fig. 5.3** Mechanical model of an AFM cantilever with constant cross-section vibrating in contact with a sample surface (clamped spring-coupled beam)



trapezoidal form, and the suspension is not infinitely stiff and symmetrical [29] but made of silicon like the cantilever (see Fig. 5.2). For example, the higher resonance frequencies of silicon cantilevers of the approximate dimensions ( $225 \mu\text{m} \times 30 \mu\text{m} \times 7 \mu\text{m}$  [30]) are slightly lower than the frequencies predicted by the flexural beam model [28]. The same tendency and order of magnitude of frequency deviation from the Euler model is obtained theoretically when the flexural vibration frequencies of AFM cantilevers are calculated with the more precise Timoshenko beam model [31]. The difference between the Euler–Bernoulli model and the Timoshenko model was examined theoretically for the free resonance frequencies and the contact-resonance frequencies including damping [32].

### 5.2.2 Contact-Resonance Models

In linear AFAM, the vibration amplitude of the tip is assumed to be small, and the tip-sample forces such as elastic forces, adhesion forces and viscoelastic forces are represented by linear springs and dashpots. The complete mechanical model for linear contact resonance vibration is shown in Fig. 5.3.

The length of the cantilever from the clamped end to the free end is  $L$ . The sensor tip is located at position  $L_1$ , and  $L_2 = L - L_1$  is the distance between the sensor tip position and the free end. Forces normal to the surface are represented by the normal contact stiffness  $k^*$  and the contact damping  $\gamma$ , and forces lateral to the surface are represented by the lateral contact stiffness  $k_{Lat}^*$  and a lateral contact damping  $\gamma_{Lat}$ . For technical reasons the cantilever is tilted with respect to the surface by an angle  $\alpha_0$  ( $11\text{--}15^\circ$ ). The characteristic equation of the model defined in Fig. 5.3 can be found by defining two solutions for the two parts of the cantilever. The boundary conditions at the clamped end (zero displacement and slope) and the free end (zero bending moment and shear force) are the same as in Eq. 5.5. At the tip position  $x = L_1$ , additional boundary conditions arise, which contain the shear force and the

bending moment caused by the tip-sample forces, and which ensure the continuity of displacement and slope at  $x = L_1$  where the two partial solutions meet.

The characteristic equation of the complete system including tip position, lateral forces and damping can be found in the literature [28]. Four simpler versions of models for quantitative AFAM without contact damping are shown in Fig. 5.4. The models and their characteristic equations are special cases of the complete solution in [28]. The characteristic equations of these models are as follows:

(a) Simple model (24):

$$\frac{1}{3} \frac{k_C}{k^*} (k_n L)^3 (1 + \cos k_n L \cosh k_n L) + (\sin k_n L \cosh k_n L - \sinh k_n L \cos k_n L) = 0 \quad (5.9)$$

(b) Tip-position model [8, 24, 33]:

$$\begin{aligned} & \frac{2}{3} \frac{k_C}{k^*} (k_n L_1)^3 (1 + \cos k_n L \cosh k_n L) \\ & + (\sin k_n L_1 \cosh k_n L_1 - \sinh k_n L_1 \cos k_n L_1) \cdot (1 + \cos k_n L_2 \cosh k_n L_2) \\ & - (\sin k_n L_2 \cosh k_n L_2 - \sinh k_n L_2 \cos k_n L_2) \cdot (1 - \cos k_n L_1 \cosh k_n L_1) = 0 \end{aligned} \quad (5.10)$$

(c) Lateral force model without tip position [13, 34]

$$\begin{aligned} & \frac{1}{3} \frac{k_C}{k^*} (k_n L)^4 A + (k_n L)^3 \frac{h^2}{L^2} \left( \sin^2 \alpha_0 + \frac{k_{\text{Lat}}^*}{k^*} \cos^2 \alpha_0 \right) D \\ & + 2 (k_n L)^2 \frac{h}{L} \sin \alpha_0 \cos \alpha_0 \left( \frac{k_{\text{Lat}}^*}{k^*} - 1 \right) \sin(k_n L) \sinh(k_n L) \\ & + k_n L \left( \cos^2 \alpha_0 + \frac{k_{\text{Lat}}^*}{k^*} \sin^2 \alpha_0 \right) B + 3 \frac{k_{\text{Lat}}^*}{k_C} \frac{h^2}{L^2} C = 0 \end{aligned} \quad (5.11)$$

(d) Lateral force and tip-position model [10]:

$$\begin{aligned} & \frac{2}{3} \frac{k_C}{k^*} (k_n L_1)^4 A + (k_n L_1)^3 \frac{h^2}{L_1^2} \left( \sin^2 \alpha_0 + \frac{k_{\text{Lat}}^*}{k^*} \cos^2 \alpha_0 \right) \cdot [D_1 A_2 - D_2 C_1] \\ & + 2 (k_n L_1)^2 \frac{h}{L_1} \sin \alpha_0 \cos \alpha_0 \left( \frac{k_{\text{Lat}}^*}{k^*} - 1 \right) \\ & \cdot [\sin(k_n L_1) \sinh(k_n L_1) A_2 + \sin(k_n L_2) \sinh(k_n L_2) C_1] \\ & + k_n L_1 \left( \cos^2 \alpha_0 + \frac{k_{\text{Lat}}^*}{k^*} \sin^2 \alpha_0 \right) [B_1 A_2 - B_2 C_1] \\ & + 3 \frac{k_{\text{Lat}}^*}{k_C} \frac{h^2}{L_1^2} C_1 A_2 = 0, \end{aligned} \quad (5.12)$$

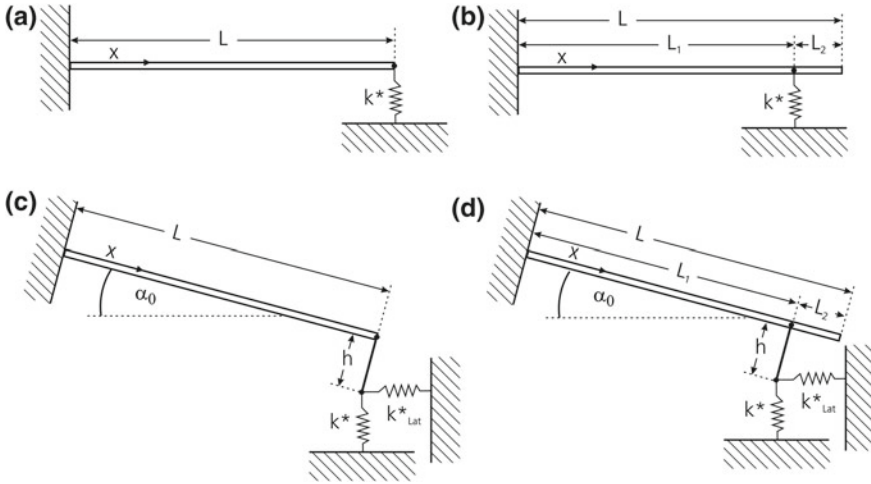


**Fig. 5.4** Mechanical models without damping for contact-resonance vibration. **a** simple model **b** tip-position model **c** lateral force model **d** tip-position and lateral force model

where

$$\begin{aligned}
 A &= 1 + \cos(k_n L) \cosh(k_n L) \\
 B &= \sin(k_n L) \cosh(k_n L) - \sinh(k_n L) \cos(k_n L) \\
 C &= 1 - \cos(k_n L) \cosh(k_n L) \\
 D &= \sin(k_n L) \cosh(k_n L) + \sinh(k_n L) \cos(k_n L).
 \end{aligned}
 \tag{5.13}$$

The subscripts 1, 2 are used in cases where the argument is  $k_n L_1$ , or  $k_n L_2$ , respectively. For example:

$$A_1 = 1 + \cos(k_n L_1) \cosh(k_n L_1) \quad \text{and} \quad A_2 = 1 + \cos(k_n L_2) \cosh(k_n L_2).
 \tag{5.14}$$

The same holds for  $B$ ,  $C$ , and  $D$ . The static flexural spring constant  $k_C$  of the cantilever is used to normalize the contact stiffness  $k^*$ . A variety of methods are known to determine the static spring constant  $k_C$  [35, 36].

The contact-resonance frequencies are obtained numerically by finding the roots  $k_n L$  of the characteristic equations, and by using the dispersion relation 5.7 to calculate the resonance frequencies  $f_n$ . In a contact-resonance experiment, the inverse problem arises: contact-resonance frequencies  $f_n$  are measured, and the aim is to calculate the contact stiffness. As already discussed above, it is favorable to use the resonance frequencies of the clamped-free beam and the known wave numbers in Table 5.1 to calculate the cantilever parameter  $c_C$ . In cases where the frequency ratio of the modes deviates from the Euler model, each contact-resonance frequency should be used in combination with the free resonance frequency of the same mode

number:

$$(k_n L)_{\text{Cont}} = c_C \sqrt{f_{n,\text{Cont}}} = (k_n L)_{\text{Free}} \sqrt{\frac{f_{n,\text{Cont}}}{f_{n,\text{Free}}}}$$

$$\text{for example: } (k_1 L)_{\text{Cont}} = 1.8751 \sqrt{\frac{f_{n,\text{Cont}}}{f_{n,\text{Free}}}} \quad (5.15)$$

Equation 5.9 describing the model in Fig. 5.4a can then be solved for the normalized contact stiffness  $k^*/k_C$ :

(a) Simple model:

$$\frac{k^*}{k_C} = \frac{(k_n L)^3 (1 + \cos k_n L \cosh k_n L)}{3(-\sin k_n L \cosh k_n L + \sinh k_n L \cos k_n L)}$$

$$= \frac{(c_C \sqrt{f_{n,\text{Cont}}})^3 [1 + \cos(c_C \sqrt{f_{n,\text{Cont}}}) \cosh(c_C \sqrt{f_{n,\text{Cont}}})]}{3[-\sin(c_C \sqrt{f_{n,\text{Cont}}}) \cosh(c_C \sqrt{f_{n,\text{Cont}}}) + \sinh(c_C \sqrt{f_{n,\text{Cont}}}) \cos(c_C \sqrt{f_{n,\text{Cont}}})]} \quad (5.16)$$

Tip position as a parameter to fit the analytical model to the real cantilever has been discussed in different publications [37, 38]. The tip position  $L_1/L$  has either to be estimated from optical micrographs or it can be determined by fitting the tip position using at least two different contact-resonance frequencies. The wave numbers of the two parts of the cantilever are:

$$(k_n L_1)_{\text{Cont}} = \frac{L_1}{L} (k_n L)_{\text{Free}} \sqrt{\frac{f_{n,\text{Cont}}}{f_{n,\text{Free}}}} \quad (k_n L_2)_{\text{Cont}} = \frac{L_2}{L} (k_n L)_{\text{Free}} \sqrt{\frac{f_{n,\text{Cont}}}{f_{n,\text{Free}}}} \quad (5.17)$$

The contact stiffness for the tip-position model is obtained by solving the characteristic Eq. 5.10 for  $k^*/k_C$ .

(b) Tip-position model:

$$\frac{k^*}{k_C} = \frac{2 (k_n L_1)^3 A}{3(-B_1 A_2 + B_2 C_1)} \quad (5.18)$$

With increasing complexity of the models, more parameters are needed for the evaluation. The height of the sensor tip  $h$  (typical values 10–17  $\mu\text{m}$ ) is usually specified by the cantilever manufacturers, and the cantilever tilt angle  $\alpha_0$  is a technical parameter of the AFM instrument. Models (c) and (d) contain two unknown tip-sample spring constants, the normal contact stiffness  $k^*$ , and the lateral contact stiffness  $k_{\text{Lat}}^*$ . The ratio  $k_{\text{Lat}}^*/k^*$  ranges between 2/3 and 18/19 for most materials with an average value of 0.85 (13). If one assumes the ratio  $k_{\text{Lat}}^*/k^*$  to be known, Eqs. 5.11 and 5.12 can be solved for  $k^*/k_C$ :

(c) Lateral force model without tip position ( $k_{\text{Lat}}^* \neq 0$ ):

$$\left(\frac{k^*}{k_C}\right)_{1;2} = -\frac{\varsigma L^2}{6c_p h^2 C} \pm \sqrt{\left(\frac{\varsigma L^2}{6c_p h^2 C}\right)^2 - \frac{(k_n L)^4 L^2 A}{9c_p L^2 C}}, \quad (5.19)$$

where  $c_P = k_{\text{Lat}}^*/k^*$  is the known lateral to normal contact stiffness ratio and

$$\begin{aligned} \varsigma = & (k_n L)^3 \frac{h^2}{L^2} \left( \sin^2 \alpha_0 + c_p \cos^2 \alpha_0 \right) D \\ & + 2 (k_n L)^2 \frac{h}{L} \sin \alpha_0 \cos \alpha_0 (c_p - 1) \sin(k_n L) \sinh(k_n L) \\ & + k_n L \left( \cos^2 \alpha_0 + c_p \sin^2 \alpha_0 \right) B \end{aligned} \quad (5.20)$$

(d) Lateral force and tip-position model ( $k_{\text{Lat}}^* \neq 0$ )

$$\left(\frac{k^*}{k_C}\right)_{1;2} = -\frac{v L_1^2}{6c_p h^2 C_1 A_2} \pm \sqrt{\left(\frac{v L_1^2}{6c_p h^2 C_1 A_2}\right)^2 - \frac{2 (k_n L_1)^4 h^2 A}{9c_p h^2 C_1 A_2}}, \quad (5.21)$$

where  $c_P$  is again the lateral to normal contact stiffness ratio and

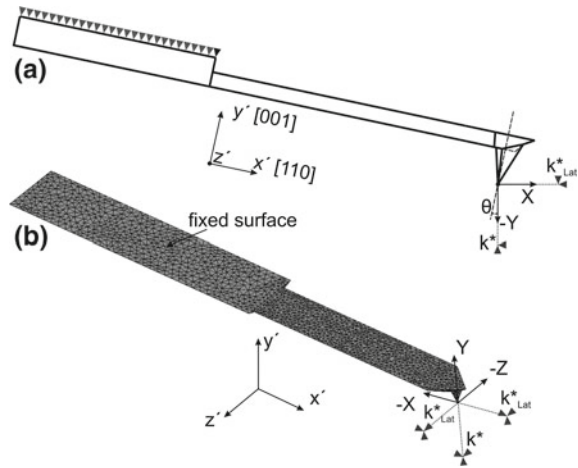
$$\begin{aligned} v = & (k_n L_1)^3 \frac{h^2}{L_1^2} \left( \sin^2 \alpha_0 + c_p \cos^2 \alpha_0 \right) [D_1 A_2 - D_2 C_1] \\ & + 2 (k_n L_1)^2 \frac{h}{L_1} \sin \alpha_0 \cos \alpha_0 (c_p - 1) \\ & \cdot [\sin(k_n L_1) \sinh(k_n L_1) A_2 + \sin(k_n L_2) \sinh(k_n L_2) C_1] \\ & + k_n L_1 \left( \cos^2 \alpha_0 + c_p \sin^2 \alpha_0 \right) [B_1 A_2 - B_2 C_1] \end{aligned} \quad (5.22)$$

The advantage of analytical models is that they can be directly solved for the contact stiffness and that they can be quickly evaluated with varying parameters. Analytical models become increasingly complicated if more details in the shape of the cantilever like the triangular end (dagger shaped cantilever) [39], the suspension [29] or shear stiffness and rotary inertia are considered [32].

### 5.2.3 Finite-Element Models (FEM)

Several publications can be found in the literature presenting numerical models and finite-element (FE) calculations of AFM cantilevers and their vibrations [14, 26] [17, 27] (Chap. 4). In order to improve quantitative evaluation of AFAM by FEM, important details in the geometric shape, the elastic anisotropy of single crystal silicon cantilevers, and the elasticity of the suspension of AFM cantilevers should be considered in the model. An FE model was created, which considers the geometrical

**Fig. 5.5** Schematic sketch of the cantilever **a** with its coordinate system  $\{x', y', z'\}$  inclined by an angle  $\theta$  relative to the sample surface coordinate system  $\{X, Y, Z\}$ . The tip-sample forces are modeled by three springs with spring constants  $k^*$  and  $k^*_{\text{Lat}}$  for vertical and lateral contact stiffness, respectively; **b** FE model of the cantilever after meshing [40]



shape of the cantilevers with a trapezoidal cross-section and a triangular free end, the cubic symmetry of silicon single crystal, and the elastic coupling of the cantilevers to the holder [40]. Figures 5.2a and 5.2b show scanning electron micrographs (SEM) of a commercial single crystal silicon cantilever. For the geometrical model, a Cartesian coordinate system with the  $x'$ -,  $y'$ -, and  $z'$ -axes in the cantilever length, thickness, and width directions, respectively, was used (Fig. 5.5). These axes coincide with the crystallographic axes  $[110]$ ,  $[001]$ , and  $[1\bar{1}0]$  of the cubic single crystal material, respectively. Figure 5.5b shows the FE model of the cantilever after meshing. It comprises 3D tetrahedral elements with linear dimensions of about  $1.5 \mu\text{m}$  in average for both the beam and the tip. In the regions where higher strain was to be expected, the density of the grid elements was increased. The tip-sample contact forces were modeled as three springs in a coordinate system  $\{X, Y, Z\}$  aligned to the sample surface (Figs. 5.5b). The coordinate system  $\{X, Y, Z\}$  was chosen to coincide with the cantilever system  $\{x', y', z'\}$  for  $\theta = 0^\circ$ . The spring constants  $k^*$  and  $k^*_{\text{Lat}}$  are the tip-sample contact stiffness values in out-of-plane ( $Y$ -axis) and in-plane ( $X$ - and  $Z$ -axes), respectively. The FE model was fitted to the experiments in a two-step iterative procedure. In a first step, the measured free resonance frequencies of the lowest bending, torsional, and lateral bending modes of an individual cantilever were used to fit the geometrical cantilever dimensions. Subsequently, tip length and cantilever inclination  $\alpha_0$  were fitted to match the measured CR frequencies of the first and the third bending mode. The FE model also allows a precise calculation of the spring constant  $k_C$  of the cantilever. With the obtained FE cantilever model, the remaining free bending as well as the torsional resonances were predicted and compared to the experimental spectra. For the first three bending modes and for the first free torsional mode errors less than 1% were achieved [40], which means that the model presented in Fig. 5.5 is able to simulate the free resonance frequencies of the cantilevers more precisely than the usual analytical models.

In order to investigate the influences of the different geometrical parameters on the resonance frequencies, several cantilevers of similar shape with only small differences in their geometrical dimensions were examined. It was shown that the modeling of the shape and elasticity of the sensor tip and of its contact to the sample surface are the most critical points rather than the differences in the analytical and the more realistic FE model of the cantilever geometry.

AFAM measurements on fused silica and nickel were numerically modeled to obtain values of out-of-plane,  $k^*$ , and in-plane,  $k^*_{\text{Lat}}$ , stiffness [40]. The normal spring constant for a cantilever inclined relative to the sample surface was determined by FEM, and used to calculate the static force from the static cantilever deflection. The obtained normal contact stiffness values were within the range covered by the theoretical values for nickel and for fused silica calculated with the Hertzian contact model and a tip radius of 80 nm. The values obtained for the in-plane surface stiffness  $k^*_{\text{Lat}}$  were too low as compared to those calculated from contact mechanics theories. This was probably due to tip-sample interactions involving contamination layers that were not included in the model.

### 5.3 Experimental Methods for Quantitative AFAM

The AFAM technique employs the contact-resonance frequencies of an AFM cantilever for quantitative measurement of elastic properties of sample surfaces. In the last years, several methods have been developed to measure the contact-resonance frequencies and to determine the sample surface properties. An important aspect of quantitative AFAM is the strategy to determine the geometrical and material parameters of the tip and the cantilever [41], which have to be known in order to calculate the sample surface properties.

#### 5.3.1 Experimental Setup

A schematic sketch of a typical AFAM setup is shown in Fig. 5.6. In the configurations discussed here, the investigated sample is placed on top of an ultrasonic transducer. The amplitude of the cantilever vibrations is measured with the laser beam deflection detector of the AFM. The frequency and the amplitude of the longitudinal wave that propagates in the sample are controlled by a waveform generator. Contact-resonance spectra are measured by recording the amplitude of the cantilever vibration as a function of the excitation frequency.

As indicated in Fig. 5.6, one can utilize different approaches to acquire a contact-resonance spectrum. One can use a lock-in amplifier to analyze the photodiode signal at the excitation frequency. In this case, the transducer is excited with a single frequency. To create the contact-resonance spectrum, the frequency is changed step-wise, and the amplitude component of the lock-in output signal is digitized, sent to



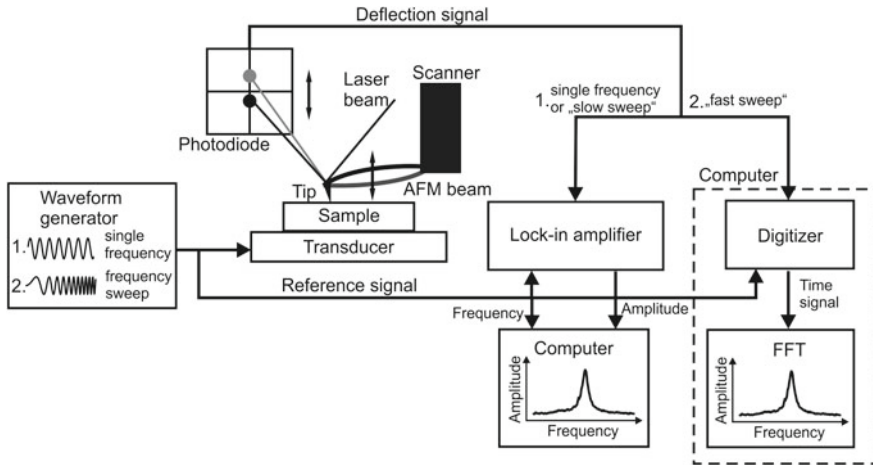


**Fig. 5.6** Schematic representation of the AFAM experimental set-up

a computer and plotted as a function of the excitation frequency. A lock-in amplifier can be easily combined with AFM instruments, and it can be used for the real-time acquisition of qualitative AFAM images, where the amplitude of the cantilever vibrations at a fixed frequency is evaluated as a function of position and used as an imaging quality. However, even in combination with a down-converter [37], lock-in amplifiers are relatively slow when used in the spectroscopy mode. A short sweep time is essential for the acquisition of a statistically significant amount of data. For a fast spectral analysis, an analog frequency modulation detector [42] and a digital-signal-processor based resonance tracking system were developed [43]. Furthermore, one can excite the transducer with a pulse and extract the spectrum by fast fourier transformation (FFT) of the cantilever vibration signal. It is favorable to tailor the frequency content of the pulse in such a way that its spectrum comprehends an appropriate interval around the center frequency of the contact resonance, like in the band excitation method [44].

### 5.3.2 *Single Point Measurements*

In the early work in AFAM single point measurements were performed, i.e., the contact-resonance spectra were acquired at a single position on the sample surface at several static loads [33, 39, 45, 46]. The CR frequencies of at least two contact modes are needed to allow for the tip-position determination required for models Fig. 5.4c and d. Figure 5.7 presents the CR frequencies measured on fused silica and single crystal silicon samples for the first and the second contact modes. A commercially

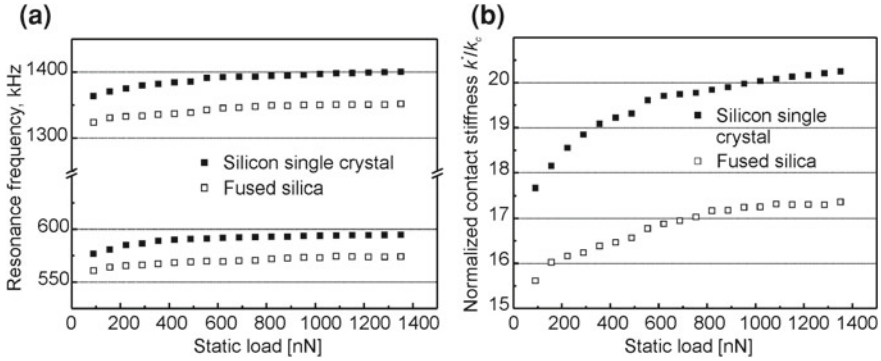


**Fig. 5.7** **a** Contact-resonance frequencies  $f_{1,Cont}$  and  $f_{2,Cont}$  measured on the single crystal silicon (Si) and fused silica reference samples. **b** Normalized contact stiffness  $k^*/k_C$  calculated from the resonance frequencies presented in **a**

available AFM beam ( $L = 225 \mu\text{m}$ ,  $b = 8 \mu\text{m}$ ,  $w = 38 \mu\text{m}$ ) was used, with free resonance frequencies of 175 kHz and 1,081 kHz for the first and the second mode, respectively. The spring constant of the cantilever was about 45 N/m. The static load applied to the tip increased from 90 nN to 1350 nN in 20 steps.

As can be seen in Fig. 5.7a, the contact-resonance frequencies recorded for the fused silica sample are significantly lower than those measured on the single crystal silicon sample because the elastic constants of fused silica are lower than those of silicon. Accordingly, the values of the normalized contact stiffness  $k^*/k_C$  calculated for fused silica are lower than those calculated for silicon for each value of the applied static load (Fig. 5.7b). In addition, the dependence of the resonance frequency values on the applied static load contains information about the tip-sample geometry. A systematic record of stiffness–load curves during a series of measurements also holds information on the changes in the tip shape and dimension.

Usually, the single point measurements are done in a precisely defined sequence. First, the contact-resonance frequencies are measured on a reference sample for at least two contact modes at several values of the static load. Then, the resonance frequencies are measured on the unknown sample at exactly the same values of the static loads like those used on the reference sample. The recurrence of the reference measurement closes the sequence, which is usually repeated several times. The repetition with recurrence to the reference sample is necessary to account for the influence of the tip wear on the accuracy of the AFAM measurement.

The single point measurements must be repeated at several random locations on the sample surface to create a statistically significant data base. The tip-sample contact occurs at an area of few tens of nanometers squared. Small local differences in the surface morphology and the unpredictable progress of the tip wear [47] influence the measurement of the CR frequency values (Chap. 13). In typical AFAM measurements with a stiff cantilever ( $k_C = 30\text{--}40\text{ N/m}$ ), the contact-resonance frequencies can be measured with an accuracy of about 0.2 and 1% for the first and the second mode,

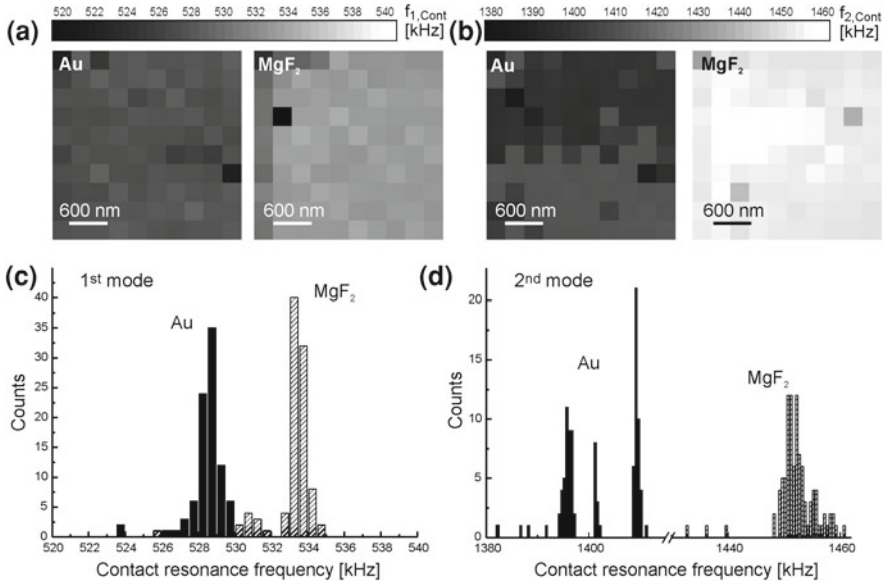


**Fig. 5.8** Grid measurements of the contact-resonance frequencies performed on surfaces of Au and MgF<sub>2</sub> samples for the (a) first and (b) second mode. Histograms of the occurrence of a contact-resonance frequency value for the (c) first and (d) second contact mode (49). The data used to create the images and histograms were provided by G. Stan, NIST, Gaithersburg, Maryland, USA

respectively [48]. These relatively small values of the measurement error may lead to about 5–10% of uncertainty in the calculated values of the tip-sample contact stiffness  $k^*$ .

### 5.3.3 Grid Measurements

An alternative to the single point measurements are grid measurements, where an array of measurement points is distributed over a certain area [49]. Figures 5.8a and b present the grid images obtained on Au and MgF<sub>2</sub> samples for the first and the second mode, respectively.

The images consist of  $10 \times 10$  points measured on an area of  $3 \times 3 \mu\text{m}$ . The free resonance frequencies of the cantilever used in this experiment were 114 and 725 kHz for the first and the second mode, respectively. The contact-resonance frequency data were evaluated statistically to obtain a histogram of occurrence of a given frequency value. Examples of such histograms calculated from the grid images presented in Fig. 5.8a and b are presented in Fig. 5.8c and d for the first and the second mode, respectively. As can be easily seen, the distribution of the contact-resonance frequency values measured for the first mode on Au and for the first and second modes

on  $\text{MgF}_2$  can be described by a Gaussian curve. The values of the second contact-resonance frequency measured for the gold sample show a bimodal distribution. In this case, the split in the values of the CR can be associated with a sudden change in the tip shape, which also explains the sudden change in the contrast of the corresponding grid image (Fig. 5.8b). The CR frequency value with the highest occurrence count is determined from the histograms and used to calculate the tip-sample contact stiffness  $k^*$ .

Grid measurements deliver low resolution images, which inform immediately on the uniformity of the samples in their elastic properties. Furthermore, the grid measurement yields values of the contact resonance-frequencies that are representative for the tested area. However, the tip scans the sample surface while relatively high static loads are applied. Continuous scanning of the sample promotes tip wear, which changes the contact-resonance frequencies. Therefore, the tip should be worn intentionally to a certain amount prior the grid measurement such that the progress in wear is less pronounced than in the case of a new, sharp tip [50]. As all the measurements are performed at the same static load, no additional information on the tip geometry is available. Such information can be either obtained by performing additional single point measurements on a reference sample or by for example SEM studies of the tip geometry [33, 51].

### 5.3.4 Contact-Resonance Frequency Images

Single-point or grid measurements work well on flat, homogenous samples. However, in case of multiphase materials, such as polycrystalline samples or composites containing phases with different elastic properties, difficulties arise in the interpretation of the frequency statistics.

Therefore, the number of points in the frequency image must be increased to generate a more detailed map. In most of the reported studies the CR images consist of  $128 \times 128$  points or more [34, 53–58]. In most of the cases, the images are acquired for the first and the second contact mode. The contact-resonance frequencies of the two modes are used later for calculation of the contact stiffness image. Figure 5.9 shows topography (a) and contact-resonance frequency images (b, c) of a blanket film of organosilicate glass (SiOC) containing trenches filled with deposited copper lines [52]. The SiOC film was approximately 280 nm thick. The topography image shows the blanket film and the copper “fingers.” The contact-resonance frequency images clearly reveal the areas corresponding to the glass and copper “fingers.”

## 5.4 Contact Mechanics and Calibration Methods

The previous sections dealt with the experimental procedures to measure contact-resonance frequencies. The contact-resonance frequencies and one of the models describing the cantilever dynamics that are explained in detail in Sect. 5.2 are

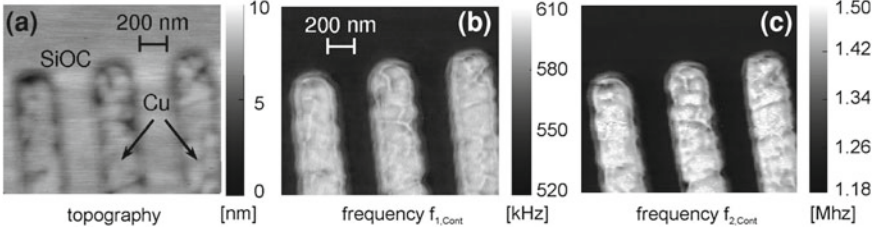


**Fig. 5.9** **a** Topography and contact-resonance frequency images obtained for **b** the first and **c** the second mode for an organosilicate glass containing copper filled trenches [52]. The images were provided by D.C. Hurley, NIST, Boulder, Colorado, USA

utilized to calculate the normalized contact stiffness  $k^*/k_C$ . In order to obtain elastic constants of the sample surface from the local contact stiffness, contact mechanics models, such as for example Hertz or Maugis models [59] are needed. The Hertzian model describes the contact between two nonconforming elastic bodies of general anisotropy [60]. In the simplest case, the bodies are mechanically isotropic, the sample is considered as flat and the sensor tip is represented by a hemisphere with radius  $R$  (see Fig. 5.1). If a normal force  $F_n$  acts, a circular contact area forms with radius  $a_C$ :

$$a_C = \sqrt[3]{3F_n R/4E^*}. \quad (5.23)$$

It is important for the validity of the model that the contact area is small compared to the tip radius, i.e.  $a_C \ll R$ . If the adhesion forces are so small that they can be neglected, the normal force  $F_n$  is given by the static deflection of the cantilever multiplied with the spring constant of the cantilever  $F_n = dk_C$ , where  $d$  is the cantilever deflection. The normal contact stiffness  $k^*$  is in this case:

$$k^* = 2a_C E^* = \sqrt[3]{6E^*2RF_n}. \quad (5.24)$$

$E^*$  is the reduced Young's modulus that combines the elastic properties of the tip (t) and the sample (s) in the following equations:

$$\frac{1}{E^*} = \frac{1 - \nu_t^2}{E_t} + \frac{1 - \nu_s^2}{E_s}, \quad (5.25)$$

where  $E_s$ ,  $E_t$ ,  $\nu_s$ ,  $\nu_t$ , are the Young's moduli and the Poisson's ratios of the surface and the tip, respectively. AFM sensor tips made of single crystalline silicon are not elastically isotropic, and this holds for other tip and sample materials as well. In special cases of symmetry Eqs. 5.24 and 5.25 remain valid if the isotropic reduced elastic modulus  $E/(1-\nu^2)$  is replaced by an indentation modulus that is calculated numerically from single crystal elastic constants [61, 62]:

$$\frac{1}{E^*} = \frac{1}{M_t} + \frac{1}{M_s}, \quad (5.26)$$

where  $M_s$  and  $M_t$  are the indentation modulus of the sample and the tip, respectively. The required symmetry holds for silicon sensor tips, which are oriented in (001) crystallographic direction.

### 5.4.1 Single Reference Method

The expression for the contact stiffness presented in Eq. 5.24 contains two unknown parameters, namely, the tip radius  $R$  and the reduced Young's modulus  $E^*$  of the sample. One method to obtain these data involves using a reference sample with known elastic properties [45]. The contact stiffness  $k^*$  is determined at several static loads for the reference sample. These values of  $k^*$  will be referred to as “reference contact stiffness”  $k_{\text{ref}}^*$ . They are compared to the values of the contact stiffness obtained for the sample with unknown elastic properties  $k_s^*$  at the same static load  $F_n$  as used for the reference measurements. Using Eqs. 5.24–5.26, an expression for the indentation modulus of the sample  $M_s$  can be derived that is independent of the tip radius and the static load:

$$\frac{k_s^*}{k_{\text{ref}}^*} = \sqrt[3]{\frac{6RF_n E_s^{*2}}{6RF_n E_{\text{ref}}^{*2}}} = \sqrt[3]{\frac{E_s^{*2}}{E_{\text{ref}}^{*2}}}, \quad (5.27)$$

$$E_s^* = E_{\text{ref}}^* \left( \frac{k_s^*}{k_{\text{ref}}^*} \right)^{3/2}, \quad (5.28)$$

$$M_s = \left( \frac{1}{E_s^*} - \frac{1}{M_t} \right)^{-1}. \quad (5.29)$$

As already mentioned in Sect. 5.3.2, the contact stiffness variation as a function of static load contains information on the tip geometry. An increase of the contact stiffness  $k^*$  with the static load  $F_n$ , follows from Eq. 5.24 if the tip apex has hemispherical geometry. As the tips wear and break, different tip shapes arise (see Fig. 5.10). If the values of  $k^*$  remain constant, a flat punch geometry can be assumed, and the radius of the contact area  $a_C$  can be assumed to be constant. Different tip shapes can be considered by introducing a tip geometry factor  $n$ , changing between 1 and 3/2 for a flat punch and a sphere, respectively. Equation 5.28 is replaced by

$$E_s^* = E_{\text{ref}}^* \left( \frac{k_s^*}{k_{\text{ref}}^*} \right)^n. \quad (5.30)$$

SEM images of various AFM tips used in AFAM experiments confirmed that the contact stiffness—load dependence is strongly influenced by the tip geometry and that consideration of the geometry factor  $n$  may improve the accuracy of the AFAM measurement [33]. Figure 5.10 shows examples of the normalized contact stiffness

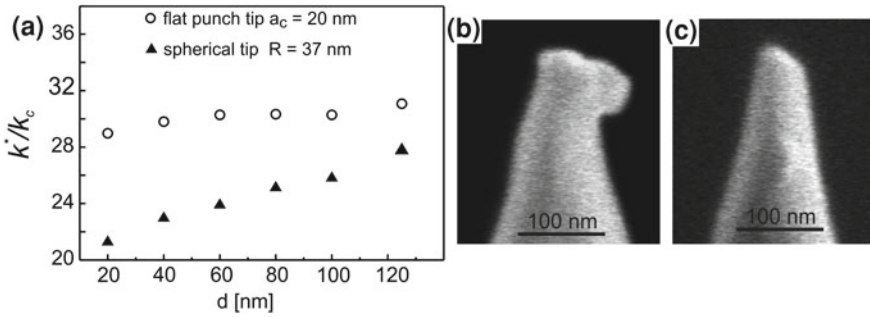


**Fig. 5.10** **a** Normalized contact stiffness  $k^*/k_C$  as a function of cantilever deflection  $d$ . The data sets were obtained with tips with geometries of **b** flat punch and **c** hemisphere confirmed by corresponding scanning electron micrographs [51]

values obtained for a fused silica sample with two cantilevers with very similar spring constants  $k_C$  but sensor tips of different geometries [51].

The single reference sample calibration does not only allow for efficient elimination of the dependence of the contact stiffness on the tip geometry but also eliminates the static spring constant of the cantilever. However, a detailed analysis of AFAM experimental data showed that the values obtained for the indentation modulus  $M_s$  were either too large if the reference sample was much stiffer than the unknown sample or too low if the reference sample was more compliant than the tested sample [48, 63]. Furthermore, the elastic constants of the sensor tips were not always known, especially in cases where the tip was coated for example with a diamond layer or diamond like carbon layer to improve its wear resistance.

### 5.4.2 Dual Reference Method

If two different reference samples are available, each of the samples can be used for calibration, and the results can be averaged, or the contact stiffness data can be used to eliminate not only the tip geometry parameter, but also the tip indentation modulus  $M_t$ . The two reference samples are chosen such that their elastic constants bracket the elastic properties of the unknown samples. By comparing the values of the contact stiffness  $k_1^*$  and  $k_2^*$  measured for two reference samples at the same static load and using Eqs. 5.24 and 5.26, the expression for the indentation modulus  $M_t$  takes the following form [48]:

$$M_t = \frac{M_1 M_2 \left(1 - \left(\frac{k_1^*}{k_2^*}\right)^n\right)}{\left(\left(\frac{k_1^*}{k_2^*}\right)^n M_2 - M_1\right)}, \quad (5.31)$$

**Table 5.2** AFAM results for the indentation modulus of a niobium film

Sample	Literature values [GPa]	AFAM results [GPa]					
		Reference: Glass		Reference: Si		Average	
		$n = 1$	$n = 3/2$	$n = 1$	$n = 3/2$	$n = 1$	$n = 3/2$
Niobium	116–133	88 ± 9	90 ± 14	127 ± 7	122 ± 10	106 ± 12	105 ± 18

The values were obtained using the single reference method for each of the two reference samples individually and subsequent averaging. Two different tip geometries, flat punch ( $n = 1$ ) and hemisphere ( $n = 3/2$ ) [39], were used

where  $M_1$  and  $M_2$  are the indentation moduli of the two different reference samples. With this method, the elastic properties of diamond coated tips [62] were determined, using silicon and strontium titanate single crystal samples as a reference. Hurley et al. [39] used two reference samples of borosilicate glass ( $M_g = 85$  GPa) and silicon single crystal ( $M_{Si} = 139$  GPa) that bracketed the expected values of the indentation modulus for a tested niobium sample ( $M_{Nb} = 116$ – $133$  GPa). The indentation modulus of niobium was calculated by using each reference material individually and subsequent averaging of the results. As can be seen from the data presented in Table 5.2, the values of the indentation modulus  $M_{Nb}$  obtained for niobium films depended strongly on the choice of the reference material. Employing the glass reference sample yielded values of  $M_{Nb}$  that were much lower than those expected from the literature values. On the other hand, using silicon as a reference sample, the values of  $M_{Nb}$  were close to the upper limit expected for the indentation modulus of niobium. Averaging yielded results that were in good agreement with the literatures data as well as the indentation modulus  $M_{Nb}$  obtained by nanoindentation measurements performed on the same niobium film.

Several authors observed an increasing difference between the expected indentation modulus and the value obtained by AFAM with increasing difference in the elastic properties of the unknown and the reference samples [48, 63]. This problem is especially pronounced for sharp tips. Stan et al. [49] used the dual reference method and Eq. 5.31 to determine the indentation modulus of a silicon tip. A variety of samples such as Au (111), CaF<sub>2</sub> (100), Si (100), and MgF<sub>2</sub> (001) were used and yielded results in the range from 60 to 180 GPa, depending on the choice of the reference sample, the tip position parameter, the influence of the lateral stiffness, and the tip geometry. The authors explained these large variations in the values of  $M_t$  by discrepancy in the actual shape of the AFM tip and the assumptions of the existing models for the contact mechanics. Despite these variations, the reason of which will have to be examined in future, it was also shown in this study that the dual reference method allows to measure the indentation modulus with an accuracy of about 3 %.



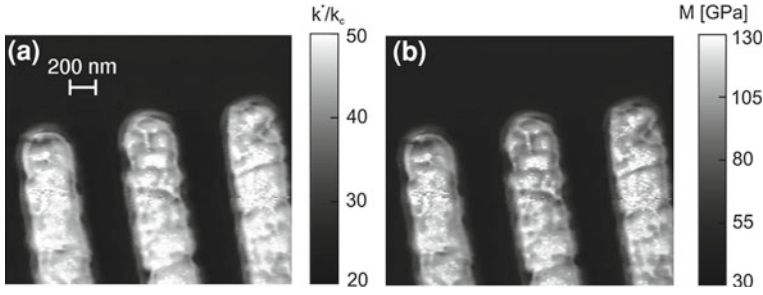


**Fig. 5.11** **a** Normalized contact stiffness and **b** indentation modulus images obtained for SiOC thin film sample with copper filled trenches [52]. The images were provided by D.C. Hurley, NIST, Boulder, Colorado, USA

### 5.4.3 AFAM Image Calibration

During the last ten years, the development of methods for fast acquisition of contact-resonance spectra [43, 42] opened the possibility to take contact-resonance frequency images with an increasing number of points. Once such contact-resonance frequency images are obtained for at least two modes, the calibration techniques discussed in the previous sections can be applied to create a contact stiffness image. Figure 5.11 shows (a) the normalized contact stiffness and (b) the indentation modulus obtained for the SiOC glass thin-film sample with the copper filled trenches presented in Fig. 5.9.

The contact stiffness image was calculated pixel-by-pixel from the contact resonance images of the two modes. To obtain a calibrated image of the indentation modulus, one can use the single or dual reference method [55, 62]. However, a calibration before or after taking an image with 16,000 points and more is problematic, as the tip shape might change because of wear. The elastic constant image in Fig. 5.11b was obtained using a part of the contact stiffness image with known elastic constants for calibration [64]. For this “self calibration,” additional single point measurements were performed directly on the SiOC film using a borosilicate glass as a reference material. Then, the value of the reduced Young’s modulus of 44 GPa obtained for the SiOC film was used as a reference  $E_{ref}^*$  for the rest of the image. In order to obtain a value for the reference contact stiffness  $k_{ref}^*/k_C$ , an average value was calculated directly from the contact stiffness image in the SiOC region. A similar self-calibrating approach was used in Refs. [53, 57].

## 5.5 Nonlinear AFAM

In most of the quantitative contact-resonance spectroscopy measurements the tip-sample contact is modeled as a system of linear springs and dashpots. However, the various physical forces acting between the tip and the surface depend nonlinearly

on the distance. Linear approximations are restricted to tip-sample displacements covering small parts of the interaction force curve, i.e., to small vibration amplitudes of the tip-sample distance. If operated beyond these limits the nonlinearity of the system becomes noticeable. In the regime of small nonlinearity, when the tip remains in contact with the sample surface during its vibration cycle, the contact resonance curves become asymmetric. They develop a steep edge at frequencies below the contact resonances, and the maximum shifts to lower frequencies in case of softening nonlinearity [65]. Hardening nonlinearity causes a reversed behavior. Nonlinear effects are further noticeable by higher or subharmonics in the spectrum of the cantilever vibration [66–68]. An experimental procedure based on perturbation analysis and higher order spectra measurements was proposed [67, 68] to identify the interaction force in a third-order polynomial approximation around the static set-point. Single mode excitation [67] and modal interactions in the presence of two-to-one auto-parametric resonance between two modes [68] was considered.

The downwards shift of the contact-resonance frequency as well as the generation of higher and subharmonics in the cantilever vibration with increasing excitation amplitude were numerically simulated for a pure Hertzian contact [69, 70] and for a Hertzian contact with adhesion forces added [71]. Experimental investigations of contact-resonance frequency variations and higher harmonics generation caused by the nonlinear part of a Hertzian contact were carried out by a scanning microdeformation microscope [72]. Different vibration amplitudes and static loads were considered.

An analytical model of the nonlinear dynamics of cantilever tip-sample interactions for various acoustic AFM modes treats the cantilever and the substrate as independent linear systems coupled by a nonlinear force acting between the sensor tip and a small sample volume [73] (Chap. 3). Equations for the maximum nonlinearity regime, i.e. around the minimum of the force curve, were obtained by perturbation theory using a second order polynomial expansion of the force curve. Equations for the hard contact (linear) regime were also derived.

### ***5.5.1 Evaluation of the Full Force Curve***

The nonlinear AFAM methods mentioned above have access only to a small part of the tip-sample interaction force curve around the static set-point. A more general approach allows the reconstruction of the full curve as a function of the tip-sample distance [74, 75]. A frequency dependent transfer function ( $T\omega$ ) was derived for the flexural contact modes of an AFM cantilever modeled as a beam with constant cross-section. The cantilever contact-vibration amplitudes were measured quantitatively at increasing amplitudes of excitation. The time signals were Fourier transformed to obtain the spectra of the cantilever vibration. By multiplying the measured cantilever vibration spectra with the transfer function and subsequent Fourier back-transformation, the nonlinear contact and adhesion forces were calculated as a function of time. Additionally, the sample surface vibration was measured

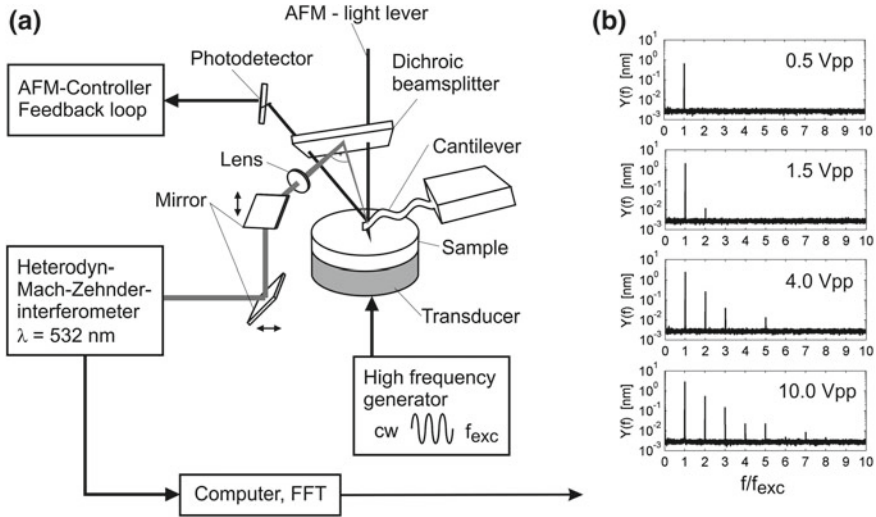


**Fig. 5.12** **a** Set-up of a commercial AFM combined with a heterodyne interferometer to measure absolute vibration amplitudes of the cantilever and the sample surface; **b** Examples for calibrated spectra  $Y(f)$  of the cantilever vibration obtained by FFT [74]

in close proximity to the cantilever tip. With these data the tip-sample interaction forces as a function of the tip-sample distance were reconstructed.

A schematic sketch of the experimental setup is shown in Fig. 5.12. Like in linear AFAM the cantilever was forced to flexural vibrations by vertical sample surface vibrations excited with an ultrasonic transducer below the sample. The static set-point of the cantilever was controlled by the beam-deflection detector and the feedback loop of the AFM. A heterodyne Mach-Zehnder interferometer (bandwidth:  $\sim 100$  kHz–80 MHz) was used for calibrated detection of ultrasonic vibrations. By a dichroic beam splitter added to the AFM the green beam of the interferometer was directed to the cantilever. Two mirrors were used to position the focal spot on the surface of the cantilever. The mirrors and the focusing lens were mounted on a motor-driven translation stage. In this way, the focal spot could be exactly positioned and the entire cantilever could be scanned during experiments to examine the shapes of the modes.

Figure 5.13 shows scans of the surface of the cantilever during nonlinear contact vibration. A single crystal silicon cantilever (Nanosensors, NanoWorld, Neuchâtel, Switzerland, length  $\sim 485$   $\mu\text{m}$ , static spring constant  $\sim 0.2$  N/m) and a polished PZT ceramic sample were used for these experiments. For reconstruction of the force curve, the focal spot of the interferometer was directed to a fixed position on the cantilever as close to the tip position as possible. The calibrated time signal of the interferometer  $y(t)$  was stored by a fast digitizer card and subsequently filtered and Fourier transformed. Thus, the spectral representation of the cantilever deflection  $Y(f)$  was obtained. Examples for spectra at different amplitudes of excitation are shown in Fig. 5.12b. The spectra contain the amplitude of the excitation frequency,

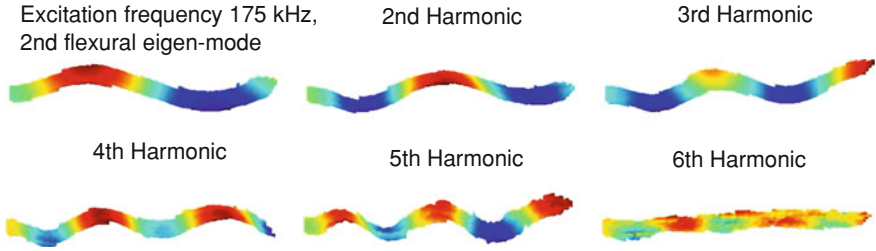


**Fig. 5.13** Measured cantilever vibration in contact with a PZT sample, excitation at the 2nd flexural contact eigen-mode of 175 kHz; the mode shapes of the vibration of the 1st to the 6th harmonic were detectable

and it can be clearly seen that the amplitudes of the harmonics increase with increasing amplitude of excitation. In order to improve the signal-to-noise ratio multiple spectra were acquired and averaged continuously. By repositioning the focal spot of the interferometer, the amplitudes and phases of the sample surface vibration were measured in the vicinity of the sensor tip. Fourier transformation revealed a spectrum containing only the excitation frequency proving that there was no signal distortion by the transducer.

The frequency dependent transfer function ( $T\omega$ ) follows from the theory of flexural vibrations of a rectangular beam of constant cross-section [74, 76]. The deflection  $y(x, t)$  of the beam is a function of the spatial coordinate  $x$  in longitudinal direction and of the time  $t$  described by the Euler–Bernoulli equation 5.1. Due to the linearity of this differential equation the principle of superposition is valid, and the general solution may be written as the sum of a part constant in time (the static deflection of the beam) and an infinite number of harmonic oscillations of circular frequency  $\omega$  [77, 78]:

$$y(x, t) = \sum_{\nu=0}^3 B_{\nu} x^{\nu} + \sum_{\omega} \left[ Y(x, \omega) e^{i\omega t} + \left( Y(x, \omega) e^{i\omega t} \right)^* \right],$$

$$y(t) = y(L_1, t), L_1 = \text{tip position}; \quad (5.32)$$

$$Y(x, \omega) = \sum_{\nu=0}^3 \left[ A_{\nu}(\omega) e^{i^{\nu} \alpha(\omega) x} \right], \alpha(\omega) = \sqrt[4]{\frac{\rho A}{EI} \omega^2 \left( 1 - i \frac{\eta}{\omega} \right)}, Y(\omega) = Y(L_1, \omega). \quad (5.33)$$

The constants  $B_{\nu}$  and  $A_{\nu}(\omega)$ ,  $\nu = \{0, 1, 2, 3\}$ , are determined by the mechanical boundary conditions of the beam.

Once the tip is in contact to the vibrating sample surface the cantilever is forced to vibrations via the tip-sample interaction forces  $F$ . The forces depend on the tip-sample distance and on the relative tip-sample velocity, which in turn are time-dependent because of the vibration. As a consequence the force acting onto the tip

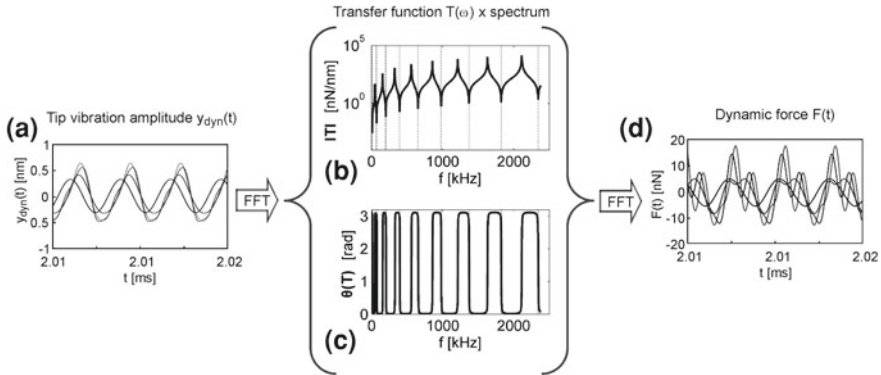


**Fig. 5.14** **a** Tip vibration  $y_{\text{dyn}}(t)$ ; **b** amplitude and **c** phase of the transfer function  $T(\omega)$ ; **d** reconstructed force  $F(t)$ . The four different signals in figures (a) and (d) correspond to four different amplitudes of excitation (0.5, 2, 5, and 10 Vpp), which were applied to the ultrasonic transducer

and indirectly onto the cantilever becomes a function of time,  $F(t)$ , which may be expressed in terms of a Fourier series  $f(\omega)$ . Note,  $F$  is not directly, but indirectly time-dependent due to its distance and velocity dependency. The described relations yield the frequency dependent transfer function  $T(\omega)$ . A detailed derivation is given in [74]. Multiplication of the cantilever vibration spectra  $Y(\omega)$  with the transfer function  $T(\omega)$  yields the Fourier components  $f(\omega)$  of the force  $F(t)$ , which then follows by Fourier back-transformation. This procedure is schematically depicted in Fig. 5.14. Figure 5.14a shows a small time interval of filtered tip vibration signals  $y_{\text{dyn}}(t)$ , Figs. 5.14b and c show amplitude  $\|T\|$  and phase  $\theta(T)$  of the transfer function  $T(\omega)$ , and Fig. 5.14d shows a small time interval of the force  $F(t)$ . The four signals in Figs. 5.14a and d were obtained with the same static deflection of the cantilever, but with different amplitudes of excitation applied to the transducer.

Dynamic interaction forces as function of the tip-sample distance can be obtained by correlating the difference of the measured cantilever vibration and sample surface vibration, i.e., the dynamic part of the tip-sample distance  $z_{\text{dyn}}(t) = y_{\text{dyn}}(t) - a(t)$ , (see Figs. 5.14a and 5.15a) and the force  $F(t)$  (Fig. 5.14d). As shown in Fig. 5.15c for several different excitation amplitudes, dynamic force–distance hysteresis loops were obtained. The extrema in distance of the loops are reversal points in the relative sample surface–sensor tip movement, i.e., points with a relative sample surface–sensor tip velocity of zero. Those points cannot contain damping forces, i.e., can be used to reconstruct the quasistatic force curve from dynamic force–distance hysteresis loops. This means that each force hysteresis loop will yield at least two points of the quasistatic force curve. The map of all extrema of 20 force loops is shown in Fig. 5.16a. The force loops were obtained from a measurement series with 20 different amplitudes of excitation ranging from 0.5 to 10 V [75].

Due to the lower cutoff frequency of 100 kHz of the heterodyne interferometer, it was not possible to measure the absolute static cantilever and sample surface posi-

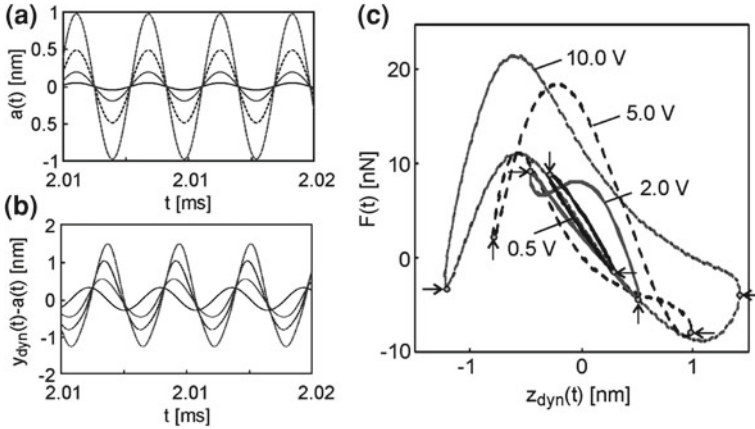


**Fig. 5.15** **a** Surface vibration amplitude  $a(t)$ ; **b** dynamic part of the tip-sample distance  $z_{dyn}(t) = y_{dyn}(t) - a(t)$ , and **c** time-dependent force as a function of tip-sample distance. The four different signals in the figures correspond to four different amplitudes of excitation 0.5, 2, 5, and 10 Vpp, which were applied to the ultrasonic transducer. The points with zero tip-sample velocity correspond to the maxima and minima of  $z_{dyn}(t)$  and are marked with *arrows* in **c** [75]

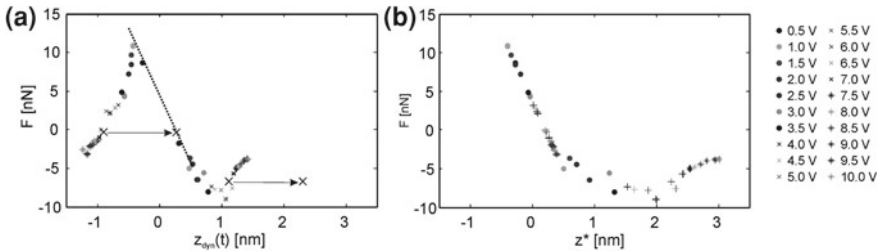


**Fig. 5.16** Reconstructed force curve, **a** quasistatic forces obtained from the turning points of the hysteresis loops some of which are shown in Figs. 5.15c and 5.15b corrected force curve obtained by shifting each pair of turning points in horizontal direction as indicated by the arrows in **a** [74, 75]

tions. The static cantilever deflection was kept constant during the measurements by the feedback loop of the AFM. Only ac-signals were applied to the ultrasonic transducer. However, the nonlinearity of the interaction forces can cause an increase of the mean tip-sample distance with increasing ultrasonic excitation amplitudes. The feedback loop of the AFM compensates for this additional static tip deflection as it does for thermal drifts. The distance between the cantilever and the rest position of the sample surface is unknown. Therefore, the force curve reconstructed as described above (Fig. 5.16a) has to be corrected with respect to an unknown static shift. In a simple tentative approach, it was assumed that the contact stiffness was approximately constant in the repulsive region entailing a force curve being approximately linear at high loads in the repulsive region. The slope of the linear force curve was

defined by the pair of turning points deduced from the elliptic hysteresis loop with the lowest amplitude of excitation stemming from a vibration, which covers only an approximately linear range of the interaction force curve. Each pair of data points from the other hysteresis loops was shifted parallel to the horizontal axis, so that the left points of the pairs formed a straight line corresponding to the contact stiffness in the repulsive region. The arrows in Fig. 5.16a show an example of how one pair of points was shifted. The quasistatic force curve corrected in this way is plotted in Fig. 5.16b. The center of the linear hysteresis loop generated by the low amplitude excitation was chosen as zero-point of the horizontal axis displaying the corrected tip-sample distance  $z^*$ . As the vibration is sinusoidal and consequently symmetric to the origin, this zero-point corresponds to the initially chosen static set-point position.

A direct and quantitative measurement of the cantilever vibrations was achieved by combining an AFM with a heterodyne Mach–Zehnder interferometer. No a priori assumptions about the shape of the force curve and the kind of forces were required. The force curve shown in Fig. 5.16c was obtained with a soft cantilever with a spring constant of approximately 0.15 N/m. In quasistatic measurements the cantilever jumps into contact when the tip-sample force gradient becomes larger than the spring constant of the cantilever. The dynamic approach presented here allows one to reconstruct intervals of the force curve which are not accessible in quasistatic measurements.

## 5.6 Conclusions

In this chapter frequently used mechanical models and experimental methods were reviewed, which have been used in quantitative AFAM. In many different applications AFAM or CR-AFM has proven to be a very useful tool for measurement of elastic constants with high local resolution. Since the invention of AFAM, there has been strong progress in its theoretical as well as in its experimental aspects. For example, the analytical and finite-element models for the theoretical description of the cantilever vibrations have been improved, the influence of the different parameters on the quantitative results, and various aspects of sensitivity have been examined. While the first quantitative AFAM results were obtained with single point measurements, the acquisition of contact-resonance frequency images is now state of the art due to the development of methods for fast acquisition of contact-resonance spectra. However, despite the advantages of CR imaging, AFAM amplitude imaging can be the technique of choice in cases where the contact-resonance frequency variations in the scanned area are small. In addition to linear AFAM, nonlinear AFAM techniques were treated. With an approach based on a transfer function of the cantilever beam, the full non-linear tip-sample force curve can be reconstructed from measurements with soft cantilevers with spring constants of approximately 0.2 N/m. In contrast to linear contact-resonance spectroscopy, which exploits the shift of the resonant frequencies, the reconstruction of the nonlinear forces is based on amplitude measurements, which are more difficult in AFM than frequency measurements.

## References

1. A. Caron, U. Rabe, M. Reinstädler, J.A. Turner, W. Arnold, Appl. Phys. Lett. **85**, 6398 (2004)
2. A. Briggs, *An Introduction to Scanning Acoustic Microscopy* (Oxford University Press, Oxford, 1985)
3. U. Rabe, W. Arnold, Appl. Phys. Lett. **64**, 1493 (1994)
4. K. Yamanaka, O. Kolosov, Jpn. J. Appl. Phys. **32**, L1095 (1993)
5. K. Yamanaka, S. Nakano, Appl. Phys. A. **66**, S313 (1998)
6. T. Hesjedahl, G. Behme, Appl. Phys. Lett. **78**, 1948 (2001)
7. B. Cretin, F. Sthal, Appl. Phys. Lett. **62**, 829 (1993)
8. P.A. Yuya, D.C. Hurley, J.A. Turner, J. Appl. Phys. **104**, 074916 (2008)
9. A. Caron, W. Arnold, Acta Materialia. **57**, 4353 (2009)
10. D.C. Hurley, J.A. Turner, J. Appl. Phys. **102**, 033509 (2007)
11. G. Stan, S. Krylyuk, A.V. Davydov, M.D. Vaudin, L.A. Bendersky, R.F. Cook, Ultramicroscopy. **109**, 929 (2009)
12. P. Maivald, H.T. Butt, S.A. Gould, C.B. Prater, B. Drake, J.A. Gurley, V.B. Elings, P.K. Hansma, Nanotechnology **2**, 103 (1991)
13. P.-E. Mazeran, J.-L. Loubet, Trib. Lett. **3**, 125 (1997)
14. R. Arinero, G. Lévêque, Rev. Sci. Instrum. **74**, 104 (2003)
15. M. Kopycinska, C. Ziebert, H. Schmitt, U. Rabe, S. Hirsekorn, W. Arnold, Surf. Sci. **532–535**, 450 (2003)
16. S. Jesse, B. Mirman, S.V. Kalinin, Appl. Phys. Lett. **89**, 022906 (2006)
17. T. Drobek, R.W. Stark, W.M. Heckl, Phys. Rev. B. **64**, 045401 (2001)
18. H.-L. Lee, W.-J. Chang, Y.-Ch. Yang, Mater. Chem. Phys. **92**, 438 (2005)
19. K.-N. Chen, J.-Ch. Huang, in *Proceedings of the 2005 International Conference on MEMS, NANO and Smart Systems (ICMENS'05)*, pp. 65–68, 2005
20. A. Caron, U. Rabe, M. Reinstädler, J.A. Turner, W. Arnold, Appl. Phys. Lett. **85**, 6398 (2004)
21. M. Reinstädler, T. Kasai, U. Rabe, B. Bhushan, W. Arnold, J. Phys. D: Appl. Phys. **38**, R269 (2005)
22. V. Scherer, M. Reinstaedtler, W. Arnold. Atomic force microscopy with lateral modulation. ed. by B. Bhushan et al. in: *Applied Scanning Probe, Methods*. 2003, pp. 75–115
23. W. Weaver, S.P. Timoshenko, D.H. Young, *Vibration Problems in Engineering* (Wiley, New York, 1990)
24. U. Rabe, K. Janser, W. Arnold, Rev. Sci. Instrum. **67**, 3281 (1996)
25. S. Nakano, R. Maeda, K. Yamanaka, Jpn. J. Appl. Phys. **36**, 3265 (1997)
26. A.W. McFarland, M.A. Poggi, L.A. Bottomley, J.S. Colton, J. Micromech. Microeng. **15**, 785 (2005)
27. D.-A. Mendels, M. Lowe, A. Cuenat, M.G. Cain, E. Vallejo, D. Ellis, F. Mendels, J. Micromech. Microeng. **16**, 1720 (2006)
28. U. Rabe, in *Applied Scanning Probe Methods II*, ed. by H. Fuchs, B. Bhushan. Atomic Force Acoustic Microscopy, (Berlin, Springer, 2006)
29. U. Rabe, S. Hirsekorn, M. Reinstädler, T. Sulzbach, Ch. Lehrer, W. Arnold, Nanotechnology. **18**, 044008 (2007)
30. Nanosensors, NCL, NANOSENSORS<sup>T</sup> M, Rue Jaquet-Droz 1, CH-2002 Neuchatel, Switzerland. <http://www.nanosensors.com>
31. J.-Ch. Hsu, H.-L. Lee, W.-J. Chang, Nanotechnology. **18**, 285503 (2007)
32. H.-L. Lee, W.-J. Chang, Jpn. J. Appl. Phys. **48**, 065005 (2009)
33. D. Passeri, A. Bettucci, M. Germano, M. Rossi, A. Alippi, S. Orlanducci, M.L. Terranova, M. Ciavarella, Rev. Sci. Instrum. **76**, 093904 (2005)
34. G. Stan, R.F. Cook, Nanotechnology. **19**, 235701 (2008); (10pp)
35. J.E. Sader, J.W.M. Chon, P. Mulvaney. Rev. Sci. Instrum. **70**, 3967 (1999)
36. N.A. Burnham, X. Chen, C.S. Hodges, G.A. Matei, E.J. Thoreson, C.J. Roberts, M.C. Davies, S.J.B. Tendler, Nanotechnology. **14**, 1 (2003)



37. E. Kester, U. Rabe, L. Presmanes, Ph. Tailhades, W. Arnold. *J. Phys. Chem. Solids.* **61**, 1275 (2000)
38. U. Rabe, S. Amelio, E. Kester, V. Scherer, S. Hirsekorn, W. Arnold, *Ultrasonics.* **38**, 430 (2000)
39. D.C. Hurley, K. Shen, N.M. Jennett, J.A. Turner, *J. Appl. Phys.* **94**, 2347 (2003)
40. F.J. Espinoza-Beltrán, K. Geng, J. Muñoz Saldaña, U. Rabe, S. Hirsekorn, W. Arnold, *New J. Phys.* **11**, 083034 (2009)
41. F. Marinello, P. Schiavuta, S. Carmingnato, E. Savio, *CIRP J. Manufact. Sci. Technol.* **3**, 49 (2010)
42. K. Kobayashi, H. Yamada, H. Itoh, T. Horiuchi, K. Matsushige, *Rev. Sci. Instrum.* **72**, 4383 (2001)
43. A.B. Kos, D.C. Hurley, *Meas. Sci. Technol.* **19**, 015504 (2008)
44. S. Jesse, S.V. Kalinin, R. Proksch, A.P. Baddorf, B.J. Rodriguez, *Nanotechnology.* **18**, 435503 (2007)
45. U. Rabe, S. Amelio, M. Kopycinska, M. Kempf, M. Göken, W. Arnold, *Surf. Interface Anal.* **33**, 65 (2002)
46. M. Kopycinska-Müller, R.H. Geiss, J. Müller, D.C. Hurley, *Nanotechnology.* **16**, 703 (2005)
47. S. Amelio, A.V. Goldade, U. Rabe, V. Scherer, B. Bhushan, W. Arnold, *Thin Solid Films.* **392**, 75 (2001)
48. M. Kopycinska-Müller, *On the elastic properties of nanocrystalline materials and the determination of elastic properties on a nanoscale using the atomic force acoustic microscopy technique.* Saarbrücken : PhD thesis, Science and Technical Faculty III, Saarland University and IZFP report No. 050116-TW, 2005
49. G. Stan, W. Price, *Rev. Sci. Instrum.* **77**, 1037071 (2006)
50. J.P. Killgore, R.H. Geiss, D.C. Hurley, *Small.* **7**, 1018 (2011)
51. M. Kopycinska-Müller, R.H. Geiss, D.C. Hurley, *Ultramicroscopy.* **106**, 466 (2006)
52. D.C. Hurley, in *Applied Scanning Probe Methods Vol. XI*, ed. by B. Bhushan, H. Fuchs. *Contact Resonance Force Microscopy Techniques for Nanomechanical Measurements*, (Berlin, New York, 2009), pp. 97–138
53. D.C. Hurley, M. Kopycinska-Müller, A.B. Kos, R.H. Geiss, *Adv. Engin. Mater.* **7**, 713 (2005)
54. D.C. Hurley, M. Kopycinska-Müller, E.D. Langlois, A.B. Kos, N. Barbosa, *Appl. Phys. Lett.* **89**, 021211 (2006)
55. D. Passeri, A. Bettucci, M. Germano, M. Rossi, A. Alippi, V. Sessa, A. Fiori, E. Tamburri, M.L. Terranova, *Appl. Phys. Lett.* **88**, 121910 (2006)
56. D. Passeri, M. Rossi, A. Alippi, A. Bettucci, D. Manno, A. Serra, E. Filippo, M. Lucci, I. Davoli, *Superlattices Microstruct.* **44**, 641 (2008)
57. A. Kumar, U. Rabe, S. Hirsekorn, W. Arnold, *Appl. Phys. Lett.* **92**, 183106 (2008)
58. F. Mege, F. Volpi, M. Verdier, *Microelectron. Eng.* **87**, 416 (2010)
59. B. Cappella, G. Dietler, *Surf. Sci. Rep.* **34**, 1 (1999)
60. K.L. Johnson, *Contact Mechanics* (Cambridge University Press, Cambridge, 1985)
61. J.J. Vlassak, W D. Nix, *Phil. Mag. A.* **67**, 1045 (1993)
62. U. Rabe, M. Kopycinska, S. Hirsekorn, J. Muñoz Saldaña, G.A. Schneider, W. Arnold, *J. Phys. D: Appl. Phys.* **35**, 2621 (2002)
63. M. Prasad, M. Kopycinska, U. Rabe, W. Arnold, *Geophys. Res. Lett.* **29**, 13 (2002)
64. D.C. Hurley, M. Kopycinska-Müller, A.B. Kos, R.H. Geiss, *Meas. Sci. Technol.* **15**, 2167 (2005)
65. U. Rabe, M. Kopycinska, S. Hirsekorn, W. Arnold, *Ultrasonics.* **40**, 49 (2001)
66. N.A. Burnham, A.J. Kulik, G. Gremaud, *Phys. Rev. Lett.* **74**, 5092 (1995)
67. E.M. Abdel-Rahman, A.H. Nayfeh, *Nanotechnology.* **16**, 199 (2005)
68. H.N. Arafat, A.H. Nayfeh, E.M. Abdel-Rahman, *Nonlinear Dyn.* **54**, 151 (2008)
69. B. Wei, J.A. Turner, in *Review of Progress in Quantitative Nondestructive Evaluation* vol 20, ed. by D.O. Thompson, D.E. Chimenti, 2001, p. 1658
70. J.A. Turner, *Nondestructive evaluation and reliability of micro- and nanomaterial systems.* *Proc. SPIE* **4703**, 74 (2002)

71. K. Shen, J.A. Turner, Nondestructive evaluation and reliability of micro- and nanomaterial systems. *Proc. SPIE.* **4703**, 93 (2002)
72. P. Vairac, R. Boucenna, J. Le Rouzic, B. Cretin, *J. Phys. D: Appl. Phys.* **41**, 155503 (2008)
73. J.H. Cantrell, S.A. Cantrell. *Phys. Rev. B.* **77**, 165409 (2008)
74. D. Rupp, U. Rabe, S. Hirsekorn, W. Arnold, *J. Phys. D: Appl. Phys.* **40**, 7136 (2007)
75. D. Rupp, Nichtlineare Kontaktresonanzspektroskopie zur Messung der Kontakt- und Adhäsionskräfte in der Kraftmikroskopie, Diploma thesis, Saarland University, IZFP report 060130-TW, 2006
76. R. Vázquez, F.J. Rubio-Sierra, R.W. Stark, *Nanotechnology.* **18**, 185504 (2007)
77. S. Hirsekorn, U. Rabe, W. Arnold, *Nanotechnology.* **8**, 57 (1997)
78. J.A. Turner, S. Hirsekorn, U. Rabe, W. Arnold, *J. Appl. Phys.* **82**, 966 (1997)

# Chapter 6

## Ultrasonic Atomic Force Microscopy UAFM

Kazushi Yamanaka and Toshihiro Tsuji

**Abstract** A version of scanning probe acoustic technique was developed as ultrasonic atomic force microscopy (UAFM), where higher order mode cantilever vibration is excited at its base (support). It enables precise imaging of both topography and elasticity of stiff samples such as metals and ceramics, without a need for bonding a transducer to the sample. By virtue of this advantage, a range of unique analysis and hardware has been developed. In this chapter, after briefly summarizing the concept of UAFM, basic mathematical analysis, mechanical, and electronic instrumentation are described, including a noise-free cantilever holder and analogue/digital fast resonance frequency tracking circuit. The final section describes illustrative examples first realized by this technique as an introduction for later chapters of applications (e.g. subsurface defects).

### 6.1 Conceptual Design

#### *6.1.1 Forced Vibration of Cantilever from the Base*

An atomic force microscope (AFM) [1] uses a cantilever to measure nanoscale irregularities on the surface of a sample, utilizing the deflection of the cantilever supporting a tip owing to the force acting between the sample surface and the tip. Methods have been proposed to measure the distribution of contact stiffness by detecting the vibration of the AFM cantilever when the sample is vibrated at or higher frequency than its resonance frequency (frequency range of ultrasound), while the vertical control is realized via the static cantilever deflection [2–5]. They can measure the elasticity of stiff materials. Note that it is not possible in the force modulation mode where the

---

K. Yamanaka (✉) · T. Tsuji  
Department of Materials Processing, Tohoku University, 6-6-02, Aramaki-Aza-Aoba,  
Sendai 980-8579, Japan  
e-mail: yamanaka@material.tohoku.ac.jp

sample is vibrated at a frequency much lower than resonance frequency in vertical direction [6], not in the lateral direction [7].

However, since the sample has to be bonded to an ultrasonic vibrator,

- (1) Selection of optimum adhesive for each sample is required.
- (2) Adhesives contaminate the sample and cannot be used with LSI wafers and other samples requiring a high degree of cleanness.
- (3) A large or irregularly shaped sample is hard to vibrate uniformly.
- (4) Unwanted resonance peaks of the sample overlap cantilever resonances, degrading the precision.

These disadvantages are overcome by the ultrasonic atomic force microscopy (UAFM) [8–21] in which the cantilever rather than the sample is vibrated, without requiring the sample to be bonded to a vibrator. With suppression of both spurious vibration of cantilever base (chip to mount the cantilever to cantilever holder) and nonlinear jumping of the tip, a wealth of information is conveniently obtained from the clear spectra of fundamental and higher order modes of deflection, torsion, and lateral bending vibration of the cantilever.

### ***6.1.2 Tracking Quantitative Information, Directional Control, and Resonance Frequency***

The cantilever vibration spectra in contact with the sample were found to be strongly dependent on the excitation power [10]. However, if the excitation power is small enough, the resonance peak width decreases and the peak frequency increases to a certain limiting value. In this condition the tip-sample contact is kept linear, and satisfactory agreement between the measured and calculated frequency is obtained. The agreement is further improved by taking into account the lateral stiffness. More quantitative information on the elasticity of the sample is obtained from the contact load dependence of the frequency, where contact stiffness of a non-spherical tip shape is derived from the Sneddon–Maugis formulation, and the tip shape index is estimated by an inverse analysis of the load–frequency relation. A further advantage is the evaluation of not only the vertical, but also the lateral stiffness by simultaneous measurement of deflection and torsional vibration [9]. It was demonstrated on a ground silicon wafer [10].

The modulus can be calculated using the resonance frequency obtained from the peak frequency of a spectrum, and the loss modulus is calculated using the Q factor defined as the ratio of the peak frequency to its width. However, measurement of spectra takes a long time (typically 5 s for one point for an average of 10 times). Consequently, mapping of the resonance frequency and the Q factor takes a very long time (~91 h for a  $256 \times 256$  pixels image).

A resonance-tracking scheme was developed to reduce the time required for mapping the resonance frequency [13]. Furthermore, if we use the analytical relationship between the peak height of resonance and the Q factor obtained by the theory of

UAFM, we can measure the  $Q$  factor from the vibration amplitude at resonance. Based on this i.e., advanced UAFM was developed for mapping both the resonance frequency and  $Q$  factor of the sample. Here the frequency is not fixed but automatically tuned to instantaneous resonance frequency determined by the stiffness of sample.

## 6.2 Analysis

### 6.2.1 *Effective Enhancement of Cantilever Stiffness*

As an essential point of UAFM, cantilever stiffness is effectively enhanced by higher order resonances, as pointed out by the first paper of UAFM [8].

As the most comprehensive introduction, the first five vibration modes are illustrated in Fig. 6.1. The cantilever with a fixed boundary at the right-hand side has an elastic boundary shown by the small rectangular column which represents stiffness of sample. The deformation is negligible in  $n = 1$  and 2 modes. Consequently, a small variation of stiffness of sample would not cause significant change in the cantilever vibration amplitude. On the other hand, the sample is significantly compressed at the  $n = 4$  mode and stretched at  $n = 5$  mode. Consequently, a small variation of stiffness of sample would cause some change in the deformation of sample and thus the cantilever vibration amplitude. And this change will be detected by the laser probe.

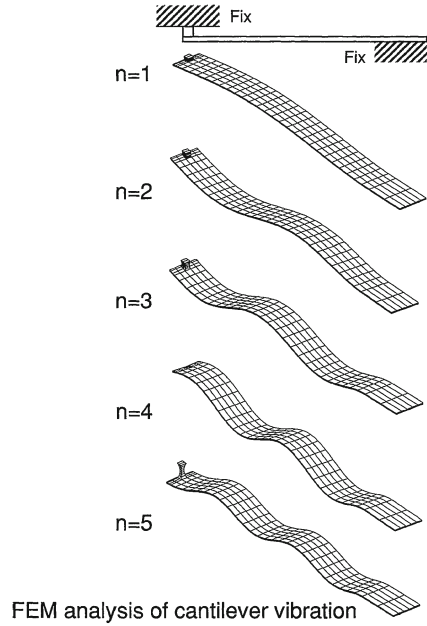
This is the clearest demonstration of the property that the cantilever softer than the sample stiffness is effectively stiffened at higher order modes. This property is used to measure elasticity of stiff samples using a soft cantilever. The reason for this stiffening is explained by the inertia of the cantilever as well as the formation of nodes along the cantilever axis. The distance between the sample and the closest node is much less than the original cantilever length, resulting in the effective shortening of the cantilever.

### 6.2.2 *Stiffness, $Q$ Factor, and Nonlinear Parameter in Resonance Spectra*

#### 6.2.2.1 **Criterion to Avoid Plastic Deformation**

The start point for any reliable measurement is the repeatability. Plastic deformation of tip and/or the sample are the most serious obstacle to repeatability since it is a irreversible process. But it is lucky that we have a good criterion to judge if plastic deformation takes place.

**Fig. 6.1** Effective enhancement of cantilever stiffness at higher modes (FEM analysis of cantilever vibration) [8]



If the von Mises stress  $\sigma_V$  calculated from stress components is larger than the yield stress, plastic deformation will take place. Maximum  $\sigma_V$  under the tip-sample contact is approximately given by

$$\sigma_v \cong 0.3\sigma_0 \quad (6.1)$$

where  $\sigma_0 = 1.5F_{\perp}/(\pi a_c^2)$  is the maximum normal stress in the contact area, where  $a_c = (3RF_{\perp}/4K^*)^{1/3}$  is the contact radius,  $R$  is the tip radius,  $K^*$  is the effective modulus of tip/sample pair, and  $F_{\perp}$  is the contact force. Assuming typical parameters of AFM,  $K^*$  of 100 GPa, and contact force of 250 and 2,400 nN, the contact diameter and Mises stress are evaluated in Table 6.1.

In Table 6.1, it is noted that  $\sigma_v$  is fairly large in spite of small  $F_{\perp}$ , due to very small  $a_c$ . Therefore, we have the following concern about;

(1) Yield and wear of samples

The cases (a) and (b) are for radius  $R = 50$  nm of slightly worn tip and (c) and (d) are for  $R = 100$  nm of severely worn tip. At (a),  $\sigma_v$  is as large as 3.2 GPa, much larger than yield stress  $\sigma_y$  of typical metals listed in Table 6.2, which is usually less than 1 GPa = 1000 MPa. Since some metals such as Gold (Au) is very soft, it easily undergo plastic deformation at the contact force  $F_{\perp}$  exceeding 1000 nN. This point should be taken care when applying not only UAFM but also related techniques in this book. One should always know approximate tip radius  $R$ . It

**Table 6.1** Von Mises stress for some sets of tip radius  $R$  and contact force  $F_{\perp}$ 

	Tip radius $R$ (nm)	Contact force $F_{\perp}$ (nN)	Contact diameter $2a_c$ (nm)	Max normal stress $\sigma_0$ (GPa)	Von Mises stress $\sigma_v$ (GPa)
(a)	50	250	6.7	10.7	3.2
(b)	50	2,400	14.2	22.7	6.8
(c)	100	250	11.4	3.6	1.1
(d)	100	2,400	24.3	7.7	2.3

**Table 6.2** Yield stress  $\sigma_y$  of typical materials

Material	Yield strength $\sigma_y$ (MPa)
Structural steel ASTM A36 steel	250
Steel, API 5L X65 (Fikret Mert Veral)	448
High density polyethylene (HDPE)	26–33
Polypropylene	12–43
Stainless steel AISI 302 –Cold-rolled	520
Titanium alloy (6% Al, 4% V)	830
Aluminum alloy 2014-T6	400
Copper 99.9% Cu	70
Silkworm silk	500
Kevlar	3620

is useful to observe the appearance of sample surface in the noncontact mode AFM image after spectra measurement.

(2) Wear of tip

Even for a silicon tip whose  $\sigma_y$  is 5 to 9 GPa, yield may occur at  $\sigma_v$  larger than 5 GPa. Moreover, the tilt of cantilever (typically about  $11^\circ$  in common AFM) further increases the  $\sigma_v$  due to surface friction. Consequently, severe wear of Si tip should take place at condition above  $\sigma_v = 5$  GPa. The tip will be worn and the radius increases to e.g. 100 nm (d), and the resonance frequency will also increase. Hence, frequent measurement of reference sample is required when they use  $F_{\perp} > 1000$  nN to obtain reliable data.

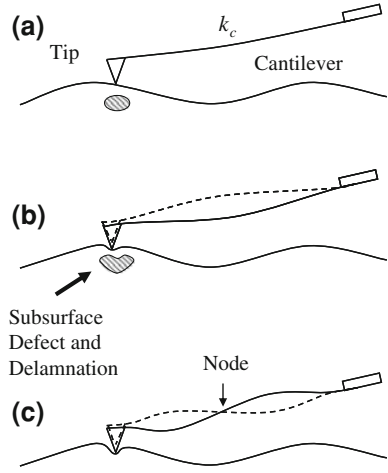
(3) Spatial resolution degradation

The contact diameter representing the resolution is more than 10 nm in Table 6.1, except for the case (a). Therefore, to achieve spatial resolution about 5 nm, contact force should be less than 250 nN with a tip without wear. Hence, users need care if images are taken at high loads.

The worn tip also causes artifacts. The contrast of grooves and grain boundary can be inverted by the compensation of multi-asperity contact. Moreover, the simple relation

$$k^* = 2a_c K^* \quad (6.2)$$

**Fig. 6.2** Principle of UAFM. **a** AFM. **b** UAFM in the first resonance. **c** UAFM in the second resonance



cannot be employed for contacts without axial symmetry. If it is used, over compensation may easily take place resulting in an inverted artifact. There is no established relation to be employed to convert the contact stiffness to local modulus value.

### 6.2.2.2 Analysis of Stiffness and Q Factor

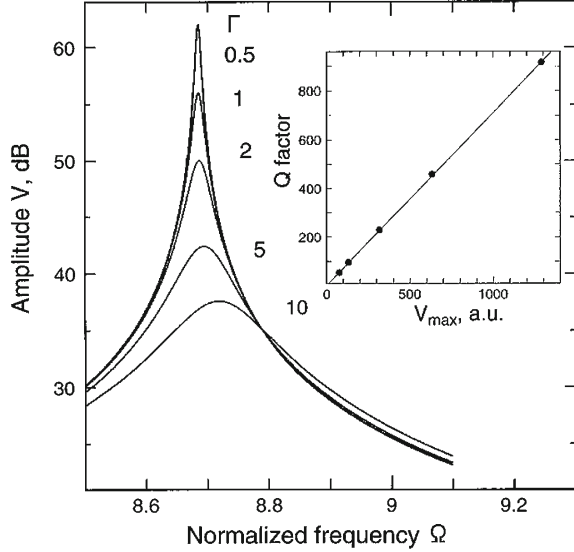
The principle of UAFM for the analysis of stiffness and subsurface defects is shown in Fig. 6.2 [10]. When resonance vibration is excited to the cantilever, elastic deformation of the sample is caused by effective stiffening of the cantilever due to the inertia effect (Fig. 6.2b) as well as shortening of the lever due to the formation of nodes (Fig. 6.2c) as proposed previously.

In a model of UAFM cantilever with distributed mass, the slope of the cantilever is given by

$$\begin{aligned}
 V(x) &= \frac{\partial z(x)}{\partial x} \\
 &= (u_0/2) \frac{\beta}{L_1} e^{i\omega t} \left[ \sinh \beta \frac{x}{L_1} - \sin \beta \frac{x}{L_1} - B(\omega) (\sin \beta \frac{x}{L_1} + \sinh \beta \frac{x}{L_1} x) \right. \\
 &\quad \left. + D(\omega) (\cos \beta \frac{x}{L_1} x - \cosh \beta \frac{x}{L_1}) \right] \\
 B(\omega) &= -\frac{SS_h + \alpha(CS_h + SC_h)}{(1 + CC_h) + \alpha(CS_h - SC_h)}, \quad D(\omega) = \frac{CS_h + SC_h + 2\alpha CC_h}{(1 + CC_h) + \alpha(CS_h - SC_h)}
 \end{aligned} \tag{6.3}$$



**Fig. 6.3** Relation between the Q factor and the maximum peak height  $V_{\max}$  of a peak formed around  $\Omega \approx 0.87$  when and  $k^*/k_c = 200$ . Five different values of  $\Gamma \equiv \gamma/\sqrt{Mk_c}$  were assumed  $\sim 0.5, 1, 2, 5,$  and  $10$



where  $z$  is the deflection of cantilever,  $u_0$  is the vibration amplitude of cantilever base,  $\omega$  is the angular frequency,  $L_1$  is the actual distance between the tip and the base (cantilever length), and  $S = \sin \beta$ ,  $S_h = \sinh \beta$ ,  $C = \cos \beta$ ,  $C_h = \cosh \beta$ ,  $\alpha = -1/\beta^3(3k^*/k_c + i\sqrt{3}\Gamma\beta^2)$ ,  $\beta = 3^{1/4}\sqrt{\Omega}$  [13]. The factor  $\Omega = \omega/\sqrt{k_c/M}$  is the normalized frequency and  $\Gamma = \gamma/\sqrt{Mk_c}$  is the normalized damping coefficient, where  $M$  is the mass of cantilever,  $k_c$  is the cantilever stiffness,  $k^*$  and  $\gamma$  are the contact stiffness and damping coefficient between tip and sample. Because the slope is proportional to the signal measured by optical-deflection AFM, Eq. (6.3) is an analytical expression of the UAFM spectrum at a given location  $x$  of the laser beam spot.

Figure 6.3 shows spectra calculated using Eq. (6.3) with  $\Gamma \equiv \gamma/\sqrt{Mk_c} = 0.5, 1, 2, 5, 10$  and  $k^*/k_c = 200$ , for the laser beam spot at the end of cantilever ( $x = L_1$ ) [13]. The Q factor is calculated as the ratio of peak frequency  $\Omega_0$  to the 3 dB-width  $\Delta\Omega$ . Inset of Fig. 6.3 shows the relation between the Q factor and the peak height of resonance  $V_{\max}$ , showing clear linearity between them. Though the linearity is an approximate relation, it holds over a reasonably wide range of normalized damping coefficient  $\Gamma$ . For example, the ratio between the Q factor and the maximum peak height  $V_{\max}$ ,  $Q/V_{\max}$ , remains almost constant (0.413~0.422) over a range of  $\Gamma$  from 0.1 to 10.0 for the normalized contact stiffness  $k^*/k_c$  of 200. For  $k^*/k_c$  larger than 200, the variation of  $Q/V_{\max}$  is even smaller. Thus, the peak height of resonance can be employed as a measure of the Q factor. The analysis can be further improved by considering the lateral stiffness [22], tilt of the cantilever [10], and shape of the tip.

The Q factor is determined by the internal friction of the sample and by the water or contaminant film on the sample. Although other factors such as the air damping,

clamp of cantilever base to the ultrasonic transducer and defects within the cantilever change the Q factor, their effect is usually small or uniform, and therefore, does not significantly affect the contrast in the image.

To verify quantitatively such an effect, we use the continuum theory to describe vibration of the cantilever with a tip in contact with the sample. For analysis of experiments, lateral stiffness [9, 22] and the oblique sample surface [23] are considered. The frequency equation of the cantilever is

$$C \cdot C_h(PQ - 1 + D^2) + S \cdot C_h(P + Q) + C \cdot S_h(P - Q) + 2S \cdot S_h\sqrt{PQ}D + 1 + PQ - D^2 = 0 \quad (6.4)$$

$$P = \frac{\beta^3}{3(k^*/k_c)(r \sin^2 \varphi + \cos^2 \varphi)} \quad Q = \frac{\beta(L_1/h)^2}{3(k^*/k_c)(r \cos^2 \varphi + \sin^2 \varphi)}$$

$$D = \frac{(1-r)^2 \tan^2 \varphi}{(r + \tan^2 \varphi)(r \tan^2 \varphi + 1)} \quad \text{and} \quad r = \frac{k_{\text{Lat}}^*}{k^*} \quad (6.5)$$

in which  $\beta = \kappa L_1$  is the product of the wavenumber  $\kappa$  and the cantilever length  $L_1$ ,  $k^*$  is the vertical (out-of-plane) contact stiffness,  $k_{\text{Lat}}^*$  is the lateral (in-plane) contact stiffness,  $k_c$  is the cantilever stiffness, and  $\varphi$  is the angle between the lever axis (the  $x$ -axis) and the sample surface. When the parameters ( $r$ ,  $\varphi$ ,  $L_1/h$ ,  $k^*/k_c$ ) are given, Eq.(6.4) is solved for  $\beta$  and Eq.(6.4) gives the resonance frequency

$$\kappa^4 = \left(\frac{\beta}{L_1}\right)^4 = \frac{\omega^2 \rho A}{EI} = \frac{3\omega^2 \rho A}{k_c L_1^3} \quad (6.6)$$

In the limit of  $r \rightarrow 0$  and  $\varphi \rightarrow 0$ , we obtain  $Q \rightarrow \infty$  and hence

$$\frac{k_c}{3k^*} \beta^3 (1 + \cos \beta \cosh \beta) = \cos \beta \sinh \beta - \sin \beta \cosh \beta \quad (6.7)$$

which is the original equation for ultrasonic AFM [5, 8].

### 6.2.2.3 Detrimental Nonlinear Spectra

Another obstacle to achieve reliable measurement is the nonlinearity. To show this, three silicon cantilevers with a silicon tip were used. The nominal length, width, thickness, and stiffness of the cantilever were  $L_1 = 444 \mu\text{m}$ ,  $a = 73 \mu\text{m}$ ,  $b = 3.5 \mu\text{m}$  and  $k_c = 1.5 \text{Nm}^{-1}$ , respectively. The spectra of tip 1 around the second resonance at the static load of 30 nN on a soda-lime glass are shown in Fig. 6.4. Different level of excitation power was applied to the piezoelectric transducer attached to the cantilever holder. For clear comparison, each spectrum is shifted by 5 dB from preceding spectra [9].

**Fig. 6.4** Deflection vibration spectra with different excitation power of cantilever

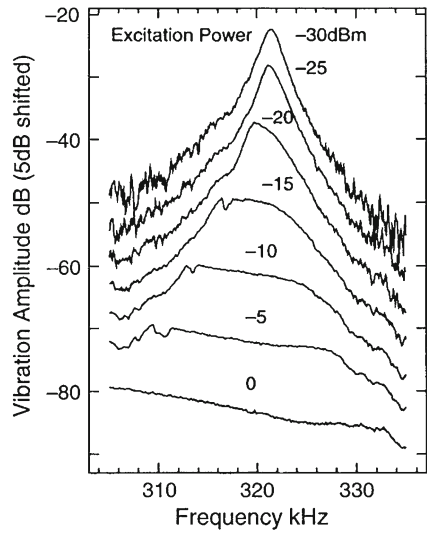
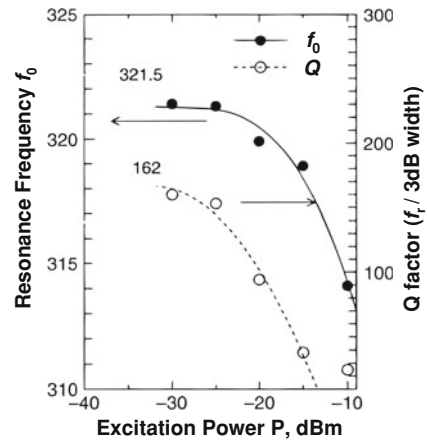


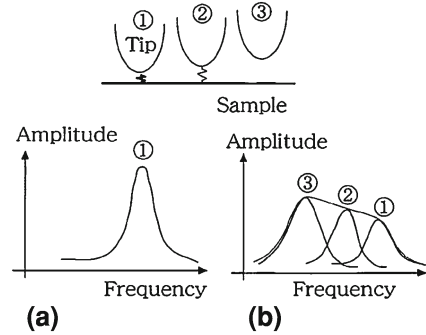
**Fig. 6.5** Variation of resonance frequency and  $Q$  factor (3 dB) with excitation power of cantilever



Although the first step for quantitative evaluation is the precise measurement of resonance frequency, it turned out that this is not an easy task. It was found that the width decreases and the peak frequency increases as the excitation power is reduced from  $-10$  to  $-25$  dBm. However, if the resonance frequency  $f_r$  and  $Q$  factor are plotted as functions of excitation power in Fig. 6.5, it was possible to estimate the limiting value of  $f_r$  and  $Q$  as 321.5 kHz and 162, respectively, as the power was extrapolated to zero. Moreover, approximately constant values were obtained by reducing the excitation power to less than  $-25$  dBm. We name the spectra measured in such conditions ‘linear spectra’.

It has been suggested that the width of the spectra is related to the viscosity or energy dissipation at the tip-sample contact [5, 22, 23] and it is possible to evaluate

**Fig. 6.6** Surface tip-sample contact vibration for different excitation power levels. **a** low power. **b** high power



the viscosity from the peak width. However, because the width is generally dependent on the excitation power, as shown in Figs. 6.4 and 6.5, it is not possible to evaluate correctly the viscosity from the nonlinear spectra. It is essential to suppress the nonlinearity for reliable viscosity measurement.

To explain the shape of the observed linear and nonlinear spectra, an intuitive model is shown in Fig. 6.6 [10]. If the excitation power is low, the variation of the tip-sample indentation during one cycle of vibration should be small and the contact stiffness at every moment can be regarded to be constant during one vibration cycle. Then the spectra consist of a single peak corresponding to a single value of contact stiffness. However, if the excitation power is increased, an intermittent contact results and the contact stiffness changes its magnitude during the vibration circle. The stiffness is small while the tip is detached from the sample. Then, the vibration spectra averaged over one cycle may be approximated by the sum of component spectra for different contact stiffness. The total spectra are therefore broader and the peak frequency is lower than the linear spectra. If the amplitude of component vibration is not uniform, then the total spectra will be asymmetric. The qualitative features of the observed spectra are consistent with this model. For quantitative prediction of the observed spectra, more precise analysis of the nonlinear vibration is introduced in later part of this chapter.

#### 6.2.2.4 Relation Between UAFM and UFM

Similar but another type of nonlinearity is described in the model of UFM [2, 3]. When an amplitude-modulated (AM) high-frequency vibration is excited on the sample or on the cantilever support, a vibration at the modulation frequency is generated by a demodulation or ‘mechanical diode’ effect due to the nonlinear tip-sample contact. In order to understand the relation between these two nonlinear effects, it is useful to compare the threshold power for linear spectra  $P_L$  with that for nonlinear demodulation of the AM vibration  $P_D$ .

According to investigation in the same experimental conditions as these of Fig. 6.4, the threshold power  $P_D$  was  $\sim 0$  dBm, which is significantly higher than the threshold

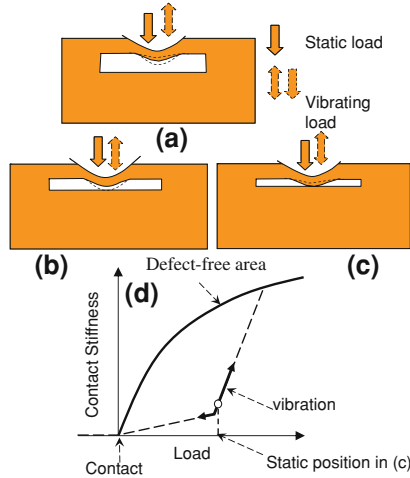


**Fig. 6.7** Contact acoustic nonlinearity (CAN) in closed crack. **a** A linear gap decreases the contact stiffness (*widest*). **b** A wide gap is closed during downward motion (*dotted line*) of the tip. **c** The narrow gap is already closed but opened during upward motion (*dotted line*) of the tip (subsurface pull off). **d** Contact stiffness as a function of tip position. *Thick arrows* indicate the variation of tip position, and the *open circle* shows the average position in the case of **(c)**

for linear spectra  $P_L$  ( $-25$  dBm, as shown previously). Correspondingly, the carrier frequency providing the maximum demodulation was 300 kHz at just above  $P_D$  which is lower than the linear resonance frequency of 321 kHz. This result shows that the tip-sample contact is still nonlinear even at a power of  $<P_D$ . The reason why  $P_D$  is higher than  $P_L$  is because a stronger nonlinearity is required for the demodulation effect than for the resonance shift.

Although both effects have the same physical origin, i.e. the nonlinear force-distance (or indentation) relation, they can be distinguished because the influence of the excitation power on the visibility of these effects is opposite. As shown in Fig. 6.4, the resonance frequency can be measured only in the low power range, where well-defined spectra are obtained. It becomes difficult to identify the peak at powers above  $-5$  dBm, where the spectra are severely broadened and distorted. On the other hand, in our theoretical study on the nonlinear imaging method UFM, we showed that the demodulation effect becomes significant only at powers higher than  $P_D$ . Moreover, it was found that above the threshold power  $P_D$  the tip is pulled off from the sample surface, overcoming the adhesion force  $F_c$ . Therefore, the nonlinear effect responsible for the demodulation depends not only on the elasticity but also on the adhesion force, bringing another complexity into play.

The images obtained in the demodulation or the mechanical diode mode are sometimes very clear and sensitive to variation of material properties or to the existence of subsurface defects. However, it is difficult to extract quantitative information from these nonlinear modes because the nature of the tip-sample contact is quite complex

at large amplitude vibration under the adhesion force, as discussed above. Further study is needed on this subject.

### 6.2.2.5 Useful Nonlinear Spectra

Although nonlinearity is usually an obstacle for reliable measurement, nonlinearity might be useful for some kinds of measurements. Which are employed in difficult objects where other method using linear measurement is not available. In macroscopic ultrasonics, the typical object is closed cracks or delaminations [16]. In UAFM, dislocations in graphite is most clearly characterized not only by linear but also by nonlinear spectra [12, 14, 15]. Though dislocation observation had been for academic interests when it was first reported, it may help diagnosis of recent graphene devices.

In Fig. 6.7, origin of the linear and nonlinear spectra at a subsurface gap is illustrated [15, 21]. First, note that the load acting on the contact area between the UAFM tip and sample is the sum of the static load and the vibration force. In terms of these two forces, the behavior of a subsurface gap is classified into three cases as shown in Fig. 6.7a–c. Solid lines represent the tip position and the gap deformation due to the static load and dotted lines represent those due to the vibration force.

Figure 6.7d shows the contact stiffness as a function of tip position. Thick solid and broken lines represent the contact stiffness at defect-free areas and defect areas, respectively. Broken arrows indicate the vibration of the tip position, and the open circle shows the average position in the case of Fig. 6.7c. When the gap is sufficiently wider than the vibration amplitude of the tip, the gap is not closed during the vibration (Fig. 6.7a). When the gap is slightly wider than the static displacement of the tip, the gap is not closed by static displacement but by the increasing load period of the vibrations (Fig. 6.7b). Since the contact stiffness increases as the gap is closed (Fig. 6.7d), it is called a stiffening nonlinear spring and may be called the ‘subsurface tapping mode’. On the other hand, when the gap is narrower than the static displacement, it is closed by static displacement but opened during the decreasing load period of the vibrations (Fig. 6.7c). Since the contact stiffness decreases as the gap is opened, it is called a softening nonlinear spring. It is similar to the typical behavior at the pull off, so it may be called the ‘Subsurface pull off’.

This type of nonlinear vibration can be analyzed by a number of different approaches. But, in this work we adopt the simplest approach using the Duffing equation for a nonlinear vibration, since it gives a simple analytic solution for the stiffening or softening stiffness during vibration. The Duffing equation is given by

$$\ddot{\zeta} + \Gamma\dot{\zeta} + \chi_1\zeta + \chi_3\zeta^3 = \zeta_E\sqrt{\Omega^2 + \Gamma^2}\cos\Omega\tau, \quad (6.8)$$

where  $\zeta$  is the tip displacement,  $\tau$  is time,  $\Gamma$  is a damping coefficient,  $\chi_1$  is a linear stiffness coefficient,  $\chi_3$  is a nonlinear stiffness coefficient,  $\zeta_E$  is an excitation amplitude,  $\Omega$  is an excitation frequency. All quantities are dimensionless. The positive  $\chi_3$

represents the stiffening spring and the negative  $\chi_3$  represents the softening spring. For the harmonic vibration, since the fundamental frequency component having the period  $2\pi/\Omega$  predominates over the higher harmonics, the periodic solution takes the form

$$\zeta = \zeta_1 \sin \Omega\tau + \zeta_2 \cos \Omega\tau. \quad (6.9)$$

Substituting Eq. (6.9) into Eq. (6.8), and equating the coefficient of the terms containing  $\sin \Omega\tau$  and  $\cos \Omega\tau$  separately to zero yields

$$\left[ \left( \Omega^2 - \chi_1 - 3/4\chi_3\zeta_0^2 \right)^2 + \Omega^2\Gamma^2 \right] \zeta_0^2 = \zeta_E^2 \left( \Omega^2 + \Gamma^2 \right), \quad (6.10)$$

where  $\zeta_0^2 = \zeta_1^2 + \zeta_2^2$ .

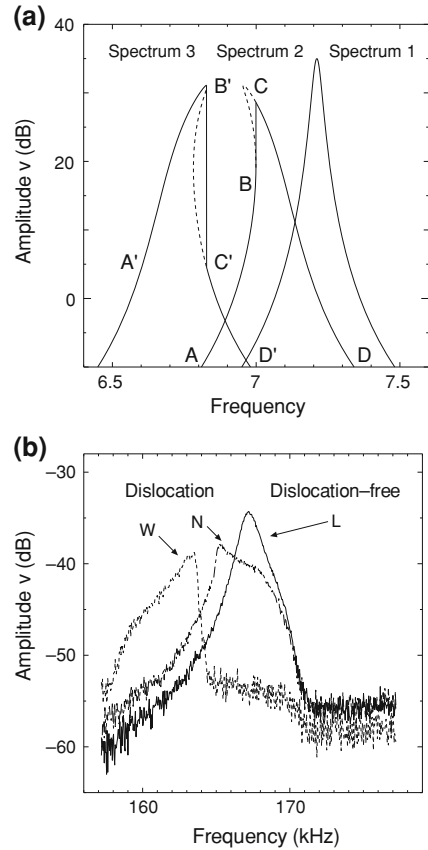
Figure 6.8a shows calculated spectra for the Duffing oscillator, where frequency is gradually increasing. Parameters are chosen so as to qualitatively reproduce the measured spectra at the subsurface dislocation in graphite shown in Fig. 6.8b where  $k_c = 4.6\text{N/m}$  and  $f_0 = 38.2\text{kHz}$ .

Spectrum 1 is a linear spectrum with  $\chi_3 = 0$  ( $\chi_1 = 52.0$ ,  $\zeta_E = 0.3$ ,  $\Gamma = 0.04$ ). The linear spectrum is symmetric with regard to the peak frequency. Spectrum 2 is a nonlinear spectrum with  $\chi_3 = -0.9$  ( $\chi_1 = 50.0$ ,  $\zeta_E = 0.3$ ,  $\Gamma = 0.05$ ), representing the softening spring since the peak is shifted to a lower frequency owing to the third-order term. Spectrum 3 is a nonlinear spectrum with  $\chi_3 = 0.9$  ( $\chi_1 = 45.0$ ,  $\zeta_E = 0.3$ ,  $\Gamma = 0.05$ ), representing the stiffening spring. The behavior is the opposite of the situation in spectrum 2 and the peak is shifted to a higher frequency. Branches represented by dashed lines are unstable solutions, which cannot be realized physically. The softening spring can be explained by the gap behavior shown in Fig. 6.7c and the stiffening spring is explained by the gap behavior shown in Fig. 6.7b.

Figure 6.9 shows the observation of the subsurface edge dislocation in a highly oriented pyrolytic graphite (HOPG) crystal where  $k_c = 2.4\text{N/m}$  and  $f_0 = 28\text{kHz}$ . Figure 6.9a is the topography showing small depression due to subsurface stacking fault. Figure 6.9b is an UAFM image showing a pair of dislocations. Figure 6.9c is a schematic illustration showing narrow and wide gaps with respect to the tip vibration amplitude ( $\sim 0.1\text{nm}$ ).

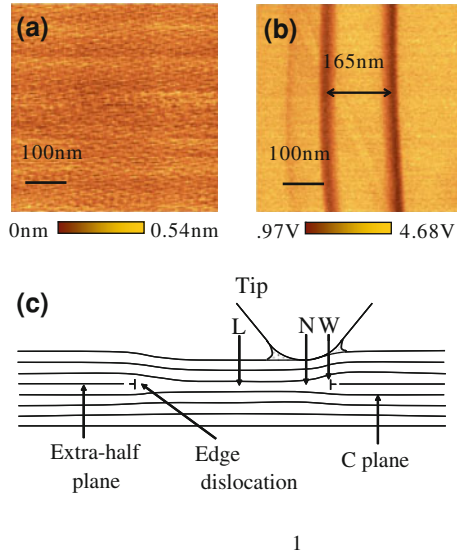
Figure 6.8b shows the resonance spectra measured at the positions L, N, and W of the images in Fig. 6.9c. Spectrum L is symmetric with regard to the peak. However, spectrum N shows the peak shifted to a lower frequency and W shows the peak shifted to a higher frequency. The essential features of these spectra are reproduced by the calculated spectra shown in Fig. 6.8a. Therefore, it has been proved that the nonlinear analysis was reasonable and the gap under position W was an open gap, given in Fig. 6.7b and that under position N was a closed gap given in Fig. 6.7c. For more rigorous analysis of nonlinear vibration, the theory of contact acoustic nonlinearity in the field of nonlinear ultrasonic nondestructive evaluation may be applied.

**Fig. 6.8** Nonlinear cantilever vibration. **a** Spectra calculated using Duffing nonlinear vibration equation. **b** Related experimental observation (see Fig. 6.9)



More practical example of nonlinear spectra is found in microelectronic devices [19–21]. A chromium (Cr) electrode was fabricated on a lead magnesium niobate–lead titanate ( $0.65 \text{ Pb}(\text{Mg}_{1/3}\text{Nb}_{2/3})\text{O}_3 - 0.35 \text{ PbTiO}_3$ , PMN–PT) substrate using the lift-off process. Figure 6.10 was obtained using the cantilever with  $k_c = 5.0 \text{ N/m}$  and  $f_0 = 36.1 \text{ kHz}$ . The topography of an area on the edge of an electrode shows a thickness of 240 nm in Fig. 6.10a. In the UAFM resonance frequency image shown in Fig. 6.10b, the darker area had lower resonance frequency, indicating lower contact stiffness. The low frequency region was probably due to delamination. To confirm this, spectra were measured at positions A, B, C, and D in Fig. 6.10b. The peak frequency decreased from A to D, indicating a decrease in contact stiffness. Moreover, asymmetric shapes of spectrum B and C indicate the contact vibration of the gap, typically predicted by the calculated spectra of Fig. 6.8a.





1

**Fig. 6.9** Edge dislocation of HOPG crystal. **a** Topography showing small depression due to subsurface stacking fault. **b** UAFM image showing a pair of dislocation. **c** Schematic illustration showing narrow and wide gaps with respect to tip vibration amplitude ( $\sim 0.1$  nm)

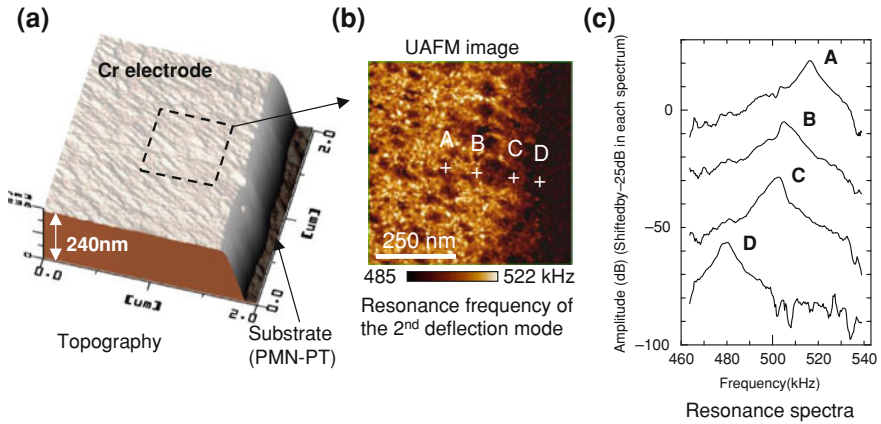


**Fig. 6.10** Observation of subsurface delamination of Cr electrode. **a** Topography of Cr electrode deposited on substrate with thickness of 240 nm. **b** UAFM resonance frequency image in second deflection mode. **c** Spectra measured at positions A to D

### 6.2.3 Quantitative Evaluation of Elasticity

When and only when the linear spectra are obtained, quantitative evaluation of elasticity becomes feasible [10].

**Fig. 6.11** Spectra of three different materials : glass, GL; graphite (HOPG), GR; polystyrene, PS

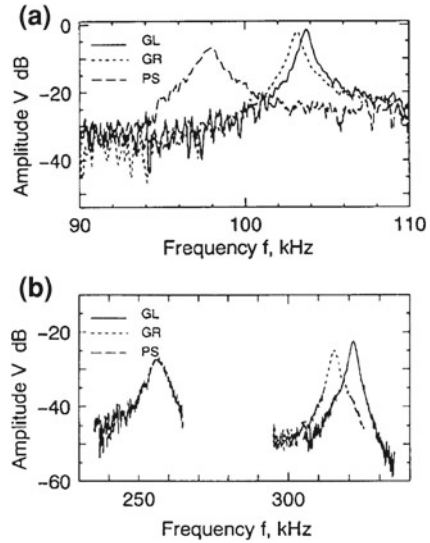
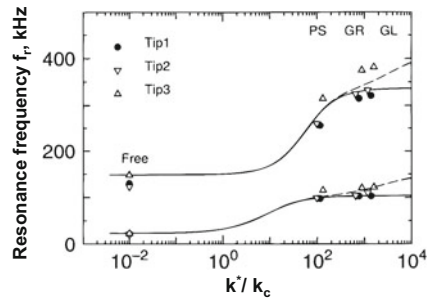


**Fig. 6.12** Calculated and measured resonance frequency as a function of relative contact stiffness over the cantilever stiffness



The linear spectra of three different materials (soda-lime glass, GL; graphite, GR; polystyrene, PS) are presented in Fig. 6.11. Figure 6.11a represents the first resonance (such as in Fig. 6.1b) and Fig. 6.11b the second resonance (Fig. 6.1c). Both spectra of different materials are separated according to the difference in contact stiffness, but the second resonance has better separation due to the effective stiffening by inertia and the formation of nodes as predicted in the reference 8. The peak frequency  $f$  of each spectra together with the free resonance frequency are plotted in Fig. 6.12 against the contact stiffness  $k^*$  normalized by the lever stiffness  $k_c$ . The contact stiffness was estimated by using the approximated equation (Eq. 6.7). For estimation of the contact radius, the tip was imaged using a porous silicon sample with remaining sharp silicon crystals within it. The contact radius  $a_c$  was estimated to be 20 nm. More precise estimation of the contact radius is presented in a later section.

The calculated resonance frequency, assuming  $E = 169 \text{ GPa}$ ,  $\rho = 2.3 \times 10^3 \text{ kgm}^{-3}$  and using Eq. (6.7), is also plotted by the solid curve in Fig. 6.12. The

agreement between measured and calculated frequencies is acceptable. Because the agreement for tip 3 at a large value of  $s_v/k$  was rather poor, we examined the effect of lateral stiffness by Eq. (6.5) and the ratio  $r = 0.8$ . The angle  $\varphi$  was assumed to be zero. The agreement was then improved as shown by dotted curve and it is shown that quantitative evaluation of the sample contact stiffness is thus possible using the linear theory of UAFM and linear spectra. We may conclude that the ‘linear’ spectra really reflect the linear tip-sample contact described by linear theory. In contrast, under conditions where the resonance frequency and  $Q$  factor vary as the excitation power varies, we have a certain kind of nonlinearity. Such nonlinear spectra should not be used in quantitative analysis. The nature of nonlinear spectra have been discussed in Sect. 6.2.2.3.

### 6.2.4 Frequency-Stiffness Relation Depending on the Type of Differential Equation

In the preceding part of this chapter, we assumed that the vibration is deflection mode shown in Fig. 6.13a. The deflection vibration of a cantilever in the  $x - z$  plane is expressed as

$$\rho A \frac{d^2 z}{dt^2} + EI \frac{d^4 z}{dx^4} = 0 \quad (6.11)$$

where  $E$  is Young’s modulus,  $\rho$  is the density,  $A$  is the cross-section and  $I$  is the area moment of inertia.

However, Eq. (6.11) has a rather special property that the spatial derivative of  $x$  is in fourth order. This property brings important feature of stiffness enhancement at higher order modes. To show this, it is useful to study another type of differential equation of torsional vibration shown in Fig. 6.13b excited by a transducer attached to a cantilever base. It was introduced into the field of this book in 1998 as lateral UAFM [9], followed by later publications (e.g. [24, 25]). The equation of motion for the torsional vibration is

$$\rho J_P \frac{\partial^2 \theta}{\partial t^2} - C_t \frac{\partial^2 \theta}{\partial x^2} = 0 \quad (6.12)$$

where  $\theta(x, t)$  is torsional angle,  $J_P$  is polar moment of inertia and  $C_t$  is torsional rigidity of the cantilever. Note that the spatial derivative of  $x$  is in second order.

For a rectangular cantilever,  $J_P = a^3 b/12$  and  $C_t = (1/3)G a b^3 (1 - 0.63b/a)$  where  $G$  is the shear modulus. The solution to (6.12) is given by

$$\theta(x, t) = \left( C_1 \cos \frac{\omega}{b} x + C_2 \sin \frac{\omega}{b} x \right) (A \cos \omega t + B \sin \omega t), \quad (6.13)$$

where  $b = \sqrt{C_t/(\rho J_P)}$ . The boundary condition at  $x = 0$  is  $\theta = 0$  (no torsion). If we assume that the tip stick to the sample and there is no slip, the boundary condition at  $x = L$  is  $C_t \partial \theta / \partial x = F_{//} h$  (balance of the torsional moment) where  $F_{//}$  is the lateral force exerted on the cantilever by the sample and  $h$  is the height of tip. Since the lateral displacement of the tip is  $h\theta$ , the lateral force is given by  $F_{//} = -k_{\text{Lat}}^* h\theta$ , where  $k_{\text{Lat}}^*$  is the shear stiffness of contact of the tip and sample. Substituting the solution of (6.13) into the boundary conditions, we obtain a frequency equation,

$$C_t \frac{\omega}{b} \cos \frac{\omega}{b} L_1 + h^2 k_{\text{Lat}}^* \sin \frac{\omega}{b} L_1 = 0. \quad (6.14)$$

A typical relation between the resonance frequencies of the first three modes and the ratio of shear stiffness  $k_{\text{Lat}}^*$  and cantilever torsional rigidity  $C_t$  is plotted in Fig. 6.14b. It is interesting to note that the resonance frequency of the three modes changes in almost the same range of  $\log(L_1 h^2 k_{\text{Lat}}^* / C_t)$  between  $-1$  to  $2$ . This is in contrast to the deflection vibration (Fig. 6.14a, where the range of  $\log(k^*/k_c)$  producing resonance frequency shift differs among the different modes. It is worthwhile mentioning here that it is not easy to establish the no-slip contact of the tip and sample, but it may be realized by increasing the normal force and monitoring the phase of the cantilever torsional vibration as the sample is laterally vibrated.

If the resonance frequency is measured,  $k_{\text{Lat}}^*$  is obtained from (6.14) as

$$k_{\text{Lat}}^* = -\frac{C_t \omega L_1}{L_1 h^2} \sqrt{\frac{\rho J_P}{C_t}} \cot \left( \sqrt{\frac{\rho J_P}{C_t}} \omega L_1 \right). \quad (6.15)$$

At first sight, (6.15) gives negative-stiffness  $k_{\text{Lat}}^*$ , but the angular resonance frequency is allowed only in the range where the cotangent term on the right-hand side is negative and hence  $k_{\text{Lat}}^*$  is always positive. The shear stiffness  $k_{\text{Lat}}^*$  is related to the shear moduli and Poisson's ratio of both tip and sample and the contact radius  $a_c$ . Since we have other two equations connecting the elastic constants, that is,  $K^* = [(1 - \nu_T^2)/E_T + (1 - \nu_S^2)/E_S]^{-1}$  and  $G_S = E_S/2(1 + \nu_S)$ , we have three equations for three unknown constants  $E_S, G_S$ , and  $\nu_S$ . Then, these constants can be uniquely determined from measurements of  $k^*$  and  $k_{\text{Lat}}^*$ . The feasibility of this approach will be investigated in a future work.

Although perfect determination of vertical and lateral stiffness is a difficult task, the simultaneous measurement of deflection and torsional vibration is the first step for this goal. The benefit of simultaneous measurement of deflection and torsional vibration is appreciated in this respect.

As an illustrative example, evaluation of defects on machined surface is shown. At ten different points on the surface of a machined silicon surface ground with a diamond wheel, second-order deflection, and first torsional spectra were recorded as in Fig. 6.15. General trends are noticed: when the deflection resonance frequency is low, the torsional resonance frequency is also low; when the deflection resonance frequency is high, the torsional resonance frequency is also high. This result shows

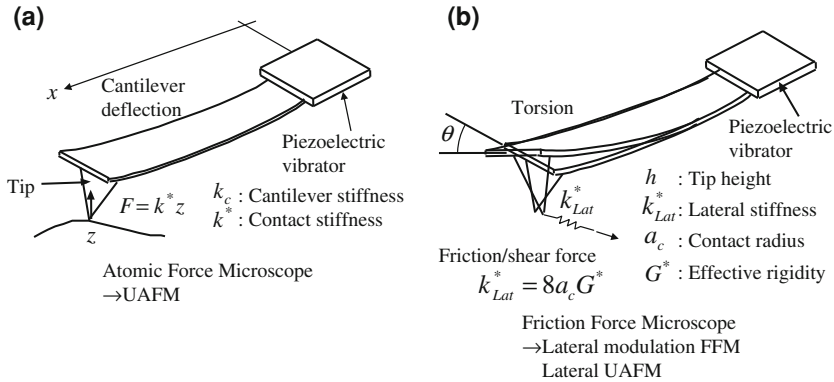


**Fig. 6.13** Different mode of vibration in scanning probe acoustic microscopy (a) Deflection mode (b) Torsional mode (lateral UAFM)

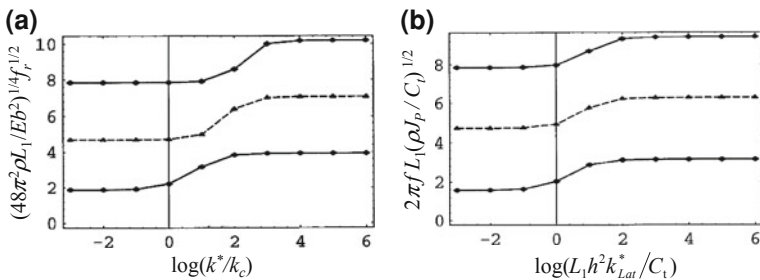


**Fig. 6.14** Relation between resonance frequency and stiffness of sample. **a** Normalized resonance frequency of deflection resonance as a function of the relative contact stiffness of sample  $\log(k^*/k_c)$ . **b** Normalized resonance frequency  $2\pi f L_1 / b$  of torsional vibration as a function of the relative shear stiffness of sample  $\log(L_1 h^2 k_{Lat}^* / C_t)$

that when the vertical stiffness is reduced due to machining damage, the lateral stiffness is also reduced, which implies that the damage is rather isotropic, probably due to averaging of numerous small defects.

Another possible reason for the variation of resonance frequency is the effect of sample tilt, as theoretically predicted by Eq. (6.4). However, although a tilt in a particular direction does not always shift the deflection and torsional resonance to the same direction, the measured resonance frequency was usually shifted to the same direction. Therefore, the effect of tilt is not so dominant as the reduction of stiffness, in the present case. This conclusion can only be derived by simultaneous measurement of deflection and torsional vibration.

Moreover, because the tilt can be measured in AFM from the topographic data, there is in principle a way to compensate for the effect of tilt on the variation of resonance frequency. To demonstrate experimentally the possibility of this approach,

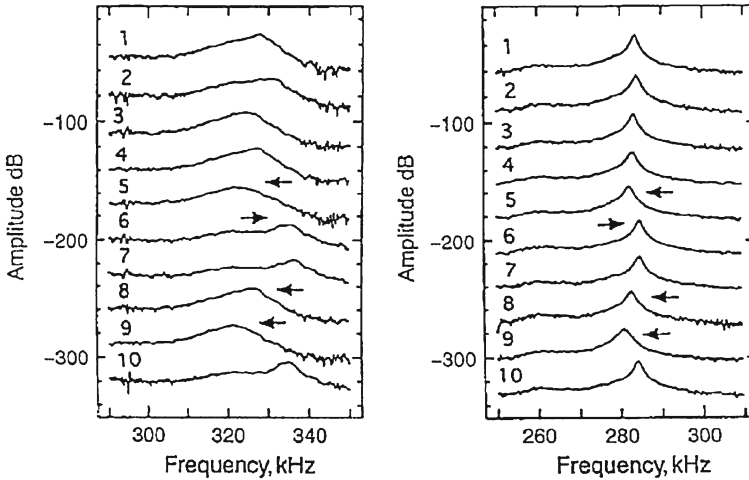


**Fig. 6.15** Deflection (*left*) and torsional (*right*) spectra of a cantilever with the tip in contact with ten different points on a ground silicon wafer

the reliability of experiment should be enhanced by using the improved measurement and analysis described in the previous sections.

## 6.3 Instrumentation

### 6.3.1 Possibility of Large Sample Stage

Figure 6.16 shows an implementation of UAFM based on a contact mode AFM. A high frequency vibrator attached to the cantilever base is driven in the high frequency range of 50 kHz to 10 MHz. Resultant vibration of the cantilever is detected by a photodiode and processed by using a lock-in amplifier, network analyzer or a special phase-locked loop (PLL) circuit. Linear and nonlinear detection schemes are employed. In the linear detection scheme, the high frequency signal is measured at the same frequency. In the nonlinear scheme, the high frequency signal is amplitude-modulated by a low frequency signal in the frequency range of 1 to 10 kHz. Instead of the high frequency signal, the low frequency signal is measured. The advantage of nonlinear scheme is that we can use commercial AFM without modification. Moreover, use of low frequency signal is favorable for achieving a high signal to noise ratio. However, the analysis is not simple and precise. Further comparison between these two modes has been discussed in Sect. 6.2.2.4.

Since we directly vibrate the cantilever in UAFM, it is similar to the noncontact (NC) mode and tapping mode AFM. However, the use of higher mode is unique

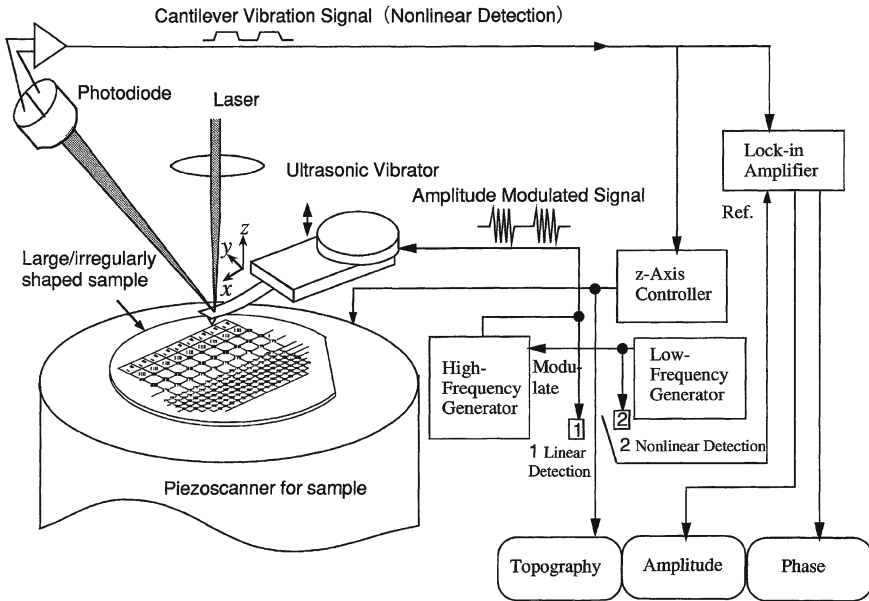


Fig. 6.16 An implementation of UAFM [8]

to UAFM. Also, we use very low vibration amplitude of less than 1 nm, so that we can control the contact force to a very low level of less than 0.1 nN. Finally, it is emphasized that there is no problem in the inspection of large samples (e.g. silicon wafers for VLSI) and irregularly shaped samples (e.g. turbine blades or magnetic disk heads), since the tedious transducer bonding to the samples is not required.

### 6.3.2 Suppression of Spurious Vibration

To improve the precision of dynamic AFM using cantilever vibration spectra, a simple but effective method for suppressing spurious response (SR) was developed. The dominant origin of SR was identified to be the bending vibration of the cantilever substrate, by the analysis of the frequency of SR.

Here, we show a convenient method for clamping the displacement of the base, where the bending rigidity of the base is enhanced by gluing a rigid plate (clamping plate: CP) to the base for the suppression of SR. The purpose of this method is not a shift of SR to higher frequencies but significant reduction of SR amplitude. Figure 6.17 shows a cantilever chip onto which a Si wafer as the CP is glued with epoxy adhesive (CP chip). The CP chip can be used with an ordinary cantilever holder.

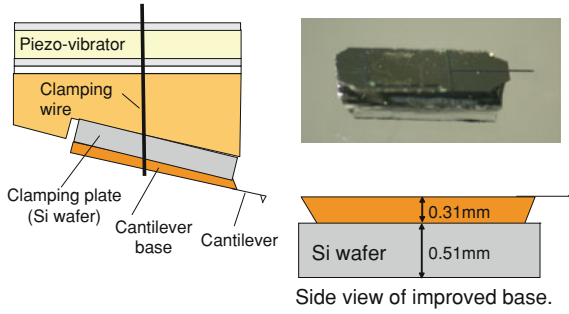


Fig. 6.17 Clamping plate (CP) for suppressing of SR

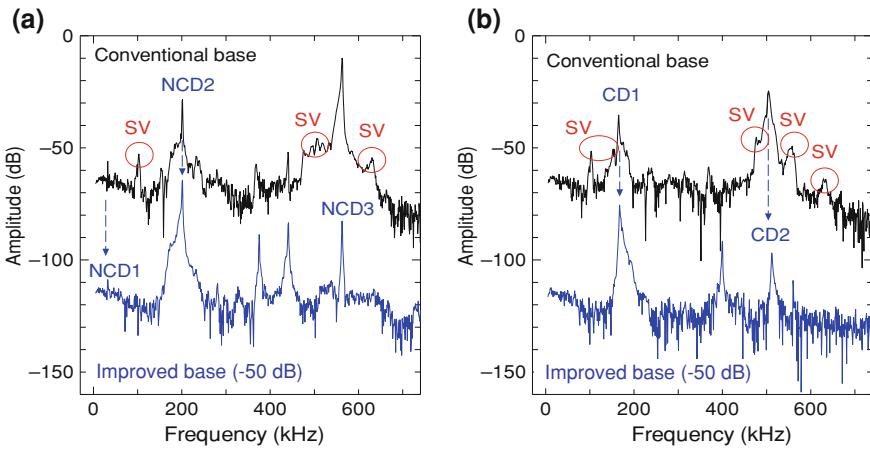


Fig. 6.18 Improvement of spectra by CP, **a** non-contact, **b** contact on Si wafer (100)

Figure 6.18 shows a set of spectra measured under the NC and contact conditions. In these figures, black curve shows spectra using the as-purchased chip and blue curve shows the CP chip, where the latter is shifted by  $-50$  dB. It was found that the response  $S$  was suppressed by the CP. Therefore, the enhancement of the bending rigidity of the base by using the CP is proved to be useful for the suppression of SR. This method is more convenient than the first method using the rigid cover, since an ordinary cantilever holder can be used here.

Successive NC spectra of the first deflection (NCD1) mode obtained to investigate the reproducibility when attaching and detaching the cantilever chip to the holder. It was shown that the reproducibility of SR suppression was sufficiently high. It was also found that the method with the CP was more effective than the method with the trenches [26], considering that the reproducibility of the former method was significantly higher than that of the latter method. It is noted that the same effect of the CP is achieved by fabricating base with a thicker plate than that used for ordinary cantilever chips.



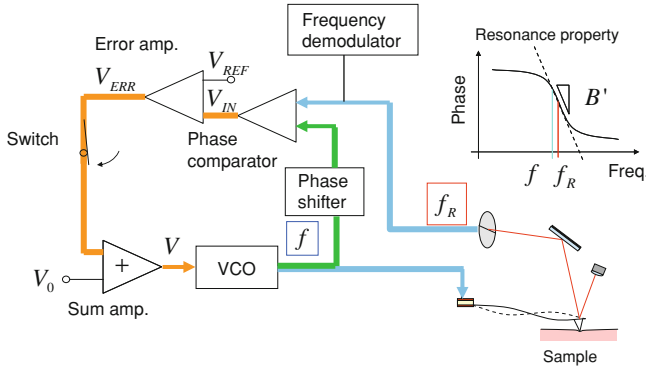


Fig. 6.19 Phase-locked loop circuit for the mapping of resonance frequency and Q factor

### 6.3.3 Electronics for Resonance Frequency Tracking and Q Factor Mapping

In the present instrumentation, the mapping of resonance frequency and Q factor is realized by the PLL circuit depicted in Fig. 6.19, where the cantilever vibration is excited by a voltage-controlled oscillator (VCO) [13, 27]. The input voltage  $V$  of the VCO is adjusted to realize resonance when the tip is in contact with the sample. Then, the cantilever deflection signal detected by the photodiode (PD) is split into two parts and one part is low-pass-filtered (LPF) to control the  $z$  position of the sample. The other part is band-pass-filtered (BPF) and its phase is compared with that of the VCO output signal. The phase difference between them is adjusted with a variable phase shifter  $\phi$  to equate the phase comparator output  $V_{IN}$  to a reference voltage  $V_{REF}$ .

After connecting the switch, we start raster scanning of sample. If the resonance frequency is changed, the phase signal is also changed. Then, the output  $V_E$  of the error amplifier caused by the phase change is added to the VCO input in order to recover the resonance. In this manner, the cantilever is always vibrated at the resonance frequency and the vibration amplitude represents the Q factor.

Whereas the resonance frequency tracking described above is similar to that of the frequency modulation mode of noncontact AFM (NC-AFM), the vibration amplitude of the cantilever is quite different. Although it is very large ( $> 10$  nm) in NC-AFM, it should be small ( $< 1$  nm) in UAFM, in order to keep the tip always in linear contact with the sample, namely the contact stiffness  $k^*$  should not deviate from its static value. Thus, we should control carefully the driving power of the cantilever in UAFM. To determine the optimum driving power, we monitor the vibration spectrum and find the largest possible power where the spectrum still remains symmetrical and sharp, immediately before becoming asymmetrical and broad. Thus, both a good signal-to-noise ratio and linear contact are realized.

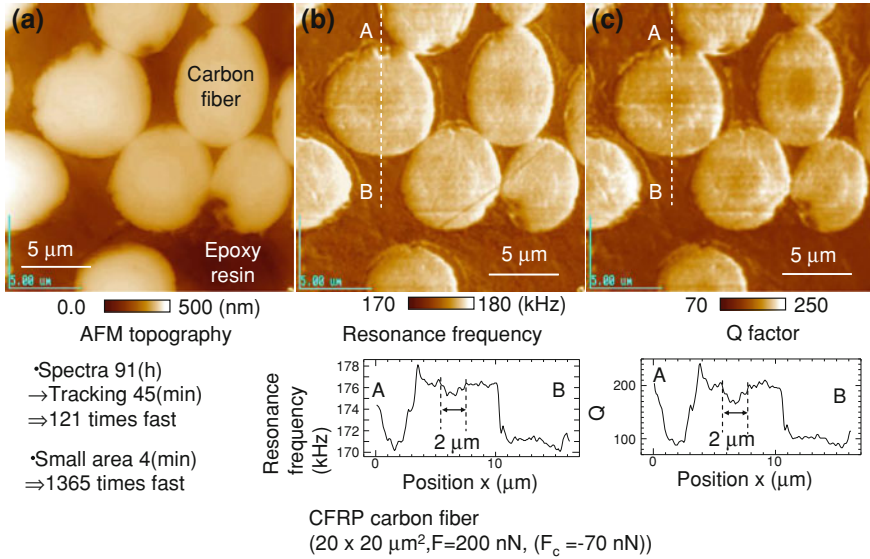


Fig. 6.20 Images of carbon fiber and epoxy resin in a CFRP

## 6.4 Illustrative Examples

### 6.4.1 Heat Treatment of Advanced Carbon Fiber for Reinforced Plastics

As an application, we show images of a carbon fiber and epoxy resin in a carbon fiber reinforced plastics (CFRP) in Fig. 6.20, at a contact force of 200 nN including an adhesion force  $F_c$  of  $-70 \text{ nN}$ , using a diamond-coated silicon tip. The cantilever had a stiffness of  $5 \text{ N/m}$  and length of  $450 \mu\text{m}$  [13]. The vibration amplitude and phase are determined by the measurement of spectra, when the piezoelectric transducer at the base of the cantilever was driven at a power of  $-35 \text{ dBm}$  ( $10^{-3.5} \text{ mW}$ ). The resonance frequency increased from  $38.5 \text{ kHz}$  at free resonance to  $176 \text{ kHz}$  for the carbon and  $171 \text{ kHz}$  for the epoxy. The Q factors were  $180\text{--}200$  for the carbon and  $100\text{--}110$  for the epoxy. The peak for both the carbon and epoxy had a symmetrical shape, indicating the linear contact stiffness at this driving power for the particular transducer used. It should be noted that we obtained the nonlinearity at power levels above  $-25 \text{ dBm}$ .

Figure 6.20b, c are the resonance frequency and Q factor images obtained at a contact force of 200 nN corresponding the topography in Fig. 6.20a. Conversion from the maximum peak height to the Q factor was experimentally performed using power spectra obtained at the carbon and epoxy area such as those shown in Fig. 6.3.

The measurement of spectra provides useful information, but it takes a long time (typically 5 s for one point for an average of 10 times). Consequently, mapping of the resonance frequency and Q factor takes a very long time ( $\sim 91$  h for a  $256 \times 256$  pixels image). On the other hand, the method using PLL circuit succeeded in mapping them in 45 min as shown in Fig. 6.20b, c. As a result, 121 times speeding up was attained. Moreover, more than 1,300 times speeding up was possible for smaller area.

The images Fig. 6.20b, c showed that epoxy was much softer and more viscous than the carbon. Within the carbon and epoxy areas, the brightness was almost uniform. However, we noted a small but reproducible variation within the carbon area. As shown in the frequency and Q factor profiles in Fig. 6.20 obtained along the vertical lines in Fig. 6.20b, c, the resonance frequency at the core was lower than that at the rim by 0.5–1 KHz. Similarly, the Q factor at the core was lower than that at the rim by 20–40. These differences are probably due to the radial difference in the degree of stabilization during heat treatment, an important parameter for achieving high strength.

### 6.4.2 *Extremely Soft Domain Boundary of Efficient Ferroelectric Materials*

The development of ferroelectric materials and devices has required the better understanding of not only the ferroelectric domain but also the ferroelectric domain boundary (DB) called domain wall. For example, the movement of ferroelectric and ferroelastic DB significantly enhanced the piezoelectric coefficient of the ferroelectric thin film. One of the origins of the polarization fatigue in ferroelectric thin film is the pinning of the movement of the ferroelectric DB.

The width of the DB was attributed in the order of 1–10 nm [28], which has been studied by several methods, such as the transmission electron microscopy [29], scanning nonlinear dielectric microscopy (SNDM) [30], and atomic force microscopy [31]. Although the SNDM may provide dielectric information, we believe that the mechanical information is also important because the piezoelectric deformation and the polarization switching are related to the mechanical behavior of the domain and the DB.

We reported an evidence of the reduction of the stiffness at the ferroelectric DB in a lead zirconate titanate ( $\text{Pb}(\text{Zr}_x, \text{Ti}_{1-x})\text{O}_3$ , PZT) ceramic [17, 18]. We observed ferroelectric domains in PZT ceramics by the 2D mapping of the resonance frequency.

For imaging the ferroelectric domains, piezoresponse force microscopy (PFM) was used [32]. Commercially available bulk PZT ceramics were investigated (sample 1: NEC Tokin Cooperation N-21, sample 2: Fuji Ceramics Cooperation C-82). Sample 1 was an unpoled material. Because sample 2 was a poled material, it was annealed in order to obtain random domain configuration. These were lapped by diamond slurry and polished by colloidal silica slurry and alumina paste for sample 1 and sample 2, respectively. They were glued to sample holders with silver paste. We

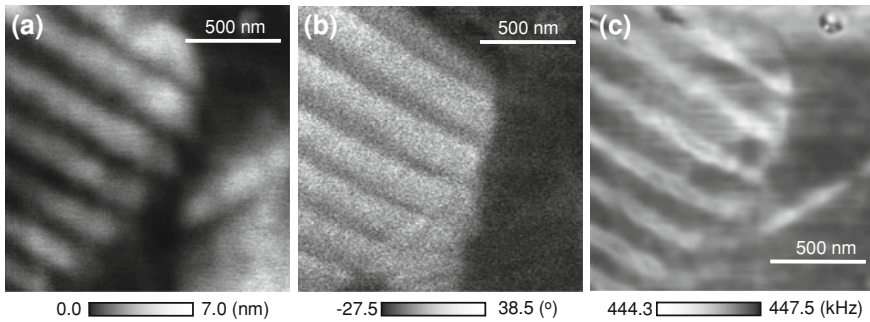


**Fig. 6.21** Observation of domains in a PZT

used an Au coated and a CVD diamond film coated Si cantilevers for sample 1 and sample 2, respectively, purchased from Nanosensor. We performed the experiments in ambient air at 23 °C with the relative humidity in the range of 40–60 %.

First, we show the applicability of the UAFM to the stiffness evaluation of the PZT. Figure 6.21(a) shows a contact AFM topography of an area of sample 1. Figure 6.21b shows a PFM image of the same area as Fig. 6.21a representing the phase shift of the deflection vibration to the AC voltage applied between the tip and the bottom electrode (PFM image). The frequency and the amplitude of the AC voltage were 4 kHz and 5 Vp-p, respectively. There was a stripe pattern with a period of 250 nm representing differently oriented domains. It may be 90° domain structure. Figure 6.21c shows a UAFM image representing the resonance frequency at the third deflection mode (UAFM image). Darker color represents higher resonance frequency, indicating higher contact stiffness. The stripe pattern in the UAFM image was related to the domains. As a result, it was demonstrated that the UAFM can evaluate the different elasticity due to the differently oriented domains of PZT. This is a result similar to Ref. [33].

After confirming the applicability of the UAFM to PZT, we now applied it to the evaluation of the stiffness at the DB. Figure 6.22a shows a topography of an area of sample 2 with the load  $F$  of 1,200 nN. Figure 6.22b shows a PFM image of the same area where the applied AC voltage was the same as that in Fig. 6.21b. Because uniformly bright and dark regions represent the ferroelectric domains, the boundaries between them represent the DBs. It may be 180° DBs because of the wavy shape. Although the phase difference was much less than 180°, it may be explained by the integral piezoelectric response due to randomly polarized grains stacked in the normal to the surface and the capacitive force between the cantilever and the bottom electrode. Figure 6.22c shows a UAFM image at the second deflection mode.

There were string-like structures showing lower resonance frequency. When we compare the same area surrounded by the dotted squares, we note that the string-like structures observed in Fig. 6.22c corresponded to the DBs observed in the PFM image, Fig. 6.22b. At the same time, it does not correspond to the edge of the surface relief because the edge is out of the zone surrounded by the dotted square in Fig. 6.22a.

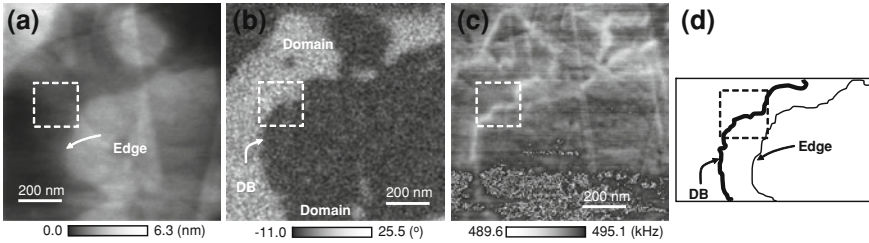


**Fig. 6.22** Images for the evaluation of the stiffness at the domain boundary (DB)

**Fig. 6.23** A bird’s-eye view of the zone surrounded by the dotted square shown in Fig. 6.22c

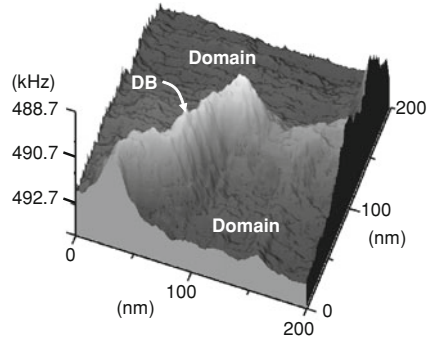


**Table 6.3** Variation in the stiffness of the DB normalized by that of domain,  $E_{DB}/E_D$ , depending on the half width of the DB,  $w$

$w$ (nm)	1	2	5	8.72
$E_{DB}/E_D$	0.179	0.587	0.826	0.880

The relation between the DB and the edge is illustrated in Fig. 6.2d. Therefore, it was verified that the string-like structures were the DBs and not topographic artifacts.

Figure 6.23 shows a bird’s-eye view of the zone surrounded by the dotted square shown in Fig. 6.22c. The apparent half width of the DB was in the range of 20–30 nm, which was widened due to finite contact area.

In order to obtain an insight into the nature of the DB based on the above observation, we analyzed the stiffness on the DB. The resonance frequency  $f_r = 492.7$  kHz within the domain gives the contact stiffness  $k^* = 1,305$  N/m, using cantilever vibration theory. When the load  $F$ , the Young’s modulus at the domain  $E_D$  and the Poisson’s ratio  $\nu$  are 1,200 nN, 117 GPa and 0.34, respectively, the tip radius  $R$  and the contact radius  $a_c$  are 55.1 and 8.72 nm, respectively, using Hertzian contact theory. When  $F, R, a_c$  are identical within the image,  $f_r = 489.7$  kHz on the DB gives the averaged Young’s modulus  $\bar{E} = 103$  GPa.

In order to evaluate the contribution of the Young’s modulus of the DB  $E_{DB}$  to the  $\bar{E}$ , we approximate the application of the stress in the experiment to that in the

unidirectional fiber-reinforced composite materials and apply the linear mixture law of the Young's modulus [34]. The averaged modulus  $\bar{E}$  is expressed by

$$\bar{E} = (1 - R_{\text{DB}}) E_D + R_{\text{DB}} E_{\text{DB}}, \quad (6.16)$$

where  $E_D$  and  $E_{\text{DB}}$  are the Young's moduli of the domain and the DB and  $R_{\text{DB}}$  is the area ratio of the DB to the total contact, respectively. The  $R_{\text{DB}}$  is expressed by

$$R_{\text{DB}} = \frac{2}{\pi} \left\{ \frac{w_{\text{DB}}}{a_c} \sqrt{1 - \left( \frac{w_{\text{DB}}}{a_c} \right)^2} + \frac{\pi}{2} - \arccos \frac{w_{\text{DB}}}{a_c} \right\}, \quad (6.17)$$

where  $w_{\text{DB}}$  is the half width of the DB. We estimated the stiffness of the DB normalized by that of the domain,  $E_{\text{DB}}/E_D$ , for 4 different values of  $w_{\text{DB}}$  as listed in Table 6.3. As a result, we found, for the first time, that the stiffness at the DB is much lower than that of the domain when we assume that the width of the DB is smaller than the calculated contact radius (8.72 nm). As shown in Table 6.3,  $E_{\text{DB}}/E_D$  is as low as 0.587 if  $w_{\text{DB}}$  is 2 nm.

Finally, we discuss possible explanations of this finding.

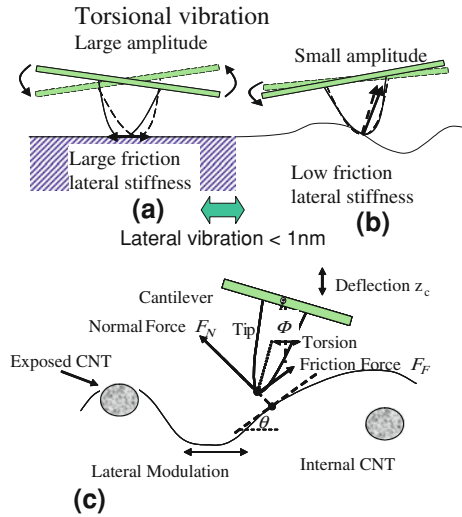
- (i) The disorder of the lattice at the DB; the imperfection of the crystal may reduce the stiffness.
- (ii) The ability of the switching of the domain; the switching accompanies the movement of the DB. It may be facilitated by the reduction of the stiffness at the DB because the polarization of the domain is constrained by the minimum state of the sum of the strain energy and the electrostatic energy. Therefore, the ability of the switching of the domain may reduce the stiffness.
- (iii) The reduction of the piezoelectric stiffening; when the polarization charge is not compensated during the application of the stress, the stiffness is enhanced because of the depolarization field (piezoelectric stiffening).

In the experiment of the UAFM, the polarization on the domain may lead to the piezoelectric stiffening, because the small contact area cannot compensate all polarization charge over the domain. On the other hand, because the spontaneous polarization of the lattice is rotated at the DB, the average polarization on the DB is smaller than that on the domain. As a result, the piezoelectric stiffening on the DB is smaller than that on the domain. Therefore, the reduction of the piezoelectric stiffening may reduce the stiffness.

We estimate the order of the reduction in the case of (iii), using the variation in stiffness coefficient  $c$  between the electrical conditions of the constant electric field and the constant electric displacement, represented by the superscripts of  $E$  and  $D$ , respectively [35]. The ratio of stiffness coefficients is expressed by

$$\frac{c^E}{c^D} = 1 - k^2, \quad (6.18)$$

**Fig. 6.24** Principle of LM–AFM. **a** High friction area **b** tilted area with low friction **c** CNT PS composite with curvature



where  $k$  represents the electromechanical coupling coefficient in the poling direction. When we use the coupling coefficient,  $c_{33}^E/c_{33}^D$  becomes 0.44 that is consistent with the result of  $E_{DB}/E_D=0.587$ .

### 6.4.3 Friction and Shear Elasticity on Surface Layer by Lateral Force Modulation

As explained in Sect. 6.2, UAFM has modes of deflection and torsion. Since the torsional stiffness of cantilever is usually comparable to that of shear stiffness of sample, lower frequency than resonance may be used for the shear stiffness evaluation. In this frequency range, vibration of sample is not difficult using standard scanner for the AFM raster scan. Therefore, a technique was developed as lateral force modulation LM–AFM [7], a closely related technique of UAFM [8]. It is useful for evaluation of friction and shear elasticity on surface layer.

Figure 6.24 shows the principle of LM–AFM where the sample is laterally vibrated at a frequency much lower than that of torsional resonance. As shown in Fig. 6.24a, a flat area with high friction leads to a small static angle  $\theta$  and a large vibration amplitude  $\Delta\theta$  of cantilever torsion when the sample is laterally vibrated. A tilted area with low friction shown in Fig. 6.24b leads to a large  $\theta$  and small  $\Delta\theta$ . Thus, when a conventional friction force microscopy (FFM) is used, it is difficult to precisely measure frictional force because of the curvature of the surface, as shown in Fig. 6.24c. However, the LM–AFM is not significantly affected by the local tilt angle  $\theta$  because it uses the vibration amplitude  $\Delta\theta$  of cantilever torsion to evaluate the friction.

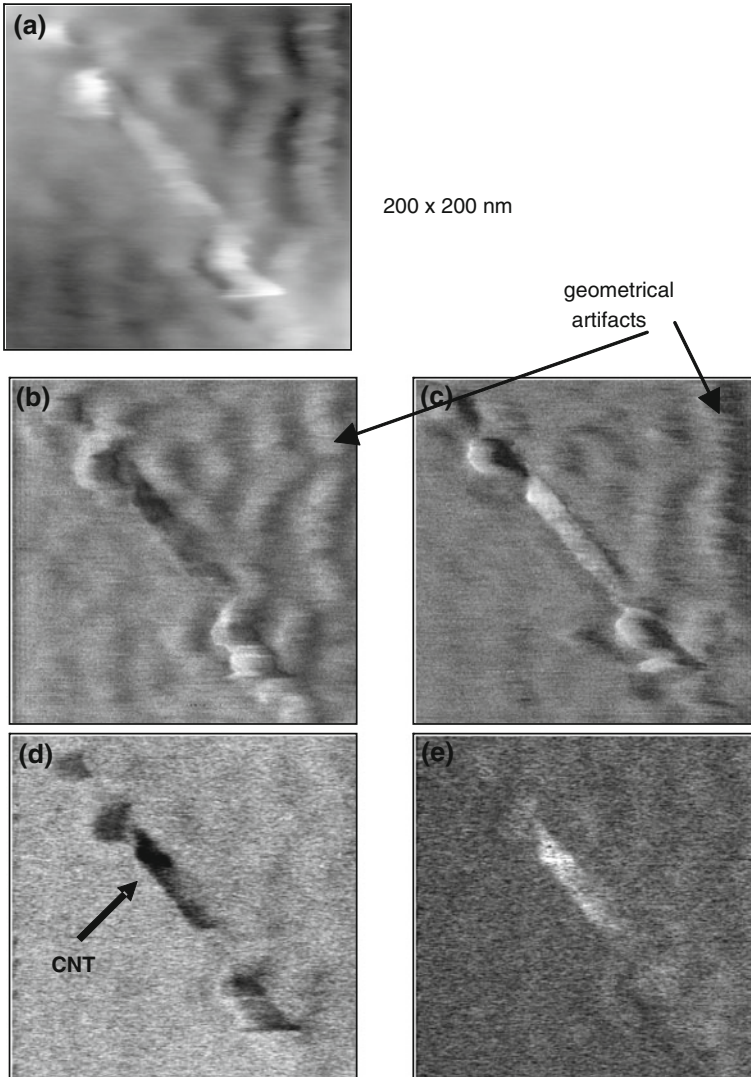


**Fig. 6.25** Observation of CNT on PS. CNT partially covered by PS. **a** Topography (0–18.9 nm). **b** FFM image of right scan. **c** FFM image of left scan. **d** LM-AFM amplitude image. **e** LM-AFM phase image

Figure 6.25 shows a carbon nanotube (CNT) PS (polystyrene) composite [21]. The CNT is emerging on a polystyrene (PS) matrix, a promising light-weight high-strength conductive material, whose section is illustrated in Fig. 6.24c. Figure 6.25a shows the topography of an area with embedded and partially exposed CNT. The



cantilever with  $k_c = 0.098 \text{ N/m}$  and  $f_1 = 11 \text{ kHz}$  was used. FFM images shown in Fig. 6.25b, c demonstrate geometrical artifacts of PS owing to the large tilt  $\theta$ .

A LM–AFM image of Fig. 6.25d demonstrates only CNT with lower friction or lateral contact stiffness. This feature of LM–AFM is useful for precise evaluation of magnetic recording instruments, lubricant on a medium, and contamination of engineering surfaces that are not necessarily atomically flat. For precise evaluation of lateral contact stiffness, the sliding of the tip needs to be suppressed. In LM–AFM, this has been achieved by monitoring the phase signal of torsion vibrations.

## 6.5 Conclusion

It was shown that the vibration spectra of UAFM and related techniques are strongly dependent on the excitation power of the cantilever vibration. The resonance peak width decreases and the peak frequency increases as the excitation power is reduced while the power is above a certain threshold level. Controlling the excitation power, we obtained linear spectra independent of the excitation power. Using the linear spectra, satisfactory agreement between the measured and calculated peak frequency was obtained by assuming a consistent tip–sample contact stiffness. Further improvement by taking into account the non-spherical tip shape will be described somewhere in this book using the Sneddon–Maugis formulation of contact elasticity, and the tip shape index was estimated by an inverse analyzes of load–frequency relation. Application to evaluation of vertical and lateral stiffness on a ground silicon wafer is described by the simultaneous measurement of deflection and torsional vibration.

## Appendix A

The deflection vibration of a cantilever is expressed in the  $x - -z$  plane as

$$\rho A \frac{d^2 z}{dt^2} + EI \frac{d^4 z}{dx^4} = 0 \quad (\text{A1})$$

where  $E$  is Young's modulus,  $\rho$  is the density,  $A$  is the cross-section and  $I$  is the area moment of inertia. In the case of a rectangular lever of width  $a$  and thickness  $b$ ,  $I = ab^3/12$ . At the end of the lever where  $x = L_1$ , the deflection of the lever  $z(x, t)$  produces a displacement of the apex of the tip of length  $h$  as  $[h(\partial z/\partial x), z]$  and the  $-z$  component of the shear force  $EI(\partial^3 z/\partial x^3)$  caused by the vertical (out-of-plane) contact stiffness  $k^*$  of sample is

$$F_v = k^* \left( -h \frac{\partial z}{\partial x} \sin \varphi \cos \varphi + z \cos^2 \varphi \right) \quad (\text{A2})$$

and the bending moment  $EI(\partial^2 z/\partial x^2)$  is

$$M_V = -hk^* \left( h \frac{\partial z}{\partial x} \sin^2 \varphi - z \sin \varphi \cos \varphi \right) \quad (\text{A3})$$

when the tip is in contact with the sample with oblique angle  $\varphi$  with respect to the  $x$ -axis. Similarly, those forces caused by the lateral (in-plane) contact stiffness  $k_{\text{Lat}}^*$  are

$$F_1 = k_{\text{Lat}}^* \left( h \frac{\partial z}{\partial x} \sin \varphi \cos \varphi + z \sin^2 \varphi \right) \quad (\text{A4})$$

and

$$M_1 = -hk_{\text{Lat}}^* \left( h \frac{\partial z}{\partial x} \cos^2 \varphi - z \sin \varphi \cos \varphi \right) \quad (\text{A5})$$

Then the boundary conditions at  $x = L_1$  are

$$EI \frac{\partial^3 z}{\partial x^3} = \hat{k}_V^* z + \hat{k}_{\text{LatV}}^* h \frac{\partial z}{\partial x} \quad (\text{A6})$$

$$EI \frac{\partial^2 z}{\partial x^2} = -\hat{k}_{\text{Lat}}^* h^2 \frac{\partial z}{\partial x} - \hat{k}_{\text{LatV}}^* h z \quad (\text{A7})$$

where  $\hat{k}_V^* = k^* \cos^2 \theta + k_{\text{Lat}}^* \sin^2 \varphi$ ,  $\hat{k}_{\text{Lat}}^* = k_{\text{Lat}}^* \cos^2 \varphi + k^* \sin^2 \varphi$  and  $\hat{k}_{\text{LatV}}^* = (k_{\text{Lat}}^* - k^*) \cos \varphi \sin \varphi$ . It is noted that if the vertical and lateral stiffness are identical ( $k^* = k_{\text{Lat}}^*$ ) then  $\hat{k}_{\text{LatV}}^* = 0$  and  $\hat{k}_V^* = \hat{k}_{\text{Lat}}^* = k^*$  and Eqs. (A6) and (A7) do not depend on the tilt angle  $\varphi$ . This is in contrast to Ref. [6] where  $\hat{k}_{\text{LatV}}^* = 0$  does not hold when  $\hat{k}_V^* = \hat{k}_{\text{Lat}}^*$ . Equation (6.4) is obtained by substituting a solution of Eq. (A1) into the boundary conditions (A6) and (A7).

## References

1. G. Binnig, C.F. Quate, Ch. Gerber, Phys. Rev. Lett. **12**, 930 (1986)
2. O. Kolosov, K. Yamanaka, Jpn. J. Appl. Phys. **32**, L1095 (1993)
3. K. Yamanaka, H. Ogiso, O. Kolosov, Appl. Phys. Lett. **64**, 178 (1994)
4. U. Rabe, W. Arnold, Ann. Physik **3**, 589 (1994)
5. U. Rabe, K. Janser, W. Arnold, Rev. Sci. Instrum. **67**, 3281 (1996)
6. M. Radmacher, R.W. Tillmann, H.E. Gaub, Biophys. J. **64**, 735 (1993)
7. K. Yamanaka, E. Tomita, Jpn. J. Appl. Phys. **34**, 2879 (1995)
8. K. Yamanaka, S. Nakano, Jpn. J. Appl. Phys. **35**, 3787 (1996)
9. K. Yamanaka, S. Nakano, Appl. Phys. A **66**, 313 (1998)
10. K. Yamanaka, A. Noguchi, T. Tsuji, T. Koike, T. Goto, Surf. Interface Anal. **27**, 600 (1999)
11. K. Yamanaka, U.S. Patent 6,006,593, 1999
12. T. Tsuji, K. Yamanaka, Nanotechnology **12**, 301 (2001)
13. K. Yamanaka, Y. Maruyama, T. Tsuji, K. Nakamoto, Appl. Phys. Lett. **78**, 1939 (2001)

14. T. Tsuji, H. Irihama, K. Yamanaka, *Jpn. J. Appl. Phys.* **41**, 832 (2002)
15. K. Yamanaka, T. Tsuji, H. Irihama, T. Mihara, *Proc. of SPIE* **5045**, 104 (2003)
16. K. Yamanaka, T. Mihara, T. Tsuji, *Jpn. J. Appl. Phys.* **43**, 3082 (2004)
17. T. Tsuji, H. Ogiso, J. Akedo, S. Saito, K. Fukuda, K. Yamanaka, *Jpn. J. Appl. Phys.* **43**, 2907 (2004)
18. T. Tsuji, S. Saito, K. Fukuda, K. Yamanaka, H. Ogiso, J. Akedo, K. Kawakami, *Appl. Phys. Lett.* **87**, 071909 (2005)
19. T. Tsuji, K. Kobari, S. Ide, K. Yamanaka, *Rev. Sci. Instrum.* **78**, 103703 (2007)
20. S. Ide, K. Kobari, T. Tsuji, K. Yamanaka, *Jpn. J. Appl. Phys.* **46**, 4446 (2007)
21. K. Yamanaka, K. Kobari, T. Tsuji, *Jpn. J. Appl. Phys.* **47**, 6070 (2008)
22. O. Wright, N. Nishiguchi, *Appl. Phys. Lett.* **71**, 626 (1997)
23. U. Rabe, J. Turner, W. Arnold, *Appl. Phys. A* **66**, S277 (1998)
24. M. Reinstadtler, T. Kasai, U. Rabe, W. Arnold, *J. Phys. D: Appl. Phys.* **38**, R269 (2005)
25. Y. Song, B. Bhushan, *J. Appl. Phys.* **99**, 094911 (2006)
26. J.D. Adams, D. York, N. Whisman, *Rev. Sci. Instrum.* **75**, 2903 (2004)
27. K. Kobayashi, H. Yamada, K. Matsushige, *Surf. Interface Anal.* **33**, 89 (2002)
28. M.E. Lines, A.M. Glass, *Principle and Applications of Ferroelectrics and Related Materials* (Clarendon, Oxford, 1977), p. 100
29. S. Stemmer, S.K. Streiffer, F. Ernst, M. Ruhle, *Philos. Mag. A* **71**, 713 (1995)
30. K. Matsuura, Y. Cho, R. Ramesh, *Appl. Phys. Lett.* **83**, 2650 (2003)
31. D. Shilo, G. Ravichandran, K. Bhattacharya, *Nat. Mater.* **3**, 453 (2004)
32. A. Gruverman, *Nanoscale Characterization of Ferroelectric Materials*, ed. by M. Alexe, A. Gruverman (Springer, New York, 2004)
33. U. Rabe, M. Kopycinska, S. Hirsekorn, J. Munoz Saldana, G.A. Schneider, W. Arnold, *J. Phys. D: Appl. Phys.* **35**, 2621 (2002)
34. S.K.U. Kuno, *Micromechanics of Composites* (Hanser, New York, 1996), p. 15
35. T. Ikeda, *Fundamentals of Piezoelectricity* (Oxford University Press, New York, 2004)

# Chapter 7

## Enhanced Sensitivity of AFAM and UAFM by Concentrated-Mass Cantilevers

Mikio Muraoka

**Abstract** The mechanical resonance of an atomic force microscopy (AFM) cantilever whose tip is in contact with a sample surface, namely the contact resonance, provides a measure of the local elasticity of a sample. It has been applied to measurements of the elastic modulus on a nanometer scale in dynamic AFM, such as atomic force acoustic microscopy (AFAM) and ultrasonic atomic force microscopy (UAFM). For stiff samples such as metals and ceramics, the contact stiffness between a tip and a sample is much larger than the stiffness of a cantilever, and thus the tip can hardly penetrate a sample. It results in a reduced sensitivity in the elasticity measurements. This chapter introduces a solution to the problem, that is the use of concentrated-mass (CM) cantilevers. We discuss the theoretical background of CM cantilevers in AFAM and UAFM to clarify the enhanced sensitivity and some advantages, and present some experimental results including the measurements of elastic modulus of thin films.

### 7.1 Introduction

It is well-known that when an atomic force microscopy (AFM) cantilever is driven to vibrate with small deflection amplitude, the presence of an interactive force  $F$  between a tip mounted on the cantilever and a sample surface, or more precisely the gradient  $dF/dz$ , modifies the resonant frequency [1]. When the force gradient is small, the vibration dynamics is approximately expressed with a point-mass model, and the fundamental resonant frequency of the cantilever is simply given by:

---

M. Muraoka (✉)  
Department of Mechanical Engineering, Akita University,  
1-1 Tegatagakuen-machi, Akita 010-8502, Japan  
e-mail: muraoka@gipc.akita-u.ac.jp

$$f_{\text{res}} = \frac{1}{2\pi} \sqrt{\frac{k_c - (dF/dz)_{z_e}}{m_{\text{eff}}}} = f_0 \sqrt{1 - \frac{(dF/dz)_{z_e}}{k_c}}, \quad (7.1)$$

where  $k_c$  and  $m_{\text{eff}}$  are the spring constant and effective mass of the cantilever, respectively. The coordinate  $z$  denotes a separation between the tip and sample, and  $z_e$  is its value at an initial equilibrium. If the sample exerts an attractive force on the tip with a positive force-gradient, the spring constant will effectively soften. As a result, the resonant frequency will decrease. Then the force gradient can be detected by measuring the amplitude, phase or frequency change of the vibration [1]. This is the principle of the so-called non-contact (NC) mode, which has been applied to magnetic-force or electrostatic-force imaging (e.g., [2, 3]).

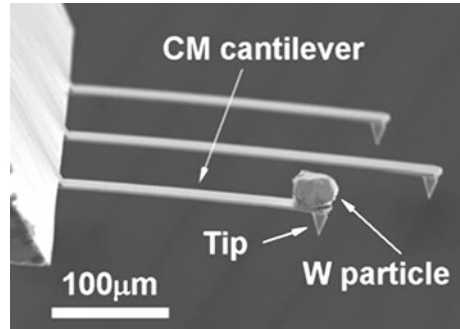
In contrast to the NC mode, where the tip is initially positioned away from a sample ( $z_e > 0$ ), let the tip be initially in contact with a sample ( $z_e < 0$ ). When the tip is driven to vibrate with amplitude small enough for linear vibration under the contact-mode operation, one can detect the contact stiffness  $k_V^*$ , which is defined as  $k_V^* = -(dF/dz)_{z_e}$ . The contact resonance is shifted to a higher frequency when the contact stiffness is larger, as expected from Eq.(7.1). Because the contact stiffness reflects the elastic modulus of the sample on the nanometer scale, one could determine the elastic modulus from measuring the contact resonant frequency. In 1996, the detection of elasticity was first achieved by sinusoidally modulating the position of the sample [4] and of the cantilever [5] at ultrasonic frequencies. The former and latter instrumentations are called atomic force acoustic microscopy (AFAM) and ultrasonic atomic force microscopy (UAFM), respectively. It is also noted that a scale-up version, i.e., micrometer-resolution version, had been reported, named scanning microdeformation microscopy (SMM) [6].

While the force gradient is significantly small in the case where the tip is separated from the sample, the contact stiffness normally takes large values. For stiff samples such as metals and ceramics, the normalized contact stiffness  $k_V^*/k_c$  reaches to around  $10^3$ . The relation of the resonant frequency ( $f_{\text{res}}$ ) versus contact stiffness ( $k_V^*$ ) drastically changes from the point-mass model that gives Eq.(7.1). The sensitivity of  $f_{\text{res}}$  to  $k_V^*$  is reduced because the vibration modes of a relatively soft cantilever tend to be in energetically low states where the tip can hardly penetrate a sample. To overcome the problem, the use of higher resonance modes of the cantilever is suggested, where effectively stiffening of the cantilever at higher modes improves the sensitivity to some extent [4, 5].

The nonzero tip height provides another difficulty in detecting the contact stiffness. The tip motion vertical to a sample surface is always accompanied by the rotational motion around the tip-mounted site of the cantilever. The resulting lateral motion of the tip apex increases with the tip height. Therefore, the resonant frequency depends on the lateral contact stiffness as well as on the vertical contact stiffness. The determination of the vertical stiffness requires additional measurements or assumptions on the lateral stiffness.

As an alternative way of enhancing the sensitivity, concentrated-mass (CM) cantilevers were introduced in 2002 [7]. CM cantilevers are fabricated by gluing

**Fig. 7.1** SEM image of a concentrated-mass (CM) cantilever for enhancing the sensitivity to the contact stiffness in the contact resonance techniques, where the tungsten particle with a mass of  $m_{\text{add}} = 540 \text{ ng}$  is glued on the tip and the mass ratio is  $\alpha = 12$ . Reprinted with permission from [9]. Copyright 2005 Institute of Physics Publishing



a heavy particle at the extremity of a cantilever, see Fig. 7.1. The particle, which is located on the tip, generates an inertia force enough for the tip to penetrate stiff samples. When the mass of an attached particle is approximately four times larger than that of the cantilever, the vibration dynamics can be approximated by that of the point-mass model. Therefore, CM cantilevers allow one to use the simple formula Eq. (7.1) even for large values of  $k_V^*/k_c$ . In addition, the inertia enhancement at the tip site reduces the rotational tip motion, and thus the resonant frequency depends only on the vertical stiffness [8]. The enhanced sensitivity due to the use of CM cantilevers has been demonstrated in AFAM [9].

Meanwhile, mass-loaded cantilevers can be found in the literatures for various purposes [7, 10–13]. To make clear the difference between the CM cantilevers and the others, we here give a brief review. Attachment of a tungsten sphere as a known mass to the end of a cantilever was used to calibrate the spring constant of the cantilever [10], where the sphere was detachable because they were attached with natural adhesion. A magnetic particle glued at the end of a cantilever was utilized to directly exert a magnetic force on the tip by applying a magnetic field to the particle in magnetic force modulation microscopy (MFMM) [11]. MFMM works below the contact resonant frequency, i.e., in quasistatic situation, to detect the elasticity of a sample. Therefore, it seems to have the less sensitivity in the detection, especially for stiff samples, than that of the resonance techniques, i.e., AFAM and UAFM. It should be noted that MFMM uses the attached particle for the magnetic force excitation, not for the inertia enhancement as in the CM cantilevers. In magnetic resonance force microscopy (MRFM), which is a scanning probe technology that measures the weak magnetic force between a microscopic magnet and the magnetic moments in a sample, a mass-loaded cantilever that was monolithically microfabricated was developed to reduce thermal noise coming from higher order modes of the cantilever [12]. A CM attachment to a certain position across the length of a cantilever was proposed to tune the resonant frequencies to coincide with the higher harmonics generated in a tapping mode AFM by the nonlinear tip–sample interaction force [13]. The mass-loaded cantilevers addressed above differ from the CM cantilevers [7] in that the attached or loaded masses are not used to enhance the inertia force of the tip.

In the contact resonance techniques, i.e., AFAM and UAFM, the cantilever vibration changes from linear to nonlinear when the excitation amplitude is increased. The nonlinear phenomena were investigated experimentally [14, 15] and theoretically [16, 17]. They suggested that the cyclic jumping of the tips near the contact resonance could be useful to experimentally determine the attractive force. The CM cantilevers would be also useful for such nonlinear applications because the vibration dynamics can be approximately simplified to that of a point-mass model.

In the subsequent sections, we discuss why the CM cantilevers make the contact resonance sensitive to the contact stiffness and obey the simple dynamics of a point mass model. We start with some investigations of theoretical formulas on forced vibrations of CM cantilevers whose tip interacts with a sample, where some closed-form solutions are given for steady-state forced-vibrations under nonlinear tip-sample interactions. Then the tip height effects on the resonant frequency are discussed. The final section demonstrates applications of CM cantilevers in AFAM and UAFM, including measurements of the elastic modulus of diamond-like carbon thin film on a substrate.

## 7.2 Theory of Concentrated-Mass Cantilevers

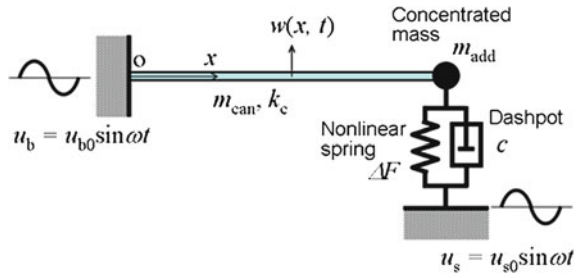
### 7.2.1 Forced Vibration

#### 7.2.1.1 Nonlinear Tip-Sample Interaction

Let us consider a typical case of the contact resonance techniques, AFAM and UAFM, in combination with a concentrated-mass (CM) cantilever. The cross-section of the cantilever is rectangular and uniform along the longitudinal axis. The fundamental natural frequency  $f_{\text{free}}^{(1)}$  of the free cantilever before the CM attachment and the spring constant ( $k_c$ ) are usually given as specifications of a commercial AFM cantilever, or can be experimentally determined [10, 18, 19]. By driving a  $z$ -scanner, a sample surface is brought into contact with the tip, and then the equilibrium contact force  $F_e$  is set to an arbitrary constant value, where  $F_e (= k_c w_e)$  is determined by measuring the equilibrium deflection  $w_e$  of the cantilever end.

After this initial setting, the cantilever in contact with the sample surface is oscillated by application of an AC voltage to the piezoelectric element attached on the base plate where the cantilever is supported in UAFM [5, 15, 20–22]. In another type of excitation, i.e., AFAM, the sample is oscillated by use of a piezoelectric element inserted beneath the sample [4, 14, 23–26]. The sample oscillation method is also used for nonlinear detection of tip-sample interactions in ultrasonic force microscopy (UFM) [27]. The induced deflection is denoted by  $w(x, t)$  (i.e., total deflection minus equilibrium deflection), where  $x$  is an axial coordinate originating at the fixed end and  $t$  is the time. To analyze  $w(x, t)$ , we consider forced vibration of a cantilever which is modeled as having its end connected to a nonlinear spring and a dashpot,

**Fig. 7.2** A model of concentrated-mass (CM) cantilevers, which are driven to vibrate by the modulation of the sample or cantilever positions, under nonlinear tip-sample interactions. The cases of  $u_{b0}=0$ ,  $u_{s0}=0$ , and  $u_{b0} = u_{s0}$ , correspond to AFAM, UAFM, and the direct force modulation, respectively



as shown in Fig. 7.2. The nonlinear spring represents the effect of tip-sample interaction on vibrations around the equilibrium position. The dashpot expresses viscous and friction damping near the tip-sample contact region. This damping is dominant over the others coming from the cantilever itself such as aerodynamic and internal damping of the cantilever. For the sake of simplicity, the CM attached at the end of the cantilever is assumed to be a point mass with a mass of  $m_{add}$ , the height and mass of the tip are neglected, and the slight tilt ( $\approx 15^\circ$ ) of the cantilever relative to a sample surface in the actual setting is also neglected. These simplifications are validated for CM cantilevers as shown in Sect. 7.2.2. The fixed end of the cantilever and the sample surface are oscillated with the forced displacements  $u_b = u_{b0} \sin \omega t$  and  $u_s = u_{s0} \sin \omega t$ , respectively, where  $\omega (= 2\pi f)$  is the angular frequency. The deflection of the simplified cantilever corresponds to  $w(x, t)$  in AFAM when  $u_{b0} = 0$  and in UAFM when  $u_{s0} = 0$ . In addition, when equating the amplitude  $u_{b0}$  with  $u_{s0}$ , one can equivalently deal with the direct force modulation where the CM is directly oscillated by force, see Sect. 7.2.1.3. The case of cantilevers without CMs in UAFM ( $m_{add} = u_{s0} = 0$ ) has already been analyzed in our work [17], which gives some analytical closed-form solutions. This section extends our analysis into the case of  $m_{add} \neq 0$  and  $u_{s0} \neq 0$ .

Let  $w_r(x, t)$  be the relative deflection defined as  $w_r(x, t) = w(x, t) - u_s$ . On the basis of beam vibration theory [28, 29], the equation of motion is described by

$$\ddot{w}_r(x, t) + \left(2\pi f_{free}^{(1)}\right)^2 \left(l/\lambda_{free}^{(1)}\right)^4 w_r''''(x, t) = u_{s0} \omega^2 \sin \omega t, \quad (7.2)$$

where the dots and the primes denote the partial derivatives with respect to  $t$  and  $x$ , respectively. The coefficient of the second term,  $\left(2\pi f_{free}^{(1)}\right)^2 \left(l/\lambda_{free}^{(1)}\right)^4$ , equals flexural rigidity  $EI$  divided by mass per unit length  $\rho A$  of the cantilever, where  $\lambda_{free}^{(1)}$  ( $=1.875$ ) is the smallest root of the frequency equation for free cantilevers without CMs, and  $l$  is the length of the cantilever. Also the coefficient is expressed by  $k_c l^4 / (3m_{can})$ , where the formula  $k_c = 3EI/l^3$  and  $m_{can} = \rho Al$  are used. The boundary conditions are given as



$$w_r(0, t) = (u_{b0} - u_{s0}) \sin \omega t, \quad w_r'(0, t) = w_r''(l, t) = 0, \quad (7.3a)$$

$$- (k_c l^3 / 3) w_r'''(l, t) = \Delta F - c \dot{w}_r(l, t) - m_{\text{add}} [\ddot{w}_r(l, t) + \ddot{u}_s]. \quad (7.3b)$$

Equation (7.3b) expresses a condition imposed on the force acting on the cantilever edge ( $x = l$ ), where the coefficient equals flexural rigidity,  $\Delta F$  is the restoring force of the nonlinear spring, and  $c$  denotes the damping coefficient.

Due to the nonlinearity of the spring,  $w_r(x, t)$  contains several frequency components (i.e., a DC component, harmonics, and subharmonics) in addition to the fundamental component of  $\omega$  in steady-state vibration. The motion can be expressed as the Fourier series:

$$w_r(x, t) = w(x, t) - u_s = W_0(x) + \sum_{n=1}^{\infty} W_n(x) \sin[n\omega t - \phi_n(x)]. \quad (7.4)$$

If the subharmonic components are negligibly small, the terms in the summation in Eq. (7.4) correspond directly to the fundamental and harmonic components. For this case, the harmonic balance method is effective for the nonlinear analyzes [30]. Using Eqs. (7.2–7.4), we can derive the following conditions imposed on harmonic balance (see Appendix I):

$$W_0(l) = \frac{1}{k_c T} \int_0^T \Delta F dt, \quad (7.5a)$$

$$\begin{aligned} & W_n(l) \sin \phi_n(l) \left[ \Psi(\lambda_n) + \frac{1}{3} \alpha \lambda_n^4 \right] + \left( \frac{cn\omega}{k_c} \right) W_n(l) \cos \phi_n(l) \\ &= \frac{2}{k_c T} \int_0^T \Delta F \cos n\omega t dt \quad (n = 1, 2, 3, \dots), \end{aligned} \quad (7.5b)$$

$$\begin{aligned} & - W_n(l) \cos \phi_n(l) \left[ \Psi(\lambda_n) + \frac{1}{3} \alpha \lambda_n^4 \right] + \left( \frac{cn\omega}{k_c} \right) W_n(l) \sin \phi_n(l) \\ &+ \left\{ (u_{b0} - u_{s0}) \Theta(\lambda_n) - u_{s0} \left[ \Psi(\lambda_n) + \frac{1}{3} \alpha \lambda_n^4 \right] \right\} \delta_{1n} \\ &= \frac{2}{k_c T} \int_0^T \Delta F \sin n\omega t dt \quad (n = 1, 2, 3, \dots), \end{aligned} \quad (7.5c)$$

where

$$\Psi(\lambda_n) = \frac{\lambda_n^3 (1 + \cos \lambda_n \cosh \lambda_n)}{3(\cos \lambda_n \sinh \lambda_n - \sin \lambda_n \cosh \lambda_n)}, \quad (7.6a)$$

$$\Theta(\lambda_n) = \Psi(\lambda_n) \left( \frac{\cos \lambda_n + \cosh \lambda_n}{1 + \cos \lambda_n \cosh \lambda_n} \right), \quad (7.6b)$$

$$\lambda_n = \lambda_{\text{free}}^{(1)} \sqrt{\frac{nf}{f_{\text{free}}^{(1)}}} = l \left( \frac{\rho A}{EI} \right)^{1/4} \sqrt{n\omega} = \left( \frac{3m_{\text{can}}}{k_c} \right)^{1/4} \sqrt{n\omega}, \quad (7.6c)$$

$$\alpha = m_{\text{add}}/m_{\text{can}}. \quad (7.6d)$$

The important parameter  $\alpha$  is the ratio of the CM ( $= m_{\text{add}}$ ) to the mass  $m_{\text{can}}$  of the cantilever without the CM.  $T = 1/f = 2\pi/\omega$ , and  $\delta_{1n}$  is the Kronecker symbol; i.e.,  $\delta_{1n} = 0$  ( $n \neq 1$ ) and  $\delta_{11} = 1$ . All the components  $W_n(l)$  ( $n = 0, 1, 2, \dots$ ) and the phase delay angles  $\phi_n(l)$  ( $n = 1, 2, 3, \dots$ ) must satisfy Eq. (7.5a–c).

The relationship between the force acting on the AFM tip and the tip–sample separation  $z$  [i.e., the force curve  $F(z)$ ] is generally complex, and an exact, explicit description is difficult. For the contact states ( $z < 0$ ), we use the half-empirical, half-theoretical formula [31]:

$$F(z) = \frac{4}{3} E^* \sqrt{-Rz^3} - F_C - \sqrt{2\pi w_{\text{ad}} E^*} (-Rz)^{3/4} \equiv F_{\text{cont}}(z) \quad (z \leq 0), \quad (7.7)$$

where  $E^*$  is the effective Young's modulus, which is defined as

$$1/E^* = (1 - \nu_s^2)/E_s + (1 - \nu_t^2)/E_t, \quad (7.8)$$

where  $E_i$  and  $\nu_i$  ( $i = s$  and  $t$ ) are the Young's moduli and the Poisson's ratios, respectively. The subscripts  $s$  and  $t$  denote the sample and the AFM tip, respectively.  $R$  is the tip radius,  $w_{\text{ad}}$  is the Dupré adhesion energy (the work per unit area for separating the interface), and  $F_C$  is the attractive force at zero separation. The first term of Eq. (7.7) represents Hertzian contact repulsion, and the remaining terms approximate the adhesion effect. The two parameters; i.e., the adhesion energy ( $w_{\text{ad}}$ ) and the attractive force at zero separation ( $F_C$ ), characterize the surface chemical properties. When the attractive effect is due to van der Waals attractive interaction, the so-called DMT theory [32] gives the simple relation  $F_C = 2\pi R w_{\text{ad}}$ . However, in the general case, relating  $F_C$  with  $w_{\text{ad}}$  is difficult.

Also, for small separations  $0 < z \ll R$ , we introduce a master curve applicable to several attractive interactions:

$$F(z) = - \sum_{k=1}^s \frac{F_k}{1 + z/D_k} - \sum_{k=s+1}^m \frac{F_k}{(1 + z/D_k)^2} \equiv F_{\text{sepa}}(z) \quad (0 < z \ll R), \quad (7.9a)$$

$$\sum_{k=1}^m F_k = F_C, \quad (7.9b)$$

where  $F_k$  and  $D_k$  ( $k=1, 2, \dots, m$ ) are fitting parameters. The first summation can represent capillary forces due to water adsorption on the surfaces, and capacitance forces due to a potential difference between the sample and tip [31]. The second summation can express van der Waals forces and electrostatic forces due to electric charges (patch charges) [31].

In our nonlinear vibration model, the restoring force from the nonlinear spring ( $\Delta F$ ) is expressed by

$$\Delta F = F[z_e + w_r(l, t)] - F_e, \quad (7.10)$$

where  $z_e (<0)$  is the equilibrium  $z$  position ( $-z_e$  is the equilibrium penetration depth) and  $F_e = F(z_e)$ . The contact stiffness ( $k_V^*$ ) corresponds to  $-dF/dz$  at  $z = z_e$ , as mentioned in Sect. 7.1. While the tip is in contact with the sample [ $z_e + w_r(l, t) < 0$ ], the first term takes the form of Eq. (7.7). For the other intervals, when the tip is jumping off the sample surface [ $z_e + w_r(l, t) > 0$ ], the first term is described by Eq. (7.9a).

It is difficult to analytically integrate Eq. (7.5a–c). Here we approximate  $w(x, t)$  by taking into account only the two main components  $W_0(x)$  and  $W_1(x)$ :

$$w_r(x, t) = W_0(x) + W_1(x) \sin[\omega t - \phi_1(x)]. \quad (7.11)$$

For  $W_0(l)$ ,  $W_1(l)$ , and  $\phi_1(l)$ , we use the simple notations  $W_0$ ,  $W_1$ , and  $\phi_1$ , respectively. The component  $W_0$  corresponds to the DC liftoff or diode effect, which has been used for detecting the tip–sample interaction in UFM [27]. Also, we may assume  $W_1 > 0$ . Then, the integrals ( $n = 1$ ) in Eq. (7.5b, c) can be related with each other as follows:

$$\frac{1}{\sin \phi_1} \int_0^T \Delta F \cos \omega t dt = -\frac{1}{\cos \phi_1} \int_0^T \Delta F \sin \omega t dt. \quad (7.12)$$

Here we introduce the function defined as

$$\chi_1(W_0, W_1; z_e) = \frac{2}{k_c T W_1 \sin \phi_1} \int_0^T \Delta F \cos \omega t dt. \quad (7.13)$$

Using Eqs. (7.5b, c), (7.12), and (7.13), we obtain the following equations for the deflection amplitudes of the cantilever end and the delay phase angle:

$$W_1^2 = \frac{\{(u_{b0} - u_{s0})\Theta(\lambda_1) - u_{s0} [\Psi(\lambda_1) + \alpha \lambda_1^4/3]\}^2}{[\Psi(\lambda_1) + \alpha \lambda_1^4/3 - \chi_1(W_0, W_1; z_e)]^2 + (c\omega/k_c)^2}, \quad (7.14a)$$

$$\tan \phi_1 = \frac{-(c\omega/k_c)}{\Psi(\lambda_1) + \alpha \lambda_1^4/3 - \chi_1(W_0, W_1; z_e)}. \quad (7.14b)$$

The DC and  $\omega$  components of amplitude must satisfy Eqs. (7.5a) and (7.14a). The delay of phase angle ( $\phi_1$ ) is determined by Eq. (7.14b). The other equations ( $n \geq 2$ ) in Eq. (7.5b, c) are neglected, in accordance with the concept of the harmonic balance method [30].

The phase angles at the transition from contact to separation  $\theta_1 (= \omega t_1 - \phi_1)$  and from separation to contact  $\theta_2 (= \omega t_2 - \phi_1)$  are described by

$$\theta_1 = \pi - \theta_2 = \text{Arc sin } \frac{-z_e - W_0}{W_1}. \quad (7.15)$$

Then, analytically integrating the right-hand side of Eq. (7.5a), we obtain

$$\begin{aligned} \bar{W}_0 &= \frac{1}{2\pi k_c R} \int_{\theta_2 - 2\pi}^{\theta_1} F_{\text{cont}}(z) d\theta + \frac{1}{2\pi k_c R} \int_{\theta_1}^{\theta_2} F_{\text{sepa}}(z) d\theta - \frac{F_e}{k_c R} \\ &= C_0(\bar{W}_0, \bar{W}_1; \bar{z}_e) + S_0(\bar{W}_0, \bar{W}_1; \bar{z}_e) - \frac{F_e}{k_c R}, \end{aligned} \quad (7.16)$$

where  $z = z_e + W_0 + W_1 \sin\theta$  and the upper bar denotes the value normalized by  $R$ ; i.e.,  $\bar{(\ )} = (\ )/R$ . The first term  $C_0(\bar{W}_0, \bar{W}_1; \bar{z}_e)$  is expressed as an infinite series, and the second term  $S_0(\bar{W}_0, \bar{W}_1; \bar{z}_e)$  is expressed in closed form (see Appendix II). Similarly, for Eq. (7.13), we have

$$\begin{aligned} \chi_1 &= \frac{1}{\pi k_c W_1 \sin \phi_1} \left[ \int_{\theta_2 - 2\pi}^{\theta_1} F_{\text{cont}}(z) \cos(\theta + \phi_1) d\theta + \int_{\theta_1}^{\theta_2} F_{\text{sepa}}(z) \cos(\theta + \phi_1) d\theta \right] \\ &= C_1(\bar{W}_0, \bar{W}_1; \bar{z}_e) + S_1(\bar{W}_0, \bar{W}_1; \bar{z}_e). \end{aligned} \quad (7.17)$$

The expressions of  $C_1(\bar{W}_0, \bar{W}_1; \bar{z}_e)$  and  $S_1(\bar{W}_0, \bar{W}_1; \bar{z}_e)$  are shown in Appendix II. Equation (7.16) gives the relationship between the shift in average position ( $W_0$ ) and amplitude ( $W_1$ ). The amplitude is determined from Eqs. (7.14a) and (7.17).

In the case of perfect contact, where the tip is always in contact with the sample surface during vibration, we obtain relatively simple formulas for nonlinear vibration (set  $\Delta\theta = \theta_2 - \theta_1$  to zero in Appendix II):

$$\bar{W}_0 = \sum_{k=1}^{\infty} \frac{g^{(k)}(\bar{z}_e)}{k!} \left[ \bar{W}_0^k + \sum_{p=1}^{\lfloor k/2 \rfloor} \binom{k}{2p} \binom{2p}{p} \bar{W}_0^{k-2p} \left( \frac{\bar{W}_1}{2} \right)^{2p} \right], \quad (7.18)$$

$$\chi_1(\bar{W}_0, \bar{W}_1; \bar{z}_e) = -\frac{1}{2} \sum_{k=1}^{\infty} \frac{g^{(k)}(\bar{z}_e)}{k!} \times \left[ \sum_{p=1}^{\lfloor (k+1)/2 \rfloor} \binom{k}{2p-1} \binom{2p}{p} \bar{W}_0^{k-2p+1} \left( \frac{\bar{W}_1}{2} \right)^{2p-2} \right], \quad (7.19)$$

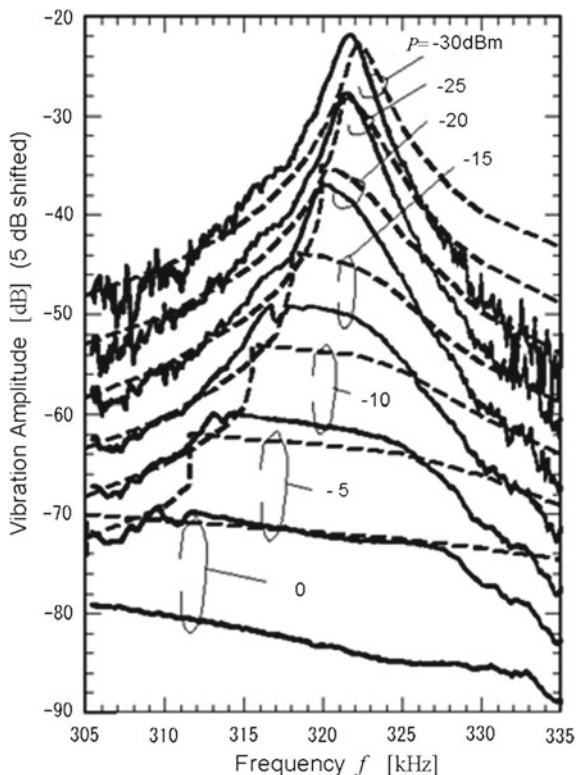
where the Gauss notation and the simple notation of a binomial coefficient are used (see Appendix II). The function  $g(\bar{z}) [=F_{\text{cont}}/(k_c R)]$  represents normalized interactive force in the contact situation, and the derivative is given by

$$\begin{aligned} g^{(k)}(\bar{z}) &= \frac{d^k g(\bar{z})}{d\bar{z}^k} \\ &= \frac{\Gamma(k-3/2)}{\Gamma(-3/2)} \left( \frac{4E^* R}{3k_c} \right) (-\bar{z})^{3/2-k} \\ &\quad - \frac{\Gamma(k-3/4)}{\Gamma(-3/4)} \left( \frac{\sqrt{2\pi w_{\text{ad}} E^* R}}{k_c} \right) (-\bar{z})^{3/4-k}, \end{aligned} \quad (7.20)$$

where  $\Gamma(x)$  is the Gamma function [ $\Gamma(x+1) = x \Gamma(x)$ ].

Figure 7.3 shows an example of theoretical predictions (broken curves) by using Eqs. (7.14–7.20) for the second resonance spectra measured in UAFM [15] (solid curves), where a glass surface was observed with a normal cantilever. The simulations were carried out by finding the roots  $W_0$  and  $W_1$  of Eqs. (7.14a) and (7.16) under the condition of  $u_{s0} = 0$  and appropriate values on the tip–sample interaction [17]. Our simulation explains well the drastic change in a shape of resonance curves due to the increase in excitation power  $P$ . For low excitation powers ( $-20$ ,  $-25$ , and  $-30$  dBm), the amplitudes simulated around the resonance frequency almost coincide with the experimental amplitudes. However, the simulation deviates from the experimental amplitudes for larger excitation powers ( $> -20$  dBm). It is noted that these cases of discrepancy correspond to large nonlinear vibrations where the tip jumps out of the sample surface. In such large nonlinear vibrations, harmonics and subharmonics appear and the damping effect becomes stronger than that at perfect contact. The discrepancy is considered to be due to the neglect of the appearance of harmonics and subharmonics and the assumption of constant damping coefficient. For the situation of perfect contact, the theory was successfully applied to the determination of the elastic modulus and adhesion energy [17].

**Fig. 7.3** A comparison of the theoretical prediction (*broken curves*) with the experimental contact spectra [15] (*solid curves*), which were observed for a glass surface by UAFM with a normal cantilever. The parameter  $P$  is the excitation power. For  $P$  less than  $-15$  dBm, the tip meets the perfect contact without any jumping out of the sample surface, where the theory well explains the measurements. Reprinted from [17]



### 7.2.1.2 Linear Tip–Sample Interaction

If the amplitude is so small that  $\bar{W}_1^{2p}$  ( $p = 1, 2, 3, \dots$ ) may be neglected, Eqs. (7.18) and (7.19) become the expressions of linear vibrations  $\bar{W}_0 = 0$  and  $\chi_1 = -g^{(1)}(\bar{z}_e) = k_V^*/k_c$ , respectively. Hereafter, we omit the subscript 1 in the symbols  $W_1$ ,  $\phi_1$ ,  $\lambda_1$ , etc. for linear vibration. Substituting  $\chi_1 = k_V^*/k_c$ , in Eq. (7.14a, b), the amplitude  $W$  and phase delay  $\phi$  at the end of the cantilever ( $x = l$ ) are described by

$$W = \frac{|(u_{b0} - u_{s0})\Theta(\lambda) - u_{s0}[\Psi(\lambda) + \alpha\lambda^4/3]|}{\sqrt{[\Psi(\lambda) + \alpha\lambda^4/3 - k_V^*/k_c]^2 + (c\omega/k_c)^2}}, \quad (7.21a)$$

$$\tan \phi = \frac{-(c\omega/k_c)}{\Psi(\lambda) + \alpha\lambda^4/3 - k_V^*/k_c}, \quad (7.21b)$$

$$\lambda = \lambda_{\text{free}}^{(1)} \sqrt{f/f_{\text{free}}^{(1)}} = (3m_{\text{can}}/k_c)^{1/4} \sqrt{\omega}, \quad (7.21c)$$

where the damping coefficient ( $c$ ) is related with the quality factor  $Q$  (see Appendix III).

For low damping, we can approximate the resonance condition as

$$\Psi(\lambda) + \alpha\lambda^4/3 = k_V^*/k_c. \quad (7.22)$$

Equation (7.22) coincides with the frequency equation of natural vibrations. For  $\alpha = k_V^* = 0$ , it gives  $\Psi(\lambda) = 0$  and thus the frequency equation of clamped-free (or fixed-free) beams,  $1 + \cos\lambda\cosh\lambda = 0$ , which is by equating the numerator of Eq. (7.6a) with zero. Let  $\lambda_{\text{free}}^{(n)}$  denote the  $n$ th order solution:

$$\lambda_{\text{free}}^{(n)} = 1.875, \quad 4.694, \quad 7.855, \quad 10.996, \quad 14.137, \dots \quad (7.23)$$

The limit  $k_V^* \rightarrow \infty$  in Eq. (7.22) leads to  $\Psi(\lambda) \rightarrow \infty$  for finite values of  $\lambda$  and thus to the frequency equation of clamped-pinned (or fixed-simply supported) beams,  $\tanh\lambda = \tan\lambda$ , which is obtained by setting the denominator of Eq. (7.6a) zero. The  $n$ th order solution  $\lambda_{\text{pin}}^{(n)}$  is given by

$$\lambda_{\text{pin}}^{(n)} = 3.927, \quad 7.069, \quad 10.210, \quad 13.352, \quad 16.493, \dots \quad (7.24)$$

When  $k_V^*$  increases, the  $n$ th order solution  $\lambda^{(n)}$  of Eq. (7.22) approaches  $\lambda_{\text{pin}}^{(n)}$ , whatever  $\alpha$  takes. Therefore, the possible range of  $\lambda^{(n)}$  is

$$0 < \lambda^{(1)} \leq \lambda_{\text{pin}}^{(1)}, \quad \lambda_{\text{pin}}^{(n-1)} < \lambda^{(n)} \leq \lambda_{\text{pin}}^{(n)} \quad (n = 2, 3, 4, \dots). \quad (7.25)$$

### 7.2.1.3 Derivation of Effective Point-Mass Models

As we have seen in the preceding sections, the vibration dynamics of cantilevers in contact with a sample seems somewhat complicated even with the linear tip-sample interaction. However, if the excitation frequency [ $f = \omega/(2\pi)$ ] is limited to close vicinities of the resonances, one may find an effective point-mass model for each of the resonances. The presence of the effective models, whose possibility depends on values of  $\alpha$  and  $k_V^*/k_c$ , could allow one to substitute the following approximation in Eq. (7.21a, b):

$$\Psi(\lambda) + \alpha\lambda^4/3 - k_V^*/k_c \approx (m_{\text{eff}}\omega^2 - k_{\text{eff}}^{(n)})/k_c, \quad (7.26)$$

where  $m_{\text{eff}}$  is the effective mass, and  $k_{\text{eff}}^{(n)} [= m_{\text{eff}}(\omega^{(n)})^2]$  is the effective spring constant near the  $n$ th order resonance. The right side of Eq. (7.26) corresponds to  $\omega X/k_c$ , where  $X$  is the mechanical reactance. Let us call the left side of Eq. (7.26) the *reactance relative*.

Here, let us seek out the effective point-mass models. For a small difference  $\Delta(\omega^2) = \omega^2 - (\omega^{(n)})^2$ , the reactance relative is approximated by

$$\begin{aligned} & \Psi(\lambda) + \alpha\lambda^4/3 - k_V^*/k_c \\ & \approx \Psi(\lambda^{(n)}) + \alpha(\lambda^{(n)})^4/3 - k_V^*/k_c \\ & + \left\{ \frac{m_{\text{can}}}{4} \left[ 1 + 3\Psi(\lambda^{(n)})\Phi(\lambda^{(n)})/(\lambda^{(n)})^3 \right] + m_{\text{add}} \right\} \left[ \omega^2 - (\omega^{(n)})^2 \right] / k_c, \end{aligned} \quad (7.27)$$

where Eqs. (7.6a, d) and (7.21c) are used, and

$$\Phi(\lambda) = \frac{2 \sin \lambda \sinh \lambda}{\cos \lambda \sinh \lambda - \sin \lambda \cosh \lambda} + \frac{3}{\lambda}. \quad (7.28)$$

If  $\lambda^{(n)}$  is the exact solution of Eq. (7.22), the first three terms in the right side of Eq. (7.27) disappear, and then Eq. (7.27) suggests that the expression in the braces corresponds to the effective mass ( $m_{\text{eff}}$ ). Unfortunately,  $m_{\text{eff}}$  is not a constant in general, but depends on the resonant frequency. The effective point-mass model does not always exist near the resonances.

When the cantilever is a normal one without the CM and the sample is very soft, that is  $\alpha \ll 1$  and  $k_V^*/k_c \ll 1$ , we have the approximation  $\Psi(\lambda^{(n)}) \approx 0$ , where  $\lambda^{(n)} \approx \lambda_{\text{free}}^{(n)}$ , and then find the effective point-mass model with the effective mass:

$$m_{\text{eff}} = m_{\text{can}}/4 + m_{\text{add}}, \quad (7.29)$$

and the effective spring constant:

$$k_{\text{eff}}^{(n)} = k_c^{(n)} + k_V^* = \left[ \left( \lambda_{\text{free}}^{(n)} \right)^4 / 12 \right] k_c + k_V^*, \quad (7.30)$$

where  $k_c^{(n)}$  is often called the dynamic (or effective) spring constant of cantilevers, which have no attached masses, and approximately equals to  $k_c$  for the fundamental resonance ( $n = 1$ ). Meanwhile, Eq. (7.30) predicts that for  $\alpha \ll 1$  and  $k_V^*/k_c \ll 1$ , the application of the higher modes does not provide any enhanced-sensitivity in detecting  $k_V^*$  because  $\Delta\omega = \omega_{\text{free}}^{(n)} k_V^*/(2k_c^{(n)}) = k_V^*/(k_c^{(n)} m_{\text{can}})^{1/2}$  is reduced when  $k_c^{(n)}$  increases. The reduced sensitivity is also predicted in the NC mode by substituting  $-(dF/dz)_{z_e}$  for  $k_V^*$ .

In AFAM and UAFM using normal cantilevers ( $\alpha \ll 1$ ),  $k_V^*/k_c$  normally takes not small values. There is no available point-mass models because the resonance condition  $\Psi(\lambda^{(n)}) \approx k_V^*/k_c$  does not allow one to find any effective mass that is independent of the resonant frequencies. Instead of the point-mass models, one is required to solve the resonance condition for  $\lambda^{(n)}$  directly. For stiff samples such as metals, the sensitivity of the fundamental resonant frequency to  $k_V^*$  is known to be reduced but can be improved by using the higher order resonances [4, 5].



Apart from the limitation of close vicinities of the resonances, let us consider now two cases in which effective point-mass models are available. One is the excitation at low frequencies with any values of  $\alpha$  ( $0 < \lambda < \lambda_U \approx 2.5$  for  $\alpha = 0$ , the upper limit  $\lambda_U$  depends on  $\alpha$ , and  $\lambda_U \rightarrow \lambda_{\text{pin}}^{(1)}$  as  $\alpha \rightarrow \infty$ ), which leads to the fundamental-mode vibration in the range of  $-1 < k_V^*/k_c < (k_V^*/k_c)_U \approx 2.5$  for  $\alpha = 0$ , the upper limit  $(k_V^*/k_c)_U$  depends on  $\alpha$ , and  $(k_V^*/k_c)_U \rightarrow \infty$  with  $\alpha$ . Using Taylor series expansion of  $\Psi(\lambda)$  around  $\lambda = 0$ :  $\Psi(\lambda) \approx -1 + (11/140)\lambda^4$  together with Eq. (7.21c), we have the approximation to the reactance relative:

$$\Psi(\lambda) + \alpha\lambda^4/3 - k_V^*/k_c \approx \left\{ [(33/140)m_{\text{can}} + m_{\text{add}}]\omega^2 - (k_c + k_V^*) \right\} / k_c, \quad (7.31)$$

where the coefficient  $33/140 \approx 0.236$ . Equation (7.31) shows the effective point-mass model with the effective mass,  $m_{\text{eff}} = 0.236 m_{\text{can}} + m_{\text{add}}$ , connected to the two parallel springs,  $k_c$  and  $k_V^*$ . This confirms that the fundamental resonant frequency for any values of  $\alpha$  takes the same form as Eq. (7.1) with  $k_V^*$  substituting for  $-(dF/dz)_{z_e}$ .

Another case in which the forced vibration can be approximated by an effective point-mass model is the use of CM cantilevers with  $\alpha > 4$ . In this case, the model is applicable at almost all the frequencies of practical interest. Figure 7.4 plots the sum of frequency-dependent terms  $\Psi(\lambda) + \alpha\lambda^4/3$  in the reactance relative, as a function of  $\lambda$ . The graphs explain the effect of the CM on the reactance relative. That is, when the mass ratio ( $\alpha$ ) exceeds around 4, the term  $\alpha\lambda^4/3$  dominates over the sum of the frequency-dependent terms [i.e.,  $\Psi(\lambda) \ll \alpha\lambda^4/3$ ], except near the specific resonances of  $\lambda = \lambda_{\text{pin}}^{(1)}$  ( $= 3.927$ ),  $\lambda_{\text{pin}}^{(2)}$  ( $= 7.069$ ), etc., which correspond to the case where the end of the cantilever is pinned (or simply supported). Hence, we are allowed to neglect  $\Psi(\lambda)$  in the reactance relative:

$$\Psi(\lambda) + \alpha\lambda^4/3 - k_V^*/k_c \approx \alpha\lambda^4/3 - k_V^*/k_c = \left( m_{\text{add}}\omega^2 - k_V^* \right) / k_c. \quad (7.32)$$

Note that Eq. (7.32), which is valid for  $\alpha > 4$ , makes relatively large errors for small values of  $\lambda (< 2)$  and  $k_V^*/k_c (< 20)$ . In this case Eq. (7.31) is available rather than Eq. (7.32). If Eq. (7.31) with  $\alpha > 4$  is extrapolated to the case for larger values of  $k_V^*/k_c$ , we see it to equal Eq. (7.32), approximately. Thus, we reach the following approximation to the reactance relative for CM cantilevers with  $\alpha > 4$ .

$$\Psi(\lambda) + \alpha\lambda^4/3 - k_V^*/k_c \approx \left[ m_{\text{eff}}\omega^2 - (k_c + k_V^*) \right] / k_c, \quad (7.33)$$

where  $m_{\text{eff}} = 0.236m_{\text{can}} + m_{\text{add}}$ , and hereafter we approximately use Eq. (7.29) for  $m_{\text{eff}}$ . The resonant frequency is given by

$$f_{\text{res}} = \frac{1}{2\pi} \sqrt{\frac{k_c + k_V^*}{m_{\text{eff}}}} = f_0 \sqrt{1 + \frac{k_V^*}{k_c}}, \quad (7.34)$$

**Fig. 7.4** Plots of the sum of frequency-dependent terms in the reactance relative,  $\Psi(\lambda) + \alpha\lambda^4/3$ , as a function of  $\lambda$ , which is a parameter proportional to  $f^{4/2}$ , see Eq. (7.21c). The broken curves show the second term,  $\alpha\lambda^4/3$

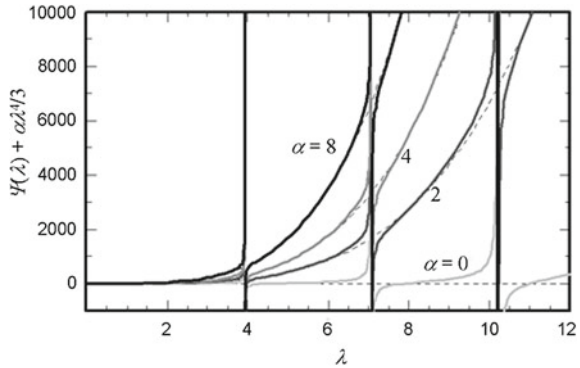
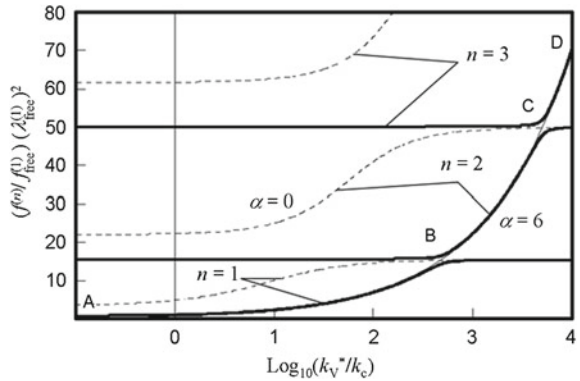


**Fig. 7.5** The normalized resonant frequency versus contact stiffness for the CM cantilever ( $\alpha = 6$ , solid curves), a normal cantilever ( $\alpha = 0$ , broken curves), and the point-mass model Eq. (7.34) (thin solid curve, which coincides the curve A-B-C-D). For the point-mass model, the normalized resonant frequency is expressed by  $(\lambda_{\text{free}}^{(1)})^2(1 + 4\alpha)^{-1/2}(1 + k_V^*/k_c)^{1/2}$  from Eq. (7.34)



where  $f_0$  is the fundamental resonant frequency of the CM cantilever in no interaction with the sample ( $k_V^* = 0$ ). Figure 7.5 shows the normalized resonant frequency  $f^{(n)}[(\lambda_{\text{free}}^{(1)})^2/f_{\text{free}}^{(1)}] = (\lambda^{(n)})^2$  versus the normalized stiffness ( $k_V^*/k_c$ ) for the CM cantilever with  $\alpha = 6$ , where the calculation is carried out by using Eq. (7.22), and the result for the CM cantilever is compared with the normal cantilever ( $\alpha = 0$ ) before the attachment of the CM. We see from Fig. 7.5 that the CM cantilever yields the apparently-connected segments A-B-C-D in solid curves, which consists of parts of the 1st to 3rd resonance curves ( $n = 1 \sim 3$ ). The segments are well fitted by Eq. (7.34) within the line width. The horizontal lines corresponds to the specific resonances  $\lambda^{(n)} = \lambda_{\text{pin}}^{(n)}$ . It should be also noted that the curve consisting of the segments for the CM cantilever looks very steep, compared to the result for the normal cantilever. The slope indicates the sensitivity in AFAM and UAFM, which will be discussed in Sect. 7.2.1.4.

Note that Eqs. (7.33) and (7.34) are applicable to almost all the range of frequency, except near the specific resonances of the cantilever with one end pinned, as mentioned above, and to each of AFAM and UAFM as long as one uses the CM cantilevers. On the other hand, the amplitude ( $W$ ) and the phase delay ( $\phi$ ) of the

relative deflection ( $w_r$ ) at the cantilever end, see Eq. (7.21a, b), are rewritten as

$$W = \frac{|k_c(u_{b0} - u_{s0})\Theta(\lambda) - u_{s0}(m_{\text{eff}}\omega^2 - k_c)|}{\sqrt{[m_{\text{eff}}\omega^2 - (k_c + k_V^*)]^2 + (c\omega)^2}}, \quad (7.35a)$$

$$\tan \phi = \frac{-c\omega}{m_{\text{eff}}\omega^2 - (k_c + k_V^*)}. \quad (7.35b)$$

With  $u_{b0} = 0$ , i.e. AFAM, the first term in the numerator of Eq. (7.35a), which contains the function  $\Theta(\lambda)$ , can be neglected for  $\lambda > 2$  and  $\alpha > 4$ , and then we acquire the complete expression that contains only quantities in the effective point-mass model. In the case of  $u_{b0} = u_{s0}$ , we also have the complete expression. If  $u_{s0}$  is changed along with  $\omega$  so as to make the term  $u_{s0}m_{\text{eff}}\omega^2$  be a constant value, denoted by  $P_0^{\text{ext}}$ , we obtain the formula on the direct force modulation for relatively high frequencies  $\omega \gg 2\pi f_0$ , where the CM is directly oscillated with an external force  $P^{\text{ext}} = P_0^{\text{ext}} \sin \omega t$ . In the formula converted in this way, the relative quantities like  $W$  should be regarded as the absolute ones. This corresponds to MFMM where the attached magnetic particle satisfies the requirement  $\alpha > 4$  for the CM cantilevers. On the other hand, UAFM where  $u_{s0} = 0$ , unfortunately, does not allow us to obtain the complete expression because there remains  $\Theta(\lambda)$ , which has some nature coming from the distributed mass of the cantilever.

When the absolute deflection  $w(l, t) = w_r(l, t) + u_s$  at the cantilever end is expressed by  $w(l, t) = W_{\text{abs}} \sin(\omega t - \phi_{\text{abs}})$ , the amplitude  $W_{\text{abs}}$  and the phase delay  $\phi_{\text{abs}}$  are related with the relative ones  $W$  and  $\phi$  as:

$$W_{\text{abs}} = W \sqrt{\sin^2 \phi + [\cos \phi + (u_{s0}/W)]^2}, \quad (7.36a)$$

$$\tan \phi_{\text{abs}} = \sin \phi / (\cos \phi + u_{s0}/W). \quad (7.36b)$$

#### 7.2.1.4 Sensitivity in Detecting Contact Stiffness

The slope in the relation of resonant frequency versus the contact stiffness, see Fig. 7.5, means the sensitivity in the detection of sample elasticity by AFAM and UAFM. First, we define the non-dimensional sensitivity  $S$  as the ratio of the normalized increase in the resonant frequency,  $\Delta f^{(n)}/f^{(n)}$ , to that in the contact stiffness,  $\Delta k_V^*/k_V^*$  [7, 17]. Using Eq. (7.22) together with Eq. (7.21c), we obtain the expression:

$$S \equiv \left( \frac{k_V^*}{f^{(n)}} \right) \frac{df^{(n)}}{dk_V^*} = \frac{2[\Psi(\lambda^{(n)}) + \alpha(\lambda^{(n)})^4/3]}{\lambda^{(n)}[\Psi(\lambda^{(n)})\Phi(\lambda^{(n)}) + (1 + 4\alpha)(\lambda^{(n)})^3/3]}. \quad (7.37)$$

For the CM cantilevers, the effective point-mass model, Eq. (7.34), simplifies the sensitivity:

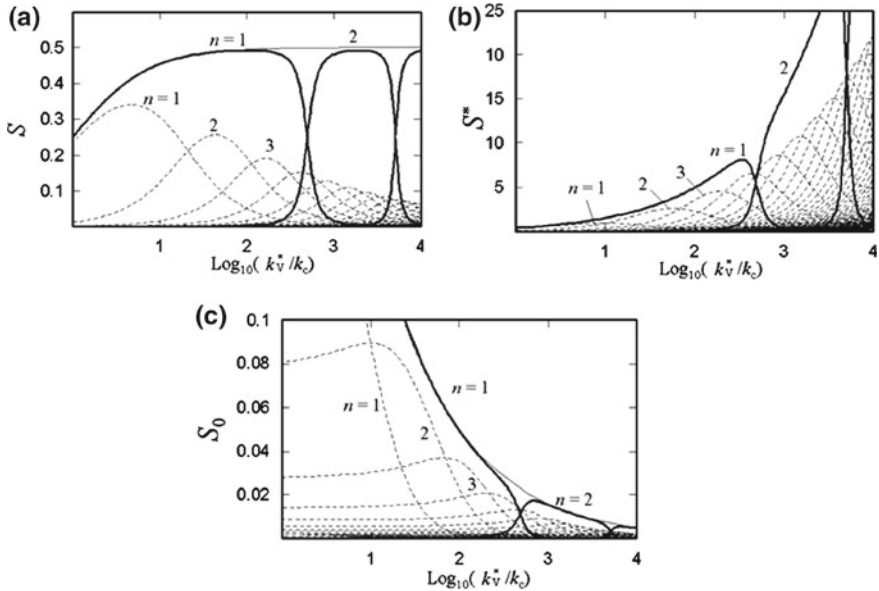


**Fig. 7.6** The sensitivity, defined by **a** Eq. (7.37), **b** Eq. (7.39), and **c** Eq. (7.40), for the CM cantilevers ( $\alpha = 6$ , solid curves) as a function of the normalized contact stiffness, in comparison with that for the normal cantilevers ( $\alpha = 0$ , broken curves). The thin solid curves in **a** and **c** show Eqs. (7.38) and (7.41), respectively

$$S \approx (1/2)(k_V^*/k_c)/(1 + k_V^*/k_c). \tag{7.38}$$

When increasing the normalized stiffness, the sensitivity increases and then reaches a constant value of 0.5. This value is the maximum of the sensitivity defined by Eq. (7.37). Figure 7.6a shows the sensitivity as a function of the normalized stiffness for the CM cantilever with  $\alpha = 6$ , compared to that for the normal cantilever ( $\alpha = 0$ ). The calculations have been made with Eq. (7.37) together with Eq. (7.22). The enhancement of the sensitivity by the use of the CM cantilever is understood from Fig. 7.6a.

When the CM and normal cantilevers having the same fundamental resonant frequency with the end free are compared, we may modify the sensitivity in the way that  $\Delta f^{(n)}$  is normalized by using each of the fundamental resonant frequencies of the cantilevers with the end free ( $f_0$  and  $f_{\text{free}}^{(1)}$  for the CM and normal cantilevers, respectively). Then, we have the sensitivity  $S^*$  for the CM cantilever:

$$S^* \equiv \left(\frac{k_V^*}{f_0}\right) \frac{df^{(n)}}{dk_V^*} = \sqrt{1 + 4\alpha} \left(\frac{(\lambda^{(n)})^2}{2\sqrt{3}}\right) S, \tag{7.39}$$

where, for the normal cantilevers ( $\alpha = 0$ ),  $f_0$  should be replaced by  $f_{\text{free}}^{(1)}$ , while the right-hand side remains valid. Figure 7.6b shows the comparison for this case. We see that the CM cantilever ( $\alpha = 6$ , solid curves) significantly improves the sensitivity within almost the entire range of the normalized stiffness.

In the sensitivities defined above, the change in the contact stiffness is normalized with the contact stiffness to which we want to know the sensitivity. These sensitivities clearly indicate the performance of detecting the contact stiffness for relatively stiff samples or soft cantilevers ( $k_V^*/k_c \gg 1$ ). Especially, in the case where macroscopically homogeneous stiff-samples are evaluated or imaged for fluctuations of the surface elasticity, the relative change in the contact stiffness is important, and thus the sensitivities would be useful. In contrast, these sensitivities would not be suitable for relatively soft samples or stiff cantilevers ( $k_V^*/k_c \ll 1$ ) because they approach zero as  $k_V^*/k_c \rightarrow 0$ . Instead, one may use the definition where the change in  $k_V^*$  is normalized with the spring constant of the cantilever  $k_c$  [27], which is similar to that in the NC mode:

$$S_0 \equiv \left( \frac{k_c}{f_0} \right) \frac{df^{(n)}}{dk_V^*} = \frac{S^*}{\Psi(\lambda^{(n)}) + \alpha(\lambda^{(n)})^4/3}. \quad (7.40)$$

The sensitivity Eq. (7.40) is applicable to making a comparison between the CM and normal cantilevers with the same fundamental resonant frequency  $f_0 = f_{\text{free}}^{(1)}$ , as shown in Fig. 7.6c. For the CM cantilevers, the effective point-mass model, Eq. (7.34), simplifies the sensitivity:

$$S_0 \approx (1/2)/\sqrt{1 + k_V^*/k_c}. \quad (7.41)$$

The sensitivity  $S_0$  takes the maximum of 0.5 as  $k_V^*/k_c \rightarrow 0$ . From Fig. 7.6c, we see that the relation of  $S_0$  versus  $k_V^*/k_c$  for the CM cantilever ( $\alpha = 6$ ) approximately coincides with that for the point-mass model Eq. (7.41), as expected, and the CM cantilever improves the sensitivity especially at higher values of  $k_V^*/k_c$ .

## 7.2.2 Effects of Lateral Stiffness

The actual cantilevers have nonzero tip heights. The deflection angle at the end of the cantilevers imposes a rotational motion on the tips, and induces a lateral motion of the contact point on sample surfaces. As a result, the resonant frequency is influenced by the lateral contact stiffness, as well as the vertical contact stiffness. In addition, a tilt of the cantilevers is given relatively to sample surfaces in the actual setup. The tilt also causes the resonant frequency to depend on the lateral contact stiffness. Some studies for AFAM and UAFM discussed these effects for normal cantilevers [14, 15, 33, 34]. In contrast, it was proved for the CM cantilevers that these effects are significantly suppressed, and that the approximation by the effective point-mass

model, such as Eq. (7.34), is still valid [8]. Furthermore, if one uses rod-like CMs that enhance the rotary inertia, see Fig. 7.7, the lateral contact stiffness can be detected independently of the vertical one from another contact resonance that depends only on the lateral stiffness [8].

In this section, we introduce the unique features of the CM cantilevers, according to the work [8]. It is assumed in the theoretical model that the CM is a thin rod of mass  $m_{\text{add}}$  and length  $l_m$ . A tip of length (height)  $h$  is attached at a distance  $l_t$  from the end of the CM rod, see Fig. 7.8. The rod is connected to the end of the flexural cantilever of mass  $m_{\text{can}}$  and length  $l$ . The gravitational center of the rod is at a distance  $l_g$  from the connected end ( $l_g = l_m/2$  for uniform rods). The tip-sample interaction is represented by the vertical contact stiffness  $k_V^*$  and the lateral contact stiffness  $k_L^*$ . The CM cantilever is tilted with an angle of  $q$ , and has a spring constant  $k_c$  relating the deflection at the tip site to the force acting in the tip direction.

Let us consider now natural flexural vibrations of the cantilever with small-amplitudes and negligible small damping. The equation of motion is described by

$$\ddot{w}(x, t) + (EI/\rho A)w''''(x, t) = 0. \quad (7.42)$$

The flexural rigidity to mass per unit length of the cantilever is described by  $EI/(\rho A) = l^4 k_{c0}/(3m_{\text{can}})$ , where  $k_{c0}$  is the spring constant of the flexural part. The spring constant  $k_{c0}$  is related to  $k_c$  by  $k_{c0} = k_c[1 + 3(l_t/l) + 3(l_t/l)^2]$ , which is obtained from elementary flexural theory. The boundary conditions are given by  $w(0, t) = w'(0, t) = 0$ . The conditions for the shear force acting the cantilever  $F = (k_{c0}l^3/3)w'''(l, t)$  and for the bending moment  $M = (k_{c0}l^3/3)w''(l, t)$  are derived from the equations of translational motion and rotational motion on the gravitational center of the CM rod:

$$F = \hat{k}_V w(l + l_t, t) + \hat{k}_{LV} w'(l, t)h + m_{\text{add}} w''(l + l_g, t), \quad (7.43a)$$

$$M = -[\hat{k}_V w(l + l_t, t) + \hat{k}_{LV} w'(l, t)h] l_t - [\hat{k}_{LV} w(l + l_t, t) + \hat{k}_L w'(l, t)h] h - m_{\text{add}} w''(l + l_g, t)l_g - J_m \ddot{w}'(l + l_g, t), \quad (7.43b)$$

where  $J_m$  is the moment of inertia on the gravitational center of the CM rod. The symbols with a hat are the effective contact stiffness that contains the effect of the tilt angle  $q$ , defined as [15]:

$$\left. \begin{aligned} \hat{k}_V &= k_V^* \cos^2 q + k_L^* \sin^2 q \\ \hat{k}_L &= k_L^* \cos^2 q + k_V^* \sin^2 q \\ \hat{k}_{LV} &= (k_L^* - k_V^*) \cos q \sin q \end{aligned} \right\}. \quad (7.44)$$

Substituting the solution form  $w(x, t) = Z(x)\sin(\Omega t - \phi_0)$  into Eq. (7.42), we have the form of the mode function  $Z(x)$ :

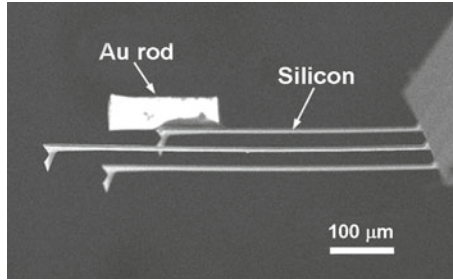
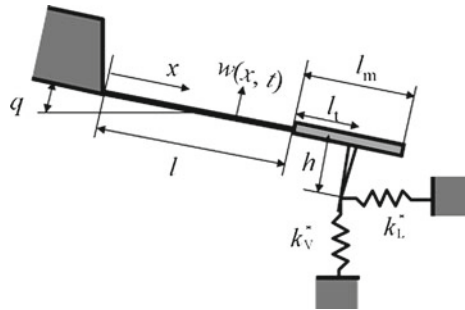


**Fig. 7.7** SEM image of the rod-like CM cantilever, where the CM is made by cutting a gold wire of  $30\ \mu\text{m}$  in diameter into a length of  $l_m = 100\ \mu\text{m}$ . The other data of the cantilever are as follows:  $k_c = 0.86\ \text{N/m}$ ,  $l = 187\ \mu\text{m}$ ,  $l_t = 0.55l_m$ ,  $h = 24\ \mu\text{m}$ ,  $m_{\text{add}} = 1.38\ \mu\text{g}$ ,  $\alpha = 44.9$ ,  $l_g = l_m/2$ , the first resonant frequency  $f_0 = 4.9885\ \text{kHz}$ , and the second resonant frequency  $f_{0\phi} = 61.5\ \text{kHz}$  with the end free. The second resonance ( $f_{0\phi}$ ) provides the rotational tip motion (see Fig. 7.10)

**Fig. 7.8** A model of vibrations of the CM cantilevers whose tip is in contact with a sample. The tip-sample interactions are represented by the linear springs in the vertical and lateral directions, where the rod-like CM is simplified as a thin rigid segment with the mass  $m_{\text{add}}$  and the length  $l_m$



$$Z(x) = K_1 \sin(\xi x/l) + K_2 \cos(\xi x/l) + K_3 \sin h(\xi x/l) + K_4 \cosh(\xi x/l), \quad (7.45)$$

where  $\xi = \Omega^{1/2}(3m_{\text{can}}/k_{c0})^{1/4}$ , and  $\Omega$  and  $\phi_0$  are natural angular frequency and constant phase angle, respectively. Again we substitute the solution together with Eq. (7.45) in all the boundary conditions. Then we have conditions on the coefficients  $K_1$  to  $K_4$ , which determine the frequency equation:

$$C_0 + C_1 \cos \xi \cosh \xi + C_2 \sin \xi \cosh \xi + C_3 \cos \xi \sinh \xi + C_4 \sin \xi \sinh \xi = 0, \quad (7.46)$$

where

$$\begin{aligned}
C_0 &= 1 + PQ - D_1 D_2 - P\alpha\xi V, & C_1 &= -1 + PQ + D_1 D_2 + P\alpha\xi V, \\
C_2 &= P + Q - PQ\alpha\xi \left\{ 1 + \xi^2 \left[ (l_g/l)^2 + J_C / (m_{\text{add}} l^2) \right] \right\} \\
&\quad + 2PD_1(l_t/l) + Q\xi^2(l_t/l)^2, \\
C_3 &= P - Q + PQ\alpha\xi \left\{ 1 - \xi^2 \left[ (l_g/l)^2 + J_C / (m_{\text{add}} l^2) \right] \right\} \\
&\quad + 2PD_1(l_t/l) + Q\xi^2(l_t/l)^2, \\
C_4 &= 2\sqrt{PQD_1D_2} - 2PQ\alpha\xi^2(l_g/l) + 2Q\xi(l_t/l), \\
V &= 1 - Q\alpha\xi^3 J_C / (m_{\text{add}} l^2) + 2D_1(l_t - l_g)/l \\
&\quad + (D_1/D_2)[J_C / (m_{\text{add}} l^2) + (l_g - l_t)^2 / l^2], \\
P &= \xi^3 / [3(k_V^* / k_{c0})(\cos^2 q + r \sin^2 q)], \\
Q &= \xi / [3(h/l)(k_V^* / k_{c0})(r \cos^2 q + \sin^2 q)], \\
D_1 &= (r - 1) \tan q / [(h/l)(r + \tan^2 q)], & D_2 &= (h/l)(r - 1) \tan q / (1 + r \tan^2 q), \\
r &= k_L^* / k_V^*, \\
J_C &= \eta(m_{\text{add}} l_m^2 / 12). \tag{7.47}
\end{aligned}$$

The coefficient  $\eta$  in the equation for  $J_C$  is an adjustment factor counting for effects of a non-zero diameter of the CM rod. The solutions  $\xi$  of Eq. (7.46), which give the natural frequencies  $\Omega$ , and also approximate the resonant frequency measured in AFAM and UAFM using the CM cantilevers.

Figure 7.9 shows an example of variation in the  $f_{\text{res}}$  versus  $k_V^*$  relation when increasing the length ( $l_m$ ) of an attached Au rod from  $l_m = 0$  with keeping the original length of the cantilever  $l + l_t = 242 \mu\text{m}$  and the diameter of the rod. The other data are the same as those in Fig. 7.7. The tilt angle  $q$  is set a typical value of  $14^\circ$ , and the stiffness ratio  $r$  is assumed 0.8. The values of  $(k_{c0}/m_{\text{can}})^{1/2}/(2\pi)$  and  $\eta$  are set 48.713 kHz and 1.582, respectively, so as to equate the prediction of the first and second resonant frequencies,  $f_0$  and  $f_{0\varphi}$ , under the free end for  $l_m = 100 \mu\text{m}$  with the experimental data shown in the caption of Fig. 7.7. With an increase in  $l_m$  a steep curve appears like ABC in Fig. 7.9b, which coincides with the effective point-mass model, namely Eq. (7.34), in spite of presence of the lateral contact stiffness. This means that the attachment of the CM suppresses a rotational motion of the tip. It is also interesting that another steep curve appears like DEF in Fig. 7.9c with a further increase in  $l_m$ .

Figure 7.10 shows the vibration modes at several points on the curves in Fig. 7.9c. It should be noted that, for the curve connecting the points A2-B2-C1-D1-E1-H2 (correspond to the curve DEF in Fig. 7.9c), the vibration modes always have a node at the tip. This means that the tip motion becomes purely rotational and interacts only with the lateral contact stiffness. The rotational vibration of the tip can be approximated with the one-freedom model shown in Fig. 7.11:



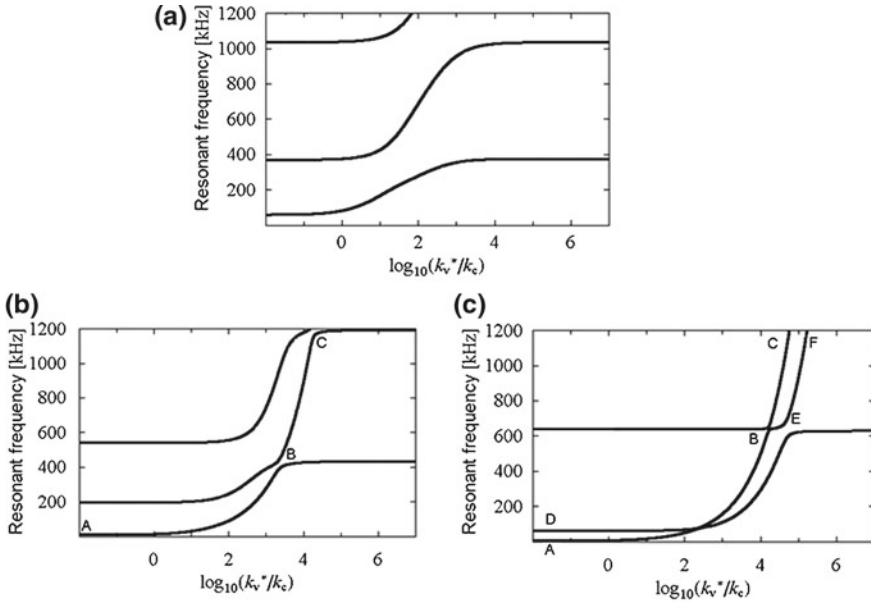


**Fig. 7.9** Effects of the length  $l_m$  of the CM on the relation between the resonant frequency and the normalized vertical contact stiffness, where the tip mass is added to  $m_{\text{add}}$  in calculation of the mass ratio  $\alpha$ . The cases are given: **a** for a normal cantilever ( $l_m = 0$ ,  $\alpha = 0.094$ , and  $\beta = 0$ ), **b** for a CM cantilever similar to the type shown in Fig. 7.1 ( $l_m = 30 \mu\text{m}$ ,  $\alpha = 11$ , and  $\beta = 0.2$ ), and **c** for a CM cantilever similar to the type shown in Fig. 7.7 ( $l_m = 100 \mu\text{m}$ ,  $\alpha = 45$ , and  $\beta = 13$ ). Reprinted with permission from [8]. Copyright 2007 Institute of Physics Publishing

$$f_{\text{res}} = f_0\phi\sqrt{1 + \frac{h^2k_L^*}{k_{c\phi}}} = f_0\phi\sqrt{1 + \left(\frac{k_V^*}{k_c}\right) \frac{3h^2r}{4(l^2 + 3l_t l + 3l_t^2)^2}}, \quad (7.48)$$

where  $k_{c\phi}$  is the spring constant of the spiral spring that provides a restoring moment  $M$  against the rotational motion with the angle  $\phi$  of the rod-like CM around the fixed axis on the tip, see Fig. 7.11b. The angular spring constant  $k_{c\phi}$  is related to the translational spring constant  $k_c$ . The relation is given by  $k_{c\phi} = M/\phi = (4/3)(l^2 + 3l_t l + 3l_t^2)^2 k_c$  from elementary flexural theory. Although the curve connecting the points A2-B2-C1-D1-E1-H2 apparently shows a dependence on the vertical stiffness  $k_V^*$  in Fig. 7.10, it is, indeed, independent of  $k_V^*$  because it is fitted well by Eq. (7.48), which predicts a dependence only on the lateral stiffness. When changing the stiffness ratio ( $r$ ), the curve connecting the points A2-B2-C1-D1-E1-H2 also changes in accordance with Eq. (7.48) while the curve connecting the points the curve connecting the points A1-B1-C2-D2-E2-H2 keep stationary.

We confirmed from additional analyzes that the effective point-mass model, Eq. (7.34), is still valid for  $k_V^*$  detection if  $\alpha$  is larger than about 4 and  $\theta$  is less than about  $15^\circ$ . Furthermore, the spiral-spring model, Eq. (7.48), is also applicable if the ratio of inertia moment,  $\beta$ , defined by the following, is larger than about 4.

**Fig. 7.10** Vibration modes of the CM cantilever that has a large moment of inertia on the tip (c in Fig. 7.9). Reprinted with permission from [8]. Copyright 2007 Institute of Physics Publishing

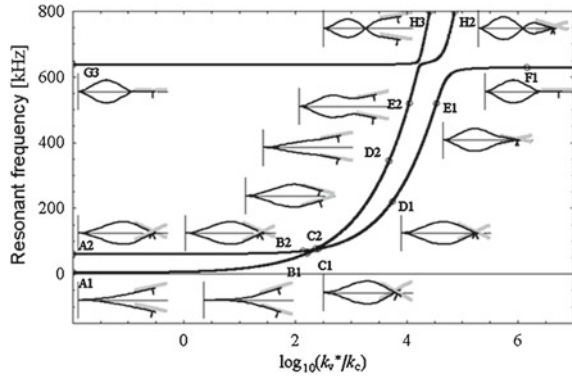
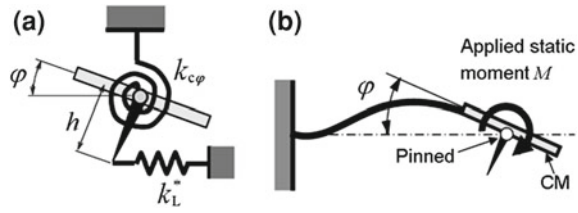


**Fig. 7.11 a** The spiral-spring model that is equivalent to the vibration mode with the rotational tip motion. **b** The static problem in which the CM cantilever pinned at the root of a tip is subject to the moment, for determining the spiral-spring constant  $k_{c\varphi}$



$$\beta = (m_{\text{add}}l_m^2)/(m_{\text{can}}l^2) = \alpha(l_m/l)^2. \tag{7.49}$$

This finding leads us to expect simultaneous detections of the vertical and lateral stiffness without their interaction. If the tip–sample friction is large, resulting in no slips of the tip, one can detect the lateral stiffness from the unique mode that provides the rotational (or lateral) tip motion by using the CM cantilevers [8], without any additional experiments such as the excitation of the torsional vibrations [15] or the assumption on the value of the stiffness ratio [14].

### 7.3 Experimental Demonstrations with CM Cantilevers

#### 7.3.1 Contact Spectra and Elasticity Mapping

##### 7.3.1.1 Experimental Procedure

A rectangular cantilever made of single-crystalline silicon ( $\mu$ Masch Co. Ltd., Type NSC12-F,  $35 \times 250 \times 2 \mu\text{m}$ , spring constant 1 N/m, fundamental resonant frequency 46 kHz) was used for the main body of the CM cantilever. The silicon tip attached to

the cantilever had an apex radius of about 10 nm and was coated with a 25-nm-thick  $W_2C$  or Pt/Ti film to prevent contact damages such as wearing. Brittleness of the  $W_2C$  coating ensures a stable tip shape but results in a relatively short lifetime due to abrupt detachment from the silicon tip. The Pt/Ti coating does not detach, but rather, easily undergoes plastic deformation. A tip with the latter coating was intentionally deformed under a contact load of 1–2  $\mu\text{N}$  to give it a flat-ended shape. The flat tip greatly simplifies the evaluation of elastic modulus in AFAM (see Sect. 7.3.2.1).

A tungsten (W) particle was selected as the concentrated mass because of its high density. An adequate-sized particle was picked up from a pinch of pure tungsten powder (Kojundo Chemical Lab. Co. Ltd., Deoxidized powder, 53  $\mu\text{m}$  mesh pass) by a micropipette in 3D micromanipulation under an optical microscope. The mass selected ranged from about 200 to 540 ng, which corresponds to  $\alpha = 5\text{--}12$ . The W particle was glued on the tip in the micromanipulation, where a UV-curable adhesive was used for convenience. Figure 7.1 shows an example that was fabricated in this way.

Atomic force microscopes (JEOL Co. Ltd., JSPM-4200 or SII Co. Ltd., SPI3700-SPA270) were used with a few modifications for imaging elasticity and acquiring contact resonance spectra. A piezoelectric element was inserted beneath a sample. Cantilever vibrations were measured by an optical lever technique using a position sensitive detector (PSD), which was a standard function of the systems (JSPM-4200 and SPA270). Because the CM cantilevers allowed the target contact-resonance to appear at lower frequencies in comparison with normal cantilevers, the built-in PSD, whose response was in the frequency range less than about 500 kHz, was available. The signal of cantilever vibrations and the sinusoidal excitation voltage as the reference signal were fed to a lock-in amplifier through a heterodyne down-converter. The function generator, the heterodyne down-converter, and the lock-in amplifier were controlled by a personal computer with GP-IB interfaces.

The cantilever was brought into contact with a sample. The contact force ( $F_e$ ) was set to several different values from 100 to 900 nN to determine a resonant peak sensitive to the contact stiffness. The time-averaged cantilever deflection signal, which corresponds to the contact force, was maintained through a built-in feedback circuit in the case of the so-called contact mode, where the electronic circuit is not subjected to sinusoidal signals at ultrasonic frequencies.

For imaging elastic heterogeneity of a surface, so-called slope detection was used for observing a shift in resonant frequency [38]. Excitation frequency was fixed near a resonant frequency sensitive to variations in contact stiffness. A shift in resonant frequency thus was observed through a change in the cantilever amplitude. When the damping is homogenous, such slope detection exhibits heterogeneity of the contact stiffness which varies with sample elasticity.

### 7.3.1.2 Contact Resonances for $W_2C$ -Coated Tips and Pt/Ti-Coated Flat Tips

The  $W_2C$ -coated tip had an apex radius of about 35 nm, i.e., a non-flat geometry. Thus, the contact force ( $F_e$ ) influenced the contact area. The contact stiffness and

**Fig. 7.12** The measurements of the contact resonance spectra for a glass surface by UAFM in combination with the CM cantilever equipped with a  $W_2C$ -coated normal tip. Reprinted with permission from [9]. Copyright 2005 Institute of Physics Publishing

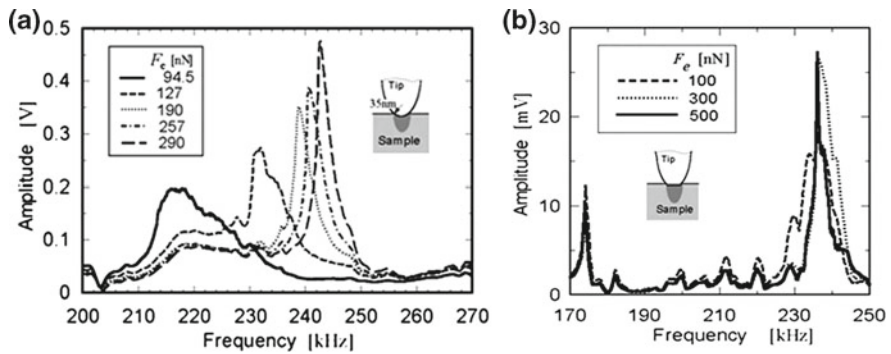
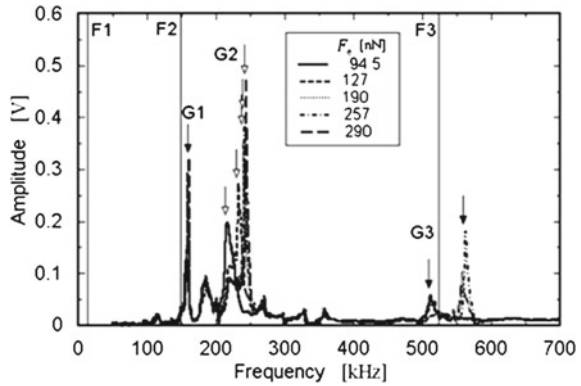


**Fig. 7.13** The second resonance spectra measured, **a** for a glass surface using the CM cantilever with the  $W_2C$ -coated normal tip (G2 in Fig. 7.12), and **b** for Si(100) wafer surface using the CM cantilever with the Pt/Ti coated flat tip. Reprinted with permission from [9]. Copyright 2005 Institute of Physics Publishing

resonant frequency are also expected to depend on the contact force. Figure 7.12 shows the spectra observed for the optical glass slide surface in UAFM using the CM cantilever with the  $W_2C$ -coated tip. The spectra are compared at several values of  $F_e$ . Arrows  $G_i$  ( $i = 1, 2, 3$ ) indicate the resonant peaks. The numeral  $i$  denotes the order of resonance. The vertical lines  $F_i$  ( $i = 1, 2, 3$ ) indicate the fundamental, second, and third resonant frequencies in no interaction with the sample. As expected, the first and third contact resonance ( $G_1, G_3$ ) arose near the free resonance ( $F_2, F_3$ ). For these trivial modes, the end deflection is zero like at a pinned end.

On the other hand, the second contact resonant frequency  $G_2$  clearly depended on  $F_e$ . Figure 7.13a shows a detail near the second resonance in Fig. 7.12, where the resonant frequency can be seen to increase with the contact force, and hence, with the contact stiffness. This indicates a contact resonance sensitive to variations in contact stiffness. In addition, all the resonant frequencies obeyed the theory of

**Fig. 7.14** The resonant frequency versus the normalized contact stiffness, where the measurements (Fig. 7.12) are compared with the theoretical prediction (see Fig. 7.5). Reprinted with permission from [9]. Copyright 2005 Institute of Physics Publishing

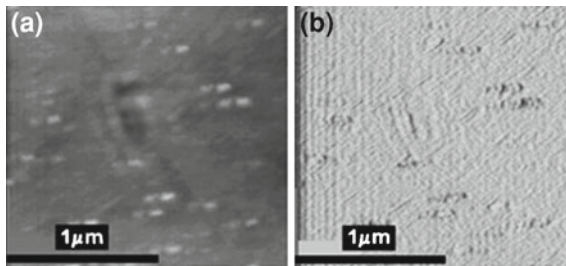
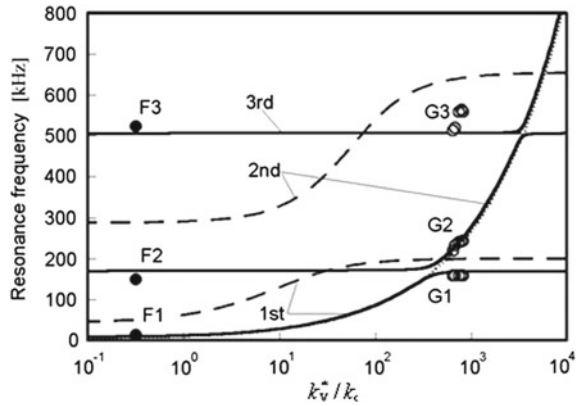


**Fig. 7.15** AFAM images of **a** topography and **b** elasticity (contact stiffness) for optical slide glass, obtained using the normal cantilever with the W<sub>2</sub>C-coated tip. The contact force was 190 nN. The 2nd resonant frequency was 532 kHz. The excitation frequency was set 528 kHz. Reprinted with permission from [9]. Copyright 2005 Institute of Physics Publishing

CM cantilevers reasonably well, as denoted by circles in Fig. 7.14, where  $k_v^*$  was estimated from a modified Hertzian contact model [31].

Figure 7.13b shows spectra for an etched Si(100) wafer, measured with the Ti/Pt-coated flat tip in AFAM. The resonant peak sensitive to the contact stiffness can be identified by the fact that the resonant peak is located apart from the trivial resonant frequencies (F2: 171.1 kHz, F3: 530.0 kHz). In contrast to the normal tip (Fig. 7.13a), the resonant frequency (around 236 kHz) seems to be independent of the contact force for the flat tip. This finding reflects the constant contact area observed in the case of the flat tip.

### 7.3.1.3 Elasticity Mapping

Figures 7.15 and 7.16 show the topography and elasticity (or more precisely contact stiffness) images for an optical glass slide. Figure 7.15 was obtained for the normal cantilever with the W<sub>2</sub>C-coated tip. Figure 7.16 was acquired by using the CM

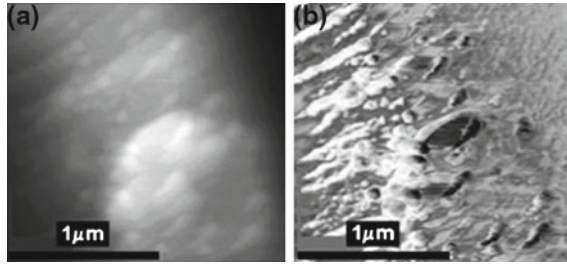
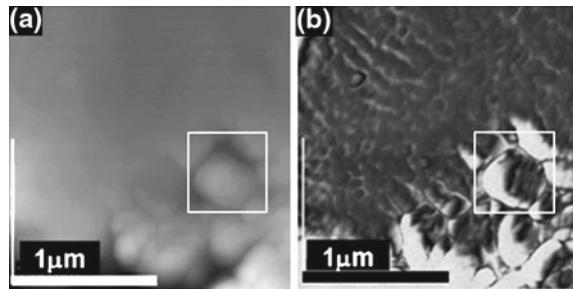


**Fig. 7.16** AFAM images of **a** topography and **b** elasticity (contact stiffness) for optical slide glass, obtained by using the CM cantilever ( $\alpha = 5$ ) with the  $W_2C$ -coated tip. The contact force was 190 nN. The 2nd resonant frequency ( $G_2$ ) was 224 kHz, and the excitation was made at 215 kHz. Reprinted with permission from [9]. Copyright 2005 Institute of Physics Publishing

**Fig. 7.17** AFAM images of **a** topography and **b** elasticity for a Ti sheet surface, obtained with the CM cantilever having the Pt/Ti flat tip, which was excited at a frequency of 286 kHz under a contact force of 875 nN. Reprinted with permission from [9]. Copyright 2005 Institute of Physics Publishing



cantilever ( $\alpha = 5$ ) with the  $W_2C$ -coated tip. In the topographical image (a), bright areas indicate high altitude. In Fig. 7.16a, the maximum difference in height ( $PV$ : Peak to Valley) is about 350 nm. In elasticity images (b), bright areas indicate soft surfaces. It is noted that the elasticity image obtained using the CM cantilever (Fig. 7.16b) reveals a clear contrast, indicative of the heterogeneous properties of the polished glass surface. By contrast, the normal cantilever does not produce meaningful contrast for elasticity (Fig. 7.15b). Unfortunately, contact resonant peaks, such as those in Fig. 7.13a, disappeared suddenly after several scans. This was due to detachment of the  $W_2C$  coated tip followed by tip disruption.

Figure 7.17 shows AFAM images of a Ti sheet (0.1 mm thick), for which the CM cantilever with a Pt/Ti-coated flat tip. The elasticity image in Fig. 7.17 reveals grains tens of nanometers in size, which are not observed in the topography. Figure 7.18 is a close-up of a large grain in Fig. 7.17. The elasticity image in Fig. 7.18 clearly shows the heterogeneity of the grain boundary. It also reveals darker (i.e., stiffer) patterns inside the grain. Contact resonance at points a, b, and c was actually shifted, as shown in Fig. 7.18c, so as to increase the contact stiffness. The pattern inside the grain seems to be due to piling up of dislocations like slip bands or crystal anisotropy of the exposed uneven surface, i.e., the fact that the crystallographic orientation normal to the exposed surface depends on the normal direction of the

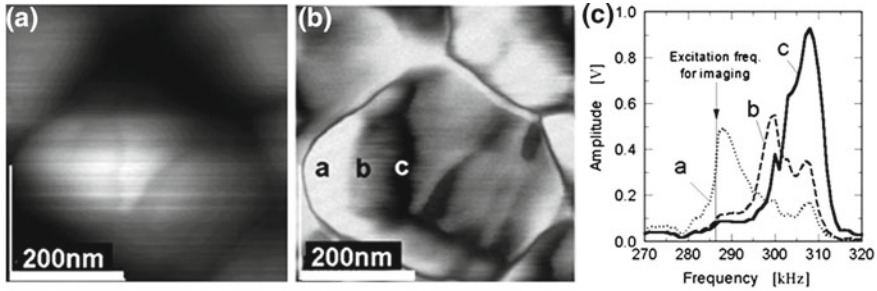


**Fig. 7.18** AFAM images of **a** topography and **b** elasticity for the Ti sheet surface, closed up at the region denoted by the rectangular in Fig. 7.17a. **c** The resonance spectra corresponding to the positions *a*, *b*, and *c* in **b**. Reprinted with permission from [9]. Copyright 2005 Institute of Physics Publishing

surface of the single grain. Each image mentioned above was acquired at an excitation frequency slightly lower than the resonant frequency. When an excitation frequency was set to be higher than the resonance, the elasticity image reversed contrast. This provides undisputed evidence that the contrast of elasticity images is mainly due to the variation of contact stiffness, rather than heterogeneous viscosity damping. It is also noted that the contact stiffness depends on local roughness within the contact area of the sample surface in addition to local elasticity. The effects of local roughness on images may not be ignored, especially for grain boundaries and slip bands. Furthermore, other geometrical artifacts should be noted, which appear on steep areas like the inclined surfaces of coarse grains in Figs. 7.17 and 7.18. In such regions, it may be difficult to achieve full contact of the flat tip due to the large tilt and the contact area may be significantly reduced. Indeed, all the bright areas in the elasticity images of Figs. 7.17b and 7.18b, corresponding to low contact stiffness, are located on the inclined surfaces of coarse grains in the topography (Figs. 7.17a and 7.18a).

## 7.3.2 Quantitative Evaluation for Elastic Modulus

### 7.3.2.1 Calibration Curve

In order to evaluate sample surfaces for elastic modulus by AFAM and UAFM, one is required to relate the contact stiffness with elastic modulus of samples. Theories of contact mechanics e.g., [35, 36] provide some theoretical formulas for the relation between the contact force and the penetration, which predicts the contact stiffness. Also, empirical formulas based on in part their theories and some experiments are available e.g., [31], see Eq. (7.7). These formulas suggest that the contact stiffness ( $k_v^*$ ) is proportional to the radius  $a$  of the contact area:

$$k_V^* = 2aE^*, \quad (7.50)$$

where the radius  $a$  normally depends on the contact force ( $F_e$ ), the tip-apex geometry, the effective Young's modulus ( $E^*$ ), see Eq. (7.8), and the adhesion between the tip and sample. Effects of the adhesion force on the contact stiffness cannot be ignored in AFAM and UAFM, where profiles of actual tip-apexes are not simple [15] but frequently assumed to be spherical (precisely parabolic) [4, 7, 14, 17, 20, 23–26, 33]. By contrast, a flat tip maintains a constant contact area independent of the adhesion force and the contact force. This ensures that the contact stiffness is also constant. A real flat tip may have a slightly rough and rounded apex surface. However, a constant contact area can be achieved provided the contact force is sufficient [9].

For stiff samples like metals and ceramics,  $k_V^*/k_c \gg 1$ , Eq. (7.34) approximates to:

$$k_V^*/k_c = (f_{\text{res}}/f_0)^2. \quad (7.51)$$

Equations (7.8), (7.50), and (7.51) give the relationship between the contact resonant frequency and the effective Young's modulus  $E_s^* [= E_s/(1 - \nu_s^2)]$  of a sample:

$$f_{\text{res}} = \sqrt{2AE_t^*E_s^*/(E_t^* + E_s^*)}, \quad (7.52)$$

where  $E_t^* [= E_t/(1 - \nu_t^2)]$  is the effective Young's modulus of the tip. The coefficient  $A$  is a factor proportional to the radius of the contact area, defined as:

$$A = af_0^2/k_c. \quad (7.53)$$

Note that the contact radius ( $a$ ) is constant for the flat tips. Predetermining values of  $E_t^*$  and  $A$  with some reference surfaces, we can evaluate the effective Young's modulus of a sample ( $f_{\text{res}}$ ) from Eq. (7.52) and measurements of the resonant frequency.

Typical references include silicon wafers Si(100), Si(111), a sapphire wafer Al<sub>2</sub>O<sub>3</sub>(0001), and a diamond wafer C(100). Their elastic moduli are calculated in [9, 37] from the crystal moduli determined by ultrasonic velocity techniques for bulk samples [38]. Figure 7.19 shows examples of spectra for the references observed by using the CM cantilever ( $\alpha = 11$ ,  $k_c = 0.65$  N/m) with the flat Pt/Ti tip, which measured  $f_0 = 9.917$  kHz. Fitting Eq. (7.52) to the relationship between the measurements of  $f_{\text{res}}$  and the effective Young's moduli calculated, we determined  $A$  and  $E_t^*$ , which are hard to measure or estimate directly. Figure 7.20 shows the least-squares fit obtained for the references. It yielded  $A = 0.2496 \pm 0.0061$  ( $\pm 2\sigma$ ) m/kg and  $E_t^* = 184.6 \pm 8.8$  ( $\pm 2\sigma$ ) GPa, where  $\sigma$  is a standard deviation. Use of the values of  $A$ ,  $k_c$  and  $f_0$  produced a reasonable contact radius  $a = 1.7$  nm. Also, the value of  $E_t^*$  is comparable to the averaged value for bulk platinum (196 GPa) and bulk titanium (129 GPa). The square of the correlation coefficient ( $r^2 = 0.9987$ ) of the fit confirms the validity of the theory on the CM cantilevers.



**Fig. 7.19** The measurements of contact resonance spectra for the reference surfaces, the Co–Cr coated substrate, and the DLC thin films on the substrate. Reprinted with permission from [37]. Copyright 2010 Springer

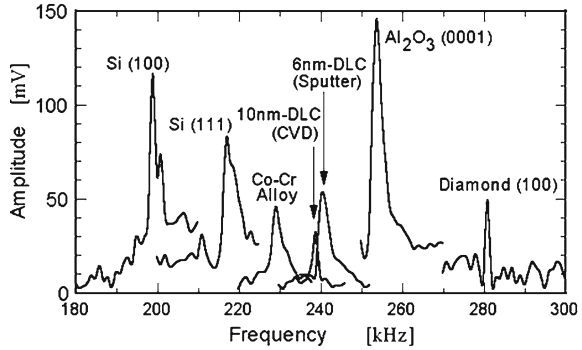
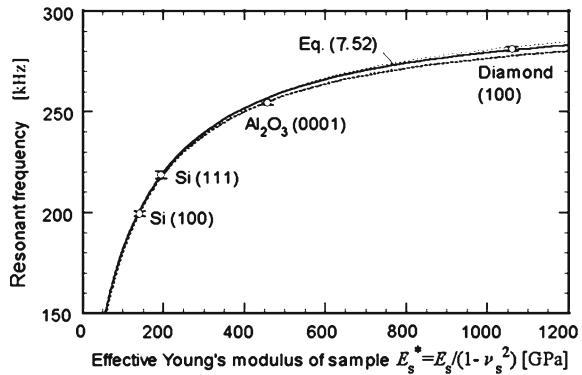


**Fig. 7.20** The calibration curve for the determination of the effective Young’s modulus of samples. Reprinted with permission from [37]. Copyright 2010 Springer



**7.3.2.2 Evaluation of Thin Films**

Let us introduce now an example of the evaluation of thin films for elastic modulus [37]. The thin films are diamond-like carbon (DLC) films of 6 nm thick and 10 nm thick, which were deposited on a substrate by sputtering a carbon target in Ar gas and by plasma-assisted chemical vapor deposition (CVD), respectively. The film thickness was estimated based on the deposition time. The substrate was a hard disk, which consisted of metallic multilayers for magnetic record and a glass substrate, namely 50-nm-thick Co–Cr-alloy layer, 70-nm-thick Ti-alloy layer, 0.6-mm-thick glass substrate. Also the substrate without DLC coating was tested for the elastic modulus.

Theoretical models on indentation of a layered half-space for a circular punch proved the validity of the following empirical formula [39]:

$$\frac{1}{E_s^*} = \frac{1}{E_{\text{film}}^*} \left[ 1 - \exp\left(-\frac{\gamma t_{\text{film}}}{a}\right) \right] + \frac{1}{E_{\text{sub}}^*} \exp\left(-\frac{\gamma t_{\text{film}}}{a}\right), \tag{7.54}$$

where  $E_{\text{film}}^*$  and  $E_{\text{sub}}^*$  are the effective Young's moduli of a film and a substrate, respectively. The coefficient  $\gamma$  is a function of  $a/t_{\text{film}}$ , where  $t_{\text{film}}$  is the film thickness. The numerical result on a relation of  $\gamma$  and  $a/t_{\text{film}}$  was graphically shown in [39]. Note that the symbol  $a$  in [39] is defined as the square root of the contact area, which differs from the definition of  $a$  (the radius of the contact area) in (Eq. 7.54), and then  $\gamma$  multiplied by  $\pi^{1/2}$  equals the symbol  $\alpha$  in [39]. The numerical data can be well fitted by the following formula [37].

$$\gamma = c_0 (a/t_{\text{film}})^{n_0} / \left[ (a/t_{\text{film}})^{n_1} + c_2 (a/t_{\text{film}})^{n_2} + c_3 \right], \quad (7.55)$$

where  $c_0 = 0.4684$ ,  $c_2 = 0.009968$ ,  $c_3 = 1.004$ ,  $n_0 = 0.4910$ ,  $n_1 = 1.736$ , and  $n_2 = 6.607$  are the coefficients determined by a nonlinear least square fit.

The samples coated with the 6-nm-thick DLC film (Sputter) and the 10-nm-thick DLC film (CVD) measured  $f_{\text{res}} = 240.4 \pm 1.6 (\pm 2\sigma)$  kHz and  $f_{\text{res}} = 239.6 \pm 0.5 (\pm 2\sigma)$  kHz, respectively. The DLC coating shifted the resonant frequency to higher than that of the sample without DLC coating [ $f_{\text{res}} = 229.8 \pm 1.6 (\pm 2\sigma)$  kHz ( $F_e = 500$  nN)]. Also, the values of  $f_{\text{res}}$  for the two DLC films were alike despite the different thickness. This does not mean that the resonance is free from the substrate effects.

The effective Young's modulus of a sample was determined from the curve in Fig. 7.20 to be  $E_s^* = 310.5 \pm 11.4$ ,  $305.2 \pm 3.5$ , and  $247.8 \pm 8.2$  GPa for the hard disks with 6-nm-thick DLC (Sputter), 10-nm-thick DLC (CVD), and without DLC coating, respectively. The errors are in the 95% confidence regions. The last one corresponds to  $E_{\text{sub}}^*$ . Substituting the values of  $E_{\text{sub}}^*$  and  $E_s^*$  into Eq. (7.54), we obtained the effective Young's moduli of the films, where  $\gamma$  was calculated using  $a = 1.7$  nm and  $t_{\text{film}} = 6$  or 10 nm. The moduli were  $E_{\text{film}}^* = 391.8 \pm 34.7 (\pm 2\sigma)$  GPa and  $345.1 \pm 8.5 (\pm 2\sigma)$  GPa for the 6-nm DLC (Sputter) and the 10-nm DLC (CVD), respectively. The presence of substrate effects was clear in that the values of  $E_s^*$  for the 6-nm-film-coated and 10-nm-film-coated samples were 20 and 10% less than the corresponding values of  $E_{\text{film}}^*$ , respectively. The values of  $E_{\text{film}}^*$  were within range of the values reported for several DLC films, from 100 to 800 GPa [40–43]. Also a good precision of  $2\sigma < 10\%$  was attained. An error in  $a/t_{\text{film}}$  also causes uncertainty of the results. A postulated error of 20% in  $a/t_{\text{film}}$  results in a relatively small error of about 5 and 2.5% in  $E_{\text{film}}^*$  for the DLC films of 6 nm thickness ( $a/t_{\text{film}} = 0.283$ ) and 10 nm thickness ( $a/t_{\text{film}} = 0.17$ ), respectively. The resulting error increases with  $a/t_{\text{film}}$ . Therefore, the contact radius ( $a$ ) should be minimized.

The indentation depth  $\delta_s$ , namely the total displacement  $\delta (= -z_e = F_e/k_V^*)$  minus the tip deformation, can be estimated by taking account of the contribution of a sample,  $k_s^* = 2aE_s^*$ , in the contact stiffness. The estimate was  $\delta_s = F_e/k_s^* = 0.57$  and  $0.77$  nm for the 6-nm-DLC and 10-nm-DLC samples, respectively. These indentation depths are 10% or less of the film thickness. The substrate effect should be carefully considered even when AFAM is applied. The present method provides the AFAM method of determining the elastic modulus for ultrathin films, eliminating the influence of a substrate. The sensitivity-enhanced AFAM in combination with the

CM cantilevers proved to be sensitive enough for the determination of the ultrathin-film elasticity and to have the excellent repeatability and reliability.

**Acknowledgments** The author acknowledges partial support from the Japan Society for the Promotion of Science (JSPS), through the Grant-in-Aid for Scientific Research (B) Grant Nos. 20360049, 21360046, 23360050, Scientific Research (A) Grant no. 20246028 and Challenging Exploratory Research Grant No. 23656077, and Ms. Y. Ishigami for her help in preparing the manuscript.

## Appendix I

Substituting Eq. (7.4) into Eq. (7.2) and then setting the coefficients of  $\sin n\omega t$  and  $\cos n\omega t$  to zero, we obtain differential equations for the vibration modes  $W_0(x)$ ,  $W_n(x)\sin\phi_n(x)$ , and  $W_n(x)\cos\phi_n(x)$ . The general solutions are obtained easily, and are of a form containing four arbitrary coefficients. Three of the four coefficients can be determined from Eq. (7.3a).

$$W_0(x) = W_0(l)x^2(3l - x)/(2l^3), \quad (\text{A.1a})$$

$$W_n(x) \sin \phi_n(x) = -A_n Y(x; \lambda_n) \quad (n = 1, 2, 3, \dots), \quad (\text{A.1b})$$

$$W_n(x) \cos \phi_n(x) = B_n Y(x; \lambda_n) + [(u_{b0} - u_{s0})U(x; \lambda_n) - u_{s0}] \delta_{1n} \quad (n = 1, 2, 3, \dots), \quad (\text{A.1c})$$

where

$$Y(x; \lambda_n) = \left( \sin \frac{\lambda_n x}{l} - \sinh \frac{\lambda_n x}{l} \right) - \left( \frac{\sin \lambda_n + \sinh \lambda_n}{\cos \lambda_n + \cosh \lambda_n} \right) \left( \cos \frac{\lambda_n x}{l} - \cosh \frac{\lambda_n x}{l} \right), \quad (\text{A.2a})$$

$$U(x; \lambda_n) = \left( \frac{\cosh \lambda_n}{\cos \lambda_n + \cosh \lambda_n} \right) \left( \cos \frac{\lambda_n x}{l} - \cosh \frac{\lambda_n x}{l} \right) + \cosh \frac{\lambda_n x}{l}. \quad (\text{A.2b})$$

The coefficients  $W_0(l)$ ,  $A_n$ , and  $B_n$  are determined from the remaining boundary condition, given by Eq. (7.3b).

Differentiating Eq. (A.1a–c) and then eliminating  $A_n$  and  $B_n$  by means of Eq. (A.1b and c), we have

$$W_0'''(l) = -(3/l^3)W_0(l), \quad (\text{A.3a})$$

$$[W_n(x) \sin \phi_n(x)]'''_{x=l} = (3/l^3)W_n(l) \sin \phi_n(l) \Psi(\lambda_n) \quad (n = 1, 2, 3, \dots), \quad (\text{A.3b})$$

$$\begin{aligned} [W_n(x) \cos \phi_n(x)]'''_{x=l} &= (3/l^3)W_n(l) \cos \phi_n(l) \Psi(\lambda_n) - (3/l^3) \\ &\times [(u_{b0} - u_{s0})\Theta(\lambda_n) - u_{s0}\Psi(\lambda_n)] \delta_{1n} \quad (n = 1, 2, 3, \dots). \end{aligned} \quad (\text{A.3c})$$

Using the remaining boundary condition Eq. (A.3b) together with Eq. (7.4), and (A.3a–c), we obtain the relationship

$$\begin{aligned}
k_c W_0(l) + \sum_{n=1}^{\infty} [k_c W_n(l) \sin \phi_n(l) \Psi(\lambda_n) + cn\omega W_n(l) \cos \phi_n(l) \\
+ m_{\text{add}}(n\omega)^2 W_n(l) \sin \phi_n(l)] \cos n\omega t \\
+ \sum_{n=1}^{\infty} \{ -k_c W_n(l) \cos \phi_n(l) \Psi(\lambda_n) \\
+ k_c [(u_{b0} - u_{s0}) \Theta(\lambda_n) - u_{s0} \Psi(\lambda_n)] \delta_{1n} \\
+ cn\omega W_n(l) \sin \phi_n(l) - m_{\text{add}}(n\omega)^2 \\
\times [W_n(l) \cos \phi_n(l) + u_{s0} \delta_{1n}] \} \sin n\omega t = \Delta F. \tag{A.4}
\end{aligned}$$

The left-hand side of Eq. (A.4) shows the Fourier expansion of the effective interaction force ( $\Delta F$ ). Therefore, we obtain Eq. (7.5a–c) from Eq. (A.4) together with the relation  $(n\omega)^2 = \lambda_n^4 k_c / (3m_{\text{can}})$ .

For the approximation of negligible higher harmonics, if the values  $W_1(l)$  and  $\phi_1(l)$  at the cantilever end are determined from Eq. (7.14a and b), one can obtain the coefficients  $A_1$  and  $B_1$  in the mode functions Eq. (A.1b and c):

$$A_1 = \frac{W_1(l) \tan \phi_1(l)}{Y(l; \lambda_1) \sqrt{1 + \tan^2 \phi_1(l)}}, \tag{A.5a}$$

$$B_1 = \frac{A_1}{\tan \phi_1(l)} - \frac{1}{Y(l; \lambda_1)} [(u_{b0} - u_{s0}) U(l; \lambda_1) - u_{s0}]. \tag{A.5b}$$

## Appendix II

For mathematical convenience, we expand  $F_{\text{cont}}(z)$  at  $z = z_e$  in a Taylor infinite series of the power of  $z - z_e (= W_0 + W_1 \sin \theta)$  and then expand each power; i.e.,  $(W_0 + W_1 \sin \theta)^k$ , into binomial series. Termwise integration of the infinite series is performed analytically by use of the following indefinite integrals:

$$\int \sin^{2p} \theta d\theta = \frac{(-1)^p}{2^{2p}} \left[ \sum_{r=0}^{p-1} (-1)^r \binom{2p}{r} \frac{\sin 2(p-r)\theta}{p-r} + (-1)^p \binom{2p}{p} \theta \right], \tag{A.6a}$$

$$\int \sin^{2p+1} \theta d\theta = \frac{(-1)^{p+1}}{2^{2p}} \sum_{r=0}^p (-1)^r \binom{2p+1}{r} \frac{\cos(2p-2r+1)\theta}{2p-2r+1}, \tag{A.6b}$$

where  $p$  is a positive integer and the following notation is used for the binomial coefficient.

$$\binom{n}{r} = \frac{n!}{r!(n-r)!}. \quad (\text{A.6c})$$

Then we obtain

$$\begin{aligned} & C_0(\bar{W}_0, \bar{W}_1; \bar{z}_e) \\ &= \left(1 - \frac{\Delta\theta}{2\pi}\right) \left\{ \frac{F_e}{k_c R} + \sum_{k=1}^{\infty} \frac{g^{(k)}(\bar{z}_e)}{k!} \left[ \bar{W}_0^k + \sum_{p=1}^{[k/2]} \binom{k}{2p} \binom{2p}{p} \bar{W}_0^{k-2p} \left(\frac{\bar{W}_1}{2}\right)^{2p} \right] \right\} \\ & \quad - \frac{2}{\pi} \sum_{k=1}^{\infty} \frac{g^{(k)}(\bar{z}_e)}{k!} \left[ \sum_{r=1}^k \binom{k}{r} \bar{W}_0^{k-r} \left(\frac{\bar{W}_1}{2}\right)^r \sum_{s=0}^{[(r-1)/2]} \binom{r}{s} \frac{\sin[(r-2s)\Delta\theta/2]}{r-2s} \right], \end{aligned} \quad (\text{A.7})$$

where  $[k/2]$  and  $[(r-1)/2]$  are the Gauss notations, which denote the largest integers less than  $k/2$  and  $((r-1)/2)$ , respectively.  $\Delta\theta$  is the interval of phase angle when the tip jumps out of the sample surface.

$$\Delta\theta = \begin{cases} 0 & (\bar{z}_e + \bar{W}_0 \leq -\bar{W}_1) \\ \pi - 2\text{Arc sin}[( -\bar{z}_e - \bar{W}_0)/\bar{W}_1] & (|\bar{z}_e + \bar{W}_0| < \bar{W}_1) \\ 2\pi & (\bar{z}_e + \bar{W}_0 \geq \bar{W}_1) \end{cases}. \quad (\text{A.8a})$$

$\Delta\theta = 0$  indicates the case of perfect contact and  $\Delta\theta = 2\pi$  the case of perfect separation during vibration. The function  $g(\bar{z})$  is the normalized interactive force:

$$g(\bar{z}) = \frac{F_{\text{cont}}(\bar{z})}{k_c R} = \left(\frac{4E^*R}{3k_c}\right) (-\bar{z})^{3/2} - \left(\frac{F_c}{k_c R}\right) - \left(\frac{\sqrt{2\pi w_{\text{ad}} E^* R}}{k_c}\right) (-\bar{z})^{3/4}. \quad (\text{A.8b})$$

The indefinite integral of  $F_{\text{sepa}}(z_e + W_0 + W_1 \sin\theta)$  can be obtained without series expansion. We obtain

$$\begin{aligned} S_0(\bar{W}_0, \bar{W}_1; \bar{z}_e) &= - \sum_{k=1}^s \left(\frac{F_k}{k_c R}\right) \bar{D}_k G_{01}(\bar{W}_0, \bar{W}_1; \bar{z}_e, \bar{D}_k) \\ & \quad - \sum_{k=s+1}^m \left(\frac{F_k}{k_c R}\right) \bar{D}_k^2 G_{02}(\bar{W}_0, \bar{W}_1; \bar{z}_e, \bar{D}_k), \end{aligned} \quad (\text{A.9})$$

where

$$\begin{aligned} G_{01}(\bar{W}_0, \bar{W}_1; \bar{z}_e, \bar{D}) &= \frac{1}{\pi \sqrt{(\bar{D} + \bar{z}_e + \bar{W}_0)^2 - \bar{W}_1^2}} \\ & \quad \times \left[ \arctan \frac{\bar{D} + (\bar{D} + \bar{z}_e + \bar{W}_0) \sin(\Delta\theta/2)}{\cos(\Delta\theta/2) \sqrt{(\bar{D} + \bar{z}_e + \bar{W}_0)^2 - \bar{W}_1^2}} \right] \end{aligned}$$

$$\left. -\text{Arc tan} \frac{\bar{D} - (\bar{D} + \bar{z}_e + \bar{W}_0) \sin(\Delta\theta/2)}{\cos(\Delta\theta/2) \sqrt{(\bar{D} + \bar{z}_e + \bar{W}_0)^2 - \bar{W}_1^2}} \right], \quad (\text{A.10a})$$

$$G_{02}(\bar{W}_0, \bar{W}_1; \bar{z}_e, \bar{D}) = \frac{\bar{D} + \bar{z}_e + \bar{W}_0}{(\bar{D} + \bar{z}_e + \bar{W}_0)^2 - \bar{W}_1^2} \times \left[ G_{01}(\bar{W}_0, \bar{W}_1; \bar{z}_e, \bar{D}) - \frac{\bar{W}_1 \sin(\Delta\theta/2)}{\pi \bar{D}(\bar{D} + \bar{z}_e + \bar{W}_0)} \right]. \quad (\text{A.10b})$$

The function  $\arctan(x)$  takes the principal value  $\text{Arctan}(x)$  when  $\bar{z}_e + \bar{W}_0 \leq 0$ , and becomes  $\pi + \text{Arctan}(x)$  when  $\bar{z}_e + \bar{W}_0 > 0$ . Equation (A.10a) is also applicable to  $(\bar{D} + \bar{z}_e + \bar{W}_0)^2 < \bar{W}_1^2$ . In this case, the elemental functions in Eq. (A.10a) may be extended to the complex region.

Similarly, we have

$$\begin{aligned} C_1(\bar{W}_0, \bar{W}_1; \bar{z}_e) &= -\frac{1}{2} \left( 1 - \frac{\Delta\theta}{2\pi} \right) \sum_{k=1}^{\infty} \frac{g^{(k)}(\bar{z}_e)}{k!} \left[ \sum_{p=1}^{[(k+1)/2]} \binom{k}{2p-1} \binom{2p}{p} \right. \\ &\quad \left. \times \bar{W}_0^{k-2p+1} \left( \frac{\bar{W}_1}{2} \right)^{2p-2} \right] \\ &+ \frac{1}{\pi} \sum_{k=1}^{\infty} \frac{g^{(k)}(\bar{z}_e)}{k!} \left[ \sum_{r=1}^k \binom{k}{r} \bar{W}_0^{k-r} \left( \frac{\bar{W}_1}{2} \right)^{r-1} \sum_{s=0}^{[r/2]} \binom{r+1}{s} \right. \\ &\quad \left. \times \frac{\sin[(r-2s+1)\Delta\theta/2]}{r-2s+1} \right] \\ &+ \frac{2}{\pi \bar{W}_1} \sin \frac{\Delta\theta}{2} \left[ \frac{F_e}{k_c R} + \sum_{k=1}^{\infty} \frac{g^{(k)}(\bar{z}_e)}{k!} \bar{W}_0^k \right], \quad (\text{A.11}) \end{aligned}$$

$$\begin{aligned} S_1(\bar{W}_0, \bar{W}_1; \bar{z}_e) &= -2 \sum_{k=1}^s \left( \frac{F_k}{k_c R} \right) \left( \frac{\bar{D}_k}{\bar{W}_1} \right) G_{11}(\bar{W}_0, \bar{W}_1; \bar{z}_e, \bar{D}_k) \\ &- 2 \sum_{k=s+1}^m \left( \frac{F_k}{k_c R} \right) \left( \frac{\bar{D}_k}{\bar{W}_1} \right)^2 G_{12}(\bar{W}_0, \bar{W}_1; \bar{z}_e, \bar{D}_k), \quad (\text{A.12}) \end{aligned}$$

where

$$G_{11}(\bar{W}_0, \bar{W}_1; \bar{z}_e, \bar{D}) = \left( \frac{\bar{D} + \bar{z}_e + \bar{W}_0}{\bar{W}_1} \right) G_{01}(\bar{W}_0, \bar{W}_1; \bar{z}_e, \bar{D}) - \frac{\Delta\theta}{2\pi \bar{W}_1}, \quad (\text{A.13a})$$

$$G_{12}(\bar{W}_0, \bar{W}_1; \bar{z}_e, \bar{D}) = \frac{(\bar{D} + \bar{z}_e + \bar{W}_0)^2}{(\bar{D} + \bar{z}_e + \bar{W}_0)^2 - \bar{W}_1^2} \times \left[ \left( \frac{\bar{W}_1}{\bar{D} + \bar{z}_e + \bar{W}_0} \right)^2 G_{01}(\bar{W}_0, \bar{W}_1; \bar{z}_e, \bar{D}) - \frac{\bar{W}_1 \sin(\Delta\theta/2)}{\pi \bar{D}(\bar{D} + \bar{z}_e + \bar{W}_0)} \right]. \quad (\text{A.13b})$$

### Appendix III

In order to relate the damping coefficient ( $c$ ) with the quality factor ( $Q$ ), let us consider the case of linear contact vibration with low damping. For the  $n$ th order resonance, the amplitude  $W^{(n)}$  at  $x = l$  is approximated by using Eq. (7.21a):

$$(W^{(n)})^2 = k_c^2 \left\{ (u_{b0} - u_{s0})\Theta(\lambda^{(n)}) - u_{s0} \left[ \Psi(\lambda^{(n)}) + \alpha(\lambda^{(n)})^4/3 \right] \right\}^2 / (c\omega^{(n)})^2, \quad (\text{A.14})$$

where  $\omega^{(n)} = (\lambda^{(n)})^2 [k_c/(3m_{\text{can}})]^{1/2}$ , and  $\lambda^{(n)}$  is the  $n$ th root of Eq. (7.22). Let  $2\Delta\omega$  denote the full width at half maximum  $W^2 = (W^{(n)})^2/2$ , where  $\Delta\omega = \omega - \omega^{(n)} = 2\omega^{(n)} \Delta\lambda/\lambda^{(n)}$ . After expanding the denominator of Eq. (7.21a) around the resonance and then neglecting higher order small terms, we substitute Eqs. (7.21a) and (A.14) in the condition  $W^2 = (W^{(n)})^2/2$ , and then obtain

$$\Delta\omega/\omega^{(n)} = \pm 2c\omega^{(n)} / \left\{ k_c \lambda^{(n)} \left[ (1 + 4\alpha) (\lambda^{(n)})^3 / 3 + \Psi(\lambda^{(n)}) \Phi(\lambda^{(n)}) \right] \right\}. \quad (\text{A.15})$$

According to the definition of  $Q$ , i.e.,  $1/Q = 2|\Delta\omega|/\omega^{(n)}$ , we can relate  $c$  with  $Q$ :

$$c = \frac{k_c \left[ \Psi(\lambda^{(n)}) + \alpha(\lambda^{(n)})^4/3 \right]}{2Q\omega^{(n)}S} = \frac{k_V^*}{2Q\omega^{(n)}S}, \quad (\text{A.16})$$

where  $S$  is the sensitivity to the contact stiffness, defined by Eq. (7.37). If a resonance spectrum is experimentally obtained for linear contact vibration, we can determine the damping coefficient from Eq. (A.16).

## References

1. G. Binnig, C.F. Quate, C. Gerber, Atomic force microscope. *Phys. Rev. Lett.* **56**, 930–933 (1986)
2. Y. Martin, H. Wickramasinghe, Magnetic imaging by ‘force microscopy’ with 1000 Å resolution. *Appl. Phys. Lett.* **50**, 1455–1457 (1987)
3. J.E. Stern, B.D. Terris, H.J. Mamin, D. Rugar, Deposition and imaging of localized charge on insulator surfaces using a force microscope. *Appl. Phys. Lett.* **53**, 2717–2719 (1988)
4. U. Rabe, K. Janser, W. Arnold, Vibrations of free and surface-coupled atomic force microscope cantilevers: theory and experiment. *Rev. Sci. Instrum.* **67**, 3281–3293 (1996)
5. K. Yamanaka, S. Nakano, Ultrasonic atomic force microscope with overtone excitation of cantilever. *Jpn. J. Appl. Phys.* **35**, 3787–3792 (1996)
6. P. Vairac, B. Cretin, Scanning microdeformation microscopy in reflection mode. *Appl. Phys. Lett.* **68**, 461–463 (1996)
7. M. Muraoka, Sensitive detection of local elasticity by oscillating an AFM cantilever with its mass concentrated. *JSME Int. J. A* **45**, 567–572 (2002)
8. M. Muraoka, Vibrational dynamics of concentrated-mass cantilevers in atomic force acoustic microscopy: presence of modes with selective enhancement of vertical or lateral tip motion. *J. Phys.: Conf. Ser.* **61**, 836–840 (2007)
9. M. Muraoka, Sensitivity-enhanced atomic force acoustic microscopy with concentrated-mass cantilevers. *Nanotechnology* **16**, 542–550 (2005)
10. J.P. Cleveland, S. Manne, D. Bocek, P.K. Hansma, A nondestructive method for determining the spring constant of cantilevers for scanning force microscopy. *Rev. Sci. Instrum.* **64**, 403–405 (1993)
11. E.-L. Florin, M. Radmacher, B. Fleck, H.E. Gaub, Atomic force microscope with magnetic force modulation. *Rev. Sci. Instrum.* **65**, 639–643 (1994)
12. B.W. Chui, Y. Hishinuma, R. Budakian, H.J. Mamin, T.W. Kenny, D. Rugar, Mass-loaded cantilevers with suppressed higher-order modes for magnetic resonance force microscopy. In: *Transducer '03, Proc 12th Int Conf on Solid State Sensor, Actuators and Microsystems @ 2003 IEEE*, pp. 1120–1123 (2003)
13. H. Li, Y. Chen, L. Dai, Concentrated-mass cantilever enhances multiple harmonics in tapping-mode atomic force microscopy. *Appl. Phys. Lett.* **92**, 151903(1–3) (2008)
14. U. Rabe, E. Kester, W. Arnold, Probing linear and non-linear tip-sample interaction forces by atomic force acoustic microscopy. *Surf. Interface Anal.* **27**, 386–391 (1999)
15. K. Yamanaka, A. Noguchi, T. Tsuji, T. Koike, T. Goto, Quantitative material characterization by Ultrasonic AFM. *Surf. Interface Anal.* **27**, 600–606 (1999)
16. S. Hirsekorn, U. Rabe, W. Arnold, Theoretical description of the transfer of vibrations from a sample to the cantilever of an atomic force microscope. *Nanotechnology* **8**, 57–66 (1997)
17. M. Muraoka, W. Arnold, A method of evaluating local elasticity and adhesion energy from the nonlinear response of AFM cantilever vibrations. *JSME Int. J. A* **44**, 396–405 (2001)
18. A. Torii, M. Sasaki, K. Hane, S. Okuma, A method for determining the spring constant of cantilevers for atomic force microscopy. *Meas. Sci. Technol.* **7**, 179–184 (1996)
19. J.E. Sader, J.W.M. Chon, P. Mulvaney, Calibration of rectangular atomic force microscope cantilevers. *Rev. Sci. Instrum.* **70**, 3967–3969 (1999)
20. K. Yamanaka, S. Nakano, Quantitative elasticity evaluation by contact resonance in an atomic force microscope. *Appl. Phys. A* **66**, S313–S317 (1998)
21. K. Yamanaka, Y. Maruyama, T. Tsuji, K. Nakamoto, Resonance frequency and Q factor mapping by ultrasonic atomic force microscopy. *Appl. Phys. Lett.* **78**, 1939–1941 (2001)
22. K. Fukuda, H. Irihama, T. Tsuji, K. Nakamoto, K. Yamanaka, Sharpening contact resonance spectra in UAFM using Q-control. *Surf. Sci.* **532/535**, 1145–1151 (2003)
23. U. Rabe, S. Amelio, E. Kester, V. Scherer, S. Hirsekorn, W. Arnold, Quantitative determination of contact stiffness using atomic force acoustic microscopy. *Ultrasonics* **38**, 430–437 (2000)



24. E. Kester, U. Rabe, L. Presmanes, Ph. Taihades, W. Arnold, Measurement of Young's modulus of nanocrystalline ferrites with spinel structures by atomic force acoustic microscopy. *J. Phys. Chem. Solid* **61**, 1275–1284 (2000)
25. S. Amelio, A.V. Goldade, U. Rabe, V. Scherer, B. Bhushan, W. Arnold, Measurements of elastic properties of ultra-thin diamond-like carbon coating using atomic force acoustic microscopy. *Thin Solid Films* **392**, 75–84 (2001)
26. M. Kopycinska-Müller, R.H. Geiss, J. Müller, D.C. Hurley, Elastic-property measurements of ultrathin films using atomic force acoustic microscopy. *Nanotechnology* **16**, 703–709 (2005)
27. O. Kolosov, K. Yamanaka, Nonlinear detection of ultrasonic vibrations in an atomic force microscope. *Jpn. J. Appl. Phys.* **32**, L1095–L1098 (1993)
28. P.S. Timoshenko, D.H. Young, W. Weaver Jr, *Vibration Problems in Engineering*, 4th edn. (Wiley, New York, 1974), pp. 415–475
29. D. Sarid, *Scanning Force Microscopy with Applications to Electric, Magnetic and Atomic Forces* (Oxford University Press, New York, 1994), pp. 1–17
30. A.H. Nayfeh, D.T. Mook, *Nonlinear Oscillations* (Wiley-VCH, Weinheim 2004), pp. 59–63
31. N.A. Burnham, R.J. Colton, H.M. Pollock, Interpretation of force curves in force microscopy. *Nanotechnology* **4**, 64–80 (1993)
32. J. Israelachvilli, *Intermolecular & Surface Forces*, 2nd edn. (Academic Press, London 1991), pp. 326–329
33. O.B. Wright, N. Nishiguchi, Vibrational dynamics of force microscopy: effects of tip dimensions. *Appl. Phys. Lett.* **71**, 626–628 (1997)
34. U. Rabe, J. Turner, W. Arnold, Analysis of the high-frequency response of atomic force microscope cantilevers. *Appl. Phys. A* **66**, S277–S282 (1998)
35. D. Maugis, M. Barquins, Adhesive contact of sectionally smooth-ended punches on elastic half-spaces: theory and experiment. *J. Phys. D: Appl. Phys.* **16**, 1843–1874 (1983)
36. D. Maugis, Adhesion of spheres: the JKR-DMT transition using a Dugdale model. *J. Colloid Interface Sci.* **150**, 243–269 (1992)
37. M. Muraoka, S. Komatsu, Characterization of films with thickness less than 10 nm by sensitivity-enhanced atomic force acoustic microscopy. *Nanoscale Res. Lett.* **6**, 33(1–6) (2011)
38. O.L. Anderson, Determination and some uses of isotropic elastic constants of polycrystalline aggregates using single-crystal data, in *Physical Acoustics III-Part B*, ed. by W.P. Mason (Academic Press, New York, 1965), p. 95
39. R.B. King, Elastic analysis of some punch problems for a layered medium. *Int. J. Solids Struct.* **23**, 1657–1664 (1987)
40. B. Schultrich, H.-J. Scheibe, D. Drescher, H. Ziegele, Deposition of superhard amorphous carbon films by pulsed vacuum arc deposition. *Surf. Coat. Technol.* **98**, 1097–1101 (1998)
41. A.C. Ferrari, J. Robertson, M.G. Beghi, C.E. Bottani, R. Ferulano, R. Pastorelli, Elastic constants of tetrahedral amorphous carbon films by surface Brillouin scattering. *Appl. Phys. Lett.* **75**, 1893–1895 (1999)
42. J.-W. Chung, C.-S. Lee, D.-H. Ko, J.H. Han, K.Y. Eun, K.-R. Lee, Biaxial elastic modulus of very thin diamond-like carbon (DLC) films. *Diam. Rel. Mater.* **10**, 2069–2074 (2001)
43. M.C. Salvadori, M.C. Fritz, C. Carraro, R. Maboudian, O.R. Monteiro, I.G. Brown, Characterization of AFM cantilevers coated with diamond-like carbon. *Diam. Rel. Mater.* **10**, 2190–2194 (2001)

# Chapter 8

## Scanning Microdeformation Microscopy: Advances in Quantitative Micro- and Nanometrology

P. Vairac, J. Le Rouzic, P. Delobelle and B. Cretin

**Abstract** The SMM is a well known scanning acoustic probe technique. Recently in the last years in order to optimize this metrological instrument a sensitivity study was carried out to adapt the stiffness of the microcantilevers to the encountered contact stiffnesses. The accuracy of the measurement is so optimized for the elasticity of the sample to characterize. Problems coming from the sliding of the tip on the surface and their effects were exhibited. New specific geometries of microcantilevers were conceived to reduce these perturbations. Their use reduced significantly the slip and so led to a better determination of the resonance frequencies, even for high amplitudes of vibration. In a last part a study of mechanical characterization was realized on polymers using DMA, SMM and nanoindentation. The use of different techniques enables to obtain complementary measures (viscoelastic characterization for several decades).

### 8.1 Introduction

Knowledge of the mechanical properties of materials at local scale has become a major issue in engineering because of the miniaturization of devices. The development of microelectromechanical systems (MEMS) was possible, all thanks to the deposition techniques of thin films (submicron thickness). Most of the time, MEMS are composed of multiple layers of different materials. However, the mechanical properties of such surfaces are difficult to predict. They can vary considerably depending on the techniques cleanroom used. Moreover, at such scales, it is difficult

---

P. Vairac (✉) · P. Delobelle · B. Cretin  
FEMTO-ST Institute, Université de Franche-comté,  
CNRS, ENSMM, UTBM, 32 avenue de l'Observatoire, 25044 Besançon Cedex, France  
e-mail: pascal.vairac@femto-st.fr

J. Le Rouzic  
Imperial College London, South Kensington Campus, London SW7 2AZ, UK

to use the laws of continuum mechanics to predict the mechanical behavior of these thin films. It is therefore vital to have reliable measurement techniques to meet these needs.

During the last 20 years, near-field microscopes have been developed in order to increase the lateral resolution and to measure different local properties of the investigated material. Main achieved systems have been derived from the AFM. The combination between AFM and acoustics, often designed AFAM emerged after 1992 [1–6]. Many features have been discovered and have been investigated from both theoretical to experimental domains. All these near-field microscopes have a behavior based on the concept of force modulation microscopy (FMM).

The force modulation microscope was first introduced by Maivald and et al. [7]. A periodic displacement at low frequency (few kHz) is imposed on the sample using a piezoelectric ceramic. The tip in contact with the sample follows the harmonic vibrations. Measuring the amplitude of the displacement of cantilever provides information on local variations of elasticity of the sample. Use of cantilevers with high stiffness leads to large applied forces and facilitates contacts plastic nature limiting the possibilities of quantitative measurements of the elasticity of the surface. A variant of this technique is to apply an external force at the end of the cantilever. This is called direct force modulation as opposed to the previous method, which is called indirect force modulation. Practically, this external force can be applied either locally with a magnet glued to the end of the lever subjected to a harmonic magnetic field created by a coil, or more broadly with a magnetic film deposited on the entire lever [8, 9]. Compared to an indirect force modulation cantilever stiffness is low enough, and reduces the risk of plastic deformation.

The scanning microdeformation microscope (SMM) is also a dynamic force microscope, but conversely to the most part of near-field microscopes based on the AFM, the sensor is magnified by one or two orders of magnitude [1, 2, 10]. The SMM can operate in transmission mode: a piezoelectric ceramic detects the acoustic amplitudes transmitted through the sample allowing subsurface imaging. The other way of detection is to measure the amplitude and the phase of the vibration of the cantilever with a high sensitive optical interferometer pointing onto the cantilever in elastic contact with the sample. The radius of the SMM sensor tip is larger than the radius of an AFM tip and for this reason models used to characterize the tip-sample interaction are easier to apply allowing “true” quantitative measurement of elastic properties of sample, even if the lateral resolution is lower than in AFM-based techniques.

The aim of this chapter is to present the last advances in term of quantitative measurement at local scale particularly with the SMM, and how it can be complementary to other mechanical tools for local characterization.

This chapter describes for the first time the SMM and the physical basis of the behavior and modeling. A specific study dedicated to optimization of the sensitivity SMM is detailed, showing that it is necessary to adapt the stiffness of the micro-cantilevers to the encountered contact stiffnesses. The accuracy of the measurement is so optimized for the elasticity of the sample to characterize. In some operating ranges of these near-field microscopes, the sliding effect of tip on the surface of

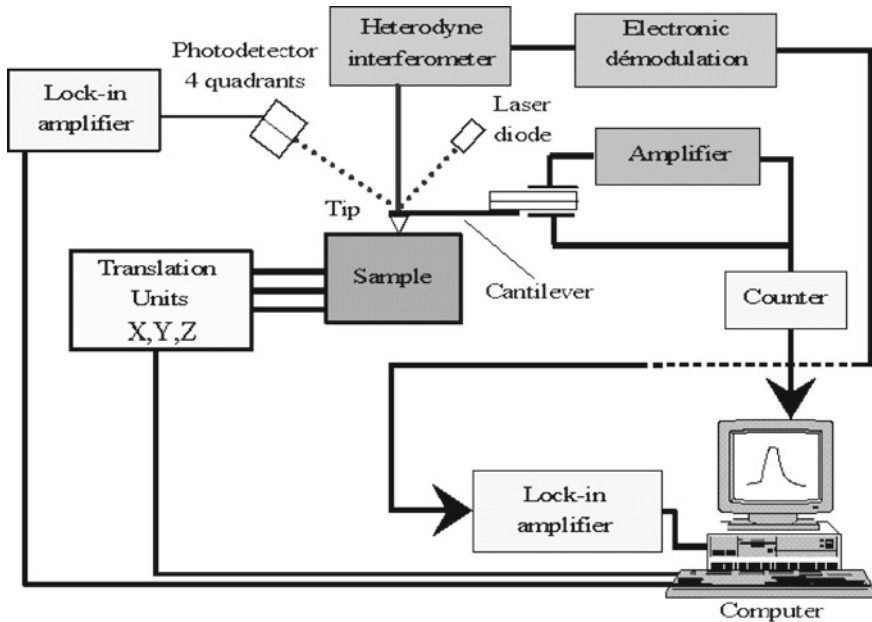


**Fig. 8.1** Experimental setup of the SMM which allows to control the static force between the tip and the sample and to measure quantitatively the vibration of the sample surface with a high sensitivity

the sample generates in many cases a problem of localization of the measurement and nonlinear perturbations. In order to reduce these effects, specific geometries of microcantilever have been studied. Their use reduced significantly the slip and so led to a better determination of the resonance frequencies, even for high amplitudes of vibration.

The last part of the chapter is devoted to a complete study of local properties of polymers by coupling the measurement results obtained with the SMM with two others techniques: nanoindentation and dynamic mechanical analysis (DMA). The use of different techniques enables to obtain complementary measures on viscoelastic characterization for several decades.

## 8.2 The Scanning Microdeformation Microscope

### 8.2.1 The Experimental Setup

The experimental setup called SMM is shown in Fig. 8.1. As in AFM a three-axis translation unit supports the sample. The vertical axis enables to adjust the value of the static contact force.

The head of the microscope is composed of a piezoelectric transducer, the cantilever and the tip (made of diamond or sapphire and not of silicon as in standard AFM where the tip is obtained by chemical etching of the cantilever). This hybrid sensor can be considered as an electromechanical resonator whose frequency is related to the tip-sample interaction. The tips can be standard pickup needles of sapphire (15–45  $\mu\text{m}$  radii), or specific diamond tips with radius down to 0.6  $\mu\text{m}$ . Depending on the tip radius and the applied force, the contact radius is in the 50 nm–2  $\mu\text{m}$  range.

The tip is kept in flexural vibration with the low frequency generator. The heterodyne interferometer is used as a noninvasive sensor to detect quantitatively the amplitude and the phase of the vibrating cantilever and the surface sample. The principle of this interferometer developed for out-of-plane vibrations measurement is completely described in Refs. [11–13]. After the electronic demodulation, a lock-in amplifier allows to obtain a high sensitivity. In ideal conditions, the ultimate sensitivity is about 1 fm/ $\sqrt{\text{Hz}}$ .

Moreover, we used on the SMM the classical optical beam deflection system modified to obtain a dynamic detection of the static deflection of the cantilever. More precisely, we modulated the laser diode and we detected the amplitude and the phase of the static deflection with a lock-in amplifier. By this way, it is possible to evaluate the static force and the static indentation on the sample.

This microscope is an effective tool to image surfaces and subsurfaces with heterogeneous local elasticity or to characterize elastic properties of a material. Some examples of images presented below demonstrate these characteristics.

First presented sample is a silicon wafer (360  $\mu\text{m}$  thickness, crystalline orientation [100]). Parallel grooves have been etched on one face, the opposite face remained polished. A cross-section of the sample which was coupled to the support with an ultrasonic gel is showed Fig. 8.2a. Scanned surface is the plane face of the sample where the grooves are optically invisibles. Figure 8.2b shows the frequency image obtained with a tip having a 40  $\mu\text{m}$  radius.

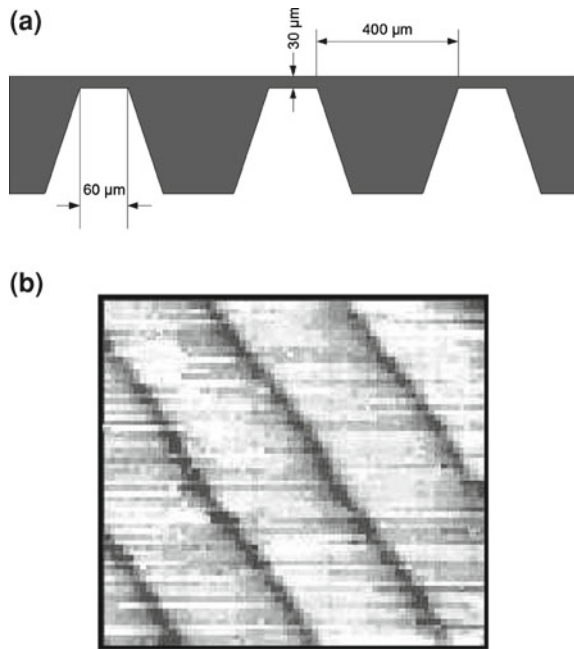
Subsurface grooves appear as parallel black stripes (the harder the sample surface, the higher the frequency).

The second sample is made of duralumin (AU4G). A 50  $\mu\text{m}$  diameter tungsten wire was inserted in a diffusion bond. The sample was cut and polished progressively, so that the tungsten wire just appeared on the sample side Fig. 8.3a. In the image area, the tungsten wire-surface spacing is estimated to be 25–35  $\mu\text{m}$ . The frequency image in Fig. 8.3b obtained at 17 kHz shows the detection capability of the SMM. Small scratches resulting from contact can be observed on the sample surface.

The presented results demonstrate that the SMM can give images of subsurface defects with image contrast related to the properties of the microdeformation volume in the case of polished surfaces.

In a more quantitative method of operation we use the SMM to determine the local Young's modulus of material. So, we put the tip in contact with the sample and we apply an additional static force by vertically displacing the clamped end of the cantilever. Then we scan the excitation frequency. The resonant frequency depends on the static force applied via the contact stiffness. Currently, measuring the resonant frequency, we can estimate the local contact stiffness and then with a suitable

**Fig. 8.2** **a** Geometry of the etched silicon sample. **b** Image of the subsurface grooves obtained at 18 kHz with a frequency variation of 100 Hz (*image size* 2,000 × 2,000 μm) [2]



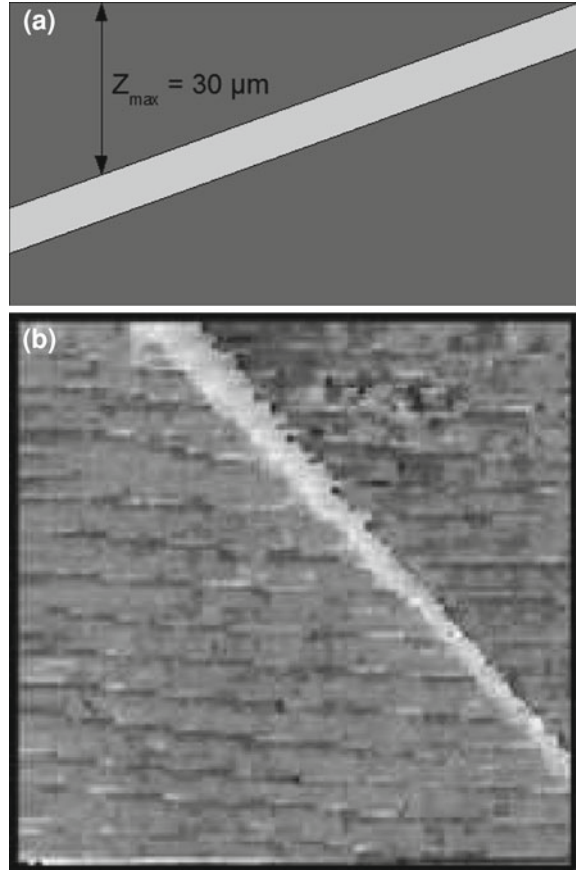
model, the local Young's modulus with high accuracy. Other ultrasonic noninvasive methods such as atomic force acoustic microscope, ultrasonic force microscopy, or AFM spectroscopy with heterodyne interferometer make such a characterization on the nanometer scale but with less accuracy, because the contact model must take into account additional forces on this scale [14–17]. We can also notice the nanoindentation and particularly Continuous Stiffness Measurement technique, which is a destructive method which enables local elasticity measurements [18].

### 8.2.2 The Basic Model

We have used a continuous model [19, 20] (Fig. 8.4) to describe the physical behavior of the SMM, and to obtain Young's moduli values of tested samples from the measured contact resonant frequencies. The cantilever is represented as a beam interacting with the sample through two springs  $k^*$  and  $k_{lat}$ . The piezoelectric bimorph transducer action on the cantilever has been modeled as simple mass  $m_p$  and spring  $k_p$ .

The longitudinal interaction stiffness  $k^*$  and the lateral interaction stiffness  $k_{lat}$  have to be known in order to evaluate the stiffness of the sample. On a mesoscopic scale and in the ideal case of flat sample,  $k^*$  can be estimated by using the classical contact theory of Hertz when the tip (assumed to be a spherical indenter of radius  $R$ ) contacts the sample [21]:

**Fig. 8.3** **a** Cross-section of the sample. **b** Microdeformation image of the tungsten wire obtained at 17 kHz with a frequency variation of 500 Hz (*image size*  $500 \times 500 \mu\text{m}$ )[2]



$$k^* = (6RE^*2 F_0)^{1/3} = 2E^*a \quad (8.1)$$

where  $a$  is the contact radius, and  $E^*$  the effective Young's modulus of the tip-sample contact.

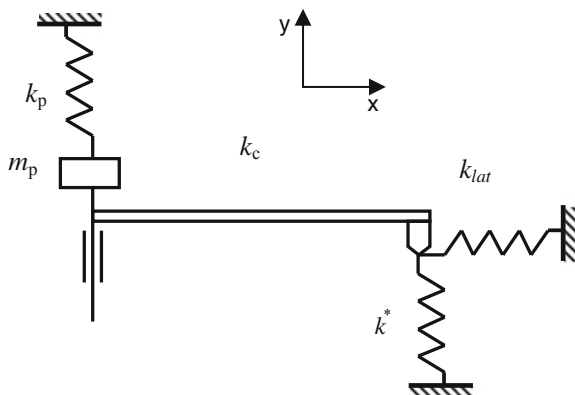
As previously described, a sinusoidal vibration of the cantilever base is used as excitation, but a variable displacement offset of the sample  $\Delta z$  is also introduced to provide a static force. Thus, this static force applied on the sample is related to  $\Delta z$  and to the longitudinal stiffness by the following expression:

$$F_0 = \frac{k_c k^*}{k_c + k^*} \Delta z \approx k_c \Delta z \quad (8.2)$$

(This approximate relation can be applied for  $k^* \gg k_c$  where  $k_c$  is the stiffness of the cantilever).

With:

**Fig. 8.4** Model used to describe the behavior of the SMM



$$\frac{1}{E^*} = \frac{1 - \nu_t^2}{E_t} + \frac{1 - \nu_s^2}{E_s} = \frac{1 - \nu_s^2}{E_s} \quad (8.3)$$

where  $E_t$ ,  $\nu_t$  and  $E_s$ ,  $\nu_s$  are, respectively, Young's modulus and Poisson ratio of the tip and the sample.

Mindlin theory on the contact between a sphere and a plane [21] makes possible to take into account the lateral stiffness and gives the relation between the longitudinal and lateral stiffness,

$$k_{lat} = 4k^* \frac{G^*}{E^*} \quad (8.4)$$

With  $G^*$  the reduced shear modulus expressed as:

$$G^* = \left( \frac{2(1 + \nu_t)(2 - \nu_t)}{E_t} + \frac{2(1 + \nu_s)(2 - \nu_s)}{E_s} \right)^{-1} \quad (8.5)$$

And finally:

$$k_{lat} \approx \frac{2(1 - \nu_s)}{(2 - \nu_s)} k^* \quad (8.6)$$

The most classical way to study this mechanical model is to solve the fourth-order differential equation for flexural vibrations of the cantilever [19, 20] with the different applied boundary conditions:

$$EI \frac{\partial^4 y}{\partial x^4} + \rho A \frac{\partial^2 y}{\partial t^2} = 0 \quad (8.7)$$

where  $E$  is Young's modulus,  $I$  the area moment of inertia,  $\rho$  the volume density, and  $A$  the cross-section of the cantilever. This equation describes the propagation of the dispersive flexural waves with the following relation:



$$EI\mu_n^4 - \rho A\omega_n^4 = 0 \tag{8.8}$$

$\omega_n$  being the angular frequencies and  $\mu_n$  the associated eigenvalues.

Assuming a general solution of the following type for Eq. 8.7:

$$y(x, t) = [C_1 (A^+) + C_2 (A^-) + C_3 (B^+) + C_4 (B^-)] e^{j\omega t} = y(x) e^{j\omega t} \tag{8.9}$$

where:  $A_{\pm}^+ = \cos(\mu x)_{\pm}^+ \cosh(\mu x)$  and  $B_{\pm}^+ = \sin(\mu x)_{\pm}^+ \sinh(\mu x)$

The constants  $C_{1-4}$  are determined by the boundary conditions applied to the cantilever.

At the excitation end of the cantilever ( $x=0$ ) the boundary conditions are:

$$\begin{cases} \frac{\partial y(x)}{\partial x} = 0 \\ \frac{\partial^3 y(x)}{\partial x^3} = \frac{k_p}{EI} y(x) + \frac{m_p}{EI} \frac{\partial^2 y(x)}{\partial t^2} \end{cases} \tag{8.10}$$

At the interaction end ( $x = L$ ), we can express the boundary conditions as:

$$\begin{cases} \frac{\partial^2 y(x)}{\partial x^2} = -l \frac{k_{lat}}{EI} (x) + \frac{m}{EI} \frac{l_c^2}{l} \frac{\partial^2 (x)}{\partial t^2} \\ \frac{\partial^3 y(x)}{\partial x^3} = \frac{k^*}{EI} y(x) + \frac{m}{EI} \frac{\partial^2 y(x)}{\partial t^2} \end{cases} \tag{8.11}$$

Assuming that the displacement of the center of the mass  $m$  in the  $x$  direction is smaller than that of the tip extremity by a factor  $l_c/l$  ( $l_c$  is the distance between the center mass of the tip and the cantilever and  $l$  the length of the tip).

The general solution (Eq. 8.9) and its derivatives are reported in these four boundary conditions and we obtain these relations between the constants  $C_{1-4}$ :

$$C_3 = 0$$

$$C_4 = \theta C_1 \text{ with } \theta = -\frac{k_p}{\mu^3 EI} + \frac{m_p \omega^2}{\mu^3 EI}$$

$$\frac{C_1}{C_2} =$$

$$\frac{\beta(\cos \mu L + \cosh \mu L) - (\sin \mu L + \sinh \mu L)}{\beta[(-\cos \mu L + \cosh \mu L) - \theta(\sin \mu L + \sinh \mu L)] - [(-\sin \mu L + \sinh \mu L) + \theta(\cos \mu L - \cosh \mu L)]} \tag{8.12}$$

$$\frac{C_1}{C_2} = \frac{(\cos \mu L - \cosh \mu L) - \alpha(\sin \mu L - \sinh \mu L)}{\alpha[-\theta(\cos \mu L + \cosh \mu L) + (\sin \mu L + \sinh \mu L)] - [\theta(\sin \mu L - \sinh \mu L) + (\cos \mu L + \cosh \mu L)]} \tag{8.13}$$

with  $\alpha = \frac{\mu^3}{\frac{k^*}{EI} - \frac{m\omega^2}{EI}}$  and  $\beta = \frac{\mu}{-\frac{k_{lql}l^2}{EI} - \frac{ml_c^2\omega^2}{EI}}$

Finally the characteristic equation of the system is obtained by:

$$\frac{\beta(\cos \mu L + \cosh \mu L) - (\sin \mu L + \sinh \mu L)}{\beta[(-\cos \mu L + \cosh \mu L) - \theta(\sin \mu L + \sinh \mu L)] - [(-\sin \mu L + \sinh \mu L) + \theta(\cos \mu L - \cosh \mu L)]} = \frac{(\cos \mu L - \cosh \mu L) - \alpha(\sin \mu L - \sinh \mu L)}{\alpha[-\theta(\cos \mu L + \cosh \mu L) + (\sin \mu L + \sinh \mu L)] - [\theta(\sin \mu L - \sinh \mu L) + (\cos \mu L + \cosh \mu L)]} \tag{8.14}$$

and the solutions  $\mu_n L$  of (8.14) computed with the software Maple, allow us to compute the resonance frequencies  $\omega_n$  by using Eq. 8.8.

The solution  $y(x, t)$  can be expressed in the form:

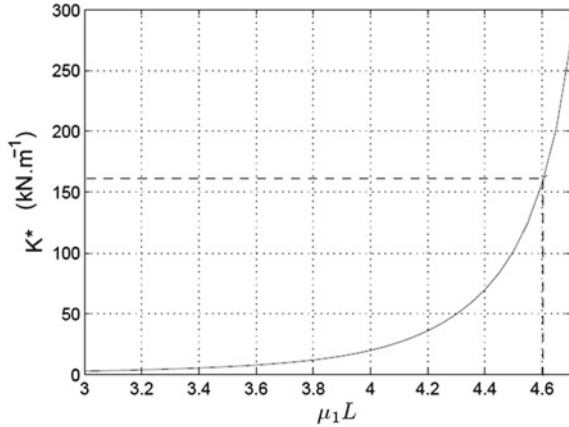
$$y(x, t) = y_0 \left[ (\cos \mu x + \cosh \mu x) + \frac{C_2}{C_1} (\cos \mu x - \cosh \mu x) + \theta(\sin \mu x - \sinh \mu x) \right] e^{j\omega t} \tag{8.15}$$

Depending on the parameters that we seek to determine, we will resolve the direct or the inverse problem.

- Direct problem: Knowing the Young’s modulus of the sample, we can evaluate, with the Hertz contact, the contact stiffness corresponding to some static force. Then from the stiffness of contact, we determine the eigenvalues  $\mu_n$ . We obtain the frequencies of vibration modes and their associated deformation shape.
- Inverse problem: We measure experimentally the resonant frequency of the cantilever that is injected into the model. We deduce the eigenvalue associated  $\mu_n$ . With the model, we can then estimate the contact stiffness  $k^*$ . Hertz’s theory provides us a final measurement of Young’s modulus of the sample.

Figure 8.5 shows the calculation performed on a silicon surface (100) with a static force of 0.8 mN. We experimentally measure a frequency of 28,050 Hz for the first mode, which corresponds to an eigenvalue  $\mu_1 L = 4.607$ . We therefore find a contact stiffness of 163,036 N.m<sup>-1</sup>. Finally, taking 0.28 for Poisson’s ratio, we calculate a Young’s modulus of 129.1 GPa.

**Fig. 8.5** Example of solution in the case of a silicon sample



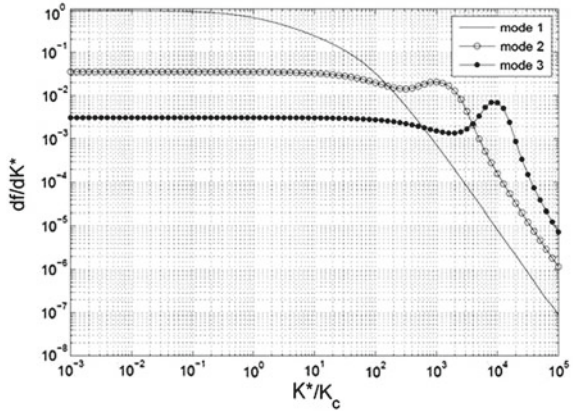
## 8.3 Optimization of the SMM

### 8.3.1 The Theoretical Study

In this part, we present the study of the sensitivity optimization of our system the SMM. The flexural contact modes of vibration of the cantilever have been modeled. We discuss the matching between the cantilever stiffness and the contact stiffness, which depends on the sample material. In order to obtain the best sensitivity, the stiffnesses must be the closest one to each other. Because the length of the cantilever directly affects its stiffness, the cantilever geometry can be optimized for different materials. We have validated this study with measurements on a soft material the Polydimethylsiloxane (PDMS) with a cantilever optimized for materials of Young's moduli of some megapascals. Experimental results obtained with two different samples have shown the high sensitivity of the method for the measurement of low Young's moduli [22, 23].

The sensitivity of our measurement system can be defined as  $\partial f / \partial k^*$  or  $\partial f / \partial E^*$  which represents the variation of resonant frequency for a variation of contact interaction or local elasticity. Actually, we need to obtain the greatest shift frequency for two materials of different Young's moduli. Such considerations have already been treated for AFM in force modulation by Chang [24], Wu et al. [25], Turner and Wiehn [26]. For all the sensitivity study we considered that the beam is clamped because the spring  $k_p$  modeling the bimorph interaction depends on the cantilever and cannot be applied here. We plotted the normalized sensitivity of the first three flexural modes versus contact stiffness for a beam with a length of 4 mm and with  $k^* = 0.68 k_{lat}$  (Fig. 8.6). We can see that for soft materials, the first mode is the most sensitive. But when contact stiffness increases and reaches nearly a hundred times the cantilever stiffness, the second mode becomes the most sensitive. And for larger values of contact stiffness the third mode becomes the most sensitive too. We can also notice that

**Fig. 8.6** Normalized flexural sensitivity  $df/dk^*$  as a function of contact stiffness  $k^*$  (normalized by the cantilever stiffness  $k_c$ ), with  $k_{lat} = 0.68 k^*$  for a cantilever with a length of 4 mm, a width of 400  $\mu\text{m}$ , and a thickness of 150  $\mu\text{m}$  for the first three modes



the first mode becomes always less sensitive when the contact stiffness is greater, whereas for the other modes the sensitivity first decreases and increases again to reach a local maximum before decreasing with the contact stiffness. We can also plot the following expression:  $S_N = (\partial f / \partial k^*) (k^* / f)$  which represents better the ability to distinguish two different materials with Young's moduli close to each other than sensitivity does. Actually,  $S_N$  is well appropriate because it takes into account the working frequency and contact stiffness.  $S_N$  has been plotted for a cantilever with a length of 4 mm versus contact stiffness (Fig. 8.7). We can see that the curves are different from those of the sensitivity.  $S_N$  has a global maximum, whereas precedent sensitivity always decreases with contact stiffness for the first mode. Besides curves appear quite symmetrical on each side from this maximum. By means of this parameter, we highlight precisely the contact stiffness which maximizes the ability to measure elastically close materials. For the first mode,  $S_N$  reaches a maximum for a contact stiffness of nearly ten times the cantilever's one, 1,000 times for the second mode, and 10,000 times for the third mode. We can also notice that the range of high value of  $S_N$  is large for the first mode but is reduced for the second mode and even more for the third one.

In order to have the best sensitivity, the cantilever stiffness  $k_c$  and the contact stiffness  $k^*$  must be close. In fact, if  $k^*$  is far bigger than  $k_c$ , the cantilever will totally bend. Whereas if  $k_c$  is far bigger than  $k^*$ , the tip will indent the sample. The cantilever stiffness  $k_c$  equals  $3E_c I / L^3$ ,  $I$  being the area moment of inertia  $I = bh^3 / 12$  for a rectangular section beam,  $w$  being the width of the beam, and  $t_c$  the thickness. Obviously, the parameters which most affect the stiffness are the length and the thickness of the beam because they are cubed in the expression of  $k_c$ . Theoretically, the effect of other parameters such as  $w$ ,  $R$ , or the tip height  $h$  are negligible for this application, but no generalization is allowed. So, we have only focused our study on the length of the cantilever it is easier and faster to fabricate on the same wafer beams of different lengths than different thicknesses by cleanroom techniques. We made the sensitivity study for a static force of 0.5 mN. Normalized first flexural mode sensitivity

**Fig. 8.7** Normalized flexural sensitivity  $(df/dk^*) \times k^*/f$  as a function of contact stiffness  $k^*$  (normalized by the cantilever stiffness  $k_c$ ), with  $k_{lat} = 0.68 k^*$  for a cantilever with a length of 4 mm, a width of 400  $\mu\text{m}$ , and a thickness of 150  $\mu\text{m}$  for the first three modes

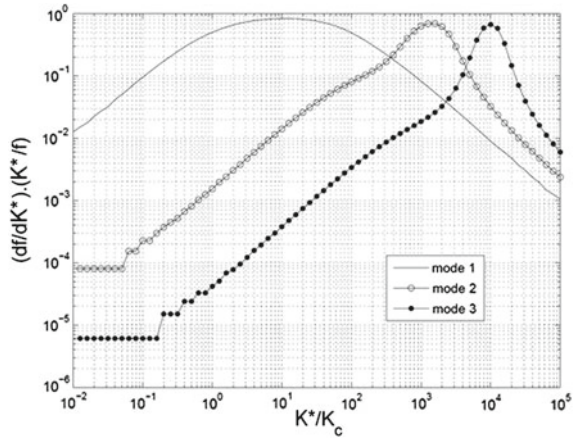
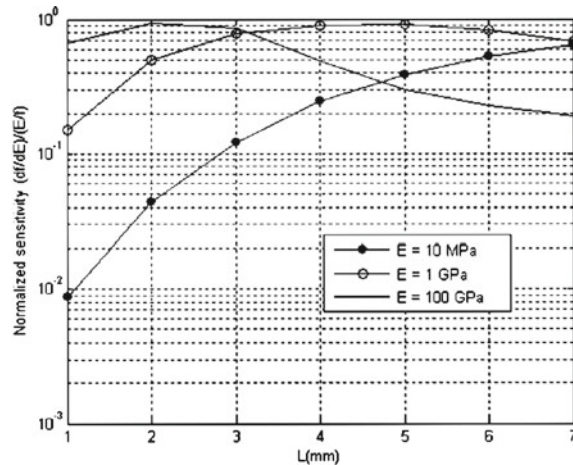
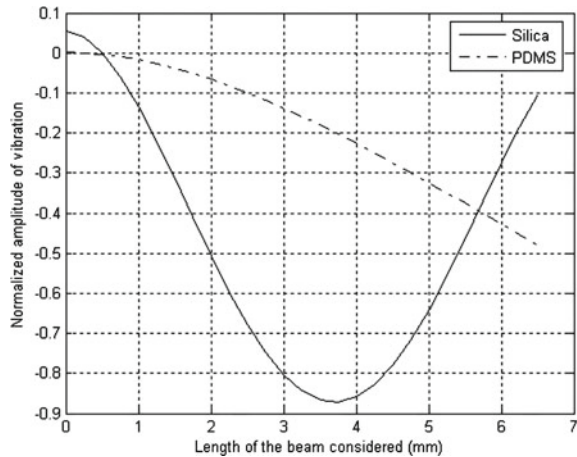


**Fig. 8.8** Normalized flexural sensitivity  $(df/dE) \times E/f$  for a cantilever with a thickness of 150  $\mu\text{m}$ , width of 400  $\mu\text{m}$  for the first contact mode (with a static force of 0.5 mN) as function of the length of the cantilever for different Young's moduli of the sample



$S_N = (\partial f / \partial k^*) (k^* / f)$  is plotted for beam lengths from 1 to 7 mm and materials of Young's moduli of 10 MPa, 1 GPa, and 100 GPa (Fig. 8.8). Thickness is assumed to be 150  $\mu\text{m}$  and width of 400  $\mu\text{m}$ . We can notice that, depending on Young's modulus, sensitivity is increasing or decreasing with the length of the cantilever. Actually for a 100 GPa Young's modulus material, the best sensitivity is obtained with a length of 2 mm, whereas for a 10 MPa Young's modulus one, it is with the length of 7 mm. So the cantilever with a length of 7 mm is optimized to characterize very soft materials. In fact with this cantilever, contact stiffness with Young's moduli of some tens of gigapascals, such as silicon or silica,  $k^*$  ( $\approx 150,000 \text{ N/m}$ ) is nearly 1,000 times greater than  $k_c$  ( $\approx 150 \text{ N/m}$ ). So  $S_N$  is a very useful parameter to compare the efficiency of our measurement system for different materials.

**Fig. 8.9** Theoretical deformation shapes of the first flexural mode in contact with SiO<sub>2</sub> and PDMS



### 8.3.2 Experimental Validation

We have validated this precedent study by characterizing a very soft material by the cantilever with a length of 7 mm. A sapphire tip with a length of 0.7 mm and a radius of curvature of 45  $\mu\text{m}$  was used. We chose PDMS. PDMS is a silicon-based viscoelastic polymer. Mechanical properties of this material vary with preparation conditions. Actually, Young's moduli values can fluctuate in the range of 100 kPa to some megapascals depending on this preparation [27].

We used two different PDMS samples with thicknesses of some millimeters prepared in different conditions and different aging times. To characterize PDMS we put the spot of the laser at the end of the cantilever because it is where the amplitude of vibration of the first contact mode is the greatest whereas for harder materials the maximum is on the middle of the beam. The model agrees with these observations (see Fig. 8.9). We can also notice that for hard materials the bimorph interaction spring  $k_p$  has a real influence on the modulus computed and has to be fitted with a known sample, whereas with PDMS the value of  $k_p$  does not hardly change the result. Figure 8.10 shows resonances on the first sample of PDMS for different static loads. We can observe the shift frequency and that the amplitude decreases versus the static force because of damping, whereas with an elastic material such as silicon we observed that amplitude increases with the force. To estimate Young's modulus of the sample we realized 15 successive measures in the same conditions. Static force applied was 150  $\mu\text{N}$  because this load provides the best sensitivity (the best slope of frequency vs. force). A new contact was obtained for each measurement and we recorded the magnitude spectrum. The dispersion of amplitude is nearly 0.75  $\text{\AA}$  and 80 Hz in frequency. So, we obtain a mean value for the frequency close to 4.18 kHz. And thanks to the model by taking 0.48 for  $\nu$ , we computed Young's modulus of 3.4 MPa. ( $\pm 0.3$  MPa by considering sensitivity and frequency dispersion). We took 1.7 MPa for the static Young modulus (dynamic mechanical measurement value).

**Fig. 8.10** Experimental spectra of amplitude of vibration (first mode) as a function of frequency in contact with the first PDMS sample for a driving voltage of the bimorph of 0.5 V and for different static forces

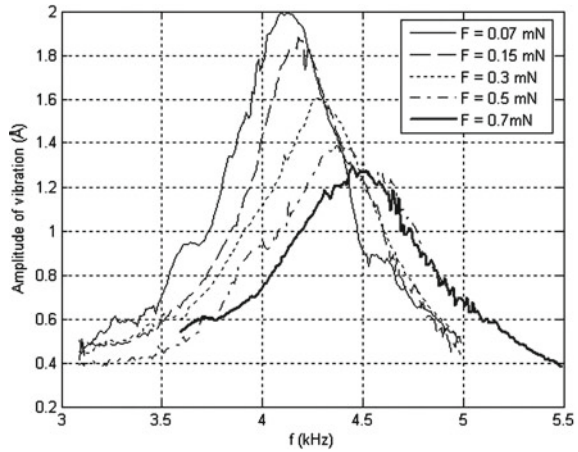
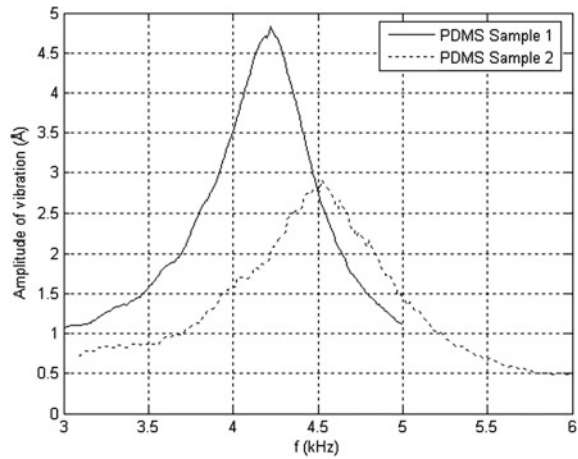


**Fig. 8.11** Experimental spectra of amplitude of vibration (first mode) as a function of frequency in contact with the two different PDMS samples for a static force of  $150\mu\text{N}$  and for a driving voltage of the bimorph of 1 V

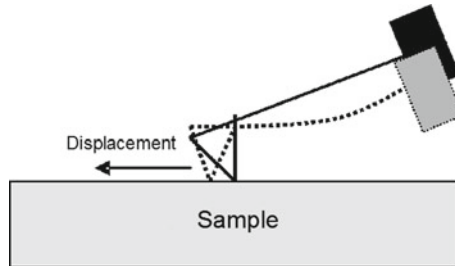


We did the same for our second PDMS sample, and we finally measure a mean resonant frequency of 4.53 kHz and also for Young’s modulus a value of 5.5 MPa ( $\pm 0.3$  MPa).

We took 2.8 MPa for the static Young modulus (dynamic mechanical measurement value). The SMM has already been tested on standard hard materials such as silicon and silica [13, 20, 28] and leaded to a precision of nearly 5% with the model we are using. We are able to characterize two very soft samples with Young’s modulus difference of some megapascals. The shift frequency difference between the two materials is 350 Hz (see Fig. 8.11). For example, the shift frequency difference with the same cantilever between silica (72 GPa) and silicon (100) (130 GPa) is nearly 1 kHz (see Table 8.1). Experimentally the sensitivity has increased by a factor of 10,000.  $S_N$  also has increased by a factor of 3.

**Table 8.1** Frequency shifts and sensitivities for stiff and flexible materials with a cantilever with a length of 7 mm

Materials	SiO <sub>2</sub> /Si	Different PDMSs
$\Delta$ shift frequency	1 kHz	350 Hz
Sensitivity	0.015 Hz/MPa	167 Hz/MPa
$S_N$	$47 \times 10^{-3}$	$136 \times 10^{-3}$

**Fig. 8.12** Illustration of the sliding of the tip on the surface during contact

### 8.3.3 New Cantilever Geometries

One of the major issues in scanning force microscopy is the application of tangential forces between the tip and the sample during contact. Actually when tangential force becomes too high, the tip slides on the surface (Fig. 8.12). This leads to prevent a good localization of the measurement and to limit the quantification of the local contact stiffness.

In atomic force microscopy, stick & slip can occur. The tip alternately sticks and slides on the surface when the force is too high. In dynamic mode, nonlinearities can appear in the contact resonance curves indicating a loss of contact stiffness, for example in lateral force microscopy [29].

Specific geometries of resonant cantilevers for scanning force microscopy aimed to reduce sliding between tip and sample have been designed and studied. These cantilevers have been designed for the SMM.

With a classic rectangular cantilever, dynamic sliding can be observed on the contact resonance curves. Actually when excitation voltage  $V_{exc}$  becomes too high, nonlinearities appear.

The amplitude of vibration does not increase linearly with the excitation and the resonance frequency decreases (Fig. 8.13). It can be explained by the loss of lateral contact stiffness due to sliding.

Sliding can be reduced by increasing the static force applied and by using a stiffer cantilever but still occurs for a bit higher amplitude of vibration. The underestimation of the contact stiffness leads to limit the quantification of the local elastic constants.



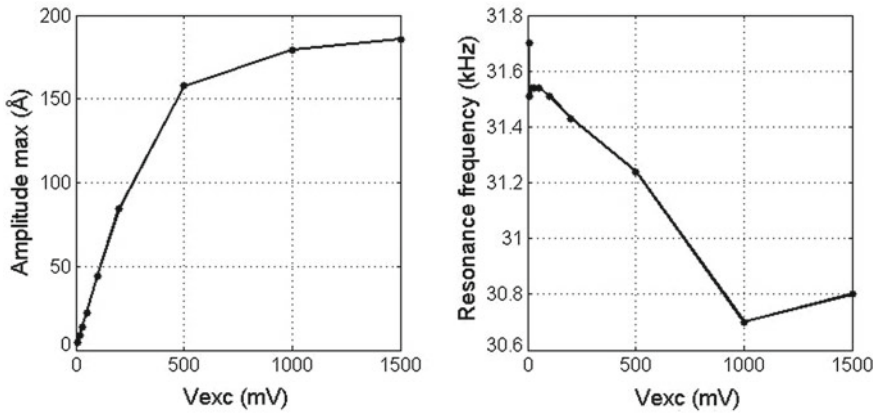
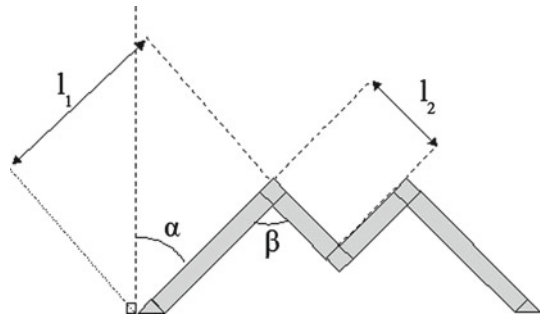


**Fig. 8.13** Evolution of the amplitude of vibration and the resonant frequency as a function of the excitation voltage

**Fig. 8.14** Scheme of the geometry of the new cantilevers conceived



So we have thought to specific geometries of resonant cantilevers to prevent the tip from sliding on the surface.

A W-shaped cantilever has been imagined, using a simple mechanism of correction, to keep the tip vertical during contact (Fig. 8.14). The tip is located on the center of the cantilever. Actually by choosing an appropriate ratio between the lengths  $l_1$  and  $l_2$ , the two beams exactly compensate the flexion of the cantilever.

The conception has been realized thanks to ANSYS software. A parametric study has been made. The thickness of the cantilevers and the width of the beams have been kept constant (respectively 150 and 400  $\mu\text{m}$ ). The other parameters have been modified and the tip torsion and the stiffness of the cantilever have been recorded. This has enabled us to choose 10 different geometries optimized to prevent sliding and with stiffnesses from 500 to 150,000 N/m (Fig. 8.15). Different stiffnesses have been chosen to optimize the sensitivity to the local contact stiffness depending on the material thanks to the precedent optimization study.

The cantilevers have been fabricated with KOH attack and DRIE process. It has enabled us to obtain satisfying vertical sides (Fig. 8.16).

**Fig. 8.15** Geometries of the 10 W-shaped cantilevers conceived with ANSYS

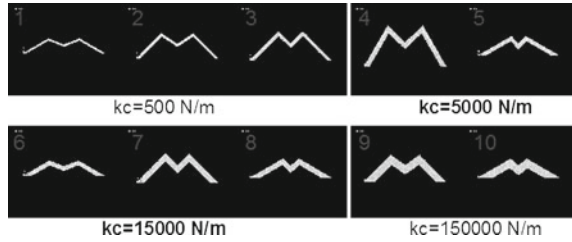


**Fig. 8.16** Photography of one of the fabricated W-shaped cantilevers

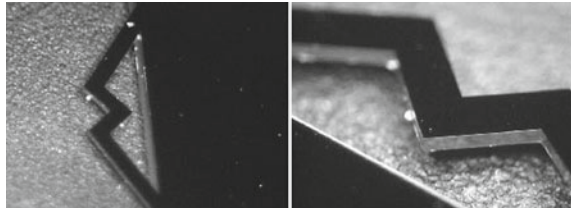
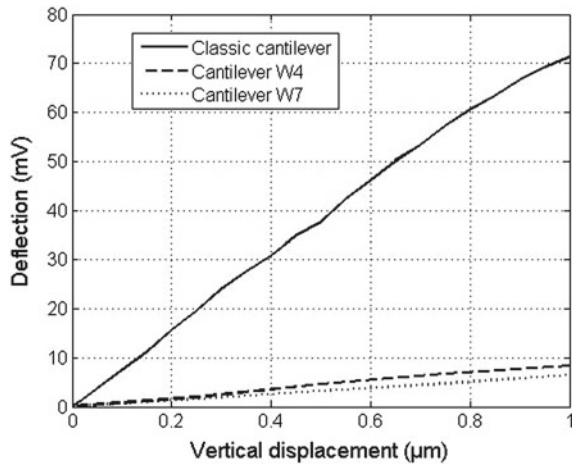


**Fig. 8.17** Static deflections measured for two W-shaped cantilevers and for a classic one on a silicon surface



- i. *Static deflections.* The static deflections of two W-shaped cantilevers (W4 and W7) have been measured on a silicon surface thanks to the deflectometer and we have compared them to those obtained with a classic cantilever (Fig. 8.17). Actually W-shaped cantilevers have shown deflections 10–20 times lower than the classic ones, indicating that the tip remains almost vertical during contact. It can be assumed that the displacement of the tip on the surface has been reduced.

Finite Element simulations have confirmed these measurements by using the software LS-DYNA. LS-DYNA simulations have shown that while lateral displacement on the surface is important with a classic cantilever (120 nm for a static displacement of 1 µm on a silicon surface), it is 6–7 times lower with a W-shaped cantilever. These simulations have confirmed the static satisfying behavior of our new cantilevers. The

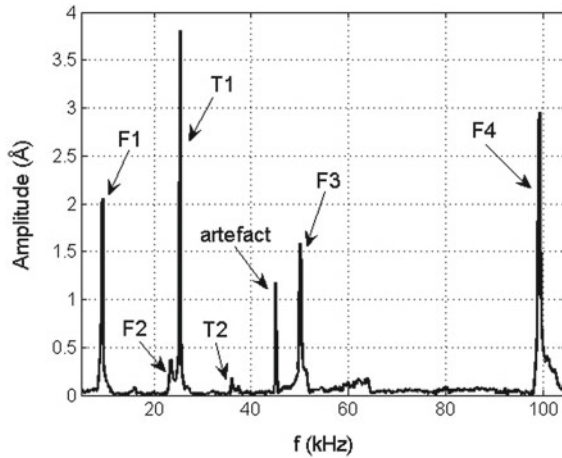


**Fig. 8.18** Free amplitude of vibration of the cantilever W4 as a function of the frequency (kHz). Flexural and torsional modes can be observed

**Table 8.2** Free vibration modes of the W-shaped cantilever W4

Mode	Experimental frequency (Hz)	FEM computed frequency (Hz)
Flexion 1	9,324	9,705
Flexion 2	25,325	24,497
Torsion 1	25,300	25,579
Torsion 2	35,928	41,505
Flexion 3	50,100	59,873
Flexion 4	99,200	82,765

tip remains vertical, so it is always the same area of the tip which is put in contact and the lateral displacement is very reduced enabling a good localization of the measurement.

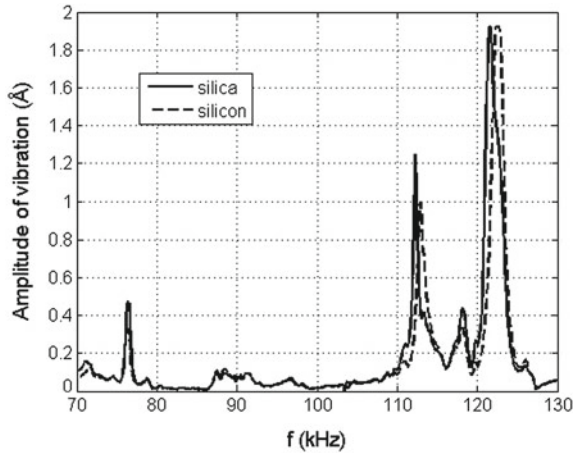
- ii. *Vibration modes.* The W-shaped cantilevers have been excited thanks to a piezo-electric ceramic. Free flexural and torsional vibration modes have been observed and compared to FEM simulations.

Figure 8.18 gives for example the spectrum of the cantilever W4.

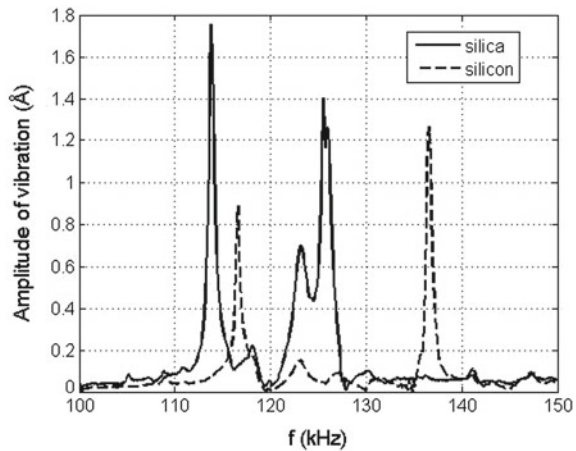
Table 8.2 compares the experimental measured frequencies and the FEM computed ones. Flexural and torsional modes have easily been observed by the same excitation. A good agreement has been obtained for the first modes but less accuracy with higher modes.

The contact modes have also been measured on silica and silicon surfaces. The best sensitivity has been obtained for the cantilever W7. The contact resonance curves can be seen in Fig. 8.19. A good frequency shift has been seen between the two materials. So it has been shown that these cantilevers enable mechanical characterization.

**Fig. 8.19** Amplitude of vibration as a function of the frequency, on silicon and silica surfaces, for the W-shaped cantilever W7, for a static force of 7.5 mN



**Fig. 8.20** Amplitude of vibration as a function of the frequency, on silicon and silica surfaces, for the W-shaped cantilever W7, for a static force of 15 mN



An even much better sensitivity has also been observed for a higher static force, especially for the torsional modes (Fig. 8.20).

LS-DYNA simulations have been realized and have shown a good accuracy for the first flexural mode but far less for the following modes (Table 8.3).

iii. *Dynamic sliding.* Finally, to verify the dynamic behavior of the W-shaped cantilevers the contact resonance curves have been measured for an increasing excitation voltage (Fig. 8.21). It can be seen that the resonance curves for the flexural mode are quite symmetric. The resonance frequency is constant even for high amplitudes of vibration. This means that dynamic sliding is reduced and it confirms the ability of the W-shaped cantilevers to prevent the tip from sliding on the surface during oscillations. But it can be observed that nonlinearities appear on the torsional mode, which indicates that there is sliding. It is normal because the

**Table 8.3** Comparison experiment/fem simulations for the vibration modes of the W-shaped cantilever W7 in contact with a silicon surface and for a static force of 7.5 mN

Mode	Experimental frequency (Hz)	FEM computed frequency (Hz)
Flexion 1	76,400	72,050
Torsion 1	112,300	84,714
Torsion 2	121,550	90,874

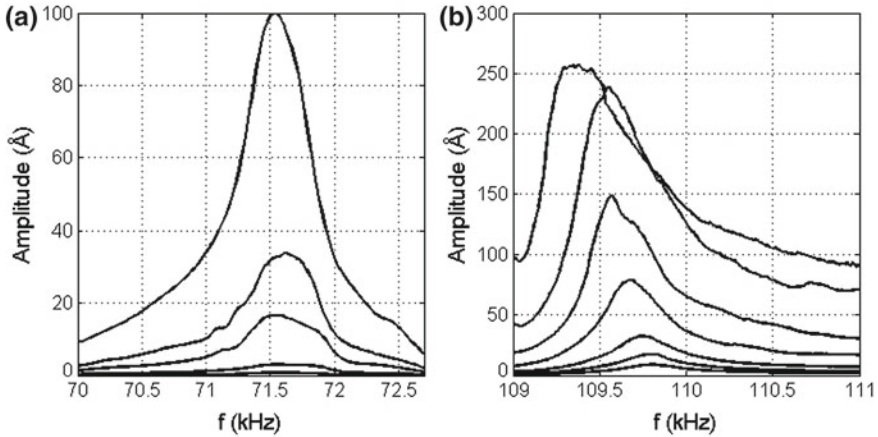


**Fig. 8.21** Contact resonance curves on a silicon surface of the W-shaped cantilever W7, for a static force of 1.5 mN, for an increasing voltage. **a** Evolution of the flexural mode, **b** evolution of the torsional mode is on the *right*

W-shaped cantilevers are designed to prevent the tip from sliding in the length direction but not from left to right.

The efficiency of the W-shaped cantilevers to reduce sliding, both in static and dynamic behaviors, has been shown in this paragraph. These cantilevers have exhibited a good sensitivity enabling mechanical characterization. The contact behavior modeling (requiring a numeric solving because of the complex shape) is quite delicate but has provided a good accuracy for the first mode.

## 8.4 Applications on Polymers

In the field of materials sciences it is quite hard to have matching mechanical characterization methods at very small scale. This has become possible only in the last few years especially thanks to scanning probe microscopy and nanoindentation [18, 30, 31]. Viscoelastic properties of polymers have also been measured for low frequencies and for higher frequencies thanks to the time temperature equivalence [32].

Yet, direct measurements at high frequencies are far less studied in the literature of materials.

In this last part, three techniques of dynamic mechanical characterization working at different scales have been used. A DMA is a technique working at macro scale by tensile tests, The SMM and at last, nanoindentation tests which can characterize materials at nano- or microscale and for quasistatic or dynamic loadings have been carried out [33]. We decided to characterize two polymers by measuring their complex Young's moduli for a wide range of frequencies to exhibit their viscoelastic properties. We chose two very different organic materials often used in MEMS applications, PDMS and SU8 resin. PDMS is a silicon-based elastomer. Mechanical properties of this very versatile material vary with preparation conditions. Young's moduli values can actually fluctuate in the range of 0.1 MPa to some tens of MPa depending on its preparation [34–38]. It exhibits important viscoelastic behavior. The other material we decided to characterize is a SU8 resin film. This resin is a polymer based on epoxies which is used for photolithography and MEMS applications and has a Young modulus in the range 3–6 GPa associated with a low viscoelastic behavior [38]. Bulk samples have been designed to allow DMA measurements and to verify the compatibility of these techniques. To our knowledge such a comparison on viscoelastic materials has not been yet reported in the literature. This is the principal aim of this study performed on these two very different polymers.

## ***8.4.1 Materials and Experimental Procedures***

### **8.4.1.1 Materials**

PDMS has become the most popular building material used in a variety of low-cost aqueous microfluidic devices aimed in particular at single use for biological or medical diagnostics. In order to have low power consumption, many groups use this material for the manufacture of mobile part (often membrane, bridge...) in active systems such as microvalves and micropumps. Therefore, the characterization of the dynamic mechanical properties of PDMS is of great interest.

Different samples have been tested. Specimen 1 was tested thanks to the three different techniques for aging times  $t_v$  of about 1,500 and 11,000 h at constant temperature  $T \approx 20 - 22$  °C in a closed Petri dish and without light exposure. Specimen 2 is a very old sample which has been aging for a long time ( $t_v > 3$  years) at room temperature (20–30 °C), without any particular precaution and whose preparation conditions are not exactly the same as those previously presented for specimen 1. Thus, these two PDMS samples must be considered as two different materials. The SU8 resin is a negative epoxy type photoresist which has been developed by IBM (Watson Research Center). This polymer is a good material for MEMS applications.

Two different samples have been tested. Specimen 1, tested with the three techniques, is a film 0.13 mm thick obtained by spin-coating liquid SU8 resin (for 30 s at 5,000 rpm/s) on a 'glass substrate. Specimen 2 is a film of 50  $\mu\text{m}$  thick deposited on

(100) silicon substrate. Due to the small thickness of these films, only nanoindentation and SMM procedures have been carried out.

#### 8.4.1.2 Dynamic Mechanical Analysis

DMA measures with frequencies in the range of  $10^{-2}$  to 100 Hz were performed on a commercial BOSE Electroforce 3200 machine, at room temperature for the three different materials and at  $T = 23, 0, -20, -40, -60$  °C for the PDMS sample 1. Thus, for this specimen the time–temperature equivalence has been analyzed over a large domain of frequency;  $10^{-2} < f < 10^5$  Hz.

For PDMS and SU8 resin (specimen 1) samples, gage lengths of the specimens were about 30 mm and 36 mm for a cross-section of about  $13 \times 3\text{--}4$  mm<sup>2</sup> and  $10.2 \times 0.13$  mm<sup>2</sup> respectively. A control on the position with a peak to peak amplitude of 0.5 mm (corresponding to a strain of  $\pm 7.6 \times 10^{-3}$ ) for a preload strain of  $9.1 \times 10^{-3}$  was realized. Thus, the samples were always in tension even at the low point of the cycles. According to the ASTM Standard Guide for Dynamic Testing the software calculates the phase angle  $\phi$  between the imposed displacement and the measured force and uses the specimen shape to convert the stiffness and the phase information to provide the values of  $E'$ , the storage modulus,  $E''$ , the loss modulus and  $\tan(\phi)$ , the tangent of the phase angle. Moreover, for the specimens 1 (PDMS and SU8), the evolution of  $E'$  and  $E''$  with the aging time  $t_v$  has been studied between 3 to about 1,300 h.

#### 8.4.1.3 Nanoindentation Tests

The Berkovich's indentations were performed with a Nanoindenter IIS (NanoInstruments). The hardness  $H_b$  and the Young's modulus  $E^*$  are deduced using the classical static procedure or the continuous stiffness method (CSM). One of the most commonly used methods for analyzing nanoindentation data is the Oliver and Pharr one [30], which expands on earlier ideas developed by Loubet et al. [39] and Doerner and Nix [40]. This analysis has often been applied to polymer characterization, for example [38, 41] and [42], even if the true contact area is underestimated due to the pushing up of the material around the indenter. In this case, the Young's modulus is slightly overestimated. However, in our method the Young's modulus has been estimated for an indentation depth close to zero and thus the pile up effect may be considered as negligible.

In the CSM method a small harmonic load oscillation is superimposed to the static one and if the tested material presents a viscoelastic character it is then possible to deduce its complex modulus [43]. If the dynamic loading is given by:

$$F = F_0 \exp(i\omega t) \quad (8.16)$$

the deformation response of the material is:

$$\Delta h = \Delta h_0 \exp(i\omega t) \exp(i\phi) \quad (8.17)$$

where  $\phi$  is the phase lag due to viscous dissipation, as for the SMM technique. The components of the complex modulus  $E^*$  can be calculated according to:

$$E'^* = S_d \frac{\sqrt{\pi}}{2\eta\sqrt{A}} \cos(\phi) \quad (8.18)$$

$$E''^* = S_d \frac{\sqrt{\pi}}{2\eta\sqrt{A}} \sin(\phi) \quad (8.19)$$

with  $S_d = F_0/\Delta h_0$ ,  $A_p$  the projected area of the elastic contact,  $\eta = 1.034$  for a Berkovich's tip and thus  $\tan(\phi) = E''^*/E'^*$ .

Nanoindentation tests were performed using a Nanoindenter IIS. As previously mentioned the study was conducted following the classical (quasistatic) and CSM (dynamic at  $f = 45$  Hz) procedures. For each tested sample and for each initial stiffness  $S_0$ , the measurement sequence consists of 5 indents with a  $50\ \mu\text{m}$  space between them with a maximum penetration depth of  $h_{\text{max}} = 4\ \mu\text{m}$ . The penetration speed was not constant but increased with depth from 2 to  $45\ \text{nm s}^{-1}$  with 8 steps such that  $\dot{\varepsilon} = (1/h)(dh/dt)$  is approximately constant and equal to  $2 \times 10^{-2}\ \text{s}^{-1}$ . The stiffness of the indentation cell  $S_i$  is  $44\ \text{N/m}$  and the values of the imposed initial stiffness are in the range  $53 < S_0 < 94\ \text{N/m}$ . For the quasistatic method, four unloadings (to 90% of the total loading) were performed at about  $h_{\text{max}} \approx 1, 2, 3$  and  $4\ \mu\text{m}$  and 50% of the unloading curves are considered to calculate the contact stiffness of the samples. For the CSM procedure, the indenter vibrates at a frequency of 45 Hz for amplitude of 1–2 nm during the indenter penetration ( $\dot{\varepsilon} \approx 2 \times 10^{-2}\ \text{s}^{-1}$ ).

In the case of the SU8 films the maximum penetration depth has been fixed at  $h_{\text{max}} = 3\ \mu\text{m}$  and the contact between the surface of the sample and the indenter tip is easily detectable. Thus, the measured values of the Young's modulus and of the hardness are constant overall the indentation depth.

#### 8.4.1.4 The SMM

In this study a simple spring-mass approximation has been introduced to take into account the damping and to determine the complex Young's modulus like Arinéro et al. [44] did for an AFM. First, the relation between the frequency  $f_0$  and  $k^*$  is obtained:

$$f_0 = \frac{1}{2\pi} \sqrt{\frac{k^* + k_c}{m_{\text{eff}}}} \quad (8.20)$$

where  $k_c$  is the beam stiffness. The linear differential equation describing the response of an oscillator, with  $m_{\text{eff}}$  the effective mass of cantilever and tip,  $\tilde{x}$  the complex value of the response,  $\omega_0$  the cantilever–tip–sample system's resonance angular frequency



and  $\lambda$  the damping coefficient is:

$$\frac{\partial^2 \tilde{x}}{\partial t^2} + 2\lambda \frac{\partial \tilde{x}}{\partial t} + \omega_0^2 \tilde{x} = \frac{F_0}{m_{\text{eff}}} \exp(i\omega t) \quad (8.21)$$

with  $\tilde{x} = X_0 \exp(i\omega t) \exp(i\phi)$ .

So,

$$X_0 \exp(i\phi) = \frac{F_0/m_{\text{eff}}}{(\omega_0^2 - \omega^2) + 2i\omega\lambda} \quad (8.22)$$

Introducing the resonance frequency of the system  $f_0$  and the 3 dB half-bandwidth  $f_1$ , given by  $f_0 = \omega_0/2\pi$  and  $f_1 = \lambda/2\pi$ , the expression of the complex contact dynamic stiffness can be obtained:

$$k_{\text{CCD}} = \frac{F_0}{X_0 \exp(i\phi)} = m_{\text{eff}}(4\pi^2(f_0^2 - f^2) + 8i\pi^2 f f_1) \quad (8.23)$$

By taking the imaginary part, and as  $f$  is close to  $f_0$ , the  $k''^*$  stiffness is obtained:

$$k''^* = 8m_{\text{eff}}\pi^2 f_0 f_1 \quad (8.24)$$

Introducing the complex effective Young modulus  $E_x^*$ :

$$E_x^* = E'^* + iE''^* \quad (8.25)$$

and writing the expression of the complex stiffness as [45]:

$$k^* = k'^* + ik''^* \quad (8.26)$$

with a static Hertz contact:

$$k^{*''} = E''^{*2/3} (6RF_0)^{1/3} \quad (8.27)$$

and thanks to Eqs. (8.20), (8.24) and (8.27), the expression of  $E''^*$  is given by:

$$E''^* = \frac{(2(k'^* + k_c) f_1)^{3/2}}{f_0^{3/2} (6RF_0)^{1/3}} \quad (8.28)$$

This relation will be used for the SU8 resin as  $E_1^* \approx E_0^*$ .

For a dynamic contact:

$$k^{*''} = \frac{E_1''^*}{E_0^{*1/3}} (6RF_0)^{1/3} \quad (8.29)$$

Thanks to Eqs. (8.20), (8.24) and (8.29), the following expression of  $E_1^{l/*}$  has been obtained:

$$E^{l/*} = \frac{2(k^{l/*} + k_c) f_1 E_0^{*1/3}}{f_0 (6RF_0)^{1/3}} \quad (8.30)$$

This relation will be used for the PDMS elastomer.

At last, it is interesting to note that the relations on the components of the complex Young's modulus determined with the hypothesis of static (st) (Eq. 8.1) or dynamic (dyn) (Eq. 8.2) Hertz contact are such that:

$$E_{\text{dyn}}^{l/*} = (E_{\text{st}}^{l/*})^{2/3} E_0^{*1/3} \quad \text{and} \quad E_{\text{dyn}}^{l/*} = (E_{\text{st}}^{l/*})^{2/3} E_0^{*1/3} \quad (8.31)$$

It is thus possible to write:

$$E_{\text{dyn}}^{(i)*} = E_{\text{st}}^{(i)*} \left( \alpha + (1 - \alpha) \left( \frac{E_0^*}{E_{\text{st}}^{(i)*}} \right)^{1/3} \right) \quad (8.32)$$

with (i) = ("or"),  $\alpha = 1$  for a nonviscous material and  $\alpha = 0$  for a viscoelastic material.

Two different cantilevers have been used for the characterization of these two materials. Thanks to the previous study on the sensitivity of the SMM, we chose 2 different cantilevers which are optimized for PDMS and SU8 resin. Actually, we showed that the cantilever stiffness must be chosen close to the contact stiffness to have the best sensitivity. As cantilever stiffness depends on the inverse of the cube of the length, a length of 7 mm for PDMS and 4.5 mm for the SU8 which is harder have been chosen. The width and the thickness of the beam are 400 and 150  $\mu\text{m}$  respectively. The tip has a cylindrical base and a conical end as shown in Fig. 8.1. The sharp end of the tip is spherical. For the beam with a length of 7 mm, the tip length  $l$  is 697  $\mu\text{m}$ , its mass  $m = 0.23 \mu\text{g}$  and its curvature radius  $R = 45 \mu\text{m}$ . For the one with a length of 4.5 mm,  $l = 976 \mu\text{m}$ ,  $m = 0.45 \mu\text{g}$  and  $R = 20 \mu\text{m}$ . The static applied force  $F_0$  was 0.15 mN for the PDMS and 0.5 mN for the SU8 resin. The frequency domain of the SMM with these cantilevers corresponds to some kHz.

With these experimental conditions the polymers are loaded in their linear viscoelastic regime. Actually, PDMS remains linear until deformations of 60% [37] and 5% for SU8 resin [38]. For a spherical tip like SMM ones, deformation of the contact area is  $\varepsilon = 0.2 a_c/R$  [46], where  $a_c$  is the contact area radius and  $R$  the tip radius. With the tips we have used,  $a_c < 5 \mu\text{m}$  and  $R > 20 \mu\text{m}$ , thus  $\varepsilon < 5\%$ .

## 8.4.2 Experimental Results

The three techniques work at different scales and at different frequencies. As previously shown, they enable us to check the viscoelastic properties of these polymers.

Actually, storage and loss moduli of polymers change depending on the frequency. We recorded the measures of  $E'$  and  $E''$  for the two specimens of PDMS and for the two SU8 resin films.

#### 8.4.2.1 Phenomenological modeling

From a material point of view and for viscoelastic materials as polymers, the crucial problem in vibration experiments concerns the accurate determination of the viscoelastic parameters over a broad range of frequency. So, in the case of sinusoidal deformation, the complex modulus can be written as [47]:

$$E^* = E^i + (E^r - E^i) \sum_{j=1}^n p_j \frac{1}{1 + i\omega\tau_j} \quad \text{with} \quad \sum_{j=1}^n p_j = 1 \quad (8.33)$$

where  $E^i$  and  $E^r$  are the instantaneous and relaxed Young's moduli, respectively. The parameters  $\tau_j$  are the different relaxation times and  $p_j$  is a ponderation coefficient for each relaxation time. It is very difficult to determine the values of the parameters  $p_j$ ,  $\tau_j$  and their number  $n$ . From a phenomenological point of view, to overcome this difficulty the empirical model of Havriliak and Negami [48] (H-N model) is considered, which combines the advantages of the modeling of Cole et al. [49] and Davidson et al. [50]. In this model, the complex modulus is given by:

$$E^* = E^i + (E^r - E^i) \frac{1}{(1 + (i\omega\tau)^\alpha)^\beta} \quad (8.34)$$

Thus, storage and loss moduli are respectively given by:

$$E' = E^i + (E^r - E^i) \frac{\cos(\beta\phi)}{(1 + 2(\omega\tau)^\alpha \cos(\alpha\pi/2) + (\omega\tau)^{2\alpha})^{\beta/2}} \quad (8.35)$$

$$E'' = (E^i - E^r) \frac{\sin(\beta\phi)}{(1 + 2(\omega\tau)^\alpha \cos(\alpha\pi/2) + (\omega\tau)^{2\alpha})^{\beta/2}} \quad (8.36)$$

$$\text{with} \quad \phi = \tan^{-1} \left( \frac{(\omega\tau)^\alpha \sin(\alpha\pi/2)}{1 + (\omega\tau)^\alpha \cos(\alpha\pi/2)} \right) \quad (8.37)$$

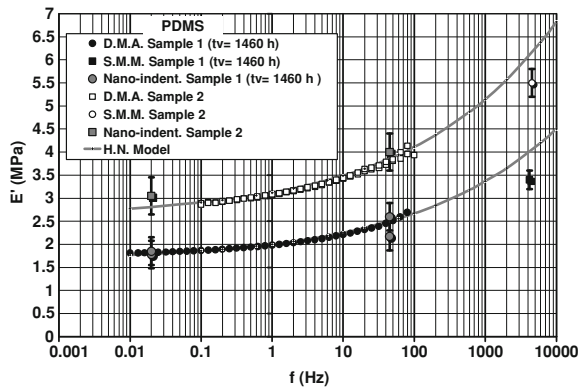
where  $\tau$  is a single parameter with time dimension and  $\alpha, \beta$  two empirical parameters.

Note that, if  $\alpha = \beta = 1$ , the Eq. (8.35) with a single relaxation time is obtained. The different experimental curves of Figs. 8.22, 8.23 and 8.24 for the PDMS and Figs. 8.25, 8.26 and 8.27 for the SU8 resin have been fitted by Eqs. (8.35), (8.36), (8.37) and the results drawn on these figures. The identified values of the parameters are listed in Table 8.4. Note that these values correspond to the working range of frequencies and cannot be used for very higher frequencies.

**Table 8.4** Parameters values of Eqs. (8.33) (8.34) and (8.35)

Specimen	$t_v$	$\alpha$	$\beta$	$\tau$	$E'$ (MPa)	$E''$ (MPa)	$F$ (Hz)
PDMS (Spec.1)	1,460h	0.236	1	$2 \times 10^{-9}$	1.65	29.6	$10^{-2}$ to $10^6$
PDMS (Spec.2)	>25,000 h	0.236	1	$2 \times 10^{-9}$	2.6	44	$10^{-2}$ to $10^6$
SU8 (Spec. 1)	1,000h	0.4	0.38	40	3,600	4,500	$10^{-2}$ to $10^5$
SU8 (Spec. 2)	1,000h	0.4	1	0.5	5,000	5,600	$10^{-2}$ to $10^5$

**Fig. 8.22** Storage modulus of PDMS samples measured by nanoindentation, DMA and SMM techniques as a function of the working frequency. Simulation with the H–N model



### 8.4.2.2 Case of the PDMS Samples

We took  $\nu = 0.48$  for the Poisson’s ratio of the PDMS (hyperelastic material). The values of  $E'$  for the two PDMS samples are plotted in Fig. 8.22 as a function of the working frequency and for the three experimental techniques. Note that for the SMM value,  $f$  is the first contact resonance frequency equals to 4.18 KHz. The measures given by the DMA and the nanoindentation methods are in a fairly good agreement. The SMM ones even if it is two decades further show a possible continuity. Static moduli  $E_0^*$  for the two samples are respectively 1.7 and 2.9 MPa. As it will be shown, this difference is principally due to the different preparation conditions and weakly to the aging time. Storage modulus increases with the frequency for the two samples, which is typical of a viscoelastic material. For these two materials the values given by the SMM at nearly 4 kHz are 3.4 and 5.5 MPa (Fig. 8.22). In the Fig. 8.23 the loss modulus is plotted as the function of the working frequency. At 0.01 Hz the values are very low, near zero, but sharply increase with the working frequency. Results between DMA and SMM show the same behavior for  $E''$  than for  $E'$ . Typically, for polymers,  $E''$  increases before reaching a maximum and then decreases with the working frequency. The SMM values of  $E''$  at 4 kHz for the two specimens are about 1 and 1.6 MPa.

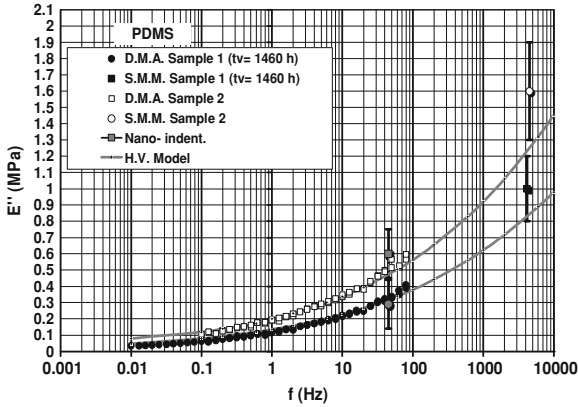


**Fig. 8.23** Loss modulus of PDMS samples measured by nanoindentation, DMA and SMM techniques as a function of the working frequency. Simulation with the H–N model

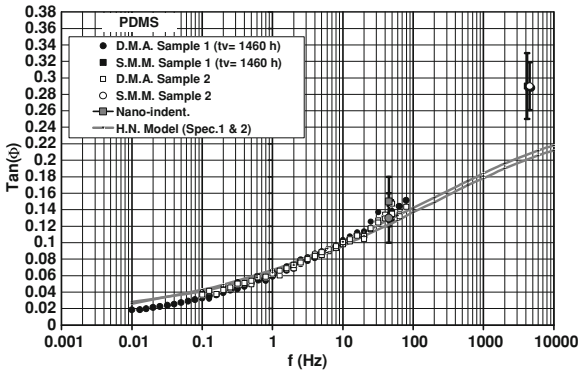


**Fig. 8.24**  $\tan(\phi)$  parameter of PDMS samples determined by the three different techniques. Simulation with the H–N model

$E'$  and  $E''$  are of the same order of magnitude which means that for this range of frequencies the material is very viscoelastic. This behavior is quantified by the parameter  $\tan(\phi) = E''/E'$  as shown in Fig. 8.24. The values estimated with the CSM nanoindentation procedure are in good agreement with those obtained by the DMA analysis. The SMM values also show a possible continuity. The  $\tan(\phi)$  parameter is an increasing function of the frequency, as expected, and the SMM values are close to 0.28 for  $f \approx 4$  kHz. It should then decrease for higher frequencies; the maximum value should be obtained at a frequency of about  $10^6$  Hz. From a material point of view, it is interesting to note that the values of the  $\tan(\phi)$  parameter are the same for the two tested specimens, indicating that this parameter seems insensitive to the elaboration conditions and the aging time as it will be shown later.

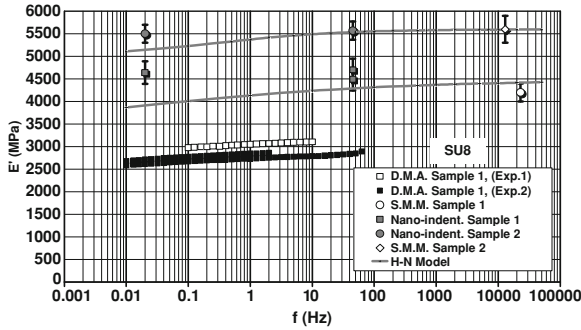


**Fig. 8.25** Storage modulus of SU8 resin samples measured with the three techniques as a function of the working frequency. Simulations with the H–N model

### 8.4.2.3 Case of the SU8 Resin

The same measures on the SU8 resin film have been carried out. For this material we took a Poisson’s ratio of  $\nu = 0.29$ . For the two specimens the evolution of the storage modulus  $E'$  with the frequency has been plotted in Fig. 8.25. This time, the three techniques do not perfectly match. Actually for sample 1, at 0.01 Hz the DMA value is about 2.9 GPa (2 different measures) whereas the nanoindentation value is about 4.5 GPa. Moreover, for these two techniques the storage modulus slightly increases with the frequency in the studied range. The SMM value at 23 kHz (first resonance frequency) confirms the indentation modulus values with a nearly equal value of 4.2 GPa. As previously mentioned, the value of the order of 4.5 GPa is in agreement with the results given in the overall literature  $E' \approx 4$  to 6 GPa. The low values obtained by DMA technique are certainly due to the too small thickness of the tested specimen (0.13 mm) and the small preload strain ( $\approx 9 \cdot 10^{-3}$ ) allowing to a certain inhomogeneity in the strain field across the specimen section. The artifacts due to the instrument compliance effects observed on rigid specimens are also not negligible. So in the typical curve of the storage modulus of a polymer, the maximum of slope has already been passed and the modulus is quite constant. The same evolution can be expected for the loss modulus in this range of frequencies. In Fig. 8.26 a loss modulus which decreases with the frequency can be observed. The nanoindentation value is a slightly greater than the DMA one. The SMM value at 23 kHz is lower and confirms the global decreasing of the loss modulus. It can be noted that the loss modulus is far lower than the storage one (20–80 MPa vs. 4–4.5 GPa). Thus, the SU8 resin presents very weak viscoelastic behavior, far less than the PDMS one.

The  $\tan(\phi)$  has also been plotted in Fig. 8.27. The maximum has been passed ( $f \approx 10^{-2}$  Hz) and this parameter decreases with the frequency. Of course, the values are much lower than for the PDMS and the maximum value is close to 0.025. It is important to observe that the three techniques perfectly match. DMA and nanoindentation values are the same at 45 Hz and the SMM value prolongs the decrease of the curve. In fact with DMA technique, the error due to the small thickness of the film (or other

**Fig. 8.26** Loss modulus of SU8 resin samples measured with the three techniques as a function of the working frequency. Simulations with the H–N model

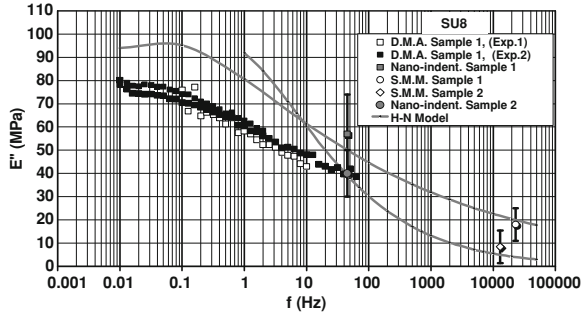
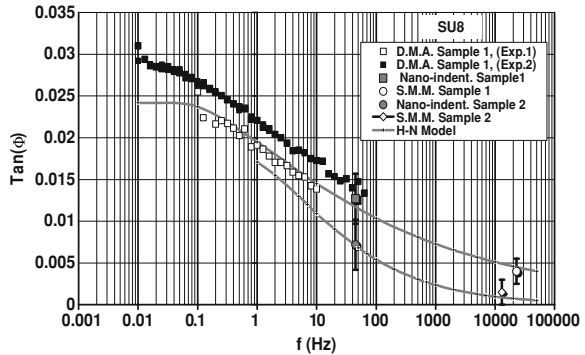


**Fig. 8.27**  $\tan(\phi)$  parameter of the two SU8 resin samples determined by the three techniques. Simulations with the H–N model



causes) has the same effect on the determination of  $E'$  and  $E''$  and disappears on the loss tangent which is equal to the ratio  $E''/E'$ .

Nanoindentation and SMM measurements have been performed on the same sample (specimen 1) but for an aging time at room temperature of about 13,000 h. Contrary to the PDMS samples, no noticeable evolution outside of the method accuracies has been pointed out.

For the SU8 film deposited on the Si substrate (specimen 2), the nanoindentation and the SMM techniques perfectly match (Fig. 8.25) and the determined values of the storage modulus are  $5.57 \pm 0.15$  GPa and  $5.6 \pm 0.3$  GPa, respectively. These values are higher than those measured on specimen 1, but close to those reported by Al-Halhouli et al. [38], i.e.: 5.2 GPa. The values of the loss modulus and the tangent of the phase lag are plotted in Figs. 8.26 and 8.27. As for the specimen 1 these two parameters decrease with the frequency, but the values are slightly lower than those determined on the previous sample, i.e.:  $E'' = 40$  MPa (at 45 Hz) and  $E'' = 8.4$  MPa (at 13 KHz) for the nanoindentation and the SMM procedures, respectively. These observations, increasing of  $E'$  and decreasing of  $E''$  compared to the values obtained on sample 1, are certainly due to the long bake during 15 h at 90 °C performed on this specimen.

Note that, the Berkovich hardnesses  $H_b$  of these different polymers are about,  $H_b = 0.33 \pm 0.05$  MPa and  $0.55 \pm 0.05$  MPa for the two PDMS samples (specimens 1

and 2 respectively) and  $H_b = 330 \pm 20$  MPa and  $H_b = 362 \pm 13$  MPa for the two SU8 films (specimens 1 and 2). This last value is in fairly good agreement with the one given by Al-Halhouli et al. [38] ( $H_b \approx 430$  MPa).

The simulations are fairly good especially considering on the one hand the three different experimental techniques that have been used and on the other hand the wide range of frequency which has been analyzed. Notice the very great difference between the time parameter of the PDMS and the SU8 resin's one; the PDMS is very viscous ( $\tan(\phi) \approx 0.21$  at  $f = 10^4$  Hz) contrary to the SU8 resin ( $\tan(\phi) \approx 0.005$  at  $f = 10^4$  Hz for sample 1). The same trend is observed on the ratio between the instantaneous and the relaxed moduli,  $E^i/E^r$ :  $E^i/E^r \approx 17$  for the PDMS and only  $\approx 1.12$ – $1.25$  for the SU8 resin.

## 8.5 Conclusion

In this chapter, we have presented different new trends concerning the field of micro and nanocharacterization with near-field microscopes, focalized on the behavior of the SMM. However, all the conclusions summarized below can be very useful for all these near-field microscopes.

Optimization of the SMM by taking into account the sample material considered and the stiffness of the cantilever can be summarized as follows: (i) the sensitivity of the three first contact modes of the SMM has been studied. Sensitivity decreases with the contact stiffness. The first mode is the most sensitive but when contact stiffness increases higher modes become the most sensitive. (ii) The parameter  $S_N$  sensitivity reduced to working contact stiffness and frequency shows for each mode a maximum corresponding to contact stiffness. Actually we saw that  $S_N$  is maximum when the contact stiffness and the cantilever stiffness are of the same order of magnitude for the first mode. (iii) The sensitivity is also depending on the stiffness of the cantilever. So, the length of the cantilever which directly affects its stiffness is a mean to optimize the cantilever with the considered material.

New cantilever geometries (W-shaped) have been investigated and allowing to give these characteristics: (i) The efficiency of the W-shaped cantilevers to reduce sliding, both in static and dynamic behaviors (ii) These cantilevers exhibit a good sensitivity enabling mechanical characterization.

In the last part, the efficiency of the three mechanical characterization methods (DMA, SMM, Nanoindentation) has been pointed out. The results of the three different scales techniques (macro, micro, and nanoscale) fairly match. The very different viscoelastic behaviors of PDMS and SU8 resin for the same frequency range have been quantified. Their storage, loss moduli and  $\tan(\phi)$  from 0.01 Hz to some kHz have been measured. Satisfying global behaviors according to the models and good agreement between measured values and literature ones have been obtained. In conclusion, these three complementary experimental techniques can be used as powerful metrology tools for the mechanical characterization at very small scale of viscoelastic materials. To our knowledge, such a comparison of these three experimental methods



applied on viscoelastic materials has not been reported in the literature and highlights the potentialities of these techniques for polymer applications.

## References

1. B. Cretin, F. Sthal, Appl. Phys. Lett. **62**, 829–831 (1993)
2. P. Vairac, B. Cretin, Appl. Phys. Lett. **68**, 461–463 (1996)
3. O. Kolosov, H. Ogiso, H. Tokumoto, K. Yamanaka, *Springer Series in Materials Sciences*, vol. 31, pp. 345–348 (Springer, Heidelberg, 1994)
4. U. Rabe, W. Arnold, Appl. Phys. Lett. **64**, 1493–1495 (1994)
5. N.A. Burnham, A.J. Kulik, G. Gremaud, P.J. Gallo, F. Ouveley, J. Vac. Sci. Technol. B **14**, 794–9 (1996)
6. E. Chilla, T. Hesjedal., H.J. Frohlich, in *Proceedings of IEEE Ultrasonics, Symposium*, pp. 363–366, 1994
7. P. Maivald, H.J. Butt, S.A. Gould, C.B. Prater, B. Drake, J.A. Gurley, V.B. Elings, P. Hansma, *Nanotechnology* **2**, 103 (1991)
8. E.L. Florin, M. Radmacher, B. Fleck, H. Gaub, Rev. Sci. Instrum. **65**, 639 (1994)
9. W.H. Han, S.M. Lindsay, T. Jing, Appl. Phys. Lett. **69**, 4111 (1996)
10. P. Vairac, Ph.D. Thesis, Thèse de l'Université de Franche-Comte, Besançon, 1996
11. B. Cretin, P. Vairac, Appl. Phys. Lett. **71**, 2082–2084 (1997)
12. P. Vairac, B. Cretin, Opt. Com. **132**, 19–23 (1996)
13. B. Cretin, P. Vairac, Appl. Phys. A Mater. Sci. Process. **66**, 227–230 (1998)
14. O. Kolosov, K. Yamanaka, Jpn. J. Appl. Phys. **32**, 1095 (1993)
15. U. Rabe, W. Arnold, Appl. Phys. Lett. **64**, 1493–1495 (1994)
16. N.A. Burnham, A.J. Kulik, G. Gremaud, P.J. Gallo, F. Ouveley, J. Vac. Sci. Technol. B **14**, 794–799 (1996)
17. E. Dupas, G. Gremaud, A. Kulik, J.-L. Loubet, Rev. Sci. Instrum. **72**, 3891 (2001)
18. X. Li, B. Bhushan, Mater. Charact. **48**, 11 (2002)
19. P. Vairac, B. Cretin, Appl. Phys. A Mater. Sci. Process. **66**, 235 (1998)
20. P. Vairac, B. Cretin, in *Scanning Microdeformation Microscopy: Subsurface Imaging and Measurement of Elastic Constants at Mesoscopic Scale, Applied Scanning Probe Methods II*, ed. by B. Bhushan, H. Fuchs (Springer, Berlin, 2006), pp. 241–281
21. K.L. Johnson, *Contact Mechanics*(Cambridge University Press, Cambridge, 1987)
22. J. Le Rouzic, P. Vairac, B. Cretin, P. Delobelle, Rev. Sci. Instrum. **79**, 033707 (2008)
23. J. Le Rouzic, Ph.D. Thesis, Thèse de l'Université de Franche-Comte, Besançon, 2009
24. W.-J. Chang, *Nanotechnology* **13**, 510 (2002)
25. T.-S. Wu, W.-J. Chang, J.-Ch. Hsu, *Microelectron. Eng.* **71**, 15 (2004)
26. J.A. Turner, J. Wiehn, *Nanotechnology* **12**, 322 (2001)
27. J.A. Walberer, A.J. McHugh, J. Rheol. **45**, 187 (2001)
28. P. Vairac, B. Cretin, Surf. Interface Anal. **27**, 588 (1999)
29. V. Scherer, W. Arnold, in *Micro/Nanotribology and Its Applications*, ed. by B. Bhushan (Kluwer Academic, Dordrecht, 1997)
30. W.C. Oliver, G.M. Pharr, J. Mater. Res. **7**, 1563 (1992)
31. W.C. Oliver, G.M. Pharr, J. Mater. Res. **19**, 3 (2004)
32. C.C. White, M.R. Vanlandingham, P.L. Drzal, N.-K. Chang, S.H. Chang, J. Polym. Sci. B **43**, 1812 (2005)
33. J. Le Rouzic, P. Delobelle, P. Vairac, B. Cretin, Eur. Phys. J. Appl. Phys. **48**, 11201 (2009)
34. J.A. Walberer, A.J. McHugh, J. Rheol. **45**, 187 (2001)
35. A. Mata, A.J. Fleischman, S. Roy, Biomed. Microdev. **7**, 281 (2005)
36. O. Roure, A. Saez, A. Buguin, R. Austin, P. Chavrier, P. Siberzan, B. Ladoux, Proc. Natl. Acad. Sci. **102**, 2390 (2005)

37. F. Schneider, T. Fellner, J. Wilde, U. Wallrabe, J. Micromech. Microeng. **18**, 065008 (2008)
38. A.T. Al-Halhouli, I. Kampen, T. Krah, S. Buttgenbach, J. Microelectr. Eng. **85**, 942 (2008)
39. J.L. Loubet, J.M. Georges, O. Marchesini, J. Tribol. **106**, 43 (1984)
40. M.F. Doerner, W.D. Nix, J. Mat. Res. **1**, 601 (1986)
41. B.J. Briscoe, L. Fiori, E. Pelillo, J. Phys. D Appl. Phys. **31**, 2395 (1998)
42. S. Roche, S. Pavan, J.L. Loubet, P. Barbeau, B. Magny, Prog. Org. Coat. **47**, 37 (2003)
43. J.L. Loubet, W.C. Oliver, B.N. Lucas, J. Mat. Res. **15**, 1195 (2000)
44. R. Arinéro, G. L'evêque, P. Girard, J.Y. Ferrandis, Rev. Sci. Instrum. **78**, 023703 (2007)
45. Y.M. Haddad, *Viscoelasticity of Engineering Materials* (Chapman and Hall, London, 1995)
46. D. Tabor, *The hardness of metals* (Clarendon Press, Oxford, 1951)
47. C. Cunat, Rev. Therm. **35**, 680 (1996)
48. S. Havriliak, S. Negami, J. Polym. Sci. Part C **14**, 99 (1966)
49. K.S. Cole, R.H. Cole, J. Chem. Phys. **9**, 341 (1941)
50. D.W. Davidson, R.H. Cole, J. Chem. Phys. **18**, 1417 (1950)

# Chapter 9

## Ultrasonic Force Microscopies

Oleg Kolosov and Andrew Briggs

**Abstract** Ultrasonic Force Microscopy, or UFM, allows combination of two apparently mutually exclusive requirements for the nanomechanical probe—high stiffness for the efficient indentation and high mechanical compliance that brings force sensitivity. Somewhat inventively, UFM allows to combine these two virtues in the same cantilever by using indentation of the sample at high frequency, when cantilever is very rigid, but detecting the result of this indentation at much lower frequency. That is made possible due to the extreme nonlinearity of the nanoscale tip-surface junction force-distance dependence, that acts as “mechanical diode” detecting ultrasound in AFM. After introducing UFM principles, we discuss features of experimental UFM implementation, and the theory of contrast in this mode, progressing to quantitative measurements of contact stiffness. A variety of UFM applications ranging from semiconductor quantum nanostructures, graphene, very large scale integrated circuits, and reinforced ceramics to polymer composites and biological materials is presented via comprehensive imaging gallery accompanied by the guidance for the optimal UFM measurements of these materials. We also address effects of adhesion and topography on the elasticity imaging and the approaches for reducing artifacts connected with these effects. This is complemented by another extremely useful feature of UFM—ultrasound induced superlubricity that allows damage free imaging of materials ranging from stiff solid state devices and graphene to biological materials. Finally, we proceed to the exploration of time-resolved nanoscale phenomena using nonlinear mixing of multiple vibration frequencies in ultrasonic AFM—Heterodyne Force Microscopy, or HFM, that also include mixing of ultrasonic vibration with other periodic physical excitations, eg. electrical, photothermal, etc. Significant section of the chapter analyzes the ability of UFM and HFM to detect subsurface mechanical

---

O. Kolosov (✉)

Department of Physics, Lancaster University, Lancaster, UK

e-mail: o.kolosov@lancaster.ac.uk

Andrew Briggs

Oxford University, Oxford, UK

inhomogeneities, as well as describes related sample preparation methods on the example of subsurface imaging of nanostructures and iii–v quantum dots.

## 9.1 Introduction

Scanning probe microscopy (SPM) offers spatial resolution approaching and often achieving the length scale of a single atom. SPM offers various contrast mechanisms, making it possible to observe object properties which would otherwise be invisible. While acoustic microscopy provides unique contrast from mechanical properties, particularly local stiffness, as well as from fine discontinuities such as cracks and delaminations [1], the task of improving resolution of acoustic microscopy seems to pose a significant challenge. The resolution of traditional acoustic microscopy (like conventional optical microscopy) is limited by the wavelength used. In order to decrease acoustic wavelength one must increase the ultrasonic frequency, which in turn leads to quadratically increasing attenuation of acoustic waves in the coupling fluid. Cryogenic liquids offer low attenuation but also poor impedance matching to the studied samples [2]. For a while it seemed that achieving spatial resolution significantly below  $1\ \mu\text{m}$  in routine acoustic microscopy would be impractical.

The first scheme to overcome the diffraction limit in acoustic microscopy used a sapphire pin attached to a piezoelectric transducer to detect the ultrasonic vibration of the sample surface [3, 4]. Figure 9.1 contains the original sketch of the concept. It was somewhat like an early car mechanic locating a fault in an engine using a long screwdriver, pressing its sharp end to different places and listening to the vibration of the handle pressed against the ear. The microscope operated at 30 MHz, and was used to detect ultrasonic waves propagating through an aluminium plate. It gave spatial resolution of  $20\ \mu\text{m}$ , which is the diameter of the bottom of the sapphire pin, and is about a tenth the wavelength of the ultrasound. These experiments demonstrated the feasibility of the idea, but it was to be several years before technology would be available for acoustic imaging with nanometer scale resolution.

The invention of scanning tunneling microscopy inaugurated a new era of SPM [5] with atomic force microscope (AFM) [6] that followed up shortly, allowing to image surfaces with nanoscale resolution. It is critical for this chapter that the interaction in AFM is the mechanical force between the tip and the sample, whose variation with separation is highly nonlinear. Scanning force microscopy has been used to image the surface elastic properties of materials, by modulating the tip-surface distance at frequencies at or below the cantilever primary resonance [7–9]. In this way the viscoelastic behaviour of relatively compliant materials such as biomaterials and polymers can be imaged [9, 10]. However for stiffer materials such as semiconductors this method does not provide good contrast. The stiffness of the contact is generally much greater than the stiffness of the cantilever, so that when relative motion occurs it is almost entirely taken up by deflection of the cantilever. The tapping mode which is widely used for imaging in atomic force microscopy to minimise surface in most cases is insensitive to materials properties [11, 12]. Making

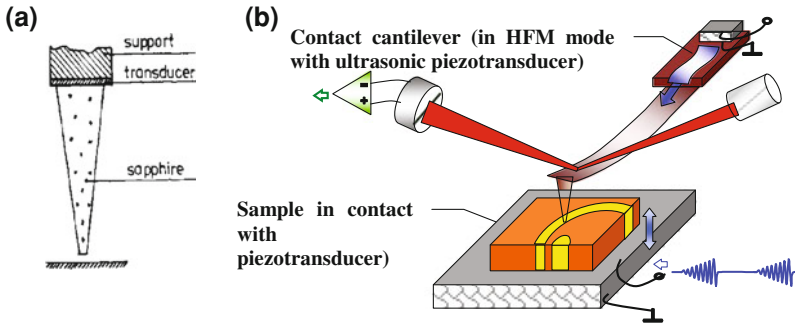


**Fig. 9.1** **a** Sketch of the world’s first ultrasonic scanning pin microscope. The scanning pin microscope operated at 30 MHz, and gave resolution of about 0.2 mm [3]. **b** Schematic of a UFM. Vertical and lateral deflections of this cantilever provide a measure of forces acting between the tip and the studied object. In Ultrasonic Force Microscope, or UFM, high frequency piezotransducers are added to the sample stage and /or to the cantilever base. The detection is the same as in the normal SFM modes [22]

the cantilever stiffer can help, but reduces the deflection sensitivity and can damage the tip and sample [13]. To overcome these limitations, the cantilever can be vibrated at ultrasonic frequencies above its primary resonance [14–17]. The effective stiffness of the cantilever then increases due to inertia. This offers sensitivity to materials with much higher stiffness, such as semiconductors, ceramics, metals, and composites. Techniques using this principle include atomic force acoustic microscopy [17] and scanning local-acceleration microscopy [16]. This chapter describes an approach which depends on the nonlinear nature of the interaction between tip and sample; this has become known as ultrasonic force microscopy (UFM) [14, 19–21]. The combination of acoustic excitation with SPM makes it possible to image and study the elastic and viscoelastic properties of materials with nanoscale spatial resolution [21].

## 9.2 Nanoscale “Mechanical Diode”: Force-Distance Nonlinearity and Detection of Ultrasonic Vibrations

The operation of and AFM is well described elsewhere [6] and is illustrated in Fig. 9.1b. In some implementations, a quadrant detector is used to measure both normal and lateral deflection, thus allowing friction forces to be measured. The data can be processed to create topographical images and lateral force images [7].

In order to understand the UFM detection, consider the non-linearity of the tip-surface interaction and what happens when the indentation depth is modulated. A schematic relationship between force and displacement is plotted in Fig. 9.2a. The force is a highly nonlinear function of tip-sample displacement, and depends on whether approach or retraction is underway. If the tip and the surface are well separated, at the far right on the graph, there is negligible interaction. During the approach,

from right to left on the graph, initially there is an attractive interaction. At closer approach the force becomes repulsive. When reversing the displacement, the tip and the surface adhere until the contact is broken at a certain pull-off distance, which is larger than the displacement at which the contact is established during the approach. The distance scale over which significant variations of force occur is only a fraction of a nanometer. Suppose the tip is in contact with the surface at an initial displacement that gives a normal force  $F_1$ . The displacement to give pull-off is  $h_1$ . An oscillatory displacement of amplitude  $a_0$  is now introduced. If the amplitude of the displacement is small,  $a_0 \ll h_1$ , the average normal force does not change appreciably. As the oscillatory amplitude is increased, the nonlinearity becomes appreciable, until at an oscillatory displacement amplitude  $a_1$  in Fig. 9.2a contact can be lost at one end of the cycle.

The stiffness of the tip-sample interaction is generally much higher than the stiffness of the cantilevers which give adequate sensitivity in SFM. Therefore if the sample surface is vibrated at a low frequency, the tip will tend to follow this motion with little relative displacement between the two. If the vibration is applied at a frequency that is much higher than any natural resonant frequency of the cantilever, then the additional inertia of the cantilever can result in a substantial enhancement of the *relative* displacement, and hence greater indentation amplitude [14]. In the limit that the cantilever motion is negligible, the relative displacement is almost equal to the normal vibration amplitude of the sample surface, giving  $a \approx \Delta h$ . This can be considered as a result of inertial increase in the effective spring constant of the cantilever at high frequency, while at low frequency the cantilever retains its high compliance and hence sensitivity to normal and lateral forces.

## 9.3 How UFM Works: Experimental Setup and Theoretical Analysis

### 9.3.1 UFM Fundamentals

In practical UFM, the feedback signal of the AFM is used to maintain a constant average deflection of the cantilever. This is necessary for obtaining a consistent UFM signal, and it also means that topographical information is available. But it presents a dilemma in separating the unique UFM contrast from the conventional SPM image. If the ultrasound were applied with constant amplitude, then it would introduce a small change to the SPM deflection, but it would be impossible to distinguish between this and topography. Instead, the ultrasonic vibration is modulated in amplitude. The feed-back circuit of the AFM will have an upper limit, or cut-off frequency, above which it does not respond. In a typical commercial AFM this may be of order 1 kHz, though the user may have some control over this. The error signal of the feedback loop is then used as the measure of the UFM response. Although for some analytical purposes one may wish to measure the full response illustrated in Fig. 9.2c,

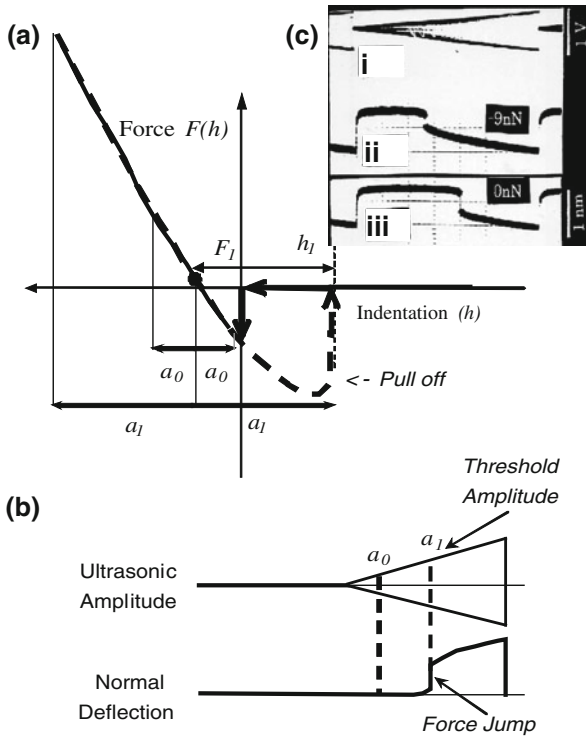


**Fig. 9.2** **a** Tip-surface interaction force versus indentation for approach and retraction (*solid and dashed* respectively). Approach (*solid*) and retraction (*dashed*) differ at the verge of the tip-surface contact; **b** Non-linear detection of ultrasound at increasing ultrasonic vibration amplitude; **c** Oscilloscope traces of ultrasound detection in a standard SFM setup [14, 20]

for most practical imaging a lock-in amplifier can be used to give phase-sensitive and amplitude sensitive detection of the UFM signal. The modulation signal is the reference and the error signal from the feed-back circuit is the input. The output of the lock-in amplifier provides the contrast signal for the UFM image.

### 9.3.2 Selection of UFM Operating Parameters

The lock-in phase and time constant can be selected to give the best contrast. The output can be chosen between two pairs:  $x$  (*in-phase*) and  $y$  (*quadrature*), or amplitude ( $R = \sqrt{x^2 + y^2}$ ) and phase ( $\theta = \arctan(x/y)$ ). Any variation in *threshold amplitude* or *force jump* produces a variation of the shape of the ultrasonically-induced normal deflection, which can be measured by the lock-in amplifier. In choosing the parameters for the ultrasonic excitation, there are three critical choices. First, the maximum applied amplitude must be higher than any *threshold amplitude* to be measured over

the whole area to be imaged. Second, the amplitude modulation frequency must be sufficient to enable several cycles to be averaged at each pixel. Finally, the profile of the amplitude modulation can be chosen from waveforms such as sinusoidal, ramp (saw-tooth), triangular and trapezoidal [14, 20]. Experience shows that the best contrast is generally obtained with a saw-tooth or triangular profile with a blank period of the same length (e.g. see the saw tooth profile in Fig. 9.2b), combined with the amplitude lock-in signal output  $R = \sqrt{x^2 + y^2}$ .

The ultrasonic frequency must be chosen carefully in order to obtain unambiguous UFM data. The frequency should be high enough to enable the inertial term ( $\omega^2 m$ ) to give sufficient enhancement of the elastic stiffness of the cantilever to make it comparable with the tip-sample stiffness or to exceed it. While frequencies of up to 60 MHz or more have been used in some experiments [23] it is more common to choose a frequency in the range 2–10 MHz. The linear response of the cantilever cannot readily be measured at these frequencies, and simulations suggest that it is likely to be negligible [24]. Once the transducer has been selected and mounted, fine tuning of the frequency then becomes pragmatic. The useful bandwidth of a piezoelectric transducer for this purpose is usually within 10% of the central frequency. There may be other resonance frequencies at which a non-linear UFM response can be excited, and many of them are not pure thickness modes. If the piezoelectric transducer frequency is not high enough, cantilever higher harmonics may interfere with the UFM detection. These harmonics are usually damped, but if they are present they can reduce the effective dynamic rigidity of the cantilever, especially if the UFM is operated in vacuum.

A practical procedure for tuning the frequency starts with acquisition of a spectrum of the nonlinear response. With amplitude modulation applied, the ultrasonic vibration frequency is swept over a wide interval centred at the nominal resonance frequency of the piezoelectric transducer. From this spectrum, one finds the frequencies at which a nonlinear response can be obtained. The second step is to analyze the ultrasonically-induced normal deflection for the frequencies at which a nonlinear response has been detected. The practical guidelines for achieving reproducible and reliable UFM data include the ones described in [20]:

1. The amplitude modulation frequency should generally be in the range 0.5–3 kHz. Below 0.5 kHz the feedback usually modifies the ultrasonically-induced normal deflection. Above 3 kHz the characteristic time constants and delays of the cantilever response can become comparable with the amplitude modulation period.
2. The maximum ultrasonic amplitude must be chosen so that the average threshold amplitude occurs at roughly three quarters of the reference period.
3. The lateral deflection signal should also be checked. If the lateral response is unstable, it is quite likely that the normal deflection is influenced, even though it might look stable.
4. In the non-filtered (high frequency included) photodetector output mainly the non-linear component is present. Significant component similar to the excitation waveform can mean either blunt tip or excitation of the higher order cantilever overtones,



5. *Increase* of the set-force *decreases* the UFM signal.
6. Friction force either vanishes or is significantly reduced with the application of ultrasound. (see more details on that effect that we call “ultrasonic induced lubricity” in Sect. 9.4.1).

### 9.3.3 Experimental Setup

The experimental setup can be based on almost any commercial AFM [14, 25]. The main mechanical modification to implement UFM is made to the sample holder to allow application of a normal ultrasonic vibration. The sample holder of the commercial system is usually a thin disc of metal, often fixed to the piezoactuator (scanner) via a magnet positioned inside the actuator. A piezoplate (ultrasonic transducer) can be permanently glued to the sample holder, e.g. with cyanoacrylate or epoxy. An insulating spacer can be inserted between the metallic sample holder and the piezoplate, to isolate the lower electrode of the piezoplate from the SFM unit. A piezoplate has a longitudinal resonance which depends inversely on its thickness (typically 1 mm gives 2 MHz). A diameter from 8 to 20 mm is common (depending on the SFM system). Very soft connecting wires (especially critical if the sample is scanned, as it is in DI Multimode<sup>TM</sup> or DI/Thermal Microscopes CP systems) should be connected with a low melting point solder to avoid depolarization of the piezoplate. The top of the piezoplate can be connected to ground, in order to avoid electrical interaction between the tip and the sample (particularly for studying conductive samples).

For the ultrasonic vibration a programmable waveform generator can be used to generate signals in a required frequency range typically from 1 to 10 MHz. It should have amplitude modulation with various modulation shapes, particularly blanked saw-tooth (Fig. 9.2b) or at least saw-tooth capability. A maximum output voltage of 10 V<sub>pp</sub> (peak-to-peak) is more than sufficient for the average piezoplate (for a typical experiment an amplitude of 1–4 V<sub>pp</sub> is used). The ultrasonically-induced normal deflection can be visualized on the oscilloscope (preferably digital for signal averaging) by using the feedback error signal (provided the ultrasonic deflection is modulated above the feedback circuit frequency cut-off). The oscilloscope and the lock-in amplifier should be synchronised to the modulation frequency.

The sample can be directly bonded to the piezoplate through an acoustic coupler such as salol (phenyl-salicylate), which melts at 42 °C; a grain of crystalline salol can be used to nucleate crystallization of the supercooled liquid. Afterwards the salol can be melted and the sample removed without damage. Epoxy and other glues are more permanent. The sample dimensions and mass must be compatible with the microscope stage and scanner, and the sample, which may be polished, cleaved or cast, must be flat enough to avoid the kind of topographical artifacts to be discussed in Sect. 9.4.1.

## 9.4 Examples of UFM Output

Figure 9.3 shows AFM and UFM images obtained in this way of a longitudinal section of a composite consisting of a silicon carbide fibre (SiC: Young modulus  $E \sim 500$  GPa) in a mullite matrix ( $\text{Al}_2\text{O}_3\text{-SiO}_x$ , Young modulus  $E \sim 150$  GPa). These are relatively stiff materials. The AFM image (a) shows the topography, with a rough trench (3) between the fibre (1) and the matrix (4). The UFM image (b) reveals elasticity, showing that the interface contains a relatively soft layer (3) coating the silicon carbide fibre between the stiffer regions of SiC and mullite. The force modulation image (d) shows little extra information with respect to the corresponding topography in (c).

UFM detection is obtained by measuring the cantilever deflection at low frequency (Fig. 9.2). The ultrasonic vibration applied to the sample is invariably from a longitudinal wave transducer fixed to the bottom, causing normal vibration of the sample surface. As the ultrasonic amplitude is increased, contact is eventually broken at the pull-off point ( $a_1 = \Delta h_1$ ), giving a discontinuity in the time-averaged displacement. We refer to this ultrasonic amplitude as the *threshold amplitude*, and the corresponding inflection in the displacement curve as the *force jump*. A further increase of the ultrasonic amplitude results in a steady increase of the time-averaged force and therefore of the quasi-static normal deflection [20].

The force on the cantilever under normal vibration of amplitude  $a$  from an initial indentation  $h_1$  is found by integrating over a period [14]:

$$F_m(h_1, a) = \frac{1}{T} \int_0^T F(h_1 - a \cos(2\pi ft)) dt, \quad (9.1)$$

where  $F(h)$  is the force dependence on the indentation depth without ultrasonic vibration,  $f_{\text{ult}}$  is the ultrasonic frequency, and the integral is taken over a period  $T_{\text{ult}} = 1/f_{\text{ult}}$ . Because of the nonlinearity of the force function  $F$ , the cantilever will acquire a new equilibrium deflection  $z_{\text{eq}}$  with a corresponding new mean indentation depth  $h_{\text{eq}}$ , so that now

$$F_m(h_{\text{eq}}, a) = k_c z_{\text{eq}}, \quad (9.2)$$

This description is based on the simplified consideration that the cantilever acts as a point mass. A fuller analysis of the cantilever takes into account its distributed mass and multiple vibration modes [24]. This allows a more rigorous description of the mode of operation of the UFM and the contrast in the images, and also provides the theoretical basis for using the cantilever as a waveguide through which vibrations can be introduced [26]. For the applications to be described in this chapter, the key components of the UFM and the mechanical diode principle are:

- (a) The inertial stiffness of the cantilever at the ultrasonic vibration frequency.
- (b) Nonlinear detection of additional forces at low frequency.
- (c) The compliance of the cantilever at the detection frequency.

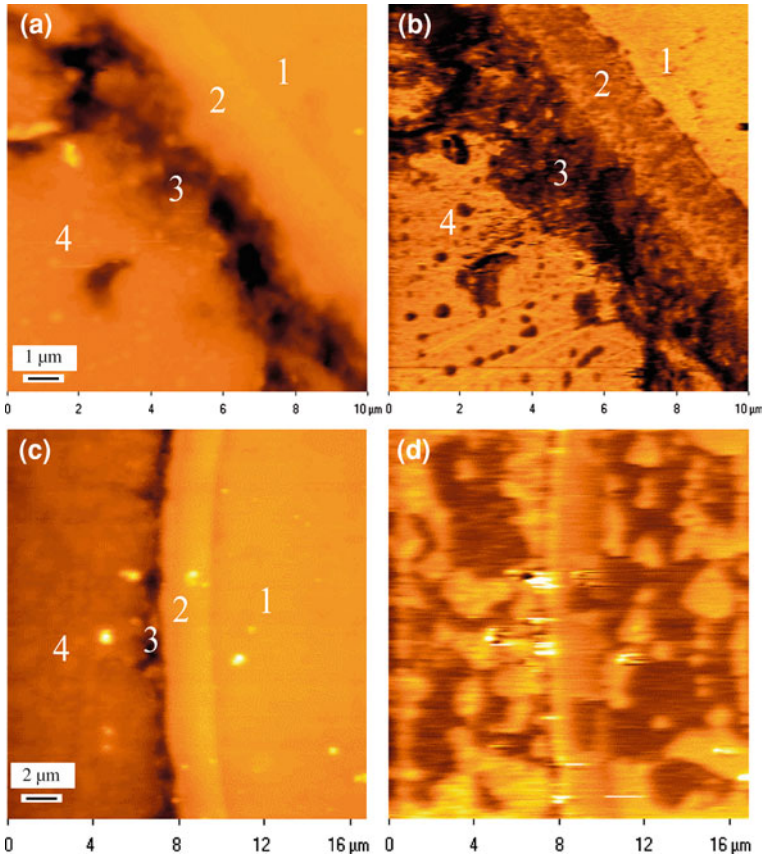


**Fig. 9.3** Topography AFM **a** and elasticity UFM **b** images of SiC ceramic fiber. The topography AFM image shows the interface as a jagged trench dividing a SiC fibre (**1**) and a mullite ( $\text{Al}_2\text{O}_3\text{-SiO}_x$ ) matrix (**4**). The elasticity image reveals the detailed structure of this interface consisting of the relatively soft intermediate concentric carbon rich layer (**2**) and a softer reaction layer (**3**) separating much stiffer regions of SiC and mullite. Image size is  $10 \times 10 \mu\text{m} \times \mu\text{m}$ . The force modulation image (**d**) shows information that is not related to the structure of the fibre interface, highlighting less relevant surface contamination [22]

The UFM signal depends on the local tip-surface force dependence, and therefore on everything that affects this, including elasticity, adhesion, and viscoelastic relaxation, together with the subsurface structure of the object, local topography and discontinuities such as cracks, and the shape of the particular tip. The dominant property is usually the elastic stiffness of the sample in the vicinity of the surface.

As we saw, the AFM cantilever response to the HF sample vibration of amplitude  $a_u$  can be described by the introduction of a new force-versus-separation dependence  $F_m(z)$ , derived from the original  $F(z)$  dependence by averaging over a vibration period  $T$  (Eqs. 9.1, 9.2). Therefore the UFM response can be relatively easy calculated, using

well-known force balance equation in SFM, provided original  $F(z)$  dependence is known.

To calculate the UFM response from Eqs (9.1) and (9.2), the force-versus-separation dependence  $F(z)$  must be known. The choice of a continuum mechanics description of the tip-surface force interaction  $F(z)$  depends on the geometry, the elastic properties, and the adhesion energy. An approximation that lends itself to analytical modelling is the Johnson-Kendall-Roberts (JKR) model [27]. The force  $F$  and the displacement  $z$  may each be expressed in terms of the radius  $a$  of the contact area [28]:

$$F = \frac{4E^*a^3}{3R} + \sqrt{16\pi\gamma E^*a^3}, \quad (9.3)$$

$$z = \frac{a^2}{R} - 2\sqrt{\frac{\pi\gamma a}{E^*}}, \quad (9.4)$$

The adhesion energy is  $\gamma$ , and the mutual plain strain modulus and radius of curvature are:

$$\frac{1}{E^*} = \frac{1 - \nu_t^2}{E_t} + \frac{1 - \nu_s^2}{E_s}, \quad (9.5)$$

$$\frac{1}{R} = \frac{1}{R_t} + \frac{1}{R_s}, \quad (9.6)$$

where  $E$  and  $\nu$  denote Young modulus and Poisson ratio, and subscripts t and s indicate the tip and sample. In the approximation that the material of the tip is much stiffer than the sample and the surface of the sample is flat, the terms  $(1 - \nu_t^2)/E_t$  and  $1/R_s$  may be neglected. Even for perfectly elastic materials, there will be hysteresis if contact is broken in the cycle of vibration; with viscoelastic samples such as polymers there will be additional hysteretic effects [29]. The JKR model is most valid for large radius and adhesion energy and small stiffness; other models are appropriate for different regimes [30]. All the continuum mechanics models give nonlinearity, which may be simply expressed by saying that the instantaneous stiffness is determined by the contact area, and this will be greater when you push than when you pull. Atomistic modelling of nanoscale contacts suggests that the contact area and hence stiffness may be two or more times what is calculated by continuum models, but does not alter the conclusion that the force-displacement relationship is highly nonlinear [31].

The UFM response is calculated for silicon and germanium surfaces in Fig. 9.4a, using the JKR model and average values of the elastic moduli for silicon and germanium [32]. The calculated UFM responses for unstrained Si and Ge (curves 1 and 2) are distinctly different, with the step in the Ge response occurring at a higher amplitude than that of Si. Careful choice of the amplitude would give a smaller UFM signal for Ge, confirming the possibility of directly mapping the elasticity of Si-Ge nanostructures. Figure 9.5 contains images showing such contrast from germanium quantum dots on silicon. The left hand image (a) is conventional AFM topography, with a line scan underneath. The right hand image (b) is UFM, with a corresponding UFM line

scan. Using engineering stiffness parameters, germanium ( $E_{\text{Ge}} = 121 \text{ GPa}$ ) is less stiff than silicon ( $E_{\text{Si}} = 164 \text{ GPa}$ ), and the Ge islands give a lower signal than the surrounding wetting layer, which consists of two or three atomic layers of Ge on the Si substrate. The bright UFM signal around the dots may be due to a topographic effect, which will be discussed further in Sect. 9.4.1 below. At the edge of the dots the contact area between the tip and substrate may be increased, especially if the dot is surrounded by a narrow moat as some are, and this would give rise to increased contact stiffness and hence UFM signal. A model based on statistical thermodynamics has been developed to account for the size and shape distributions of these dots [33]. UFM images have been obtained of individual antimonide particles [34]. The nanoparticles were formed by aggregation and spontaneous rapid crystallization of thermally deposited Sb onto the basal planes of highly oriented pyrolytic graphite (HOPG) and molybdenum disulfide ( $\text{MoS}_2$ ). The UFM contrast was interpreted in terms of variations in local stiffness, which correlated with evidence from transmission electron microscopy of strained regions within the nanocrystals.

The shape of the force versus indentation curve depends on surface adhesive and elastic properties. Variations in these parameters affect the ultrasonically-induced deflection. Conversely, the variations in the shape of the ultrasonically-induced normal deflection contain information on surface adhesive and elastic properties. Figure 9.2 illustrates how the threshold amplitude should depend on the normal force value. If the normal force is set at a higher value  $F_2 > F_1$ , then the threshold amplitude ( $a_2 = h_2$ ) needed to reach the pull-off point should be higher than the threshold amplitude ( $a_1 = h_1$ ) for  $F_1$ . If the threshold amplitude values ( $a_1$  and  $a_2$ ) are measured for two different normal force values ( $F_1$  and  $F_2$ ), the contact stiffness is

$$S_{\text{eff}}(F_{\text{av}}) = \frac{F_2 - F_1}{a_2 - a_1}, \quad (9.7)$$

where:

$$F_{\text{av}} = (F_2 + F_1)/2. \quad (9.8)$$

The beauty of the differential UFM approach is that the absolute value of the contact stiffness of a nanoscale contact at a known force level  $F$  is directly measured in terms of the ultrasonic vibration amplitude and the applied force (independent of the adhesion or other contact parameters). The contact geometry would need to be known in order to determine the elastic stiffness of the sample.

The differential UFM approach is based on three main assumptions:

1. It is possible to identify a threshold amplitude, defined as the amplitude at which the contact breaks, and pull-off occurs, for part of the ultrasonic cycle. It can be identified as the amplitude at which the inflection occurs in the normal deflection signal.
2. The threshold amplitude depends on the applied normal force.
3. The cantilever vibration at the ultrasonic working frequency is negligible. Therefore the difference in threshold amplitude at different values of normal force is equal to the difference in indentation  $\Delta h = h_2 - h_1$

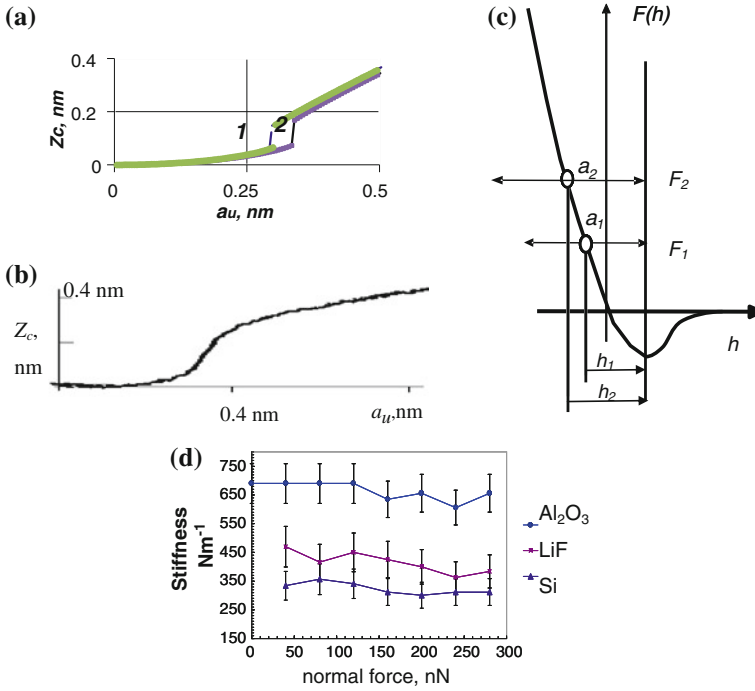


**Fig. 9.4** **a, b** theoretical calculation of the UFM response on Si (1) and Ge (2) surface, using the parameters  $E_{\text{Si}} = 164 \text{ GPa}$ ,  $E_{\text{Ge}} = 121 \text{ GPa}$ , surface energy in an ambient environment  $W = 1 \text{ N m}^{-1}$ , and the manufacturer’s data for tip radius  $R = 10 \text{ nm}$ . **c** Illustration of the differential UFM approach to the measurement of contact stiffness [35]. If one measures the threshold amplitude values ( $a_1$  and  $a_2$ ) for two different normal force values ( $F_1$  and  $F_2$ ), the contact stiffness  $S_{\text{eff}}$  is given by  $S_{\text{eff}} = (F_2 - F_1)/(a_2 - a_1)$  **d** Experimental stiffness measurements obtained using differential UFM for sapphire, silicon (100) and LiF (100) [36]. (Nominal cantilever stiffness was  $k_c = 2.8 \text{ N/m}$ , and radius of curvature  $R = 10 \text{ nm}$ )

The second assumption is based on contact mechanics models in which viscoelastic effects that might influence the instability point (pull-off) and adhesion are negligible or can be allowed for. The third assumption is based on representing the cantilever with a point mass model.

Simulations using a distributed mass model indicate that ultrasonic vibration of the cantilever is relatively small and in many cases less than 0.05 of the UFM normal deflection [24].

Figure 9.4d presents experimental stiffness measurements using differential UFM for three high modulus materials: sapphire, silicon (100) and LiF (100) [36]. The samples were probed with the same silicon tip on a V-shaped cantilever (nominally cantilever stiffness was  $k_c = 2.8 \text{ N/m}$ , and radius of curvature  $R = 10 \text{ nm}$ ). The surface RMS roughness of the surfaces was less than 0.2 nm over a few square micrometers for all three samples. The relative difference between the three sets of data reveals that the elastic properties of these three materials can be distinguished

by differential UFM; the relative independence of the applied force may indicate the fact that the tip had been flattened by extended contact with such hard samples.

### 9.4.1 *Imaging of Elastic Properties with UFM: From Semiconductors to Biopolymers*

UFM is able to give contrast from samples over a wide range of elastic properties, from stiff crystalline materials like semiconductors or ceramics, including composites of hard materials (metals, metal oxides, carbon fibre) and polymers, to soft rubbery inclusions and proteins.

Figure 9.5c,d shows a double GaSb-InAs superlattice with periodicities of 40 and 8 nm. The superlattice was cleaved and immediately mounted on the sample stage. The topographical image shows that the surface is flat (RMS roughness  $<0.2$  nm over  $1 \mu\text{m}^2$  area). Wider layers (arrow i) are barely visible whereas the finer ones (arrow ii) are not visible at all. The UFM contrast is different from the topography, even while the difference in elastic moduli is only of about 6% ( $E_{\text{GaSb}} = 88$  GPa,  $E_{\text{InAs}} = 82$  GPa). UFM detects this difference, with the GaSb layers brighter than the InAs layers. The very fine superlattice (arrow ii) of only 4 nm wide layers is observable in the UFM image (d).

The resolution of scanning probe techniques is full of happy surprises. The original estimates of the resolution of the scanning tunnelling microscope assumed a smooth sphere of radius 100 nm. The actual resolution obtained far surpassed this, because so far from being a smooth sphere the tip is always atomically rough. Though a Darwinian process of natural selection, by the time the user is ready to record a picture the tip has one atom protruding significantly further than the others, giving subnanometer resolution. For UFM, it is not obvious how the lateral resolution might compare with the corresponding AFM. During the ultrasonic vibration the contact size varies from zero to something larger than a conventional AFM working in contact mode at the same normal force. The UFM signal arises from nonlinearity in the force-displacement curve, and this nonlinearity is greatest when the diameter of the contact area is least. Hence it might be expected that the UFM lateral resolution should be at least as good as the AFM lateral resolution, and perhaps even better. This is borne out by the UFM resolution of the finer periodic lattice in Fig. 9.7d.

High density interconnects on semiconductor chips link various parts of the processor with memory and other functions. In the Damascene process, the underlying silicon oxide insulating layer is patterned with open trenches, which are then overfilled with metal. Chemical-mechanical polishing is then used to remove the metal to the level of the top of the insulating layer. The term comes from metallurgical processes associated with pattern-welded swords from Damascus. AFM and UFM images of a Damascene interconnect test structure are shown in Fig. 9.5e. They show trenches  $0.32 \mu\text{m}$  wide. The UFM images Fig. 9.5f display little topographical sensitivity, while UFM contrast is material specific, delineating polymer and Al regions uniformly across the scan area. The image contrast corresponding to Al is

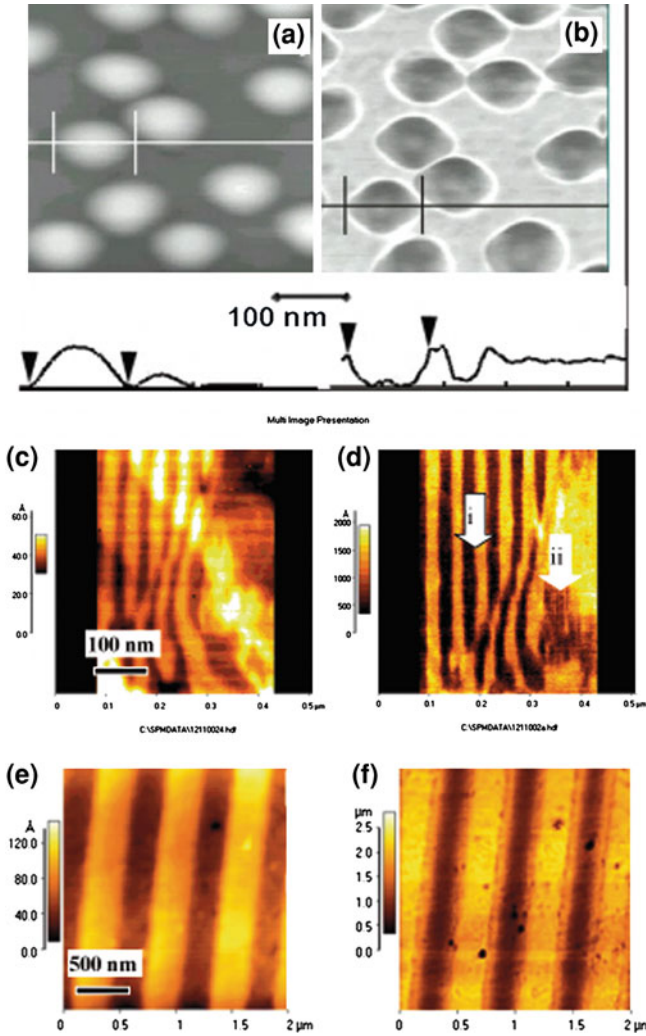


**Fig. 9.5** **a** and **b** are, correspondingly, topographical and UFM images of Ge quantum dots on a Si substrate (image size is  $400 \times 400 \text{ nm}^2$ ); [32, 20]. Topography **c** and UFM **d** images of GaSb-InAs superlattice with periodicity of 40 nm (*arrow i*) and 8 nm (*arrow ii*) respectively. The superlattice was cleaved and immediately mounted on the sample stage. The topographical image shows that the surface is very flat (RMS roughness  $< 0.2 \text{ nm}$  over  $1 \mu\text{m}^2$  area). Wider layers (*arrow i*) are barely visible whereas the finer layers (*arrow ii*) are not visible at all. The very fine superlattice (*arrow ii*) of only 4 nm wide layers is observable in the UFM image **d** [20]. **e** AFM and **f** UFM images in the trench region of an Al/BCB (*aluminium/benzo-cyclo-butene*) damascene test structure. The contrast inverts between topography and elasticity scans. There is interfacial variation of the elasticity between the Al and BCB regions. The interface between hardened and unmodified BCB is denoted by the white arrow **i** [38]



uniform across the trench region, the 10  $\mu\text{m}$  wide lead, and the contact pad. The white areas in the topographic images are polymer (benzo-cyclo-butene, or BCB) spacers with low dielectric constant (low- $k$ ) to increase the speed of data transfer on the chip. The dark areas in the topography image are the aluminium connects. The topography results from the different speed of removal of material during chemical-mechanical polishing process. The UFM contrast arises primarily from the difference between the Al and BCB elastic moduli. The UFM images reveal elastic nonuniformity across the top of the BCB wall. Two distinct regions are apparent. The center portion of the BCB wall displays a lower contact stiffness compared to high-contrast regions near the Al/BCB interfaces that may betoken an increase in the BCB rigidity in the vicinity of the Al/BCB interface [38].

The samples in Fig. 9.6 are of lower stiffness. Figure 9.6a,b shows a composite consisting of injection molded poly(methylmethacrylate) PMMA ( $E_{\text{PMMA}} = 4.5 \text{ GPa}$ ) with spherical PMMA-rubber inclusions ( $E_{\text{rubber}} < 0.1 \text{ GPa}$ ) in order to increase its fracture toughness [39]. The structure of the inclusions is illustrated in the inset. Each inclusion is made of a rubber core and alternate layers of PMMA and rubber of a few nanometer thickness, with an outer layer is of PMMA. In the UFM images the inclusions have a texture which may be due to topographical deformations induced either by the manufacturing process or by the scanning itself. They exhibit a different elastic behaviour from the surroundings. The difference in contrast between inclusions may be due to the depth of a given inclusion relative to the surface or the amount of the outer layer of PMMA remaining around the rubber.

Figure 9.6c, d show images of amylin fibres deposited on mica in water solution and then dehydrated. The proteins have lower stiffness. Mica is a suitable substrate as its cleavage planes are atomically flat and it provides good bonding to the proteins. In conventional contact mode AFM, no clear topographical image of these samples could be obtained, because the scan usually sweeps soft materials away. The application of the ultrasound signal for UFM allowed a topographic image to be obtained through a mechanism to be described as superlubricity in Sect. 9.4.1. The UFM image shows that the fibres of 50–100 nm in size are more compliant than the surrounding area and reveals the internal structure reflecting packing of the fibres.

This gallery of pictures illustrates how UFM can image the elastic properties of a broad range of materials from very stiff engineering ceramics to very soft polymers and biopolymers. The secret lies in the use of high frequencies to give inertial stiffness combined with low frequencies to give sensitive detection. There is an analogy with using a four point probe to measure an electrical device, combining a low impedance current source with a high impedance voltmeter. The next section addresses some of the artifacts which may be present in UFM images, and how to recognise them, take account of them, and if possible avoid them.

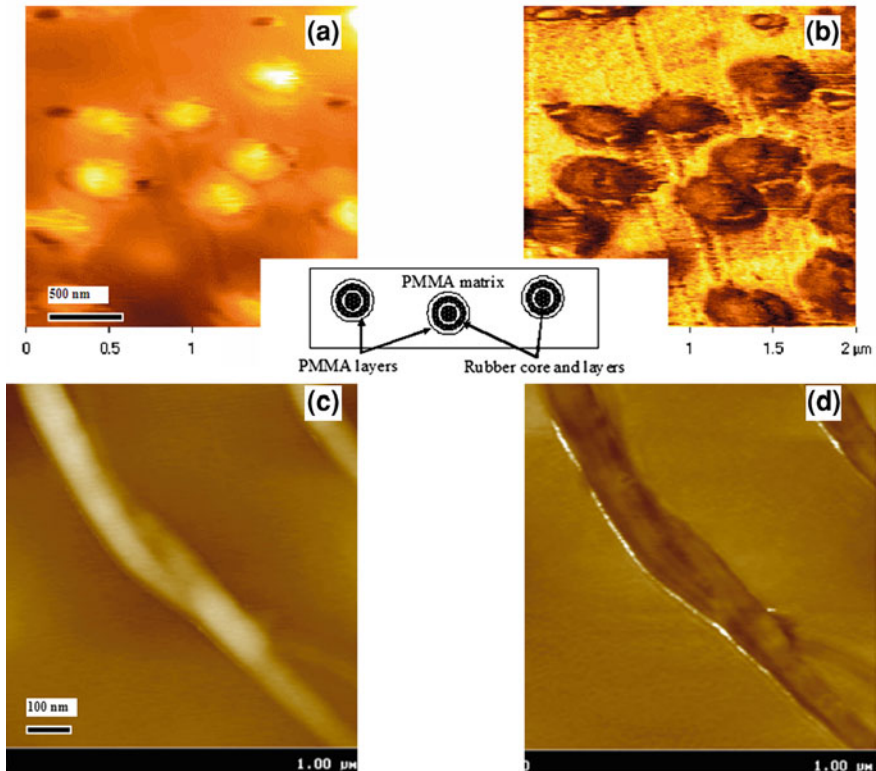


**Fig. 9.6** **a** Topography and **b** UFM images of a compliant sample made of injection molded poly(methylmethacrylate) PMMA ( $E_{\text{PMMA}} = 4.5 \text{ GPa}$ ) with spherical PMMA-rubber inclusions ( $E_{\text{rubber}} < 0.1 \text{ GPa}$ ) [39]. **c** (topography) and **d** (UFM) images of amylin fibres on a freshly cleaved sheet of mica. The amylin fibres are less stiff than mica and UFM reveals internal structure reflecting packing of the fibres [20, 37]

#### 9.4.2 “Director’s Cut” of UFM Imaging: Artifacts (and ways to avoid them) and Unique Benefits of UFM

In addition to the elastic properties which UFM is intended to image, anything else which affects the tip-surface interaction will also affect the UFM contrast. Prominent among these are surface adhesion and abrupt topographical features. The shape of the ultrasonically-induced normal deflection (that can be qualitatively described using *threshold amplitude* and the *force jump*, as in Sect. 9.1) is affected by both elasticity and adhesion. If there is no appreciable variation in adhesive properties, a variation in *threshold amplitude* gives a good indication of variations in stiffness. While this is generally valid for most stiff inorganic samples, some samples, particularly polymeric samples with plasticized surface, highly hydrophilic samples or samples with soft surface layers can deviate from this behaviour.

Figure 9.7 shows an organic thiolipid Langmuir-Blodgett film (LB) deposited on a hydrophilic substrate of a freshly cleaved mica. The elongated molecules of the film have been compressed to such an extent that a fluid phase and a solid phase coexist at the air-water interface. In the fluid phase the molecules are not spatially organized although their mobility is inhibited. In the solid phase, the molecules are mutually aligned and tend to form stars made of six sectors, each of them with a different packing orientation (Gourdon et al. 1997). The topographical image (a) contains edges of such stars with liquid in between. Small dust particles on the surface can nucleate the ordering of the molecules in fluid phase, creating islands between the main regions of solid phase. In the fluid phase the molecules are tilted at random angles to the normal giving a mean height about 2 nm lower than the solid phase. In the UFM image, a higher output from the lock-in amplifier is displayed as a brighter color. This typically results from a lower *threshold amplitude* and therefore a stiffer material. In the UFM image (b) the fluid phase is brighter than the solid one. To avoid the naïve conclusion that the fluid phase is stiffer than the solid one, one should perform a safety check and monitor the actual shape of the ultrasonically-induced normal deflection on each phase.

In Fig. 9.7c the two ultrasonically-induced normal deflection signals on solid and fluid phase are presented. The fluid *threshold amplitude* is higher than the solid *threshold amplitude*, but the *force jump* on reaching the pull-off point is higher for the fluid phase. The output of the lock-in amplifier is determined by the integrated area between the deflection curve and zero (indicated by the broken line; the deflection is here displayed as lower than zero). The fluid response gives a higher lock-in amplifier output because its signal area is bigger. For samples with high adhesion variation, the difference in shape in Fig. 9.7c is a warning sign that the interpretation should take into account how the lock-in amplifier responds to such behaviour. Theoretical modelling may be needed to determine how the *threshold amplitude* is affected by the variation of the adhesive properties. An alternative approach is to use the differential force method for contact stiffness measurement described in Sect. 9.2, to compensate for variations in the adhesive contribution. Whenever adhesion may be significant, the shape of ultrasonically-induced deflection and its consistency throughout the sample serves as a good check against artifacts associated with adhesion, and as a corollary can provide information on variability of adhesion properties of the sample.

Another significant influence on UFM contrast comes from its sensitivity to variations of the tip-surface geometry. The geometry is affected by both stiffness and adhesion, but it can also be affected by topography. For the contrast to arise solely from variations in stiffness, an ideal sample would be one with a surface smooth to the scale of the tip curvature. Since this is not always possible, it is important to understand how topographical variations manifest themselves in order to be able to identify them whenever they occur. Figure 9.7d illustrates some possible situations. An increase of the contact area, due to a negative value of the local curvature or to a high asperity, makes the contact stiffer and therefore a lower *threshold amplitude* is needed to break the contact. This could be wrongly interpreted as the presence of a stiffer material. On the other hand if the contact area diminishes due to a positive value of the local curvature, the stiffness decreases and the *threshold amplitude*

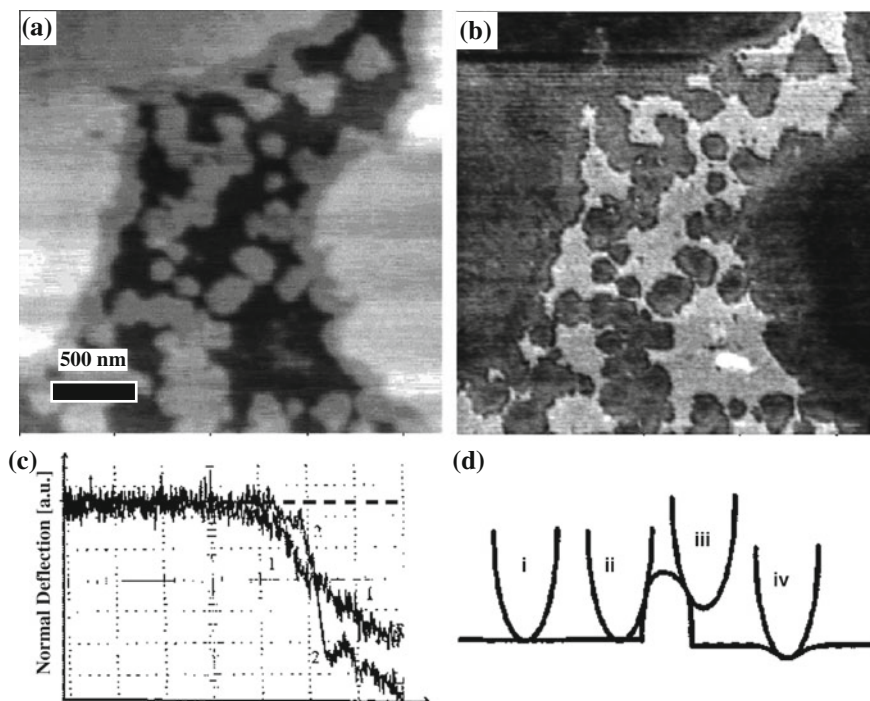


**Fig. 9.7** Adhesive and topographic contributions to the contrast. **a** topographical image of Langmuir-Blodgett thiolipid film having ordered areas of solid-like (*bright*) and disordered liquid-like phase (*dark areas*). **b** UFM image of liquid areas shows inverted (*brighter*) contrast for liquid area linked with the variation of the shape of UFM response **c** due to strong adhesion, rather than change in the threshold amplitude alone. **d** Schematic representation of contact area increase leading to apparent increased local stiffness of the sample [20]

increases. As a result, the region could be incorrectly interpreted as a more compliant material. The bright halo around the Ge quantum dots in Fig. 9.6b is another artifact of an edge effect in areas where the rounded AFM tip simultaneously touches the protruding dot *and* the substrate, increasing the effective tip-surface contact stiffness (and UFM response). Under certain growth conditions a moat forms around Ge/Si dots, and this would introduce a further geometrical effect. It is similar to the case **ii** in the Fig. 9.7d. Such a halo allows one to estimate an upper limit of the size of the contact region and hence the UFM resolution; in this case it was about 5–10 nm.

The UFM approach has several further beneficial features which are explained in the rest of this section. A unique collateral benefit of using ultrasonic vibration in SPM is the reduction of friction between sample and cantilever. Although the ultrasound increases the additional average force acting on a tip, the friction vanishes when the tip-surface contact breaks for part of the vibration cycle [40]. The friction force is reduced even at amplitudes at which no break in contact occurs, and this reduction does not greatly depend on the normal load. Once contact is broken, the lateral force

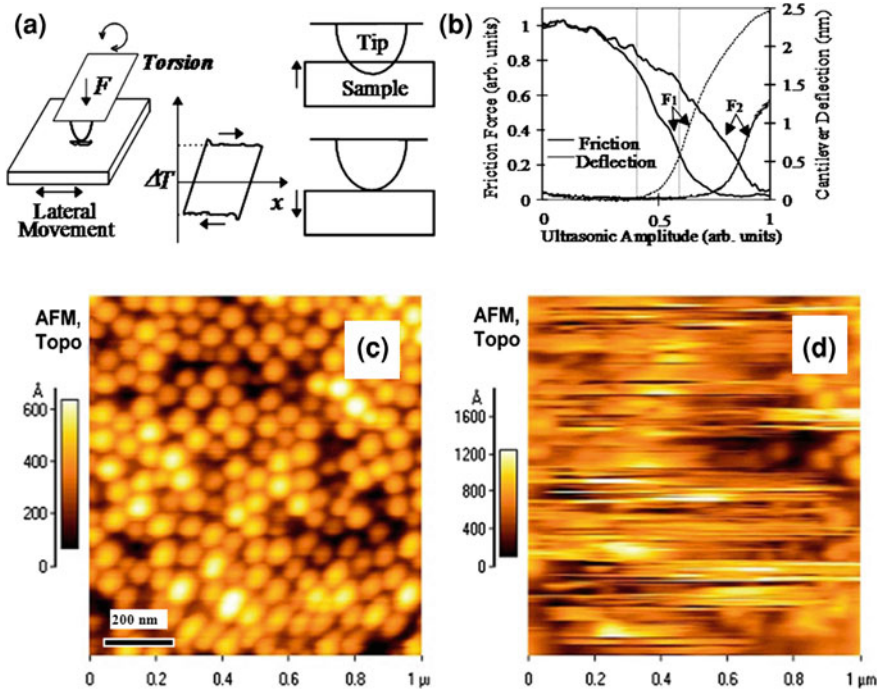


**Fig. 9.8** Ultrasound induced lubricity. **a** Schematic of the experiment **b** measurements of dynamic friction and cantilever deflection dependencies on the ultrasonic amplitude (Si sample,  $\text{Si}_3\text{N}_4$  microlever). The loads applied are  $F_1$ : 0;  $F_2$  2 nN. The sliding speed is  $50 \text{ nm s}^{-1}$  [40]. **c**, **d** Topography images of  $90 \mu\text{m}$  polystyrene spheres imaged in **c** with ultrasound (*UFM mode*) and **d** in standard contact topography mode without application of ultrasound. In **c** the ultrasound was on during the topography image; in **d** it was off. Without ultrasound the sample became damaged, as clearly seen in **d**

vanishes and the cantilever almost instantly slides to a new equilibrium position where there are no lateral forces—and there is therefore no friction! Figure 9.8 illustrates the effect of the ultrasonic amplitude on the friction force and cantilever deflection. Figure 9.8a is a sketch of the experiment, in which the frictional force is measured by the torsional deflection of the cantilever. In Fig. 9.8b, the effect of ultrasound amplitude is shown for a  $\text{Si}_3\text{N}_4$  microlever on a polished Si sample, at two different values of the normal load, 0 and 2 nN. As the ultrasonic amplitude is increased from zero, the friction force decreases at first slowly, commencing at low ultrasonic amplitudes irrespective of the normal load. When the amplitude reaches a threshold value (indicated by the vertical dotted lines) which depends on the normal load, the cantilever deflects due to the strong nonlinearity of the force curve. At amplitudes above this threshold, the friction force rapidly goes to zero. This phenomenon of vanishing friction has applications to micro-electromechanical (MEMS) and nano-electromechanical (NEMS) systems [41].

This reduction in friction has been exploited to image 90 nm polystyrene spheres in Fig. 9.8c, d. The ordered arrangement of the spheres can be seen in topography in the presence of ultrasonic vibration (c). The contact mode AFM image in the absence of ultrasound (d) shows only hazy streaks. Subsequent UFM examination of the same area shows how the arrangement of the latex spheres was disrupted by the AFM scan. Ultrasonic superlubricity allows UFM to be used to study delicate samples in a way similar to the tapping mode AFM.

Another exciting feature of UFM is its ability to operate under liquid. It is beneficial for both exploration of surface modifications in liquids as well as for creating controlled environment and friction reduction. One might think that it would not be possible as ultrasound at UFM frequencies can easily propagate through the liquids and will create overwhelming nonlinear signal on the cantilever surface (due to rectification of the ultrasonic vibration also known as a radiation pressure). Nevertheless as it is reported in [22] and seen in Fig. 9.9 the UFM (and “mechanical diode”) operate very successfully in liquid environment, owing to extreme force-distance nonlinearity of the tiny nanometer size tip-surface contact that is not swamped by the acoustical pressure on the cantilever, despite its vastly greater area. The nonlinearity of the tip-surface contact is crucial for this application, acoustic AFM modes with linear detection of ultrasound (such as atomic force acoustic microscopy, or AFAM [17]) will have not allow such a capability. Some further work in this area [42] have shown that lipid bi-layers can be successfully investigated by operating UFM under liquid, opening the way for investigation biosystems in their natural environment.

Magnetic recording materials have oxide particles embedded in a polymer binder. As a quaint reminder of the past, the bottom two images in Fig. 9.9 are of the materials in a floppy disk. The images were taken underwater, and illustrate that the mechanical diode of the UFM can work well in a liquid. The topography image (a) gives little contrast between the polymer and binder particles, of the kind that is readily apparent in the UFM image (b). In each case the contrast arises from the difference between the oxide and polymer elastic properties.

### ***9.4.3 Subsurface Imaging in UFM: From Delaminations to Subsurface Elasticity Mapping***

Since the acoustic wave responsible for the UFM excitation passes through the sample, it is to be expected that the UFM contrast will be sensitive to subsurface defects or discontinuities. One of the first reports on this was study of such subsurface defects in UFM is given in Fig. 9.10, which shows a polyethylene terephthalate (PET) substrate several micrometers thick coated with a 20 nm  $\text{SiO}_x$  layer, where  $1 \leq x \leq 2$  [20], other publications using related approaches followed more recently [43]. Such nanocomposites are used in packaging, with the glass layer providing a barrier against the permeation of gas through the polymer. There is a crack running across the sample, probably caused by strain deformation, which would provide a path for gas perme-

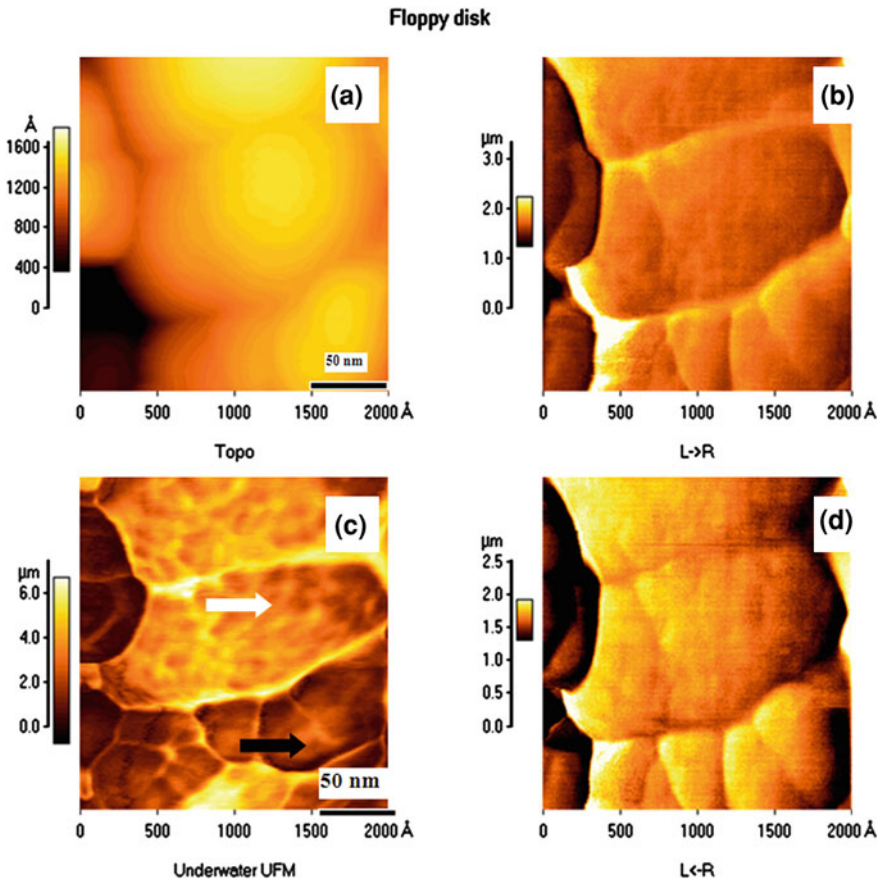


**Fig. 9.9** UFM imaging under liquid. **a** Topography image of a floppy disk and the corresponding UFM image **b**. The fine contrast within the magnetic metal coated oxide particles (*white arrow*) observed in UFM and contrast between different particles (*black arrow*) is due to the different properties of the oxide particles and the polymer binder. No such contrast can be observed in friction images **c** (*left-right*) and **d** (*right-left*). Image was taken underwater that illustrates the ability of UFM (and “mechanical diode”) to operate in liquid environment [22], owing to extreme force-distance nonlinearity of the tiny nanometer size tip-surface contact that is not mask by the acoustical pressure on the many of orders of magnitude bigger area of sub-mm size cantilever

ation. Also visible in the UFM image (b), though not in the topography image (a), are several discs of diameter 3 μm or so. These are interpreted as delaminations between the polymer and the SiO<sub>x</sub> glass. The UFM frequency was 2 MHz. At this frequency the wavelength in PET is about 1 mm. Although the thickness of the delaminations is likely to be much less than this, the impedance mismatch between the air in the void and the materials on either side is so great that transmission across a delamination is negligible. The thickness of the glass layer is much less than the lateral extent of the delaminations, and the UFM signal above the delaminations is small, yielding the

dark patches seen in Fig. 9.10b. In this way UFM can detect subsurface defects that would not be directly revealed by other AFM techniques [44]. A further example is given in c, d) where a single graphene layer was deposited on Si/SiO<sub>2</sub> surface. Some areas of graphene are not adhered to the substrate forming shallow ( $\sim 1$  nm height) “nano-domes” that are barely visible in topography images Fig. 9.10c. Area of graphene “nano-domes” is less stiff than the area of graphene on the substrate resulting in superior contrast in Fig. 9.10d UFM images, therefore revealing areas of poor adhesion. Perhaps most clear so far demonstration of superior ability of UFM to image subsurface features is given in Fig. 9.10e,f [?]. Here a thicker multilayer graphene—graphite flake ( $\sim 50$  nm thickness) on the patterned COC (cyclic olefin co-polymer) substrate is imaged in both the topography and UFM modes. Whereas topography Fig. 9.10e shows perfectly smooth flake, UFM magically allows observation of areas of contact even through 50 nm thick layers in Fig. 9.10f. It should be noted that UFM was used to image few nm in size subsurface defects in layered structure of graphite [19, 45]. These pictures were taken long before the discovery of the remarkable properties of single layers of graphene.

One could wonder what happens if the elastic inhomogeneity is not a strong one like crack or delamination where the ratio of acoustic impedances (or contact stiffness is orders of magnitude different). It was shown that even these nanoscale structures can be observed in UFM, but the requirement is that the surface quality should be close to atomically flat, in order not to mask the subsurface elasticity information. In Fig. 9.11 such true subsurface nanoscale resolution elastic imaging of a semiconductor quantum dot (QD) nanostructure is shown. It is InAs quantum dots in GaAs matrix (the difference in elastic moduli is approximately 20%) under capping layer. The surface topography Fig. 9.11b had some vague indication of underlying structures, whereas UFM images Fig. 9.11b revealed identifiable QD structures.

There is no universal formula for the depth of subsurface objects probed by UFM. If the ultrasonic wavelength is long compared with any relevant sample dimensions, which is usually the case, then a good approach is to consider the equivalent problem in static elasticity. A subsurface delamination, such as the ones shown in Fig. 9.11, will generally give edges in the UFM images whose sharpness is comparable with the depth of the delamination below the surface. If the phase of the cantilever response could be measured, then it would be possible to use depth reconstruction algorithms from optical and acoustic near-field imaging [46].

In order to provide any noteworthy improvement of subsurface sensitivity, such a reconstruction requires non-negligible phase differences  $\Delta\phi \gg 1$  in the HF vibration reaching the point of tip-surface contact where the phase is detected. The phase difference can be estimated as  $\Delta\phi = k\Delta z$ , where  $k$  is the wavevector of acoustic wave and  $\Delta z$  is the characteristic depth of subsurface feature. For the typical frequency of ultrasound in UFM and HFM  $f = 2\text{--}10$  MHz and the speed of sound in semiconductor materials generally in the range of  $c_s = 3\text{--}10 \times 10^3$  m/s,  $k = f/c_s$  is on the order of  $10^{-3}$  m<sup>-1</sup>. For the typical depths of location of nanostructures  $\Delta z$  of 10–100 nm ( $1\text{--}10 \times 10^{-7}$  m),  $\Delta\phi$  is estimated as  $3 \times 10^{-4}$ , or less than  $0.1^\circ$ . Such a small phase difference implies that using phase detection as used in HFM [47] and its modifications [43] would not significantly improve the subsurface sensitivity of



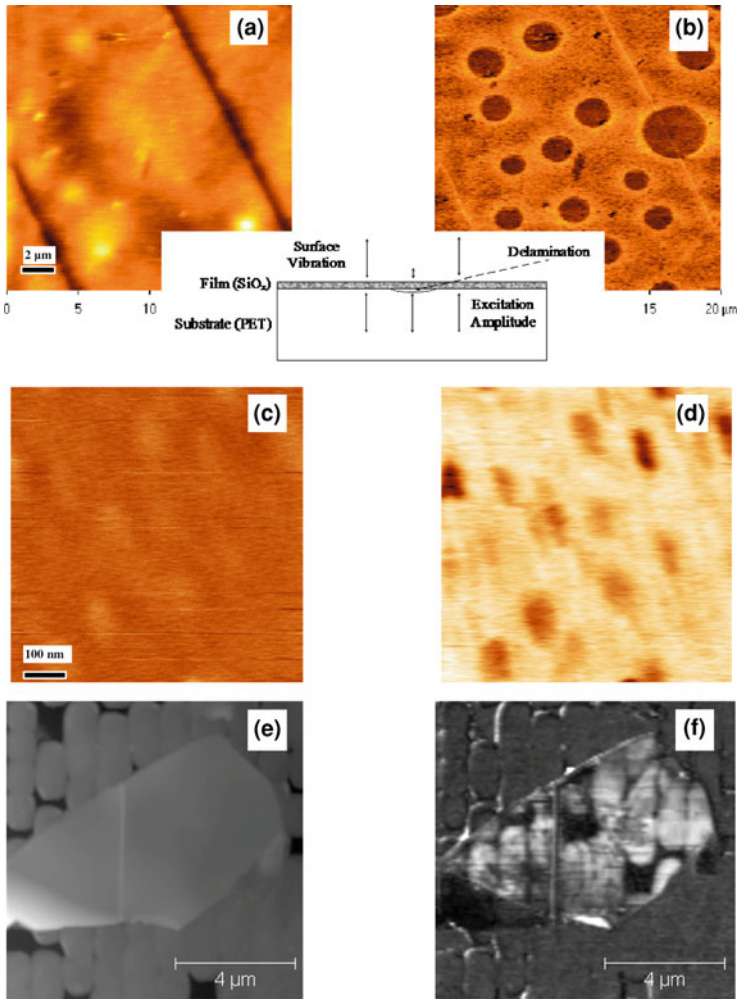


**Fig. 9.10** Subsurface imaging of delaminations in UFM. **a, b** Original report on UFM observation of subsurface delaminations—the sample of a PET substrate coated with a 20 nm SiOx layer. “Bubbles” visible in the UFM image **b** are delaminations at the oxide-polymer interface—schematically illustrated by **c** are only barely visible in the topography image **a** [20]. **c, d** Topography and UFM image of single graphene layer on Si/SiO<sub>2</sub> surface. Some areas of graphene are not adhered to the substrate forming shallow (~1 nm height) “nano-domes” that are barely visible in topography images **c** [?]. Area of graphene “nano-domes” is less stiff then the area of graphene on the substrate resulting in superior contrast in **d**—UFM images revealing areas of poor adhesion. **e, f** Thicker multilayer graphene—graphite flake (~50 nm thickness) on the patterned COC (*cyclic olefin co-polymer*) substrate. Whereas topography **e** shows perfectly smooth flake, UFM allows to observe areas of contact even through 50 nm thick layers (image courtesy Dinelli, Pinque and Kolosov, [? ])

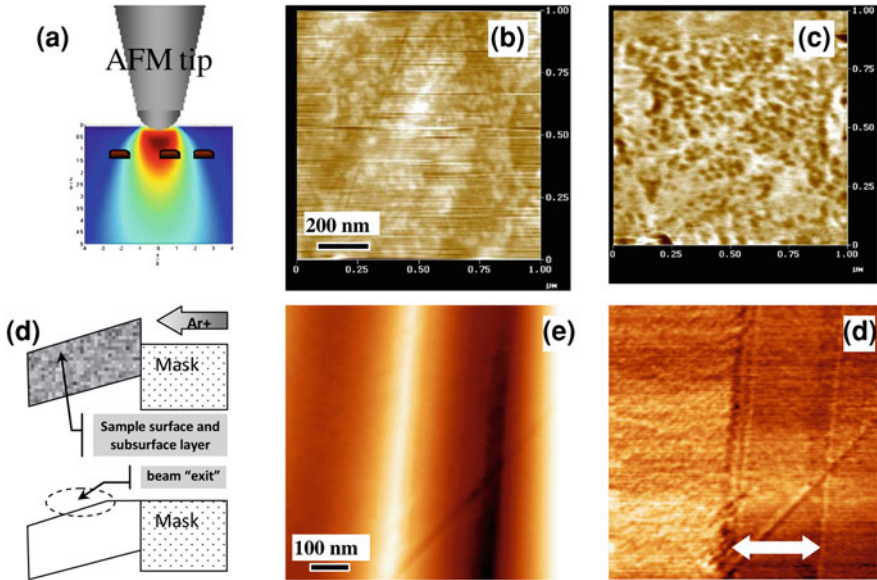


**Fig. 9.11** Subsurface imaging of elastic properties with UFM. **a** Oscillating elastic field in UFM penetrates surface at depth on the order of several diameters of contact area. **b** Topography and UFM **c** image of InAs quantum dots (QD) on GaAs substrate partly covered with GaAs capping layer. UFM images reveal features similar to topography but provide much better discrimination and localisation of QD structures (eg. in fuzzy areas in topography indicated by *arrows*) [?]. **d–f** Material sensitive UFM imaging of ion cross-sectional polishing (BEXP). **d** Schematic illustration of the principle of beam exit Ar ion cross-section polishing (BEXP). A surface layer of interest is exposed to the beam exit only and therefore is not perturbed by the proximity of the shadow mask. **e** Topography and **f** UFM image of an InSb superlattice layers in GaAs matrix (arrow indicates *superlattice region*). The first two superlattice layers positioned at 5 nm and 25 nm depth are clearly observable (average concentration of InSb in the superlattice zone was around 1 weight %)

UFM in nanostructures. That, though, should be clearly differentiated from the high sensitivity of HFM to the near-surface dynamic phenomena (eg. viscolastic relaxation, vibrational modes, etc.) on the time scale of 1–100 ns, that can be accessed with the spatial resolution determined by the contact area as described in Sect. 9.4.4.

For most purposes, less abrupt variations in properties can be considered by turning the problem the other way round. A Hertzian contact gives a field with a characteristic depth comparable with the diameter of the contact area [28]. Since the resolution of the UFM is determined by the size of the contact area, the depth over which the UFM is most sensitive to small variations in elastic properties is comparable with its resolution. Bigger variations in elastic properties can give contrast from greater depths; by Saint Venant's principle the resolution will not then depend much on the geometry of the tip-sample contact.

In cases when the depth penetration of the elastic field is not sufficient, recently a novel imaging principle involving UFM nanoscale resolution material sensitivity

was developed [48]. A novel method uses Ar ion beam cross-section polishing via beam exiting the sample (BEXP). In this approach, a sample is tilted at a small angle with respect to the polishing beam that enters from underneath the surface of interest and exits at a glancing angle similar to the edge mechanical polishing [49]. This creates an almost perfect nanometer scale flat cross-section with close to open angle prismatic shape of polished and pristine sample surfaces ideal for SPM imaging. Using the new method and material sensitive UFM it was possible to map internal structure of an InSb/InAs QD's superlattice of 18 nm layer periodicity with the depth resolution on the order of 5 nm (Fig. 9.11d–f). BEXP with UFM imaging is also applicable to revealing details of interfaces in VLSI low-k dielectric interconnects similar to ones in Fig. 9.5e–f, porous Si and details of mechanical nanostructure of abalone shells.

#### ***9.4.4 “Mechanical Diode” Versus “Mechanical Heterodyne”: Sensing Nanosecond Time Scale Dynamic Phenomena in Nanostructures***

The difference in the stiffness of the AFM cantilever at low and high frequencies, which is so crucial to the operation of the UFM, can be described more rigorously in terms of a dispersive mechanical waveguide. The high compliance at low frequencies corresponds to low impedance, and the high stiffness at high frequencies corresponds to high impedance. A flexural wave can be launched down the cantilever, leading to a modulation of tip-surface distance rather similar to the effect of the ultrasonic wave propagating through the sample in the simple UFM [23]. The mechanical diode effect can still be used to detect the tip-surface interaction. This technique is known as a waveguide UFM (W-UFM). It gives contrast similar to the simple UFM, with the difference that the sample does not need to be able support ultrasonic wave propagation, and in a sample with strong bulk heterogeneities the contrast will be dominated by the properties within the Hertzian contact zone.

If a vibration is also applied through the sample, it is possible to perform heterodyne detection. Ultrasonic vibration is applied simultaneously to the cantilever (at frequency  $\omega_c$ ) and sample (at frequency  $\omega_s$ ). The AFM tip detects the oscillating force at the difference frequency  $\omega_c - \omega_s$ , very much like a heterodyne radio receiver. This technique is known as heterodyne force microscopy (HFM) [50]. Once again, the tip-surface force nonlinearity plays critical role. The low frequency beating oscillation carries information on the phase of the original high frequency oscillations.

Generally, there could be several ways of how two vibration frequencies can be applied to the tip-surface junction. The first uses two surface acoustic waves (SAWs) propagating in opposite directions along the sample surface with the tip sensing the vertical component of resulting vibration [51]. The second uses the vertical vibration of the tip as in HFM and the sample [52]. In an interesting modification pioneered by Cuberes [53] ultrasonic vibration is applied simultaneously with the AFM tapping

mode. This has a distinctive feature of two frequencies being very different, often with ratio of several times. Another method uses SAW and is very sensitive to the in-plane delays of the SAW wave propagation, as we will see below, it is HFM that provides the ability to sense relaxation and time dependent phenomena of the tip-surface elastic response.

In order to evaluate phase sensitivity and operation of HFM, we consider a simple model of the tip-surface force nonlinearity

$$F(z) = k_s(z_t - z_s) + \chi_s(z_t - z_s)^2, \quad (9.9)$$

where  $z_t$  and  $z_s$  are the instantaneous displacements of the tip and the sample, and  $k_s$   $\chi_s$  are coefficients describing the linear and quadratic force-displacement response. Any time dependent phenomena on the time scale  $\tau$ , such as viscoelastic relaxation or resonance, can be represented by a phase delay of the sample vibration  $\phi = \omega_s \tau$ , with

$$z_s = a_u \cos(\omega_s t + \omega_s \tau). \quad (9.10)$$

Preserving only the low frequency terms in the AFM cantilever response (since the high frequency terms will be filtered out by the mechanical response, and possibly also the electronic circuitry), the additional force due to the vibration of the tip and the surface is

$$F = \chi_s \{a_t^2/2 - a_t a_s \cos[(\omega_t - \omega_s)t - \omega_s \tau] + a_s^2/2\}, \quad (9.11)$$

where  $a$  and  $\omega$  are the amplitude and angular frequency of displacement, and the subscripts t and s refer to the cantilever and the sample. The first term in parentheses represent the nonlinear detection of cantilever vibration or W-UFM [47], the last term describes the nonlinear detection of the sample vibration UFM and the middle term describes the mixing (HFM). An experimental demonstration of such mixing is presented in Fig. 9.12. The HFM mechanically mixed signal has good signal-to-noise ratio and closely follows the reference signal from electronic mixing of the electrical signals driving the sample and cantilever piezoelectric transducers. Even a short relaxation time  $\tau$  will cause a significant phase shift  $\omega\tau$  in the resulting non-linear LF cantilever response. For example, if the difference frequency is a few kilohertz, and the phase of the cantilever vibration is measured with a precision of  $1^\circ$ , a relaxation time of 300 ps can be detected by HFM.

Amplitude HFM images (Fig. 9.12c) generally provide contrast similar to UFM images showing the equivalence of what is learnt from their closely related cousin. The phase HFM image (Fig. 9.12d) shows contrast that comes from differences in the response of the tip-surface interaction of the sub- $\mu$ s time scale. HFM can also be used to investigate directly the nature of the mechanical properties of biological composite materials.

HFM can also be performed using a combination of modulated optical excitation with ultrasonic excitation for optical HFM (OHFM). Figure 9.13a shows an experimental setup, which may be based on a commercial AFM. A transparent silicon

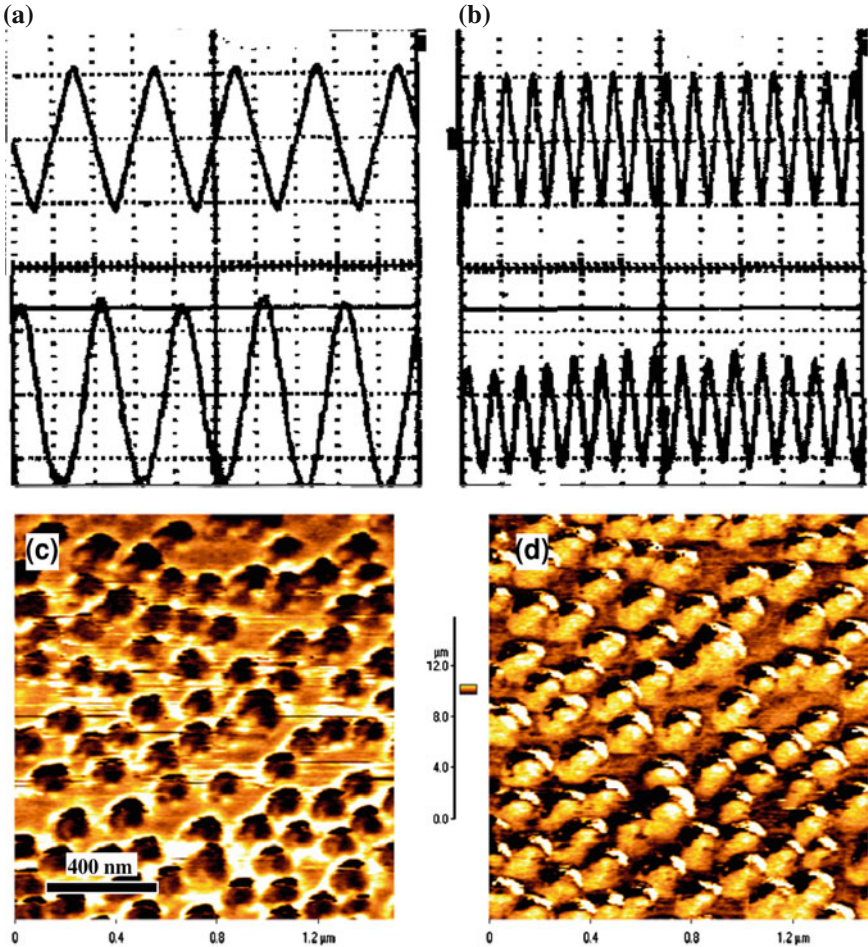


**Fig. 9.12** a, b Heterodyne mixing of two ultrasonic vibrations of sample and the cantilever at excitation frequencies around 9 MHz and difference frequencies of a 5 kHz and b 15 kHz. HFM “mechanically” mixed signal is of good signal-to-noise ratio and closely follows oscillations of reference signal that uses conventional high frequency mixer [50]. c Amplitude Heterodyne Force Microscopy (HFM) image of Ge quantum dots similar to ones in Fig. 9.5a, b reveals lower elastic moduli of Ge QD’s. Phase HFM image d reveals changes in the temporal response of the QD’s linked potentially with some adhesion differences in the QD’s and underlying substrate (*full delay scale* 10 ns)

nitride tip is vibrated while the sample is irradiated from above by light chopped at a slightly different frequency. The sample undergoes periodic temperature variations of a few degrees, causing the surface to vibrate with an amplitude of a few picometers. Because of the nonlinearity of the tip-sample force curve, a vibration of the contacting tip is induced at the difference frequency. This frequency is chosen to be lower than the fundamental cantilever resonance but higher than the response

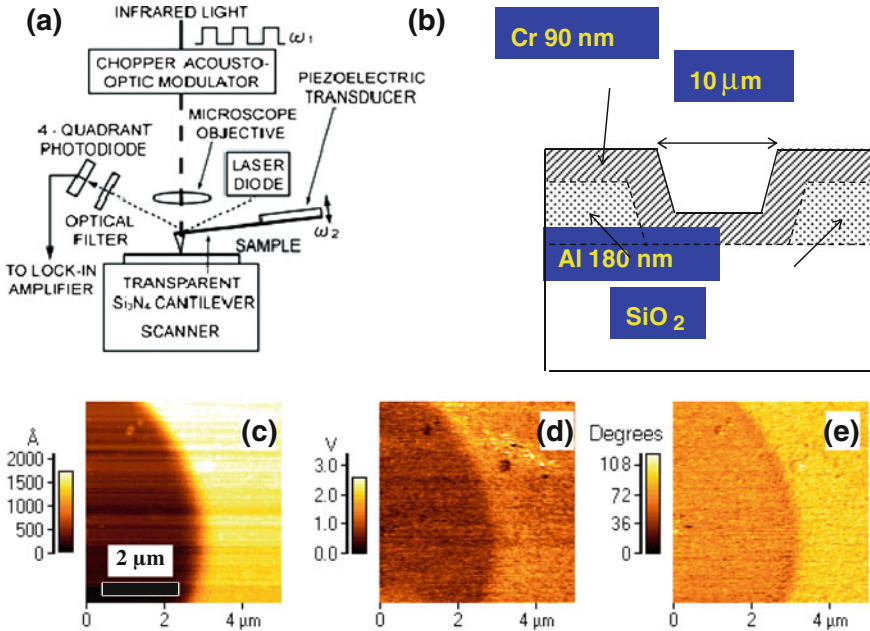


**Fig. 9.13** Optical heterodyne force microscopy (OHFM)—**a** principle and experimental setup. The transparent silicon nitride tip was vibrated in contact with the sample at a frequency  $f_2 = 4.190$  kHz while the sample is irradiated from above by light chopped at a slightly different frequency  $f_1 = 4.193$  kHz, focused through the tip to a spot  $\sim 2 \mu\text{m}$  in diameter with incident power  $P = 0.5$  mW and wavelength 830 nm. The sample undergoes periodic temperature variations  $\sim 3$  K, causing the surface to vibrate at  $f_1$  with an amplitude  $\sim 10$  pm. Through the nonlinearity of the tip-sample force-displacement curve, a vibration of the contacting tip is induced at the difference frequency  $f_1 - f_2 = 3$  kHz. The cantilever resonance frequency is 38 kHz. **c** topography, **d** amplitude and **e** phase OHFM images for a chromium coated region of Al on  $\text{SiO}_2$  structure. Al on  $\text{SiO}_2$  layer and  $\text{SiO}_2$  only areas are clearly visible under a Cr layer of thickness 90 nm with resolution on the order of 150 nm [54]

frequency of the AFM feedback loop. The cantilever deflection is measured in the standard way, generally through the deflection of an optical beam reflected from the cantilever. The amplitude and phase of the heterodyne signal are used to form the OHFM image through lock-in detection of the cantilever deflection. Separating the individual contributions to the signal can be difficult, but the technique can be illustrated by the thermal contrast from a sample with a flat surface covered with a homogeneous layer. Figure 9.13d–e shows correspondingly OHFM amplitude and phase images for a system illustrated in 9.13b where the thermally inhomogeneous nanostructure of Al and  $\text{SiO}_2$  substrate is overcoated with Cr layer of 90 nm thickness. Both phase as well as amplitude of OHFM shows clear discrimination between these materials.

## 9.5 In Lieu of Conclusion: Ultrasound in SPM—Expanding the Alliance

The high resolution acoustic microscope was the brainchild of Cal Quate. He was also one of the inventors of the AFM. One of the first attempts to combine HF acoustics and AFM also came from Quate's lab [13], which later stimulated more practical realization in UFM [14]. The principle of HFM highlights the future potential of expanding UFM family of methods. We have shown here that it works well for the mixing of two mechanical vibrations and for optically stimulated thermal expansion. And, more generally, any SPM is by definition uses the steep dependence of the output signal on distance that is always nonlinear. This nonlinearity can be generalized so that any combination of excitation signals, and mechanical displacement of the tip at the adjacent frequency, will result in the frequency mixing and easy detection of SPM response at low frequency [56]. That will provide any SPM with both nanosecond or better time resolution and nanometer spatial resolution [50] that we hope will become a reality soon.

Many emerging and established approaches in SPM including these higher harmonics modes of cantilevers, video rate AFM's, high frequency tapping etc. are using tip-surface interaction at increasing ultrasonic frequencies. The authors of this chapter firmly believe that this is a natural part of the development of both acoustic microscopy and SPM that will allow more thorough investigation of intricate properties of novel materials, devices and physical phenomena with nanoscale spatial resolution and nanosecond and picosecond time scale sensitivity.

**Acknowledgments** Authors would like to thank all those who have collaborated with us in the development of UFM and related techniques, in particular Franco Dinelli, Kazushi Yamanaka, Teresa Cuberes, Bryan Huey, Oliver Wright, Walter Arnold, Nancy Burnham, Martin Castell, Gerard Germaud, Andrew Kulik, Tony Krier, Manus Hayne, Alex Robson, Mohammed Henini, and Hubert Pollock and OVK would like to thank his wife Tatiana and daughter Ksenia for tremendous and much needed support while preparing this manuscript. Part of material used in this chapter is based on the material from Acoustic Microscopy, 2nd edition by G.A.D. Briggs and O. V. Kolosov (2010), reproduced by © permission of Oxford University Press.

## References

1. A. Briggs, *Acoustic Microscopy* (Oxford University Press, Oxford, 1992)
2. J. Foster, C.F. Quate, Acoustic microscopy in Superfluid-helium. *Phys. Today* **37**, S4–S (1984)
3. J.K. Zieniuk, A. Latuszek, Ultrasonic pin scanning microscope: a new approach to ultrasonic microscopy. *IEEE Ultrason. Symp.* 1037–1039 (1986)
4. Zieniuk J K and Latuszek A 1987 Ultrasonic pin scanning microscope: A new approach to ultrasonic microscopy. *Ieee Transactions on Ultrasonics Ferroelectrics and Frequency Control* 34 414-.
5. G. Binnig, H. Rohrer, C. Gerber, E. Weibel, Tunneling through a controllable vacuum gap. *Appl. Phys. Lett.* **40**, 178–80 (1982)
6. G. Binnig, C.F. Quate, C. Gerber, Atomid force microscope. *Phys. Rev. Lett.* **56**, 930–3 (1986)

7. Y. Martin, C.C. Williams, H.K. Wickramasinghe, Atomic force microscope force mapping and profiling on a sub 100-Å scale. *J. Appl. Phys.* **61**, 4723–9 (1987)
8. A.L. Weisenhorn, P. Maivald, H.J. Butt, P.K. Hansma, Measuring adhesion attraction, and repulsion between surfaces in liquids with an atomic-force microscope. *Phys. Rev. B* **45**, 11226–11232 (1992)
9. T. Miyatani, M. Horii, A. Rosa, M. Fujihira, O. Marti, Mapping of electrical double-layer force between tip and sample surfaces in water with pulsed-force-mode atomic force microscopy. *Appl. Phys. Lett.* **71**, 2632–2634 (1997)
10. P. Gunther, U. Fischer, K. Dransfeld, Scanning near-field acoustic microscopy. *Appl. Phys. B-Photophysics Laser Chem.* **48**, 89–92 (1989)
11. O.P. Behrend, F. Oulevey, D. Gourdon, E. Dupas, A.J. Kulik, G. Gremaud, N.A. Burnham, Intermittent contact: tapping or hammering? *Appl. Phys. Mater. Sci. Process.* **66**, S219–S21 (1998)
12. N.A. Burnham, O.P. Behrend, F. Oulevey, G. Gremaud, P.J. Gallo, D. Gourdon, E. Dupas, A.J. Kulik, H.M. Pollock, G.A.D. Briggs, How does a tip tap? *Nanotechnology* **8**, 67–75 (1997)
13. C.F. Quate, B.T. Khuri-Yakub, S. Akamine, B.B. Hadimioglu, Near field acoustic ultrasonic microscope system and method US Patent 5, 319, 977, 1994
14. O. Kolosov, K. Yamanaka, Nonlinear detection of ultrasonic vibrations in an atomic-force microscope. *Japanese J. Appl. Phys. Part 2 Lett.* **32**, L1095–L1098 (1993)
15. W. Rohrbeck, E. Chilla, H.J. Frohlich, J. Riedel, Detection of surface acoustic-waves by scanning tunneling microscopy. *Appl. Phys. Mater. Sci. Process.* **52**, 344–347 (1991)
16. N.A. Burnham, A.J. Kulik, G. Gremaud, P.J. Gallo, F. Oulevey, Scanning local-acceleration microscopy. *J. Vac. Sci. Technol. B* **14**, 794–799 (1996)
17. U. Rabe, W. Arnold, Acoustic microscopy by atomic-force microscopy. *Appl. Phys. Lett.* **64**, 1493–1495 (1994)
18. U. Rabe, W. Arnold, Acoustic microscopy by atomic force microscopy. *Appl. Phys. Lett.* **64**, 1493–1495 (1994)
19. K. Yamanaka, H. Ogiso, O. Kolosov, Ultrasonic force microscopy for nanometer resolution subsurface imaging. *Appl. Phys. Lett.* **64**, 178–180 (1994)
20. F. Dinelli, M.R. Castell, D.A. Ritchie, N.J. Mason, G.A.D. Briggs, O.V. Kolosov, Mapping surface elastic properties of stiff and compliant materials on the nanoscale using ultrasonic force microscopy. *Philos. Mag. Phys. Condens. Matter Structure Defects Mech. Prop.* **80**, 2299–323 (2000)
21. B.D. Huey, AFM and acoustics: fast, quantitative nanomechanical mapping. *Ann. Rev. Mater. Res.* **37**, 351–385 (2007)
22. O. Kolosov, UFM shakes out the details at the nanoscopic scale. *Mater. World* **6**, 753–754 (1998)
23. K. Inagaki, O.V. Kolosov, G.A.D. Briggs, O.B. Wright, Waveguide ultrasonic force microscopy at 60 MHz. *Appl. Phys. Lett.* **76**, 1836–1838 (2000)
24. S. Hirsekorn, U. Rabe, W. Arnold, Theoretical description of the transfer of vibrations from a sample to the cantilever of an atomic force microscope. *Nanotechnology* **8**, 57–66 (1997)
25. F. Dinelli, H.E. Assender, N. Takeda, G.A.D. Briggs, O.V. Kolosov, Elastic mapping of heterogeneous nanostructures with ultrasonic force microscopy (UFM). *Surf. Interface Anal.* **27**, 562–567 (1999)
26. K.K. Inagaki, O.V. Briggs, G.A.D. Muto, S. Horisaki, Y. Wright, Ultrasonic force microscopy in waveguide mode up to 100 MHz. *IEEE Ultrason. Symp. Proc.* **1**, 2, 1255–1259 (1998)
27. K.L. Johnson, K. Kendall, A.D. Roberts, Surface energy and contact of elastic solids. *Proc. Roy. Soc. London Ser. Math. Phys. Sci.* **324**, 301–313 (1971)
28. K.L. Johnson, *Contact Mechanics* (Cambridge University Press, Cambridge, 1985)
29. J.A. Greenwood, K.L. Johnson, Oscillatory loading of a viscoelastic adhesive contact. *J. Colloid Interface Sci.* **296**, 284–291 (2006)
30. K.L. Johnson, J.A. Greenwood, An adhesion map for the contact of elastic spheres. *J. Colloid Interface Sci.* **192**, 326–333 (1997)



31. B.Q. Luan, M.O. Robbins, The breakdown of continuum models for mechanical contacts. *Nature* **435**, 929–932 (2005)
32. O.V. Kolosov, M.R. Castell, C.D. Marsh, G.A.D. Briggs, T.I. Kamins, R.S. Williams, Imaging the elastic nanostructure of Ge islands by ultrasonic force microscopy. *Phys. Rev. Lett.* **81**, 1046–1049 (1998)
33. R.E. Rudd, G.A.D. Briggs, A.P. Sutton, G. Medeiros-Ribeiro, R.S. Williams, Equilibrium distributions and the nanostructure diagram for epitaxial quantum dots. *J. Computational Theor. Nanosci.* **4**, 335–347 (2007)
34. M.T. Cuberes, B. Stegeman, B. Kaiser, K. Rademann, Ultrasonic force microscopy on strained antimony nanoparticles. *Ultramicroscopy* **107**, 1053–1060 (2007)
35. O.V. Kolosov, H. Ogiso, K. Yamanaka, Ultrasonic Force Microscopy a New Technique for a Nondestructive Investigation on Nanometer Scale Viscoelastic Properties. In: *Proceedings of the 3rd Japan International SAMPE Symposium (Nondestructive Evaluation)*, (Tokyo, Japan, 1993) pp. 2196–2201
36. F. Dinelli, S.K. Biswas, G.A.D. Briggs, O.V. Kolosov, Measurements of stiff-material compliance on the nanoscale using ultrasonic force microscopy. *Phys. Rev. B* **61**, 13995–14006 (2000)
37. Nanoscale SPM Characterisation of Nacre Argonite Plates and Synthetic Human Amyloid Fibres, I. Grishin, C. Tinker, D. Allsop, A. Robson, O.V. Kolosov, In: *Proceedings of Techconnectworld-2012, Nanotech-2012*, (Santa Clara, USA, 2012)
38. R.E. Geer, O.V. Kolosov, G.A.D. Briggs, G.S. Shekhawat, Nanometer-scale mechanical imaging of aluminum damascene interconnect structures in a low-dielectric-constant polymer. *J. Appl. Phys.* **91**, 4549–4555 (2002)
39. K. Porfyrakis, O.V. Kolosov, H.E. Assender, AFM and UFM surface characterization of rubber-toughened poly(methyl methacrylate) samples. *J. Appl. Polym. Sci.* **82**, 2790–2798 (2001)
40. F. Dinelli, S.K. Biswas, G.A.D. Briggs, O.V. Kolosov, Ultrasound induced lubricity in microscopic contact. *Appl. Phys. Lett.* **71**, 1177–1179 (1997)
41. V. Sherer, W. Arnold, B. Bhushan, Tribology Issues and Opportunities in MEMS. in *Proceedings of the NSF/AFOSR/ASME Workshop on Tribology Issues and Opportunities in MEMS*, ed. by B. Bhushan (Kluwer, USA, 1998)
42. M.T. Cuberes, in *Proceedings of the 17th International Vacuum Congress/13th International Conference on Surface Science/International Conference on Nanoscience and Technology*, ed. by L.S.O. Johansson et al. (Iop Publishing Ltd, Bristol, 2008)
43. G.S. Shekhawat, V.P. Dravid, Nanoscale imaging of buried structures via scanning near-field ultrasound holography. *Science* **310**, 89–92 (2005)
44. A.P. McGuigan, B.D. Huey, G.A.D. Briggs, O.V. Kolosov, Y. Tsukahara, M. Yanaka, Measurement of debonding in cracked nanocomposite films by ultrasonic force microscopy. *Appl. Phys. Lett.* **80**, 1180–1182 (2002)
45. K. Yamanaka, UFM observation of lattice defects in highly oriented pyrolytic graphite. *Thin Solid Films* **273**, 116–121 (1996)
46. B.R.T. Rosner, D.W. van der Weide, High-frequency near-field, microscopy **2505**, (2002)
47. M.T. Cuberes, H.E. Assender, G.A.D. Briggs, O.V. Kolosov, Heterodyne force microscopy of PMMA/rubber nanocomposites: nanomapping of viscoelastic response at ultrasonic frequencies. *J. Phys. D-Appl. Phys.* **33**, 2347–2355 (2000)
48. O.V. Kolosov, I. Grishin, R. Jones, Material sensitive scanning probe microscopy of subsurface semiconductor nanostructures via beam exit Ar ion polishing. *Nanotechnology* **22**, 8 (2011)
49. F.P. Bowden, D. Tabor, *Tribology* (Anchor Press, New York, 1973)
50. O.V. Kolosov, G.A.D. Briggs, Atomic Force Microscopy and Method Thereof. In: *UK patent application 9617380.2*, 1996
51. W. Rohrbeck, E. Chilla, H.J. Frohlich, J. Riedel, Detection of surface acoustic waves by scanning tunneling microscopy. *Appl. Phys. Mater. Sci. Process.* **52**, 344–347 (1991)
52. O. Kolosov, A. Briggs, Atomic Force Microscopy Apparatus and Method Thereof, UK patent application, no. 9617380.2, 19 August 1996

53. M.T. Cuberes, Intermittent-contact heterodyne force microscopy. *J. Nanomater.* **5**, 716–721 (2009)
54. M. Tomoda, N. Shiraishi, O.V. Kolosov, O.B. Wright, Local probing of thermal properties at submicron depths with megahertz photothermal vibrations. *Appl. Phys. Lett.* **82**, 622–624 (2003)
55. O.V. Kolosov, K. Yamanaka, Nonlinear detection of ultrasonic vibrations in an atomic force microscope. *Jpn. J. Appl. Phys. Part 2 Lett.* **32**, L1095–L1098 (1993)
56. N. Kumano, K. Inagaki, O. Kolosov, O. Wright, Optical heterodyne force microscopy. *IEEE Ultrason. Symp. Proc.* **1, 2**, 1269–1272 (1998)

# Chapter 10

## Scanning Near-Field Ultrasound Holography

Shraddha Avasthy, Gajendra S. Shekhawat and Vinayak P. Dravid

**Abstract** Non-invasive nanoscale characterization is becoming exceedingly important to study complex nanosystems, such as dynamic biological processes controlled by nanosized subcellular components and microelectronic devices with nano-sized components that control their operation. Scanning Probe Microscopy (SPM) is a technique that has been shown to have the capability to adapt to surface characterization of several material properties in a non-destructive manner. Scanning Near-Field Ultrasound Holography (SNFUH) is a Scanning Probe Microscopy (SPM) based technique that employs ultrasonic waves for characterization of elastic properties of the surface as well as subsurface materials in a studied system. The characterization method involves launch of ultrasonic plane waves through the bottom of a sample and ultrasonic excitation of the SPM cantilever probe tip with piezoelectric transducers. Phase signal of the difference in excitation frequency between the sample and tip is recorded as an image. The phase contrast in the image is contributed to by both the near-field ultrasonic wave scattering and surface tip-sample interactions. SNFUH has already been demonstrated to be able to characterize elastic properties of not only hard but also soft material systems. Development of this method by further understanding its operation principles and contrast mechanisms will help to integrate it as a mainstream nanoscale characterization method for any system with hard and soft materials.

---

S. Avasthy · G. S. Shekhawat · V. P. Dravid  
Department of Materials Science and Engineering, Northwestern University, Evanston,  
IL 60208, USA  
e-mail: shraddhaavasthy2013@u.northwestern.edu

G. S. Shekhawat (✉) · V. P. Dravid  
Institute for Nanotechnology, 2220 Campus Drive, Cook Hall, Evanston 60208, USA  
e-mail: g-shekhawat@northwestern.edu

G. S. Shekhawat · V. P. Dravid  
NUANCE Center, 2220 Campus Drive, Cook Hall, Evanston, IL 60208, USA  
e-mail: v-dravid@northwestern.edu

## 10.1 History of Development of Acoustic Methods for Imaging

Acoustic microscopy is widely used for quality control to ensure reliability through failure analysis for applications in life sciences, structural components, and electronic devices. Its ability to image optically opaque objects non-destructively makes it a powerful microscopy technique for such applications. Contrast in an acoustic image results from acoustic scattering caused by a difference in mechanical properties of materials interacting with incident acoustic waves.

The idea for developing an acoustic microscope imaging device was conceived by Sergei Sokolov in the early twentieth century [1, 2]. Sokolov et al. [2] conducted the first experiments to get acoustic images using high-frequency acoustic waves. Considerable progress in the field was made after Lemons and Quate developed the first Scanning Acoustic Microscope (SAM) that was mechanically driven and operated in transmission mode [3, 4]. Around the same time another group led by L.W. Kessler at Zenith Radio Research Labs also came up with a version of SAM [4]. Several improvements were made to this instrument to enhance image resolution and automation of image collection before Kessler et al. [5–7] developed a SAM that operated in the transmission mode when aligned sapphire acoustic lenses were used to supply and collect acoustic waves from the sample. With further advancements SAMs began using reflection mode imaging that worked on the concept of time-of-flight signal processing. These microscopes used pulsed acoustic waves, instead of continuous acoustic waves used by transmission mode, to differentiate between the source and reflected acoustic wave signals [8]. The design of this microscope is the basis for nearly all of the acoustic microscopes in use today. This development led to later advances to SAMs, such as cross-sectional acoustic imaging, 3D acoustic imaging, and others. Conventionally SAM images measured just the signal amplitude at the receiver end. However, Reinholtsen et al. [9] demonstrated that measurement of both amplitude and phase of the SAM signal improved subsurface image reconstruction. They demonstrated that numerically processing images with both amplitude and phase measurements enabled quantitative non-destructive evaluation.

By the late twentieth century researchers had started expanding the capability of conventional acoustic microscopy to make measurements at the nanoscale by integrating it with the Scanning Probe Microscopy (SPM) platform that has a spatial resolution of  $\sim 10$  nm or even less [10, 11].

## 10.2 Introduction to Acoustic Methods Developed on SPM Platform

Several high-resolution techniques, such as electron beam microscopy, scanning probe microscopy, near-field scanning optical microscopy, and x-ray imaging, are currently in use for material evaluation. However, when it is required to evaluate soft as well as hard materials not only for surface but also subsurface properties

these techniques are limited. Some of the limitations include ability to image only surface properties/topography, cumbersome/invasive specimen preparation, inability to image subsurface properties of opaque or soft materials, and inability to focus beams to a sub-100 nm scale. Based on the above discussion there is clearly a need for some means to non-destructively evaluate material properties of embedded structures with nanoscale resolution [12].

As discussed earlier, a popular traditional technique for non-destructive evaluation is the use of scanning acoustic microscopes that may be operated in either reflection or transmission mode. Acoustic waves in these microscopes are focused on an area of evaluation and are coupled into the sample via some acoustic coupling interface, such as water. However, Abbe's principle establishes that lateral resolution of techniques that use focused beams cannot get better than a wavelength due to diffraction [13]. Lateral resolution limit of scanning acoustic microscopy is a few microns and hence, not very suitable for detecting features at the nanoscale. This limit can be overcome by using SPM-based techniques that have lateral resolution capabilities of  $\sim 10$  nm or even less. Although SPM techniques offer high lateral resolution, they are sensitive to only surface features and phenomena. Therefore, establishing acoustic microscopy on an SPM platform is a potential way to image mechanical as well as geometric properties of subsurface feature as illustrated in Fig. 10.1. Integration of these two microscopy techniques requires acoustic excitation of either or both the sample and SPM probe while the SPM probe is scanning the surface of the sample for imaging.

An important requirement to detect subsurface features in a set up where bulk acoustic waves are scattered to sense subsurface features, length of the acoustic near-field region of these subsurface features should extend to the top of sample surface. To achieve this for nanoscale features acoustic signal wavelengths need to be small enough to avoid diffraction and the signal amplitude large enough to be detected over the environmental acoustic noise. Other means of detecting subsurface features is indentation by the SPM probe to sense changes in stress field within the sample. Yamanaka et al. [14] and Rabe et al. [11] first adapted the SPM platform for detection of mechanical or elastic properties using ultrasonic excitation and introduced the techniques Ultrasonic Force Microscopy (UFM) and Atomic Force Acoustic Microscopy (AFAM), respectively.

In case of UFM, the sample is excited at ultrasonic frequencies. Sample vibrations are constrained to follow the standard SPM force separation curve [15]. The extent of the sample vibration following the repulsive and attractive regimes of the force separation curve depends on the force set point and amplitude of vibration. The amplitude of vibration is chosen such that the nonlinear regime of the force-distance curve is scanned and an average nonlinear force (over and above the set point force) acts on the cantilever [16]. This average force causes SPM probe tip to indent the sample periodically and an average force is experienced by the tip. This average force magnitude depends on the elastic property of the material being probed. Contrast in UFM is a strong function of the ratio of spring constant of cantilever and the tip-sample contact's spring constant [14, 17–21].

Atomic Force Acoustic Microscopy (AFAM) has the capability of detecting out-of-plane and in-plane vibrations of cantilever in the frequency range of 100 kHz to

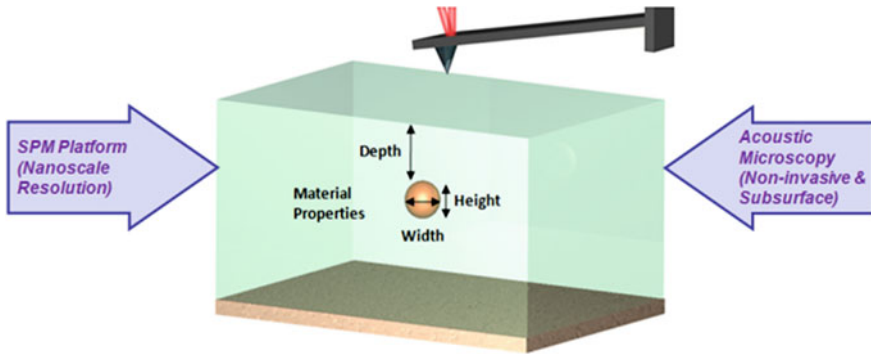


**Fig. 10.1** High lateral resolution capability of SPM and non-invasive subsurface imaging capability of acoustic microscopy when combined on the same platform offer a promising solution to high resolution surface and subsurface imaging of mechanical properties

several Megahertz. Contrary to UFM, amplitude of vibration in AFAM is kept low enough to keep the net force in repulsive or linear regime of the force-distance curve. This technique helps to determine a quantitative estimate of the elastic properties of a sample. The sample is vibrated in the range of hundreds of kilohertz to a few megahertz frequencies with the cantilever in contact with the sample. Based on the flexural and torsional modes excited in the cantilever the stiffness constant of the contact between tip and sample is determined. A numerical method to determine quantitative elastic properties with the measurements of contact stiffness has been developed by Rabe et al. [22] Considerable progress has been made in the understanding and development of imaging with AFAM for determining quantitative surface and subsurface elastic properties [23–29].

Cuberes et al. [30] introduced another nonlinear technique called Heterodyne Force Microscopy (HFM) executed in SPM contact mode. This was followed by a modified nonlinear method named Intermittent Contact Heterodyne Force Microscopy (IC-HFM) [31] executed in tapping mode. The experimental set up is such that both the tip and sample are vibrated at Megahertz frequencies such that the tip-sample distance is modulated at a beat frequency. Beat frequency in case of IC-HFM is chosen as the second cantilever eigenmode while in case of HFM it is chosen to be a few Kilohertz. Both these techniques are capable of imaging dynamic viscoelastic and/or adhesive responses with a high temporal sensitivity of the order of nanoseconds.

Resonant Difference-Frequency Atomic Force Ultrasonic Microscopy is yet another technique proposed by Cantrell et al. [32] where the cantilever and sample are each vibrated at Megahertz frequencies. Vibration frequencies are chosen such that the beat frequency corresponds to one of the contact resonance frequencies of the tip-sample assembly. A theoretical basis of the contrast observed in images has also been developed. The theory is based on the fact that image contrast is a con-

sequence of changing tip-sample contact stiffness due to elastic properties of surface and subsurface features [33].

### 10.3 Challenges and Difficulties with SPM Acoustic Methods

Extensive efforts are being made to enhance the reliability of SPM-based acoustic microscopy for enabling wide-scale use not only by researchers but also the industry. Here, we briefly describe some of the challenges that need to be considered to interpret the images collected through these acoustic methods.

Considerable research is being devoted to quantifying image contrast by these methods. Both surface and subsurface elastic properties have been shown to contribute to this contrast. A major challenge here is to differentiate the contribution to contrast by surface versus subsurface material properties. Such interpretations become even more challenging due to contributions from additional factors such as surface adhesion properties, that need to be considered when quantifying the observed image contrast.

Contribution to image contrast by just the subsurface features has its own set of challenges. Subsurface features cause scattering (reflection and refraction) of incident bulk ultrasonic waves due to acoustic impedance mismatch between the bulk material and material of the subsurface feature. The net effect of these scattered waves interacting with the incident acoustic waves is a perturbed region originating from the subsurface feature as shown in Fig. 10.2a. This region of perturbation is called the near-field region and its length depends on the wavelength of incident acoustic waves and effective size of the subsurface feature. Beyond the near-field region perturbations flatten out and the acoustic waves again become plane bulk waves. Therefore, detection of perturbation by an SPM tip at the surface (Fig. 10.2b) is possible only if the near-field region of a subsurface particle extends up to the surface and causes an acoustic signal perturbation at the surface greater than system's acoustic noise.

Perturbed acoustic waves also experience diffraction within the near-field region. It is due to this diffraction phenomenon that the image of subsurface features always has blurred edges and the size of feature in an image appears greater than the actual size of subsurface feature. The Full Width Half Maximum (FWHM) of a feature size imaged at the top surface depends on its depth and geometry. Diffraction can be countered by using higher frequency signals. Acoustic transducers in this case need to be designed such that amplitude of a high-frequency signal supplied to the sample and cantilever is not compromised.

Finally some of these imaging methods rely on lock-in-amplifiers to differentiate the signal amplitude or phase from the reference signal supplied to the system. If this signal magnitude is lower than the detection limits of the lock-in due to electrical or acoustic noise sources then it will not be possible to detect it. Therefore, stray sources of noise such as environmental acoustic vibrations, mechanical resonance

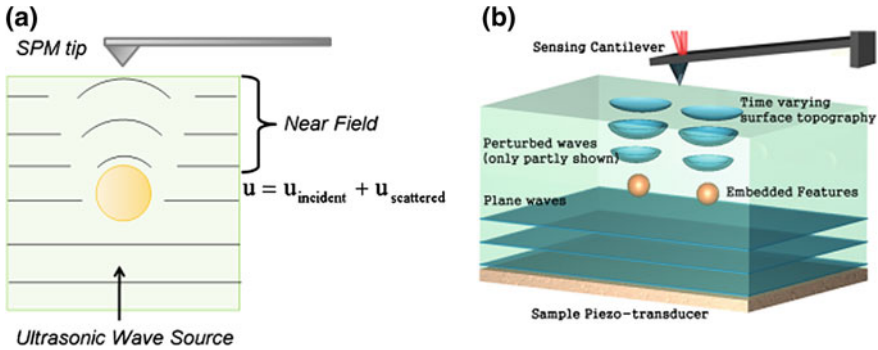


**Fig. 10.2** **a** Acoustic plane waves propagating through bulk of a vibrated sample get perturbed by features in their path. The perturbations in acoustic waves travel to *top* of the sample surface and undergo diffraction while doing so. Perturbation of these acoustic waves extends to only a certain length called the near-field distance, governed by the size of the feature and wavelength of acoustic waves from the source. **b** If the *top* surface is within the acoustic near-field distance and the perturbation amplitude is greater than environmental sources of acoustic noise, then the perturbation can be detected by an SPM tip scanning the sample surface. [16]

of piezo-transducer [34], and phase delay in electric signals caused by connecting cables need to be controlled.

## 10.4 Introduction to Scanning Near-Field Ultrasound Holography (SNFUH)

### 10.4.1 Description of the SNFUH Method

SNFUH was developed for non-destructive subsurface material characterization via ultrasonic excitation on an SPM platform [12, 16, 35–39]. This method finds wide applicability given that it is equally amenable to biological as well as electronic materials. Both the sample and SPM probe are vibrated at Megahertz frequencies in contact mode, as shown in Fig. 10.3 [12]. Ultrasonic excitation at the base of sample generates bulk acoustic waves through the sample and that at the base of SPM probe enables it to respond to such high-frequency elastic waves from the sample bulk.

Besides piezotransducers ultrasonic wave generation can be done using pulsed laser (causing a thermo-acoustic effect) [40, 41] and electron beams [42]. Difference frequency ( $\Delta f$ ) between the sample and probe is chosen such that the system operates at contact resonance (resonance of the tip-sample spring system) to enhance signal to noise ratio for imaging. As discussed in Sect. 10.3, differentiating surface from subsurface signal is a challenge. Given that images are collected at contact resonance there is expected to be a contribution from surface contact stiffness. A more detailed



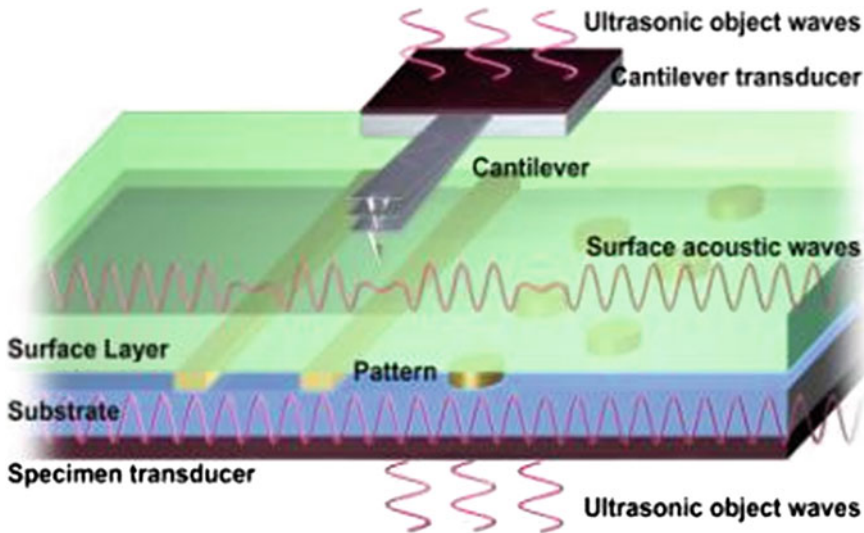


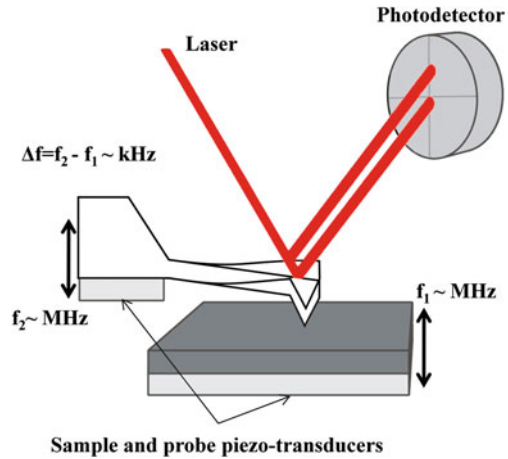
**Fig. 10.3** Scanning near-field ultrasound holography (SNFUH) images nanoscale mechanical properties of soft as well as hard materials by sensing acoustic perturbations at the sample surface. These perturbations are caused by changing mechanical properties of surface and subsurface features [12]

quantitative description of signal contribution from surface and subsurface features has been developed by Cantrell et al. [32, 33]. As illustrated in Sect. 10.4.2, surface measurements are made using height imaging of sample surface and is compared against the SNFUH image to identify the subsurface features. However, changing contact stiffness of the surface can also contribute to the image contrast and hence, result in the appearance of features not visible in height image. Some model samples were, therefore, designed with a uniform surface material (Sect. 10.4.2.1) and imaged to confirm the subsurface imaging capability of SNFUH. For samples with unknown surface and subsurface materials this is a subject of further research. A limitation to the choice of the difference frequency is that it should be within the frequency detection limit of the photodetector collecting the deflection error signal from SPM cantilever (Fig. 10.4).

The phase signal is then used to image the elastic properties of defects, inclusions, features, etc. The deflection error signal (cantilever flexural deflection) from the AFM photodetector is sent to the lock-in-amplifier to extract the amplitude and phase of the signal detected by the cantilever. Further details on the experimental setup have been illustrated elsewhere [16].

To explain the physical significance of the SNFUH phase signal we illustrate the AFM tip-sample interaction by a mass-spring model undergoing simple harmonic motion as illustrated in Fig. 10.5a, b Normal force on the tip-sample spring system is  $F_N$  and the contact stiffness of this coupled system is  $k^*$ . It is important to ensure that the operation parameters are setup such that the interaction force between the

**Fig. 10.4** Schematic illustration of experimental setup of SNFUH where the conventional electronic feedback system of an SPM system has been modified to adapt to ultrasonic sensing. Function generators are used to excite piezoelectric transducers for the sample and the cantilever. The A-B signal is processed to extract the phase signal for SNFUH Phase imaging



SPM tip and sample changes with changing mechanical properties of the sample. This is possible if the SPM tip-sample force scans the nonlinear regime of a standard force-distance curve [15] and as a consequence of that there is a nonlinear tip-sample interaction force. Multiple means may be used for modulating tip-sample interaction force, which in turn depends on distance between the SPM tip and sample. Changing difference frequency (frequency of excitation of tip relative to sample), amplitudes of vibration of tip/sample, force set point, and the average tip height above the sample surface are all parameters that can be changed to control tip-sample interaction force. As seen in Fig. 10.5c if there is no change in interaction force between the tip and sample then the mass oscillates about the same equilibrium position. In other words the modulation of tip-sample distance does not change. This means that there is no change in the phase signal being sensed by the system's SPM probe. However, when there is a change in mechanical properties or geometry of the sample it changes normal force to  $F'_N$  and the mass-spring system starts oscillating about a different equilibrium position. The tip-sample distance is now being modulated at a different amplitude and phase of the frequency. This change is imaged as a differential amplitude and phase of vibration with respect to the applied or reference signal, for each image pixel. The differential phase signal is reconstructed by an automated imaging system to generate the SNFUH phase image.

## 10.4.2 Applications of SNFUH

### 10.4.2.1 Semiconductors Structures, Interfaces, and Devices

Problems are getting worse as current technology node is moving beyond the conventional metrology tool set such as advancement in lithography, new advanced

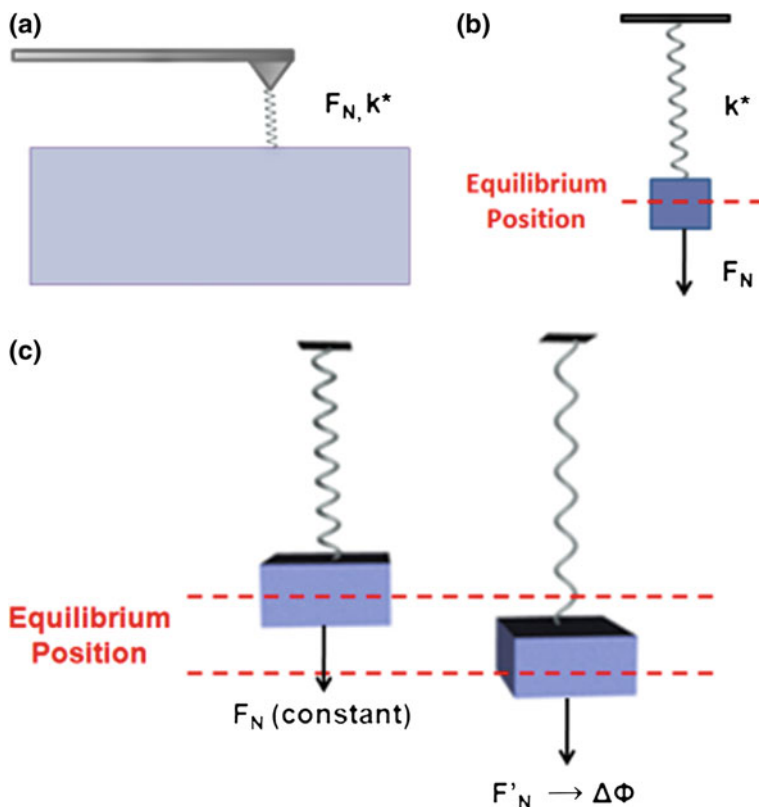


**Fig. 10.5** **a** An SPM tip-sample system can be depicted with a simple mass-spring model where  $k^*$  is the contact stiffness of the tip-sample system and  $F_N$  is the normal force acting on the probe tip. Any change in  $F_N$  causes a change in phase of optical feedback signal to the standard SPM system and thereby, contributes to SNFUH phase image contrast. **b** When a constant average force over a vibration cycle acts on the spring then the equilibrium position of the oscillating spring remains constant. **c** However, when there is a change in the average force over a vibration cycle due to changing contact stiffness or mechanical properties of the sample then the equilibrium position changes resulting in a change in phase of the vibration of tip-sample spring system. This phase change is imaged across the scan area of the sample to generate a SNFUH phase image

materials, and structures and devices for beyond CMOS. According to International Technology Roadmap for Semiconductors (ITRS) 2007 [43], metrology requirements continued to be driven by advanced lithography processes. New concepts in nanometrology are required to solve the critical problems. The ITRS 2007 identifies the principal technologies to be required within the Roadmap timeframe. Some of the metrology challenges in semiconductor industry that need innovative metrology developments to identify them are [44, 45]:

- Identification of buried defects in Extreme Ultraviolet Lithography (EUVL) multilayers blanks (foreign particles, stress), metrology capabilities for actinic-patterned mask inspection
- Buried microcracks in patterned Deep Ultraviolet (DUV) photomasks, defects in thin layers e.g. threading dislocations, HF defects, particle detection on multilayered surfaces
- Striae, bubble, stress, inclusions in Lorentz Transmission Electron Microscopy (LTEM) substrates used in EUVL. Buried defects in transistors under several multilayers.
- Voiding in vias and trenches in low-K dielectric materials, non-destructive measurements of the barrier layer and copper seed layer, along trench sidewall is a big challenge in semiconductor industry as the device size continues to shrink.
- 3D interconnect metrology, such as Through Silicon Vias (TSV) depth and profile through multilayers, detection of damage to metal layers during TSV process, defects in vias between wafers, defects after thinning wafers.

Other major challenges in this critical microelectronics step include voiding, delamination, and cracking at the polymer-trench interface. Conventional techniques for characterization of voids and stresses in narrower trenches include destructive approaches such as cross-sectional Scanning Electron Microscopy (SEM) or Transmission Electron Microscopy (TEM), which are not only laborious and time-consuming but require the wafer to be sacrificed. Electrical testing is nondestructive but spatially insensitive, and it requires contact to the wafer. Clearly, a non-destructive subsurface imaging approach is warranted to identify and isolate such defects or delamination and thereby improve the process yield.

Mask defect specifications are ultimately determined by the yield impact to device performance which correlates to resist Critical Dimension (CD) which is often measured by SEM. One of the major metrology challenges in semiconductor industry is to image buried defects, such as inclusions, pits, and bumps in EUV Multilayer (ML) blank which use quartz substrates with Mo/Si layers on top of it non-destructively. EUVL requires a reflective mask with Mo/Si film stack designed to reflect light with a wavelength of 13.5 nm. Very small particles or pits on the substrate surface can nucleate critical phase defects in reflective coatings and can significantly degrade the imaging performance of the mask [46–49]. Details of the material imperfections in these ML blanks are described in [47].

Both pits and bumps can cause disturbances to the ML and affect the phase and/or amplitude of the reflected EUV light. These defects on the surface propagate through the ML stack by so-called the decorative effect of the ML coating. To study the ML defects Programmed Defect Mask (PDM) was used as a ‘model’ test sample. Defects were produced with controlled growth on a ML blank and accurate placement in varying proximity to absorber patterns on the mask. PDM defects includes absorber line and shapes of different Critical Dimensions (CDs) and pitches, a wide range of ML defect sizes and shapes, and varied proximity of ML defects to the adjacent absorber patterns. ML defects were comprised of nanopatterned SiO<sub>2</sub> lines and bumps (size

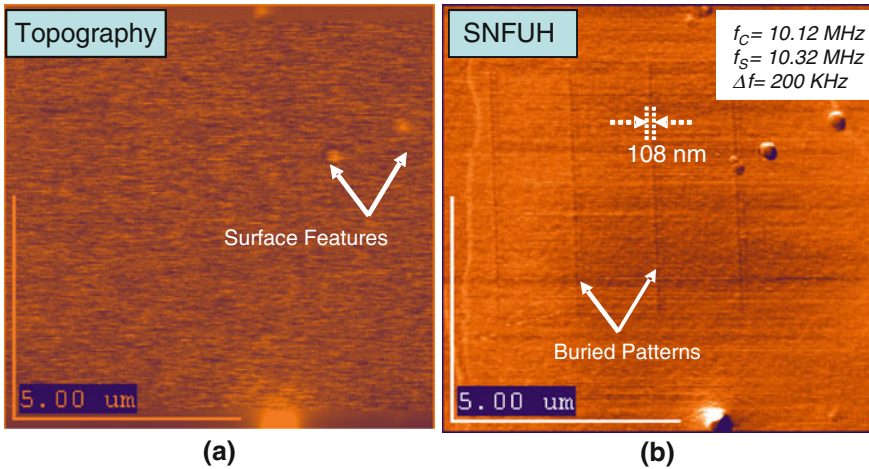
100 and 60 nm, respectively), fabricated by electron beam lithography and buried under 280 nm thick ML stacks.

Figure 10.6a depicts the conventional topography image of EUV mask, while Fig. 10.6b is the corresponding (simultaneously recorded) SNFUH phase image. The topography scan shows uniform and featureless surface except a few surface defects. However, the corresponding SNFUH phase image shown in Fig. 10.6b clearly reveals the phase contrast reminiscent of buried electron beam patterned lines under the multilayer stack. The bright contrast in the phase image corresponds to buried patterned lines, which undergoes a distinct viscoelastic response to the specimen ultrasound wave. The measured FWHM line width was around 108 nm. The ultrasonic waves launched in the sample and cantilever system was around 10.12 and 10.32 MHz, respectively. This result demonstrates a new application of SNFUH system in recognizing buried patterns while maintaining high resolution. Defects in these multilayer blanks such as lines and bumps appears as regions of dark contrast in ultrasound holography imaging due to large acoustic impedance mismatch at the defect locations [50].

#### 10.4.2.2 Low-K Dielectrics and Interconnects

The major challenge that industry is facing with this technology is voiding, delamination, and cracks at the polymer-trench interface. Conventional techniques for characterization of voids and stresses in narrower trenches include wet chemical etching and electrical testing, which is spatially insensitive and it requires contact to the wafer. In the case of *via* chains, several metal levels must be fabricated before the electrical test can be completed. Figure 10.7 illustrates imaging of a copper low-dielectric interconnect system [51]. Typical AFM topography image in Fig. 10.7 shows periodic polymer and copper lines. The copper lines are about 60 nm wide and the polymer lines around 200 nm. SNFUH Phase image in this figure reveals the surface elastic contrast and subsurface voiding in the copper lines. A line profile of a section of the phase image observed across a void has also been shown.

Another nice application of SNFUH in low-K dielectric interconnects is in identifying underlying defects in narrower trenches. We fabricated shallow trench structures as shown in Fig. 10.8a. The trenches were etched in Spin-On Dielectric (SOD) with a 50 nm layer of Low-Pressure Chemical Vapor Deposition (LPCVD)  $\text{Si}_3\text{N}_4$  as a capping layer, and trenches (1  $\mu\text{m}$  deep) were etched into  $\text{Si}_3\text{N}_4$  by wet processing [39]. A layer of polymer (Benzocyclobutene) 500 nm thick was spin coated, followed by thermal annealing to cure the polymer. A conventional topography scan (Fig. 10.8b), 7.5 by 7.5  $\mu\text{m}$ , shows uniform and contiguous polymeric coating on  $\text{Si}_3\text{N}_4$  and inside the trenches. On the other hand, the corresponding (simultaneously recorded) SNFUH phase image shown in Fig. 10.8c reveals phase contrast reminiscent of embedded voiding within the polymer and at the  $\text{Si}_3\text{N}_4$ -polymer interfaces. The dark contrast in the phase image in polymer coated  $\text{Si}_3\text{N}_4$  lines corresponds to voids at  $\text{Si}_3\text{N}_4$  polymer interfaces (i.e., voiding underneath the contact). The contrast is due to the distinct viscoelastic response from the specimen acoustic wave from the



**Fig. 10.6** **a** Typical AFM (topography) image shows featureless and smooth surface with few isolated features on the surface and **b** shows a remarkable SNFUH phase image clearly showing the *buried lines* with high definition under multilayer film stack. The measured line width is around 108 nm [50]

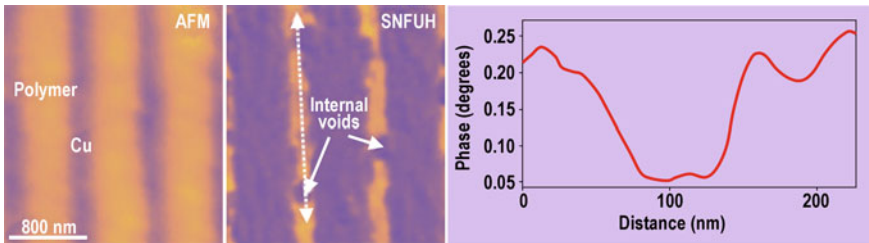
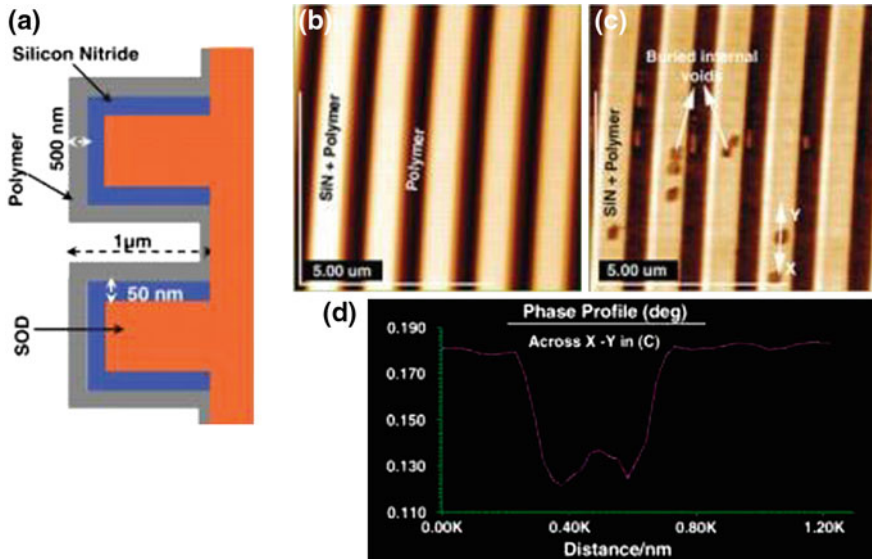


**Fig. 10.7** SNFUH imaging of a copper low-dielectric interconnect system. *Left* typical AFM (topography) image shows periodic polymer and copper features. The *copper lines* are about 60 nm wide and the polymer one around 200 nm. *Middle* phase image of SNFUH that clearly reveals the surface elastic contrast and subsurface voiding in the *copper lines*. *Right* line profile across the voids [51]

voids. Interestingly, a notable hardening of the polymer in the trench and its sidewall is also evident in the phase image, which results from thermal annealing and possibly poor adhesion with SOD. Because it is nondestructive, SNFUH is an ideal toolset for such subsurface metrology needs.

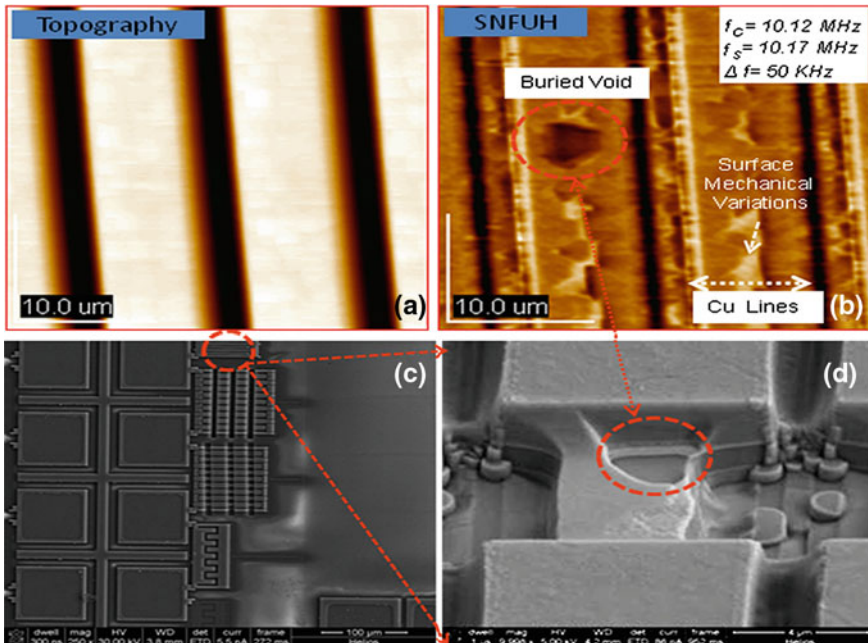
### 10.4.2.3 Probing Buried Defects for Advanced Interconnect Architectures

Figure 10.9 shows a series of copper lines having thickness of around 500 nm [35]. Figure 10.9a shows the conventional topography image, while Fig. 10.9b is



**Fig. 10.8** **a** Schematic of the model test sample for detecting embedded defects/voiding in shallow trenches. **b** Typical AFM topography image shows a coating of low-dielectric material [benzocyclobutene (BCB)], 500 nm thick, uniformly covering the trenches. Trench width is  $\sim 400$  nm and height is  $\sim 1$   $\mu\text{m}$ . **c** Phase image of SNFUH clearly reveals the surface elastic contrast and embedded voiding in polymer coating over nitride and hardening of it at the trench walls, a result of its curing. This is evident from the contrast at the trench walls. **d** The line profile across the void, marked across X-Y in (c). Remarkably high subsurface phase resolution is achieved. [39]

the corresponding (simultaneously recorded) SNFUH phase image. The typical  $25 \times 25$   $\mu\text{m}$  topography scan shows uniform and contiguous polymer and copper lines. However, the corresponding SNFUH phase image shown in Fig. 10.9b reveals phase contrast reminiscent of subsurface voiding in copper lines. The dark contrast in the phase image of copper lines corresponds to voids underneath the metal. The presence of this contrast in phase image implies that there is insufficient metal plating at the bottom, i.e. voiding underneath the contact, which undergoes a distinct viscoelastic response. Some of the topographical mechanical variations are also evident more prominently in the SNFUH image. These topographical mechanical variations originate from the chemical mechanical polishing of these interconnects lines. After SNFUH imaging, sample location was precisely marked and put down in FEI dual beam Focused Ion Beam (FIB) to cross-validate what we got in ultrasound holography. Figure 10.9c depicts the planar view of the FIB image showing the area that we cut down to see the buried defects. Figure 10.9d depicts the FIB image of a defect found during SNFUH imaging. The lines were cut exactly at the same location where SNFUH was performed and the image clearly demonstrates the same buried defect that was found in ultrasound imaging. Thus, we validated the SNFUH buried imaging capabilities with FIB.



**Fig. 10.9** Schematic illustration of a copper interconnects lines. The thickness of the lines is around 500 nm. **a** Shows the uniform topographical interconnect lines with some features visible. **b** Shows the remarkable SNFUH phase image clearly demonstrates the voiding in these *copper lines* and other surface mechanical variations. **c** Depicts the FIB image highlighting the area that was cut down to cross-validate the SNFUH image and **d** the cross-section of one of the trench shows the buried defects when it was etched down from top by ion-milling [35]

These images clearly demonstrate the reliability of this method not only as a microscopy technique but also as an extremely sensitive probe of the mechanical reliability of the interfaces. Recently, extensive research is being conducted to fill shallow trenches with polymers to prevent extra processing steps. The trench isolation technique can be used to fabricate memory, logic, and imager devices which can exhibit reduced current leakage and/or reduced optical cross-talk.

### 10.4.3 Non-Invasive Nanomechanics of Subcellular Structures

As biology gets increasingly quantitative, a comprehensive understanding of biological structures and processes from the molecular to cellular level has become imperative. Among the many roadblocks that still exist, characterization of the complex dynamics of biological processes, and especially signal pathways at nanoscale resolution remains a formidable challenge. The existence of multiple kinetic pathways and transient intermediate states often make these processes difficult to dissect,



as individual steps of a multistep process are typically not synchronized among molecules. Molecular imaging of subcellular features provides the ability to study their molecular processes that have potential to impact many facets of biomedical research. Advances in electron and optical microscopy have spurred tremendous growth in biological imaging. Several electron and optical imaging are used to monitor the biological systems *in vitro* as well as *in vivo*. Such techniques include confocal, fluorescent imaging, and cryo-based electron microscopy modalities. Many applications require a combination of these imaging modalities, which gives rise to huge data sets. However, lack of powerful information extraction and quantitative analysis tools poses a major hindrance to exploiting the full potential of the acquired data, which is very crucial for monitoring the intracellular biological processes.

Despite recent advances, conventional imaging with non-invasive radiations, such as light and acoustic waves, suffers from classical diffraction limit to attain sub 100 nm resolution [52–55]. Fluorescence confocal microscopy [56–58] is a traditional way to monitor biological interactions, but it suffers from poor spatial resolution and requires fluorescent dyes. Scanning probe microscopy (SPM) and its analogs offer superb spatial resolution but are sensitive only to surface or shallow surface features [59, 60]. These techniques provides only the qualitative and structural information, but not quantitative. In summary, no single modality currently meets the needs of high sensitivity, high spatial, and temporal resolution.

Emergence of quantitative non-destructive imaging approaches based on acoustic and light-optical microscopy is limited by classical diffraction which limits the spatial resolution in the far-field regime. Further they are also limited by the need of lenses, coupling fluid, relatively low resolving power, high cost, and complexity for the user. Moreover, detectability is variable dependence.

Our SNFUH technology demonstrated the high sensitivity, resolution, and nanomechanical quantification of subcellular structures. The novelty of our findings lies in the fact that it provides an unique way to study intracellular features under ambient and their natural conditions, that is, without placing them in vacuum, coating it with metal, bombarding it with electrons, or inserting other molecules, as in the case with other techniques such as electron and fluorescent microscopy. Our nanomechanical bioprobe synergistically combines the non-invasive nature and sensitivity to deeply buried intracellular using ultrasound waves in lift-mode operation, and a holography detection paradigm which provides exquisite sensitivity to “phase” of scattered ultrasound wave.

#### 10.4.3.1 Non-Invasive Nanomechanics of Malaria Parasites

Unique example for real-time *in vitro* biological imaging is demonstrated in Fig. 10.10. It depicts high resolution and remarkably high contrast arising from malaria parasites inside infected Red Blood Cells (RBCs). It seems to show an early stage presence of parasites inside RBCs, without any labels or sectioning of cells, and under physiologically viable conditions. In addition to several other features reminiscent of membrane proteins and subcellular contents, multiple parasites

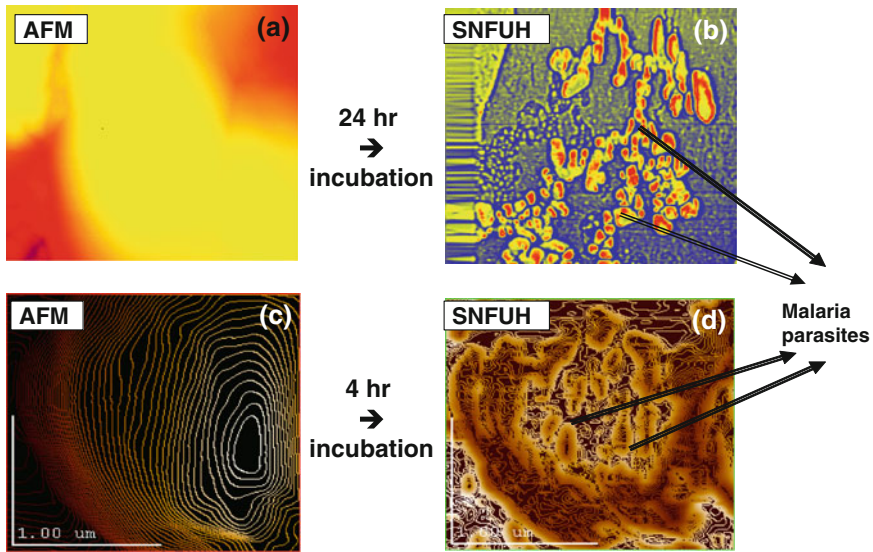


**Fig. 10.10** **a** and **c** AFM topography, and **b** and **d** SNFUH phase images from malaria-infected RBCs. Images **a** and **b** were obtained from 24 h incubation. Topography shows typical surface features of RBCs with scan size of 10 by 10  $\mu\text{m}$ , while SNFUH phase image demonstrates remarkable contrast from parasites inside the RBC at nanoscale spatial resolution. Images **c** and **d** represent early-stage incubation of parasite infection 8

are clearly evident. *Plasmodium falciparum* strain 3D7 was cultured in vitro [61]. Parasites were synchronized to within 4 h using a combination of Percoll purification and sorbitol treatments, cultured to 10 % parasitemia, and harvested at the indicated times.

#### 10.4.3.2 Viscoelastic (nanomechanical) Holography for Imaging Nanoparticles in Cells

Nanostructured materials have numerous potential biomedical applications but their possible adverse effects and cytotoxicity are receiving equal attention [62, 63]. Inhalation of nanoparticles is of great concern because nanoparticles can be easily aerosolized. Imaging techniques that can visualize local populations of nanoparticles at nanometer resolution within the structures of cells are therefore important [64]. We have demonstrated that cells [36, 37] obtained from mice exposed to Single Walled Carbon Nanohorns (SWCNH) can be probed using SNFUH. These results suggest a new paradigm for non-invasive imaging with SNFUH, for probing the interactions of engineered nanomaterials in biological systems, both for intentional and desirable purpose as well as to monitor unintended environmental/toxic response.

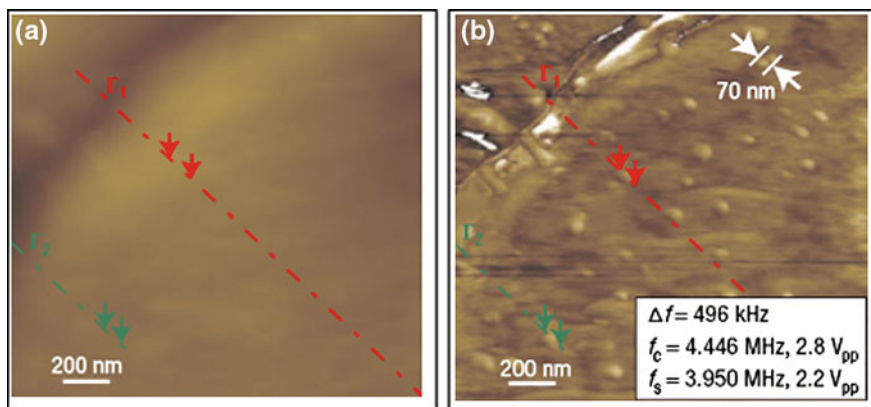


**Fig. 10.11** Nanoparticles detected inside red blood cells. AFM topography **a** and SNFUH phase **b** images of erythrocytes obtained from the BAL fluid of SWCNH-exposed mouse 24 h post-aspiration [36]

Interestingly, as in the case of macrophages from SWCNH-exposed mice, we encounter nanoparticles within erythrocytes that were present (although rare) in Broncho Alveolar Lavage (BAL) samples. Figure 10.11a,b, show the topography and SNFUH phase images of erythrocytes that were present in BAL fluid extracted from a mouse 24 h after SWCNH exposure. While the topography only resolves nanoparticles on the cellular surface of the erythrocytes (Fig. 10.11a), a surprisingly large number of additional particles are detected in the SNFUH image captured at the same location as the surface topography (Fig. 10.11b). Higher resolution images of topography (Fig. 10.11a) and SNFUH (Fig. 10.11b) consistently compare and show the particles that have an average diameter of 70 to 110 nm [36].

#### 10.4.4 Future Development

Given the ever decreasing scales of features being evaluated by the scientific community and introduced in commercial products by the industry, every microscopy technique endeavors to push limits of resolution to even smaller scales. To achieve the same for SNFUH it is envisioned that high frequency oscillators that vibrate at up to Gigahertz frequencies will be employed to image features a few nanometers in size that are embedded as deep as several microns into a sample.

Like the other SPM-based acoustic techniques it is imperative to further SNFUH by enhancing the quantitative understanding of phase measurements made using it. Modeling and experiments to this effect will enable determination of subsurface material properties and geometries, and also give an insight into mechanisms for enhancing phase contrast.

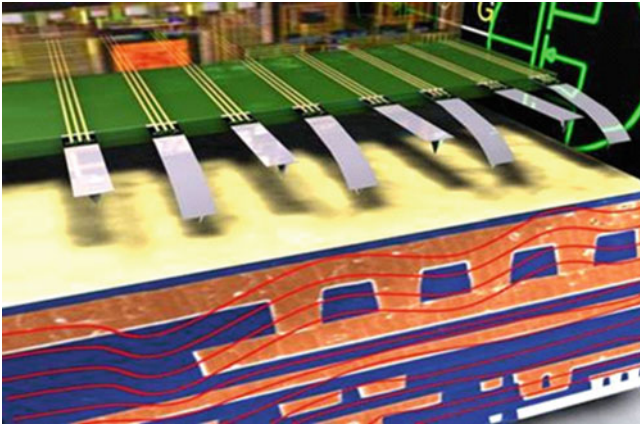


**Fig. 10.12** Schematic of the envisioned high speed SNFUH platform integrated with an array of MOSFET cantilevers for feedback and high frequency actuators. [12]

Once the above stated developments have been achieved it is envisioned that SNFUH can be taken to the next level to achieve 3D tomography and faster scan speeds compared to traditional SPM imaging. A 3D tomography map of elastic properties of embedded features can be obtained if SNFUH phase information recorded in 2D space by modeling depth distribution of phase, which is a direct consequence of depth, material, and geometry of the embedded features.

Faster scan speeds can be achieved by using an array of MOSFET embedded cantilevers with electronic feedback instead of a single cantilever with optical feedback, as illustrated in Fig. 10.12 [12]. This will allow massively parallel electronic feedback and hence, faster image collection times. Another advantage of electronic feedback with MOSFET embedded cantilevers is that the limitation of keeping difference frequencies up to a few Megahertz only, is eliminated. Difference frequencies greater than a few MHz are difficult to detect due to low cut-off frequencies of photodetectors (1–5 MHz) used in the present SPM systems, which is not expected to be the case for electronic feedback through MOSFETs. Finally, seamless integration of such MOSFET embedded cantilever arrays with commercially available SPM systems is another driver to pursue this development in the future.

## 10.5 Conclusions

Reliable nanoscale characterization of material properties and geometries of surface and subsurface features in a non-invasive manner is an essential requirement. SNFUH is a promising characterization method for such an application. This characterization method has been successfully used for imaging biological cells and samples relevant to the semiconductor industry. This has motivated further understanding of SNFUH

to develop it for unambiguous characterization of elastic properties of materials at the nanoscale. It is envisioned that this method will become a complementary method to other techniques presently being used by the industry for characterization of materials at the nanoscale.

## References

1. S.Y. Sokolov, Ultraacoustic methods of studying properties of hardened steel and detecting intrinsic flaws of metal articles. *Zhurnal Tekhnicheskoi Fiziki*. **XI**(1–2), 160–169 (1941)
2. S.Y. Sokolov, The ultrasonic microscope. *Doklady Akademia Nauk SSSR*. **64**, 333 (1949)
3. R.A. Lemons, C.F. Quate, A scanning acoustic microscope. in *Proceedings of the IEEE Ultrasonics Symposium*, 1973, p. 18–21
4. R.A. Lemons, C.F. Quate, Acoustic microscope—scanning version. *Appl. Phys. Lett.* **24**(4), 163–165 (1974)
5. L.W. Kessler, A. Korpel, P.R. Palermo, Simultaneous acoustic and optical microscopy of biological specimens. *Nature* **239**, 111–112 (1972)
6. A. Korpel, L.W. Kessler, P.R. Palermo, Acoustic microscope operating at 100 Mhz. *Nature* **232**(5306), 110–111 (1971)
7. L.W. Kessler, A. Korpel, Acoustic imaging with a focused light beam. *J. Acoust. Soc. Am.* **47**(1A), 81 (1970)
8. Andrew Briggs, Acoustic microscopy—a Summary. *Rep. Prog. Phys.* **55**(7), 851–909 (1992)
9. Paul A. Reinholdtsen, Butrus T. Khuriyakub, Image-processing for a scanning acoustic microscope that measures amplitude and phase. *IEEE Trans. Ultrason. Ferroelectr. Freq. Control* **38**(2), 141–147 (1991)
10. O.V. Kolosov, K. Yamanaka, Nonlinear detection of ultrasonic vibrations in an atomic-force microscope. *Jpn. J. Appl. Phys. Part 2 Lett.* **32**(8A), L1095–L1098 (1993)
11. U. Rabe, W. Arnold, Acoustic microscopy by atomic-force microscopy. *Appl. Phys. Lett.* **64**(12), 1493–1495 (1994)
12. V. Dravid, G. Shekhawat, Seeing the invisible: non-destructive subsurface nanoscale metrology with scanning near-field ultrasound holography. *Small Times* **9**(2) (2010)
13. V.E. Borisenko, S. Ossicini, *What is What in the Nanoworld : a handbook on nanoscience and nanotechnology*, 2nd edn. (Wiley, Weinheim, 2008), p. 522
14. Kazushi Yamanaka, Hisato Ogiso, Oleg V. Kolosov, Ultrasonic force microscopy for nanometer resolution subsurface imaging. *Appl. Phys. Lett.* **64**(2), 178–180 (1994)
15. F. Dinelli, S.K. Biswas, G.A.D. Briggs, O.V. Kolosov, Measurements of stiff-material compliance on the nanoscale using ultrasonic force microscopy. *Phys. Rev. B* **61**(20), 13995–14006 (2000)
16. S. Avasthy, G. Shekhawat, V. Dravid, in *Scanning near-field ultrasound holography*, ed. by R.A. Meyers. *Encyclopedia of Analytical Chemistry: supplementary volumes S1–S3 : applications, theory and instrumentation* (Wiley, Hoboken, 2010), a9146, pp. 1–9
17. K. Inagaki, O.V. Kolosov, G.A.D. Briggs, O.B. Wright, Waveguide ultrasonic force microscopy at 60 MHz. *Appl. Phys. Lett.* **76**(14), 1836–1838 (2000)
18. K. Inagaki, O.V. Kolosov, G.A.D. Briggs, S. Muto, Y. Horisaki, O.B. Wright. Ultrasonic force microscopy in waveguide mode up to 100 MHz. in *Proceedings of the IEEE Ultrasonics Symposium*, Vols. 1 and 2 (1998), p. 1255–1259
19. O.V. Kolosov, M.R. Castell, C.D. Marsh, G.A.D. Briggs, Imaging the elastic nanostructure of Ge islands by ultrasonic force microscopy. *Phys. Rev. Lett.* **81**(5), 1046–1049 (1998)
20. O. Kolosov, A. Briggs, K. Yamanaka, W. Arnold, in *Nanoscale imaging of mechanical-properties by ultrasonic force microscopy (UFM)*, eds. by P. Tortoli, L. Masotti. *Acoustical Imaging*, vol. 22 (Plenum Press, New York, 1996), p. 665–668

21. K. Yamanaka, H. Ogiso, O.V. Kolosov, Analysis of subsurface imaging and effect of contact elasticity in the ultrasonic force microscope. *Jpn. J. Appl. Phys. Part 1-Regul. Pap. Short Notes Rev. Pap.* **33**(5B), 3197–3203 (1994)
22. U. Rabe, S. Amelio, M. Kopycinska, S. Hirsekorn, M. Kempf, M. Göken, W. Arnold, Imaging and measurement of local mechanical material properties by atomic force acoustic microscopy. *Surf. Interface Anal.* **33**, 65–70 (2002)
23. D.C. Hurley, M. Kopycinska-Muller, A.B. Kos, Mapping mechanical properties on the nanoscale using atomic-force acoustic microscopy. *J. Miner.* **59**(1), 23–29 (2007)
24. D.C. Hurley, M. Kopycinska-Müller, A.B. Kos, R.H. Geiss, Nanoscale elastic-property measurements and mapping using atomic force acoustic microscopy methods. *Meas. Sci. Technol.* **16**(11), 2167–2172 (2005)
25. D.C. Hurley, K. Shen, N.M. Jennett and Joseph A. Turner, Atomic force acoustic microscopy methods to determine thin-film elastic properties. *J. Appl. Phys.* **94**(4), 2347–2354 (2003)
26. U. Rabe, K. Janser, W. Arnold, Acoustic microscopy with resolution in the nm-range. in *Proceedings of 24th International Symposium on Acoustical Imaging*, vol. 22 (1996), p. 669–676
27. U. Rabe, K. Janser, W. Arnold, Vibrations of free and surface-coupled atomic force microscope cantilevers: theory and experiment. *Rev. Sci. Instrum.* **67**(9), 3281–3293 (1996)
28. U. Rabe, M. Dvorak, W. Arnold, The atomic-force microscope as a near-field probe for ultrasound. *Thin Solid Films* **264**(2), 165–168 (1995)
29. D.C. Hurley, in *NanoScience and Technology*, ed. by B. Bhushan, F. Harald. Applied Scanning Probe Methods I, Vol. XI (Springer, New York, 2009)
30. M. Teresa Cuberes, H.E Assender, A. Briggs, O.V. Kolosov, Heterodyne force microscopy of PMMA/rubber nanocomposites: nanomapping of viscoelastic response at ultrasonic frequencies. *J. Phys. D Appl. Phys.* **33**(19), 2347–2355 (2000)
31. M. Teresa Cuberes, Intermittent-Contact heterodyne force microscopy. *J. Nanomater.* **2009**(762016), 1–5 (2009)
32. S.A. Cantrell, J.H. Cantrell, P.T. Lillehei, Nanoscale subsurface imaging via resonant difference-frequency atomic force ultrasonic microscopy. *J. Appl. Phys.* **101**(11), 114324–114324-8 (2007)
33. J.H. Cantrell, S.A. Cantrell, Analytical model of the nonlinear dynamics of cantilever tip-sample surface interactions for various acoustic atomic force microscopies. *Phys. Rev. B* **77**(16) 165409, 1–16 (2008)
34. S. Avasthy, J.H. Kim, G. Shekhawat, S.P. Shah, V.P. Dravid, Improving accuracy of nanoscale mechanical property imaging with AFM-based contact resonance force microscopy (2011) (submitted)
35. G. Shekhawat, A. Srivastava, S. Avasthy, V.P. Dravid, Ultrasound holography for noninvasive imaging of buried defects and interfaces for advanced interconnect architectures. *Appl. Phys. Lett.* **95**(263101), 1–3 (2009)
36. L. Tetard, A. Passian, K.T. Venmar, R.M. Lynch, B.H. Voy, G. Shekhawat, V.P. Dravid, T. Thundat, Imaging nanoparticles in cells by nanomechanical holography. *Nat. Nanotechnol.* **3**(8), 501–505 (2008)
37. L. Tetard, A. Passian, R.M. Lynch, B.H. Voy, G. Shekhawat, V. Dravid, T. Thundat, Elastic phase response of silica nanoparticles buried in soft matter. *Appl. Phys. Lett.* **93**(13), 133113, 1–3 (2008)
38. G. Shekhawat, V. Dravid, Seeing the invisible: scanning near-field ultrasound holography (SNFUH) for high resolution sub-surface imaging. *Microsc. Microanal.* **12**(S02), 1214–1215 (2006)
39. G. Shekhawat, V.P. Dravid, Nanoscale imaging of buried structures via scanning near-field ultrasound holography. *Science* **310**(5745), 89–92 (2005)
40. S.G. Pierce, B. Culshaw, Q. Shan, Laser generation and detection of ultrasound for materials characterisation, in *International Conference on Applied Optical Metrology*, vol. 3407 (1998), p. 437–442

41. W. Arnold, Generation of Ultrasound by Short Laser-Pulses and Its Application in Physics and NDE. *Acta Physica Slovaca* **36**(1), 5–16 (1986)
42. Ch. Thomas, R. Heiderhoff, L.J. Balk, Acoustic near-field conditions in an ESEM/AFM hybrid system. *J. Phys. Conf. Ser.* **61**, 1180–1185 (2007)
43. Semiconductor Research Corporation, ITRS Grand Challenges (2007), Available from: <http://www.src.org/program/grc/about/grand-challenges/2007/>
44. A.C. Diebold, Metrology for Emerging Materials, Devices, and Structures. International Conference on Frontiers of Characterization and Metrology for Nanoelectronics, University at Albany, New York, 2009
45. C.M. Garner, E.M. Vogel, Metrology challenges for emerging research devices and materials. *IEEE Trans. Semicond. Manuf.* **19**(4), 397–403 (2006)
46. B. Fay, Advanced optical lithography development from UV to EUV. *Microelectron. Eng.* **61–62**, 11–24 (2002)
47. T. Liang, E. Ultanir, G. Zhang, S-J. Park, E. Anderson, E. Gullikson, P. Naulleau, F. Salmassi, P. Mirkarimi, E. Spiller, S. Baker, Growth and printability of multilayer phase defects on extreme ultraviolet mask blanks. *J. Vacuum Sci. Technol. B* **25**(6), 2098–2103 (2007)
48. T. Liang, P. Sanchez, G. Zhang, E. Shu, R. Nagpal, A. Stivers, Understanding and reduction of defects on finished EUV masks. in *Proceedings of the Metrology, Inspection, and Process Control for Microlithography XIX*, Pts 1–3, vol. 5752 (2005) pp. 654–662
49. E.M. Gullikson, S. Mrowka, B.B. Kaufmann, Recent developments in EUV reflectometry at the advanced light source. *Emerg. Lithog. Technol. V* **4343**, 363–373 (2001)
50. G. Shekhawat, S. Avasthy, A. Srivastava, S-H. Tark, V. Dravid, Probing buried defects in extreme ultraviolet multilayer blanks using ultrasound holography. *IEEE Trans. Nanotechnol.* **9**(6), 671–674 (2010)
51. A. Diebold, Subsurface imaging with scanning ultrasound holography. *Science* **310**(5745), 61–62 (2005)
52. Y. Su, Z. Fan, K. Xu, Y. Jianquan, R.K. Wang, A photoacoustic tomography system for imaging of biological tissues. *J. Phys. D Appl. Phys.* **38**, 2640–2644 (2005)
53. H.G. Abdelhady, S. Allen, S.J. Ebbens, C. Madden, N. Patel, C.J. Roberts, Z. Jianxin, Towards nanoscale metrology for biomolecular imaging by atomic force microscopy. *Nanotechnology* **16**(6), 966–973 (2005)
54. M. Moloney, L. McDonnell, H. O’Shea, Immobilisation of semliki forest virus for atomic force microscopy. *Ultramicroscopy* **91**(1–4), 275–279 (2002)
55. A. Briggs, O.V. Kolosov, Acoustic microscopy. 2nd edn. in *Monographs on the Physics and Chemistry of Materials xxii*, (Oxford University Press, New York, 2010), p. 356
56. T.M. Nelson, R.W. Smith, Scanning acoustic microscopy. *Adv. Mater. Process.* **162**(12), 29–32 (2004)
57. S. Weiss, Fluorescence spectroscopy of single biomolecules. *Science* **283**(5408), 1676–1683 (1999)
58. A. Ishijima, T. Yanagida, Single molecule nanobioscience. *Trends Biochem. Sci.* **26**(7), 438–444 (2001)
59. C.F. Quate, A. Atalar, H.K. Wickramasinghe, Acoustic microscopy with mechanical scanning—review. *Proc. IEEE* **67**(8), 1092–1114 (1979)
60. C.F. Quate, The AFM as a tool for surface imaging. *Surf. Sci.* **300**(1–3), 980–995 (1994)
61. K. Haldar, M.A.J. Ferguson, G.A.M. Cross, Acylation of a plasmodium-falciparum merozoite surface-antigen Via Sn-1,2-diacyl glycerol. *J. Biol. Chem.* **260**(8), 4969–4974 (1985)
62. A. Nel, T. Xia, L. Mädler, N. Li, Toxic potential of materials at the nanolevel. *Science* **311**(5761), 622–627 (2006)
63. B.J. Panessa-Warren, J.B. Warren, S.S. Wong, J.A. Misewich, Biological cellular response to carbon nanoparticle toxicity. *J. Phys. Condens. Matter* **18**(33), S2185–S2201 (2006)
64. V. Stone, K. Donaldson, Nanotoxicology—Signs of stress. *Nat. Nanotechnol.* **1**(1), 23–24 (2006)

# Chapter 11

## Mapping of the Surface's Mechanical Properties Through Analysis of Torsional Cantilever Bending in Dynamic Force Microscopy

Andrzej Sikora and Łukasz Bednarz

**Abstract** In atomic force microscopy, the cantilever probes provide sensing of the tip-sample forces, therefore are used for the surface's topography imaging as well as the mechanical properties mapping at nanoscale. As in most techniques developed for local stiffness imaging based on so-called contact mode, the force applied to the surface exceeds acceptable level often causing damage to the sample. On the other hand, the most popular measurement technique based on the intermittent contact mode, where dynamic tip-sample interaction is measured and processed in order to provide surface's shape tracking as well as imaging of energy dissipation, allows to perform the measurements with much less force and can be applied to a wide range of samples. This method, however, is insufficient in many cases, as it cannot provide detailed information about certain mechanical properties of the sample. Therefore, a new approach has been lately developed and successfully utilized in a number of applications. By the analysis of higher harmonics of the cantilever's oscillation, one can obtain more specific information about the tip-sample interaction than in the case of phase imaging. Moreover, the time-resolved tapping mode, where advanced high-bandwidth signal processing is implemented, allows performing fast imaging of the stiffness, adhesion, peak force, and energy dissipation. As this technique provides gentle interaction with the surface, it can be used in imaging of fragile objects, such as biological samples. Due to the mechanical properties of the cantilever causing significant deformations of the detection bandwidth, the torsional bending of the cantilever is utilized in order to obtain the desired signal. In this chapter we discuss the principles of the implementation of this method and its application issues.

---

A. Sikora (✉) · Ł. Bednarz  
Division of Electrotechnology and Materials Science,  
Electrotechnical Institute, M. Skłodowskiej-Curie 55/61,  
50-369 Wrocław, POLAND  
e-mail: sikora@iel.wroc.pl

Ł. Bednarz  
e-mail: l.bednarz@iel.wroc.pl



## 11.1 Introduction

Atomic force microscopy as one of the very few methods allowing subnanometer imaging of the surface [1–3], offers also the possibility of measuring the forces acting between the scanning tip and the sample. Its role as a diagnostic tool in various fields of science and technology has undoubtedly been appreciated and widely used for over two decades [4, 5]. Among the wide range of the measurement modes allowing observation of the distribution of morphological, electrical, magnetic, thermal, and optical properties of the surface, information about certain mechanical properties can also be obtained. The Force Modulation Microscopy mode, for example, provides a mapping of the local stiffness. It may, however, relatively easily cause modifications of the surface due to large forces applied to the sample [6]. Although the Force Volume Microscopy method utilizing contact mode and force spectroscopy acquisition [7, 8] was successfully utilized in investigations of biological or chemical samples, it is, nevertheless, time-consuming and provides the force mapping resolution significantly lower than the topography imaging (e.g.  $32 \times 32$ ). Jumping mode scanning force microscopy [9, 10] and digital pulse force mode [11, 12] were also proposed as techniques allowing to investigate the mechanical properties of the surface; however, the mapping speed was still insufficient. To compensate the drawbacks mentioned before, another approach, described in this chapter, was required in order to provide high-speed mapping of the mechanical properties of the sample.

In dynamic detection methods of the tip-sample interaction known as intermittent contact mode (semicontact mode, tapping mode) the tip acts on the sample with significantly smaller force than in contact mode, allowing one to investigate fragile objects [13]. Also the wear of the tip, as well as the risk of its contamination is significantly lower than in contact related modes [14, 15]. In this technique the tip oscillates with a frequency near to its resonant frequency, perpendicularly to the surface [16, 17]. During every oscillation cycle, the tip presses the sample for a certain time period. When the tip experiences attractive and repulsing forces, the oscillation amplitude of the cantilever is damped, which is used to control the tip-sample distance while the surface imaging is being performed [18]. Also the phase shift between the excitation signal and the cantilever's response is present and can be utilized to create a map of the energy dissipation which is related to the viscous and elastic forces [19–23]. This feature is very helpful when the non-homogeneities of the material should be investigated. An example of such a result obtained on the polymer film containing nanofillers is presented in Fig. 11.1a. This imaging mode can also be used as a source of information about the molecular structure of the material, such as  $C_{60}H_{122}$  alkane, when the topography data does not provide sufficient contrast (Fig. 11.1b).

It should be emphasized, however, that it is very difficult to distinguish the origin of the interaction responsible for the observed phase shift. Moreover, determining of the relation between the change of the specific property and signal's variations requires certain procedures and varies depending on some settings of the instrument. Therefore, the interpretation of the obtained results is challenging. Additionally, the

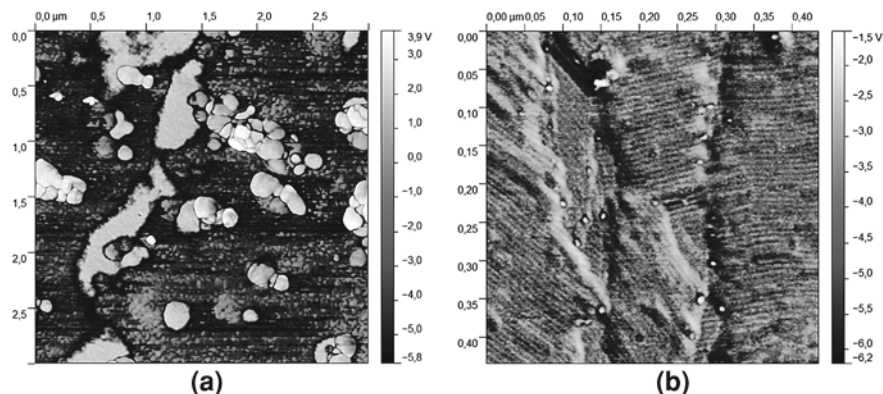


**Fig. 11.1** Examples of phase imaging maps revealing certain details invisible in topography images. Complex polymer film containing various compounds mixed up (a), molecular chains of the  $C_{60}H_{122}$  alkane deposited on mica substrate (b)

complexity of the tip-sample interaction phenomena can also be a source of misinterpretation resulting in imaging artifacts [17]. The best-known issue is the nonlinear dynamics effect causing the appearance of artifacts in the topography as well as in the phase image [24]. Although one can perform comparison procedures in order to establish some relation between the change of the properties and the system response, it cannot be used as an infallible approach in data analysis. Moreover, the response of the setup depends on settings of the detection system (e.g. tip oscillation amplitude, set-point,...). Therefore, performing all the measurements in precisely the same conditions in order to avoid any misinterpretation would be necessary. An example of unwanted features (artifacts) in phase imaging data is shown in Fig. 11.2, where the nonlinear dynamics effect introduced both: the instability in keeping the tip-sample distance constant as well as rapid phase shift changes. Consequently, one needs to analyze carefully the behavior of the measurement setup and the obtained results in order to avoid such situations. Concerning the number of above-mentioned drawbacks of the phase imaging feature, another approach basing on intermittent contact mode is needed. The alternative solution can be implemented using the detection of higher harmonic of the cantilever's oscillation.

In the remaining sections of this chapter we describe methods that enable acquisition and processing of the time-varying tip-sample force waveforms in intermittent contact AFM. The simple model to calculate the time-varying tip-sample force waveforms and the relation between those forces and the sample properties is presented. We also describe the way the reconstruction of the tip-sample force curve known also as the force spectroscopy curve is performed. The technical issues of the real-time signals processing in developed measurement system are also presented. Then an alternative method of utilization of the high-harmonics analysis as surface's stiffness mapping is described. Finally we present examples of the utilization of this method in mapping of mechanical properties of the surface.

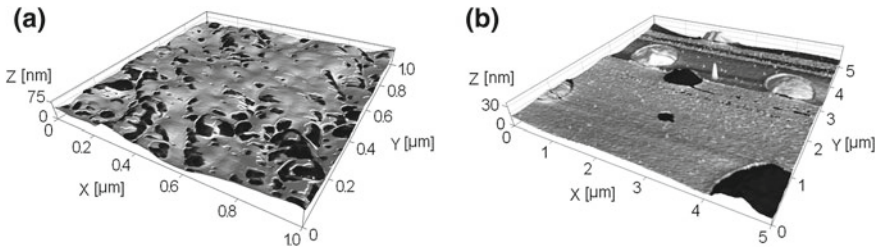


**Fig. 11.2** Examples of phase imaging artifacts presented as color palette on a 3D view of the topography. Transitions of the bistable tip-sample interactions (attractive and repulsive) cause the presence of jumps over several degrees as well as topography artifacts (a). Switching of the detection phase reverses the indication of the energy dissipation (b)

## 11.2 Time-Resolved Tapping Mode in Mapping of the Mechanical Properties of the Surface

Intermittent contact mode is one of the most popular AFM imaging techniques. Therefore, a number of theoretical and experimental studies of this method have been carried out and published [4, 5, 16–24]. Nevertheless, some specific phenomena and measurement solutions are in the field of interest of various research groups, including newly developed time-resolved tapping mode technique, which enabled high-resolution and high-speed mapping of the mechanical properties of the surface. As the principles of the tip-sample interactions in intermittent contact method are well-documented, in following subsections we focus on particular issues referring to the high-bandwidth tip-sample interactions detection and processing. In order to provide the impression of the differences between the typical tapping mode and the new approach, we present also the practical aspects of its implementation on commercially available AFM system, with typical cantilever’s deflection detection feature [25]. Implemented solution allowed to acquire some experimental data which are presented here in order to illustrate certain issues of the system’s development.

### 11.2.1 Modeling of Tip–Sample Interaction Forces in Intermittent Contact AFM

As during the scanning process the tip repeatedly presses the sample and retracts, a dynamically changing signal can provide much more information than the amplitude and the phase shift as deduced from typical intermittent contact mode. Figure 11.3 illustrates the relation between the distance–force curve and two dynamic phenomena: the cantilever’s oscillation and the tip-sample interaction forces curve. It can be noted that as the cantilever repetitively moves toward the sample and retracts, the tip senses the attractive and repulsive forces every cycle of the oscillation. As in the intermittent contact mode, the lock-in amplifier-based detection system allowed to detect only

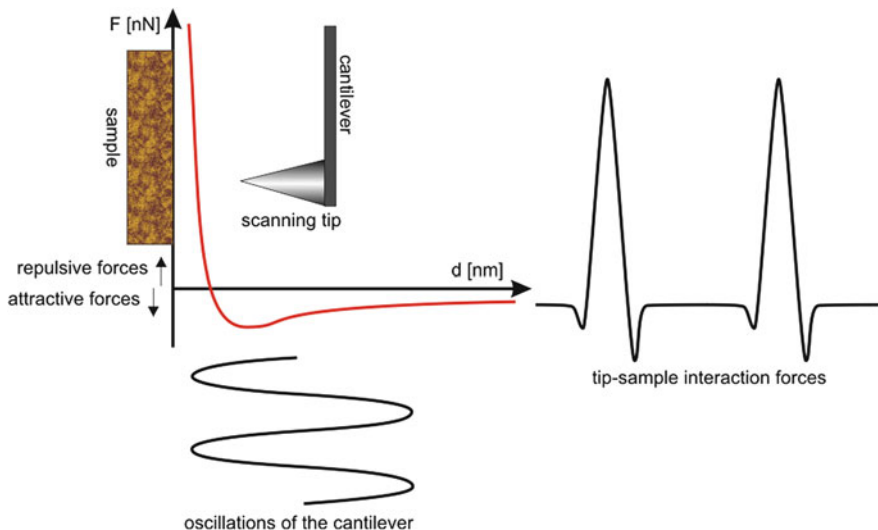


**Fig. 11.3** The tip-sample forces graph with correlated path of the cantilever’s oscillation and the tip-sample interaction forces caused by tapping of the tip against the surface. Some of the proportions have been disturbed in order to provide good readability of the curves

the amplitude and phase shift of the cantilever’s oscillation, the complex tip-sample interaction forces waveform was not accessible and remained unused. A specific approach was developed in order to obtain the access to this information and utilize it in terms of determining local mechanical properties of the surface.

Since most of the tip-sample interactions can be described with the Derjaguin–Muller–Toporov (DMT) model [26], one can see that dynamics of the force change along one tap cycle varies depending on the stiffness of the sample (Fig. 11.4). In order to verify the relation between the mechanical properties of the surface and the shape of the tip-sample interaction force curve, the modeling was performed.

Equations 11.1 and 11.2 were used to calculate time-resolved waveforms [27, 28].

$$F_{ts} = \begin{cases} -\frac{HR}{6d^2}, & d > a_0 \\ -\frac{HR}{6a_0^2} + \frac{4}{3}E^*\sqrt{R(a_0 - d)^{3/2}} + \left(-\frac{4\pi\gamma_{H_2O}R}{1 + d/h}\right), & d \leq a_0 \end{cases} \quad (11.1)$$

$$E^* = \left[ \frac{1 - \nu_{tip}^2}{E_{tip}} + \frac{1 - \nu_{sample}^2}{E_{sample}} \right]^{-1} \quad (11.2)$$

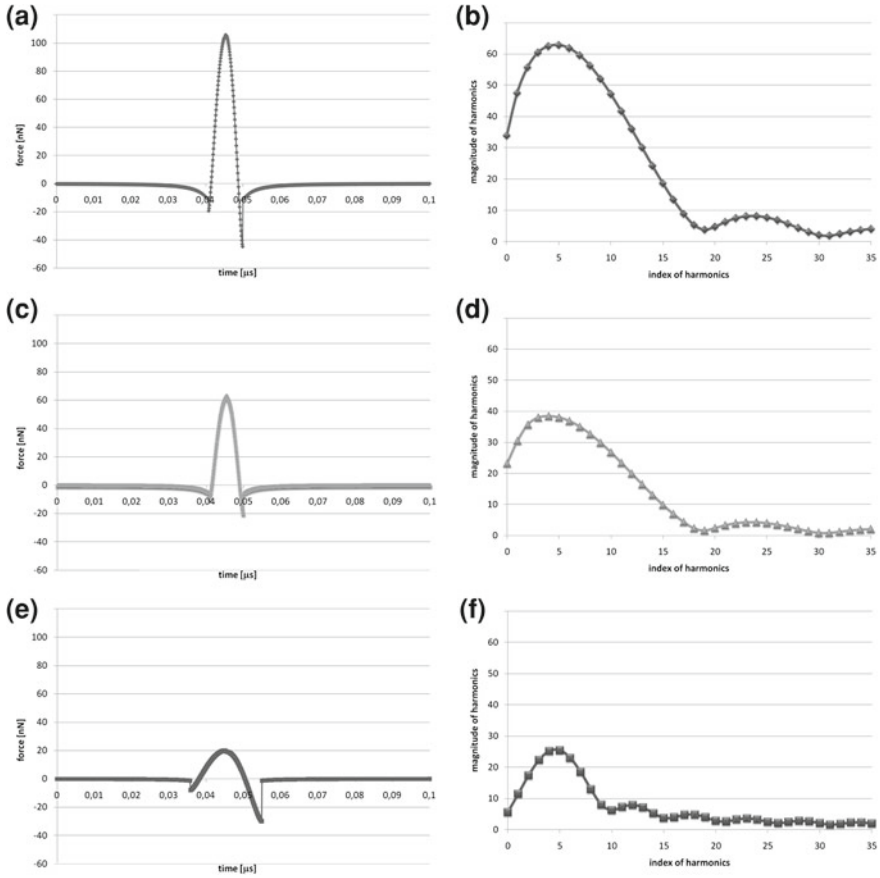


**Fig. 11.4** The results of the simulation of the tip-sample interaction during the tip oscillation, basing on the DMT model (a, c, e). The FFT transformation of the simulated graphs (b, d, f). The Young moduli of the surface used in the simulation are: 10 GPa (a, b), 5 GPa (c, d) and 1 GPa (e, f)

where:

$\gamma_{H_2O}$  is the liquid–vapor interfacial energy of water,  $E^*$  is the effective elastic modulus between the tip and the sample system,  $d$  is the tip-sample gap,  $a_0$  is the intermolecular distance and  $h$  is thickness of the water film.

Also the variables were used: the driving frequency, which is chosen close to the fundamental frequency of the cantilever  $f_0 = 50$  kHz, Young modulus of the tip  $E_t = 130$  GPa, Young modulus of the surface  $E_s = 1, 5$  and  $10$  GPa, respectively, radius of the tip  $R = 20$  nm, Poisson’s ratio respectively tip and sample  $\nu_t = \nu_s = 0.3$ , spring constant of the cantilever  $k_c = 40$  N/m, quality of the cantilever’s resonance  $Q = 400$ , Hamaker constant  $H = 7 \times 10^{-12}$  J.

Figure 11.4 presents the time-force graphs calculated using the formula (11.1). It can be noted that, as the stiffness of the sample  $E_s$  increases, the slope of the tip-sample interaction force increase becomes steeper.

As the intermittent contact mode bases on periodic oscillations of the cantilever, its movement influenced by the tip-sample interaction can be represented using frequency-domain methods. These methods will be mostly important for the signal analysis described in the next sections.

The tip-sample force  $F_{ts}$ , can be represented as a Fourier series:

$$F_{ts}(t) = \sum_{n=0}^{\infty} a_n \cos(n\omega t) + b_n \sin(n\omega t) \quad n = 0, 1, 2, \dots \quad (11.3)$$

where  $\omega$  is the driving frequency, as previously mentioned, near to the resonant frequency of the cantilever. The coefficients can be expressed:

$$a_n = \frac{\omega}{\pi} \int_0^{\frac{2\pi}{\omega}} F_{ts} \cos(n\omega t) dt \quad (11.4)$$

$$b_n = \frac{\omega}{\pi} \int_0^{\frac{2\pi}{\omega}} F_{ts} \sin(n\omega t) dt \quad (11.5)$$

Therefore the  $n$ th harmonic of the signal can be described as follows:

$$F_{ts_n} \cos(n\omega t + \theta_n) = a_n \cos(n\omega t) + b_n \sin(n\omega t) \quad (11.6)$$

where  $F_{ts_n} = \sqrt{a_n^2 + b_n^2}$  and  $\theta_n$  are magnitude and phase of the  $n$ th harmonic force. Therefore, the movement of the tip can be analyzed as a superposition of harmonic forces and the utilization of harmonics measurement can be a source of information about the stiffness of the sample [29].

In order to provide one equation describing the steady state dynamics of the tapping cantilever in terms of analysis of the balance of the total harmonic force (driving force plus the first harmonic of the tip-sample force), the vibration amplitude, and phase, Sahin et al. developed formula, showing that these resonant harmonics are sensitive to variations of the mechanical properties of the material [30]. Moreover, by performing a series of measurements, Sahin et al. showed [31], that independently measured time-varying tip-sample forces quantitatively satisfy the steady state equations for the cantilever dynamics described by Eq. (11.7).

$$F_T e^{i[\omega t + \beta(\omega)]} = F_D e^{i[\omega t + \phi]} + F_{ts1} e^{i[\omega t + \theta]} \quad (11.7)$$

which can be described as follows:

$$K_1 A_S T(\omega) e^{i\beta(\omega)} = K_1 A_0 T(\omega) e^{i\phi} + F_{ts1} e^{i\theta} \quad (11.8)$$

where:

$$\tan[\beta(\omega)] = \frac{\frac{\omega\omega_0}{Q}}{\omega^2 - \omega_0^2}, \quad \beta \in \{0, \pi\} \quad (11.9)$$

$$T(\omega) = \left\{ 1 - \left( 2 - \frac{1}{Q^2} \right) \left( \frac{\omega}{\omega_0} \right)^2 + \left( \frac{\omega}{\omega_0} \right)^4 \right\} \quad (11.10)$$

$$F_{ts1} e^{i\theta} = \frac{\omega}{2\pi} \int_{\frac{2\pi}{\omega}} f_{ts}(t) e^{-i\omega t} dt \quad (11.11)$$

and  $F_T$ ,  $F_D$ , and  $F_{ts1}$  are the magnitudes of the total harmonic force, driving force, and the first harmonic of the tip-sample force, respectively,  $\omega$  is the drive frequency,  $\omega_0$  is the resonance frequency,  $Q$  is the quality factor of fundamental resonance,  $K_1$  is the effective spring constant of the fundamental flexural mode,  $A_0$  is the free vibration amplitude,  $A_s$  is the vibration (set point) amplitude,  $\phi$  is the phase difference between the driving force and the cantilever motion (reference),  $\theta$  is the phase difference between the driving force and the first harmonics.

### 11.2.2 Extraction of the High Bandwidth Oscillation of the Cantilever

In order to provide appropriate conditions for the measurement of the high bandwidth phenomena, the detection system should respond linearly, without major distortions. Otherwise, the acquired signal is useless, as every frequency is attenuated or amplified in a different way. Figure 11.5 shows two responses of the HMX cantilever from Bruker AXS Inc. (Madison, WI, USA): (a) flexural and (b) torsional response (Fig. 11.5a, b, respectively). As the torsional response allows one to obtain only slightly distorted signal with nicely visible harmonic frequencies, it proves its usability in detecting the tip-sample interactions during every cycle of the oscillation. The flexural response, however, allows to detect only the base frequency along with very few higher harmonics of the signal. Therefore, it is useful only in an intermittent contact mode setup, where the base frequency response is utilized. The visible bending of the detected signal spectrum is connected to the properties of the electronic detection setup (3 dB cutoff frequency) and to some extent can be compensated relatively easy. Some measurement systems have relatively wide plateaus of the detection bandwidth, therefore further signal processing does not require any compensation of the band reduction [29].

The mechanical response of cantilevers with rectangular cross-section shapes can be calculated using the Euler–Bernoulli equation [24]. The first resonance frequency

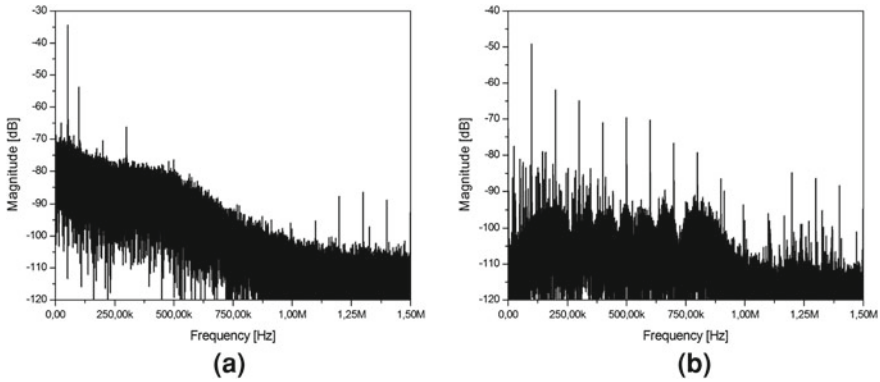


**Fig. 11.5** Vibration spectra of a HMX cantilever measured in an intermittent contact mode AFM. The excitation signal is equal to the fundamental resonance frequency. The flexural response (a) contains only few frequencies due to the specific behavior of the cantilever, while the torsional response (b) shows a wide spectra of frequencies

in torsional direction is about 20 times the flexural base frequency (Fig. 11.6). Therefore, the above-mentioned condition of the linear response of the cantilever can be achieved that way. This approach was proposed by Sahin et al. [29, 30, 32]. As a consequence of this solution one must assume that in the case of a typical cantilever, when the tip is placed on the symmetry axis of the cantilever, the bending momentum is too small to cause sufficient torsional bending of the cantilever in order to provide reasonable signal detection. Therefore, Sahin et al. designed a series of cantilevers applicable for torsional bending [33–35] (Fig. 11.7). Recently the T-shaped cantilevers have become a commercially available product (Table 11.1). Another method of the longitudinal resonance frequency increase was proposed by Sarioglu et al. [36, 37]. The developed finger-like micromachined cantilever and differential interferometric measurement of the oscillation allowed one to obtain very high sensitivity of the force detection. It requires, however, utilization of a specific signal detection setup. Moreover, as the design of the probe is relatively complex, one can expect that the price would also be considerably higher than in the case of T-shaped cantilevers.

In order to detect the torsional signal in the case of the T-shaped cantilevers, typically quadrant photodiodes are used. As for the detection of the flexural oscillations the top–bottom pairs of sections are used, the torsional oscillations can be detected using the left–right pairs of the detector (Figs. 11.7 and 11.8). A similar approach is applied in case of friction force microscopy (FFM) [38] known also as lateral force microscopy (LFM). One should, however, take into account that due to the specific application of that detection channel, its bandwidth can be significantly reduced in order to provide a low noise level when FFM is active. Therefore, this issue should be verified if one is intend to implement the described solution in a commercially available AFM system.



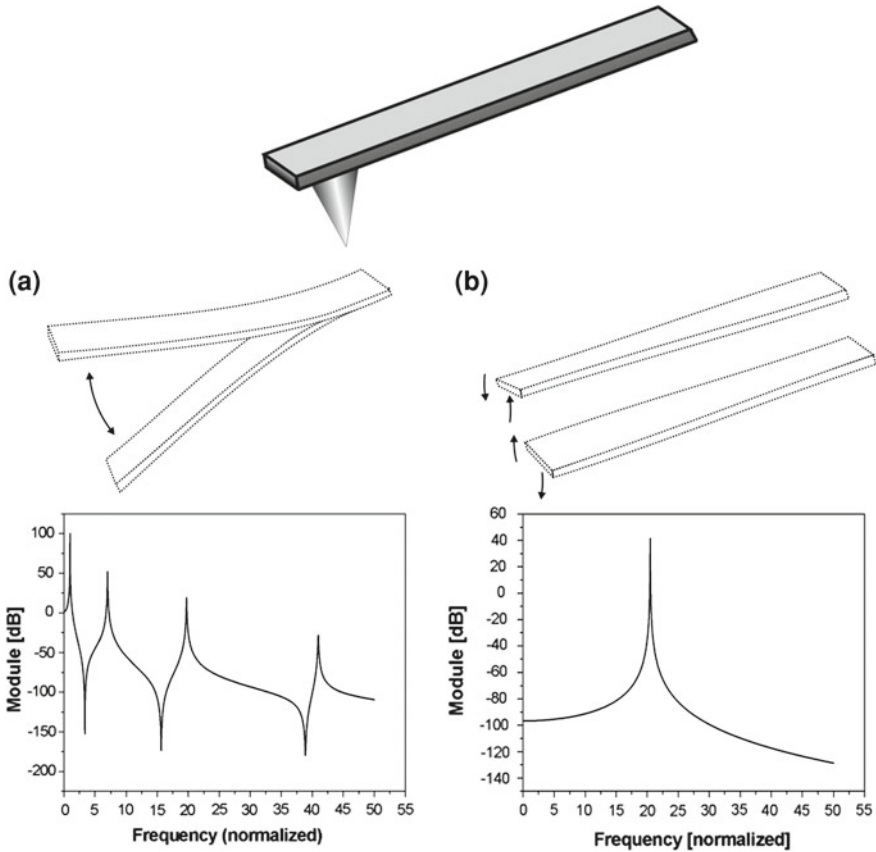


**Fig. 11.6** The flexural (a) and torsional (b) oscillation modes of a rectangular cantilever. Frequency responses calculated using Euler-Bernoulli equation [10] for both oscillation modes, respectively

**Table 11.1** The list of commercially available T-shaped cantilevers and their specifications

Manufacturer	Name	$f_0$ (kHz)	$f_{tr}/f_{fl}$	$k^*$ (N/m)	Length ( $\mu\text{m}$ )	Width ( $\mu\text{m}$ )	Thickness ( $\mu\text{m}$ )
Bruker	HMX	60	17	4,0	300	25	4
Bruker	HMX-S	40	17	1,0	300	25	3
MicroMasch	TL01	90	10	2,0	180	20	2
MicroMasch	TL02	60	17	3,0	300	20	5

### 11.2.3 Recovering the Time-Varying Interaction Signal of the Tip-Sample Forces

Although the torsional bending of the T-shaped cantilever enables convenient detection of the high-bandwidth waveform of the tip-sample interaction, it should be underlined, that signal processing is necessary as one expects to recover the shape

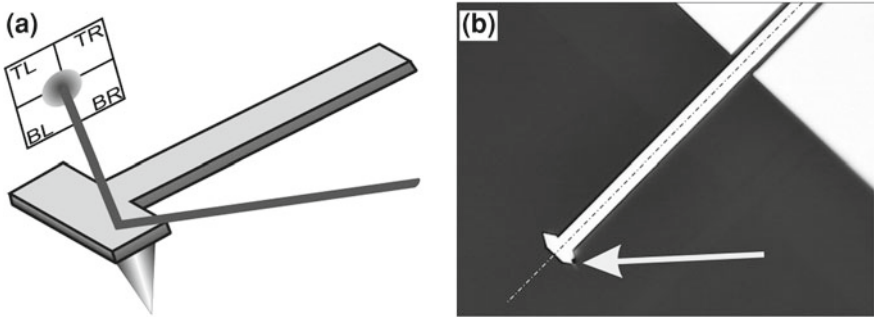


**Fig. 11.7** A typical setup for the optical detection of the cantilever's bending (a). The  $(TL + BL) - (TR + BR)$  signal is used for the detection of the flexural bending,  $(TL + TR) - (BL + BR)$  signal is used for torsional bending detection. The optical microscope view of the HMX cantilever (b). The arrow points at the location of the hammer-shaped end of the cantilever with the asymmetrically placed tip

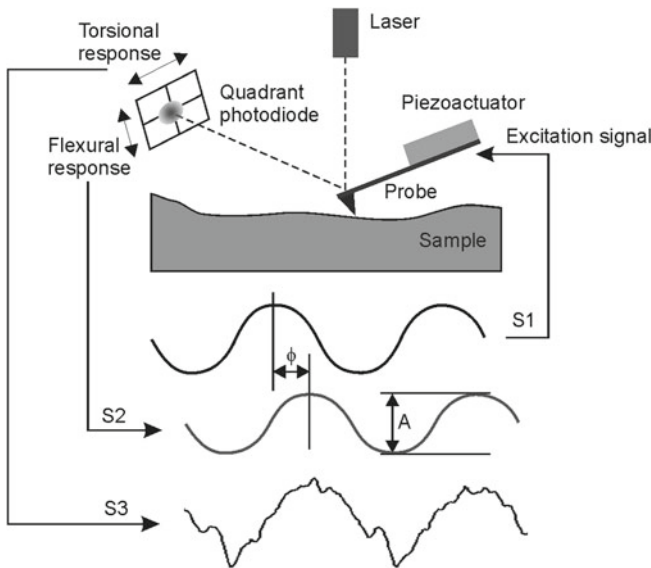


**Fig. 11.8** The principles of the detection system and the acquired signals. Signals: S1, excitation; S2, flexural response; S3, torsional response. The amplitude  $A$  is used for keeping the tip-sample distance constant, while the phase shift  $\phi$  is used for energy dissipation imaging

allowing to perform further interpretation. Figure 11.9a represents both: vertical and torsional signals acquired at the four-quadrant photodiode [5]. As explained before, the vertical signal contains very few harmonics, with major fraction of the base resonant frequency of the cantilever. Therefore, this waveform cannot be used in extracting of the tip-sample interaction curve. The torsional signal, however, is more complex, and after some filtering steps it can enable access to desired informa-

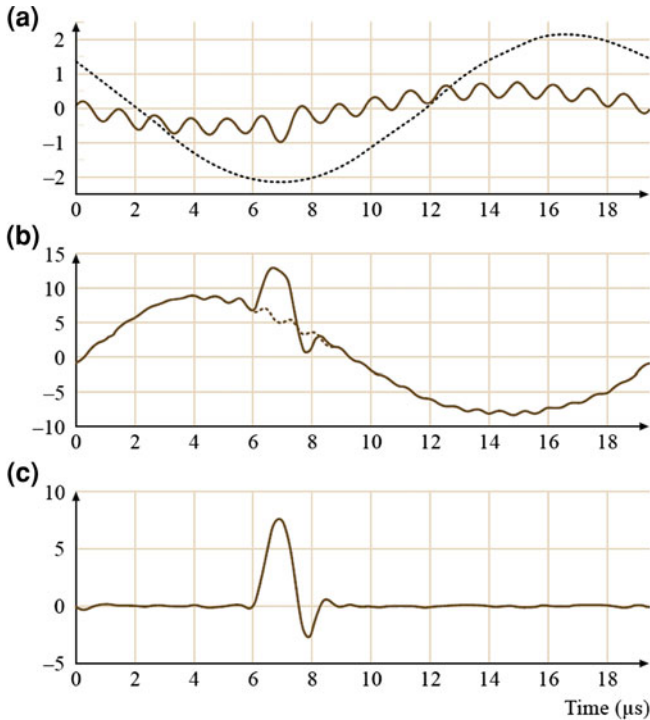


**Fig. 11.9** Vibration signals from flexural and torsional motions, and tip-sample forces. **a** The signals at the four-quadrant photodetector for vertical and torsional displacement. The *solid curve* is the torsional signal. The torsional signal was multiplied by a factor of 10 to provide clear view of both curves in one graph. **b** The torsional vibration signal after being divided by the torsional frequency response. Except for the pulse located between the 300 and 400th time steps, the tip-sample forces should have been close to zero, because the tip is far away from the surface at those times. The measured signals when not in contact come from crosstalk from the flexural deflection signal. The *dashed curve* estimates the error introduced by these curves. When it is subtracted from the *solid curve* one gets the time-varying forces plotted in **c** [5]

tion. It should be noted, that even though the special T-shaped cantilever is utilized, the torsional signal is still much smaller than the vertical one, therefore the detection (ADC conversion) feature must provide appropriate sensitivity and resolution. Additionally, special effort must be taken in order to obtain the signal–noise ratio high enough to provide the acquisition of legible waveforms that could be interpreted.

Once the torsional signal is divided by the torsional signal response (Fig. 11.9b), one can observe the shape containing the tip-sample interaction feature that was obtained during the simulation. The rest of the waveform does not contain any useful data as the tip is away from the surface and the interaction force is nearly zero. One can, however, notice presence of waviness of the curve, which is caused by the crosstalk signal (the harmonic of the flexural base frequency of the cantilever), which has to be removed. Also the base frequency of the torsional oscillations of

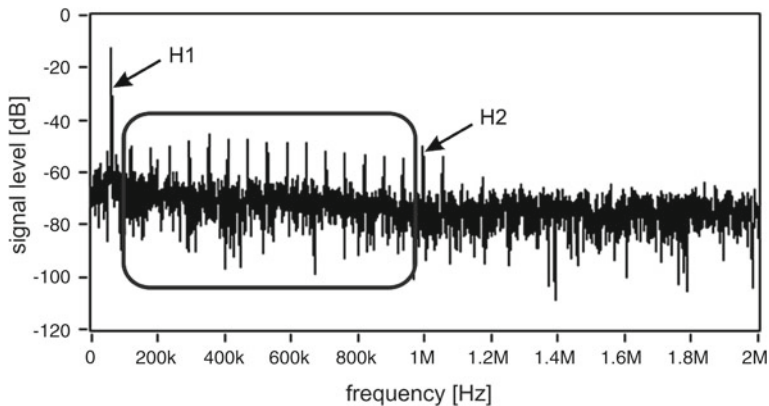


**Fig. 11.10** The spectrum of the torsional oscillation of the cantilever after primary deconvolution process. The harmonics marked with H1 and H2 should be removed, the marked group of the harmonics are useful for the interaction signal recovery

the cantilever is undesired feature. Those frequencies can be filtered out relatively easily by applying the FFT filtering (Fig. 11.10). Finally, the time-varying tip-sample interaction waveform is obtained (Fig. 11.9c). Various signal processing approaches were described in detail by Sahin et al. [29, 30, 33, 34] and Stark et al. [39].

It should be emphasized, that the stage of the signal processing is the most complex task in development of the technique, as the filtering should provide extraction of certain signals without losing any relevant information. Therefore, advanced tools are utilized in order to obtain the optimal results in terms of filtering quality and the process efficiency. The most popular way is the implementation of the procedure including conversion of the waveform into the frequency domain (FFT), and then elimination of unwanted frequencies (Fig. 11.10) and obtained data converting back into the time domain (Inverted FFT). Legleiter et al. presented solution, where the cross talk and high background noise was removed with advanced software tools like comb filter and spectral filtering [40]. Sahin applied the least square-fitted waveform filtering in order to remove the unwanted components of the signal [32]. Quite different approach based on direct observation and interpretation of the oscillation signal was presented by Sarioglu and Solgaard [36]. It was however, possible as their setup introduced much less distortion than in case of T-shaped based solution.

Once the tip-sample interaction curve is acquired, it is processed in order to obtain a reconstruction of the force-distance curve. In order to obtain that, the dividing of the waveform must be performed, as each peak has to be in separated dataset. Eventually, on each dataset, the stitching like operation must be done, as the spectroscopy curve contains two lines related to the decrease and increase the tip-sample distance. In order to provide the best possible result of the curve reconstruction, the DMT model fitting can be implemented as one of the last steps.

As the developed NanoSwing setup [25] allowed to extract certain data during following signal processing steps, the selected stages are illustrated in Fig. 11.11.

The direct signal from the photodiode (Fig. 11.11a) is acquired, and the FFT as well as the comb filtering is performed to remove unwanted components of the signal (Fig. 11.11b). Eventually as the tip-sample force interaction waveform is available, the algorithm performs dividing the signal into sections (dividing lines—“d”) and the stitching operation is carried out (Fig. 11.11c). The stitching points “s” are related to the highest values of the tip-sample interaction force. Finally, the reconstructed force spectroscopy curve is available, containing approach and retract parts (Fig. 11.11d). It should be underlined, that unlike in typical force spectroscopy measurement, in time-resolved tapping mode the cantilever’s movement is driven with the sinusoidal waveform. Therefore, additionally, the linearization of acquired response is necessary in order to avoid the distortions of reconstructed curve. As the tip-sample contact event occurs with the frequency typical for certain cantilever (Table 11.1), which is in range of 50–90 kHz, the averaging of obtained curve is possible. Typically one can define the number of averaged curves in range of few to few hundreds. One must be aware that the reconstructed force-distance curve obtained with the time-resolved tapping mode and the typical force spectroscopy measurement procedure can differ due to imperfections of the processing algorithms as well as differences in dynamics of various phenomena as for instance the adhesion [41–43]. It should be mentioned, that there are AFM systems with such functionality commercially available [44].

It should be mentioned, that during preparation of the AFM system for the measurement procedure, certain factors should be taken into account. Because the quality of the force spectroscopy curve reconstruction is essential, the tip-sample interaction signals must be at an appropriate level. Therefore, one should be able to verify key steps of the reconstruction process. As the number of analyzed harmonic frequencies has a direct impact on the amount of processed data, one should be able to observe the real-time behavior of the signal’s spectra. Due to varying properties of the probes, it is also important to adjust the detection frequency range that is considered to be useful in a certain case. By displaying the time-resolved tip-sample interaction signal one can verify, if the filtering feature is adjusted properly and the shape of the curve meets the expectation of the operator. Finally, the real-time view of the reconstructed force-distance curve allows one to verify if the tip-sample interaction is stable and allows one to perform the measurement. As the amount of the oscillations is relatively high, the averaging feature allows reducing the noise. The number of the averaged periods of the cantilever’s oscillation should also be adjusted carefully.

Appropriate mapping of the mechanical properties of the surface is much more challenging than usual topography measurement in intermittent contact mode. The major settings: the free oscillation amplitude of the cantilever and the setpoint must be chosen very carefully. Figure 11.12 presents three cases, where, by changing the setpoint, we were able to adjust the tip-sample interaction in order to modify the response of the cantilever and, eventually, to observe changes in the reconstruction result. As the setpoint is too high (93 % of free oscillation amplitude), the interaction is too weak and one can see very few harmonics or too low level of the signal. The reconstruction in such case is possible, however, due to insufficient tip-sample interaction in the repulsive forces area, the stability of interactions is not satisfying and the stiffness of the surface cannot be estimated correctly. The appropriate value

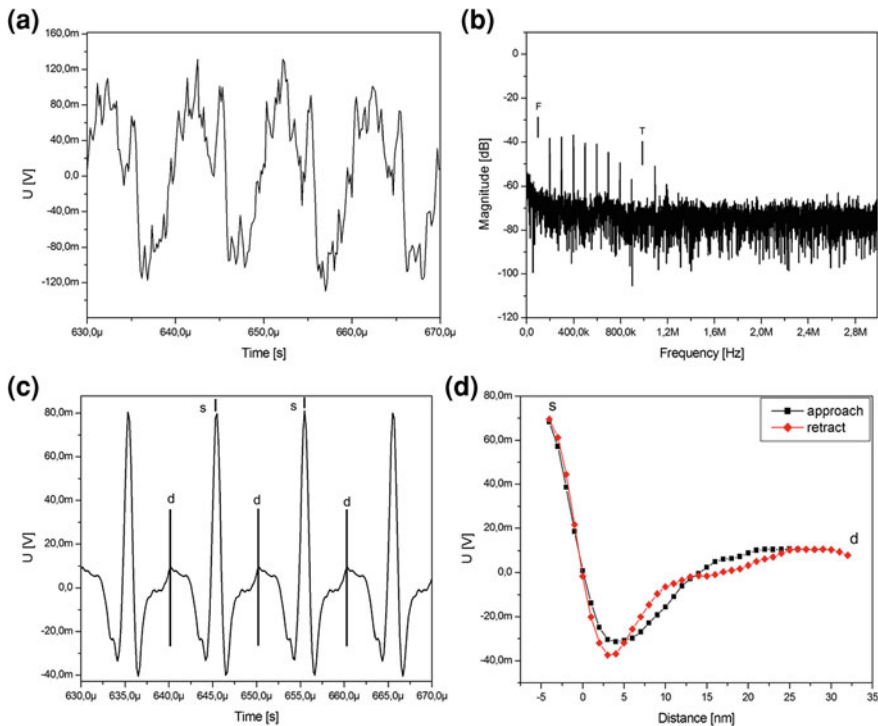


**Fig. 11.11** Following steps of the force curve reconstruction: raw signal (a), FFT spectrum of the signal after removing the harmonics related to flexural and torsional base frequencies of the cantilever (b), time-domain interaction signal with marked dividing lines “d” and central points for stitching operation “s” (c), distance domain force spectroscopy curve with marked dividing ends “d”, and central point for stitching operation “s” (d)

of the setpoint (70 %) allows one to perform the scanning process with desired quality of the obtained maps. It can be noted that apparently insignificant differences of the signal spectra in the first two cases, have a severe impact on the final result. On the other hand, a too small value of the setpoint (40 %) causes permanent damping of the torsional oscillations of the cantilever and precludes the reconstruction of the force-distance spectrum. Such behavior is not observed in the intermittent contact mode, as the scanning process can be successfully performed in a much wider range of setpoint values. Although one must be aware of possible consequences, such as surface modification or tip contamination, it is possible to obtain still a correct topography image. Therefore, utilization of the time-resolved intermittent contact mode requires much more attention and expertise.

In order to estimate the range of the setpoint values that can be applied to obtain a correct force spectroscopy reconstruction, its impact on the Young modulus estimation was investigated. As this method was designed to visualize the non-homogenous materials, the relation was verified for two materials present on

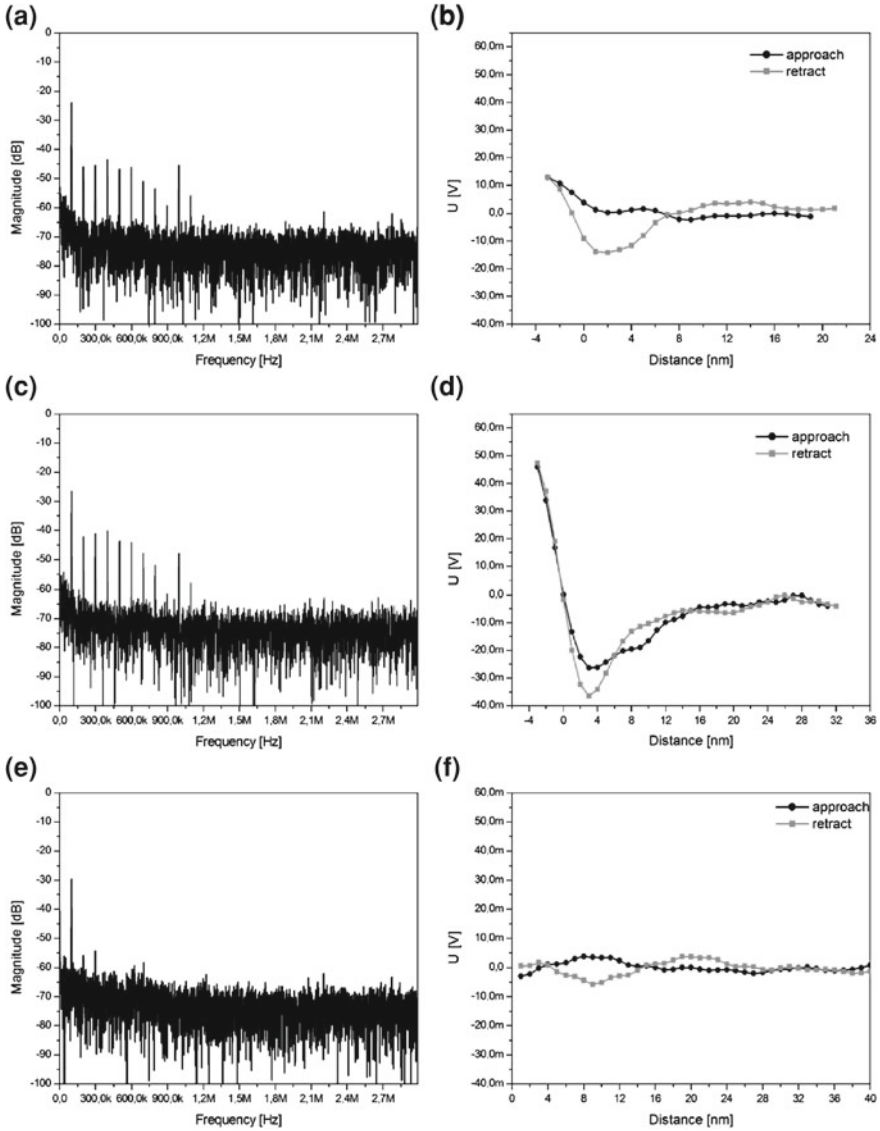


**Fig. 11.12** Examples of the force spectroscopy reconstruction quality for various setpoint values (**b, d, f**) and the correlation to the FFT spectra used as an indicator of the tip-sample interaction (**a, c, e**). The setpoint values were as follows: 0.93 (**a, b**), 0.7 (**c, d**), and 0.4 (**e, f**) with a free oscillation amplitude  $A_0 = 18$  nm

the test sample used in the previous section. The obtained results are presented in Fig. 11.13. Fixing the setpoint within the range 0.58–0.81 allowed us to acquire stable readouts for both materials. As presented above, too high or too small values

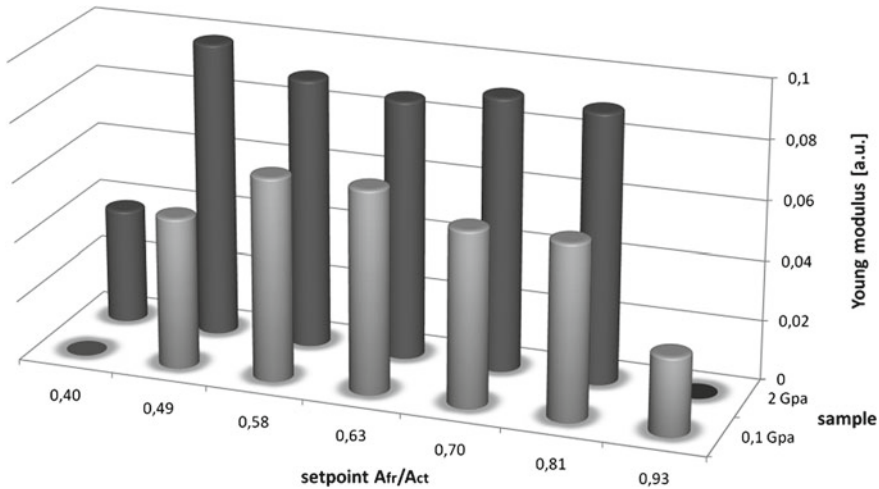


**Fig. 11.13** Comparison of the Young moduli as a function of the setpoint value. Free oscillation amplitude  $A_0 = 18$  nm

of the setpoint can lead to incorrect determinations of the properties of the surface. Therefore, one should verify the response of the measurement system, if the applied scanning factors provide reliable signal processing.

The oscillation amplitude of the cantilever also determines the way the reconstruction is performed. When too small amplitudes are applied, the tip is not retracted far enough from the surface to acquire a full force–distance curve. On the other hand, too large amplitudes can cause tip and surface wear as well as an introduction of significant errors of the reconstruction due to utilization of a wrong interaction model as the tip would indent the surface much deeper than previously assumed. As the use of torsional harmonic cantilevers in the tip-sample interactions detection is a very complex problem, it was analyzed both theoretically and experimentally [45–48].

The additional advantage of the force spectroscopy reconstruction observation is the ability of tip contamination detection. While in intermittent contact mode one can perform the measurements with a contaminated tip, it is very difficult to obtain the force spectroscopy curve in such a situation. Therefore, the probability of the presence of topography artifacts can be significantly reduced.

### ***11.2.4 Mapping of the Mechanical Properties Basing on Advanced Signal Processing***

After the force spectroscopy curve is reconstructed, it can be analyzed by software in order to determine following mechanical properties: stiffness, peak force, adhesion, energy dissipation for deformation, and energy dissipation for tip-sample separation.



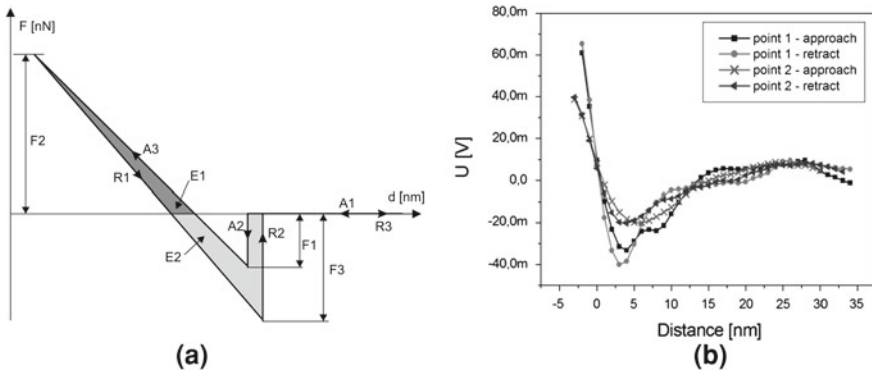


**Fig. 11.14** Typical force spectroscopy curve and the related mechanical properties of the surface (a). The parameters are: F1, snap-in force; F2, peak force; F3, adhesion. R1 (slope), elasticity; E1, energy dissipation for deformation; E2, energy dissipation for tip-sample separation. Two reconstructed force spectroscopy curves measured in different areas of the test sample (b)

The relation between the listed properties and the shape of the reconstructed force spectroscopy curve is shown in Fig. 11.14.

As the tip approaches the surface (A1), it can experience attractive forces, the snap-in event (A2), and then repulsive forces (A3). During retraction (R1) the repulsive forces decrease and again the attractive forces are present up to the snap-off moment (R2). During such cycle one can observe changes of all presented sections of the curve. Therefore, their determination and mapping is essential. Two reconstructed force spectroscopy curves are presented in order to show the differences of various details. By continuous signal acquiring, filtering, processing, and analyzing, one can perform the mapping of the mechanical properties of the sample. The example of the obtained maps is presented in Fig. 11.15. Additionally, the topography as well as the phase imaging map are shown in order to correlate all available data. The measurement was performed in ambient conditions ( $T = 26^\circ\text{C}$ ,  $\text{RH} = 32\%$ ) at a scanning speed of 0.3 Hz.

In order to observe the efficiency of the imaging mode, a commercially available test sample [25] was used: a blend of polystyrene (PS) and polyolefin elastomer (ethylene-octene copolymer) deposited on a silicon substrate with a spin-cast method. The PS regions of the sample have elastic modulus value approximately 2 GPa, while the copolymer regions have elastic modulus value approximately 0.1 GPa. Such a range of stiffness values on the same surface allowed to clearly show the difference of the system's response for various values of the Young modulus.

The interpretation of the results is intuitive, as the brightness of the map represents higher values of certain parameters. Although one may guess that all maps are qualitatively identical, but the distribution histograms presented in Fig. 11.16 show significant differences between most of the properties.

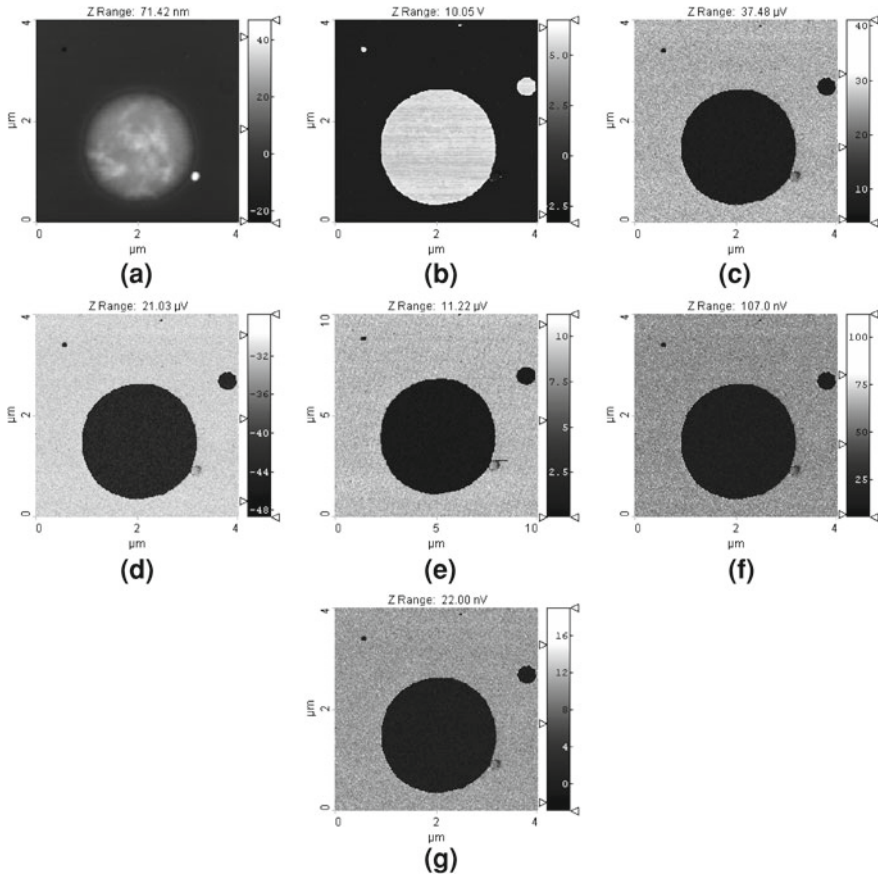


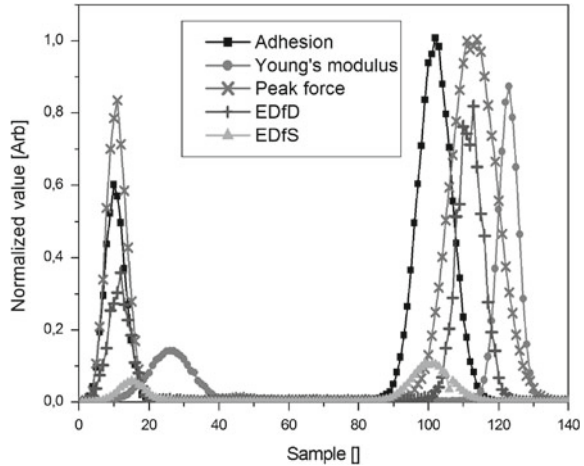
**Fig. 11.15** The results of scanning of the test structure: topography (a), phase imaging (b), adhesion (c), stiffness (d), peak force (e), energy dissipation for tip-sample separation (f), and energy dissipation for deformation of the surface (g)

The presented data are no absolute values, it is, however, possible to calibrate the system in order to provide specific information about the values of the forces, the stiffnesses, or the energies.

As one expects to obtain quantitative information, the relation between the real tip-sample force and its electrical representation in the measurement system must be established. The formula correlating the corrected voltage waveform  $V_{TC}$  acquired at the photodiode and the tip-sample forces can be written as follows [49]:

$$V_{TC}(\omega) = \frac{\omega_T^2 - \omega^2 + \frac{i\omega\omega_T}{Q_T}}{\omega_T^2} V_T(\omega) = c_{\text{optical}} \frac{d}{k_T} F_{TS}(\omega) \quad (11.12)$$

**Fig. 11.16** The comparison of spectrum histograms from Fig. 11.20



where the  $\omega_T$  and  $Q_T$  are torsional resonance frequency and quality factor are denoted, respectively,  $k_T$  is a torsion constant of the first torsional mode, defined as the angular deflection for a unit torque around the long axis of the lever,  $d$  is an offset distance from the longitudinal axis of the lever,  $c_{\text{optical}}$  is the detector signal for a unit torsional deflection angle,  $V_{T(w)}$  is the Fourier transform of the detector signal  $v_T(t)$ . The frequency response of the detector can be neglected if is properly compensated, or the cutoff frequency is well above the harmonic frequencies. As one can note, in time domain both waveforms  $V_{TC}$  and  $F_{TS}$  has the same shape within scalar factor.  $V_{TC}$ , however, still remains in electrical unit. Therefore, it has to be determined.

Typical routine based on determining the cantilever's deflection detection sensitivity and the cantilever's spring constant [44] is similar to the procedure performed in typical force spectroscopy measurements, when contact cantilevers must be evaluated (thermal tuning feature implemented in AFM software). Additionally, the tip radius must be determined in order to calculate properly the Young modulus. In order to obtain such data, one can use high resolution electron microscopy or perform the blind reconstruction of the tip's shape [50, 51]. However, this solution is time-consuming, it was successfully utilized by Ihalainen et al. [52] in determination of mechanical properties of pigment-latex coated paper samples.

An alternative method, is utilization of the reference sample, where at least two well-defined components can be measured [44]. Lanniel et al. used reference surface of polystyrene and low density polyethylene thin film, knowing that the stiffness of the polystyrene sample is 1.6 GPa [53]. As the response of the system is linear [54], one can extrapolate the response of the measurement system within the range of the Young modulus values related to the spring constant of the cantilever. For instance, the HMXS and HMX cantilevers can properly measure the values from 0.5 MPa to 1 GPa and from 10 MPa to 10 GPa, respectively. Below and beyond this range, one can perform successfully imaging of the mechanical properties, however, the estimation of the certain values can suffer very low accuracy. The reference sample-

based approach is less effort-consumable, however, one must be aware, that the mechanical properties of the sample can vary with time as well as the environmental conditions. Therefore, it should be verified periodically, as every standard or reference sample. In order to do that, one can perform typical force spectroscopy measurement, or to calibrate time-resolved tapping mode system as described above and then to scan the sample in order to compare expected and measured values.

### ***11.2.5 The Principles of the Measurement Setup***

Although only few commercial AFM systems were designed to utilize the T-shaped cantilevers [44], the detection of the torsional bending of the cantilever can be performed in a number of commercially available and homemade setups. As mentioned above, the only condition is an access to the raw left–right signal of the quadrant photodiode detection module. Due to requirement of a high-bandwidth, the minimum amount of filters and other signal processing/adapting modules are recommended before signal acquisition, as every such an object can introduce distortions.

In order to develop the time-resolved tapping mode with detection of the torsional bending of the T-shaped cantilever, commercially available AFM system working in typical tapping mode was used [25]. Therefore, some modifications were necessary in order to perform experiments described in following sections. The access to the high-bandwidth  $(TL + TR) - (BL + BR)$  signal was obtained by changing a few internal connections in the scanning head. Additionally, the synchronizing signal from the AFM controller was used to connect an auxiliary computational unit providing A/D signal conversion, data acquisition, processing, and storage (Fig. 11.17). The role and importance of the synchronization of the modules involved in the measurement process will be explained in the last section of this chapter. As the performance of the signal processing is essential, commercially available real-time signal acquisition and data processing unit was utilized. The data processing algorithms were developed using commercially available graphical programming environment. This solution provided useful tools and processing modules in order to develop the software quickly and flexibly. The correctness of the scanning head's modifications could be verified with an oscilloscope (Fig. 11.18) when the torsional signal was observed. One can see the complex waveform of the signal as well as its Fast Fourier Transform revealing presence of the expected high-order harmonic frequencies. It is distinctive that only odd multiple values of the driving frequency are present in the spectrum.

One should be aware that processing of wide-bandwidth signals requires utilization of a high-speed analog–digital converting unit. As typically one can observe the presence of the relevant harmonic frequencies up to 1 MHz, the converter should provide at least 2 Ms/s sampling ratio according to Nyquist-Shannon-Kotelnikov criteria. Practically, however, the signal processing provides better accuracy when 4 or even 10 Ms/s sampling ratio is utilized [25]. Also the resolution and the input voltage range of the converter are crucial, as the signal rarely exceeds 400 mV peak-peak value.

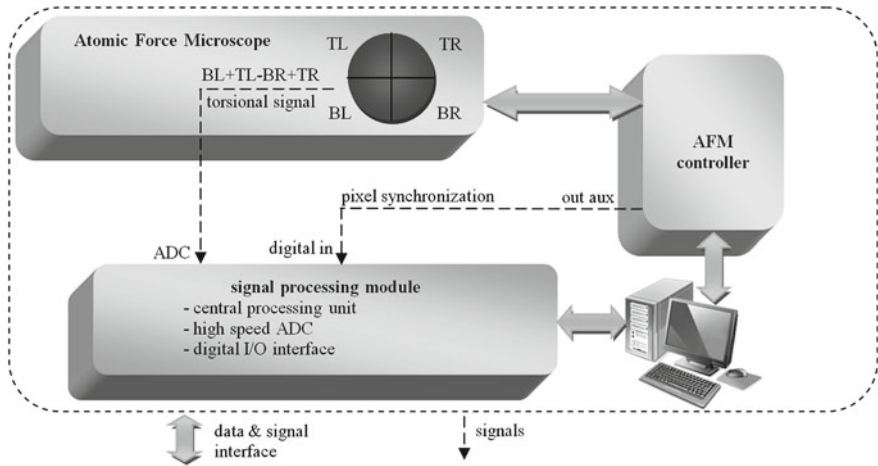


**Fig. 11.17** Simplified diagram illustrating the hardware configuration of the detection setup to measure the torsional bending of the cantilever

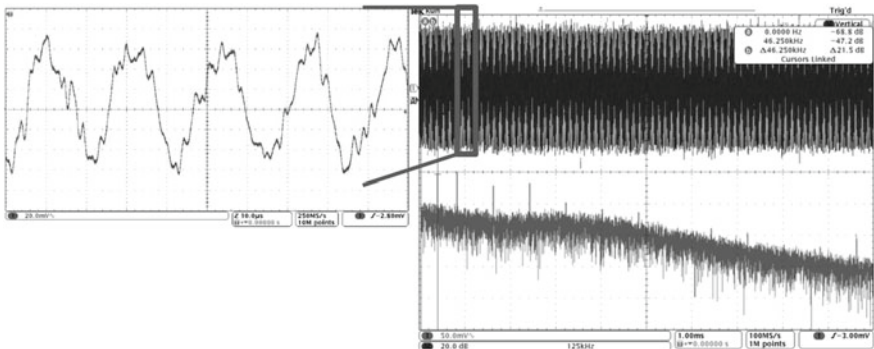


**Fig. 11.18** The torsional response signal in time and frequency domain as acquired directly from the optical detection system. The complexity of the signal as well as the high-order harmonics are clearly visible

### 11.2.6 Signal Acquisition and Processing Issues in Terms of the Algorithm's Efficiency Demands

As the data acquisition and processing unit should work simultaneously with the AFM controller, it is essential that every cycle of the signal processing is performed within certain time limits. When the development of the AFM system is planned, one of the most important issues is the synchronization of the central unit and the auxiliary computational device. The problems with fulfilling those conditions can lead to improper image creation and the presence of the artifacts [40].

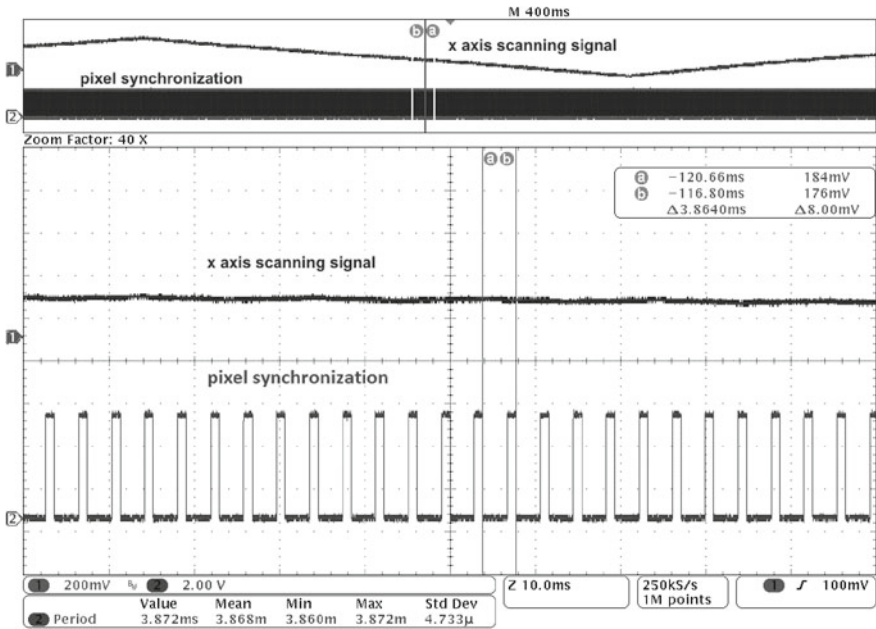


**Fig. 11.19** View of the signals present in the AFM system. The fast scanning signal (X axis) and the pulse synchronization signal are necessary to simultaneously work with the AFM controller and the auxiliary computational unit. The signals were obtained during scanning with 0.6 Hz scanning speed and  $512 \times 512$  resolution

In the case of utilized commercial system [25], the synchronizing signal is available, which delivers the electrical pulse at every single acquired pixel (Fig. 11.19). Therefore, it is possible to provide precisely the same data acquisition timing for the external software as for the original one. Thanks to this, the data gathered by the two devices is fully coherent. As one can see from the time between two pixels, the time period available for single pixel calculation is smaller than 4 ms. According to our tests, even 10 ms can be insufficient, when complex NanoSwing operations are to be performed on a Windows-based platform. Therefore, a real-time solution was implemented in order to provide necessary stability and repeatability of the computational tasks. Figure 11.20 shows the difference between the real-time system and often utilized software solution. Every signal processing task has to be finished within a certain time. If it takes longer, the information can be lost and a void pixel is acquired. Moreover, such situation can also induce a permanent delay in data processing and eventually cause a major data corruption. On the other hand, the real-time solution provides very stable computation conditions. In this case, the software procedure is performed with a very small standard deviation of the processing time.

As the AFM acquires more than 65,000 pixels during a single measurement procedure, it is important to avoid any delays or glitches in signal processing. In order to verify the efficiency of the real-time solution implemented in the described setup,

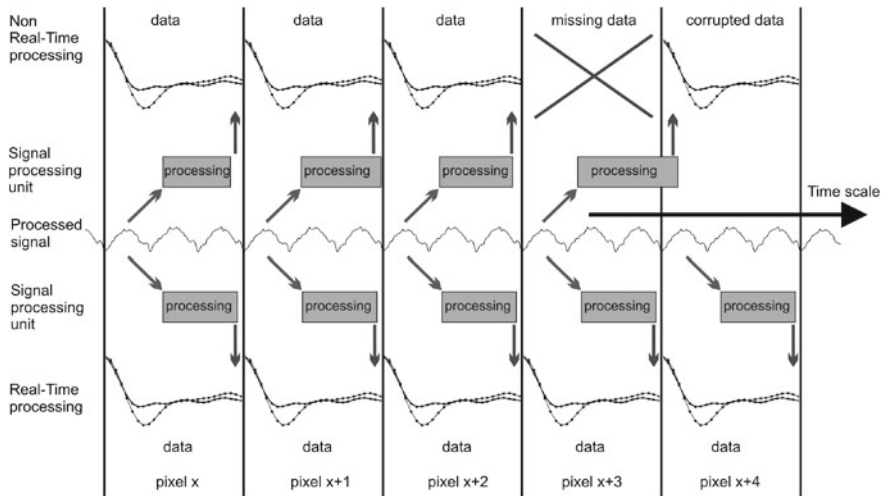


**Fig. 11.20** Time diagram showing the difference between real-time (*lower part*) and non real-time (*upper part*) signal processing in advanced signal processing during surface scanning with the AFM

a test procedure was performed. The data processing loop was performed 5,000 times and every execution time was measured and saved in the statistical data set. The tests were carried out also for the Windows-based solution in order to illustrate the impact of the specific behavior of such a system. Additionally, three levels of the algorithm optimization were evaluated, as one of the aim was to maximize the efficiency of the software. The first level of optimization was the code rearrangement, the second—enabling the pipeline processing, and the third one—enabling multithreading. The improvement of the efficiency is significant. The distribution of the measured processing time is shown in Fig. 11.21. It should be underlined, that the average time of the processing in such an application should not be taken into account, as the worst result determines the real performance of the system. Therefore, Table 11.2 summarizes the standard deviation as well as the maximum duration of the single loop execution.

As one can see, the Windows-based solution cannot be applied in such systems, as it is not possible to control or predict the maximum time of the signal processing. Considering the amount of data that is calculated during every measurement, it is very likely that practically every set of results would contain artifacts.

### ***11.2.7 Utilization of High-Order Harmonics of the Cantilever's Oscillations for the Surface's Stiffness Mapping***

As the bandwidth of the cantilever's response signal is related to the stiffness of the sample (Fig. 11.3), it can be used for the mapping of this particular property

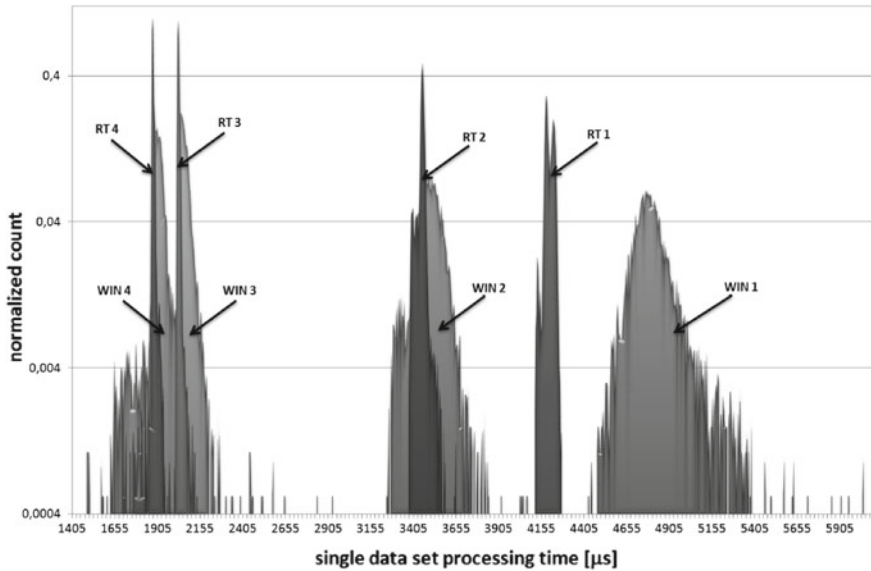


**Fig. 11.21** The distribution of the time periods for performing a single signal processing cycle for a single pixel, for two solutions: non real-time—“WIN” (Windows 7 based) and real-time—“RT” and various levels of the algorithm performance (1-raw algorithm, 2-optimized algorithm, 3-pipeline processing, 4-multithreading) are also presented

**Table 11.2** Comparison of the standard deviation and average time of the data processing duration for a single pixel

Time (μs)	Performance 1	Performance 2	Performance 3	Performance 4
	Std. dev./average	Std. dev./average	Std. dev./average	Std. dev./average
Real-time	26/4325	28/3848	15/2366	20/2077
Windows7	180/6756	125/6949	90/3959	69/3787
Windows7 <sup>a</sup>	2493/59157			

<sup>a</sup>Measured during induced activity of other applications

[29, 35, 55, 56]. By measuring the power of certain high-order harmonic frequencies, one can relatively easily perform the imaging processing. Therefore, a lock-in amplifier should be used in order to provide necessary selectivity and sensitivity. Such approach cannot deliver quantitative information about mechanical properties of the surface, nevertheless it is useful in terms of interpretation of the results. It also simpler to implement than the time-resolved tapping mode technique.

In order to verify the usability of certain frequencies in the mapping process, we have developed a software-based eight-channel lock-in amplifier [57]. The structure of the hard-/software setup is shown in Fig. 11.22. The user can select the value of the multiplier for every channel independently, therefore the flexibility of detection is provided. The number of channels allows, however, to cover almost all useful harmonic frequencies of the torsional oscillation signal. It should be underlined, that



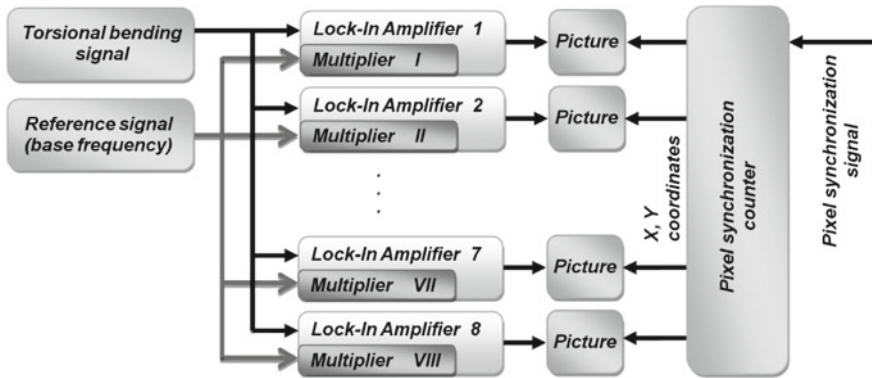


**Fig. 11.22** The diagram showing the concept of the implementation of the eight-channel software-based lock-in amplifier with the signal imaging feature

such an approach permits to perform the experiment within a reasonable time period, without acquiring additional expensive hardware. Additionally, all the obtained data refer to the same area, therefore the comparison of data from different frequency ranges is easy and reliable.

In order to verify the stiffness imaging ability of developed system, the test sample described in previous subsection was used. Figure 11.23 shows the topography scan and the Fourier transform spectra related to the spots where they were obtained. One can see that at some specific frequencies of the signal the differences are significant. Therefore, mapping of appropriate harmonics can deliver the desired kind of information. As we can verify from the spectra of the signal, the coverage of the bandwidth with eight-channel setup was satisfying, while further frequencies were very close to the torsional resonance of the cantilever. As previously mentioned and confirmed with the spectra graphs, only odd multiplications of the base frequency should be considered as the source of useful information. Therefore, the software was configured in order to perform the mapping of the following harmonic frequencies: 1, 3, 5, 7, 9, 11, 13, 15. As the base frequency of the HMX-S cantilever used was approximately 49.24 kHz, the values were analyzed in the range: 98.48–787.84 kHz. The measurement was performed in ambient conditions ( $T = 25^\circ\text{C}$ ,  $\text{RH} = 34\%$ ) at a scanning speed of 0.2 Hz.

Obtained results are presented in Fig. 11.24. Also the topography and phase imaging maps are shown in order to allow correlating all available data. It can be noted that the first harmonic does not provide sufficient contrast, however, the maps of higher harmonics show very clearly a good relation between theoretical consideration and the obtained data. The softer area is presented by darker colors, as the values of certain harmonics are lower in a such case. It should be underlined, that higher frequencies (13, 15) are not as distinct as the lower ones, as they would reach higher values in case of mapping stiffer surfaces. In order to compare the effectiveness of the stiffness imaging, the distributions of acquired maps are presented in Fig. 11.25.

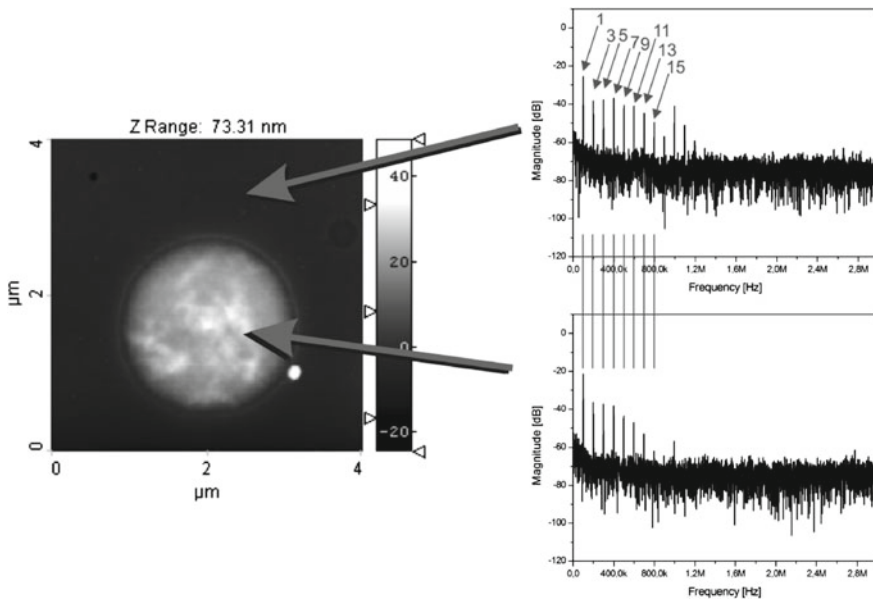


**Fig. 11.23** The results of the comparison of two spectra obtained on the test sample containing materials of different stiffness: 2 GPa (surrounding) and 0.1 GPa (*round object*)

The height of the peaks as well as the distance between them indicates how legible a certain map is. Therefore, it can be considered as an estimation of the detection sensitivity. The comparison of the distances between peaks is additionally shown in Fig. 11.26. It shows clearly that the largest values were obtained in the case of the 5, 7 and 9th harmonics. Concerning the height of the peaks, the 5 and 9th harmonics provided the higher values. This factor plays very important role as a derivative of the steepness of the tip-sample force curve. Therefore, it can be considered as the indicator of the stiffness detection resolution.

It should be emphasized that in the presented solution, the flatness of the system's detection bandwidth is not essential, as every harmonic is monitored and mapped independently. Therefore, the mutual relations of certain signals is not as relevant as in case of the force spectroscopy curve reconstruction process described in the following section. Moreover, in the case of a single harmonic with one lock-in amplifier, the simplicity of the presented approach makes it very attractive for a wide range of applications and can be implemented easily in many AFM systems.

It should be noted, that also flexural high-order oscillations were analyzed in terms of mapping of the mechanical properties of the surface.

In numerical analysis based on equivalent electrical circuits to model and simulate the higher harmonics generation in tapping mode, Sahin et al. concluded, that third harmonics is highly sensitive to the tip-sample interaction [58]. Experimental work showing the mapping of mechanical properties of the etched silicon wafer using 13th harmonic was presented by Hillenbrand et al. [59]. The utilization of such

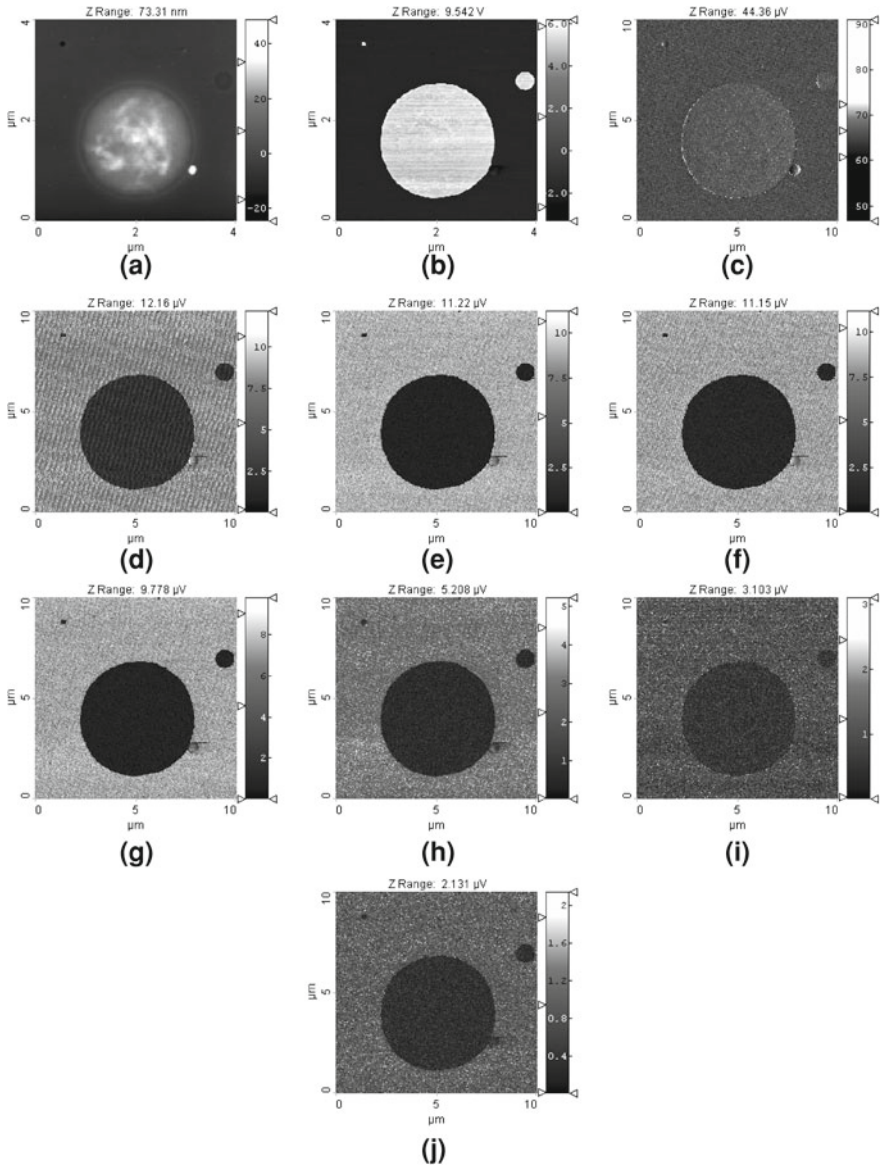


**Fig. 11.24** The scanning results of the test structure. From left to right: topography (a), phase imaging (b), and following harmonics: 1, 3, 5, 7, 9, 11, 13, 15 (c–j, respectively) for the base frequency 49, 24 kHz

solution was more effective than phase imaging technique. In this work, the idea of reconstruction of the tip-sample interaction curve was also proposed. Also Sahin et al. used 10th harmonic to generate maps of the local stiffness changes while the temperature of PS-PMMA polymer film increased [29].

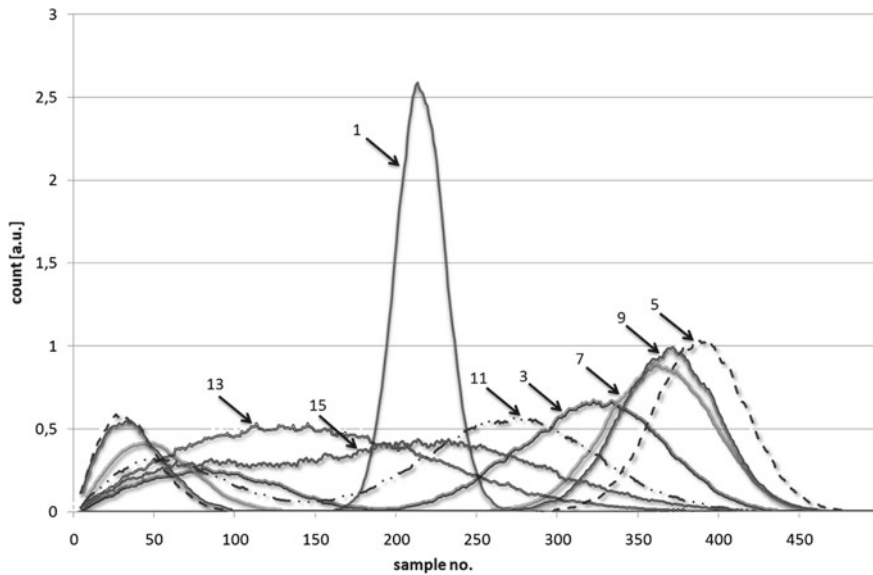


Fig. 11.25 The comparison of the distributions of the harmonics acquired with the 8-channel lock-in amplifier

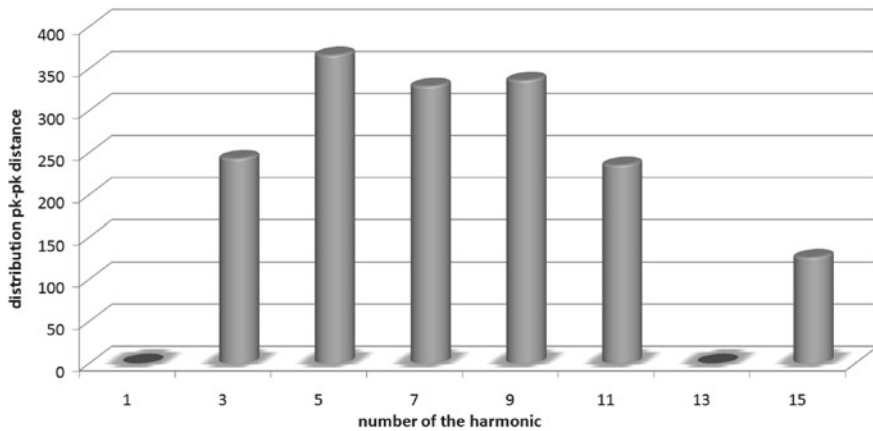
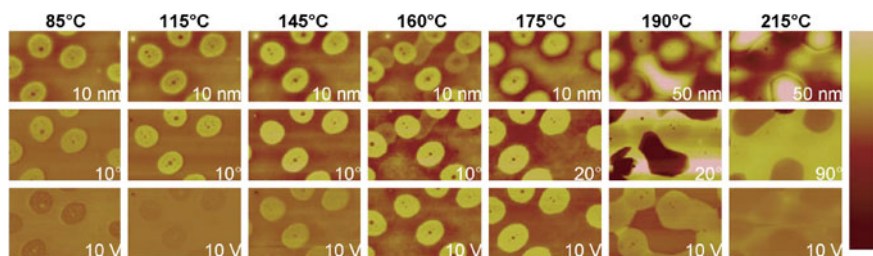


Fig. 11.26 The comparison of the peak–peak distances for acquired histograms of the harmonic changes distribution

### 11.3 Application Examples

The utilization of time-resolved tapping mode technique in various fields of science allows to obtain more information about the properties of the sample. Therefore, much more complex materials and phenomena can be observed and interpreted.



**Fig. 11.27** Changes in the mechanical properties of a polymer blend near the glass transition. Topography, phase, and tenth-harmonic images of a thin polymer film composed of PS and PMMA recorded at different temperatures. The circular features are PMMA, and the matrix is PS. Brighter color represents larger height, phase, or harmonic amplitude. The scan area is  $2.5 \times 5 \mu\text{m}$ . The color bar represents different height and phase ranges at each temperature (the range is given in the *top left* corner of each panel). For the harmonic images, the color bar represents a 10 V lock-in output signal at all temperatures. Note that height and phase contrast increases with temperature, whereas the harmonic contrast is first increasing and then decreasing [29]

As one can analyze separate maps of various properties of the surface (stiffness, adhesion) as well as the tip-sample interaction (peak force, energy dissipation), significantly deeper insight into the nanoscale world can be enabled. It should be emphasized, that due to the complexity of the measurement technique, mostly commercially available systems are utilized. Additionally, as we have presented in Sect. 11.2.3, optimizing the scanning parameters in terms of appropriate force-distance curve reconstruction and effective mapping of the mechanical properties requires much more expertise and effort than in case of contact or intermittent contact mode. Therefore, this imaging technique can be underestimated. In this subsection, we present few examples of research that gained from utilization of time resolved tapping mode.

Observation of dynamically changing properties of the material due to temperature increase was presented by Sahin et al. [29]. In this case, however, the mapping was performed using the 10th harmonic of the flexural cantilever's base signal instead of recovering the force-distance curve. With this method, the behavior of the polymer film composed of the PS and PMMA near the glass transition was imaged (Fig. 11.27). It was possible to observe that near the 190 °C, the grain boundaries become unclear and the material gained mobility, starting rearrangements of the formerly stable forms.

The mapping of the mechanical properties of pigment-latex coated paper samples was performed by Ihalainen et al. [52]. It was noted, that although being the minor component in the coating color formulation, the latex was appeared to be one of the major components on the surface. Additionally, the tip-sample thermodynamic work of adhesion of the composite materials on the coated surface correlated with the surface energy values obtained by contact angle measurements, showing a higher tip-sample work of adhesion as a function of a higher surface energy.

Lanniel et al. [53] observed the increase of the Young modulus of the hydrogen silesquioxane, as it was exposed to the electron beam. As the map of the stiffness

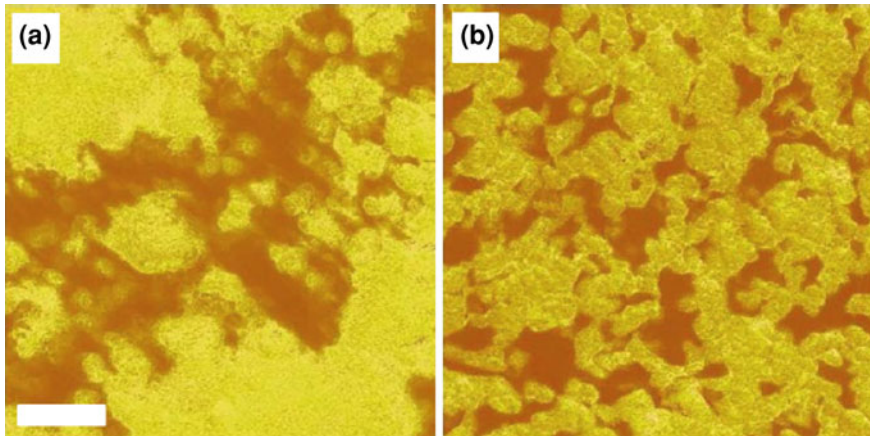


**Fig. 11.28** DMT modulus images of SBR/EPDM blends filled with 20 phr Ultrasil VN3; **a** 30/70 SBR/EPDM; **b** 50/50 SBR/EPDM [59]

was acquired, its uniform distribution was observed. Since the Young modulus was determined with nanoindentation method, one could confirm, that locally measured properties were representative.

The mapping of surface elastic moduli in silica-reinforced rubbers and rubber blends was presented by Schön et al. [60]. Styrene–butadiene rubbers (SBR) and ethylene–propylene–diene rubbers (EPDM) and SBR/EPDM rubber blends with varying concentrations of silica nanoparticles were investigated (Fig. 11.28). The results allowed to reveal an increase of the areal fraction of silica particles with rising concentration in the compound preparation mixture. Additionally, measurements revealed the formation of larger silica aggregates in EPDM in contrast to SBR where isolated silica particles can be observed.

Another experiment focused on quantitative mapping of elastic moduli at the nanoscale in phase separated polyurethanes was also performed by Schön et al. [61]. As observed morphology as well as elastic modulus strongly depends on stoichiometric ratio, it was possible to identify the sample. Additionally, the comparison of two commercially available mechanical mapping techniques was performed: torsional oscillations-based time-resolved tapping mode, and based on peak-force detection and feedback next generation imaging technique.

Qu et al. by mapping of the elastic modulus obtained confirmation of presence of the interphase of rubber-particle nanocomposites in hydrogenated nitrile butadiene rubber (HNBR)–carbon black composites [62]. As the bound rubber exhibits mechanical properties distinct from rubber matrix and the particles, it was possible to determine the thickness of the interphase to be below 20 nm.

Also newly developed materials can be investigated in order to determine their properties. In particular, very promising nanomaterial as the graphene, still requires a number of investigations, as its values can enable new technologies and applications.

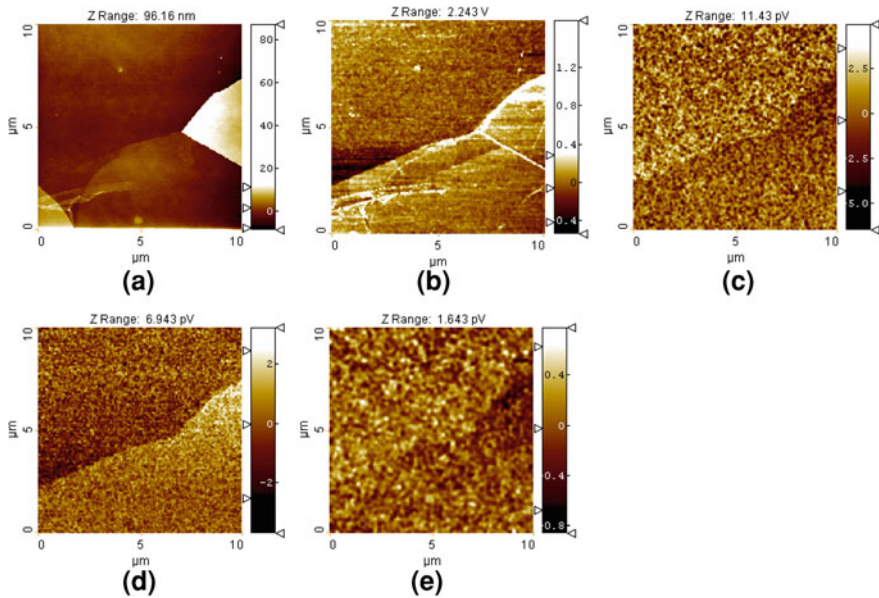


**Fig. 11.29** The results of scanning of the exfoliated graphene: topography (a), phase imaging (b), adhesion (c), stiffness (d), and peak force (e)

In present example the exfoliated graphene flakes were placed on silicon wafer covered with 300 nm thick silicon dioxide layer [63]. As we expected, the stiffness of graphene is higher than the stiffness of the silicon dioxide (Fig. 11.29). Moreover, we could observe that the change of the thickness: monolayer and multilayers (from 4 up to over 40) does not affect the stiffness significantly. Additionally, we could observe slightly smaller adhesion on the graphene surface in relation to the substrate. Moreover, the peak force map revealed almost homogenous value, except the right side of the image, which can be related to very thick layer as well as the graphene detaching. One can note, that the phase image could not provide such valuable information. It should be emphasized, that the quantitative measurement in such case would not provide accurate data, as the Young modulus of graphene is far beyond the range of linear response of the system. Nevertheless obtained information can be useful in terms of technology of development of particular devices.

The utilization of time-resolved tapping mode in biological and medical sciences was also significant. Dague et al. observed interaction forces between the pig gastric mucin (PGM) and *Lactococcus lactis* as the model for lactic acid bacteria [64]. As the *L. lactis* cells were immobilized on the AFM tip, it was possible to observe the interaction forces between bacteria (lacto probe) and PGM-coated polystyrene.

Cross-correlational research comparing time-resolved tapping mode and conventional nanoindentation technique was performed, concerning investigation of the elasticity of bacterial nanowires from *Shewanella oneidensis* MR-1 cultured under electron-acceptor limiting [65]. Leung et al. demonstrated good consistency of the

results obtained with both methods. Mapping of the elasticity of the bacteria wires did not reveal significant variations, therefore its mechanical homogeneity was verified.

Husale et al. presented utilization of time-varying tip-sample forces analysis in determination of the unique mechanical signatures of the DNA and RNA molecules [66]. Presented solution enabled direct quantification and counting hybridized molecules attached to the surface. The advantage of the method is relatively low cost, high speed, and attomolar-level detection sensitivity while it eliminates the biochemical processes.

## 11.4 Outlook and Conclusions

In this chapter we have presented the principles, specific issues of the implementation, and example results of the time-resolved intermittent contact technique based on the detection of the torsional cantilever oscillation. In particular, we showed a successful implementation of the NanoSwing solution based on this method. As this technique allows to perform high-speed and high-resolution mapping of the mechanical properties of the surface in intermittent contact mode regime, its range of application is very wide. The obtained maps of: topography, stiffness, adhesion, peak force, and energy dissipation enables the study of the structure of non-homogenous materials, where ingredients can be identified. Although the use of such a technique is much more complex than typical intermittent contact mode and the experience of the operator in setting the scanning parameters determines the effectiveness of its utilization, the advantages of the achieved measurement results are unquestionable as they provide much more detailed insight into the structure and properties of the investigated object.

We have also presented the possible methods of implementation of two measurement techniques utilizing the torsional bending of the cantilever. The presented solutions can be implemented on many AFM systems, where one is able to obtain access to the high-bandwidth unprocessed signals of all sections of the quadrant photodetector.

It should be underlined, that by enabling an access to information about certain tip-sample interaction phenomena, the experiments are performed in order to utilize available information to improve the topography imaging process, as the scanning tip can cause significant deformation of the surface. Such drawback can be reduced by developing new idea of the Z-axis feedback solution [67, 68].



**Acknowledgments** The authors would like to thank Roman Szeloch (Wrocław University of Technology, Wrocław, Poland), Hans-Ulrich Danzebrink, Miriam Friedemann and Mirosław Woszczyna (Physikalisch-Technische Bundesanstalt, Braunschweig, Germany) and other colleagues and coworkers for support and collaboration. This work was supported financially by the Polish Ministry of Science and Higher Education (MNiSW) within the framework of the research project no. N N505 466338.

## References

1. G. Binnig, C.F. Quate, C.H. Gerber, Atomic force microscope. *Phys. Rev. Lett.* **56**(9), 930–933 (1986)
2. Y. Martin, C.C. Williams, H.K. Wickramasinghe, Atomic force microscope-force mapping and profiling on a sub 100-Å scale. *J. Appl. Phys.* **61**(10), 4723–4729 (1987)
3. F.J. Giessibl, AFM's path to atomic resolution. *Mater. Today* **8**(5), 32–41 (2005)
4. S. Morita (ed.), *Roadmap of Scanning Probe Microscopy* (Springer, Berlin, 2006)
5. B. Bhushan (ed.), *Springer Handbook of Nanotechnology* (Springer, Berlin, 2010)
6. P. Maivald, H.J. Butt, S.A.C. Gould, C.B. Prater, B. Drake, J.A. Gurley, V.B. Elings, P.K. Hansma, Using force modulation to image surface elasticities with the atomic force microscope. *Nanotechnology* **2**, 103 (1991)
7. W.F. Heinz, J.H. Hoh, Spatially resolved force spectroscopy of biological surfaces using the atomic force microscope. *Trends Biotechnol.* **17**(4), 143–150 (1999)
8. C. Reynaud, F. Sommer, C. Quet, N. El Bounia, T.M. Duc, Quantitative determination of Young's modulus on a biphasic polymer system using atomic force microscopy. *Surf. Interface Anal.* **30**, 185–189 (2000)
9. P.J. de Pablo, J. Colchero, J. Gomez-Herrero, A.M. Baro, Jumping mode scanning force microscopy. *Appl. Phys. Lett.* **73**(22), 3300–3302 (1998)
10. F. Moreno-Herrero, J. Colchero, J. Gómez-Herrero, A.M. Baró, J. Ávila, Jumping mode atomic force microscopy obtains reproducible images of Alzheimer paired helical filaments in liquids. *Eur. Polym. J.* **40**(5), 927–932 (2004)
11. A. Gigler, C. Gnahn, O. Marti, T. Schimmel, S. Walheim, Towards quantitative materials characterization with digital pulsed force mode imaging. *J. Phys. Conf. Ser.* **61**, 346–351 (2007)
12. A. Rosa-Zeiser, E. Weilandt, S. Hild, O. Marti, The simultaneous measurement of elastic, electrostatic and adhesive properties by scanning force microscopy: pulsed-force mode operation. *Meas. Sci. Technol.* **8**, 1333–1338 (1997)
13. M. Grandbois, H. Clausen-Schaumann, H.E. Gaub, Atomic force microscope imaging of phospholipid bilayer degradation by phospholipase A<sub>2</sub>. *Biophys. J.* **74**, 2398–2404 (1998)
14. C. Su, L. Huang, K. Kjoller, K. Babcock, Studies of tip wear processes in tapping mode<sup>TM</sup> atomic force microscopy. *Ultramicroscopy* **97**(1–4), 135–144 (2003)
15. A.G. Khurshudov, K. Kato, H. Koide, Wear of the AFM diamond tip sliding against silicon. *Wear* **203**(204), 22–27 (1997)
16. B. Anczykowski, D. Krueger, H. Fuchs, Cantilever dynamics in quasiconcontact force microscopy: spectroscopic aspects. *Phys. Rev. B* **53**, 15485 (1996)
17. R. Garcia, R. Perez, Dynamic atomic force microscopy methods. *Surf. Sci. Rep.* **47**, 197–301 (2002)
18. U. Rabe, K. Janser, Vibrations of free and surface-coupled atomic force microscope cantilevers: theory and experiment. *Rev. Sci. Instrum.* **67**, 3281–3293 (1996)
19. R. Garcia, A. San Palo, Attractive and repulsive tip-sample interaction regimes in tapping-mode atomic force microscopy. *Phys. Rev. B* **60**, 4961–4967 (1999)
20. P.J. de Pablo, J. Colchero, M. Luna, J. Gomez-Herrero, A.M. Baro, Tip-sample interaction in tapping-mode scanning force microscopy. *Phys. Rev. B* **61**(20), 14179–14183 (2000)

21. B. Anczykowski, B. Gotsmann, H. Fuchs, J.P. Cleveland, V.B. Elings, How to measure energy dissipation in dynamic mode atomic force microscopy. *Appl. Surf. Sci.* **140**, 376–382 (1999)
22. A. San Palo, R. Garcia, Tip-surface forces, amplitude and energy dissipation in amplitude modulation (tapping mode) force microscopy. *Phys. Rev. B* **64**, 193411 (2001)
23. J. Melchera, C. Carrascob, Xua 11, J.L. Carrascosad, J. Gómez-Herrerob, P.J. de Pablob, A. Ramana, Origins of phase contrast in the atomic force microscope in liquids. *PNAS* **106**(33), 13655–13660 (2009)
24. R.W. Stark, Bistability, higher harmonics, and chaos in AFM. *Mater. Today* **13**, 24–32 (2010)
25. A. Sikora, L. Bednarz, Mapping of mechanical properties of the surface by utilization of torsional oscillation of the cantilever in atomic force microscopy. *Cent. Eur. J. Phys.* **9**(2), 372–379 (2011)
26. B.V. Derjaguin, V.M. Muller, Y.U.P. Toporov, Effect of contact deformations on the adhesion of particles. *J. Colloid Interface Sci.* **53**, 314–326 (1975)
27. L.D. Landau, E.M. Lifshitz, *Theory of Elasticity* (Pergamon, New York, 1986)
28. L. Zitzler, S. Herminghaus, F. Mugele, Capillary forces in tapping mode atomic force microscopy. *Phys. Rev. B* **66**, 155436 (2002)
29. O. Sahin, C. Su, S. Magonov, C.F. Quate, O. Solgaard, An atomic force microscope tip designed to measure time varying nanomechanical forces. *Nature Nanotechnol.* **2**, 507–514 (2007)
30. O. Sahin, C.F. Quate, O. Solgaard, A. Atalar, Resonant harmonic response in tapping-mode atomic force microscopy. *Phys. Rev. B* **69**, 165416 (2004)
31. O. Sahin, Time-varying tip-sample force measurements and steady-state dynamics in tapping-mode atomic force microscopy. *Phys. Rev. B* **77**, 115405 (2008)
32. O. Sahin, *Harmonic force microscope: a new tool for biomolecular identification and characterization based on nanomechanical measurements* (Stanford University, Ph.D. Dissertation, 2005)
33. Sahin O., Atalar A., Quate C.F., Solgaard O., (2005) Harmonic cantilevers and imaging methods for atomic force microscopy, US Patent No. US6935167.
34. Sahin O., Quate C.F., Solgaard O., (2006) Torsional harmonic cantilevers for detection of high frequency force components in atomic force microscopy, US Patent No. US7089787.
35. Sahin O., Quate C.F., Solgaard O., (2008) Atomic force microscope using a torsional harmonic cantilever, US Patent No. US7404314.
36. A.F. Sarioglu, O. Solgaard, Cantilevers with integrated sensor for time-resolved force measurement in tapping-mode atomic force microscopy. *Appl. Phys. Lett.* **93**, 023114 (2008)
37. Bharat Bhushan (ed.), *Scanning Probe Microscopy in Nanoscience and Nanotechnology*, vol. 2 (Springer, Berlin, 2011)
38. G. Meyer, N.M. Amer, Simultaneous measurement of lateral and normal forces with an optical-beam-deflection atomic force microscope. *Appl. Phys. Lett.* **57**, 2089 (1990)
39. M. Stark, R.W. Stark, W.M. Heckl, R. Guckenberger, Inverting dynamic force microscopy: from signals to time-resolved interaction forces. *Proc. Natl. Acad. Sci. U. S. A.* **99**, 8473–8478 (2002)
40. J. Legleiter, M. Park, B. Cusick, T. Kowalewski, Scanning probe acceleration microscopy (SPAM) in fluids: mapping mechanical properties of surfaces at the nanoscale. *Proc. Natl. Acad. Sci. U. S. A.* **103**, 4813–4818 (2006)
41. E. Evans, K. Ritchie, Strength of a weak bond connecting flexible polymer chains. *Biophys. J.* **72**, 1541 (1997)
42. G.I. Bell, Models for the specific adhesion of cells to cells. *Science* **200**, 618 (1978)
43. A. Ptak, M. Kappl, H.-J. Butt, Modified atomic force microscope for high-rate dynamic force spectroscopy. *Appl. Phys. Lett.* **88**, 263109–263111 (2006)
44. HarmoniX User Guide, doc. no 004–1024–000, Veeco Instruments Inc. Santa Barbara USA, 2008.
45. S.D. Solares, H. Holscher, Numerical analysis of dynamic force spectroscopy using a dual-oscillator sensor. *J. Vac. Sci. Technol. B* **28**, 3305338 (2010)
46. S.D. Solares, H. Holscher, Numerical analysis of dynamic force spectroscopy using the torsional harmonic cantilever. *Nanotechnology* **21**, 075702 (2010)

47. J. Legleiter, The effect of drive frequency and set point amplitude on tapping forces in atomic force microscopy: simulation and experiment. *Nanotechnology* **20**, 245703 (2009)
48. N. Mullin, C. Vasilev, J.D. Tucker, C.N. Hunter, C.H.M. Weber, J.K. Hobbs, "Torsional tapping" atomic force microscopy using T-shaped cantilevers. *Appl. Phys. Lett.* **94**, 173109 (2009)
49. O. Sahin, Harnessing bifurcations in tapping-mode atomic force microscopy to calibrate time-varying tip-sample force measurements, *Rev. Sci. Instrum.* **78**, 103707–1–1103707-4 (2007).
50. J.S. Villarrubia, Scanned probe microscope tip characterization without calibrated tip characterizers. *J. Vac. Sci. Technol. B* **14**(2), 1518 (1996)
51. P.M. Williams, K.M. Shakesheff, M.C. Davies, D.E. Jackson, C.J. Roberts, S.J.B. Tendler, Blind reconstruction of scanning probe image data. *J. Vac. Sci. Technol. B* **14**(2), 1557 (1996)
52. P. Ihalainen, J. Järnström, A. Määttänen, J. Peltonen, Nano-scale mapping of mechanical and chemical surface properties of pigment coated surfaces by torsional harmonic atomic force microscopy. *Colloids Surf. Physicochem. Eng. Aspects* **373**, 138–144 (2011)
53. M. Lanniel, B. Lu, Y. Chen, S. Allen, S. Buttery, P. Williams, E. Huq, M. Alexander, Patterning the mechanical properties of hydrogen silsesquioxane films using electron beam irradiation for application in mechano cell guidance. *Thin Solid Films* **519**, 2003–2010 (2011)
54. O. Sahin, N. Erina, High resolution and large dynamic range nanomechanical mapping in tapping-mode atomic force microscopy. *Nanotechnology* **19**, 445717 (2008)
55. R.W. Stark, W.M. Heckl, Higher harmonics imaging in tapping-mode atomic-force microscopy. *Rev. Sci. Instr.* **74**(12), 5111–5114 (2003)
56. M. Balantekin, A. Atalar, Enhanced higher-harmonic imaging in tapping-mode atomic force microscopy. *Appl. Phys. Lett.* **87**, 243513 (2005)
57. A. Sikora, L. Bednarz, The implementation and the performance analysis of the multi-channel software-based lock-in amplifier for the stiffness mapping with atomic force microscope (AFM). *Bull. Pol. Acad. Sci: Tech. Sci.* **60**(1), 83–88 (2012)
58. O. Sahin, A. Atalar, Simulation of higher harmonics generation in tapping-mode atomic force microscopy. *Appl. Phys. Lett.* **79**(26), 4455 (2001)
59. R. Hillenbrand, M. Stark, R. Guckenberger, Higher-harmonics generation in tapping-mode atomic-force microscopy: insights into the tip-sample interaction. *Appl. Phys. Lett.* **76**(23), 3478 (2000)
60. P. Schön, S. Dutta, M. Shirazi, J. Noordermeer, G.J. Vancso, Quantitative mapping of surface elastic moduli in silica-reinforced rubbers and rubber blends across the length scales by AFM. *J. Mater. Sci.* **46**, 3507–3516 (2011)
61. P. Schön, K. Bagdi, K. Molnár, P. Markus, B. Pukánszky, Quantitative mapping of elastic moduli at the nanoscale in phase separated polyurethanes by AFM. *Eur. Polym. J.* **47**, 692–698 (2011)
62. M. Qu, F. Deng, S.M. Kalkhoran, A. Gouldstone, A. Robisson, K.J. Van Vliet, Nanoscale visualization and multiscale mechanical implications of bound rubber interphases in rubber-carbon black nanocomposites. *Soft Matter* **7**, 1066–1070 (2011)
63. A. Sikora, M. Woszczyna, M. Friedemann, M. Kalbac, F.-J. Ahlers, AFM diagnostics of the graphene-based quantum Hall devices. *Micron* **43**, 479–486 (2012)
64. E. Dague, D.T. Le, S. Zanna, P. Marcus, P. Loubière, M. Mercier-Bonin, Probing in vitro interactions between *Lactococcus lactis* and mucins using AFM. *Langmuir* **26**(13), 11010–7 (2010)
65. K.M. Leung, G. Wanger, Q. Guo, Y. Gorby, G. Southam, W.M. Lau et al., Bacterial nanowires: conductive as silicon, soft as polymer. *Soft Matter* **7**, 6617 (2011)
66. S. Husale, H.J. Persson, O. Sahin, DNA nanomechanics allows direct digital detection of complementary DNA and microRNA targets. *Nature* **462**, 1075–U1138 (2009)
67. Z. Parlak, R. Hadzadeh, M. Balantekin, F.L. Degertekin, Controlling tip-sample interaction forces during a single tap for improved topography and mechanical property imaging of soft materials by AFM. *Ultramicroscopy* **109**, 1121–1125 (2009)
68. A. Sikora, L. Bednarz, Direct measurement and control of peak tapping forces in atomic force microscopy for improved height measurements. *Meas. Sci. Technol.* **22**, 094005 (2011)

# Chapter 12

## Quantitative Measurements of Elastic Properties with Ultrasonic-Based AFM and Conventional Techniques

D. C. Hurley

**Abstract** A prime motivation for the original development of ultrasonic-based AFM methods was to enable measurements of elastic properties with nanoscale spatial resolution. In this chapter, we discuss the quantitative measurement of elastic modulus with ultrasonic-based AFM methods and compare it to measurement by more conventional or established techniques. First, we present the basic principles of modulus measurement with methods that involve contact resonance spectroscopy, such as atomic force acoustic microscopy (AFAM) and ultrasonic AFM (U-AFM). Fundamental concepts of modulus measurement with more established approaches, especially instrumented (nano-) indentation (NI) and surface acoustic wave spectroscopy (SAWS), are then discussed. We consider the relative strengths and limitations of various approaches, for example measurement accuracy, spatial resolution, and applicability to different materials. Example results for specific material systems are given with an emphasis on studies involving direct intercomparison of different techniques. Finally, current research in this area and opportunities for future work are described.

### 12.1 Introduction

A key reason for the original development of ultrasonic-based AFM methods was to enable measurements of elastic properties with nanoscale spatial resolution. This measurement need is motivated partly by the fact that new applications often involve structures with nanoscale dimensions (e.g. nanoelectromechanical systems, nanoimprint lithography). Other new structures have larger overall dimensions, but integrate

---

Contribution of NIST, an agency of the US government; not subject to copyright.

---

D. C. Hurley (✉)  
National Institute of Standards & Technology, 325 Broadway,  
Boulder, Colorado 80305, USA  
e-mail: donna.hurley@nist.gov

disparate materials on the micro- or nanoscale (e.g. electronic interconnect, composites). In both cases, successful development of new materials, devices, and thin films requires understanding and control of nanoscale mechanical properties. In particular, many applications require knowledge about elastic properties. Accurate information is essential not only to predict the performance of a system before use, but also to evaluate its reliability during or after use.

Since the invention of atomic force microscopy over 25 years ago, numerous AFM-based approaches have been demonstrated to sense elastic and mechanical properties. However, most of these methods provide only “pretty pictures” of qualitative or relative contrast. For advanced materials research, we seek quantitative information—numerical data—of actual material properties. We furthermore desire some level of confidence in the accuracy of the quantitative values obtained. Accuracy can be validated, for example, by comparing results obtained with different methods or by tracing results back to established quantities.

In this chapter, we discuss the quantitative measurement of elastic modulus with ultrasonic-based AFM methods and compare it with measurement by more conventional or established techniques. The discussion primarily concerns those ultrasonic-based AFM methods that involve contact resonance spectroscopy. Contact resonance spectroscopy is a general name encompassing closely related techniques such as atomic force acoustic microscopy (AFAM) [1, 2], ultrasonic AFM (u-AFM) [3, 4], and contact resonance force microscopy (CR-FM) [5]. The discussion is limited to contact resonance spectroscopy, because of all ultrasonic-based AFM methods it has provided by far the most quantitative results to date. First, we briefly review the contact resonance spectroscopy concepts pertinent to modulus measurements. Confidence in the validity of any measurement method can be obtained by comparison with other established techniques. Although numerous methods exist for measurement of modulus on the micro- to nanoscale, many comparisons with contact resonance spectroscopy have involved two approaches: instrumented (nano-) indentation (NI) and surface acoustic wave spectroscopy (SAWS). We therefore familiarize the reader with the basic measurement concepts of NI and SAWS. Next, we consider each method’s relative strengths and limitations in such areas as measurement accuracy, spatial resolution, and range of material applicability. Example results for specific material systems are given with an emphasis on studies involving direct intercomparison of different techniques. Finally, current research and opportunities for future work are described. In this way, we intend to provide an overview of current progress in quantitative ultrasonic-based AFM modulus measurements, as well as placing it in context with other quantitative techniques.

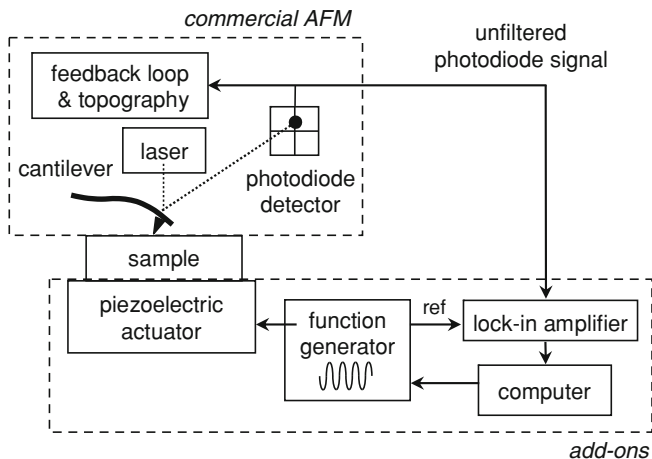


Fig. 12.1 Schematic of apparatus for contact resonance spectroscopy experiments

## 12.2 Overview of Measurement Methods

### 12.2.1 Contact Resonance Spectroscopy

Detailed explanations of the theory, experiment, and analysis of contact resonance spectroscopy have been presented both in the earlier chapters and in previously published reviews [2, 4, 5]. The discussion here is therefore limited to a short overview. In brief, contact resonance spectroscopy involves measurements of the AFM cantilever's resonant vibrations while its tip remains in contact with the sample. Unlike some other AFM methods that monitor the magnitude or phase of the cantilever's motion in vibration, contact resonance spectroscopy techniques measure the frequency at which the free and contact resonances occur. Experiments usually involve the lowest order flexural (bending) eigenmodes of the cantilever. For typical cantilevers, the flexural modes possess frequencies in the acoustic or ultrasonic range, from several tens to a few hundreds of kilohertz for the tip in free space and several hundreds of kilohertz to a few megahertz for the tip in contact (see, for instance, Ref. [5]). The mechanical properties of the sample are deduced from the measured frequencies with the help of two models: one for the dynamic motion of the cantilever and another for the contact mechanics between the tip and the sample. A practical advantage to this approach is that relative frequency shifts can often be measured more easily and accurately than absolute magnitudes or phases.

Figure 12.1 shows the schematic of an apparatus for contact resonance spectroscopy experiments. A number of research groups worldwide have independently developed a version of this apparatus. In addition, a few commercial instruments

exist with the capability for contact resonance measurements<sup>1</sup> [6–8]. The apparatus makes use of a commercial AFM instrument and a few additional off-the-shelf components. The typical frequency range involved ( $\sim 10$  kHz to 2 MHz) requires access to the high-frequency (unfiltered) photodiode signal of the AFM instrument. The specimen is usually bonded to a piezoelectric actuator mounted on the translation stage of the AFM instrument. Actuation at the clamped end of the cantilever is also possible and has been shown to yield equivalent results [2, 4, 9]. The actuator is excited with a continuous sine-wave voltage by a function generator. The excitation voltage is kept sufficiently low so that the tip remains in contact with the sample, ensuring a linear tip-sample interaction. The amplitude of the cantilever deflection is monitored by the AFM's internal position-sensitive photodiode with a laser beam-bounce technique. A lock-in amplifier is used to isolate the component of the photodiode signal at the excitation frequency. By sweeping the transducer excitation frequency and recording the output signal of the lock-in amplifier, a spectrum of the cantilever response versus frequency can be obtained.

Experiments are performed with a static force  $F_{\perp}$  applied to the tip.  $F_{\perp}$  is determined through the relation  $F_{\perp} = k_c z_{\text{eq}}$ , where  $k_c$  is the cantilever spring constant and  $z_{\text{eq}}$  is the static deflection of the cantilever. Measurements on stiff materials (modulus  $\sim 50$  GPa or higher) involve relatively stiff cantilevers ( $k_c \approx 30$  to 50 N/m). In such experiments,  $F_{\perp}$  is typically in the range from several hundred nanonewtons to a few micronewtons. Such forces ensure that the tip-sample contact is predominantly elastic. In experiments on more compliant (“softer”) materials such as polymers (see, for instance, Refs. [10] and [11]), more compliant cantilevers ( $k_c \approx 0.2$  to 3 N/m) with correspondingly lower values of  $F_{\perp}$  ( $< 100$  nN) are used. In such cases, it is important to ensure that elastic interactions still dominate, so that analysis with an elastic model is valid.

To perform modulus measurements, an apparatus like that in Fig. 12.1 is used to acquire spectra for two different resonant eigenmodes while the tip remains stationary at a fixed sample position. Figure 12.2 shows examples of free and contact resonance spectra obtained in this fashion. From the measured values of the contact resonance frequency, values for the normalized contact stiffness  $k^*/k_c$  are determined. The calculations employ analytic [2, 4, 5] or numerical [12–14] models for the cantilever dynamics. It should be noted that a distributed-mass model is used, because a simplified point-mass model for the cantilever does not yield accurate results [2]. Spectra are obtained on two samples in alternation: (i) the test or unknown sample and (ii) a reference or calibration specimen whose elastic properties are known. Elastic properties of reference specimens can be determined by various means, including pulse-echo ultrasonics [15], instrumented (nano-) indentation [16, 17], or other methods discussed in this chapter. For accurate measurements,

---

<sup>1</sup> Commercial equipment and materials are identified only in order to adequately specify certain procedures. In no case does such identification imply recommendation or endorsement by the National Institute of Standards and Technology, nor does it imply that the materials or equipment identified are necessarily the best for the purpose.

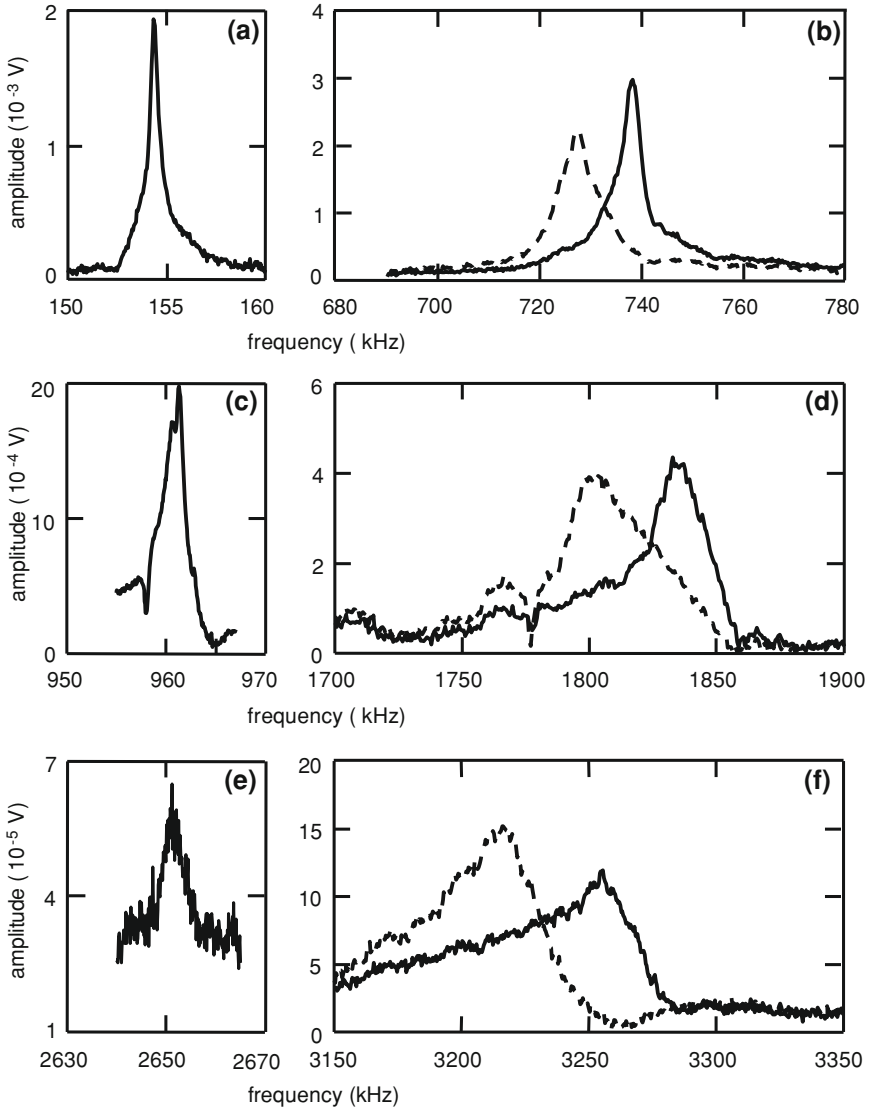


**Fig. 12.2** Examples of experimental results for contact resonance spectroscopy. (a), (c), and (e): Spectra of the first, second, and third free-space flexural resonances for a cantilever with nominal spring constant  $k_c = 48 \text{ N/m}$ . (b), (d), (f): Corresponding contact resonance spectra for the tip in contact with a  $\langle 102 \rangle$   $\text{SnO}_2$  nanobelt. The spectra were acquired at two different static deflections,  $z_{\text{eq}} = 15 \text{ nm}$  (dashed line) and  $z_{\text{eq}} = 45 \text{ nm}$  (solid line)

the elastic properties of the reference specimen should be similar to those of the test specimen [13, 18, 19].



If measurements are performed on the test (subscript  $s$ ) and reference (subscript  $ref$ ) samples at the same values of  $F_{\perp}$ , it can be shown that [18]

$$E_s^* = E_{ref}^* \left( \frac{\frac{k_s^*}{k_c}}{\frac{k_{ref}^*}{k_c}} \right)^m = E_{ref}^* \left( \frac{k_s^*}{k_{ref}^*} \right)^m, \quad (12.1)$$

where the exponent  $m$  describes the tip shape. For Hertzian contact,  $m = 3/2$ ; for a flat punch,  $m = 1$ .  $E^*$  is the reduced modulus between the tip (subscript  $t$ ) and the sample given by

$$\frac{1}{E^*} = \frac{1}{M_t} + \frac{1}{M_s}. \quad (12.2)$$

For elastically isotropic materials, the indentation or plane strain modulus  $M$  is given by  $M = E/(1 - \nu^2)$ , where  $E$  is Young's modulus and  $\nu$  is Poisson's ratio. For elastically anisotropic materials, more complicated formulas have been derived to relate  $M$  to the elastic tensor  $c_{ijkl}$  [20]. The indentation modulus  $M_s$  of the test specimen can thus be determined from the experimental values of contact stiffness  $k^*/k_c$  with Eqs. 12.1 and 12.2 and knowledge of the tip modulus  $M_t$ . This approach eliminates the need for precise knowledge of quantities that are difficult to determine accurately, such as  $F_{\perp}$ , the tip radius of curvature  $R$ , and the tip-sample contact radius  $a_c$ . Because the true shape of the tip is usually intermediate between a hemisphere and a flat, the values calculated with  $m = 3/2$  and  $m = 1$  are considered to set upper and lower limits on  $M_s$  [18, 21].

Measurements are typically made at several sample locations. At each location, data are acquired at several different values of the applied static force  $F_{\perp}$ . Measurements are performed on the reference material immediately before and after each set of measurements on the unknown material. Multiple data sets are obtained by analyzing each set of measurements on the unknown sample with both sets of reference measurements. This procedure also minimizes the impact of tip wear on the measured values [18, 21]. In a typical experiment, approximately 20 to 40 individual values for the indentation modulus  $M_s$  of the unknown sample are obtained with this approach. Combining all of the data yields a single average value and standard uncertainty for  $M_s$ .

### 12.2.2 Instrumented (Nano-) Indentation

Instrumented (nano-) indentation (also known as depth-sensing indentation or nanoindentation, NI) [16, 17] is a more established or conventional method for measuring near-surface mechanical properties. In addition to elastic modulus, quantities such as hardness, fracture toughness, and viscosity can be determined with NI methods. A schematic of the basic NI apparatus is shown in Fig. 12.3a. Measurements involve a probe tip, typically made of diamond with a defined geometry. Although tip shapes such as spherical, conical, or cube corner can be used, the Berkovich (triangular

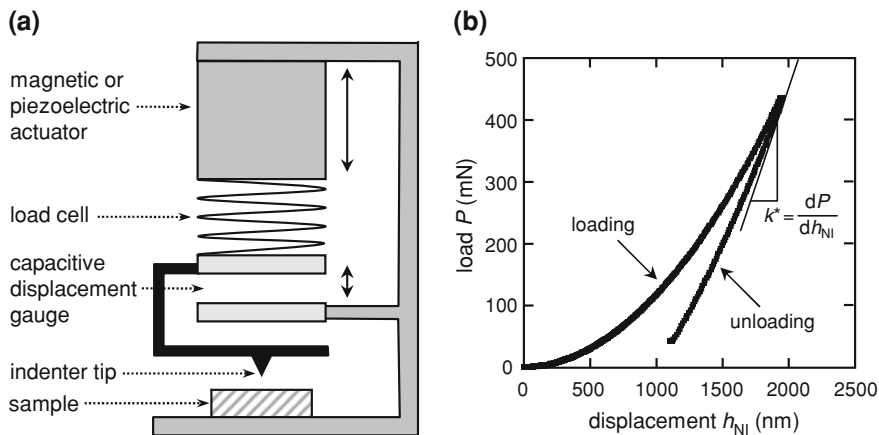


**Fig. 12.3** **a** Schematic of apparatus for instrumented (nano-) indentation experiments. **b** Example of experimental NI results, showing the applied force  $P$  and the resulting sample deformation  $h_{\text{NI}}$ . The elastic indentation modulus  $M$  is determined by the slope of the initial unloading portion of the curve, which is the tip-sample contact stiffness  $k^*$  [Data courtesy of S. E. Campbell, NIST (unpublished)]

pyramidal) geometry is most common. The stiff probe tip is pressed against the sample with known force  $P$  and then withdrawn. The resulting vertical deformation  $h_{\text{NI}}$  of the material is recorded throughout the entire cycle. Figure 12.3b shows a typical force displacement curve obtained in NI experiments. Similar to contact resonance AFM methods, a key element of NI is the tip-sample contact. However, indentation approaches are arguably simpler, in that the load is applied perpendicular to the sample and the resulting displacement in the same (normal) direction is measured.

To determine the sample's elastic properties, the initial unloading (retraction) portion of the force displacement curve is examined. The tip-sample contact stiffness  $k^*$  is found from the slope in this region:  $k^* = dP/dh_{\text{NI}}$ . Values for the indentation or plane strain modulus  $M_s$  are obtained from the experimental values of  $k^*$  by use of the same contact mechanics models discussed above for contact resonance spectroscopy AFM. Because the NI indenter tip is larger than that used in AFM (a few micrometers), measurements of the tip shape and contact area are more accessible. Therefore, the direct comparison or referencing approach described for contact resonance spectroscopy methods is not used. The reference ratio in Eq. 12.1 is replaced by the general Sneddon relation,

$$k^* = 2\beta \sqrt{\frac{A_c}{\pi}} E^*, \quad (12.3)$$

which relates the absolute contact stiffness  $k^*$  to the reduced modulus  $E^*$  and the contact area  $A_c$ . Here,  $\beta$  is a constant (on the order of unity) that depends on

the specific geometry of the tip. For an ideal or perfect tip of known geometry, the contact area  $A_c$  is a function of the contact depth. However, because real tips are not perfect,  $A_c$  is usually determined by calibration measurements on a reference material of known modulus  $M$  to determine the so-called area function. Traditionally, fused quartz is used for this purpose. The growth of NI measurements on polymers and other soft materials may necessitate alternative area-function techniques. With a known value of the tip-sample reduced modulus  $E^*$  and measured values of  $k^*$  versus deformation depth  $h_{\text{NI}}$ , Eq. 12.3 can be solved for  $A_c$  as a function of  $h_{\text{NI}}$ . Measurements are then fit to a functional form, often a polynomial in orders of  $h_{\text{NI}}$ . Once the area function has been obtained in this way, indentation measurements are made on the unknown material. The values of  $k^*$  determined from the unloading slope are combined with values of  $A_c$  from the area function to yield values of  $E^*$  for the test material from Eq. 12.3. Finally, the indentation modulus  $M_s$  of the sample is determined from  $E^*$  with use of Eq. 12.2 and knowledge of the tip modulus  $M_t$ .

The applied forces in NI are usually sufficiently large (micronewtons to millinewtons) that the resulting stress causes plastic as well as elastic deformation. This means that NI techniques are destructive and permanently damage the sample. Plastic deformation in nonideal materials such as biological tissues and polymers may fundamentally alter the material beneath the indenter tip (e.g. compaction of collagen fibers, displacement of water) and thus affect the measured modulus values. In addition, the residual indent restricts the achievable lateral spatial resolution. Care must be taken to ensure that the plastically deformed zone of a previous measurement does not affect subsequent results. Given a typical indent area of approximately one square micrometer, NI measurements must be spaced a few to several tens of micrometers apart. Another consequence of the length and force scales characteristic to NI is the constraint that they impose upon thin films. To ensure that the substrate properties do not substantially influence the measurements, experiments usually follow the rule of thumb that the deformation  $h_{\text{NI}}$  should remain less than 10% of the film thickness. As a result, measurements become increasingly challenging as film thickness decreases below  $\sim 1 \mu\text{m}$ , and accurate measurements on films thinner than a few to several hundreds of nanometers are very difficult, if not impossible. More complicated analysis models that include substrate effects have been developed in attempts to overcome this constraint.

Numerous refinements to the basic technique outlined above have been implemented for improved measurement capabilities. For instance, AFM topography imaging of both the probe and the indent can be performed to obtain precise information about the tip shape and area function. Hybrid approaches that utilize nanoindentation techniques on the AFM platform are also available for improved spatial resolution. Additional effort has gone into the development of more sophisticated analysis procedures and correction factors [17, 22]. The above approach assumes the sample to be perfectly elastic and plastic and thus works well for relatively stiff materials such as metals and ceramics. However, more complex systems such as polymers present measurement challenges (e.g. creep, pile-up), a result of their more pronounced viscoelasticity. To overcome such obstacles, modified or dynamic approaches such as force modulation and continuous stiffness measurement have been developed [17,

23, 24]. In addition, improved analysis models have been developed to incorporate material time dependence [25].

In closing, we note that instrumented (nano-) indentation methods have become sufficiently widespread and mature that technical standards have been established. In this context, technical standards are formal documents that describe testing methodologies or protocols for a measurement approach. Standards are developed by committees of technical experts under the auspices of organizations such as ASTM International (formerly the American Society for Testing and Materials) and ISO (International Organization for Standardization). Standards exist for numerous methods to measure the elastic and other mechanical properties of bulk or macroscale materials. In order for ultrasonic-based AFM methods to achieve widespread acceptance as practical measurement tools, it is very likely that standards concerning their use will eventually be required.

### 12.2.3 Surface Acoustic Wave (SAW) Spectroscopy

A third approach for measuring near-surface elastic properties on the micro- to nanoscale is surface acoustic wave (SAW) spectroscopy or SAWS [26–29]. The excellent reviews in Refs. [27] and [29] provide much greater detail than given here. It should be noted that SAWS is almost exclusively applied to determine the properties of thin supported films. SAWs are well suited for this purpose, because their energy is concentrated at the surface and the rate of decay of energy away from the surface is frequency dependent. As the SAW frequency increases, its energy is concentrated more closely to the surface, so that the film's elastic properties have an increasing influence on the velocity. SAWS exploits this principle by measuring the frequency dependence of the phase velocity, that is, the dispersion relation. Measured dispersion relations are then compared with those predicted by analytical models for wave propagation in order to determine the film's elastic moduli.

SAW spectroscopy experiments typically involve the simultaneous generation and detection of SAWs over a very broad frequency range. To obtain sufficient measurement sensitivity for thin films (thicknesses of a micrometer or less), acoustic wavelengths on the order of tens to hundreds of micrometers are needed, corresponding to acoustic frequencies of several hundred megahertz to a few gigahertz. Such frequencies are extremely high from a conventional ultrasonic testing perspective. To meet these measurement challenges, approaches based on laser-based ultrasonic methods are often used [27–29]. Besides enabling broadband generation and detection of SAWs, laser-based ultrasonic methods are noncontacting, usually nondestructive, and easily adapted to scanning. A commercial SAWS instrument that utilizes a broadband piezoelectric detection method is also available [26, 30].

A schematic of an experimental apparatus for laser-ultrasonic SAW spectroscopy is shown in Fig. 12.4. This particular instrument was created in our own laboratory [28] but is similar to systems developed elsewhere [26, 27]. The SAW generation source is a pulsed laser (wavelength  $\lambda = 532$  nm, nominal full pulse width at half maximum  $T \approx 0.2$  ns, repetition rate 20 Hz). The generation laser spot is focused

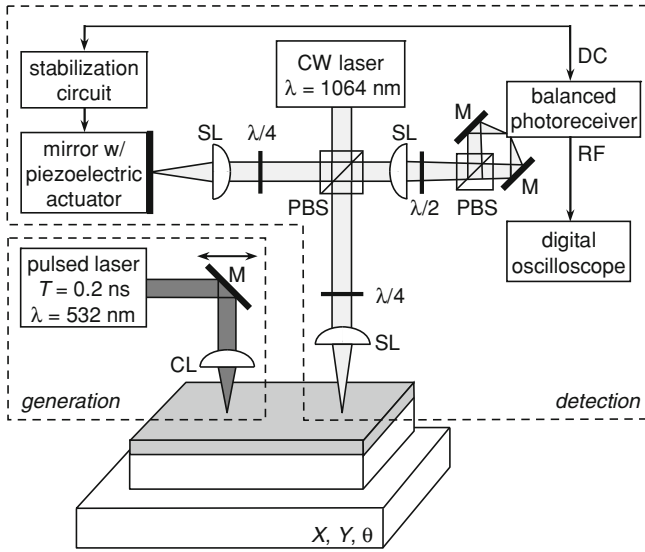


**Fig. 12.4** Schematic diagram of a laser-ultrasonic apparatus for SAWS experiments incorporating a pulsed line source and a high-frequency Michelson interferometer. The separate components for generation and detection of SAWs are indicated by the two dashed boxes. *CL* cylindrical lens; *SL* spherical lens; *M* mirror; *PBS* polarizing beamsplitter;  $\lambda/2$ , half-wave plate;  $\lambda/4$ , quarter-wave plate

onto the surface with a cylindrical lens, creating a line source several millimeters long in order to minimize diffraction effects in the generated SAWs. The energy per pulse (typically  $\sim 50 \mu\text{J}$  or less) is sufficiently low that SAWs are generated thermoelastically, causing little or no damage to the sample. In this apparatus, the propagating SAWs are detected by a path-stabilized Michelson interferometer incorporating a continuous wave laser ( $\lambda = 1064 \text{ nm}$ ) and a high-frequency differential photodiode. The interferometer measures the absolute amplitude of the SAW's out-of-plane displacement. Other optical detection schemes (e.g. Fabry–Perot interferometer, knife edge) have also been implemented. Source and detector lasers at other wavelengths have been used for applications involving materials such as silicon with poor optical absorption and/or reflectance at these wavelengths.

With the use of a translation stage beneath the sample, the relative distance between the source (pulsed laser line) and the detector (interferometer spot) can be easily changed. Data acquisition involves acquiring several waveforms of the SAW displacement amplitude versus time as the source-detector separation  $x$  is incrementally varied. Typically in our experiments, ten waveforms from  $x = 5 \text{ mm}$  to  $x = 15 \text{ mm}$  are acquired. Figure 12.5a shows a waveform for a titanium nitride (TiN) film on a silicon (Si) substrate. From measured waveforms such as this, an experimental dispersion relation for the SAW phase velocity  $v_{\text{phase}}$  versus frequency  $f$  is calculated [26, 28]. The phase velocity is obtained by first calculating the phase versus frequency of the waveform at each position  $x$ . From this, the cumulative phase

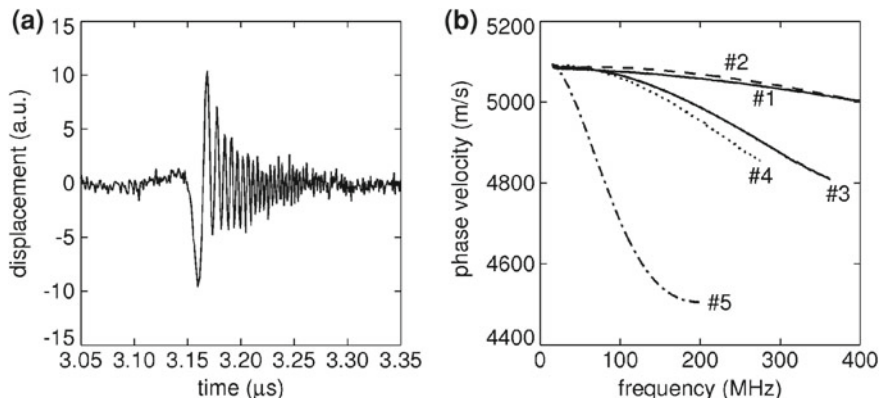


**Fig. 12.5** **a** Example of experimental SAWS results showing the displacement waveform for a TiN film with thickness  $t = (287 \pm 27)$  nm on a (100) Si wafer. SAW propagation was along the Si (110) direction. **b** Calculated SAW dispersion relations for samples containing TiN films on Si substrates. The curves represent SAW propagation in the Si (110) direction. The film thickness  $t$  for each sample is as follows: #1:  $t = (287 \pm 27)$  nm; #2:  $t = (348 \pm 30)$  nm; #3:  $t = (793 \pm 135)$  nm; #4:  $t = (949 \pm 150)$  nm; #5:  $t = (3330 \pm 242)$  nm

spectrum  $\Phi(x, f)$  is calculated by summing the incremental phase differences. Finally, the dispersion relation for the phase velocity  $v_{\text{phase}}$  versus frequency  $f$  is obtained with the relationship  $v_{\text{phase}}(f) = 2\pi x/f\Phi(x, f)$ . The use of waveforms acquired at several different positions minimizes the effects of scatter at any individual position and reduces the experimental uncertainty in  $v_{\text{phase}}(f)$ . Figure 12.5b shows experimental dispersion relations for TiN films of varying thickness on Si.

After calculating the dispersion relations, it is still necessary to interpret them to determine values for physical properties such as the film elastic moduli, density, and thickness. A common approach is Adler’s matrix method [31], in which the film and substrate properties serve as input parameters to a wave propagation model that predicts the dispersion relation. Predictions are compared to measurements, and the input parameters are adjusted iteratively until optimum agreement is obtained. The values of the physical properties that produce the best agreement between model predictions and measurements are considered the film’s actual properties. In our work, we used a Green’s-function approach to solve the inverse problem [28]. With this approach, the film and substrate can be modeled as either elastically isotropic or anisotropic and the corresponding properties determined. This approach also avoids difficulties due to crossing branches or identification of the correct mode branch [31].

It is important to realize that SAW spectroscopy methods can be used to determine a variety of film properties: not only elastic moduli, but also film thickness and density. This is because SAW propagation in a layered system, and thus the SAW dispersion relation, is affected by all of these parameters to some extent. Dispersion relations also possess different degrees of sensitivity to changes in different parameters, which can affect the ability to determine parameters accurately. The number of

parameters that can be determined from a given SAW dispersion relation depends on its specific frequency dependence [26, 31]. Typically, values for only one or two parameters are obtained. Input values for the remaining parameters must be provided, with the use of either literature values or values obtained from complementary measurements. It should also be noted that SAWS methods usually interrogate a sample region with lateral dimensions of a few square centimeters. Therefore, SAW spectroscopy results represent the average properties of a much larger sample region than that measured by either contact resonance spectroscopy or NI.

### 12.2.4 Other Techniques

Many other measurement approaches exist to characterize elastic and mechanical properties on the nanoscale and microscale. The literature describing each method's physical principles, experimental and analysis techniques, and application to specific material systems is extensive. Below, we briefly discuss a few of the most pertinent approaches.

Closely related to contact resonance spectroscopy, ultrasonic force microscopy (UFM) [32–34] is an ultrasonic-based AFM method that has achieved progress toward quantitative measurement of elastic properties. UFM differs fundamentally from contact resonance approaches because the tip and sample do not remain in contact at all times, resulting in a nonlinear tip-sample interaction. The UFM variation most suited to quantitative modulus measurement is differential UFM (d-UFM). In d-UFM, the displacement or threshold amplitude necessary to drive the tip out of contact is measured along with the corresponding force jump of the cantilever. The difference in threshold amplitude for two applied forces is used to determine the contact stiffness  $k^*$ . Values of the indentation modulus  $M$  are obtained from  $k^*$  in a fashion similar to that used for contact resonance spectroscopy. Although it can be argued [35] that nonlinear d-UFM provides a somewhat more direct measurement of  $k^*$  than linear contact resonance methods, a complete uncertainty analysis of both methods is required for strict comparison. For instance, UFM methods usually require a contact mechanics model more complicated than that used in contact resonance methods, involving several nonlinear parameters to model tip adhesion and jumpoff [34]. Nonetheless, d-UFM methods have been used to determine quantitative values of contact stiffness [33] and elastic modulus [36–38] in systems ranging from microelectronic interconnect [36] to nanotubes [38].

We also mention SAW-assisted SPM or SAW-AFM [39], a hybrid technique in which interdigital transducers generate two counterpropagating SAWs at relatively high frequencies (typically several hundred megahertz). The nonlinear interaction between the SAWs creates a third SAW at the difference frequency (typically tens of kilohertz), which is detected by the AFM tip. Phase images of the difference wave provide the SAW phase velocity relation, from which elastic property information with the spatial resolution of AFM can be obtained.

Another AFM-based technique that is widely used to obtain quantitative material data is the force-distance ( $F$ - $D$ ) method [40, 41]. In  $F$ - $D$  measurements, the cantilever

tip is pressed into the sample by use of the AFM's vertical ( $Z$ ) piezoelectric actuator, and the corresponding cantilever deflection is measured. The actuator motion is converted into an applied force by calibration of the actuator and the cantilever spring constant  $k_c$ . The resulting plot of cantilever deflection or distance  $D$  versus applied force  $F$  provides information about several material properties. In particular, the tip-sample contact stiffness  $k^*$  is found from the slope of  $F$  versus  $D$ . Quantitative values of elastic modulus are determined from  $k^*$  with the same contact mechanics models described above for contact resonance spectroscopy and instrumented (nano-) indentation. Because  $F$ - $D$  measurement sensitivity is best when  $k^*$  is less than or comparable to the cantilever stiffness  $k_c$ ,  $F$ - $D$  methods are typically suited to compliant systems such as polymers and biomaterials. Although the point-by-point nature of  $F$ - $D$  seriously hampers acquisition speed, a recently introduced commercial technique based on  $F$ - $D$  principles promises rapid, quantitative imaging [42].

Other methods involve more conventional acoustic and ultrasonic approaches. In many of these methods, the acoustic dispersion relation over a portion of the frequency spectrum is determined experimentally. As in SAW spectroscopy, the dispersion relation can then be analyzed to determine elastic properties of thin films or structures. Perhaps the most established and widely used of such methods is scanning acoustic microscopy [43, 44], in particular the  $V(z)$  method involving SAWs with frequencies from approximately 0.2 to 2 GHz. In this method, the voltage  $V$  of the acoustic transducer is measured as a function of the distance  $z$  between the focus of the lens and the specimen surface. Periodic variations in the  $V(z)$  curve can be used to determine the ultrasonic velocity, from which the elastic modulus is obtained if the film thickness and mass density are known. Also well established is Brillouin light scattering (BLS) [29, 45], which employs optical methods to probe the ambient population of acoustic phonon modes from about 0.3 to 30 GHz. Other related methods utilize ultrafast laser acoustic techniques [46, 47] in the approximate frequency range from 0.1 to 1 GHz. Detailed reviews of these methods, both individually and in comparison, are given elsewhere [29, 35, 46].

### 12.3 Relative Merits of Individual Methods

Above, we have explained the basic principles of several methods to determine micro- and nanoscale elastic properties. While all of these methods have proven their value in obtaining information about elastic properties, each may be considered more or less suitable for a particular application. Before presenting studies in which the measurement results from different methods were compared, we discuss some of the advantages and disadvantages of the various techniques. The main points of this discussion are summarized in Table 12.1.

The above measurement techniques vary significantly in their lateral spatial resolution. For contact resonance spectroscopy methods, both lateral and depth resolution are determined by the tip-sample contact radius  $a_c$ . With a Hertzian contact mechanics model,  $a_c$  depends on the tip radius of curvature  $R$ , the reduced tip-sample modulus



**Table 12.1** Summary of comparison of main techniques discussed in this chapter for quantitative measurements of elastic properties. Included for each technique are its primary merits or advantages, potential limitations or drawbacks, and type(s) of systems to which it is typically applied. The references denote sources of additional information.

Technique	Advantages	Limitations	Main application	References
Ultrasonic-based AFM	<ul style="list-style-type: none"> <li>• nanoscale resolution</li> <li>• imaging capability</li> <li>• nondestructive</li> </ul>	<ul style="list-style-type: none"> <li>• accurate methods still under development</li> </ul>	<ul style="list-style-type: none"> <li>• thin films</li> <li>• nanostructures</li> </ul>	[2], [5]
Instrumented (nano-) indentation	<ul style="list-style-type: none"> <li>• nm to <math>\mu\text{m}</math> resolution</li> <li>• methods well developed</li> </ul>	<ul style="list-style-type: none"> <li>• destructive</li> <li>• point mapping only</li> </ul>	<ul style="list-style-type: none"> <li>• films &amp; coatings</li> <li>• bulk materials</li> </ul>	[16], [17]
Surface acoustic wave spectroscopy	<ul style="list-style-type: none"> <li>• noncontact</li> <li>• nondestructive</li> </ul>	<ul style="list-style-type: none"> <li>• limited spatial resolution</li> <li>• no imaging</li> </ul>	<ul style="list-style-type: none"> <li>• films &amp; coatings</li> </ul>	[26], [27]

$E^*$ , and the applied static load  $F_{\perp}$ . The lateral spatial resolution is determined by the stress distribution surrounding the tip and is therefore not simply  $a_c$ , but approximately 2 to  $3a_c$ . For representative values of  $R$ ,  $E^*$ , and  $F_{\perp}$ ,  $3a_c \approx 10\text{ nm}$  to  $20\text{ nm}$  is a conservative estimate of the lateral spatial resolution [5]. In contrast, the spatial extent of the plastically deformed zone in instrumented (nano-) indentation is of the order of  $1\ \mu\text{m}$  under typical experimental conditions. As explained in Sect. 12.2.3, SAW spectroscopy involves the collection of several ultrasonic waveforms, typically spaced one or more millimeters apart. Therefore, the lateral resolution of this technique is of the order of a centimeter. This might be reduced to a few millimeters through use of more sophisticated optical and mechanical equipment. The resolution of optical methods such as BLS is determined by the diffraction limit of the focused light and is therefore approximately  $0.5$  to  $1\ \mu\text{m}$ . The resolution of scanning acoustic microscopy is also constrained by diffraction-limited focusing, but in this case ultrasonic waves are focused. For high-frequency (gigahertz) operation, ultrasonic spot sizes of a few micrometers can be achieved. Comparing the resolution of the different techniques, it can be seen that AFM methods provide at least one to two orders of magnitude higher lateral resolution than other methods. With this in mind, the interest in AFM methods for modulus measurements is hardly surprising.

The different methods also vary in their suitability to different material systems. In terms of absolute modulus, contact resonance spectroscopy has been successfully applied to systems with modulus ranging from a few gigapascals to a few hundred gigapascals. To obtain the maximum measurement sensitivity over this wide range, it is important to employ a cantilever with spring constant suited to the given material compliance [5]. Instrumented (nano-) indentation methods have been used for measurements over a fairly similar modulus range. Because NI methods use a diamond tip ( $M_t \approx 1150\text{ GPa}$ ), they are arguably better suited than ultrasonic-based AFM methods ( $M_t \approx 165\text{ GPa}$  for a silicon tip) for samples with modulus val-

ues greater than approximately 100 GPa. Nonetheless, SAW spectroscopy outshines both of these methods in the limit of extremely stiff materials such as wear-resistant coatings. Any method based on contact mechanics is difficult to apply in cases where the compliance of the probe tip is similar to (or even less than) that of the sample. As a noncontacting method, SAWS furthermore does not suffer from tip wear effects on hard materials. In terms of sample thickness that can be measured, the small depths probed by ultrasonic-based AFM methods means they can be applied to systems ranging from ultrathin supported films (as low as  $\sim 50$  nm [21]) to bulk samples. Similarly, instrumented (nano-) indentation can be applied to bulk materials and films thicker than a few hundred nanometers. In contrast, SAWS methods are appropriate for films and coatings only, but can be applied to systems with a wide range of film thicknesses (tens of nanometers to many micrometers).

Another factor to consider when choosing a method for measurement of elastic properties is its relative destructive or nondestructive nature. Ultrasonic-based AFM techniques, even those that use contact mode, generally do not involve stresses sufficient to permanently damage the sample. Although this statement holds true for measurements on stiffer materials, it may be necessary to modify existing contact resonance techniques to prevent damage as they are applied more frequently to compliant materials such as polymers. Other AFM methods are typically nondestructive, except for AFM-based nanoindentation that induces plastic deformation by means of a diamond tip and relatively high applied forces. Similarly, instrumented (nano-) indentation methods are almost always destructive. SAW spectroscopy is typically nondestructive due to the optical nature of the source and detector, but material damage can occur from ablation by the source laser. More conventional acoustic and opto-acoustic methods (SAM, BLS, ultrafast acoustics) are generally noninvasive and nondestructive. Scanning acoustic microscopy requires immersion of the sample in water or other acoustic couplant, which may be problematic for some materials.

It is beyond the scope of this chapter to provide a complete uncertainty analysis of each measurement method, but some general comments can be made. Earlier calculations of absolute accuracy with contact resonance spectroscopy [10, 48] gave conservative estimates as high as 40%. However, when the uncertainty is considered as simply the scatter in individual measurements, experiments achieve standard deviations as low as  $\pm 1\%$  [5]. There are many reasons for the variation in uncertainty from experiment to experiment, for instance, sample smoothness or uniformity, the amount of tip wear during measurements, and assumptions made in the data analysis concerning tip shape. The lowest values of uncertainty are often achieved in imaging experiments, which yield very large numbers of measurements for statistical analysis. In comparison, rigorous analysis of instrumented (nano-) indentation methods [48] indicates that they can achieve overall accuracies of approximately  $\pm 5$  to  $\pm 10\%$ . In SAW spectroscopy methods, absolute measurement accuracy of the acoustic waveforms has been estimated to be much less than one percent [26, 28]. However, the nonlinear fitting approach used to determine elastic-property values makes it difficult to convert this into a modulus uncertainty. Furthermore, the uncertainty of the elastic properties determined by the model depends significantly on assumed values

and accuracy of many input parameters (film thickness and density, substrate elastic properties and density). However, experiments often achieve precision of a few percent.

Lastly, we consider the extent to which different methods have been commercialized. A commercial AFM with contact resonance spectroscopy functionality has been available for several years [6]. More recently, other approaches for contact resonance AFM measurements have been implemented in commercial instruments [6–8]. However, the evolution of contact resonance from a research technique in academic laboratories to a practical tool in industrial settings has just begun. Other ultrasonic-based AFM methods such as UFM and SAW-AFM remain as laboratory methods based on custom modifications to commercial AFMs, although the required modifications are generally not too difficult to implement. Because instrumented (nano-) indentation is more mature as a technique and is widely used in the industry, turnkey NI tools are readily available from a number of companies. At least one commercial SAWS instrument exists [30], and this method has gained some industrial acceptance for advanced product development. Several brands of commercial scanning acoustic microscopes also exist, again in part due to the relative maturity of the technique. The other optical and acoustical methods mentioned in Sect. 12.2.4 (BLS, ultrafast laser acoustics, etc.) are still considered primarily research laboratory techniques, involving extensive customized instrumentation.

## 12.4 Results of Measurement Comparisons

In this section, we summarize the results of several studies involving direct inter-comparison of contact resonance spectroscopy and other measurement techniques. This discussion is not intended to serve as a comprehensive review of contact resonance measurements, which is available elsewhere [5, 35, 49]. Indeed, given the burgeoning interest in contact resonance methods as evidenced by a growing number of publications, it is now almost impossible to maintain a complete, up-to-date summary. It should be noted that many comparison studies involved model systems such as blanket thin films. Such systems facilitate comparison with other methods that possess inferior spatial resolution. Quantification of truly nanoscale elastic properties with ultrasonic-based AFM has been showcased in other studies on structures such as nanowires and nanotubes [50, 51], piezoelectric and nanocrystalline films [48, 52], and micro- and nanocomposites [11, 53, 54].

Figure 12.6 shows a relatively early comparison of measurement results. The bar graph compares experimental values of the indentation modulus  $M$  obtained with three different methods: CR-FM point measurements (equivalent to AFAM); instrumented (nano-) indentation (NI); and surface acoustic wave spectroscopy (SAWS) [55]. The samples consisted of supported thin films that ranged in thickness from a few hundred nanometers to a few micrometers. The film materials comprised relatively stiff metals and ceramics with modulus values from approximately 50 GPa to more than 200 GPa. The graph shows that the values obtained by the various methods are in good agreement, with differences of less than 10% for all samples. It is

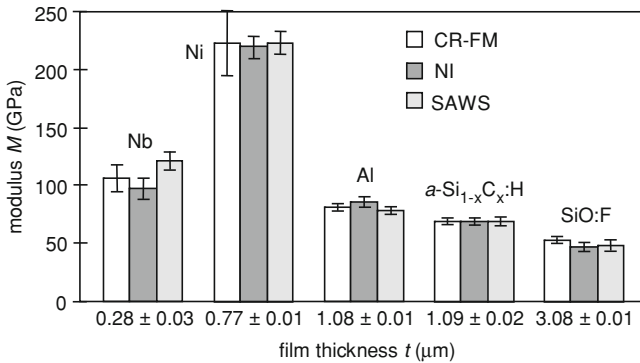


**Fig. 12.6** Indentation modulus  $M$  of thin supported films obtained by contact resonance force microscopy (CR-FM), instrumented (nano-) indentation (NI), and surface acoustic wave spectroscopy (SAWS). The thickness  $t$  of each film was determined by cross-sectional SEM analysis or by stylus profilometry methods. Film materials include fluorinated silica glass (FSG), amorphous hydrogenated silicon carbide ( $\alpha\text{-Si}_{1-x}\text{C}_x\text{:H}$ ), aluminum (Al), niobium (Nb), and nickel (Ni). The error bars represent one standard deviation of the individual measurements

important to remember the characteristic length scale for each technique:  $\sim 10$  nm for AFAM,  $\sim 1 \mu\text{m}$  for NI, and  $\sim 1$  cm for SAWS.

Another study [56] compared measurements with four different techniques on a nanocrystalline nickel film (thickness  $t \approx 800$  nm) deposited on silicon: AFAM, SAWS, NI, and microtensile testing (not discussed here). Because the external forces in microtensile testing are applied in the plane of the film, it primarily senses the in-plane or transverse elastic properties. The normal (out-of-plane) forces used in NI and AFAM mean that these techniques probe a different combination of elastic properties, while the ultrasonic strain fields in SAWS sense a third combination. Values obtained by AFAM and NI for the indentation modulus (220 to 223 GPa) and by SAWS for Young's modulus (177 to 204 GPa) were lower than those theoretically predicted for randomly oriented polycrystalline nickel. The observed behavior was attributed to grain-boundary effects in the nanocrystalline film. In addition, the different measurement results were not self-consistent when interpreted assuming elastic isotropy. Agreement was improved by adopting a transversely isotropic model corresponding to the film's preferred  $\langle 111 \rangle$  orientation and reducing the elastic moduli by 10 to 15%. The SAW spectroscopy results indicated that the film density was 1 to 2% lower than expected for bulk nickel, consistent with models for nanocrystalline materials. Similar reductions in modulus and density were observed for two additional films approximately 200 nm and 50 nm thick when measured with AFAM and SAWS. These results illustrate how complementary methods can provide a more complete understanding of film properties.

In another study involving blanket thin films [57], contact resonance spectroscopy methods were used for point measurements on low- $k$  dielectric thin films. Several amorphous hydrogenated silicon carbide ( $a\text{-SiC:H}$ ) and oxycarbide ( $a\text{-SiOC:H}$ ) films

(thickness  $t \approx 500$  nm) on silicon substrates were created by plasma-enhanced vapor deposition. Different films were created by varying the combination of precursor gases used for deposition ( $\text{SiH}_4$ , methylsilanes,  $\text{H}_2$ , He, etc.). Contact resonance experiments were performed while the applied load  $F_{\perp}$  was varied. Several contact mechanics models were applied to the entire curve of contact stiffness  $k^*$  versus  $F_{\perp}$  to extract best-fit values of the modulus  $M$ . From the contact resonance values of  $M$ , values for Young's modulus  $E$  were obtained from the relation  $M = E/(1 - \nu^2)$  with Poisson's ratio  $\nu = 0.25$ . The values of  $E$  obtained in this way ranged from approximately 10 to 160 GPa. The modulus values  $E_{\text{CR}}$  measured by contact resonance methods were compared directly with the values  $E_{\text{PLA}}$  determined by picosecond laser acoustic methods [47]. The average deviation between measurements as defined by the quantity  $|1 - E_{\text{CR}}/E_{\text{PLA}}|$  was 23%. Possible reasons for this systematic discrepancy (e.g. value used for  $\nu$ , length scale effects, material inhomogeneity) were not explored. The results nonetheless represent reasonably good agreement, given that the two methods are based on very different physical concepts. These results also highlight the versatility of contact resonance methods to determine local modulus over a wide range ( $\sim 1$  to  $>100$  GPa).

An extensive comparison was performed on specimens of nanocrystalline nickel fabricated by pulsed electrodeposition [58]. Processing steps such as the length of post-deposition anneal were varied in order to obtain different average grain sizes. AFAM measurements of the indentation modulus  $M$  were compared to results obtained by NI. The first set of experiments involved five specimens with average grain diameter from approximately 155 to 480 nm. The values of  $M$  obtained by AFAM and NI were similar within the measurement uncertainty. However, the AFAM and NI modulus values were lower than those determined by ultrasonic velocity measurements, which were comparable to those for coarse-grained nickel. The AFAM values displayed relatively large scatter in measurements (20 to 30%). In a second set of experiments with five additional specimens, the grain size varied from about 14 to 68 nm. For these samples, AFAM values for  $M$  were systematically higher than those obtained by NI, even when the measurement uncertainty was included. The results are consistent with the fact that AFAM and NI measurements probe a few grains (or even single grains), while ultrasonic measurements yield an effective modulus averaged over numerous grains. Moreover, nanocrystalline materials contain significant amounts of intercrystalline material with lower modulus than that of the crystalline grains. These facts were used together to explain the systematic differences in measurements by different methods. This work emphasizes that intercomparison measurements should not always be expected to yield identical results, due to the different length scales probed by different methods.

Other work [37] compared measurements by different methods on micro- to nano-sized structures. Study of small structures was possible in this case because both the techniques involved, namely contact resonance spectroscopy and differential UFM (d-UFM), provided nanoscale spatial resolution. AFAM point measurements, CR-FM modulus mapping, and d-UFM experiments were performed on tin oxide ( $\text{SnO}_2$ ) nanobelts approximately 900 nm wide, 45 nm thick, and several micrometers long on silicon. As determined by electron backscatter diffraction, the surface

normal of the nanobelt was parallel to the (102) reciprocal lattice vector. Indentation modulus measurements yielded values of  $M_{\text{d-UFM}} = (151 \pm 14)$  GPa and  $M_{\text{AFAM}} = (154 \pm 18)$  GPa. It is interesting to note the difference in depth probed by the two methods. For AFAM, applied forces between 0.6 and 1.8  $\mu\text{N}$  resulted in a probed depth of about 45 to 60 nm; in d-UFM, applied forces from 25 to 125 nN resulted in estimated depths of 14 to 24 nm. The good agreement between the contact resonance and d-UFM results provides confidence in the accuracy of both methods for comparison with other approaches. However, these modulus values were significantly lower than the value  $M = 358$  GPa for the (102) direction predicted from the bulk single-crystal elastic constants of  $\text{SnO}_2$ . The observed behavior was consistent with previous studies in which instrumented (nano-) indentation measurements yielded  $M_{\text{NI}} = (66 \pm 10)$  GPa for a (IOT)-oriented  $\text{SnO}_2$  nanobelt, much lower than the predicted value of 308 GPa. Structural and compositional characterization with Auger electron spectroscopy and electron backscatter diffraction did not indicate any difference between the nanobelts and bulk  $\text{SnO}_2$  in terms of porosity, stoichiometric ratio, or average density. This work exemplifies a prime driver for the development of ultrasonic-based AFM methods, namely for modulus measurements on new micro- and nanomaterials that cannot be accessed by more conventional techniques.

Comparison of any new or emerging measurement technique with more established methods is a necessary step in its development. Obtaining agreement between different methods, or understanding the reasons for disagreement, validates experimental and analysis procedures for quantitative measurements. Comparisons such as those described above establish a high level of confidence in the ability of contact resonance spectroscopy methods to provide accurate mechanical property information.

## 12.5 Summary and Outlook

In this chapter, we have summarized concepts for quantitative measurement of modulus at the nanoscale with ultrasonic-based AFM techniques. Contact resonance spectroscopy approaches, encompassing such methods as AFAM, U-AFM, and CR-FM, were emphasized. Basic principles of complementary techniques were also described, in particular instrumented (nano-) indentation (NI) and surface acoustic wave spectroscopy (SAWS). Relative advantages and disadvantages of individual techniques were considered in the context of other methods. Results of direct measurement comparisons between contact resonance spectroscopy and other approaches were presented. In many cases, it was found that within the measurement uncertainty, values obtained by contact resonance methods agreed well with those obtained by more conventional approaches. In cases where the results from different techniques did not agree, discrepancies could usually be attributed to the difference in length scales probed by the techniques. This highlights a strength of ultrasonic-based AFM methods, namely their exquisite spatial resolution. When taken together, the numerous comparison studies performed in the past decade establish the validity of contact resonance spectroscopy methods as a means for measurement of elastic properties.

As shown in this and in preceding chapters, ultrasonic-based AFM methods have reached sufficient maturity that they can be confidently used as a quantitative tool. Yet, room for improvement remains. Extensions and refinements to current procedures could yield better measurements: more accurate, more precise, over a wider modulus range, or for thinner films. Examples of improvements include custom-fabricated cantilevers for enhanced sensitivity and robust tips to minimize tip wear. Refinements to current idealized models for cantilever dynamics and contact mechanics could also be made, for example, to more realistically describe the tip-sample interaction at lower applied loads in the presence of adhesive forces. Intercomparisons with other methods will remain necessary in order to ensure the validity of new techniques as they evolve and emerge.

Several areas for future research with ultrasonic-based AFM methods relate to the themes of this chapter. For example, instead of further studies that directly compare modulus measurements with different techniques, work to integrate measurements made on different length scales could prove extremely valuable. Multiscale models could be used to relate the nanoscale properties measured with AFM methods to the micro- and macroscale properties and performance determined by more conventional, larger scale methods. In this way, a richer understanding of heterogeneous systems ranging from composites to biomaterials could be obtained.

Many new and emerging applications involve compliant materials such as polymers and biomaterials, and there is widespread interest in nanomechanical mapping of such systems. Yet, highly compliant materials present numerous challenges to the original ultrasonic-based AFM approaches developed for stiff materials. It remains to be seen just how fully ultrasonic-based AFM methods can satisfy the need for accurate nanomechanical measurements of soft materials. It is likely that a number of refinements and modifications to existing approaches will be required. For instance, sub-micronewton static forces are typically needed to prevent sample damage, requiring the use of more compliant cantilevers (spring constant  $k_c \sim 1$  N/m or lower). Measurements may involve higher order eigenmodes in order to optimize the sensitivity of such cantilevers at low load. However, adhesion and damping forces become more significant for lower applied forces, necessitating more sophisticated contact mechanics models for correct data analysis.

Moreover, many new applications target knowledge of not only elastic properties, but nanoscale viscoelastic properties as well. Progress has been made toward viscoelastic measurements with various other AFM approaches [59]. In recent collaborations with other groups, we have begun to explore the potential of contact resonance spectroscopy for quantitative viscoelastic measurements [60, 61]. Initial results are promising, but further effort is essential to demonstrate the validity of our methods and to determine their limits of applicability. Intercomparisons similar to those described above for elastic properties are essential in this endeavor. Likely candidates for careful comparison studies include instrumented (nano-) indentation and dynamic mechanical analysis (DMA) or its microscale counterpart. As discussed above, the length scale of different measurement methods must be taken into account for accurate comparisons. Moreover, because viscoelastic effects are fre-

quency dependent, each method's characteristic time scale must also be considered, further complicating matters.

It is hoped that the information presented here provides readers with confidence in ultrasonic-based AFM as a tool for nanoscale mechanical measurements and stimulates them to apply these methods to their own research. A growing body of work by groups worldwide points to the utility of ultrasonic-based AFM methods for a wide range of applications. By providing quantitative nanomechanical information for a variety of material systems, ultrasonic-based AFM techniques will contribute to the rapid growth of nanoscale materials science and will play a significant role in future nanotechnology efforts.

**Acknowledgments** Many current and former NIST coworkers contributed to this work, including S. Campbell, C. Flannery, R. Geiss, J. Killgore, M. Kopycinska-Müller, A. Kos, E. Langlois, P. Rice, D. Smith, C. Stafford, and G. Stan. I value many interactions over the years with researchers from other institutes, especially with J. Turner and students (Univ. Nebraska-Lincoln), and W. Arnold, U. Rabe, and S. Hirsekorn (Fraunhofer Institute for Nondestructive Testing IZFP, Saarbrücken, Germany). I also value collaborations and discussions with R. Geer and students (State University of New York at Albany), B. Huey (Univ. Connecticut-Storrs), N. Jennett and coworkers (National Physical Laboratory, Teddington, UK), T. Murray (Univ. Colorado-Boulder), and G. Pharr (Univ. Tennessee-Knoxville).

## References

1. U. Rabe, W. Arnold, *Appl. Phys. Lett.* **64**, 1493 (1994)
2. U. Rabe, Atomic force acoustic microscopy, in *Applied Scanning Probe Methods Vol. II*, ed. by B. Bhushan, H. Fuchs (Springer, Berlin, 2006), Chap. 2, p. 37
3. K. Yamanaka, S. Nakano, *Jpn. J. Appl. Phys.* **35**, 3787 (1996)
4. K. Yamanaka, K. Kobari, T. Tsuji, *Jpn. J. Appl. Phys.* **47**, 6070 (2008)
5. D. C. Hurley, Contact resonance force microscopy techniques for nanomechanical measurements, in *Applied Scanning Probe Methods Vol. XI*, ed. by B. Bhushan, H. Fuchs (Springer, Berlin, 2009), Chap. 5, p. 97
6. <http://www.ntmdt.com/page/afam>. Accessed May 2012
7. B.J. Rodriguez, C. Callahan, S.V. Kalinin, R. Proksch, *Nanotechnology* **18**, 475504 (2007). <http://www.asylumresearch.com/Applications/BimodalDualAC/BimodalDualAC.shtml>. Accessed May 2012
8. S. Jesse, S.V. Kalinin, R. Proksch, A.P. Baddorf, B.J. Rodriguez, *Nanotechnology* **18**, 435503 (2007), <http://www.asylumresearch.com/Applications/BandExcitation/BandExcitation.shtml>. Accessed May 2012
9. T. Tsuji, K. Kobari, S. Ide, K. Yamanaka, *Rev. Sci. Instr.* **78**, 103703 (2007)
10. M. Prasad, M. Kopycinska, U. Rabe, W. Arnold, *Geophys. Res. Lett.* **29**, 13 (2002)
11. S.S. Nair, S. Wang, D.C. Hurley, *Composites A* **41**, 624 (2010)
12. R. Arinero, G. Lévêque, *Rev. Sci. Instr.* **74**, 104 (2003)
13. D.C. Hurley, K. Shen, N.M. Jennett, J.A. Turner, *J. Appl. Phys.* **94**, 2347 (2003)
14. F.J. Espinoza Beltrán, J. Muñoz-Saldaña, D. Torres-Torres, R. Torres-Martínez, G.A. Schneider, *J. Mater. Res.* **21**, 3072 (2006)
15. E.P. Papadakis, The measurement of ultrasonic velocity, in *Physical Acoustics Vol. XIX*, ed. by R.N. Thurston, A.D. Pierce (Academic Press, San Diego, 1990), Chap. 2, p. 81
16. J.B. Pethica, R. Hutchings, W.C. Oliver, *Philos. Mag. A* **48**, 593 (1983)
17. W.C. Oliver, G.M. Pharr, *J. Mater. Res.* **19**, 3 (2004)



18. U. Rabe, S. Amelio, M. Kopycinska, S. Hirsekorn, M. Kempf, M. Göken, W. Arnold, *Surf. Interf. Anal.* **33**, 65 (2002)
19. W. Price, G. Stan, *Rev. Sci. Instr.* **77**, 103707 (2006)
20. J.J. Vlassak, W.D. Nix, *J. Mech. Phys. Solids* **42**, 1223 (1994)
21. M. Kopycinska-Müller, R.H. Geiss, D.C. Hurley, *Ultramicroscopy* **106**, 466 (2006)
22. T. Chudoba, N.M. Jennett, *J. Phys. D: Appl. Phys.* **41**, 215407 (2008)
23. S.A. Syed Asif, K.J. Wahl, R.J. Colton, *Rev. Sci. Instrum.* **70**, 2408 (1999)
24. X. Li, B. Bhushan, *Mater. Charact.* **48**, 11 (2002)
25. M. Oyen, R. Cook, *J. Mater. Res.* **18**, 139 (2003)
26. D. Schneider, T. Schwarz, B. Schultrich, *Thin Solid Films* **219**, 92 (1992)
27. A. Lomonosov, A.P. Mayer, P. Hess, Laser controlled surface acoustic waves, in *Handbook of Elastic Properties of Solids, Liquids, and Gases Vol. 1*, ed. by M. Levy, H.E. Bass, R.R. Stern (Academic Press, New York, 2001), Chap. 7, p. 137
28. D.C. Hurley, V.K. Tewary, A.J. Richards, *Meas. Sci. Technol.* **12**, 1486 (2001)
29. A.G. Every, *Meas. Sci. Technol.* **13**, R21 (2002)
30. [http://www.ccl.fraunhofer.org/download/LA\\_Wave.pdf](http://www.ccl.fraunhofer.org/download/LA_Wave.pdf). Accessed May 2012
31. G.W. Farnell, E.L. Adler, Elastic wave propagation in thin layers, in *Physical Acoustics Vol. 9*, ed. by W.P. Mason, R.N. Thurston (Academic Press, San Diego, 1972), Chap. 2, pp. 35–127
32. F. Dinelli, M.R. Castell, D.A. Ritchie, N.J. Mason, G.A.D. Briggs, O.V. Kolosov, *Phil. Mag. A* **80**, 2299 (2000)
33. F. Dinelli, S.K. Biswas, G.A.D. Briggs, O.V. Kolosov, *Phys. Rev. B* **61**, 13995 (2000)
34. B.D. Huey, *Annu. Rev. Mater. Res.* **37**, 351 (2007)
35. D. Passeri, A. Bettucci, M. Rossi, *Anal. Bioanal. Chem.* **396**, 2769 (2010)
36. L. Muthuswami, R.E. Geer, *Appl. Phys. Lett.* **84**, 5082 (2004)
37. Y. Zheng, R.E. Geer, K. Dovidenko, M. Kopycinska-Müller, D.C. Hurley, *J. Appl. Phys.* **100**, 124308 (2006)
38. L. Muthaswami, Y. Zheng, R. Vajtai, G. Shehkawat, P. Ajayan, R.E. Geer, *Nano Lett.* **7**, 3891 (2007)
39. T. Hesjedal, *Rep. Prog. Phys.* **73**, 016102 (2010)
40. B. Cappella, G. Dietler, *Surf. Sci. Rep.* **34**, 1 (1999)
41. H.-J. Butt, B. Cappella, M. Kappl, *Surf. Sci. Rep.* **59**, 1 (2005)
42. B. Pittenger, N. Erina, C. Su, Quantitative mechanical property mapping at the nanoscale with PeakForce QNM, [http://www.bruker-axs.com/application\\_notes\\_afm.html](http://www.bruker-axs.com/application_notes_afm.html). Accessed May 2012
43. J.D. Achenbach, J.O. Kim, Y.-C. Lee, Measuring thin-film elastic constants by line-focus acoustic microscopy, in *Advances in Acoustic Microscopy Vol. 1*, ed. by G.A.D. Briggs (Plenum, New York, 1995), Chap. 5, pp. 153–208
44. G.A.D. Briggs, O.V. Kolosov, *Acoustic Microscopy*, 2nd edn. (Oxford University Press, New York, 2010)
45. P. Mutti, C.E. Bottani, G. Ghislotti, M. Benghi, G.A.D. Briggs, J.R. Sandercock, Surface Brillouin scattering—extending surface wave measurements to 20 GHz, in *Advances in Acoustic Microscopy Vol. 1*, ed. by G.A.D. Briggs (Plenum, New York, 1995), Chap. 7, pp. 249–300
46. J.A. Rogers, A.A. Maznev, M.J. Banet, K.A. Nelson, *Annu. Rev. Mater. Sci.* **30**, 117 (2000)
47. G.A. Antonelli, B. Perrin, B.C. Daly, D.G. Cahill, Characterization of mechanical and thermal properties using ultrafast optical metrology. *MRS Bull.* **31**, 607 (2006)
48. E. Kester, U. Rabe, L. Presmanes, P. Tailhades, W. Arnold, *J. Phys. Chem. Solids* **61**, 1275 (2000)
49. D.C. Hurley, Measuring mechanical properties on the nanoscale with contact resonance force microscopy methods, in *Scanning Probe Microscopy of Functional Materials: Nanoscale Imaging and Spectroscopy*, ed. by S. Kalinin, A. Gruverman (Springer, Berlin, 2011)
50. G. Stan, C.V. Ciobanu, P.M. Parthangal, R.F. Cook, *Nano Lett.* **7**, 3691 (2007)
51. G. Stan, C.V. Ciobanu, T.P. Thayer, G.T. Wang, J.R. Creighton, K.P. Purushotham, L.A. Bendersky, R.F. Cook, *Nanotechnology* **20**, 035706 (2009)

52. T. Tsuji, S. Saito, K. Fukuda, K. Yamanaka, H. Ogiso, J. Akedo, K. Kawakami, *Appl. Phys. Lett.* **87**, 071909 (2005)
53. D. Passeri, M. Rossi, A. Alippi, A. Bettucci, M.L. Terranova, E. Tamburri, F. Toschi, *Physica E* **40**, 2419 (2008)
54. M. Preghenella, A. Pegoretti, C. Migliaresi, *Polym. Test.* **25**, 443 (2006)
55. D.C. Hurley, M. Kopycinska-Müller, A.B. Kos, *JOM* **59**, 23 (2007)
56. D.C. Hurley, R.H. Geiss, M. Kopycinska-Müller, J. Müller, D.T. Read, J.E. Wright, N.M. Jennett, A.S. Maxwell, *J. Mater. Res.* **20**, 1186 (2005)
57. G. Stan, S.W. King, R.F. Cook, *J. Mater. Res.* **24**, 2960 (2009)
58. M. Kopycinska-Müller, A. Caron, S. Hirsekorn, U. Rabe, H. Natter, R. Hempelmann, R. Birringer, W. Arnold, *Z. Phys., Chem.* **222**, 471 (2008)
59. P. Attard, *J. Phys.: Condens. Matter* **19**, 473201 (2007)
60. P.A. Yuya, D.C. Hurley, J.A. Turner, *J. Appl. Phys.* **104**, 074916 (2008)
61. J.P. Killgore, D.G. Yablon, A.H. Tsou, A. Gannepalli, P.A. Yuya, J.A. Turner, R. Proksch, D.C. Hurley, *Langmuir* **27**, 13983 (2011)

# Chapter 13

## Data Processing for Acoustic Probe Microscopy Techniques

F. Marinello, D. Passeri, P. Schiavuta and E. Savio

**Abstract** One of the merits of acoustic probe microscopy techniques is the possibility of exploiting traceable quantitative mechanical characterization of surfaces. To this end, after measurement proper data processing is needed in order to eliminate or compensate artifacts and distortions and eventually optimize extrapolated information. This chapter discusses the main points of data post processing, providing hints and strategies for repeatable analysis of surface data sets.

### 13.1 Introduction

Extrapolation of quantitative results from a measurement is the result of a set of operations, and in particular proper instrument setup, reproducible measurement conditions, instrument calibration, data processing. This is even more important

---

F. Marinello (✉)

TeSAF, Department of Land, Environment, Agriculture and Forestry,  
University of Padua, Viale dell'Università 16,  
35020 Legnaro (Padua), Italy  
e-mail: francesco.marinello@unipd.it

D. Passeri

BASE, Department of Basic and Applied Sciences for Engineering,  
University of Rome Sapienza, Via A. Scarpa 16, 00161 Rome, Italy  
e-mail: Daniele.Passeri@uniroma1.it

P. Schiavuta

Interuniversity Consortium for Nanotechnology of the Veneto Region, CIVEN Association, Via  
delle Industrie 9, 30175 Marghera (Venezia), Italy  
e-mail: schiavuta@civen.org

E. Savio

DII, Department of Industrial Engineering, University of Padua,  
Via Venezia 1, 35131 Padua, Italy  
e-mail: enrico.savio@unipd.it

in the case of Scanning Probe Microscopes (SPMs), where new measuring techniques (high temperature, fast scanning, near-field measurements) and new field of applications (as biological samples, polymers, soft materials, nanoparticles, unstable interfaces, heterogeneous composite materials, etc.) are frequently introduced, and where standard procedures are still far from being defined.

An optimal measurement setup encompasses a number of factors:

- sample preparation
- sample installation and fastening
- probe preparation, functionalization and protection
- instrument insulation
- scanning parameters setting

Such factors are very much depending on the analyzed sample and on the specific implemented scanning technique. Most of these issues have been treated for specific acoustic techniques (as for instance ultrasonic force microscopy [1–4], atomic force acoustic microscopy (AFAM) [5–8], microdeformation microscopy [9–11], scanning near-field ultrasound holography [12–15]) and for specific fields of application (polymers and thin films [16–18], biological [19–21] and other samples) in the related chapters of this book.

Calibration is the fundamental step for achieving traceable quantitative measurements. A number of publications discuss calibration of geometrical AFM characteristics for exploitation of dimensional measurements [22–24]. On the other hand, calibration of other signals from SPMs have to be specifically calibrated as discussed in the chapters of this book and in other publications [5, 7, 25].

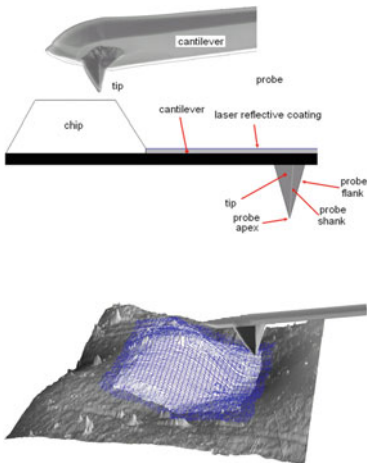
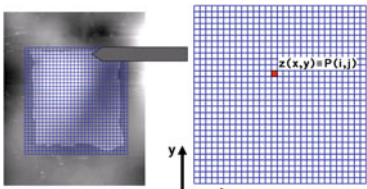
Data processing closes the chain from the instrument to the measurement result. Indeed data processing allows compensation of distortions, filtering and segmentations of surface regions, and eventually extrapolation of quantitative parameters.

In the following data processing is discussed, keeping a general approach valid for different acoustic microscopes and also presenting specific examples taken from the AFAM technology.

## 13.2 Basic Terminology

This chapter starts with a summary of most recurrent and important terms (Table 13.1). These will be of help for a proper comprehension and correct interpretation of the topics discussed in the following. In particular, the pixels matrix presented in the last row is the model commonly used by commercial instruments and analysis software for topography representation [26, 27].

**Table 13.1** Basic terminology for data processing [28]

Representation	Description
	<p>Surface topography measurements are achieved by scanning a probe over a surface. The probe is generally made of silicon and consists of a sharp tip sticking out of a cantilever</p> <p>The probe is scanned over the surface in a raster fashion. Surface topography is reconstructed through a collection of parallel profiles</p> <p>Normally, two main directions are used to describe SPMs probe movement: <math>x</math>, the so-called “Fast Scan Direction”, parallel to the profiles, and <math>y</math> the “Slow Scan Direction”, perpendicular to the first one. Each profile is normally scanned twice: one forward and one backward. The two movements are normally indicated as “scan” or “trace” and “back-scan” or “retrace”</p>
	<p>Surface is eventually characterized by an array of points (often referred to as pixels) called “image”. Positions <math>i, j</math> in the matrix correspond to physical positions <math>x, y</math> in the surface. The value stored in <math>i, j</math> cell of the matrix is the vertical elevation <math>z</math></p>

### 13.3 Distortions and Artifacts

All SPMs generate results that are affected by a number of error sources. An identification and organization of the main distortions occurring during acoustic imaging is proposed in Table 13.2. Lines within the table are dotted on purpose: even if a main source has been identified, generally those distortions have to be regarded as the result of multiple interactions rather than the effect of a single direct origin.

**Table 13.2** Main distortions in acoustic scanning probe microscopy

Source	Effect	Distortion
Scanning system	Scaling	Geometrical
	crosstalk and bow effect	
	non-linearity	
	creep overshoots	
Probing system and sample topography	Installation slope	Geometrical/acoustic
	convolution	
	tip artifacts	
Acoustic wave generator and feedback	noise	acoustic
	Acoustic drift	
Environment	acoustic shift	Geometrical/acoustic
	noise	
	drift	
Data-processing	noise	Geometrical/acoustic
	Filtering	
	levelling	Geometrical/acoustic

This table is divided by the sources that originate the problem; five main sources can be identified in acoustic SPM techniques: the scanning system, the probing in concert with the sample topography, the acoustic wave generator with the feedback system, the environment, and the image processing. The “environment” class stands for those phenomena coming from the complex instrument-operator-room system and affecting the measurement operation.

A number of publications discuss the issue of geometrical distortions [28–38], for such reason here the focus is kept on acoustic imaging.

### 13.4 Drift and Leveling

A typical software operation performed on SPM measurements is data leveling. The aim of this correction is to remove the installation slope, i.e., the tilt occurring between the microscope  $x - y$  scanning plane and sample surface. Such tilt is typically lower than  $5^\circ$ , but accurate sample positioning can reduce the tilt to angles lower than  $1^\circ$  [28–32].

Data leveling is also implemented in order to compensate distortions introduced by vertical drift. Drift is the gradual uncontrolled movement of the system over time, normally more accentuated along the slow scan direction. It is not easy to uniquely define sources of drift, but most probably one of the primary causes has to be ascribed to changes in temperature and in temperature gradients. Most microscopes are covered and many are insulated or placed in a temperature-controlled environment, but anyway it is difficult to achieve drift to velocities lower than 30–60 nm/h. This means

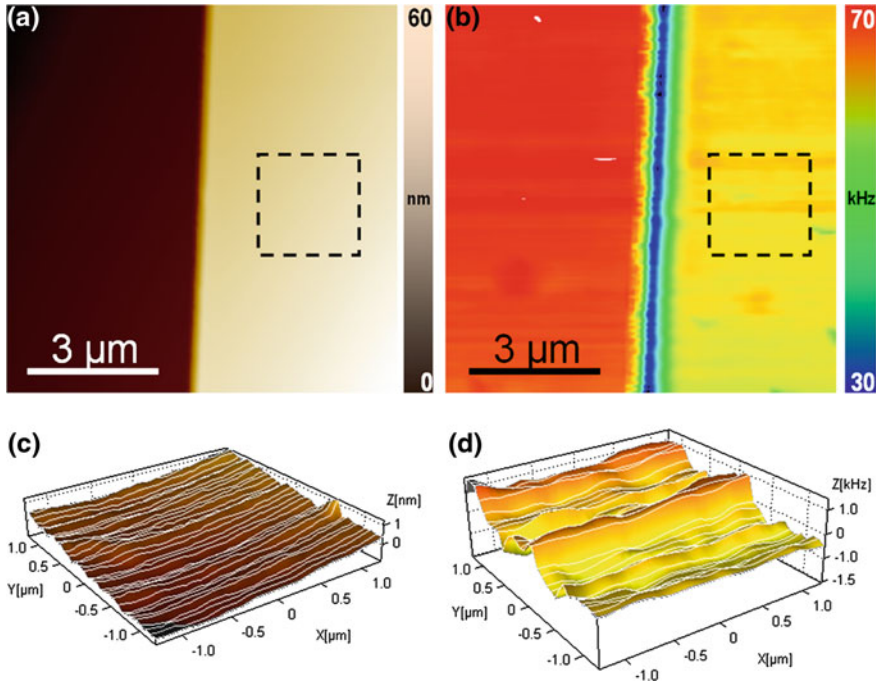


**Fig. 13.1** AFAM measurement of a  $\text{SiO}_2$  step on a Si wafer: topography (a) and local resonance frequency map after (b). In the second row three-dimensional rendering of the areas evidenced with the *dashed line* square both for topography (c) and resonance frequency (d)

that uncontrolled relative movements between the tip and the surface occur, with a speed in the order of a nanometer per minute. Acoustic SPM characterizations are normally quite slow, especially when the resonance spectrum is acquired point by point. Therefore, considerable drift distortions may occur. The effect of drift is clearly visible on topography, and also the acoustic map undergoes to some distortions due to small variations in the position of the probe relative to the sample surface. An example is given in Fig. 13.1, where a measurement of a silicon dioxide ( $\text{SiO}_2$ ) step on a silicon (Si) wafer is reported. The average roughness  $S_a$  of the surface both for the silicon and for the silicon oxide is less than 0.3 nm, however, a close look to the surface (see the three-dimensional rendering in Fig. 13.1c) evidences relative shifts in a range of  $\pm 1$  nm between subsequent profiles along the slow scan direction  $y$ . Correspondingly, relative shifts between subsequent profiles can be recognized in the three-dimensional rendering of the acoustic map in a range of  $\pm 2$  kHz (Fig. 13.1d).

Such distortions can be partially compensated during data processing. In particular correction of single profiles (normally implemented in commercial SPM software such as [26, 27]) is in general applicable. Each profile is fitted with a polynomial function, which is afterwards subtracted to the generating profile [28–32].

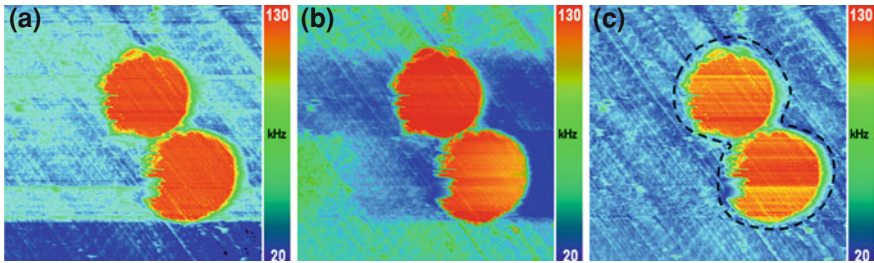


**Fig. 13.2** AFAM measurement of glass fibers on a polypropylene matrix (a). After first degree data leveling drift is compensated, but a depressed *blue* region appears in the center (b). Data leveling looks correct if the area of the fibers (enclosed by the *dashed line*) is excluded by the polynomial function computation of the single profiles

The polynomial can be:

- a zero degree function: in this case all the profiles are set to the same average height;
- a first degree function: in this case profile by profile the best fitting line is calculated and subtracted, resulting in a compensation of any tilt distortion;
- a second or higher degree function: in this case the best fitting curve is calculated profile by profile and subtracted, resulting in a compensation of any tilt or curvature distortion.

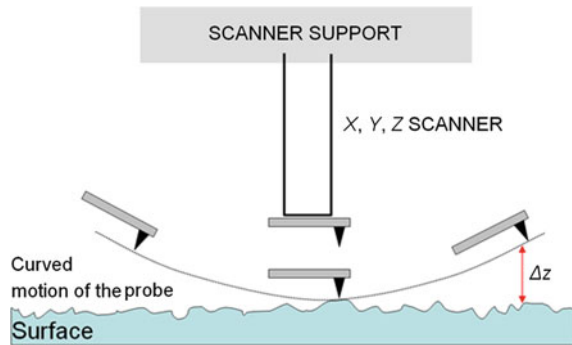
Normally second or higher order compensation should be avoided: indeed they alter the average distribution of data, therefore they should applied only if a reasonable physical meaning is associated to the choice, as discussed for the case of the bow second degree distortion discussed in next Sect. 13.5.

It is worth to note that in case of non-homogeneous surfaces, as in the case of heterogeneous compounds, correction of single profiles has to be carefully implemented. Indeed, the presence of isolated areas with an average value even only slightly higher or lower than the rest of the surface can distort the computation of the best fitting polynomial function. An example is reported in Fig. 13.2, where an AFAM measurement of glass fibers on a polypropylene matrix is reported. Drift distortions are clearly visible in the first image as light blue lines parallel to the ruler (Fig. 13.2a). After a first degree data leveling, drift distortions disappear, but a blue region appears in the center (Fig. 13.2b): this is due to a bad polynomial function computation of the single profiles, altered from the presence of the glass fibers (red regions) which exhibit an average frequency value definitely higher than the surrounding polypropylene matrix (blue region).

Proper data leveling in general can be carried out excluding from the polynomial function computation of the single profiles regions with higher or lower average values. To exclude surface areas from computation it is sufficient to apply segmentation operations (commonly implemented in commercial software), typically based on local average values or on local gradients. This is how the map reported in Fig. 13.2c



**Fig. 13.3** Representation of a tube scanner movement producing a paraboloidal trajectory and causing a bow distortion



was got, excluding from the computation the area of the glass fibers enclosed by the dashed line (Fig. 13.2c).

### 13.5 Bow Effect and Installation Slope

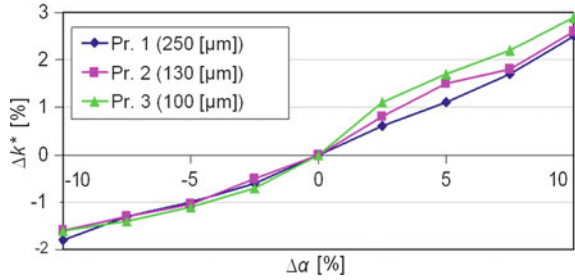
A combination of nonlinearity associated with coupling between the vertical axis and the  $x - y$  directions is frequent, known as bow distortion. This is a nonlinear scan artifact that has the appearance of a false curvature superimposed to the actual specimen topography. This kind of artifact is not due to hysteresis phenomena, but due to the particular probe movement, associated in particular with tube scanner architectures. In fact the tip raster scan pattern is achieved by lateral bending of the piezo-tube: this movement is not horizontal but follows a curved trajectory with a radius of curvature generally in the order of some tens of millimeter [22, 38].

In Fig. 13.3, a representation is given of the spherical or paraboloidal movement (depending on the scanner architecture) causing bow artifacts.

The influence of the bow distortion is in general negligible when measurements are performed in reduced scan ranges, but gets more severe as the scanning range increases. This is true not only when topography is acquired, but also when secondary signals are revealed. In fact, in particular when constant height measurements are carried out, the spherical or paraboloidal trajectory causes a variation of the angle between the cantilever and the surface. Evidently, the same problem arises whenever the probe is scanned in an horizontal trajectory but symmetrically the surface exhibits a curved shape. In such cases the variation of the angle causes a variation of the projection of the distance between the contact point located at the tip apex and the chip, with an effect well described in the case of AFAM in [39] and summarized by the graph reported in Fig. 13.4.

The same problem arises whenever the SPM for acoustic mapping is calibrated with a specific calibration standard and afterwards the calibration is used to get quantitative measurements from other samples. Normally it is very difficult to position surfaces always with the same installation slope with respect to the cantilever. For

**Fig. 13.4** Effect of cantilever incidence angle  $\alpha_0$  relative to the surface on contact stiffness  $k^*$  computation, for three different probes with different lengths as indicated in the legend [39]



that reason the installation slope both for the calibration surface and for other samples has to be recorded: this can be done simply measuring the tilt of the best fitting plane. Angles have to be compared and eventually compensated when applying the conversion models, in order to avoid errors which can rise up to a few percents.

## 13.6 Tip Geometry

Acoustic SPM techniques can provide not only qualitative but also quantitative mapping of surface mechanical properties. However, extrapolation of quantitative data is not trivial: indeed acoustic measurements are influenced by many parameters which may significantly increase uncertainty. Influencing parameters can be divided into two main groups: constant and nonconstant. Parameters related to the probe cantilever can be regarded as constant, including cantilever length, stiffness, or incidence angle. On the other hand, tip-related parameters should be better regarded as nonconstant parameters: in fact, as a consequence of severe interaction between the probe and the surface, tip undergoes significant wear phenomena during scanning (Fig. 13.5). Conversely, only minor wear phenomena are recognized on sample interface.

The tip geometry plays a double role on imaging distortions. First, from a geometrical point of view, the tip shape convolutes with the sample surface causing a topography dilation. Second, the tip radius variation enters the conversion model for mechanical characterization causing an apparent increase in contact stiffness estimation.

### 13.6.1 Geometrical Dilation

A basic principle in Scanning Probe Microscopy (with the only exception of Scanning Tunneling Microscopy) is that the probe senses the presence of features with dimensions smaller than  $1/2$ – $1/10$  the tip apex radius  $R$  or the tip apex contact radius  $a_c$  but cannot image them with a sufficient resolution. Indeed, due to the tip width, the tip flank touches the sample before the tip apex (Fig. 13.6). Since the image is

**Fig. 13.5** Scanning electron microscope image of a silicon tip: after a few hours of AFAM measurements, the tip apex looks more like a flat punch rather than a cone

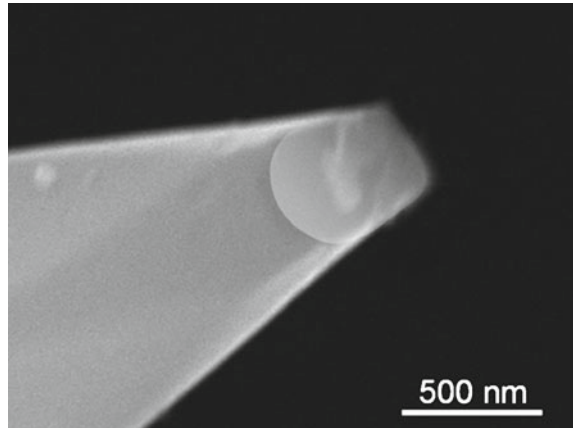
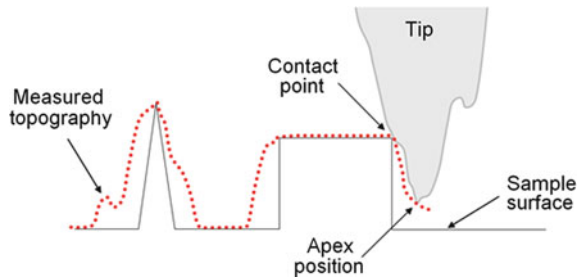


**Fig. 13.6** Schematic view of surface convolution



created only by the position of the tip apex, the measured topography is different from the sample topography; this means that the apex is not always the actual contact point, originating a dilation distortion [17].

As a result, the imaged topography is the replica of the surface obtained if an inverted tip is placed at all points on the surface. The envelope produced by these inverted tip images is the image of the surface [32, 41] as represented in Fig. 13.7.

A schematic representation is sketched in Table 13.3. The example simulates the effect of four probes with a flat punch apex exhibiting different geometries (circular, square, triangular, and irregular) and different average apex contact radius, when scanning over three circular features with diameters of 25, 100, and 400 nm, respectively.

As evidenced by the simulations, the convolution dilates the geometries, with an influence which is more evident when small details are to be analyzed, or when relatively large tips are used. A second effect is the blurring of the features edges, more evident not only when tips are relatively large, but also when the probe exhibits an irregular apex shape.

In the case of acoustic SPM techniques probes with a tip radius  $R$  in the range 5–50 nm are normally implemented: this means that features smaller than some tens of nanometers are not properly imaged.

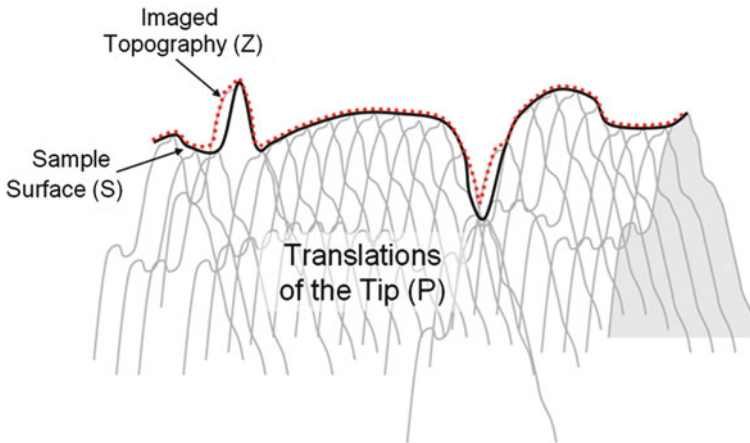


**Fig. 13.7** Image formation after topography dilation

From a mathematical point of view, with reference to Fig. 13.7,  $Z$ ,  $S$ , and  $P$  are the sets of which the function  $z$ ,  $s$ , and  $p$  are the respective tops.  $P$  is defined as the reflection of the tip, through the origin.

The amount of dilation depends on the shape and orientation of the probe as well as on the surface topography. The description the dilation process can be defined through Eq. (13.1):

$$Z = S \oplus P \quad (13.1)$$

The operator  $\oplus$  is used to indicate the convolution; it can be more extensively expressed as (13.2):

$$z(x, y) = \max_{(u,v)} [s(x - u, y - v) + p(u, v)] \quad (13.2)$$

where  $u$  and  $v$  are the components of a vector defining the translation related with the convolution phenomenon.





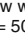




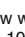




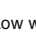




Partial compensation for dilation (deconvolution operation) can be achieved through erosion operations, as described by Villarrubia [17]. Erosion is not the inverse operation of dilation, but the dual of the dilation.

In fact, although it is not possible to define an actual contour of those surface regions not touched by the tip during scanning, an approximation  $S_r$  of the real image of the sample surface can be evaluated as follows (Eqs. (13.3) and (13.4)):

$$S = Z \ominus P \quad (13.3)$$

The deconvolution operator  $\ominus$  can be more extensively expressed as:

**Table 13.3** Simulations on effect of different tip apex sizes and geometries on an acoustic SPM measurement

Tip apex shape Contact radius $a_c$	 Circular shape	 Square shape	 Triangular shape	 Irregular shape
Low wear $a_c = 50$ nm 				
Low wear $a_c = 100$ nm 				
Low wear $a_c = 200$ nm 				

$$s_r(x, y) = \min_{(u,v)} [z(x + u, y + v) - p(u, v)] \tag{13.4}$$

In particular when small features area or segmentation are needed with high accuracy, proper deconvolution procedures are needed. Erosion procedures have to be applied separately for topographies and for acoustic images. For this reason two reflections  $P$  of the tip are needed: a physical reflection  $P_P$  of the tip for topography and an acoustic reflection  $P_A$  for deconvolution, respectively, of topography and of the acoustic map. For reverse imaging of tip reflection  $P_P$ , several papers have been reported and proper samples are also available featuring high aspect ratio and sharp nanostructures (as for instance niobium oxyde nano-needles) [28, 32, 40, 41]. With regard to acoustic tip reflection there is still a lack of knowledge, however, extending physical tip principles, an ideal sample would feature very flat (say with an average roughness  $S_a$  less than at least one tenth the radius of curvature of the tip) and soft surface (as for instance a polymer) with stiff nanostructures (say with a diameter smaller than at least half of the contact radius  $a_c$ ) embedded at the interface. Software tools for reconstruction of tip reflection are already implemented in commercial software, as for instance in [26, 27]. An example is reported in Fig. 13.8, where together with the topography of a Styrene Butadiene Styrene (SBS)-Poly(methyl methacrylate) (PMMA) polymer blend (Fig. 13.8a), the acoustic map is reported before (Fig. 13.8b) and after deconvolution (Fig. 13.8c). After deconvolution SBS phase (green islands in the red PMMA matrix) appears slightly shrunk, with dimensions better fitting the topography appearance. In the second row, representations of the physical tip apex shape (Fig. 13.8d) and of the acoustic tip (Fig. 13.8e) are reported. They were both

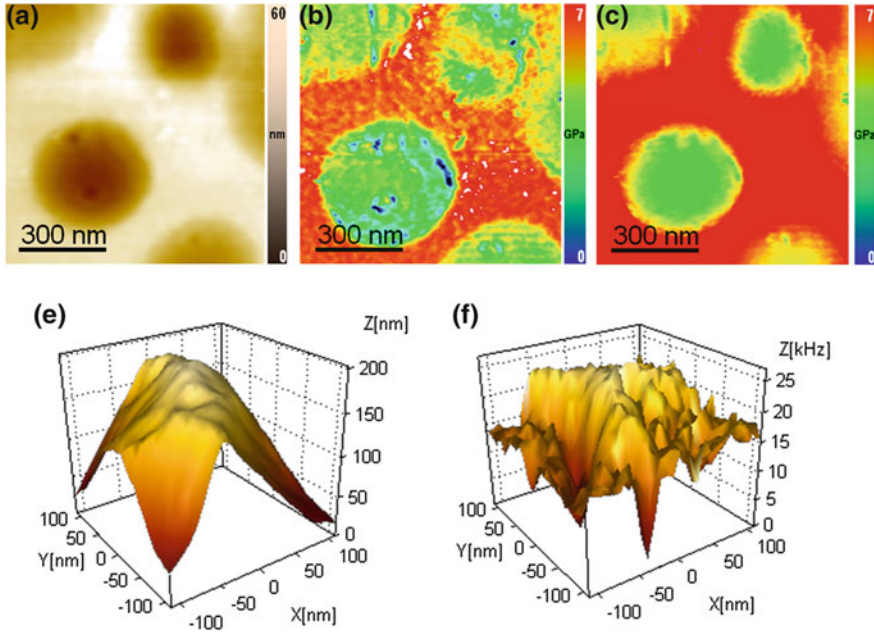


**Fig. 13.8** Topography (a) and mechanical map (b) of a PMMA/SBS polymer blend surface. After deconvolution (c) SBS islands appear slightly smaller and better defined. In the second row three-dimensional rendering of the physical tip (physical reflection  $P_P$ ) and of the acoustic tip ( $P_A$ )

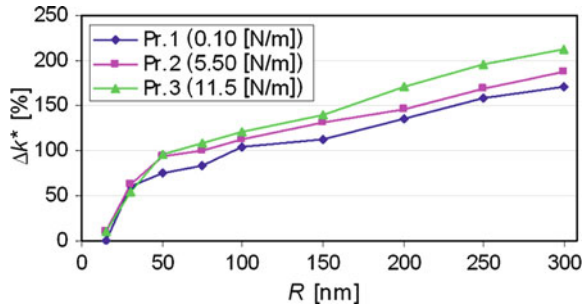
obtained by means of a blind tip reconstruction through the commercial software SPIP™ [26] implementing the algorithm described by Villarrubia [17].

It is worth to note that such blind tip reconstruction and subsequent deconvolution are applicable in particular when low noise measurements are taken and when scan resolution is comparable with tip apex dimensions. In case of noisy measurements or in case of large area or low resolution scans blind tip reconstruction can be distorted in the first case and distorted or not necessary in the second case.

### 13.6.2 Geometrical Dilatation

As reported by Marinello et al. [25, 39] wear phenomena affecting the tip and its corresponding changes in geometry is the major impediment for exploitation of quantitative AFAM. Indeed, at constant deflection scanning, variations in tip radius during measurement cause a modification in the tip to surface interaction, with a variation in the contact dynamic. The direct effect of tip radius on contact stiffness for three different probes is reported in Fig. 13.9.

**Fig. 13.9** Effect of radius of curvature  $R$  on contact stiffness  $k^*$  computation. In the legend the three probes with the three different force constants are indicated [39]



As described by [25], during AFAM interaction tip wear rate can rise up to 1–2 nm/min in the case of stiff measured surfaces, which means a variation of up to 40–50 nm in the tip radius between the beginning and the end of measurement scan. Such large variations in tip radius correspondingly cause very significant variations in contact stiffness computation (see Fig. 13.9) and even larger deviations are to be expected when multiple measurements are taken with the same probe. To limit such influence two preventative approaches can be adopted:

- implementation of tips with hard coatings, where the wear rate can be reduced down to 0.1 nm/min [25];
- use of warm up procedures (at least half an hour standstill scan with the tip approached to the surface) before a set of measurements is run, in order to stabilize as much as possible tip condition.

Anyhow, whatever is the chosen approach, in order to get quantitative measurements it is necessary to define the best approximation of the tip shape. To this end, best practice procedures advice to monitor tip geometry through deconvolution scans right before and right after the acoustic scan. Deconvolution scans can be performed on a proper sample for tip reconstruction featuring high aspect ratio and sharp nanostructures. However, such procedure is quite time spending and needs double sample exchange for each acoustic measurement. Therefore an alternative procedure, even though less accurate, is to use the same topography revealed together with the acoustic map to make a blind reconstruction of the reflection of the tip: afterwards such reconstruction can be used to carry out a corrected calibration of the acoustic map [42].

## 13.7 Conclusions

In order to exploit traceable quantitative mechanical characterization of surfaces, after measurement proper data processing is needed. Indeed data processing allows elimination or compensation of artifacts and distortions and eventually optimization of quantitative information.

In this chapter some of the main issues have been discussed, with particular reference to sample installation slope and bow distortion, drift and leveling, and tip-related issues.

Best practice procedures however recommend, together with data processing, implementation of frequent calibration operations, where attention is paid to reproduce as similar as possible measurement conditions between calibration specimens and samples to be tested.

## References

1. F. Dinelli, M.R. Castell, D.A. Ritchie, N.J. Mason, G.A.D. Briggs, O.V. Kolosov, Mapping surface elastic properties of stiff and compliant materials on the nanoscale using ultrasonic force microscopy. *Philos. Mag. a-Phys. Cond. Matter Struct. Defects Mech. Prop.* **80**, 2299–323 (2000)
2. F. Dinelli, S.K. Biswas, G.A.D. Briggs, O.V. Kolosov, Measurements of stiff-material compliance on the nanoscale using ultrasonic force microscopy. *Phys. Rev. B* **61**, 13995–4006 (2000)
3. A.P. McGuigan, B.D. Huey, G.A.D. Briggs, O.V. Kolosov, Y. Tsukahara, M. Yanaka, Measurement of debonding in cracked nanocomposite films by ultrasonic force microscopy. *Appl. Phys. Lett.* **80**, 1180–2 (2002)
4. O.V. Kolosov, I. Grishin, R. Jones, Material sensitive scanning probe microscopy of subsurface semiconductor nanostructures via beam exit Ar ion polishing. *Nanotechnology* **22**, 8 (2011)
5. D.C. Hurley, M. Kopycinska-Muller, A.B. Kos, R.H. Geiss, Nanoscale elastic-property measurements and mapping using atomic force acoustic microscopy methods. *Meas. Sci. Technol.* **16**, 2167–2172 (2005)
6. M. Kopycinska-Müller, A. Caron, S. Hirsekorn, U. Rabe, N. Natter, R. Hempelmann, R. Birringer, W. Arnold, Quantitative evaluation of elastic properties of nano-crystalline nickel using atomic force acoustic microscopy AFM modeling MST. *Z. Phys. Chem.* **222**, 471–498 (2008)
7. U. Rabe, S. Amelio, E. Kester, V. Scherer, S. Hirsekorn, W. Arnold, Quantitative determination of contact stiffness using atomic force acoustic microscopy. *Ultrasonics* **38**(1–8), 430–437 (2000)
8. E. Kester, U. Rabe, L. Presmanes, P. Tailhades, W. Arnold, Measurement of mechanical properties of nanoscaled ferrites using atomic force microscopy at ultrasonic frequencies. *Nanostruct. Mater.* **12**(5–8), 779–782 (1999)
9. P. Vairac, B. Cretin, Scanning microdeformation microscopy: experimental investigations on non-linear contact spectroscopy. *Surf. Interface Anal.* **27**, 588 (1999)
10. P. Vairac, B. Cretin, in *Scanning Microdeformation Microscopy: Subsurface Imaging and Measurement of Elastic Constants at Mesoscopic Scale, Applied Scanning Probe Methods II*, ed. by B. Bhushan, H. Fuchs, (Springer, Berlin, 2006) pp. 241–281
11. P. Vairac, S. Ballandras, B. Cretin, Finite element analysis of the behavior of the scanning microdeformation microscope. *Ultrason. Ferroelectr. Freq. Control* **48**(4), 895–899 (2001)
12. S. Avasthy, G. Shekhawat, V. Dravid, Scanning near-field ultrasound holography. in: *Meyers Encyclopedia of analytical chemistry: supplementary volumes S1–S3 : applications, theory and instrumentation*, vol. a9146, ed. by A. Robert (Wiley, Hoboken, 2010), pp. 1–9
13. G. Shekhawat, V. Dravid, Seeing the invisible: scanning near-field ultrasound holography (SNFUH) for high resolution sub-surface imaging. *Microsc. Microanal.* **12**(S02), 1214–1215 (2006)
14. G. Shekhawat, V. Dravid, Nanoscale imaging of buried structures via scanning near-field ultrasound holography. *Science* **310**(5745), 89–92 (2005)



15. G. Shekhawat, S. Avasthy, A. Srivastava, S.H. Tark, V. Dravid, Probing buried defects in extreme ultraviolet multilayer blanks using ultrasound holography. *IEEE Trans. Nanotechnol.* **9**(6), 671–674 (2010)
16. Y. Liu, S. Chen, E. Zussman, C.S. Korach, W. Zhao, M.H. Rafailovich, Diameter-dependent modulus and melting point behavior in electrospun semi-crystalline polymer fibers. *Macromolecules* **44**(11), 4439–4444 (2011)
17. D. Passeri, M. Rossi, A. Alippi, A. Bettucci, M.L. Terranova, E. Tamburri, F. Toschi, Characterization of epoxy/single-walled carbon nanotubes composite samples via atomic force acoustic microscopy. *Physica E* **40**, 2419–2424 (2008)
18. W. Zhao, C.S. Korach, Measurement of Epoxy Stiffness by Atomic Force Acoustic Microscopy. *Proceedings ASME 2009 International Mechanical Engineering Congress and Exposition*, Vol. 12: Micro and Nano Systems, Part A and B, 85–87, 2009
19. A. Ebert, B.R. Tittmann, J. Du, W. Scheuchenzuber, Technique for rapid in vitro single-cell elastography. *J. Ultrasound Med. Biol.* **32**(11), 1687–1702 (2006)
20. C. Miyasaka, B.R. Tittmann, Ultrasonic Atomic Force Microscopy on Spray Dried Ceramic Powder. in *Acoustic Imaging*, vol. 27, ed. by W. Arnold, S. Hirsekorn (Kluwer Academic Publishers, Dordrecht, Netherlands, 2004), pp. 715–720
21. D. Doroski, B.R. Tittmann, C. Miyasaka, Study of biomedical specimens using scanning acoustic microscopy. *Acoust. Imaging* **28**(1), 13–20 (2007)
22. F. Marinello, P. Bariani, S. Carmignato, E. Savio, Geometrical modelling of scanning probe microscopes and characterization of errors. *Meas. Sci. Technol.* **20**(8), 084013 (2009)
23. F. Marinello, E. Savio, Use of cylindrical artefacts for AFM vertical calibration. *Meas. Sci. Technol.* **18**(2), 462–468 (2007)
24. J. Garnæs, A. Kule, L. Nielsen, F. Borsetto, True three-Dimensional Calibration of closed loop scanning probe microscopes. in *Nanoscale Calibration Standards and Methods: Dimensional and Related Measurements in the Micro- and Nanometer Range*, ed. by G. Wilkening, L. Koenders (Berlin, Wiley-VCH, 2004), pp. 193–204
25. F. Marinello, P. Schiavuta, S. Vezzù, A. Patelli, S. Carmignato, E. Savio, Atomic force acoustic microscopy for quantitative nanomechanical characterization. *Wear* **271**(3–4), 534–538 (2011)
26. Scanning Probe Image Processor (SPIP™, developed by Image Metrology A/S, [www.imagemet.com](http://www.imagemet.com))
27. Window Scanning x Microscope (WSxM), developed by Nanotec Electronica, [www.nanotec.es](http://www.nanotec.es)
28. F. Marinello, Atomic Force Microscopy in nanometrology: modeling and enhancement of the instrument. Ph.D dissertation, University of Padova and Technical University of Denmark, (2007) [http://paduaresearch.cab.unipd.it/1295/01/PhD\\_Thesis\\_Marinello.pdf](http://paduaresearch.cab.unipd.it/1295/01/PhD_Thesis_Marinello.pdf)
29. R. Arinéro, G. Leveque, P. Girard, J.Y. Ferrandis, Image processing for resonance frequency mapping in atomic force modulation microscopy. *Rev. Sci. Instrum.* **78**, 023703 (2007)
30. R.V. Gainutdinov, P.A. Arutyunov, Artifacts in atomic force microscopy. *Russ. Microelectron.* **30**(4), 219–224 (2001)
31. T.G. Lenihan, A.P. Malshe, W.D. Brown, L.W. Schaper, Artifacts in SPM measurements of thin films and coatings. *Thin Solid Films* **270**, 356–361 (1995)
32. ASTM E 1813-96, Standard practice for measuring and reporting probe tip shape in scanning probe microscopy, (1998), pp. 1–11, (reapproved 2002)
33. H.U. Danzebrink, L. Koenders, G. Wilkening, A. Yacoot, H. Kunzmann, Advances in scanning force microscopy for dimensional metrology. Keynote paper *Ann. CIRP* **55**(2), 841–878 (2006)
34. D. Kim, D.Y. Lee, D.G. Gweon, A new nano-accuracy AFM system for minimizing Abbe errors and the evaluation of its measuring uncertainty. *Ultramicroscopy* **107**(4–5), 322–328 (2007)
35. L. Mingzhen, G. Sitian, J. Qihai, C. Jianjun, D. Hua, G. Hongtang, An atomic force microscope head designed for nanometrology. *Meas. Sci. Technol.* **18**(6), 1735–1739 (2007)
36. J.F. Jorgensen, C.P. Jensen, J. Garnæs, Lateral metrology using scanning probe microscopes, 2D pitch standards and image processing. *Appl. Phys. A* **66**, 847–852 (1998)

37. A. Sikora, Correction of structure width measurements performed with a combined shear-force/tunnelling microscope. *Meas. Sci. Technol.* **18**(2), 456–461 (2007)
38. F. Marinello, S. Carmignato, A. Voltan, E. Savio, L. De Chiffre, Error sources in atomic force microscopy for dimensional measurements: taxonomy and modeling. *ASME—J. Manuf. Sci. Eng.* **132**(3), 031003–1-8 (2010)
39. F. Marinello, P. Schiavuta, S. Carmignato, E. Savio, Critical factors in quantitative atomic force acoustic microscopy. *CIRP J. Manuf. Sci. Technol.* **3**(1), 49–54 (2010)
40. J.S. Villarrubia, Algorithms for scanned probe microscope image simulation, surface reconstruction, and tip estimation. *J. Res. Natl. Inst. Stand. Technol.* **102**(4), 425–454 (1997)
41. J.S. Villarrubia, Morphological estimation of tip geometry for scanner probe microscopy. *Surface Sci.* **321**(3), 287–300 (1994)
42. M. Kopycinska-Müller, R.H. Geiss, D.C. Hurley, Contact mechanics and tip shape in AFM-based nanomechanical measurements. *Ultramicroscopy* **106**, 466–474 (2006)

# Chapter 14

## Friction and Internal Friction Measurements by Atomic Force Acoustic Microscopy

A. Caron and W. Arnold

**Abstract** Atomic force acoustic microscopy (AFAM) is a contact-resonance spectroscopy technique originally designed to determine elastic properties at the nanometer scale. While the load dependent shift of contact-resonance frequencies has been exploited to determine the elasticity of sample surfaces, less attention has been given to the damping of contact resonances. In this chapter, the authors show how the atomic force microscopy technique can be used to measure interfacial and internal friction by analyzing the Q-factor of contact-resonance curves.

### 14.1 Introduction

With the development of micro-mechanical devices and materials whose properties are governed by nanoscale interfaces, characterization techniques with high spatial resolution have become crucial. To this end several techniques have been developed, based on dynamic atomic force microscopy (AFM), such as the tapping mode [1], force modulation mode [2], atomic force acoustic microscopy (AFAM) [3], and ultrasonic atomic force microscopy (UAFM) [4]. AFAM and UAFM are contact-resonance spectroscopy techniques where a microfabricated AFM cantilever is excited to its contact resonances. The spatial resolution of these techniques is given by the tip-sample contact radius  $a$ , which is usually around a few nanometers,

---

A. Caron (✉)

INM – Leibniz-Institute for New Materials, D-66123 Saarbrücken, Germany  
e-mail: arnaud.caron@inm-gmbh.de

A. Caron

WPI-Advanced Institute of Materials Research, Tohoku University, Sendai 980-8577, Japan

W. Arnold

Department of Materials, Saarland University, Saarbrücken, Germany

W. Arnold

Physikalisches Institut, Universität Göttingen, D-66123 Göttingen, Germany

typically 10 nm. When bringing the tip of an AFM cantilever in contact with a sample surface, one observes a shift of the resonance frequencies to higher values and a decrease of the  $Q$ -factor. The frequency shift can be used to determine the contact stiffness  $k^*$  [5–7], which is related to the elastic properties of the sample, allowing one to obtain its indentation modulus  $M$ . Similarly, injecting transversal ultrasound waves into the sample instead of longitudinal waves, torsional and lateral bending contact vibration of the cantilever can be excited and used to determine the shear elasticity of the sample surface and ultimately to determine the Poisson's ratio of the sample [8].

Beside the contact-resonance frequencies, efforts have been undertaken to exploit the  $Q$ -value of AFM contact resonances in order to perform local internal friction measurements, for example in polymers, and relate them to the various relaxation mechanisms, both locally and globally [9]. Also,  $Q$ -mapping of the contact resonances of AFM cantilevers has been suggested to image areas of high absorption [10] in materials. Similarly, the decrease of the  $Q$ -factor of torsional contact resonances as a function of the amplitude of the exciting transversal ultrasonic signal has been associated with the onset of micro-sliding [11], thus further broadening the application range of AFAM to nanoscale friction measurements.

In this chapter, the authors give an overview of the applications of AFAM in the field of materials science. The first part of this chapter focuses on the working principles of AFAM and its application, in order to determine local elastic properties. In the second part, results are presented on internal friction measurements and their relation to the dislocation activity in nanocrystalline (nc-) nickel. Finally, the contribution of friction to the contact damping of an AFM cantilever in contact with a sample surface is discussed.

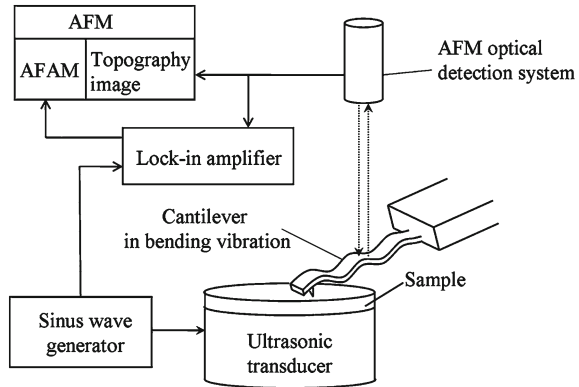
## 14.2 Atomic Force Acoustic Microscopy and Elasticity Measurements at the Nanoscale

Figure 14.1 shows the experimental setup of AFAM where a transducer injects longitudinal ultrasonic waves into the sample leading, to periodic normal displacements at the sample surface that couples to the tip of a microfabricated cantilever and excites it to bending vibration.

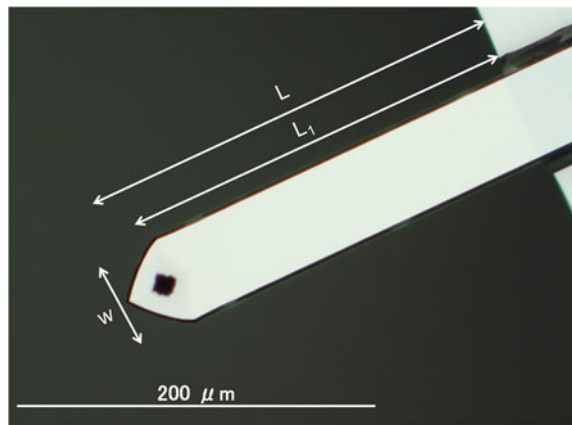
The free bending resonances of an AFM cantilever are determined by its geometry, its elastic properties and its mass density, and are characterized by  $Q$ -values of typically 200–1000 in ambient air. Neglecting the damping caused by frictional losses in air, the first free bending-resonance frequency of a cantilever beam is given by

$$f_{01} = \frac{(1.8751)^2}{2\pi} \frac{1}{L^2} \sqrt{\frac{EI}{\rho A}} \quad (14.1)$$

**Fig. 14.1** Experimental setup of AFAM



**Fig. 14.2** Optical image of single-crystal silicon AFM cantilever (type contsc, manufactured by Nanosensors GmbH, Germany)



where  $L$  is the length of the cantilever,  $E$  is the Young’s modulus of the cantilever material,  $I$  is the area moment of inertia,  $\rho$  is the mass density, and  $A$  is the cross-sectional area. The length and the width  $w$  of the cantilever can be measured by optical microscopy (see Fig. 14.2) to determine the cantilever spring constant  $k_c$  according to [12]

$$k_c = \frac{Ewb^3}{4L^3} \tag{14.2}$$

When bringing a cantilever into contact with a sample surface, one observes a shift of the resonance frequencies to higher values and a decrease of the  $Q$ -values down to 20–100 due to the stiffening and damping effect of the contact. The still appreciable  $Q$ -values of the contact resonances lead to resonance amplification, and therefore also allow one to detect the cantilever resonances in contact with a high signal-to-noise ratio. Depending on the tip and sample properties, the contact forces can be hydrostatic, electrostatic, adhesive, or elastic. Using stiff cantilevers and hence high static loads, the contact forces can be adjusted such that they are in the elastic regime,

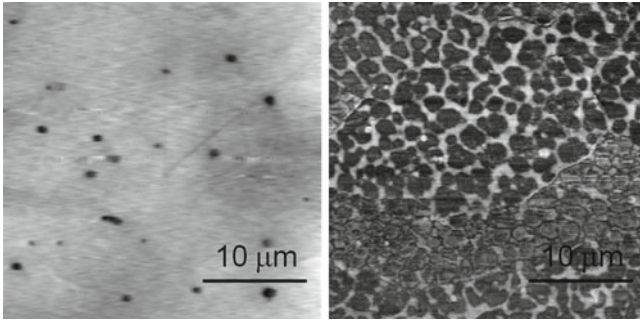


**Fig. 14.3** *Left* AFM topography image recorded on a rapidly cooled bi-phased NiMnSn alloy with a single-crystal silicon cantilever of stiffness  $k_c = 42 \text{ N/m}$  and an applied load  $P \approx 60 \text{ nN}$ . The z-scale of the image is  $70.8 \text{ nm}$ . *Right* Simultaneously recorded vibration amplitude image at the frequency  $f = 720 \text{ kHz}$

while adhesive forces can be neglected. AFAM can be used to qualitatively map local elasticity changes on a sample surface (see Fig. 14.3). During the image recording in Fig. 14.3, the cantilever was excited at a fixed frequency near its resonance, here  $f = 720 \text{ kHz}$ . The contact-resonance frequency then shifts according to the local changes in the contact stiffness, which results in changes in the vibration amplitude of the cantilever at the working frequency. Likewise, the contact-resonance frequency value has been used as an imaging quantity [13, 14]. In [15] also, the recording of the contact-resonance frequency was used to quantitatively characterize the elastic landscape of a microalloyed steel.

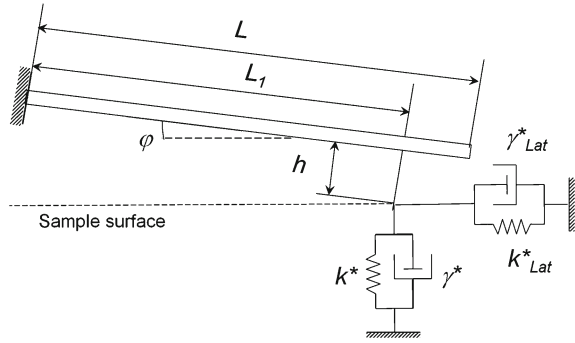
Numerous papers have described the cantilever vibrations in AFAM experiments in order to relate the cantilever contact-resonance behavior to the properties of the sample surface (see for example Refs. [6, 7, 16, 17]). In most cases, the cantilever is assumed to be a forced rectangular beam for which the following equation of motion applies:

$$EI \frac{\partial^4 y}{\partial x^4} + \eta_{\text{air}} \frac{\partial y}{\partial t} + \rho A \frac{\partial^2 y}{\partial t^2} = F \delta(x - x_0) e^{i\omega t} \quad (14.3)$$

where  $\eta_{\text{air}}$  is the damping constant of the cantilever for viscous losses in air and  $y(x, t)$  is the vertical displacement of the beam. The position along the beam is  $x$  and  $t$  is the time.  $F$  is the force acting on the tip at the position  $x_0$ .

Considering repulsive elastic forces and small vibration amplitudes, the interaction forces between tip and sample surface can be approximated linearly and are often represented by linear springs as shown in the mechanical model for the cantilever in Fig. 14.4. There, accounting for the tilt angle  $\phi$  of the cantilever length axis with regard to the sample surface, the contact forces acting on the tip are represented by two linear springs for the vertical and lateral contact stiffness  $k^*$  and  $k_{\text{Lat}}^*$  and the two dashpots  $\gamma^*$  and  $\gamma_{\text{Lat}}^*$  for the vertical and the lateral contact damping, respectively. Following earlier work by Mazeran and Loubet [18], the lateral contact forces  $P_{\text{lat}}$  can be set as a fraction of the vertical forces  $P$  according to

**Fig. 14.4** Mechanical model of a rectangular cantilever beam in contact with a sample surface



$k_{Lat}^*/k^* \approx P_{Lat}/P = 2(1 - \nu)/(2 - \nu)$ , where  $\nu$  is the Poisson's ratio. The boundary conditions for the displacement and the slope of the cantilever beam are expressed as:

$$x_0 = L_1 \text{ or } x' = L - L_1 : \begin{cases} y(x) = y'(x') \\ \frac{\partial y(x)}{\partial x} = \frac{\partial y'(x')}{\partial x'} \end{cases} \quad (14.4)$$

Further, from the equilibrium between the shear forces arising from the cantilever deflection and the contact restoring forces one obtains the following boundary condition:

$$EI \frac{\partial^3 y(x)}{\partial x^3} \Big|_{x=L_1} = k^* y(L_1, t) + \gamma^* \frac{\partial y(L_1, t)}{\partial t} \quad (14.5)$$

which holds for the case when only vertical forces are present ( $\phi = 0$ ) [16, 17]. The contact resonances of the cantilever are determined by the cantilever stiffness  $k_c$ , the contact stiffness  $k^*$ , and the contact-damping constant  $\gamma^*$ . An analytical solution for the equation of motion of the mechanical model depicted in Fig. 14.4 has been developed by Rabe [7]. Also a finite difference method has been applied to calculate the contact vibrating behavior of cantilevers [16], and FEM methods for cantilevers taking into account their complex geometries [19, 20]. These solutions can then be used to determine the contact stiffness from the contact-resonance frequencies of a cantilever [5–7, 21, 22].

With the development of depth-sensing techniques, such as nanoindentation the relation of the contact stiffness to the elastic properties has been the subject of intensive research. Based on the work of Sneddon [23], Oliver and Pharr formulated the contact stiffness  $k^*$  for the case of an elastic contact between a rotationally symmetric indenter and a flat surface as [24]:

$$k^* = \frac{2}{\sqrt{\pi}} E^* \sqrt{A_c} \quad (14.6)$$

where  $A_c$  is the contact area and  $E^*$  is the reduced modulus of elasticity. For isotropic solids  $E^*$  is given by

$$E^* = \left( \frac{1}{M_{\text{tip}}} + \frac{1}{M_s} \right)^{-1} \quad (14.7)$$

where  $M_{\text{tip}}$  and  $M_s$  are the indentation moduli of the tip and the sample, respectively [25]. For isotropic bodies the indentation modulus is calculated as  $M = E/(1 - \nu^2)$ . If there exists a three- or fourfold rotational symmetry axis perpendicular to the boundary, the contact area is still circular. In this case, the same equations hold as for isotropic materials if the indentation moduli  $M$  are calculated from single-crystal elastic constants [25].

Unlike nanoindentation experiments, in AFAM measurements the geometry of the tip, and hence the contact area between tip and sample are not known and may also change during measurements due to wear [26]. Usually, the tip is considered to be either spherical or to act as a flat punch (see for example Ref. [27]), in such cases the contact stiffness can be expressed by Eqs. (14.8) and (14.9), respectively [23, 28].

$$k_{\text{sph}}^* = \sqrt[3]{6R_{\text{sph}} P E^* 2} \quad (14.8)$$

$$k_{\text{fp}}^* = 2R_{\text{fp}} E^* \quad (14.9)$$

where  $R_{\text{sph}}$  and  $R_{\text{fp}}$  are the radii of a spherical tip and of a flat punch. Accounting for intermediate geometries between a sphere and a cylinder, an empirical model for the contact stiffness has been proposed, which allows a direct fit of the experimental data [6, 29]:

$$k^* = 2^{\frac{2n+1}{3}} R^{2n-1} P^{1-n} E^{*n} \quad (14.10)$$

where  $R$  and  $n$  are fit parameters. The parameter  $n$  describes the curvature of the tip: For a spherical indenter  $n = 2/3$  and Eq. (14.10) reduces to Eq. (14.8), whereas for a flat punch  $n = 1$  and Eq. (14.10) reduces to Eq. (14.9). Inserting Eq. (14.10) in Eq. (14.6), leads to the following expression of the contact radius:

$$a_c = 2^{\frac{n-1}{3}} R^{2n-1} P^{1-n} E^{*n} - 1. \quad (14.11)$$

In a Hertzian contact the indentation depth  $\delta$  is given as [28]:

$$\delta = \frac{3P}{4E^* a_c}. \quad (14.12)$$

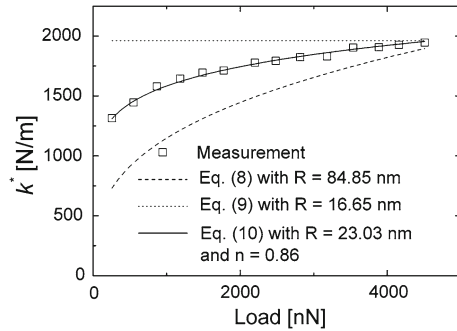
Inserting Eq. (14.11) into Eq. (14.12), leads to:

$$\delta = 3P^n 2^{-\frac{n+5}{3}} R^{1-2n} E^{*-n} \quad (14.13)$$

Figure 14.5 shows the contact stiffness  $k^*(P)$  as a function of applied load  $P$  measured on quartz glass with a diamond-coated silicon tip mounted on a cantilever



**Fig. 14.5** Contact stiffness measured on quartz glass with a diamond-coated single-crystal silicon cantilever ( $k_c = 42 \text{ N/m}$ ) (open squares). Measurement data are fitted with Eq. (14.8) for the case of a spherical tip (dashed line), with Eq. (14.9) for the case of a flat punch (dotted line), and with Eq. (14.10) for an intermediate tip geometry (solid line)



of stiffness  $k_c = 42 \text{ N/m}$ . In Fig. 14.5 the experimental data are fitted with Eq. (14.10) using  $E^* = 58.43 \text{ GPa}$ , corresponding to  $M_{\text{quartz}} = 75.8 \text{ GPa}$  and  $M_{\text{tip}} = 255 \text{ GPa}$ , while  $R = 23 \text{ nm}$  and  $n = 0.86$ . The indentation modulus of the tip  $M_{\text{tip}}$  was determined upon calibration on two calibration samples with known elastic properties, i.e., quartz glass and (111) nickel [29]. The best fits with Eqs. (14.8, 14.9) are also shown for the cases of a spherical tip with  $R = 84.85 \text{ nm}$  and a flat punch with  $R = 16.65 \text{ nm}$ . From Fig. 14.5 one can see that Eq. (14.10) provides a much better fit of the experimental data than Eqs. (14.8, 14.9), even at the cost that the fit parameters  $R$  and  $n$  do not necessarily correspond to their real values. Further, Fig. 14.6 shows the calculated plots of the contact radius  $a_c(P)$  and the penetration depth  $\delta(P)$  for the  $R$  and  $n$  values determined in Fig. 14.5 on quartz glass and the same  $E^*$  value as above.

Elasticity measurements using AFAM usually consist of calibrating the tip properties on elastically well-defined test materials before and after measurements on the sample of interest (see for example [6, 17, 27, 29–31]). In Refs. [6, 29] AFAM was used to measure the elasticity of nc-Ni with grain sizes varying from 14 to 67 nm. Based on the model shown in Fig. 14.4 and described in detail including damping [7], contact-resonance spectra as measured by a beam deflection detector were analyzed to determine the contact stiffness and the contact damping (see Sect. 14.4 of this chapter). The contact damping increases the stiffness of the contact [16] but as already mentioned above, the  $Q$ -value of the contact resonances measured was about 50, allowing one to neglect the influence of the contact damping on the contact stiffness  $k^*$  [29]. The calibration procedure consisted of successive continuous recordings of contact-resonance curves as a function of the static load on quartz glass ( $M_{\text{quartz}} = 75.8 \text{ GPa}$ ) and (111)-oriented nickel ( $M_{(111)\text{-Ni}} = 255 \text{ GPa}$ ) as calibration samples, and the material under test. For these measurements, a new stiff diamond-coated silicon single-crystal cantilever was used for each sample, with  $k_c = 39\text{--}41 \text{ N/m}$ . The ratio  $L_1/L$  of the tip position was determined for each cantilever from the first and the second contact bending-resonance frequencies recorded on quartz glass [7]. The indentation modulus  $M_{\text{tip}}$  of each cantilever tip was evaluated from the  $k^*(P)$ -plots recorded on the reference samples by fitting the experimental results with Eq. (14.10) and assuming a common value of the tip indentation modulus

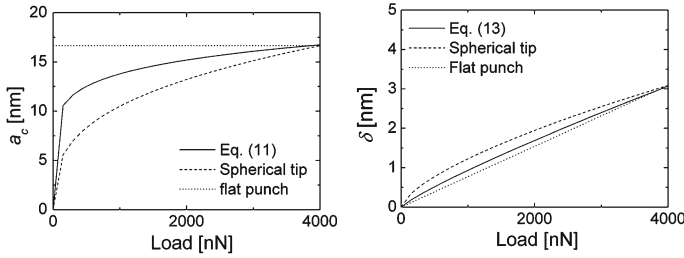


**Fig. 14.6** *Left* Calculated contact radius  $a_c$  as a function of load  $P$  using Eq. (14.11) with  $E^* = 58.43$  GPa,  $R = 23$  nm and  $n = 0.86$ , and compared to the cases of a spherical tip with  $R_{\text{sph}} = 84.85$  nm and of a flat punch with  $R_{\text{fp}} = 16.65$  nm, *Right* elastic penetration depth  $\delta$  calculated using Eq. (14.13) with the same values for  $E^*$ ,  $R$ ,  $n$ ,  $R_{\text{sph}}$ , and  $R_{\text{fp}}$  as above

$M_{\text{tip}}$  and individual parameters  $R$  and  $n$  for quartz glass and (111)-oriented Ni single crystal, respectively. Assuming a starting value  $M_{\text{tip}} = 250$  GPa, the parameters  $R$  and  $n$  were optimized until slight variations in the value for  $M_{\text{tip}}$  did not significantly affect any longer the values of  $R$  and  $n$ . Figure 14.7 shows successive measurements on the calibration samples before (a, b) and after (c, d) measurement on nc-Ni with a grain size of 14 nm (nc-Ni $_{d=14\text{nm}}$ ). For the measurements shown in Figs. 14.7a, b the values for  $R$  and  $n$  were found to vary from  $R = 18.8$  nm and  $n = 0.93$  to  $R = 11.2$  nm and  $n = 0.88$ , for quartz glass and (111)-oriented Ni single crystal, respectively. After measurement on nc-Ni $_{d=14\text{nm}}$ , the tip calibration procedure yielded  $R = 23.3$  nm and  $n = 0.86$  on quartz glass, and  $R = 13.3$  nm and  $n = 0.86$  on (111)-oriented Ni single crystal. According to Eq. (14.11) these changes in  $R$  and  $n$  correspond to changes in  $a_c$  of 23 and 2% for quartz glass and (111)-oriented Ni single crystal. While the values of the contact radii obtained from the first and second calibration procedures are in good agreement, the measurements performed on quartz glass and (111)-oriented Ni single crystal yield significantly different values for  $a_c$  that may reflect the different surface roughness of both calibration samples. This statement is also supported by recent work by Stan and Cook [31]. There, the authors have used AFAM results to calculate the local indentation moduli of 100 nm thick nc-Au films with grain size distributions from 80 to 120 nm. Stan and Cook showed that surface roughness and the local grain anisotropy lead to a distribution of the indentation modulus.

Further, from these measurements the indentation modulus of the cantilever tip was determined to be  $M_{\text{tip}} = 243.3 \pm 11.1$  GPa. Considering five different diamond-coated silicon cantilevers the indentation modulus of the tip was found to vary from  $M_{\text{tip}} = 210$  GPa to  $M_{\text{tip}} = 297$  GPa with a mean value of  $M_{\text{tip}} = 236.1$  GPa. This variation is quite reasonable considering the data published for diamond-like carbon layers [30, 32–34].

Using the same procedure as for the calibration samples, the reduced elasticity moduli of the nc-Ni samples were obtained by fitting the experimental results for  $k^*(P)$  with Eq. (14.10) (Fig. 14.7), where  $R$  and  $n$  were selected within the values

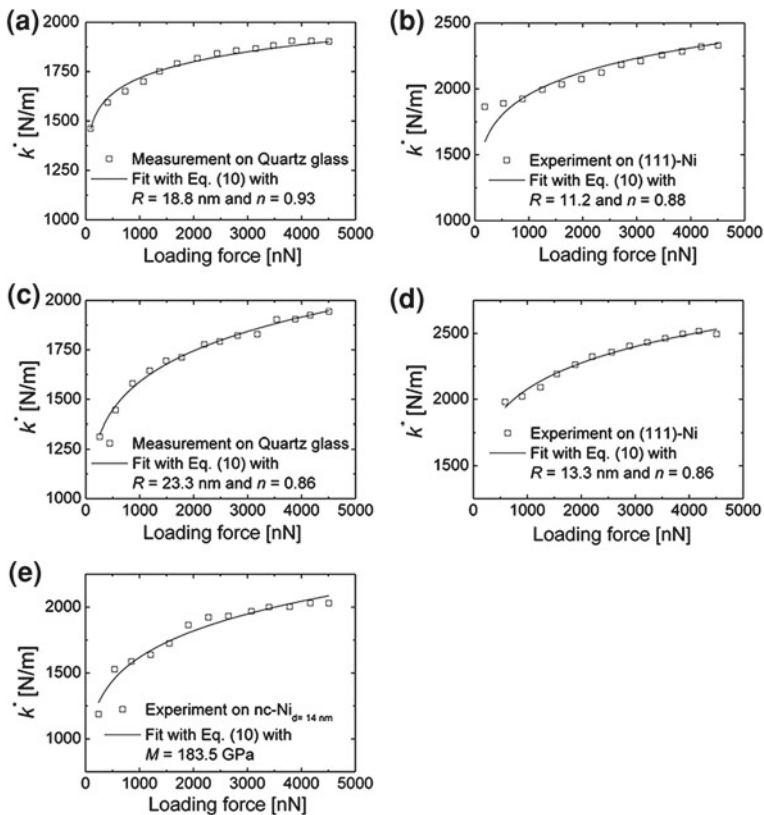


**Fig. 14.7** Contact stiffness  $k^*(P)$ -plots recorded on (a, c) quartz glass and (b, d) (111) Ni single crystal (a, b) before and (c, d) after measurement on (e) nc-Ni with a grain size of 14 nm (nc-Ni<sub>d=14 nm</sub>). From these measurements the indentation modulus of the tip was found to be  $M_{tip} = 243.3 \pm 11.1$  GPa. Before measurement on (nc-Ni<sub>d=14 nm</sub>) the tip calibration procedure yielded  $R = 18.8$  nm and  $n = 0.93$  on quartz glass, and  $R = 11.2$  nm and  $n = 0.88$  on (111)-oriented Ni single crystal. After measurement on (nc-Ni<sub>d=14 nm</sub>) the tip calibration procedure yielded  $R = 23.3$  nm and  $n = 0.86$  on quartz glass, and  $R = 13.3$  nm and  $n = 0.86$  on (111)-oriented Ni single crystal. The changes in tip parameters obtained before and after measurement on (nc-Ni<sub>d=14 nm</sub>) correspond to changes in  $a_c$  of 23 and 2% for quartz glass and (111)-oriented Ni single crystal, respectively. Setting the tip parameters in the range of values determined on the calibration samples the indentation modulus of (nc-Ni<sub>d=14 nm</sub>)  $M = 183.5$  GPa was obtained

determined for the reference measurements. Table 14.1 shows the indentation moduli of five of nc-Ni samples with grain sizes ranging from  $d = 14$  nm to  $d = 67$  nm as obtained with AFAM. In Table 14.1, the errors given for  $M_{tip}$  and  $M_{nc-Ni}$  were determined from the standard deviation obtained for three different calibration measurements yielding errors varying from 4.4 to 58%. Also, the error average associated with the fit to Eq. (14.10) was calculated from the difference between the measurement and fitting curve, yielding  $\Delta k^*$ . This produced errors in  $M$  in the range of

**Table 14.1** Indentation modulus of nc-Ni with different grain sizes. A new AFM cantilever with different  $M_{\text{tip}}$  was used for each nc-Ni sample [6, 29]

Grain size $d$ (nm)	$\Delta k^*$ (%)	$M_{\text{tip}}$ (GPa)	$M_{\text{nc-Ni}}$ (GPa)
$14 \pm 3$	5.1	$255 \pm 37$	$192 \pm 48$
$34 \pm 22$	2.8	$248 \pm 3$	$124 \pm 14$
$35 \pm 19$	5.1	$248 \pm 3$	$152 \pm 90$
$50 \pm 7$	5.9	$224 \pm 2$	$186 \pm 35$
$66 \pm 4$	6.1	$216 \pm 6$	$193 \pm 9$

2.8–6.1%. These errors are mainly due to the deviation of the fit from the measured data at loads  $P \approx 1\text{--}2 \mu\text{N}$  (Fig. 14.7). This deviation was also accompanied by a maximum in the contact damping, and its origin will be discussed in Sect. 14.4 of this chapter.

From the results shown in Table 14.1 one can see that the values for  $M_{\text{nc-Ni}}$  are smaller than for the (111)-oriented Ni single-crystal sample. However, no grain size dependence of  $M_{\text{nc-Ni}}$  can be observed. Using Eq. (14.11) with  $R = 18.8 \text{ nm}$ ,  $n = 0.93$  and  $M = 192 \text{ GPa}$ , as found for (nc-Ni) <sub>$d=14 \text{ nm}$</sub> , leads to a contact radius  $a_c = 8 \text{ nm}$  at a loading force  $P = 4.5 \mu\text{N}$ . The stress field of the tip extends about  $3a_c$  into the depth and most probably stressed the neighboring grains. The measured values for  $M$  are for all nc-Ni samples below the indentation moduli of the Ni single-crystal values:  $M_{100} = 219 \text{ GPa}$ ,  $M_{110} = 249 \text{ GPa}$ , and  $M_{111} = 255 \text{ GPa}$  [6].

The elastic properties of nc-Ni have already been reported to be smaller than for single and polycrystalline nickel [35–40]. In Kopycinska-Müller et al. [35] used AFAM to measure the elasticity of nc-Ni thin films with grain sizes ranging from 8 to 50 nm. In these measurements also, the probed volume included several grains and grain boundaries. The reduced elasticity modulus of nc-Ni compared to the one of (111)-oriented Ni single crystal was attributed to the effect of the grain boundaries. Similarly, Yang et al. [36, 37] attribute the reduction of elastic properties measured on nc-Ni by nanoindentation to the involvement of several grains and grain boundaries in the deformation of the probed volume. Further, Zhou et al. [39] and Shen et al. [40] observed a clear dependence of the Young' modulus as a function of grains size for grain sizes below 20 nm, which was attributed to the softening effect of the grain boundaries and triple junction.

To further analyze the contribution of the grain boundaries to the elastic behavior of nc-Ni using AFAM, automated measurements on many individual grains of nc-Ni with grain sizes below 20 nm should be performed. Provided the microstructure of the samples was statistically isotropic and homogeneous, this would allow one to compute effective elastic properties, despite local elastic anisotropy [41]. Recently, such a measurement technique was implemented in order to measure local statistical properties of a metallic glass [42].

### 14.3 Contact Damping

From Eq. (14.5) one can see that the contact force  $P$  is complex, describing a viscoelastic contact. In case of periodic displacements of the tip relative to the sample surface, one can write:

$$P_{\text{complex}} = \int (k^* + i\omega\gamma^*) d\delta \quad (14.14)$$

with the complex contact stiffness

$$k_{\text{complex}}^* = \frac{\partial P_{\text{complex}}}{\partial \delta} = k^* + i\omega\gamma^* \quad (14.15)$$

where  $k^*$  is the real part and  $\omega\gamma^*$  is the imaginary part of the contact stiffness, respectively. For sufficiently small damping, it is intuitive to relate the  $Q$ -factor of the vibrating contact to the contact damping  $\gamma^*$  and contact stiffness  $k^*$  [29, 43]

$$Q_{\text{contact}}^{-1} = \frac{\omega\gamma^*}{k^*} \quad (14.16)$$

which is analog to its definition in ultrasonic wave propagation

$$Q^{-1} = E''/E' \quad (14.17)$$

where  $E'$  and  $E''$  are the storage modulus and the loss modulus, respectively. The experimental resonance curve in Fig. 14.8 (left) was recorded with a diamond-coated single-crystal silicon cantilever on the surface of a quartz-glass sample with a loading force  $P = 936$  nN. Figure 14.8 (middle part) shows contact-resonance curves recorded on quartz glass as a function of the load. From these curves, one can see that the resonance is Lorentzian and that there is an increase of the contact resonance as a function of the load which has been observed in many AFAM applications. In addition, the resonance curves narrow with increasing load (Fig. 14.8 middle part), i.e.,  $Q^{-1}$  decreases which follows from Eq. (14.16) because  $k^*$  increases with load.

Several authors have examined the behavior of the cantilever in the first free resonance and in the first contact resonance based on the first mode approximation (FMA) model including damping and compared it to the beam model [16, 44–46]. In the FMA model, the cantilever is replaced by an effective mass  $m_{\text{eff}} \approx m/4$ , oscillating between two parallel arrangements of springs and damping elements. The spring with the stiffness  $k_c$  corresponds to the cantilever stiffness and the dashpot element represents the viscous damping with the damping constant  $\eta'_{\text{air}}$ . The contact is modeled as a parallel arrangement of a linear spring with the contact stiffness  $k^*$  and the damping element  $\eta'_{\text{contact}}$  (see Fig. 14.9).

In the FMA, the quality factor of the free resonance is the same as in the beam model:

$$Q = \omega_{01}/\eta'_{\text{air}} \quad (14.18)$$

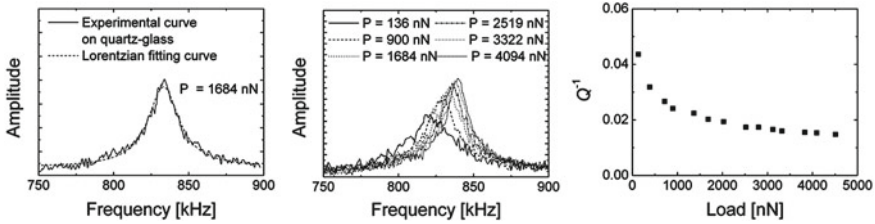
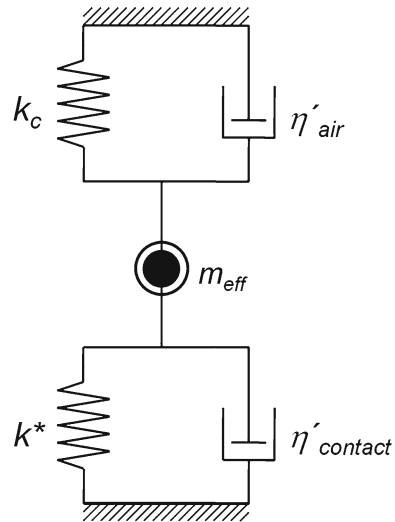


**Fig. 14.8** *Left* First contact bending-resonance curve of a stiff single crystalline silicon cantilever recorded on the surface of a quartz-glass sample with a loading force  $P = 936 \text{ nN}$ . The experimental curve (solid line) is well represented by a Lorentzian (dashed line). *Middle* Load dependence of the contact-resonance behavior. *Right*  $Q^{-1}$  as a function of load.  $Q^{-1}$  decreases as a function of load. Here,  $Q^{-1} \propto P^{-0.44}$  in the load range from 100 to 4,000  $\mu\text{N}$ . In the same load range  $k^* \propto P^{0.14}$

**Fig. 14.9** First mode approximation (FMA) model of a cantilever in contact with a sample surface. The cantilever is described by a parallel linear spring  $k_c$  and a damping element  $\eta'_{air}$  that is connected to an effective point mass  $m_{eff}$ . The contact itself is modeled as a parallel linear spring  $k^*$  and a damping element  $\eta'_{contact}$  as well. (According to [43] with permission from Elsevier)



where  $\omega_{01} = 2\pi f_{01}$  and  $f_{01}$  is the first free bending-resonance frequency of the cantilever. In contact one obtains

$$Q = \omega_{c1} / (\eta'_{air} + \eta'_{contact}) \tag{14.19}$$

where  $\omega_{c1} = 2\pi f_{c1}$  is the first contact bending-resonance frequency of the cantilever. Since the resonance curves are Lorentzian,  $Q_{total}^{-1} = \sum_i Q_i^{-1}$  must hold as well. The damping constant  $\eta_{air}$  and  $\eta'_{air}$  in Eqs. (14.3) and (14.18) are related by  $\eta'_{air} = \eta_{air} / \rho A$  while for the contact-damping constants  $\gamma^*$  and  $\eta'_{contact}$  in Eqs. (14.5) and (14.19)  $\eta'_{contact} = \gamma^* / m_{eff}$  holds. In the FMA, the free resonance frequencies and the contact-resonance frequencies are  $\omega_{01} = \sqrt{k_c / m_{eff}}$  and  $\omega_{c1} = \sqrt{(k_c + k^*) / m_{eff}}$ , respectively.

For the contact-resonance curve shown in Fig. 14.8 and using the mechanical models in Figs. 14.4 and 14.9, we find  $k^* = 1145 \text{ N/m}$  and  $\gamma^* = 2.08 \times 10^{-6} \text{ Ns/m}$ , which corresponds to  $Q_c^{-1} = 7.8 \times 10^{-3}$  when Eq. (14.16) is used.

The  $Q^{-1}$ -value can also be measured from the contact-resonance curve with  $Q^{-1} = \Delta\omega/\omega$ , where  $\Delta\omega$  is the half-width of the resonance curve [12]. The contact damping can then be derived according to  $Q_c^{-1} = Q_t^{-1} - Q_f^{-1}$  where  $Q_f$  is the  $Q$ -factor of the free resonance curve. For the contact-resonance curve shown in Fig. 14.8, we find  $Q_c^{-1} = \Delta\omega_t/\omega_t - \Delta\omega_f/\omega_f = 1.59 \times 10^{-3}$ . For the same measurement, the  $Q^{-1}$ -values determined from the resonance curve and by using Eq. (14.16) differ by a factor 2. The difference may be caused by using the FMA instead of using the beam model as discussed in the next paragraph.

The viscoelastic part of the contact force in combination with the beam model has been examined by Yuya et al. [17] by introducing a complex reduced elastic modulus  $E^*\omega = E' + E''$ . The reduced storage modulus  $E'$  and the reduced loss modulus  $E''$  were related to the contact stiffness and the contact damping according to

$$E'^* = (k^*/2) \sqrt{\pi/A_c} \quad (14.20)$$

and

$$E''^* = (\omega\gamma^*/2) \sqrt{\pi/A_c} \quad (14.21)$$

Taking the ratio of  $E''^*$  and  $E'^*$  one recovers Eq. (14.17). However, one has to keep in mind that the  $Q^{-1}$ -value measured from the cantilever resonance curve contains the damping of the cantilever in air as well, and that it is not evident that reciprocal quality factors are additive. In a subsequent paper, Yuya et al. [47] showed first that indeed  $Q_{\text{total}}^{-1} = \sum_i Q_i^{-1}$  holds, and second that the resonance curves are Lorentzian, as shown in Fig. 14.8 and in references [43, 47]. This allows one to separate the contact stiffness and damping in a two-step process. The  $Q^{-1}$ -value of the cantilever oscillations depends on the contact damping and on the contact stiffness and for a certain parameter range the quality factor might even increase. For the data in Fig. 14.8 right  $Q^{-1} \propto P^{-0.44}$  in the load range from 100 to 4,000 nN and  $k^* \propto P^{0.14}$ .

The description of the contact stiffness as a complex quantity has also been used in the resonance ultrasonic spectroscopy (RUS) technique, where a tip attached to a small bar is operated in its first contact extensional resonance [48]. The RUS oscillator is governed by a second-order differential equation based on the FMA.

## 14.4 Observation of Internal Friction Due to Dislocations in Nanocrystalline Nickel

Owing to their microstructural length in the nanometer range, nc-materials exhibit physical and mechanical properties different from those of their polycrystalline counterparts which is attributed to their high grain boundary volume [49]. For example,

for grain sizes below 10 nm the mechanical properties of nc-metals have been observed to follow an inverse Hall–Petch relation [50–53]. These results gave evidence that there are additional plastic deformation mechanisms acting as compared to polycrystalline materials, where the plastic deformation is determined by dislocation motions [54]. Computer simulation has contributed to the understanding of the response of nc-microstructures subjected to temperature and stress [55, 56]. Several plastic deformation mechanisms have been identified as a function of the grain size, such as dislocation motion, grain boundary sliding, and grain rotation in the order of decreasing grain size [56–59]. Further, simulations of nanoindentation experiments on nc-metals have been used to investigate the dislocation activity and the dislocation/grain boundary interactions [60, 61]. In computer simulations the indenter sizes are set in the range of 1 to 10 nm and are therefore much smaller than the indenters used in experiments with typical sizes of the order of 100 nm. Experimental nanoindentation results are thus averaging over several nano-grains and there is still a need for experimental techniques with higher spatial resolution.

We used AFAM to investigate the dynamic behavior of dislocations nucleated in grains of nc-Ni with sizes between 14 and 76 nm. To this aim, the same continuous records of contact-resonance curves as a function of the loading force  $P$  are used as for the elasticity measurements (see Sect. 14.2). From spectroscopic AFAM measurements contact stiffness  $k^*(P)$ -plots and contact-damping  $Q^{-1}(P)$ -plots were obtained, which are shown in Fig. 14.10 for the same nc-Ni samples as discussed in Sect. 14.2. For comparison, the data for the (111)-oriented Ni single-crystal calibration sample are also shown. The contact damping was determined by using Eq. (14.16). For the nc-Ni samples with grain sizes of 14 nm (nc-Ni<sub>*d*=14 nm</sub>), 50 nm (nc-Ni<sub>*d*=50 nm</sub>), and 66 nm (nc-Ni<sub>*d*=66 nm</sub>), a damping peak and a slight reduction of the contact stiffness can be observed at the loads  $P_c = 1196, 1870, \text{ and } 1107 \text{ nN}$ , respectively (the loads  $P_c$  are indicated by arrows in Fig. 14.10. For nc-Ni<sub>*d*=14 nm</sub> and nc-Ni<sub>*d*=50 nm</sub> this behavior also repeats itself at higher loads. The maximal shear stress  $\tau_{\max}$  exerted in the contact zone between tip and sample at  $P_c$  is  $\tau_{\max} = \frac{0.45P_c}{\pi a_c^2}$ , using the Hertzian theory of elastic contact for a spherical indenter [28] on a plane surface. One obtains  $\tau_{\max} = 2.3, 2.1 \text{ and } 1.2 \text{ GPa}$ , with  $a_c = 8.6, 11.2, \text{ and } 11.4 \text{ nm}$ , for nc-Ni<sub>*d*=14 nm</sub>, nc-Ni<sub>*d*=50 nm</sub> and nc-Ni<sub>*d*=66 nm</sub>, respectively. The contact softening  $\Delta k^*/k^*$  at the load  $P_c$ , where the damping peaks occur varies, from 14 to 34 % while the corresponding  $Q^{-1}$ -values were between 0.1 and 0.12. Furthermore, the damping peaks and the change of the contact stiffness were reversible upon unloading. In this context it is interesting to note that in the case of high-purity oriented graphite (HPOG), Tsuji et al. observed a decrease of the contact stiffness upon the generation of an edge dislocation [62].

To explain the contact-damping peaks and the simultaneous reduction of the contact stiffness that we observed on three nc-Ni samples out of five, we propose that plasticity effects play a role in the contact zone due to the mechanical stresses exerted by the tip.

Mishalske and Houston suggested that indenting a sample at a critical load should lead to the nucleation of a dislocation loop confined in the stress field of the contacting



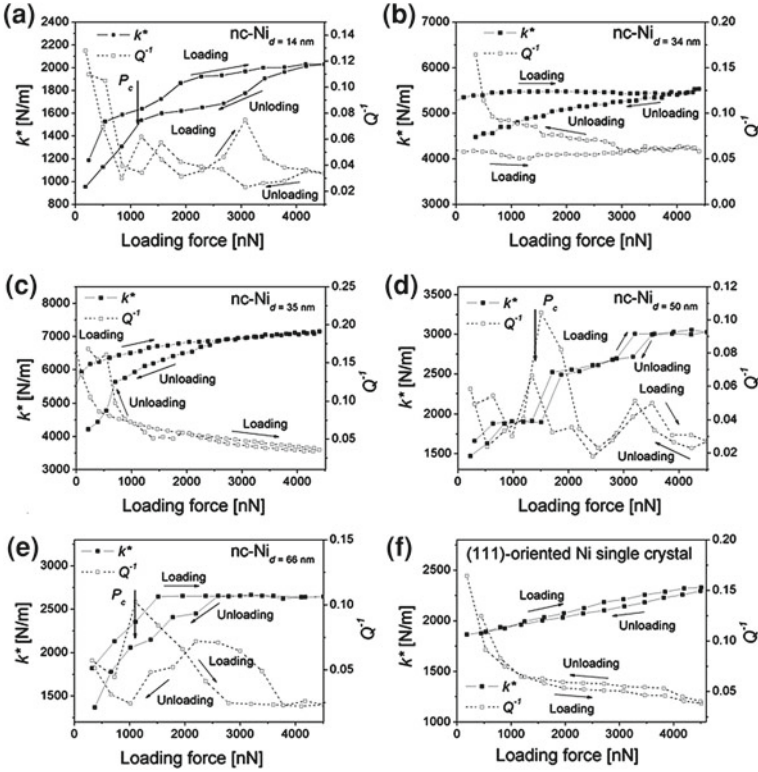


**Fig. 14.10** Contact-stiffness  $k^*(P)$ -plots and contact-damping  $Q^{-1}(P)$ -plots for nc-Ni samples with grain sizes **a**  $d = 14$  nm, **b**  $34$  nm, **c**  $35$  nm, **d**  $50$  nm, and **e**  $66$  nm. For comparison the  $k^*(P)$  and  $Q^{-1}(P)$ -plots are also shown for a (111)-oriented Ni single crystal in **(f)**. (According to [43] with permission from Elsevier)

bodies [63]. From the theory of dislocation, the free energy  $\Delta\Gamma$  of a dislocation loop of radius  $r$  can be expressed as [64]

$$\Delta\Gamma = 2\pi rW + \pi r^2(\gamma - b\tau) \quad (14.22)$$

where the line tension  $W$  of a dislocation loop of radius  $r$  is given by

$$W = \frac{2 - \nu}{2(1 - \nu)} \frac{Gb^2}{4\pi} \left( \ln \frac{3r}{r_0} - 2 \right). \quad (14.23)$$

Here,  $G$  is the shear modulus,  $b$  is the Burger's vector, and  $\gamma$  is the stacking fault energy per unit area. In Eq. (14.22), the term  $\pi r^2 b\tau$  represents the work dissipated by the expansion of the dislocation loop under the shear stress  $\tau$  and the term  $\pi r^2 \gamma$  only applies for partial dislocation loops. With computer simulations of nanocryst-

talline face-centered cubic (fcc-) metals, it has been shown that the emission of partial dislocation with  $b = 1/6 [211]$  from grain boundaries or triple junction is the main mechanism for dislocation activity [65]. The emission of dislocations from a grain boundary has been investigated by various groups [66–68]. However, the obtained results were of qualitative nature since the critical shear stress of dislocation nucleation could not be clearly stated. Further, Soer et al. [69] proposed that the emission of a dislocation from a grain boundary is facilitated by the stress acting on a grain boundary dislocation. There, the following expression was used to predict the critical stress for the nucleation of a dislocation at a grain boundary

$$\tau_{\text{GB}} = \tau^* - \frac{Gb}{\pi(1-\nu)} \frac{1}{\xi} \quad (14.24)$$

where  $\tau^*$  is the critical shear stress for homogeneous nucleation and  $\xi$  is the half-width of the grain boundary. For nickel and assuming  $\xi = 1.3$  nm, one obtains  $\tau_{\text{GB}} = \frac{G}{32} = 2.64$  GPa for the critical shear stress to nucleate a partial dislocation loop from a grain boundary. Inserting this result in Eq. (14.22) allows one to determine the critical nucleation radius by analyzing  $\Delta\Gamma(r)$ . For nickel one obtains  $r_{\text{GB}} = 3$  nm. Considering the above expression for  $\tau_{\text{max}}$  and setting  $\tau_{\text{max}} = \tau_{\text{GB}}$ , one can estimate the critical loading force  $P_c$  for the heterogeneous nucleation of partial dislocation in Ni. Using the values for  $R$ ,  $n$ , and  $E^*$  determined in Sect. 14.2 for nc-Ni<sub>d=14 nm</sub>, one obtains  $P_c = 1.3$   $\mu\text{N}$ . This value is in good agreement with the load corresponding to the observed contact-damping peaks in Fig. 14.10. For this particular  $P_c$ -value and according to Eq. (14.11) the contact radius is  $a_c = 8.7$  nm.

The effect of the generation of a dislocation on the contact damping can be evaluated from the stored energy in the contact volume and the necessary amount of energy to nucleate a dislocation. For a forced and damped oscillator  $Q^{-1}$  is given by

$$Q^{-1} = \frac{W''}{2\pi W'} \quad (14.25)$$

where  $W'$  is the elastic energy stored in the system and  $W''$  is the dissipated energy. In the present case  $W'$  can be set as the work of deformation for indentations for depths up to  $\delta_c$ , which corresponds to  $P_c$  [29, 43]

$$W' = \int_0^{\delta_c} P d\delta \quad (14.26)$$

Using the expression of  $d$  in Eq. (14.13) and inserting it into Eq. (14.26) yields

$$W' = \frac{n}{n+1} \sqrt[2^{(5-n)/3} R^{2n-1} E^* \delta^{(n+1)/n}] \quad (14.27)$$

Using again the same value as above for  $R$ ,  $n$ ,  $E^*$ , and using  $P_c = 1 \mu\text{N}$ , one obtains  $W' \approx 0.6 \times 10^{-15} \text{ J}$ . Intuitively, the dissipated energy corresponding to the nucleation of a dislocation loop is its elastic energy. Assuming  $r = 0.5a_c$ , which corresponds approximately to the diameter of the field of maximal resolved shear stress in the contact zone between tip and sample [28] and using Eqs. (14.23) and (14.11) with the same values for  $R$ ,  $n$ , and  $P_c$  as above, one obtains  $W'' \approx 2.55 \times 10^{-17} \text{ J}$  with  $G = 83 \text{ GPa}$  and  $\nu = 0.32$ , as typical values for nickel. This corresponds to  $Q^{-1} \approx 6.7 \times 10^{-3}$  for the heterogeneous nucleation of a single partial dislocation loop.

In addition, internal friction by dislocation loop oscillations in the dynamic elastic strain field of the tip is also likely to contribute to the observed  $Q^{-1}$ -values. This internal friction arises from the interaction of a dislocation loop with phonons and electrons in analogy to the vibrating string-model [70]. In the vibrating string-model, the energy loss of a dislocation loop caused by the interaction with the phonon and electron population is described by the parameter  $B$ , which is of the order of  $10^{-4} \text{ N s/m}^2$  [70]. The corresponding energy loss caused by a single dislocation can be estimated according to  $W''' = Bv_s \iota l$ , where  $v_s$  is the shear velocity with which the dislocation moves and  $\iota$  is the dynamic displacement of the dislocation line of length  $l$ . Taking  $\iota = \delta_c \approx 1 \text{ nm}$  for  $P_c = 1.3 \mu\text{N}$  and the dislocation loop length  $l = 30 \text{ nm}$  yields  $W''' \approx 10^{-17} \text{ J}$ . Using Eq. (14.25), one obtains  $Q^{-1} \approx 2.6 \times 10^{-3}$  for a single dislocation. Adding up both contribution leads to  $Q^{-1} \approx 10^{-2}$  for a single dislocation loop. Compared to the experimental observations in Fig. 14.10, this value is smaller by a factor of 5 to 10. At this point one should keep in mind however, that the elastic strain field in the contact zone is inhomogeneous [28] and that, assuming a linear damping element in the mechanical models shown in Figs. 14.4 and 14.9, the  $Q^{-1}$ -values analyzed from AFAM experiments are estimates. Also, our estimations do not account for the background loss.

Besides the interaction with dislocations, there are several mechanisms leading to absorption in the ultrasonic frequency range in crystalline, polycrystalline and nanocrystalline solids [70–73]. One of them is the interaction of dynamic stress fields with electrons, in which case the stress fields modulate the electron distribution on the Fermi surface. In AFAM experiment on metals, the electron mean free path is comparable to the dimension of the deformed volume in the contact zone. The relaxation strength for the interaction of ultrasound with the electrons is  $\approx nE_f/M_0$ , where  $n$  is the density of electron,  $E_f$  is the Fermi energy, and  $M_0$  is the appropriate elastic constant. Estimating the relaxation strength based on the same principle as for anelasticity due to inhomogeneous heat flow [70–73] in a polycrystalline ensemble, one obtains a  $Q$ -value of approximately 20, which is in agreement with the measurements in Fig. 14.10 [43].

The effect of the nucleation of a partial dislocation loop on the contact stiffness can be estimated from the spreading of a plastic zone associated with the release of mechanical work:

$$W = \pi r^2 (\gamma - b\tau) \quad (14.28)$$

Using Eq. (14.28), the effect of a spreading dislocation loop on the contact stiffness has been estimated in [29, 43] as follows

$$k^* = k_{\text{elast}}^* - (2\pi (\tau_n b - \gamma))_{\tau_n \geq \tau^*} \quad (14.29)$$

where  $k_{\text{elast}}^*$  is defined as in Eq. (14.10) and  $\tau^*$  is the stress at which dislocation nucleation occurs. From Eq. (14.29) one can see that the nucleation of a dislocation loop and its subsequent spreading leads to a reduction of  $k^*$ , though the reduction is small compared to the overall contact stiffness. Using the same value for  $R$ ,  $n$ ,  $E^*$  as above and setting  $P = 1, 200$  nN according to the experiments,  $\tau^* = G/32$ ,  $b = 1/6[2\ 1\ 1]$ , and  $\gamma = 140$  mJ/m<sup>2</sup> as typical values for nickel, the softening effect of the nucleation of a single dislocation loop to the contact stiffness can be estimated to be of the order of 1%. Internal friction is always accompanied by a stiffness reduction, which is usually expressed as the defect modulus. The defect modulus corresponding to dislocation damping is  $\Delta G/G = \pi Q^{-1}$  [74], which in our case should be analog to  $\Delta k^*/k^*$ . From the measurement in Fig. 14.10 one obtains  $\Delta k^*/k^* \approx 10\%$ . Further, the reversibility of the observed effects can be explained by considering the size of the field of maximal shear stress, which according to [28] is approximately half as big as the contact radius  $a_c$ . From Fig. 14.10 and using Eq. (14.11) one obtains at  $P_c$ :  $a_c/2 = 4.3, 5.6,$  and  $5.7$  nm for nc-Ni<sub>d=14 nm</sub>, nc-Ni<sub>d=50 nm</sub> and nc-Ni<sub>d=66 nm</sub>, respectively. These values are very close to the above estimated value for the critical radius of a dislocation loop  $r_c$ , thus implying that the dislocation loops nucleated in these experiments could not be maintained. Yamakov et al. [65] and Budrovic et al. [75] made similar observations upon loading and unloading fcc nc-metals during computer simulations and X-ray diffraction experiments.

For nc-Ni<sub>d=34 nm</sub> and nc-Ni<sub>d=35 nm</sub> the effects described above could not be observed. It is probable that in these cases the measurements were not performed on favorably oriented grains. Likewise, for the (111)-oriented Ni single crystal, neither contact-stiffness softening nor contact-damping peaks were observed. This further supports the above discussion, since heterogeneous dislocation nucleation did not occur in this case.

## 14.5 Friction Measurements at the Nanoscale

With the emergence of nano/micro-mechanical devices, the assessment of tribological properties at the nanoscale has become crucial. The high spatial resolution of AFM-based techniques has provided new insights into the fundamental mechanisms of friction and wear (see for example Refs. [76, 77]) in conjunction with modeling efforts of tribological contacts. By exploiting torsional contact resonances, the application of AFAM and related techniques has been extended to the investigation of friction at the nanometer scale [11, 31]. The decrease of the  $Q$ -factor of torsional contact resonances as a function of the excitation amplitude of transversal shear waves perpendicularly polarized to the cantilever length axis has been associated with micro-sliding [11]. At frequencies much below the contact resonances, the frictional properties of an AFM tip-sample contact have been measured based on the relative motion of the sample and the tip parallel to the cantilever length axis [78].

**Table 14.2** Elastic properties of the samples obtained by ultrasonic time-of-flight measurement and by LSAW

Sample	$E$ (GPa)	$G$ (GPa)	$\nu$
Quartz glass	76.23	33.14	0.15
nc-Al	76.2	28.32	0.345

In this section, measurements of the contact damping  $\gamma^*$  of the bending contact resonances of AFM cantilevers as a function of the loading force  $P$  are presented for two samples: quartz glass and a 100 nm thick nc-aluminum film. The observed behavior of the contact damping  $\gamma^*$  as a function of the loading force  $P$  is discussed, taking into account micro-sliding at the tip/sample surface interface [79].

The elastic properties of the quartz-glass sample were determined from time-of-flight data of ultrasonic pulse echoes [80], and the elastic properties of the nc-aluminum sample were measured by the laser acoustic surface wave technique (LASW) [81] (see Table 14.2). Further, the surfaces of the samples were characterized by AFM topography imaging, from which the roughness parameter  $Rq$  was calculated. In the case of the nc-Al thin-film sample, AFAM imaging was also used to reveal the nanostructure and to determine the average grain size by analyzing the images with the *gwyddion* software [82]. Both AFM and AFAM images of the samples are shown in Fig. 14.11.

The geometrical data of the employed cantilevers were measured by scanning electron microscopy (SEM) and were used together with the free bending-resonance frequencies to calculate the corresponding cantilever stiffness  $k_c$  according to Eqs. (14.1) and (14.2). We obtained  $k_c = 42\text{--}45$  N/m. Similar to the measurements shown in Sect. 14.4, the AFAM measurements consisted in the recording of the first contact bending-resonance curves as a function of the loading force  $P$  (Fig. 14.12). For both samples a monotonous increase of the resonance frequency and a monotonous increase of the  $Q$ -factor with increasing loading force  $P$  are observed. The mechanical models in Figs. 14.4 and 14.9 have been used to calculate the contact stiffness  $k^*(P)$  and the contact damping  $\gamma^*(P)$  (see Fig. 14.12). Using the measured elastic values in Table 14.2 and  $M_{tip} = 165$  GPa for the indentation modulus of the silicon tip, the measured  $k^*(P)$  were fitted with Eq. (14.11) to obtain  $R = 12.4$  nm and  $n = 0.941$  for the quartz-glass sample, and  $R = 15.4$  nm and  $n = 0.919$  for the nc-Al thin-film sample.

Figure 14.12 shows the  $k^*(P)$  and  $\gamma^*(P)$ -plots for both samples. The  $\gamma^*(P)$ -plots exhibit a power dependence  $\gamma^* \propto P^m$ , where  $m \approx -0.29$  for quartz glass and  $m \approx -0.42$  for nc-Al. Caron et al. have suggested that this behavior arises from friction at the contact interface between tip and sample [79]. In AFM instruments, the cantilevers are tilted by an angle  $\phi$  of typically  $12^\circ$ , with regard to the sample surface, thus giving rise to static and dynamic in-plane forces in the contact. These forces act parallel to the cantilever axis. At loading forces  $P$  as high as applied in these experiments (see Fig. 14.12), the periodic lateral force  $P_{ld}$  parallel to the beam axis is comparatively small. The angular momentum due to this force acting

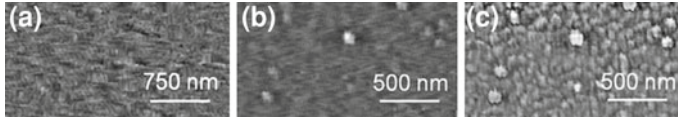


**Fig. 14.11** AFM topography images recorded on **a** quartz glass and **b** nc-Al with a loading force  $P = 60$  nN. The z-scales are 9.1 and 37 nm, respectively. **b** Topography image and **c** AFAM image recorded on nc-aluminum of the same area. The AFAM image was recorded at the contact resonance  $f = 660$  kHz. The width of the images is  $3 \mu\text{m}$  in **(a)** and  $1.5 \mu\text{m}$  in **(b)** and **(c)**. The roughness parameter  $Rq$  of the quartz-glass sample was 1.3 nm and for the nc-Al thin-film sample we found  $Rq = 1.9$  nm. From the AFAM image on the nc-Al thin-film sample we obtained an average grain size  $d = 75$  nm

at the tip is  $M_{\text{ld}} = h \times k_{\text{Lat}}^* \times \Delta y$ , where  $\Delta y = u_0 \times \sin\phi$  is the lateral vibration amplitude at the tip and  $u_0$  the out-of-plane amplitude [83]. Correspondingly, the force  $P_{\text{ld}} = M_{\text{ld}}/h = u_0 \times k_{\text{Lat}}^* \times \sin\phi$ , where  $k_{\text{Lat}}^* = 2 \times G \times a_c$  and  $G^* = ((2 - \nu_t)/G_t + (2 - \nu_s)/G_s)^{-1}$  is the reduced shear modulus with the subscripts  $t$  and  $s$  referring to the tip and the sample, respectively. With  $a_c = 10$  nm as a typical value and  $G^* = 12.2$  GPa for a silicon tip in contact with the quartz-glass sample, one obtains  $k_{\text{Lat}}^* = 244$  N/m. Assuming  $u_0 = 0.1$  nm this leads to  $P_{\text{ld}} \approx 5$  nN.

In [79], the authors have discussed the observed  $\gamma^*(P)$  behavior on the basis of micro-slip at the tip-sample interface subjected to a static loading force  $P$  and an oscillating lateral force  $P_{\text{ld}}$  [28], as has already been suggested for the case of torsional contact resonances [11], and which has been observed in dynamic friction measurements, where a cantilever was excited by a sawtooth signal at 80 Hz with amplitudes of 1.5 nm on an NbSe<sub>2</sub> sample in ultrahigh vacuum [84]. Likewise, a torsional friction experiment on Si<sub>3</sub>N<sub>4</sub> has been carried out recently, interpreting the data also in terms of a micro-slip [85]. In contrast to our conditions, in the experiments reported in [84, 85], the static forces were much less than in our case and hence adhesion had to be taken into account.

In micro-slip the contact area is partially subjected to frictional movement at its periphery  $A_p = \pi(a_c - c)^2$ , while the central part of the contact area  $A_c = \pi c^2$  remains sticking. The width  $(a_c - c)$  of the circular segment depends both on the vertical static load  $P$  and the oscillating lateral force  $P_{\text{ld}}$  and can be described by the  $c/a_c$ -ratio [28]

$$c/a_c = (1 - P_{\text{ld}}/\mu P)^{1/3}, \quad (14.30)$$

where  $\mu$  is the friction coefficient. From Eq. (14.30) one can see that with increasing  $P$ ,  $c$  tends to zero. This corresponds to the case where  $\gamma^*$  becomes minimal. Correspondingly, at small loading forces  $P$ , where micro-sliding occurs,  $\gamma^*$  increases. The dissipated energy associated to micro-sliding has been calculated by Mindlin as [28, 86]

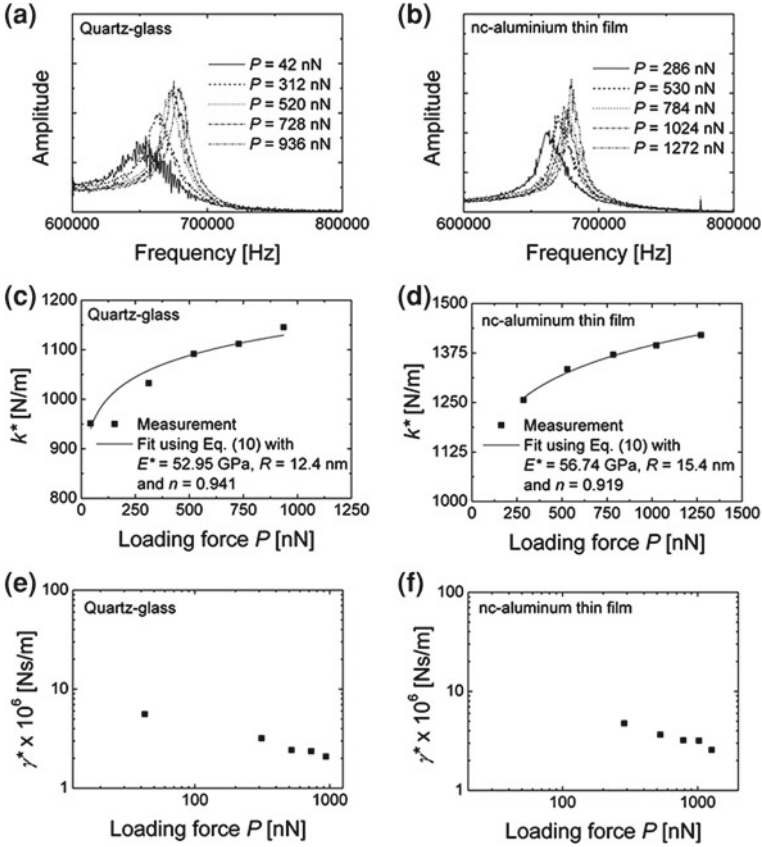


**Fig. 14.12** Contact-resonance curves recorded as a function of load on **a** quartz glass and **b** nc-aluminum thin film with cantilevers with  $k_c = 42 - 46$  N/m. **(c, d)** Contact stiffness  $k^*(P)$ -plots and **(e, f)** contact damping  $\gamma^*(P)$  plots calculated from the contact-resonance curves in **(a, b)** for **(c, e)** quartz glass and **(d, f)** nc-Al. (According to [79] with permission from APEX/JJAP)

$$\begin{aligned}
 W'' = & \frac{9\mu^2 P^2}{10a_c} \left( \frac{2 - \nu_t}{G_t} + \frac{2 - \nu_s}{G_s} \right) \\
 & \times \left[ 1 - \left( 1 - \frac{P_{ld}}{\mu P} \right)^{5/3} - \frac{5P_{ld}}{6\mu P} \left\{ 1 - \left( 1 - \frac{P_{ld}}{\mu P} \right)^{2/3} \right\} \right] \quad (14.31)
 \end{aligned}$$

where  $G_{t,s}$  are the shear moduli of the sample and the tip, respectively.

Similar as in Sects. 14.3, and 14.4, the dissipated energy  $W''$  can be computed following [43, 79]

$$W'' = 2\pi W' \frac{\omega \left( \gamma^* - \gamma_{\text{background}}^* \right)}{k^*} \quad (14.32)$$

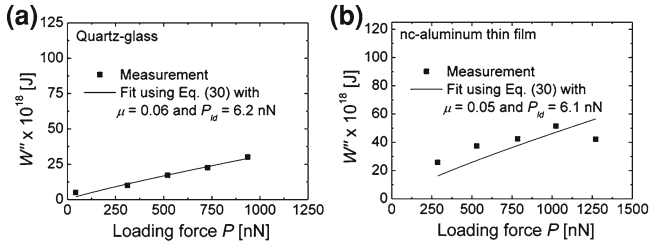


**Fig. 14.13** Dissipated energy per cycle calculated according to Eq.(14.32) with  $\gamma_{\text{background}}^* = 1 \times 10^{-6}$  Ns/m for **a** quartz glass and **b** nc-aluminum thin film. The experimental data have been fitted with Eq.(14.31) (*solid lines*) to obtain  $\mu = 0.06$  and  $P_{ld} = 6.2$  nN for **(a)** quartz glass and  $\mu = 0.05$  and  $P_{ld} = 6.1$  nN for **(b)** nc-aluminum thin film. (according to [79] with permission from APEX/JJAP.)

where  $W'$  is the stored elastic energy expressed, according to Eqs. (14.26) and (14.27). The background damping  $\gamma_{\text{background}}^* \approx 10^{-6}$  Ns/m has been discussed in Sect. 14.4 and in [43]. Figure 14.13 shows the calculated plots of  $W''(P)$  corresponding to the measurement on quartz glass and nc-Al shown in Fig. 14.12. The calculated values were further fitted with Eq.(14.31) to determine  $P_{ld}$  and  $\mu$ . For the quartz-glass sample  $P_{ld} = 6$  nN and  $\mu = 0.06$  were obtained and for nc-Al  $P_{ld} = 10$  nN and  $\mu = 0.05$ . These values for  $P_{ld}$  are in good agreement with the above estimated values.

The obtained values for the friction coefficient are within the range of reported values measured by Friction Force Microscopy (FFM), usually  $0.01 < \mu < 0.1$  [87]. In FFM experiments however, the sliding velocity is in the range of 0.01–1  $\mu\text{m/s}$  [88], while in AFAM experiments the sliding is of oscillatory nature and the maximal velocity is  $v_0 = \omega_c \times u_0$ . In this particular case  $v_0 \approx 2$  mm/s with  $f_c = \omega_c/2\pi \approx 700$  kHz and  $u_0 \approx 0.5$  nm, as a typical value for ultrasound amplitude. The sliding velocity corresponding to AFAM experiments is thus several orders of magnitudes higher than in FFM experiments.

The loading forces applied here were high and the friction between tip and sample surface may have been affected by plastic deformation of asperities in the contact area. Varying the experimental conditions, such as the choice of the cantilever stiffness, should allow one to study the velocity dependence of friction in a controlled way, and over a larger velocity range than has been done by FFM [89–93], by means of measuring the damping in AFAM experiments. Further, the damping values  $\gamma^*$  in AFAM experiments should allow investigating the ultrasonically induced lubrication in more detail, such as suggested in [94–97].



## 14.6 Conclusions

Besides the characterization of local elastic properties, measuring contact resonances by using AFAM allows one to investigate friction and internal friction at the nanoscale. On nc-nickel an increase of the contact damping  $Q^{-1}$  at specific applied static loads has been observed and attributed to dislocation activities and interaction with grain boundaries. Owing to its high spatial resolution capacity, AFAM should help to understand ultrasonic absorption in materials of complicated microstructures like steels [98] or fatigued materials [99] and to apply this knowledge in non-destructive testing. A first step in this direction has been made by Kumar et al. [15], where the authors investigated the elasticity of microalloyed steel.

Also, the damping  $\gamma^*$  of stiff silicon AFM cantilevers in contact with different surfaces, has been discussed on the basis of micro-sliding. The decrease of  $\gamma^*$  with the loading force  $P$  was analyzed using the model developed by Mindlin to calculate the dynamic friction coefficient  $\mu$  from the dissipated energy in the contact area between tip and sample surface. The sliding velocity between tip and sample was significantly higher than in typical FFM experiments and AFAM as an alternative technique thus promises to advance the investigation the velocity dependence of friction and the ultrasound lubrication at the nanoscale. Further, the loading forces applied in the presented experiments were high and may have led to plastic deformation of asperities in the contact area. It has been known that lubricating layers such as glazes can form under severe wear [100, 101]. With the formation mechanisms of such layers still being under investigation, AFAM is a good candidate to investigate these mechanisms with higher spatial and time resolution than available with macroscopic techniques and FFM.

**Acknowledgments** The results presented in this chapter were obtained when the authors were with the Fraunhofer Institute for Non-Destructive Testing (IZFP) Saarbrücken, Germany (A.C and W.A.), and the Institute of Micro- and Nanomaterials (IMNM), University of Ulm, Ulm, Germany (A.C.).

## References

1. V.B. Elings, J.A. Gurley, US Patent 5,266,801, (1993)
2. P. Maivald, H.J. Butt, S.A.C. Gould, C.B. Prater, B. Drake, J.A. Gurley, V.B. Elings, P.K. Hansma, *Nanotechnology* **2**, 103 (1991)
3. U. Rabe, K. Janser, W. Arnold, *Rev. Sci. Instrum.* **67**, 3281 (1996)
4. K. Yamanaka, A. Noguchi, T. Tsuji, T. Koike, T. Goto, *Surf. Interf. Anal.* **27**, 600 (1999)
5. U. Rabe, S. Amelio, E. Kester, V. Scherer, S. Hirsekorn, W. Arnold, *Ultrasonics* **38**, 430 (2000)
6. M. Kopynciska-Müller, A. Caron, S. Hirsekorn, U. Rabe, H. Natter, R. Hempelmann, R. Birringer, W. Arnold, *Z. Phys. Chem.* **222**, 471 (2008)
7. U. Rabe, *Applied Scanning Probe Methods* (Springer, Heidelberg, 2006), p. 90
8. D.C. Hurley, J.A. Turner, *J. Appl. Phys.* **102**, 033509 (2007)
9. F. Oulevey, G. Gremaud, A. Semoroz, A.J. Kulik, N.A. Burnham, E. Dupas, *Rev. Sci. Instrum.* **72**, 3891 (2001)

10. K. Yamanaka, Y. Maruyama, T. Tsuji, K. Nakomoto, Appl. Phys. Lett. **78**, 1939 (2001)
11. M. Reinstaedtler, U. Rabe, V. Scherer, U. Hartmann, A. Goldade, B. Bhushan, W. Arnold, Appl. Phys. Lett. **82**, 2604 (2003)
12. J.P. Den Hartog, *Mechanical Vibrations* (Dover Publication Inc., New York, 1985)
13. D.C. Hurley, M. Kopycinska-Mueller, A.B. Kos, R.H. Geiss, Meas. Sci. Technol. **16**, 2167 (2005)
14. T. Tsuji, S. Saito, K. Fukuda, K. Yamanaka, H. Ogiso, J. Akedo, Y. Kawakami, Appl. Phys. Lett. **87**, 071909 (2005)
15. A. Kumar, U. Rabe, W. Arnold, Jap. J. Appl. Phys. **47**, 6077 (2008)
16. J.A. Turner, S. Hirsekorn, U. Rabe, W. Arnold, J. Appl. Phys. **82**, 966 (1997)
17. P.A. Yuya, D.C. Hurley, J.A. Turner, J. Appl. Phys. **104**, 074916 (2008)
18. P.E. Mazeran, J.L. Loubet, Tribol. Lett. **3**, 125 (1997)
19. F.J. Espinoza-Beltrán, K. Geng, J. Muñoz-Saldanã, U. Rabe, S. Hirsekorn, W. Arnold, New J. Phys. **11**, 083034 (2009)
20. F.J. Espinoza Beltrán, T. Scholz, G.A. Schneider, J. Muñoz-Saldanã, U. Rabe, W. Arnold, J. Phys. Conf. Ser. **61**, 293 (2007)
21. D. Passeri, A. Bettucci, M. Germano, M. Rossi, A. Alippi, A. Fiori, E. Tamburri, S. Orlanducci, M.L. Terranova, J.J. Vlassak, Microelectron. Eng. **84**, 490 (2007)
22. D. Passeri, A. Bettucci, M. Rossi, Anal. Bioanal. Chem. **396**, 2769 (2010)
23. I.N. Sneddon, Int. J. Eng. Sci. **3**, 47 (1965)
24. W.C. Oliver, G.M. Pharr, J. Mater. Res. **7**, 613 (1992)
25. U. Rabe, M. Kopycinska, S. Hirsekorn, J. Muñoz-Saldanã, G.A. Schneider, W. Arnold, J. Phys. D **35**, 2621 (2002)
26. M. Kopycinska-Müller, R.H. Geiss, D.C. Hurley, Ultramicroscopy **106**, 466 (2006)
27. D. Passeri, A. Bettucci, M. Germano, M. Rossi, A. Alippi, S. Orlanducci, M.L. Terranova, M. Ciavarella, Rev. Sci. Instrum. **76**, 093904 (2005)
28. K.L. Johnson, *Contact Mechanics* (Cambridge University Press, Cambridge, 1985)
29. A. Caron, Akustische Rasterkraftmikroskopie an nanokristallinem Nickel: Von der Elastizität zum elastisch-plastischen Uebergang, Ph.D. Thesis, Science and Technical Faculty III, Saarland University, Germany (2009) (unpublished)
30. S. Amelio, A.V. Goldade, U. Rabe, V. Scherer, B. Bhushan, W. Arnold, Thin Solid Films **392**, 75 (2001)
31. G. Stan, R.F. Cook, Nanotechnology **19**, 235701 (2008)
32. B. Bhushan, Diam. Relat. Mater. **8**, 1985 (1999)
33. X. Li, B. Bhushan, J. Mater. Res. **14**, 2328 (1999)
34. D. Schneider, T. Schwarz, H.J. Scheibe, M. Panzner, Thin Solid Films **295**, 107 (1997)
35. G. Kopycinska-Müller, R.H. Geiss, J. Müller, D.C. Hurley, Nanotechnology **16**, 703 (2005)
36. B. Yang, Grain size effects on the mechanical behaviour of polycrystalline nickel from micro to nanoscale, Ph.D. Thesis, Science and Technical Faculty III, Saarland University, 2006. Shaker, ISBN 978-3-8322-5833-7 (2007)
37. B. Yang, H. Vehoff, A. Barnoush, Z. Phys. Chem. **222**, 499 (2008)
38. K. Fujiwara, H. Tanimoto, M. Mizubayashi, Mater. Sci. Eng. A **442**, 336 (2006)
39. Y. Zhou, U. Erb, K.T. Aust, G. Palumbo, Z. Metallk. **94**, 10 (2003)
40. T.D. Shen, C.C. Koch, T.Y. Tsui, G.M. Pharr, J. Mater. Res. **6**, 1012 (1991)
41. J. Tian, H. Ogi, M. Hirao, Appl. Phys. Lett. **87**, 204107 (2005)
42. H. Wagner, D. Bedorf, S. Küchemann, M. Schwabe, B. Zhang, W. Arnold, K. Samwer, Nat. Mater. **10**, 1–4 (2011)
43. A. Caron, W. Arnold, Acta Mater. **57**, 4353 (2009)
44. N. Burnham, A.J. Kulik, G. Gremaud, P.J. Gallo, F. Oulevey, J. Vac. Sci. Technol. B **14**, 794 (1996)
45. U. Rabe, Akustische kraftmikroskopie im ultraschallfrequenzbereich, Ph.D. Thesis, Technical Faculty, Saarland University, 1996, (unpublished)
46. M.C. Junger, D. Feit, *Sound, Structures and Their Interactions* (MIT Press, Cambridge, 1972)
47. P.A. Yuya, D.C. Hurley, J.A. Turner, J. Appl. Phys. **109**, 113528 (2011)

48. H. Ogi, H. Niho, M. Hirao, Appl. Phys. Lett. **88**, 141110 (2006)
49. C. Suryanarayana, D. Mukhopadhyasay, S.N. Patankar, F.H. Froes, J. Mater. Res. **7**, 2114 (1992)
50. A.H. Chokshi, A. Rosen, J. Karch, H. Gleiter, Scripta Metall. **23**, 1679 (1989)
51. R.O. Scattergood, C.C. Koch, Scripta Metall. Mater. **27**, 1195 (1992)
52. M. Gutkin, I. Ovid'ko, I.M. Gutkin, *Plastic Deformation of Nanocrystalline Materials* (Springer, Berlin, 2004)
53. B. Yang, H. Vehoff, Mater. Sci. Eng. A **400–401**, 467 (2005)
54. D. Hull, D.J. Bacon, *Introduction to Dislocations* (Pergamon Press, Oxford, 1965)
55. A.J. Haslam, V. Yamakov, D. Moldovan, D. Wolf, S.R. Phillpot, H. Gleiter, Acta Mater. **52**, 1971 (2004)
56. A.J. Haslam, D. Moldovan, V. Yamakov, D. Wolf, S.R. Phillpot, H. Gleiter, Acta Mater. **51**, 2097 (2003)
57. A.G. Froseth, P.M. Derlet, H. Van Swygenhoven, Acta Mater **52**, 5863 (2004)
58. D. Wolf, V. Yamakov, S.R. Phillpot, A. Mukherjee, H. Gleiter, Acta Mater. **53**, 1 (2005)
59. J. Schiotz, F.D. Di Tolla, K. Jakobsen, Nature **391**, 561 (1998)
60. E.T. Lilleoden, J.A. Zimmerman, S.M. Foiles, W.D. Nix, J. Mater. Res. **51**, 901 (2003)
61. D. Fechtinger, P.M. Derlet, H. Van Swygenhoven, Phys. Rev. B **67**, 024113 (2003)
62. T. Tsuji, H. Irihama, T. Mihara, K. Yamanaka, Key Eng. Mater. **262–263**, 1067 (2004)
63. T.A. Michalske, J.E. Houston, Acta Mater. **46**, 391 (1998)
64. J.P. Hirth, J. Lothe, *Theory of Dislocations* (Krieger, Malabar, 1982)
65. V. Yamakov, D. Wolf, M. Salazar, S.R. Phillpot, H. Gleiter, Acta Mater. **49**, 2713 (2001)
66. J.C.M. Li, J. Appl. Phys. **32**, 525 (1961)
67. H. Gleiter, J. Less-Common Met. **28**, 297 (1972)
68. C.W. Price, J.P. Hirth, Mater. Sci. Eng. **9**, 15 (1972)
69. W.A. Soer, K.E. Aifantis, JThM De Hosson, Acta Mater. **53**, 4665 (2005)
70. A.S. Nowick, B.S. Berry, *Anelastic Relaxation of Solids* (Academic Press, New York, 1972)
71. R.T. Beyer, S.V. Letcher, *Physical Ultrasonics* (Academic Press, New York, 1969)
72. B. Lüthi, *Physical Acoustics in the Solid State* (Springer, Berlin, 2007)
73. A. Bhatia, *Ultrasonic Absorption* (Oxford University Press, Oxford, 1967)
74. A.V. Granato, K. Lücke, J. Appl. Phys. **27**, 583 (1956)
75. Z. Budrovic, H. Van Swygenhoven, P.M. Derlet, S. Van Petegem, B. Schmitt, Science **304**, 273 (2004)
76. B. Bhushan (ed.), *Nanomechanics and Nanotribology*, 2nd edn. (Springer, Berlin, 2008)
77. E. Gnecco, E. Meyer (eds.), *Fundamentals of Friction and Wear on the Nanoscale* (Springer, Berlin, 2007)
78. T. Göddenhenrich, S. Müller, C. Heiden, Rev. Sci. Instrum. **65**, 2870 (1994)
79. A. Caron, W. Arnold, H.-J. Fecht, Jap. J. Appl. Phys. **49**, 120204 (2010)
80. R. Truell, C. Elbaum, B.B. Chick, *Ultrasonic Methods in Solid State Physics* (Academic, New York, 1969)
81. D. Schneider, T. Schwarz, H.-J. Scheibe, M. Panzner, Thin Solid Films **295**, 107 (1997)
82. <http://www.gwyddion.net>
83. P.E. Mazeran, J.L. Loubet, Tribol. Lett. **7**, 199 (1999)
84. M.A. Lantz, S.J. O'Shea, M.E. Welland, K.L. Johnson, Phys. Rev. B **55**, 10776 (1997)
85. P.E. Mazeran, M. Beyaoui, Tribol. Lett. **30**, 1 (2008)
86. R.D. Mindlin, W.P. Mason, J.F. Osmer, H. Deresiewicz, in *Proceeding of the 1st US National Congress Applied Mechanics*, ed. by E. Sternberg. (E. Brothers, Ann Harbor, 1952), p. 203
87. B. Bhushan, *Nanotribology, Nanomechanics and Materials Characterization in Nanotribology and Nanomechanics*, 2nd edn, ed. by B. Bhushan (Springer, Berlin, 2008), pp. 311–416
88. E. Gnecco, R. Bennewitz, O. Pfeiffer, A. Socoliuc, E. Meyer, *Friction and Wear on the Atomic Scale in Nanotribology and Nanomechanics*, 2nd edn, ed. by B. Bhushan (Springer, Berlin, 2008), pp. 557–605
89. O. Zwoerner, H. Hoelscher, U.D. Schwarz, R. Wiesendanger, Appl. Phys. A **66**, 263 (1998)

90. R. Bennewitz, T. Gyalog, M. Guggisberg, M. Bammerlin, E. Meyer, H.-J. Guentherodt, *Phys. Rev. B* **60**, R11301 (1999)
91. E. Gnecco, R. Bennewitz, T. Gyalog, Ch. Loppacher, M. Bammerlin, E. Meyer, J. Guentherodt, *Phys. Rev. Lett.* **84**, 1172 (2000)
92. N.S. Tambe, B. Bhushan, *Nanotechnology* **15**, 1561 (2004)
93. N.S. Tambe, B. Bhushan, *Nanotechnology* **16**, 2309 (2005)
94. F. Dinelli, S.K. Biswas, G.A.D. Briggs, O.V. Kolosov, *Appl. Phys. Lett.* **71**, 1177 (1997)
95. M.T. Cuberes, *Nanoscale Friction and Ultrasonics in Fundamentals of Friction and Wear on the Nanoscale*, ed. by E. Gnecco, E. Meyer (Springer, Berlin, 2007), pp. 49–71, and references therein
96. V. Scherer, B. Bhushan, U. Rabe, W. Arnold, *IEEE Trans. Magn.* **33**, 4077 (1997)
97. V. Scherer, W. Arnold, B. Bhushan, *Surf. Interface Anal.* **27**, 578 (1999)
98. K. Goebbels, in *Research techniques in NDT*, vol. IV, ed. by R.S. Sharpe (Academic Press, New York, 1980), p. 87
99. S. Luxenburger, W. Arnold, *Ultrasonics* **40**, 797 (2002)
100. I.A. Inman, S. Datta, H.L. Du, J.S. Burnell-Gray, Q. Luo, *Wear* **254**, 461 (2003)
101. C.H. Hager Jr, J. Hu, C. Muratore, A.A. Voevodin, R. Grandhi, *Wear* **268**, 1195 (2010)

# Chapter 15

## Quantitative Subsurface Imaging by Acoustic AFM Techniques

Zehra Parlak and Levent F. Degertekin

**Abstract** We review the modeling techniques developed for analyzing the effects of 2-D and 3-D subsurface structures on the stiffness measurements by acoustic AFM. Starting from the analytical Hertzian model, we describe important parameters such as penetration depth and subsurface resolution for acoustic AFM imaging. These definitions point to the need for analytical–numerical models based on mechanical surface impedance method and finite element modeling of arbitrary 2-D and 3-D structures buried under the surface. By using the 2-D and 3-D models, the dependence of penetration depth and subsurface resolution on material properties, subsurface structure geometry, and imaging parameters are investigated. It has been shown that high contrast between subsurface structure and substrate increases the detectability of the structure and the visible depth of the structure depends highly on the contact radius. Soft subsurface structures or voids can be detected with appropriate tip radius and force even if they are as deep as 450 nm. However, the sensitivity is higher while detecting stiff structures under thin soft layers. These results can be extrapolated for different applications using the presented guidelines.

### 15.1 Introduction

Although AFM is primarily used for imaging surface topography, many important AFM applications, such as measurement of thin films, require understanding of how the finite surface stiffness measured by the AFM tip is affected by the material prop-

---

L. F. Degertekin (✉)

School of Electrical and Computer Engineering and G.W. Woodruff

School of Mechanical Engineering, Georgia Institute of Technology, Atlanta G30332, USA

e-mail: levent.degertekin@me.gatech.edu

Z. Parlak

Mechanical Engineering and Material Science, Duke University, Durham, NC 27208, USA

e-mail: Zehra.parlak@gmail.com

erties and subsurface features [1, 2]. Acoustic and dynamic AFM techniques provide important information for this purpose by significantly increasing the range of surface stiffness measurement [3, 4]. Using experimental and analytical tools related to these techniques, 2-D and 3-D structures and interfaces between different materials beneath the surface can be identified and measured. The application space of these measurements is broad, including thin film thickness and property measurement, testing reliability, and repeatability of the fabrication processes of layered surfaces, detecting nanoscale subsurface defects, such as electromigration voids in microelectronics circuits, to provide more insight into the manufacturing and testing of multi-layered complex nanoscale structures [5–8].

In this chapter we review the modeling techniques specifically developed for acoustic AFM imaging of layered materials and subsurface defects, and present results relevant to several important applications. Starting from the analytical Hertzian model, we describe important parameters such as penetration depth and subsurface resolution for acoustic AFM imaging. These definitions point to the need for analytical–numerical models based on mechanical surface impedance method and finite element modeling of arbitrary 2-D and 3-D structures buried under the surface. We discuss the dependence of penetration depth and subsurface resolution on material properties, subsurface structure geometry, and imaging parameters and provide several illustrative examples before the concluding remarks.

## 15.2 Ultrasonic AFM for Contact Stiffness Imaging

Acoustic AFM techniques, such as AFAM and UAFM, aim for sensitive elasticity measurements with high lateral resolution [4, 9]. In these methods, while the cantilever scans the surface with a constant contact force, the cantilever tip-surface contact is vibrated at ultrasonic frequencies. At these high vibration frequencies, the cantilever beam is dynamically stiffened to increase and ideally match the stiffness of the contact, improving the measurement resolution.

Although it is not applicable to layered media, one can use the simple Hertzian model to define some of the parameters such as lateral resolution, sensitivity, and contact stiffness resolution for contact-based AFM techniques. This model was first introduced by Hertz for the contact between two elastic axisymmetric bodies [10]. It is a valuable tool for analyzing the effects of the applied force and the tip radius on the contact deformation in AFM. It can also be used to calculate the reduced Young's modulus from the contact stiffness measured by the AFM on half-spaces. The assumptions for this model can be summarized as the following [10, 11]:

- Continuous and non-conforming surfaces;
- Small strains;
- Elastic and homogeneous bodies;
- Frictionless surfaces.

For an elastic sphere with the radius  $R_t$ , like the AFM tip, in contact with a flat and elastic surface, the contact region is circular. According to this theory, the contact radius, which can be considered the lateral resolution for ultrasonic AFM is given as:

$$a_c = \sqrt[3]{\frac{3F_{\perp}R}{4M}}, \quad (15.1)$$

where  $F_{\perp}$  is the applied normal load,  $R$  is the equivalent radius of curvature, and  $M$  is the indentation modulus. The indentation modulus,  $M$ , is derived from the Young's modulus,  $E_t$ ,  $E_s$ , and Poisson ratio,  $\nu_t$ ,  $\nu_s$ , of the tip and the sample, respectively, by using the following equation:

$$\frac{1}{M} = \frac{1}{M_t} + \frac{1}{M_s}, \quad (15.2)$$

where  $M_t$  and  $M_s$  are:

$$\frac{1}{M_t} = \frac{1 - \nu_t^2}{E_t} \quad \text{and} \quad \frac{1}{M_s} = \frac{1 - \nu_s^2}{E_s}. \quad (15.3)$$

The equivalent radius of curvature is calculated by the AFM tip radius,  $R_t$  and the radius of curvature of the surface,  $R_s$ :

$$\frac{1}{R} = \frac{1}{R_t} + \frac{1}{R_s}. \quad (15.4)$$

For many cases,  $R_s$  is much higher than  $R_t$  and it is infinite for a flat surface which means  $R$  is equal to  $R_t$ .

The mutual approach of the AFM tip and the surface with the normal contact force of  $F_{\perp}$ —the maximum deformation on the contact—,  $\delta$ , is given as:

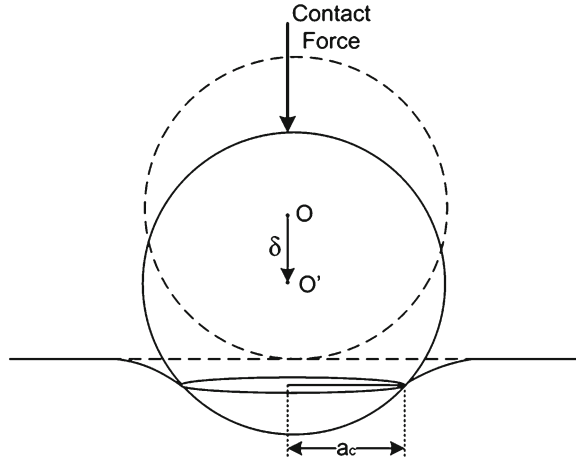
$$\delta = \frac{a_c^2}{R} = \sqrt[3]{\frac{9F_{\perp}^2}{16RM^2}}. \quad (15.5)$$

Ultrasonic AFM techniques measure the stiffness of the AFM tip-sample contact by monitoring contact resonances [3, 12, 13]. The stiffness of the contact, or contact stiffness,  $k^*$ , is the rate of change in contact force with respect to the deformation. For the contact of AFM tip and surface,  $k^*$  is calculated as [2] (Fig. 15.1):

$$k^* = -\frac{\partial F_{\perp}(\delta)}{\partial \delta} = \frac{3F_{\perp}}{2\delta}. \quad (15.6)$$

On homogeneous materials,  $k^*$  is used to calculate Young's modulus of the materials since it is a function of  $M$ :

**Fig. 15.1** The contact of a spherical object with a surface



$$k^* = \sqrt[3]{6F_{\perp}RM^2}. \quad (15.7)$$

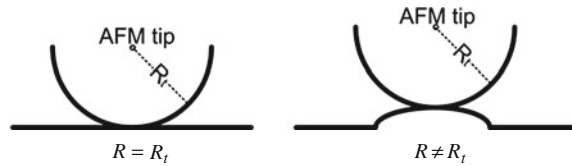
If the tip radius, tip material, and the applied force are known,  $M_s$  can also be computed by using Eq. 15.7 and 15.3.

Since the effective cantilever stiffness is close to the contact stiffness at ultrasonic frequencies, it is possible to measure contact stiffness accurately by detecting the cantilever's resonant vibrations. The resolution of the measurement can be quantified by defining a minimum detectable contact stiffness change,  $\Delta k_{\min}$ , which is determined by the stiffness sensitivity of the selected contact resonance around a certain contact stiffness and the signal-to-noise ratio (SNR). The signal to noise ratio is a function of the mechanical, electronic, and optical detection noise of the system. Various studies have reported ultrasonic AFM setups with  $\Delta k_{\min}$  as small as 10 N/m [2, 14, 15]. One can then use Eq. 15.7 to determine the resolution of indentation modulus measurement for given  $\Delta k_{\min}$ . For example, when  $\Delta k_{\min}$  is 10 N/m around 1,000 N/m contact stiffness, measured  $M$  has 1.5% error. The error increases to 6% when  $\Delta k_{\min}$  is 10 N/m around a contact stiffness of 250 N/m.

It is known that environmental factors, such as humidity may affect the  $k^*$  measurements and require some correction of the results [16, 17]. Another factor that affects the resolution of the contact stiffness measurement by AFM is the surface topography. When the surface is not flat,  $R$  differs from  $R_t$  and the measured contact stiffness changes even when the material is the same [17] (Fig. 15.2). To obtain sensitive elasticity mapping of samples, the surface should be flat or the topography effects should be taken into consideration when interpreting the results. The tip radius affects the contact stiffness significantly (Eq. 15.7) and the ambiguities about the tip radius cause errors [18]. Since subsurface imaging demands highly sensitive contact stiffness data in order to detect the slight differences caused by subsurface structures, the contact stiffness data should be reliable. One of the solutions is to



**Fig. 15.2** Contact of the AFM tip with a smooth and rough surface. Equivalent radius of curvature is equal to tip radius for a smooth surface



blunt the tip prior to the experiments so that it does not change during the imaging with some loss of lateral resolution in return [14].

A significant advantage of AFM over other elasticity measurement techniques such as nanoindentation is its high lateral resolution. Ultrasonic AFM retains this advantage and one can obtain non-destructive, sensitive elasticity measurement while imaging the topography of a sample with a resolution limited by the contact radius. This capability is especially important for imaging samples with different material regions [19–21]; such as highly oriented pyrolytic graphite (HOPG) [9], carbon fiber [22], and ferrites with nanoscale features [23].

The high lateral resolution of the elasticity images by ultrasonic AFM revealed interesting results. Researchers observed distinct features between steps of the HOPG and small areas of stiffness variation on the carbon fibers [22] such as shown in Fig. 15.3. These variations are different from the topography changes and they may appear even when the material at the top surface is the same over the image, pointing out the heterogeneous nature of the sample. These heterogeneities can be due to the subsurface defects [8, 14, 24, 25] or thin films [5, 8, 17].

The mechanism behind this contrast is the penetration of the stress fields into the sample. For homogeneous samples, the elastic stress fields extend into the sample as much as  $3a_c$  [26]. As described by Eq. 15.1, this figure increases with the compliance of the material, size of the tip, and the contact force. Therefore, even for a simple half-space one can adjust imaging parameters to achieve a certain lateral resolution as well as depth of imaging.

The situation gets more complicated as soon as any subsurface structure is introduced in the sample and models that more complex than the Hertzian approach are required to analyze the field distributions created by the tip-sample contact. The simplest subsurface structure that one can consider is a thin film layer with infinite lateral extent over a substrate (half-space). With this additional complexity some new imaging parameters need to be defined and calculated. For example, one can imagine that the substrate will affect the contact stiffness at the surface if the film-substrate interface lies close enough to the surface. In this case, we define the maximum distance between the surface and the interface that is enough to change the surface stiffness by  $\Delta k_{\min}$  as the penetration depth [2]. This parameter can also be applied for finite size subsurface structures and it becomes the maximum distance from the surface that a subsurface structure can be detected through contact stiffness measurement. The penetration depth would depend on factors such as the applied force, tip radius, size of the subsurface structures, and the contrast between the mechanical properties of the substrate and the subsurface structure among others.

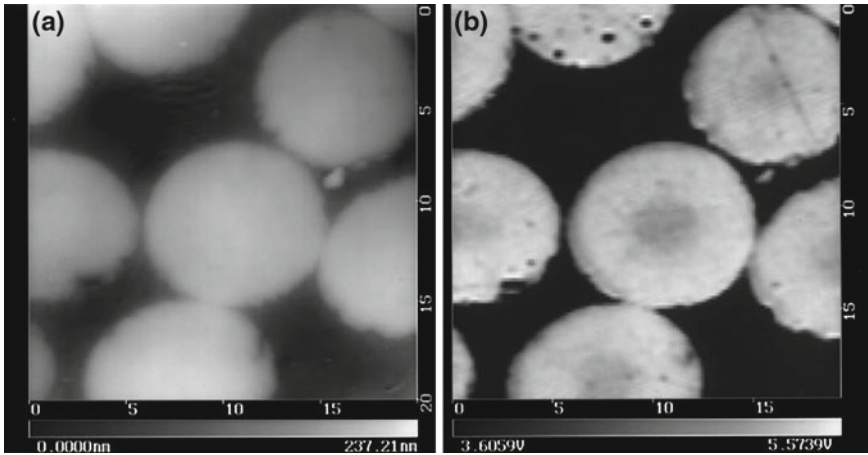


**Fig. 15.3** Images of a cross section of carbon-fiber-reinforced-plastic (CFRP). **a** Topography image **b** Vibration amplitude distribution at cantilever's resonance frequency [22]

Similarly, when a 2-D or 3-D finite size subsurface structure is present in the sample, such as the case of Fig. 15.3, the lateral subsurface resolution of an ultrasonic AFM image cannot be defined only by the contact radius at the surface. A more complicated analysis is needed to find the minimum separation between two subsurface structures that would result in  $\Delta k_{min}$  at the surface. This subsurface resolution will also depend on applied force, tip radius, and depth and size of the subsurface structures among others. Calculation of these imaging parameters requires different approaches. The following section reviews contact stiffness modeling for layered media and finite size subsurface structures leading to the discussion of penetration depth and lateral subsurface resolution in ultrasonic AFM applications.

### 15.3 Contact Stiffness Models of Samples with Subsurface Structures

Since acoustic AFM methods rely on contact stiffness for mechanical measurements, modeling of this parameter for samples including thin films and more complex subsurface structures is critical. Only with a proper, validated model can one quantitatively interpret the resulting measurements and images. In this section, we review several methods for contact stiffness modeling for samples with increasingly complex subsurface structures.

#### (a) Layered Media with Infinite Extent

Substrates with multiple thin layers are encountered in many practical applications from microelectronics, optics to biologically functionalized surfaces. Measuring

the thickness and material properties and examining the adhesion at the interfaces between layers are crucial to have reliable and repeatable fabrication processes. For modeling purposes, in the simple case, one can assume that these layers are infinitely wide as compared to contact radius, and axisymmetry applies for a spherical or conical tip.

Numerical methods like finite element analysis (FEA) can be used to analyze the AFM tip contact with layered substrates [2, 27]. Since the acoustic AFM techniques use vibration frequencies in the order of 1–10 MHz resulting in wavelengths much larger than the contact radius and the dynamic changes in contact radius is very small, the contact can be assumed quasistatic [2]. Then, contact elements can be applied to axisymmetric structural elements with static contact assumption. Although FEA is a powerful tool for modeling the AFM tip-sample contact, it requires excessive computation time. Therefore, for infinitely wide layered media, closed-form numerical solutions for calculating indentation modulus have been studied [1, 28] and used by many researchers [17, 29]. Although useful, these methods rely on many approximations and do not predict effects of the interface defects.

Another approach to the same problem emerges when one realizes that AFM at ultrasonic frequencies is a form of common ultrasonic non-destructive evaluation (NDE) methods for layered media. Although AFM deals with interactions at a much smaller scale, this fact does not prevent one from using the wave propagation-based models used in ultrasonic NDE for this particular application. Radiation impedance approach is one of these methods adapted to AFM problems [2]. In ultrasonic AFM, a vibrating AFM tip contacts the surface with a DC contact force and creates a circular ultrasonic source radiating acoustic waves into the sample. For flexural vibration modes, this source applies a traction field normal to the surface with radius  $a_c$ . Since the contact radius,  $a_c$ , is much smaller than the wavelength,  $\lambda_s$ , at that ultrasonic frequency; the generated waves into the solid are mostly inhomogeneous waves [2]. It is possible to combine the radiation impedance of this acoustic radiator [30] with Hertzian contact theory to explain the AFM tip-sample contact [2]. The radiation impedance method uses the surface impedance tensor which relates the stress and velocity fields on the surface of a sample with arbitrary number of anisotropic layers in the general case [31]. Furthermore, different defects can be introduced at the interfaces between these layers, making this approach a powerful tool for calculating the contact stiffness for a broad range of layered samples [2, 5, 6].

In this method, first the surface stiffness,  $k_s$ , is calculated from the effective radiation impedance seen by the tip on the contact area.

$$k_s = \frac{\text{normal force on the contact}}{\text{displacement}} = j\omega Z_s, \quad (15.8)$$

where  $Z_s$  is the mechanical impedance and  $\omega$  is the angular vibration frequency. Given that the waves radiated from the contact are inhomogeneous, the radiation impedance is predominantly imaginary and the contact acts as a lossless spring [30, 31].

The contact stiffness is then calculated from surface stiffness using the elements of Hertzian contact theory. An iterative algorithm, called contact stiffness algorithm (CSA) combines these two methods [2]. The algorithm can be summarized in 5 steps:

- An initial contact radius,  $a_{s[i]}$ , is estimated for the given contact force and material.
- Surface stiffness,  $k_s$ , is calculated by radiation impedance (Eq. 15.8).
- $M_s$  (the indentation modulus of the sample) is calculated:

$$M_s = \frac{k_s}{2a_s}. \quad (15.9)$$

- The contact radius associated with this  $M_s$  and  $F$  is calculated:

$$a_{s[i+1]} = \sqrt[3]{\frac{3FR}{4M_s}}. \quad (15.10)$$

If  $a_{s[i+1]}$  is close to  $a_{s[i]}$ , then it means the initial estimate is true. If not, the first 4 steps are repeated until the contact radius value converges. After this step the reduced equivalent Young's modulus and contact stiffness are calculated (Eqs. 15.1 and 15.7).

Contact stiffness calculations using CSA agree well with analytical solutions for half-space samples. The calculations for layered media have been validated by finite element modeling [2] and experiments [5]. In addition to contact stiffness calculation as a single lumped parameter, the surface impedance method enables one to obtain relevant stress and displacement fields in the layered media, which provides further insight into effect of material properties and interfaces on ultrasonic AFM. As an example, in Fig. 15.4, the normal displacement fields for 5 nm thick photoresist polymer and tungsten films on silicon substrate are plotted [2]. It is seen that in the case of the soft polymer film the displacement (indentation) is very large and confined to the polymer layer, whereas in case of tungsten film the displacement field penetrates well into the silicon substrate. This type of additional information is useful in interpreting the contact stiffness and penetration depth calculation results.

Bonding problems such as delaminations are common and detrimental in many applications of layered media. It is possible to incorporate different interface conditions or defects into CSA calculations, such as delaminations or slippery bonds between layers [6]. These conditions are included in the calculations by imposing different stress and displacement boundary conditions at the interfaces between layers in the surface impedance calculations. As an example, contact stiffness calculations for a silicon oxide/copper/silicon substrate are shown in Fig. 15.5 for perfect bonding and void-delamination conditions at the oxide/copper interface. The results show that the changes in the bonding condition drastically affect both the contact stiffness value at the surface and also the penetration depth for the measurements. Therefore, ultrasonic AFM measurements on such a sample can be used to detect this kind of subsurface layer problems.

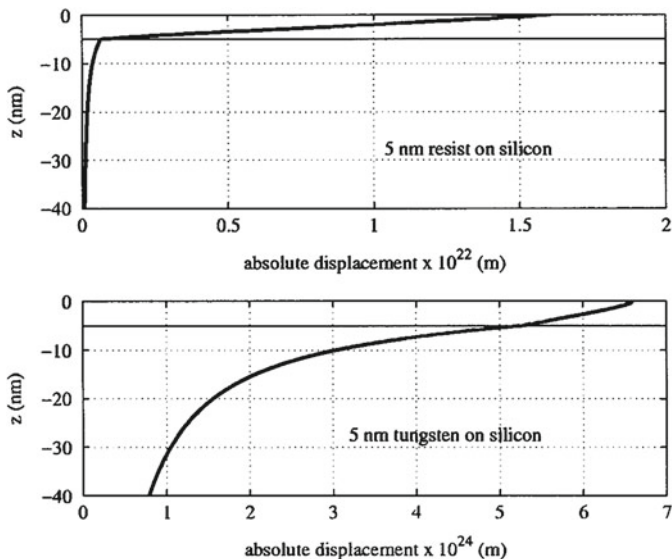
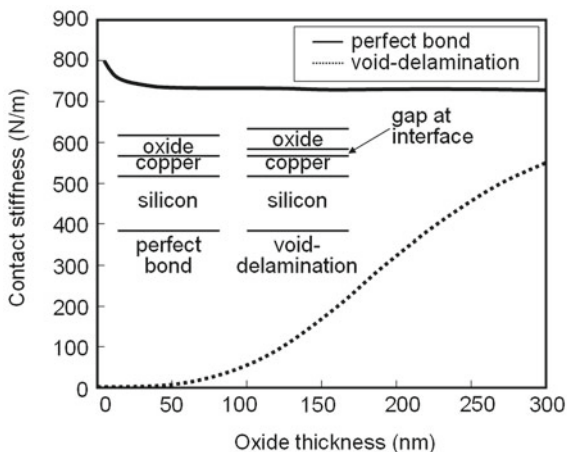


**Fig. 15.4** Side view of normal displacements into the silicon substrates with 5 nm thick resist and tungsten films on top [2]

**Fig. 15.5** Contact stiffness on oxide layer with and without a bonding defect [6]



In addition to delaminations, other adhesion problems can be investigated by using the CSA [6]. For example, when gold is deposited on silicon, usually a thin layer of titanium is needed in between to provide good adhesion. Otherwise a slippery bond occurs between gold film and silicon substrate. This slippery bond affects the contact stiffness measured on the surfaces and these effects can be simulated by using CSA [6]. Hurley et al. deposited a thin gold layer on a silicon sample with and without titanium in between. Figure 15.6b shows the contact stiffness image on the surface

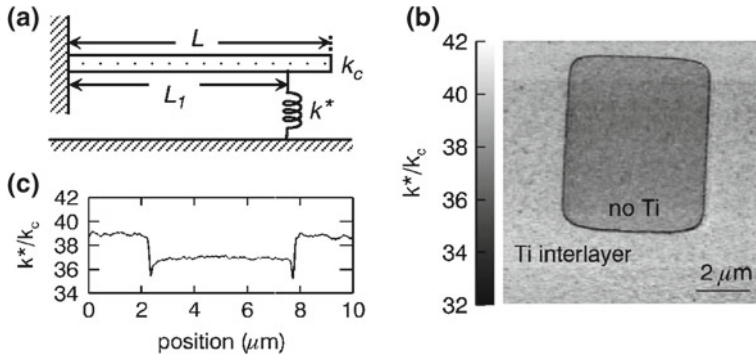


**Fig. 15.6** **a** Model for cantilever dynamics. **b** Image of the normalized contact stiffness  $k^*/k_c$  calculated from the contact resonance frequency. **c** Average stiffness versus position across the center of the image in **b** [8]

with these regions. Since the lack of the titanium causes poor adhesion and slippery bonds, these regions have lower contact stiffness than the regions with titanium. A section view of the contact stiffness image (Fig. 15.6c) shows that experimental results match with CSA results [8]. In summary, the radiation impedance method used in conjunction with the CSA provides a solid tool for calculating contact stiffness for AFM when infinite layers with various material and interface conditions need to be considered. We use this method in evaluating important parameters such as penetration depth in the later sections.

### (b) Finite-sized Subsurface Structures

Although many samples measured by acoustic AFM may have structures much larger than the tip-sample contact radius, and thus can be modeled by the radiation impedance method, many other subsurface structures are of finite size. FEA is best suited to model contact stiffness changes due to these subsurface structures.

A 2-D axisymmetric FEA model of the AFM tip-sample contact is easier to construct as compared to a 3-D model, and it is useful in defining penetration depth for spherical and pillbox shaped structures [15, 32]. A 3-D FEA model of the AFM tip-sample contact on the other hand, can be used to quantitatively characterize the effects of various subsurface structures with arbitrary shape and lateral position relative to the AFM tip. The experimental contact stiffness results can then be analyzed for subsurface imaging by using this model. Here, we review some salient aspects of a 3-D FEA model development.

In principle, 3-D FEA models are capable of simulating AFM tip-sample contact for any geometry. One could define the tip and the sample geometry much larger than the contact radius and the contact area, and finely mesh the whole structure. This brute force approach requires extensive computational resources. Since the aim of the simulation is to calculate the effective Young's modulus of the sample, using a smaller tip area decreases the computation time immensely, i.e.,  $M_S$  is of interest

and  $M_T$  can be calculated by using the mechanical properties of the silicon tip. In another approach, an infinitely rigid tip material is assumed in the simulations instead of the actual  $M_T$ , because in this case the elastic parameters of the tip do not affect the results anymore [15, 33]. The effect of the deformation in the AFM tip can be included later analytically to calculate the actual contact stiffness,  $k^*$  values as discussed below. In other words, in this model the AFM tip is simulated as a rigid indenter. This configuration gives the opportunity of using a smaller tip structure since the tip does not need to be a half-space.

For an infinitely stiff tip ( $M_T \rightarrow \infty$ ),  $M$  is simply given by  $M_S$  according to Eq. 15.2. Consequently, Eq. 2.11 below provides surface stiffness,  $k_S$ , assuming Hertzian contact:

$$k_S = \frac{3F_{\perp}}{2\delta}. \quad (15.11)$$

Note that, this equation is different from Eq. 15.6 since that equation is computed for the contact stiffness.

In order to obtain  $k^*$ , three more steps are required. First,  $M_S$  is calculated using the following equation:

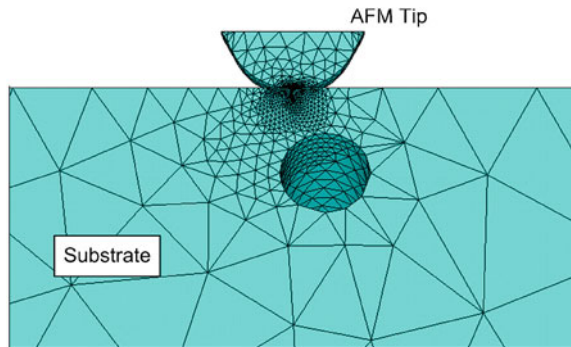
$$M_S = \sqrt{\frac{k_S^3}{6F_{\perp}R}} \quad (15.12)$$

$M_S$  is a reduced indentation modulus for the sample, which incorporates the effects of finite size subsurface structures with the bulk material properties. By substituting  $M_S$  of Eq. 15.12 into Eq. 15.2 and using actual  $M_T$ ,  $M$  is obtained. Contact stiffness can be easily calculated after this point, by using Eq. 15.7.

3-D FEA calculations can be implemented by ANSYS 11.0.25. For ANSYS, the 3-D structural solid element (SOLID92) can be used to mesh the tip and the substrate. In addition, the possible contact area should be meshed with 3-D contact elements (TARGE170, CONTA174). Figure 15.7 shows a typical 3-D FEA mesh. With this type of mesh one can simulate an AFM scan over subsurface structures such as spheres, cylinders, or rectangular prisms. Also, more than one structure can be present. The bottom of the tip is spherical and always touches the center of the substrate which is a cylindrical volume with at least 2  $\mu\text{m}$  radius. Convergence studies show that any smaller sized substrate does not agree with Hertzian contact validation for half-space case because of the close boundaries. To simulate a scan over the surface, the subsurface structures are relocated to different positions and the contact stiffness is calculated for those positions.

One of the drawbacks of the 3-D FEA contact model is the computation time, which is mainly determined by the nonlinear contact analysis and the number of nodes. The number of nodes should be high for more accurate results, but a high node number leads to excessive computation time. The SMRTSIZE command of ANSYS can be used with medium size to control the distribution of the elements on whole volume. This command provides coarse meshing. However, fine meshing around the contact, especially around the contact elements, is necessary. Thus, it is suggested to refine the meshing around the contact by using NREFINE command.

**Fig. 15.7** The computational grid on the Y surface [14]



Accordingly, the 3-D model of AFM tip-substrate contact with an acceptable number of nodes can be obtained. Each simulation run takes approximately 15 minutes on average on an Intel P 4 3.0GHz.

Convergence analysis of the 3-D FEA model of the AFM tip-substrate contact for the half-space material is performed through comparison with Hertzian contact theory. According to the convergence analysis, the simulated contact stiffness for a half-space converges to values obtained from Hertzian contact theory with less than 1% difference for different materials. Although this result verifies the FEA approach, it does not provide a comparison for the simulation of the finite size subsurface defects. For this purpose, additional ultrasonic AFM experiments were performed and the 3-D FEA model was verified [14].

The capability of imaging simulation is demonstrated in Fig. 15.8, which shows the contact stiffness variation when an AFM tip with 100 nm radius is pressed on the surface with  $1 \mu\text{N}$  contact force and scanned over a 300 nm radius spherical 500 nm under the silicon surface. The silicon half-space results in contact stiffness of 1,427 N/m in the simulations for the given parameters. The lowest contact stiffness resulted by this spherical cavity is 1,411 N/m. In comparison, an infinitely long cylinder with the same radius and depth results in 1,395 N/m of contact stiffness when the AFM tip is located at its center. With these types of simulations, one can use the 3-D FEA simulations to define subsurface image resolution of AFM in addition to the topographical resolution dominated by the contact radius.

The 3-D FEA contact model is verified on a silicon substrate with well-known finite sized subsurface structures by using AFAM. The cantilever, the tip radius, and the contact force are determined prior to the experiments by following routine calibration processes [4, 26] and these parameters are used in the simulation without any parameter fitting. The experimental data is compared with 3-D FEA contact simulations for the same subsurface structures and the comparison is shown in Fig. 15.9 [14]. The experimental analysis verified that one can use 3-D FEA contact models to calculate the contact stiffness on finite size subsurface structures [14]. It has also been shown that one can quantitatively characterize nanoparticles embedded in polymers by using 3-D FEA contact models as guidelines [25].



**Fig. 15.8** The contact stiffness simulations for an embedded spherical cavity [14]

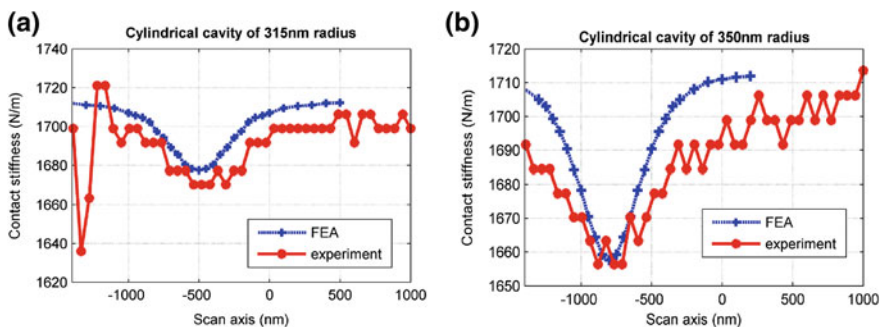
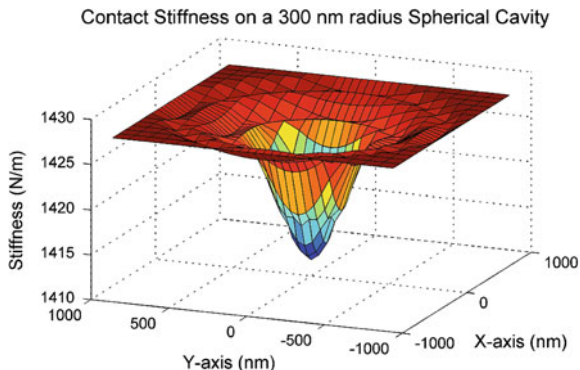


**Fig. 15.9** Measured and simulated contact stiffness on cylindrical cavities with 315 nm and 350 nm radius in silicon substrate. The center of the cavity lies under 550nm material and parallel to the surface [14]

### 15.4 Penetration Depth and Subsurface Resolution in Acoustic AFM

As introduced earlier, penetration depth is an important parameter for thin film characterization and subsurface imaging. The models discussed in the previous section enables us to evaluate this parameter for a wide variety of applications.

Penetration depth in layered media depends on the applied force, tip radius, and material properties. In order to understand how these variables affect penetration depth on thin films, the CSA approach described in Sect. III-a) is used. Figure 15.10 shows the penetration depth for a thin layer of SiO<sub>2</sub> ( $M_{SiO_2} = 72$  GPa) deposited on silicon substrate. In this figure, the penetration depth is calculated by assuming  $\Delta k_{min} = 10$  N/m for different tip radius and applied force combinations. For example, 100 nm of tip radius and 100 nN applied force results in a penetration depth of 42 nm. As a general trend, the simulation results show that for thin film layers, the penetration depth can be expressed as proportional to the cube root of the force—tip radius product, similar to the contact radius equation (Eq. 15.1). This does not mean

**Fig. 15.10** Penetration depth of SiO<sub>2</sub> film on the Si substrate versus the force-radius product

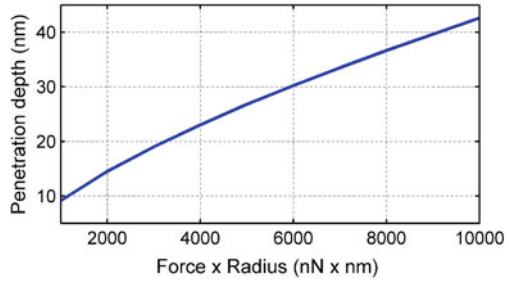
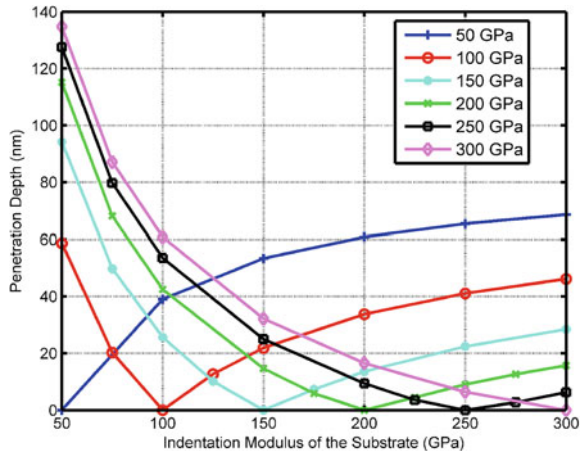


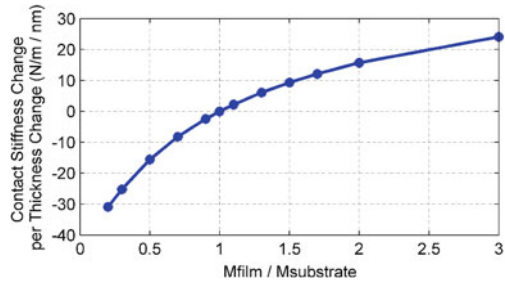
**Fig. 15.11** Penetration depth of thin films (indentation modulus of 50, 100, 150, 200, 250, and 300 GPa) on different samples



that penetration depth can be calculated from the contact radius as in the case of a half-space. But once the penetration depth for a material combination is known for a particular case, one can determine penetration depth for different force and radius values.

The data presented in Fig. 15.10 are obtained for a specific thin film/substrate material combination and it is highly affected by the indentation modulus of the materials and their contrast. To study these effects, the thin film layers with indentation modulus between 50 GPa and 300 GPa are studied. In the CSA simulations, penetration depths of these films on different substrates are calculated (Fig. 15.11). The data in this figure are obtained for 100 nN contact force and 100 nm tip radius. However, it is possible to extract results for different force and radius combinations by using the cube-root relation. When the contrast between the indentation moduli of the film and the substrate is high, the penetration depth is also high. Another result that can be obtained from this figure is that, for a thin film the penetration depth is higher when the substrate is softer than the film. For example, when the film material has 100 GPa indentation modulus, the penetration depth is 59 nm for a substrate with 50 GPa modulus. Penetration depth value decreases to 34 nm for a substrate with 200 GPa indentation modulus.

**Fig. 15.12** Contact stiffness sensitivity to thickness change of the thin films for different films

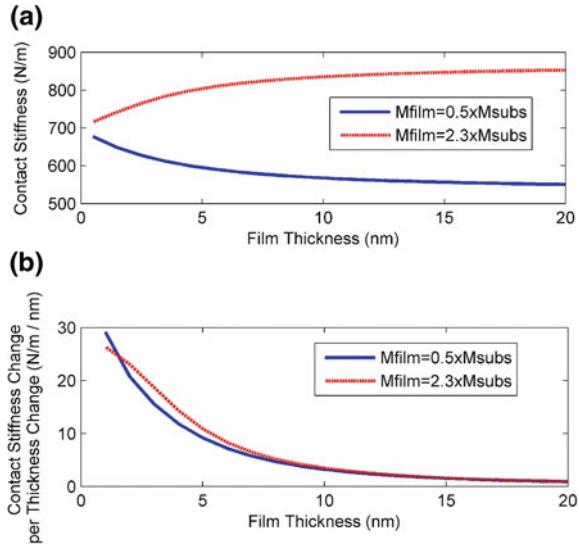


To understand the thickness sensitivity of the contact stiffness measurement by ultrasonic AFM, a simulation is conducted by CSA for a 3 nm thick film on silicon substrate ( $M_{\text{subs}} = 150$  GPa). In this simulation, different indentation modulus values are assigned to the film and the contact stiffness change for one nm of film thickness change is calculated for each material (Fig. 15.12). As expected, when the material elasticity has high contrast with the substrate, the contact stiffness change is higher.

Generally, if a film on a substrate has high penetration depth, then film thickness measurements are more sensitive. We also investigated the case where the penetration depth is the same for two different combinations. The simulations show that when a 75 GPa film is deposited on silicon substrate ( $M_{\text{film}} = 0.5 \times M_{\text{subs}}$ ), the penetration depth is 36.5 nm. This penetration depth value is also valid for a 345 GPa film ( $M_{\text{film}} = 2.3 \times M_{\text{subs}}$ ). CSA simulations are performed to understand the stiffness change associated with these films. As expected, increasing the thickness of the soft film decreases the contact stiffness while increasing the thickness of the stiff film increases the contact stiffness (Fig. 15.13a). As the rate of the stiffness change is investigated, an interesting result is observed. For very thin films (as thin as 1 nm) the stiffness change is more sensitive for a soft film, i.e., measuring the effects of the substrate is easier through a soft film than a stiff film for thin layers. When the film thickness is in the 3–10 nm range stiffer films are advantageous. For film thicknesses higher than 15 nm, the rate of contact stiffness change is the same for softer or stiffer film.

Materials of interest in nanotechnology are not limited to layered media. Finite size defects, voids, inclusions under the surface are also of interest for many researchers. One interesting parameter to investigate for finite size subsurface structure is the effect of the elastic properties of these structures on the detection limits. As in the case of infinite structures, the penetration depth changes with the elastic properties of the finite subsurface structures. This type of information is important in determining proper force and tip radius used in the experiments. For this purpose, long cylindrical inclusions in silicon made of  $\text{SiO}_2$  and tungsten are simulated by 3-D FEA model. To simulate the limiting cases, the results for a cylindrical cavity or a perfectly rigid inclusion of the same shape are also generated. A contact force of  $1 \mu\text{N}$  and tip radius of 100 nm is used in the simulations. As mentioned before,  $\Delta k_{\text{min}}$ , is 10 N/m. In Fig. 15.14, the minimum defect size and depth required for the detection

**Fig. 15.13** **a** Contact stiffness on the surfaces with 75 GPa and 345 GPa films for different thicknesses **b** Contact stiffness sensitivity for different layer thicknesses



of these subsurface defects are plotted. Each line shows the depth and the radius of the corresponding inclusion that results in  $\Delta k_{\min}$ . For each material, the region to the left of the contour shows the detectable range of the cylindrical defect radius and depth. According to Fig. 15.14, when there is higher contrast between substrate and structure, smaller inclusions can be detected. Consequently, the lines corresponding to rigid structure and void defects are the rightmost curves. Similarly, the tungsten ( $M_W = 478 \text{ GPa}$ ) inclusion generates more contrast than a similar silicon dioxide ( $M_{SiO_2} = 74 \text{ GPa}$ ) structure. Rigid inclusions can be detected easier than the voids of similar size when they are close to the surface. The steep increase in detectable rigid cylinder radius shows that the penetration depth for this type of defects is limited to about 280 nm regardless of its size for this particular tip radius, tip, and substrate material. In contrast, a void located deeper in the substrate can still be detected if it has large enough diameter. The results presented here are specific for finite size subsurface structures modeled as cylindrical inclusions. When the structure is much larger than the contact radius, the results converge to the layered media as expected. Note that although the results in this figure are valid for this particular example they can serve as a guideline for subsurface detection.

A similar study is performed for investigating the effects of the tip radius on penetration depth for finite size structures. Tip radius of 50 nm, 100 nm, and 150 nm are simulated in the 3-D FEA model. The applied force is  $1 \mu\text{N}$  force in this case and there is a cylindrical cavity in the silicon substrate. The curves show the penetration depth for different cylinder radii (Fig. 15.15). The left of the curves are the detectable regime for each tip radius. As expected, increasing the tip radius increases the penetration depth. When the ratios of the penetration depth for different tip radii are examined, it can be concluded that tip radius affects penetration depth with cube

**Fig. 15.14** The detection limit contours for the cylindrical defects in silicon substrate [14]

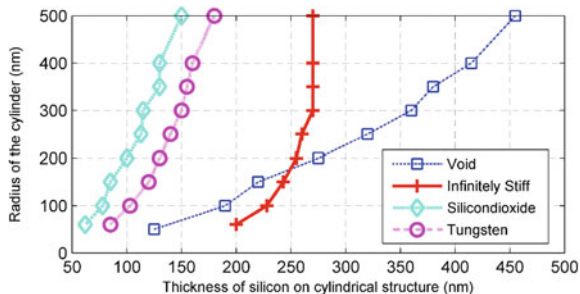
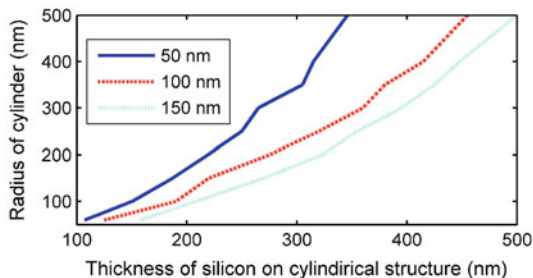


**Fig. 15.15** Penetration depth on a substrate with cylindrical cavity for 50 nm, 100 nm, and 150 nm radius tips



root. This result is consistent with the contact radius equation of the Hertzian model and CSA simulations on layered media.

Although layered media and finite size subsurface structures require more complex models than Hertzian contact theory, when examining the penetration depth it is possible to extrapolate data points by using contact radius equation (Eq. 15.1). One can either use the models for the desired material combination or use the data shown in this chapter and apply it for the desired force and tip radius combination in order to determine whether a subsurface structure can be detected or not.

The lateral resolution of an AFM scan is defined by the contact radius. When it comes to resolution in subsurface imaging, a more complicated analysis is needed. As an example, in the following figure (Fig. 15.16), two cylindrical cavities with 300 nm radius are placed at 200 nm depth in a silicon substrate. The contact stiffness measurement on this substrate is simulated by 3-D FEA mode for 1  $\mu$ N force and 100 nm tip radius. In order to analyze the lateral resolution of subsurface imaging, the distance between the centers of the cylinders is assigned as 800 nm, 1  $\mu$ m, and 1.2  $\mu$ m. The lateral resolution of subsurface imaging is the distance at which the contact stiffness image can resolve each structure independently. With that definition, when the distance between cylinders is 800 nm, the center shows a contact stiffness change of 13 N/m. This value is higher than  $\Delta k_{\min}$  that we had assumed earlier in this section, therefore these two structures can be resolved. Similarly, for the distances of 1  $\mu$ m and higher, the stiffness changes are also larger than  $\Delta k_{\min}$  and these structures are resolvable. Therefore, for this sample configuration, there should be at least 800 nm distance between the centers of the cylinders so that they can be

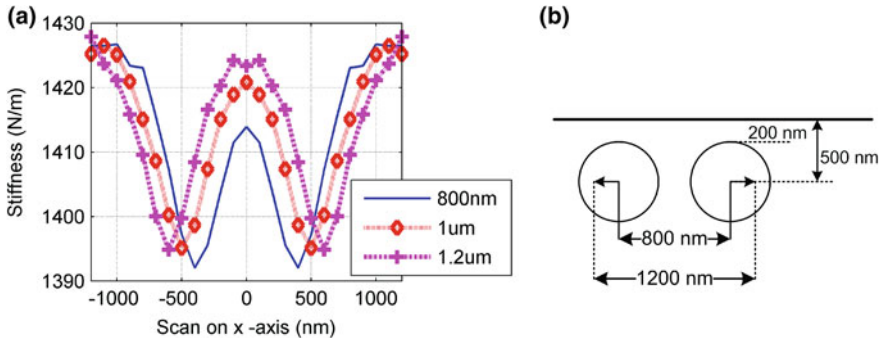


**Fig. 15.16** **a** Contact stiffness scan on two cylindrical cavities of 300 nm radius. **b** Schematic of the simulated sample

imaged at this particular depth. For different types of subsurface structures a similar analysis based on 3-D FEA can be performed.

## 15.5 Conclusion

Ultrasonic AFM provides a means for subsurface imaging at the nanoscale through contact stiffness measurements. Analysis methods that can simulate contact stiffness variations with different types of subsurface structures are essential for quantitative interpretation of the ultrasonic AFM measurements and images. Wave propagation-based analytical models have been shown to be an effective method to evaluate several key parameters such as penetration depth for layered media with various material combinations and interface defects. For more complicated 2-D and 3-D subsurface structures, FEA methods have been developed and verified. When combined, this array of methods provide the toolbox necessary to guide ultrasonic AFM studies for quantitative non-destructive evaluation of a variety of subsurface structures well beyond the few examples discussed here.

This material is based upon work supported by the National Science Foundation under Grant No. 0725618.

## References

1. V.V. Tsukruk, Surface Nanomechanical Properties of Polymer Nanocomposite Layers. *Langmuir* **17**(21), 6715–6719 (2001)
2. G.G. Yaralioglu, Contact stiffness of layered materials for ultrasonic atomic force microscopy. *J. Appl. Phys.* **87**(10), 7491–7496 (2000)
3. U. Rabe, K. Janser, W. Arnold, Vibrations of free and surface-coupled atomic force microscope cantilevers: Theory and experiment. *Rev. Sci. Instrum.* **67**(9), 3281–3293 (1996)
4. U. Rabe et al., Quantitative determination of contact stiffness using atomic force acoustic microscopy. *Ultrasonics* **38**(1–8), 430–437 (2000)
5. K.B. Crozier, Thin film characterization by atomic force microscopy at ultrasonic frequencies. *Appl. Phys. Lett.* **76**(14), 1950–1952 (2000)

6. A.F. Sarioglu, A. Atalar, F.L. Degertekin, Modeling the effect of subsurface interface defects on contact stiffness for ultrasonic atomic force microscopy. *Appl. Phys. Lett.* **84**, 5368 (2004)
7. M. Kopycinska-Muller et al., Elastic-property measurements of ultrathin films using atomic force acoustic microscopy. *Nanotechnology* **16**, 703 (2005)
8. D.C Hurley et al., Mapping substrate/film adhesion with contact-resonance-frequency atomic force microscopy. *Appl. Phys. Lett.* **89**(2), 021911 (2006)
9. K. Yamanaka, H. Ogiso, O. Kolosov, Ultrasonic force microscopy for nanometer resolution subsurface imaging. *Appl. Phys. Lett.* **64**(2), 178–180 (1994)
10. K.L. Johnson, *Contact Mechanics* (Cambridge University Press, Cambridge, 1985)
11. B. Bhushan, in *Nanotribology and Nanomechanics: An Introduction*, ed. by B. Bhushan (Springer, Berlin, 2005)
12. J.A. Turner et al., High-frequency response of atomic-force microscope cantilevers. *J. Appl. Phys.* **82**, 966 (1997)
13. U. Rabe, J. Turner, W. Arnold, Analysis of the high-frequency response of atomic force microscope cantilevers. *Appl. Phys. A Mater. Sci. Process.* **66**(7), S277 (1998)
14. Z. Parlak, F.L. Degertekin, Contact stiffness of finite size subsurface defects for atomic force microscopy: Three-dimensional finite element modeling and experimental verification. *J. Appl. Phys.* **103**(11), 114910–8 (2008)
15. T. Tsuji, K. Yamanaka, Observation by ultrasonic atomic force microscopy of reversible displacement of subsurface dislocations in highly oriented pyrolytic graphite. *Nanotechnology* **12**(3), 301–307 (2001)
16. D.C. Hurley, J.A. Turner, Humidity effects on the determination of elastic properties by atomic force acoustic microscopy. *J. Appl. Phys.* **95**, 2403 (2004)
17. D. Passeri, A. Bettucci, M. Rossi, Acoustics and atomic force microscopy for the mechanical characterization of thin films. *Anal. Bioanal. Chem.* **396**(8), 2769–2783 (2010)
18. S. Amelio et al., Measurements of elastic properties of ultra-thin diamond-like carbon coatings using atomic force acoustic microscopy. *Thin Solid Films* **392**(1), 75–84 (2001)
19. M. Prasad et al., Measurement of Young's modulus of clay minerals using atomic force acoustic microscopy. *Geophys. Res. Lett.* **29**, 1172 (2002)
20. T. Vanorio, M. Prasad, A. Nur, Elastic properties of dry clay mineral aggregates, suspensions and sandstones. *Geophys. J. Int.* **155**, 319 (2003)
21. D. Passeri et al., Atomic force acoustic microscopy characterization of nanostructured selenium-tin thin films. *Superlattices Microstruct.* **44**(4–5), 641–649 (2008)
22. K. Yamanaka, S. Nakano, Quantitative elasticity evaluation by contact resonance in an atomic force microscope. *Appl. Phys. a-Mater. Sci. Process.* **66**, S313–S317 (1998)
23. E. Kester et al., Measurement of mechanical properties of nanoscaled ferrites using atomic force microscopy at ultrasonic frequencies. *Nanostruct. Mater.* **12**, 779 (1999)
24. H. Cunfu, Subsurface defect of the SiO<sub>x</sub> film imaged by atomic force acoustic microscopy. *Opt. Lasers Eng.* **48**(11), 1108–1112 (2010)
25. J.P. Killgore et al., Quantitative subsurface contact resonance force microscopy of model polymer nanocomposites. *Nanotechnology* **22**(17), 175706 (2011)
26. U. Rabe, Imaging and measurement of local mechanical material properties by atomic force acoustic microscopy. *Surf. Interface Anal.* **33**(2), 65–70 (2002)
27. G.S. Batog et al., Calculation of the thicknesses and elastic properties of thin-film coatings using atomic-force acoustic microscopy data. *Tech. Phys.* **51**(8), 1084–1089 (2006)
28. G. Huajian, C. Cheng-Hsin, L. Jin, Elastic contact versus indentation modeling of multi-layered materials. *Int. J. Solid. Struct.* **29**(20), 2471–2492 (1992)
29. A. Kovalev et al., Nanomechanical probing of layered nanoscale polymer films with atomic force microscopy. *J. Mater. Res.* **19**(3), 716–728 (2003)
30. G.S. Kino, C.S. DeSilets, Design of slotted transducer arrays with matched backings. *Ultrason. Imaging* **1**(3), 189–209 (1979)
31. B. Honein et al., Wave Propagation in Piezoelectric Layered Media with Some Applications. *J. Intell. Mater. Syst. Struct.* **2**(4), 542–557 (1991)

32. H. Geisler et al., in *Elastic Mapping of Sub-surface Defects by Ultrasonic Force Microscopy: Limits of Depth Sensitivity*, in *Microscopy of Semiconducting Materials 2001*, ed. by A.G. Cullis, J.L. Hutchison (Iop Publishing, Bristol, 2001), pp. 527–530
33. G. Batog et al., Calculation of the thicknesses and elastic properties of thin-film coatings using atomic-force acoustic microscopy data. *Tech. Phys.* **51**(8), 1084–1089 (2006)



# Chapter 16

## Polymer Material Characterization by Acoustic Force Microscopy

Chad S. Korach

**Abstract** Acoustic force microscopy has been used for the measurement of the nanomechanical response in a number of materials and applications in materials science and engineering. The use of acoustic techniques to study polymeric materials has only recently drawn interest from the technique. Here, a review of recent accomplishments in the use of acoustic techniques to measure polymer nanomechanical properties will be discussed and the measurements of polymer fibers and bulk materials will be presented.

### 16.1 Introduction

Nanomechanical property measurement of materials with nanostructure and nanoscale dimensions provide a challenge to well-established techniques such as instrumented-indentation. This is primarily due to the depths and contact areas necessary for accurate property assessment that reduces the spatial resolution. A class of techniques based upon Scanning Probe Microscopy (SPM) which utilize analysis of Atomic Force Microscope (AFM) cantilever dynamics to determine the mechanical response of materials has evolved over the past 15–20 years. The techniques modulate samples or cantilevers and measure the cantilever response while probe–sample contact occurs; using contact modeling, quantitative properties can be accurately measured at the nanoscale and can be combined with high resolution rastering of sample surfaces to create property maps. Acoustic modulation has been used by Atomic Force Acoustic Microscopy (AFAM) [1], Contact Resonance-AFM [2], Ultrasonic-AFM [3], Ultrasonic Force Microscopy (UFM) [4], Resonant Difference-Frequency Atomic Force Ultrasonic Microscopy (RDF-AFUM) [5], Scanning Microdeforma-

---

C. S. Korach (✉)

Department of Mechanical Engineering, State University of New York at Stony Brook,  
Stony Brook, New York, NY 11794-2300, USA  
e-mail: chad.korach@stonybrook.edu

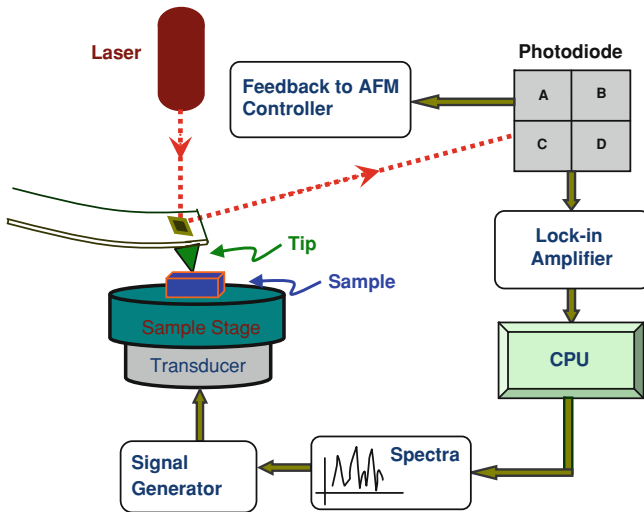


**Fig. 16.1** Schematic of an acoustic microscopy technique (AFAM) setup showing location of sample on an ultrasonic transducer (Reprinted with permission from Zhao et al. [17]. Copyright 2009 Elsevier Ltd.)

tion Microscopy (SMM) [6], Scanning Near-Field Ultrasound Holography (SNFUH) [7], and Torsional Harmonic-AFM [8] to measure quantitative nanomechanical properties. Each technique provides a means, either through the sample or the probe tip, to perturb the AFM cantilever which serves as the force transducer of the tip-sample contact stiffness.

A schematic of an acoustic technique (in this case AFAM) in Fig. 16.1 demonstrates the key components of the setup which utilizes ultrasonic frequency oscillations to excite an atomic force microscope cantilever when the tip is in contact with a sample placed on an ultrasonic transducer. The high-resolution piezo scanner of the AFM is utilized to gain precise spatial positioning, and the laser-photodiode system provides high-resolution determination of tip position and cantilever vibration modes and frequencies. Acoustic techniques can be utilized in a direct contact mode with a sample or by rastering the sample. The latter provides a stiffness map of the imaged surface. Depending on the technique, loads that are approximately two orders larger than typical AFM imaging loads are used so that a sufficient contact exists between the tip and sample and provides transduction of the oscillations induced by the ultrasonic transducer. Elastic modulus of the sample surface can be extracted from the resulting measured contact resonance frequency and using a vibration model for the cantilever is related to the tip-sample boundary condition, which is the contact stiffness [1]. Using an appropriate contact mechanics model, which assumes tip geometry, the modulus may be calculated from the contact stiffness. For polymers, both damping and plastic deformation are more likely to occur than when testing metallic or ceramic surfaces, and are necessary to consider. The technique has been used to study

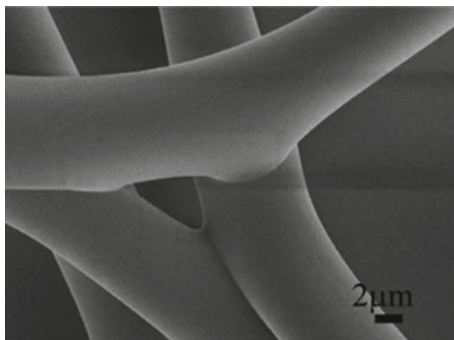
material systems with structure or features on the order of nanometers. For example, layered and thin-film polymers [9, 10], patterned wafers [11], thin-film magnetic ferrite grains [12], nanocrystalline Ni [13], and flexible electronic circuits [14], have all been measured with a form of acoustic force microscopy. These examples have been able to measure features on the order of nanometer resolution, which can be applied to measuring mechanical property variations in polymers and soft materials, such as epoxy matrix regions in composites and nanocomposites, subsurface imaging of polymer thin films, polymer nanofibers embedded in bicomponent fibers, and electrospun fibers of varying diameter. Here, these applications of acoustic microscopy techniques to heterogeneous polymeric materials will be presented, along with the effects of probe geometry and viscoelasticity.

## 16.2 Characterization of Electrospun Polymer Fibers

The measurement of mechanical properties of thin polymer fibers at the scale of the fiber diameter dimension is important for understanding surface and structural effects. The high resolution of the atomic force acoustic microscope provides the capability to measure mechanical properties at the fiber scale. Confinement of the semicrystalline polymers, poly-(ethylene-co-vinyl acetate) (PEVA) and low-density polyethylene (LDPE), produced by electrospinning has been observed to produce fibers with large protrusions, which have not been previously observed in fibers of comparable diameters produced by other methods [15]. Measurement of the mechanical properties of these fibers, by both AFAM and shear modulation force microscopy (SMFM) [16], a lateral modulation technique, indicates that the moduli of these fibers increases with decreasing diameter, with the onset at  $\sim 10 \mu\text{m}$ . Here, the measurement of the fiber stiffness will be detailed and presented.

The materials used for the fibers were PEVA and purchased from Dupont Co. with the commercial name Elvax 260 (PEVA260). Chloroform was purchased from Fisher Science. Electrospinning of PEVA polymer fibers was done by dissolving PEVA with different weight concentration in chloroform. The solutions were left at room temperature overnight and then heated on a hot plate until the solution completely dissolved. PEVA solutions were electrospun directly. In the electrospinning process, 3 mL of the solution was drawn into the 5 mL glass syringe (Hamilton Co., Reno, NV) that was then secured onto the graduated pump (KD Scientific, Holliston, MA), and the flow rate was set to be  $50 \mu\text{L}/\text{min}$ . The high-voltage power supply (Gamma High Voltage Research, Ormond Beach, FL) was set to 10 kV and attached to the needle. Because of the relatively poor solubility of PEVA in conventional solvent system at ambient temperature, a heating system was appended to the conventional electrospinning setup: (1) A flexible Kapton tape heater was attached the syringe and wrapped around the barrel and needle, in order to control solution temperature during electrospinning and the Taylor cone. The heating temperature was adjusted according to the melting point of different polymers. The solution temperature was maintained at  $78 \text{ }^\circ\text{C}$  for the PEVA260. (2) An infrared lamp was also used to maintain

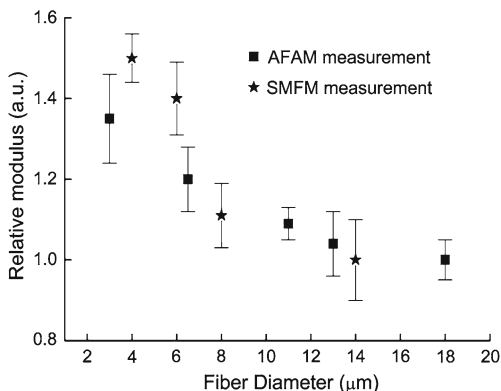
**Fig. 16.2** SEM images of electrospun PEVA260 fibers, showing smooth surface morphology (Reprinted with permission from Liu et al. [15]. Copyright 2011 American Chemical Society)



the elevated temperature between the spinner and collector. Electrospun fibers were collected on cleaned aluminum foils or silicon wafers as randomly oriented fiber mat on the aluminum target, which was horizontally placed 10 cm away from the tip of the needle. The electrospun fibers were then placed in a vacuum oven, at 25 °C overnight, in order to remove residual solvent. The morphologies of the fibers were imaged by using scanning electron microscopy (SEM, LEO 1550, LEO, Germany) with 2.5 kV acceleration voltage and at working distance of 2–4 cm. All fiber samples were sputter-coated with gold to improve the surface conductivity. Figure 16.2 shows an SEM image of the electrospun PEVA260 fiber morphology. From the figure, it is observed that the fiber surfaces are smooth and free of features.

Relative stiffness of the electrospun fibers were measured by the AFAM technique. A conventional AFM (NT-MDT SolverProM) was used with the sample mounted on an ultrasonic transducer which emits longitudinal acoustic waves [1]. The AFM cantilever is brought into contact with the sample, and the resulting vibrational frequencies in the cantilever were measured with the laser-photodiode system. The AFAM technique has successfully been used to measure the elastic modulus of thermoset epoxies [17]. The tip-sample contact stiffness is modeled as a linear spring, and using a cantilever beam model the equations of motion can be solved analytically if amplitudes are kept sufficiently small, yielding the contact stiffness as a function of vibrational frequency. An AFM cantilever (AIST fpN11S) with spring constant of 6.1 N/m, calibrated by the thermal tuning method [18], was used for all measurements. An indium film was used to calibrate the AFM cantilever and determine the tip radius of curvature. A normal load of 1 μN was applied by the cantilever to the tip-substrate interface through the cantilever bending calibration. Fibers were distributed randomly on a silicon substrate that was then mounted on an ultrasonic transducer with a small volume of honey which is allowed to set for at least 1 h. The built-in zoom microscope was used to identify fibers of interest and measure fiber widths. Small diameter fibers (<7 μm) were imaged directly with the AFM in a semi-contact (tapping) mode, and AFAM measurements were made at the apex of the fiber. When computing the elastic modulus from the measured contact stiffness, a linear elastic isotropic Hertzian contact model was utilized, which did not take into

**Fig. 16.3** Relative modulus of electrospun PEVA260 fibers measured by AFAM and SMFM methods as a function of fiber diameter. Increase of  $\sim 40\%$  is observed for fibers of  $< 10\ \mu\text{m}$ . (Reprinted with permission from Liu et al. [15]. Copyright 2011 American Chemical Society)



consideration any time-dependent effects such as viscoelastic or viscoplasticity. For larger diameter fibers, the AFM tip was located directly on the fiber and the surface imaged to determine the location of the apex. At least four AFAM measurements were performed on each fiber size. For comparison, measurements of the relative modulus of the PEVA fibers were also performed by a Veeco/DI Dimension 3000 AFM using the principle of the SMFM method [16]. The SMFM technique works by oscillating the  $x$ -piezo in a scanning probe microscope to generate a small displacement parallel to the surface. This is accomplished while a normal load of  $\sim 25\ \text{nN}$  is applied. The  $x$ -piezo amplitude is varied while the change in lateral cantilever position from the photodiode is recorded with a lock-in amplifier at 1,400 Hz. Qualitative comparison of the polymer surface stiffness can be made by the recorded cantilever lateral response amplitude for different surfaces. The technique has also successfully been applied to determine glass transition temperature ( $T_g$ ) of polymers [16]. When the drive signal amplitude was varied from 7.5 to 125 mV, which corresponded to an  $x$ -piezo displacement of 1.5–25 nm, the cantilever response was recorded to estimate the stiffness of the fibers. At least three fibrils were measured for the same diameter of each material. Each fiber was measured using at least three locations and three measurements were done at each location. Hence, the data represented an average of 27 measurements.

The relationship between the mechanical properties and fiber size can be compared by the AFM-based stiffness measurements. By keeping the ethylene content fixed, the effect of fiber diameter on the modulus can be compared. Figure 16.3 plots the relative stiffness values of PEVA260, which were measured by two separate, but complementary, techniques. The figure demonstrates clearly that the moduli increase by 40% as the fiber diameters decrease from 18 to 2  $\mu\text{m}$ . The moduli are relative to the largest fiber diameter tested, 14 and 18  $\mu\text{m}$ , for the SMFM and AFAM, respectively. A similar increase in modulus with decreasing fiber diameter was previously reported by Arinstein et al. [19] In their systems, the onset occurred for a diameter below 1  $\mu\text{m}$ , in contrast to the PEVA260 systems where the onset occurs for diameters less than 10  $\mu\text{m}$ . This observation seems to confirm their interpretation of the results as being

due to supramolecular structures internal to the fibers, rather than surface induced alignment, since it is very difficult to explain surface orientation propagating into the interior of the fibers for these larger distances. Since the AFAM technique is sensitive to the bulk response of the fiber, this establishes that the increased modulus occurs throughout the entire fiber. The AFM probe tip radius ( $\sim 50$  nm) is small compared with the fiber diameters ( $3\text{--}18\ \mu\text{m}$ ), where the maximum sub-surface stress will be  $< 100$  nm in depth. Thus, the contact stress field is contained within the fiber material and the substrate effect will be consistent from fiber to fiber size. The relative moduli obtained by AFAM and SMFM are plotted together in Fig. 16.3, where the results are in good agreement, indicating that the increased modulus with decreasing fiber diameter is characteristic of the fiber and are not simply a surface phenomenon.

Since polymeric chains have multiple degrees of freedom, confinement alone can impart special properties. In semicrystalline polymers, such as PEVA, confinement brought by electrospinning can change the melting point while at the same time improving the mechanical properties. The relationship between fiber diameter, which imparts a polymer orientation during the spinning process, and mechanical properties was successfully measured by the AFAM technique and shown to begin for fibers as large as  $10\ \mu\text{m}$ . This study demonstrates the viability of using AFAM on complex surfaces due to its high lateral resolution and ability to land on individual fibers.

### 16.3 Characterization of Bicomponent Polymer Fibers

Nanofibers spun from bicomponent extrusion are capable of unique structural and physical properties due to the unusual polymer flow in the confined elastic boundaries. Bicomponent extrusion is capable of generating up to thousands of continuous nanofibers within a sacrificial material [20]. When the fibers are at diameter scales of  $10$  nm, unusual flow patterns occur resulting in increased strength due to crystallization kinetics and induced superdrawing. The velocity profile within the extrusion generates the unusual flow and creates variations in nanofiber stiffness within the bicomponent fiber. Due to the nanoscale feature size of the fibers and the difference in modulus between the nanofibers and sacrificial material, high-resolution techniques such as AFAM may be used to quantitatively assess differences in stiffness. AFAM images of the cross-section of a bicomponent fiber, of the Islands-on-the-Sea type, obtained using conjugated extrusion are shown in Fig. 16.4. The island domains are composed of polyamide and the sea matrix is composed of polyester. AFAM is able to detect minor differences in the storage modulus between the two soft materials with nanoscale resolution. The differences in the modulus of the island domains are attributed to differential cooling and enhanced drawing of the fibers during the spinning process.

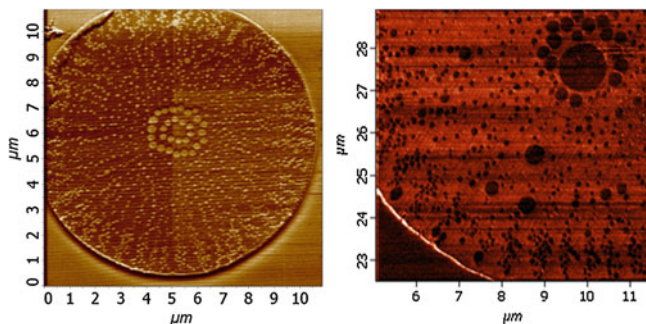


**Fig. 16.4** AFAM frequency images of bicomponent fibers. *Left* lighter regions represent higher stiffness, scale 1–6 kHz (*dark to light*). *Right* darker regions represent stiffer fibers, scale 372–387 kHz (*dark to light*). (Images courtesy of the Hinestroza Group, Cornell University, USA)

## 16.4 Characterization of Fiber-Reinforced Epoxy Composites

Composite materials have become ubiquitous in applications that demand high strength to weight ratios for improved efficiency and performance. Polymer matrix composites are multi-phase materials with fillers in the form of fibers, ribbons, or particulates with length scales ranging from millimeters to nanometers. The region surrounding the filler, the matrix interphase, is believed to control the fundamental load-transfer process and thereby bulk mechanical properties of composites. Depending on the size of the filler and the dispersion, the interphase region can range from tens of nanometers to microns. SPM-based techniques lend themselves to imaging and characterizing composite materials due to the high spatial resolution. Accurate mechanical property measurements at these scales prove challenging, and the AFAM technique has been demonstrated as a viable method to determine highly local mechanical properties. Zhao et al. [17] have successfully used AFAM to characterize carbon fiber-reinforced epoxy composite nanomechanical properties as a function of moisture exposure time, and the first to quantitatively evaluate the fiber–matrix interphase.

Fiber-reinforced polymer composites are used in infrastructure and other engineering structures applications, however, it is critical that composites prove their superior mechanical characteristics in terms of long-term durability when used in harsh and demanding environments. Moisture is readily absorbed by most polymer matrices and leads to changes in mechanical characteristics [21–23]. Research on moisture based degradation has been qualitatively shown to affect the properties of the interphase [24, 25], the region, which is on the order of sub-micrometers, between a fiber and matrix in composites, and controls the fundamental load-transfer. Hence, quantitative measurement of the mechanical properties at or near the fiber–matrix interphase is of critical importance. AFAM, a technique that retains the same excellent lateral resolution of a scanning probe microscope, but combines with an ultrasonic transducer to achieve quantitative mechanical property measurements

[1, 26], is used to characterize the epoxy interphase as a function of degradation time. This is achieved in part due to tip radius of curvature on the order of 10 nm and the ability of the piezo-stack scanner to achieve subnanometer lateral resolution.

Specimens were machined from vacuum bag fabricated  $[0]_8$  and  $[0/90]_{2S}$  laminates of IM7/997 carbon-fiber/epoxy composite. IM7 is a  $5\ \mu\text{m}$  diameter, Polyacrylonitrile (PAN)-based carbon fiber, while 997 is a  $177^\circ\text{C}$  ( $350^\circ\text{F}$ ) curing, thermoplastic modified, toughened epoxy resin with a proprietary formulation. All specimens were preconditioned in a desiccator at ambient temperature and 10% relative humidity for 1–2 weeks, and a diamond saw was used to cut samples in order to mount them onto the AFAM stage for testing. Due to the low roughness requirement to obtain results with AFAM, samples underwent metallographic polishing steps with 3, 1, and  $0.05\ \mu\text{m}$  particles. Boiling water degradation of composite samples took place in a deionized water filled boiling flask [27]. A silicone oil bath was used to provide indirect heat input and to generate an average heat distribution for the deionized water. Cold water was continuously running through a condenser to retain evaporate. During degradation, the temperature of the silicone oil was controlled within the range of  $130\text{--}135^\circ\text{C}$ . Samples for testing were placed into the degradation system all together, and two pieces were taken out after every 24 h of exposure. Six conditions, which have been degraded for 0, 24, 48, 72, 96, and 120 h, were tested with AFAM.

AFAM is performed by insonifying a sample mounted on an ultrasonic transducer that emits longitudinal acoustic waves [1], in conjunction with an AFM. An AFM cantilever is modeled as a clamped beam with a distributed mass that can vibrate in different modes, such as flexural, torsional, and extensional. Closed form solutions of the equations of motion have been used [28–30] in flexural and torsional vibration modes for analysis of the free vibrations. If the beam is fixed at any length  $L_1$  and coupled to a surface through a linear spring with stiffness  $k^*$ , the altered boundary conditions representing the forces due to tip–sample contact, the equations of motion can be solved analytically using a simplified beam contact model, if amplitudes are kept sufficiently small. For larger amplitudes, a nonlinear representation of the surface forces would be necessary [31]. A representative characteristic equation for the modal flexural stiffness is given as:

$$\begin{aligned} & \frac{k^*}{k_c} \left[ -(\cosh k_n L_1 \sin k_n L_1 - \sinh k_n L_1 \cos k_n L_1) (1 + \cos k_n L' \cosh k_n L') \right. \\ & \quad \left. + (\cosh k_n L' \sin k_n L' - \sinh k_n L' \cos k_n L') (1 - \cos k_n L \cosh k_n L) \right] \\ & = 2 \frac{(k_n L_1)^3}{3} (1 + \cos k_n L \cosh k_n L) \end{aligned} \quad (16.1)$$

where  $k^*$  is the tip–sample contact stiffness,  $L$  is the total cantilever length,  $L_1$  is the tip position along the cantilever, and  $L' = L - L_1$ . The wave number,  $k_n$ , is given by (16.2),



$$k_n = c_c \sqrt{f_n} \quad (16.2)$$

$$c_c^2 = \sqrt{\frac{48\pi^2 \rho}{b^2 E_i}} \quad (16.3)$$

$$k_c = \frac{E_i b^3 a}{4L_1^3} \quad (16.4)$$

where  $f_n$  are the vibration frequencies ( $n = 1, 2, \dots$ ),  $c_c$  is a characteristic cantilever constant,  $k_c$  is the cantilever spring constant,  $E_i (= 169 \text{ GPa})$  is the modulus of the cantilever material (silicon),  $\rho$  is the mass density of the cantilever material,  $a$  is the cantilever width, and  $b$  is the cantilever height. Typical values of cantilever spring constants used in the AFAM measurements are larger than used for contact imaging, allowing higher normal loads to be applied to the contact interface while retaining small cantilever deflections. If smaller  $k_c$  values are used, the adhesive interaction forces between the AFM tip and the sample surface are on the same order or larger than the contact forces applied by the cantilever. Viscous damping and lateral forces can be added into the theoretical model [28] though their influence on  $k^*$  is small compared with the normal forces and errors generated by tip geometry and position [32]. The resonance frequencies are sensitive to the applied normal loads and increase with applied load due to a stiffer contact created between the tip and sample, though are stable within a certain range of loads.

A Hertzian contact model provides the elastic modulus of the sample surface, after obtaining the contact stiffness. In the 3D Hertz analysis [33], the contact is assumed to be a parabolic indenter in contact with a flat surface. The indenter tip and the surface have elastic modulus of  $E_i$  and  $E_s$ , and Poisson's ratios of  $\nu_i (= 0.33)$  and  $\nu_s (= 0.36)$ , where  $i$  and  $s$  represent the indenter and the surface, respectively. For a statically applied force,  $F_c = k_c \times \Delta z$ , where  $\Delta z$  is the cantilever deflection. In these experiments the tip-sample forces  $F_c$  are sufficiently large to overcome surface interaction forces to ensure that the elastic contact forces are the main contribution to the analysis. For small deflections, the radius of contact,  $a_c$ , and the effective elastic modulus,  $E^*$ , are given as,

$$a_c = \sqrt[3]{\frac{3F_c R}{4E^*}} \quad (16.5)$$

$$\frac{1}{E^*} = \frac{1 - \nu_s^2}{E_s} + \frac{1 - \nu_i^2}{E_i} \quad (16.6)$$

where  $R$  is the radius of curvature of the indenter tip.

Using (16.5) and the mutual approach between surfaces,  $\delta = \frac{a^2}{R}$ , the contact stiffness can be represented by,

$$k^* = \sqrt[3]{6E^*2RF_c} \quad (16.7)$$

and relates the contact stiffness  $k^*$  to the sample surface elastic modulus ( $E_s$ ), and is a function of the applied contact force and the radius of curvature of the indenter tip. The analysis makes the assumption of an isotropic, linear elastic material locally. Viscoelastic effects will cause an increase in contact depth over time; the effect was minimized in the experiment by allowing the tip to contact the sample for  $\sim 1$  min prior to beginning the test, which was found to have a constant depth displacement as measured by the z-piezo and cantilever deflection. Compensation for viscoplastic effects due to yielding of the epoxy at the high contact pressures present have been attempted using a plastic core–shell contact model to estimate the contact stiffness [34].

Cantilever geometry ( $L'$ ) was measured by combination of scanning electron and optical microscopy. Tip radius of curvature is typically in the range of 10–100 nm, and was checked for accuracy during experiments using a polished silica sample [28]. Initial topography scanning to locate matrix regions for testing was performed at low applied loads, making radius of curvature a consistent value throughout all documented experiments.

The cantilever spring constant ( $k_c$ ) measurement is of essential importance, since as (16.7) shows, contact force  $F_c$  is the only unknown parameter that relates contact stiffness,  $k^*$ , and the reduced elastic modulus,  $E^*$ . Although AFM cantilever manufacturers provide a typical range for  $k_c$ , for accurate nanomechanical results the direct calibration of the spring constant was determined by the thermal turning method [18].

The ratio of  $k^*/k_c$  guides selection of the appropriate cantilever to provide the best sensitivity. Since composites contain two or more materials of different stiffness ( $E_{\text{fiber}} \sim 275$  GPa;  $E_{\text{epoxy}} \sim 4.14$  GPa [35]), to obtain correct results each material should be tested with a cantilever of an appropriate spring constant. Incorrect cantilever selection can lead to erroneous evaluation of AFAM results, due to contact stiffness ( $k^*$ ) of tip–material pairs which are out of range. Equation (16.1) can be rewritten as,

$$\begin{aligned} k^*/k_c = & (1 + \cos(L' C_C \sqrt{(f_n)}) \cosh(L' C_C \sqrt{(f_n)})) / \\ & (\sinh(L' C_C \sqrt{(f_n)}) \cos(L' C_C \sqrt{(f_n)}) \\ & - \sin(L' C_C \sqrt{(f_n)}) \cosh(L' C_C \sqrt{(f_n)})) \\ & \cdot (L' C_C \sqrt{(f_n)})^3 / 3. \end{aligned} \quad (16.8)$$

By evaluating (16.8), it is found that only some frequency ranges are possible for the contact stiffness, since physically it is a positive value. Also,  $k^*$  has singularities at the contact resonance frequencies, which could lead to sensitivity problems in calculating the sample elastic modulus,  $E_s$ . This implies that for a specific sample, cantilevers should be chosen with caution to achieve accurate results. Due to the large normal loads needed for stable results using AFAM, single point testing has been performed for all the quantitative measurements so as not to increase the tip radius of curvature significantly by high load scanning. Cantilevers with lower spring

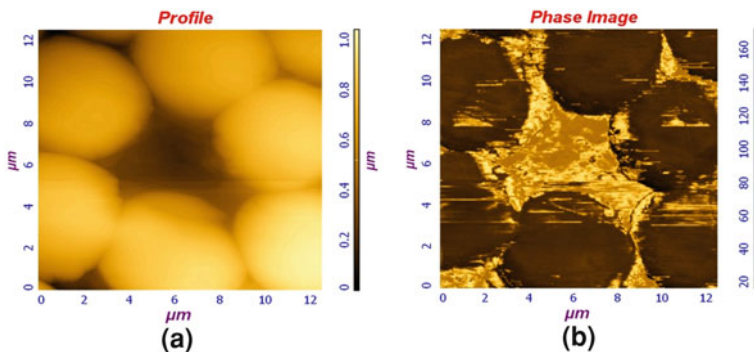


**Fig. 16.5** AFAM scan of a fiber-reinforced composite surface at 1123.509 KHz, **a** surface topography image, **b** AFAM phase image. Location of AFAM point measurements is between the fibers. (Reprinted with permission from Zhao et al. [17]. Copyright 2009 Elsevier Ltd.)

constants,  $k_c = 6\text{N/m}$  were found suitable for testing the degraded epoxy matrix region.

AFAM measurements were performed in the epoxy matrix region near the fibers for the undegraded and degraded composites (Fig. 16.5). The matrix between the fibers in Fig. 16.5b shows variation between stiffer (lighter color), near the fibers, and compliant (darker color), in the center, material response. The low AFAM phase angle results on the fibers are not considered since they are out of the range of measurement for the cantilever. This is an important consideration, in that materials of large stiffness mismatch will not be capable of simultaneous quantitative AFAM measurements due to the large difference in  $k^*$ , and is an area of further research to develop methods to resolve this issue. For each exposure case two samples were used and five independent locations were measured and the data averaged. Locations were sought out that avoided fiber-debonding which was observed for degraded samples. Phase changes in the cantilever resonance frequency while in contact with the ultrasonically perturbed composite specimen were recorded.

Specimen perturbation ranged between frequencies of 1,100–2,300 kHz. Frequency results are used in (16.1)–(16.3) to determine the contact stiffness,  $k^*$ , which is used in (16.6) and (16.7) to determine the sample modulus. Measurements were made for samples exposed to the boiling water degradation at intervals of 1 day. The samples were allowed to sit at room temperature for 2 h prior to measurement, thus any moisture on the surface in contact with the probe would have evaporated at the scale of the experiment. Quantitative decrease in the epoxy matrix stiffness near the carbon fibers was found as a function of degradation exposure. As seen in Fig. 16.6, stiffness values leveled off at  $\sim 72\text{h}$  exposure. The observed decrease in stiffness is believed to be a contribution of moisture absorption into the polymer matrix as well as degradation of the polymer cross-links due to the temperature and humidity exposure. In addition, the sensitivity of the results was evaluated as a function of the applied tip load ( $F_c$ ). Figure 16.7 shows a consistent value of  $E_s$  versus the

**Fig. 16.6** Near-fiber epoxy matrix elastic modulus (GPa) versus boiling degradation period (hours) (Reprinted with permission from Zhao et al. [17]. Copyright 2009 Elsevier Ltd.)

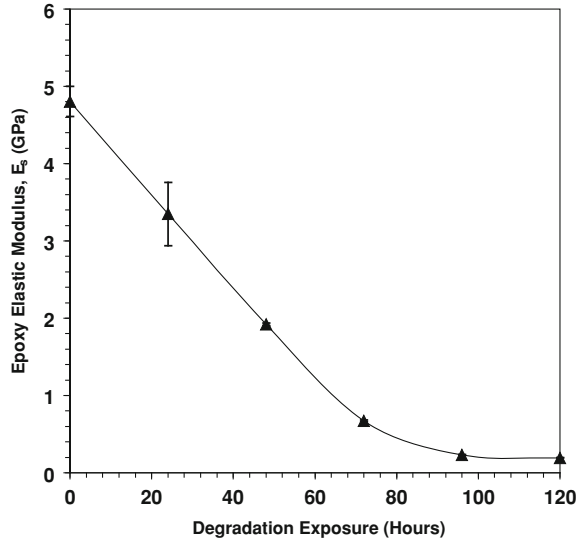
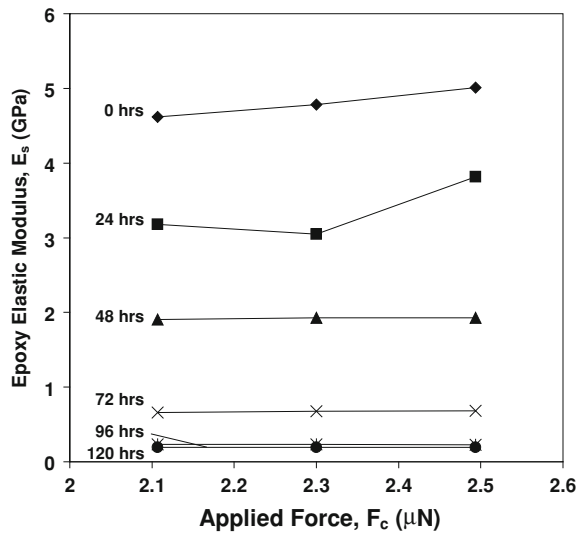


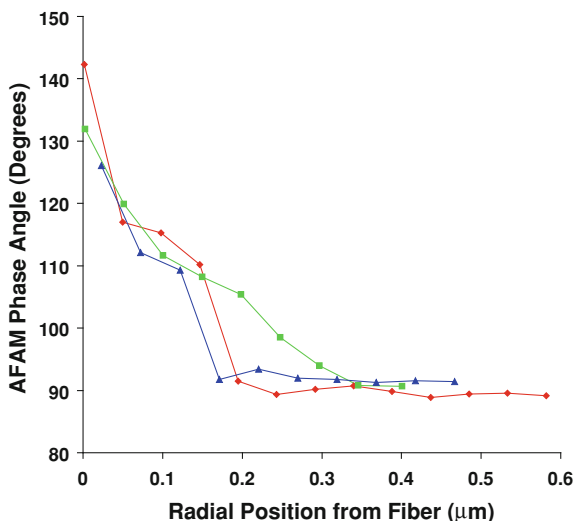
**Fig. 16.7** Epoxy elastic modulus versus applied normal force for 0–120 h boiling degradation exposure (Reprinted with permission from Zhao et al. [17]. Copyright 2009 Elsevier Ltd.)



applied normal load for undegraded and degraded samples indicating the stability of the reported measurements. These results are expected over a certain range, as long as the load is sufficient for contact, since the contact force is proportional to the load bearing contact area.

Spatial imaging of the matrix stiffness as a function of distance away from a fiber can be obtained utilizing AFAM due to the high spatial resolution of the technique. A measurement of the contact resonance frequencies of a degraded specimen matrix

**Fig. 16.8** Spatial variation from the fiber–matrix interface (*left*) toward the bulk matrix (*right*) in the AFAM phase angle signal, which represents a stiffer material for higher phase angle changes. Three discrete locations are plotted from around a fiber. Interphase is estimated from the results to be 200–300 nm in width (Reprinted with permission from Zhao et al. [17]. Copyright 2009 Elsevier Ltd.)



(see Fig. 16.8) from the edge of the fiber–matrix interface (left side of Fig. 16.8) demonstrates the decrease in phase angle moving away from the fiber. In this experiment, the AFAM phase signal relates to the change in stiffness of the matrix. The phase angle represents a change in the contact resonance frequency from a chosen datum, thus the region close to the fiber–matrix interface (left side of Fig. 16.8) is stiffer than the matrix further from the fiber–matrix interface. This is believed to be affected by a surface sizing that is present on the fibers from the manufacturer. From the spatial measurement results, the interphase is estimated to be  $\sim 200\text{--}300\text{ nm}$  in width, which corresponds to measurements by others using AFM phase imaging [36]. The results demonstrate that localized degradation of the epoxy matrix can be quantified using AFAM, and has direct implications on long-term performance of polymer matrix reinforced composites exposed to environmental conditions.

AFAM has been shown to be a viable technique for use in quantitative stiffness measurements of epoxy-based composites with fiber reinforcement. For hygrothermal degraded carbon-fiber-reinforced epoxy composites, the elastic modulus decreased from 4.8 GPa until reaching a constant after 72 h of exposure, and spatial measurements showed an interphase region with thickness of 200–300 nm.

## 16.5 Polymer Nanocomposite Imaging and Characterization

Composites made from nanoscale filler can provide different effects in the bulk thermal and mechanical properties when compared to traditional microcomposites. These effects have been attributed to the fact that nanofiller has a far larger interfacial surface area with the polymer matrix. Due to the small scale of the filler, SPM-

based techniques are widely used for local characterization of properties versus bulk techniques which would average out the small-scale filler. The use of AFAM on nanocomposites has been explored by Preghenella et al. [37], where elastic modulus distributions of epoxy-silica nanocomposites were obtained. The morphology of the nanocomposite fracture surfaces was related to the AFAM modulus distributions. Passeri et al. [38] used AFAM to evaluate dispersion of single-walled carbon nanotube (SWCNT) epoxy nanocomposites, and to provide quantitative mapping of the elastic modulus. Multiple techniques have been utilized to image the subsurface effect of nanoparticles in composites: CR-AFM has been used to map locations and depth of silica nanoparticles in polystyrene [39]; using the SNFUH technique, Shekhawat and Dravid imaged gold nanoparticles beneath a polymer film, as well as voids [7]; gold nanoparticles were also imaged beneath a polyimide thick film using RDF-AFUM [5]; and three-layer rubber nanoparticles used for toughening were imaged by UFM beneath the surface of injection molded Poly(methyl methacrylate) (PMMA) [40].

Fumed silica-epoxy nanocomposites of filler volume % ranging from 3 to 9 were fabricated and tested for bulk thermal-mechanical properties [37]. AFAM was used on fracture surfaces of the nanocomposites, where local elastic modulus distributions were calculated from the recorded contact resonance frequencies over multiple  $1 \times 1 \mu\text{m}$  regions. Filled samples were found to have broader distributions than unfilled, which accounted for the higher modulus silica content. Since particles with varying degrees of surface exposure would be present, a distribution occurs instead of a bimodal response. This was confirmed by SEM. For the highest volume loading of filler the modulus distribution was found to decrease for high moduli correlated to the fumed silica; this phenomena was shown to occur due to a lower degree of particle pullout from the matrix, indicating high interfacial interactions at the particle-matrix interphase, and correlated with the bulk mechanical response of the material which had the highest modulus and yield strength. The AFAM technique was capable of resolving local mechanical response to the bulk properties. Lastly, the study indicated higher than expected peak matrix modulus, which may be due to the limitations of a linear elastic contact model for the contact stiffness determination. These effects will be commented on in the next section. Carbon nanotubes (CNT) based composites take advantage of the remarkable physical properties of CNTs such as strength, toughness, and conductivity in polymer matrices. SWCNT composites of 1 % weight loading were fabricated for AFAM testing [38]. Raster scans of  $4 \times 4 \mu\text{m}$  were made on the surface and contact resonance frequency distributions obtained which were used to generate indentation modulus distributions. The inhomogeneous modulus distributions are attributed to CNT bundling, and provides the capability of the AFAM technique to study nanocomposite dispersion properties. Moreover, the results again indicated higher than expected elastic modulus values for the epoxy, which are believed to be due to increased adhesion forces. The results may also be affected by plastic deformation, which is a concern when performing AFAM on polymeric or soft materials. The effects of accurate contact area determination for polymer AFAM will be discussed in the next section.

The ability to image distributions, spatial locations, and morphology of nanoparticles in the subsurface of polymer nanocomposites and thin films provides researchers

a greater understanding of the materials processing and location of particles within the material. For instance, localizations of nanoparticles near the surface may provide wear resistance in nanocomposite coatings. Although techniques such as SEM can provide high-resolution imaging, they cannot provide depth sensing into the material. Acoustic force microscopy techniques allow the combination of high lateral resolution with depth sensing capabilities, since the subsurface nanoparticles will alter the tip-sample contact stiffness. A number of researchers utilizing different acoustic microscopy techniques have shown evidence of imaging subsurface nanoparticles. Shekhawat and Dravid [7] established the technique of SNFUH to image nanoscale features below compliant surfaces [7]. SNFUH places sample substrates (here nanocomposites and thin polymer films) on an ultrasonic transducer as in most acoustic microscopy techniques, though additionally generates vibrations in the cantilever via a separate transducer. The interference produces a surface acoustic standing wave which is sensitive to variations in the specimen surface. Imaging of 15 nm diameter gold nanoparticles embedded to a depth of 500 nm in a polymer film were successfully made and distributions of nanoparticles determined. The technique was employed to measure integrity of polymer films on patterned Si wafer vias, where voids and film delaminations will cause open circuits and increased resistivity. Nanoscale sub-surface voids were imaged and have application to micro-electronic circuit evaluation and reliability. Cellular materials have similar compliance as to polymers, and the ability to use SNFUH on the early detection of malaria parasites within red blood cells was also established [7]. Malaria parasites within red blood cells were imaged after only 4 h of incubation and can provide an early-stage pathological assay to malaria. A similar technique to SNFUH is Resonant Difference-Frequency Atomic Force Ultrasonic Microscopy (RDF-AFUM) [5], which also employs a perturbation of the SPM cantilever as well as the sample, though enhances the oscillations at the contact resonance frequencies. A layer of gold nanoparticles (10–15 nm diameter) embedded in polyimide were imaged using RDF-AFUM to a remarkable depth of 7  $\mu\text{m}$ . The effect of the nanoparticles on the polyimide bulk properties was quantitatively measured to be 24 % higher than for neat polyimide. The result demonstrated the effective modulus increase due to the integration of the nanoparticles. The subsurface nanoparticle imaging also revealed changes in the RDF-AFUM phase in regions directly surrounding the particles, which the authors believed to be a crystalline phase (interphase) of the polymer.

Other studies of nanocomposites have focused on resolving the depth and orientations directly using acoustic microscopy techniques. Killgore et al. [39] mapped the planar locations and depth of 50 nm silica particles embedded in polystyrene (PS) of varying thickness ranging from 30 to 160 nm using CR-AFM [39]. They were successful in determining variations in contact stiffness related to particle depth. Their study used the Finite Element Method (FEM) modeling of an elastic, isotropic axisymmetric contact between the probe tip and PS to compute the embedded nanoparticle effect on contact stiffness, and compared with their experiments. Although, in practice the authors found it necessary to utilize multiple scans at different loads to differentiate differences in particle depth due to contact stiffness variations. The morphological changes in rubber nanoparticles embedded in

injection molded PMMA has been undertaken using UFM [40], where three-layer rubber particles of  $\sim 300$  nm in diameter were observed after the bulk material was mechanically tested. The study found that UFM could image the direction and the elongation of the particles within the PMMA. Additionally, the core-shell structure of the hardening particles was able to be resolved with UFM. Particle orientation was observed to coincide with the melt flow direction of the PMMA in the material skin (surface region), and demonstrates the use of UFM to link processing conditions to nanoparticle morphology that is not observable by the SEM.

The use of acoustic microscopy techniques to study dispersions in nanocomposites has been demonstrated for SWCNTs, and fumed silica, gold, and rubber nanoparticles, as well as nano-voids in polymers and malaria parasites within cells. Successful correlation between the local elastic nanomechanical properties of the nanocomposites and the bulk properties were achieved, as well as measurements of morphological changes and depth dependency, demonstrating the capabilities of acoustic microscopy techniques in relating quantitative microstructural results to bulk material response, though work is still needed in determining accurate quantitative values.

## 16.6 Characterization of Polymer Films and Surfaces

Polymer films and surfaces have application in the areas of microelectronics, flexible electronics, solid lubricants for wear and friction reduction, and biological systems and tissue substrates. The films can be formed through spin-casting or direct deposition onto substrates, and may be found at thicknesses of only 10–100 nm up to thick films on the order of tens of micrometers. Due to the fact in many applications the films are typically deposited on stiffer substrates, the detection and imaging of subsurface defects is an important area of research [7, 14, 41]. The high-resolution capabilities of acoustic force microscopy techniques (SMM and UAFM) allows precise observations of such irregularities. The ability to measure film thickness accurately and non-destructively can also be achieved by these techniques [10], as demonstrated by Phase Sensitive Acoustic Microscopy (PSAM). Differences in the polymer film materials and morphology have also been demonstrated using UFM [42], Scanning Acoustic Microscopy (SAM) [9], and PSAM [10]; as well as quantitative stiffness assessment of films using SMM [6] and TH-AFM [43].

Films of polymer used on stiff substrates for protection or electrical insulation are prone to adhesive failure due to thermal and mechanical cycling. Critical locations are typically along high aspect ratio features which present a sharp singularity in the interface between film and substrate. To study the subsurface defects which may arise due to the delamination in the films a technique such as acoustic microscopy is needed, since typical optical or electron microscopes will only image the near surface of the material. Multiple researchers have been able to demonstrate the usefulness of acoustic force microscopy in the non-destructive detection of voids and delaminations below polymer film surfaces [7, 14, 41]. Vairac et al. [41] used SMM to detect silicon



gratings buried beneath SU8 films of 15  $\mu\text{m}$  thickness [6]. SMM is a mesoscopic-scale technique, and takes advantage of the large probe size to render accurate control of probe tip geometry, and to insure negligible interfacial forces. Although these attributes limit the possible imageable feature sizes, the authors observed that SMM was sensitive to substrates below polymer films. In a similar study, using UAFM, defect detection was performed on flexible electronic circuits which may be prone to delamination defects [14]. A Cu substrate was covered with a 25  $\mu\text{m}$  thick polyimide film, which has application to hard disk drive flexible circuits. Nalladega et al. [14] raster scanned the surface and imaged nanometer-scale defects between the copper and polymer covering film with UAFM, but topography scans of the same region with AFM did not show any defects. The study demonstrated the effectiveness of using UAFM as a quality control technique for flexible circuit defect detection, which otherwise would show no defects on the surface.

Paper surface coatings containing a combination of latex and kaolin have been mapped for adhesion and stiffness properties using TH-AFM to ascertain the thickness of the latex film between and on the surface of kaolin pigment [43]. The TH-AFM technique uses a unique cantilever design which contains a tip offset from the centerline that enhances the torsional response. The cantilever is vibrated at resonance and taps the surface causing torsional movement of the cantilever which is measured by the photo diode. No sample transducer is used with TH-AFM, simply a different cantilever is installed. Ihalainen et al. [43] made quantitative measurements of the elastic modulus for the latex coatings containing kaolin pigment, though found for the stiffer kaolin phase the modulus was underestimated. Quantitative mechanical characterization has also been made of PDMS bulk polymer films using SMM and compared with nanoindentation and dynamic mechanical analysis (DMA) for benchmarking [6]. The authors performed a detailed sensitivity analysis of SMM and determined an optimum sensitivity for each vibration mode, where sensitivity decreased with increasing mode number, but the highest sensitivity shifted to higher modes for stiffer materials. Thus, for compliant materials, the first mode was most sensitive. Quantitatively, the modulus of PDMS was determined by SMM and was found to be between 3.4 and 5.5 MPa. Compared with nanoindentation and DMA for a range of working frequencies, the SMM results showed consistency with the other techniques and potential as a continuity of results for higher frequencies.

Bulk film samples of polycarbonate (PC) have been studied by UFM for their nanoscale wear and fatigue properties [42]. PC specimens were cycled on the order of 10,000 cycles using a small stage beneath an AFM, and then topography imaging using AFM was performed and subsequently UFM of the surfaces. The surfaces of the fatigued PC were found to become increasingly rougher with higher fatigue cycles, and the contact stiffness of the surfaces decreased with fatigue cycles as measured by UFM. To observe the effect of fatigue on the nanoscale wear properties, using a higher load the fatigued surfaces were scratched with an AFM probe after different fatigue cycles. By using UFM on the worn regions, the contact stiffness was found to become more uniform for an increasing number of fatigue cycles. The results demonstrated by UFM that a different nanowear process was occurring for the fatigued specimens, and is important for the near-surface wear of PC components.

Stacked layers of polymer films to create a two-phase material were successfully imaged by Scanning Acoustic Microscopy (SAM) [9]. The two polymer phases created changes in the flexural and torsional vibrations of the cantilever as the sample was raster scanned, creating a distinct map of the material whereas topography showed a uniform height. Measurable changes in the frequency of the cantilever vibration response while scanning were made and can be used for quantitative assessment. Another two-phase material, a polymer blend (PS/PMMA) film was measured by an acoustic microscopy technique, PSAM, which uses no cantilever tip [10]. The technique places a liquid water coupling medium between a sapphire rod that acts as a focusing lens for the acoustic vibrations and the sample surface. The rod has an acoustic transducer attached at the opposite end driven at GHz frequencies. A piezo driven scanner allows submicron lateral resolution of the sample, and height variation of  $\sim 2.5$  nm can be achieved. PSAM has been employed to image structural properties and morphology of the PS/PMMA polymer blend films, and was demonstrated to measure film thicknesses on the order of 300 nm non-destructively.

Acoustic microscopy techniques have proven to be of great use in the areas of polymer films and in polymer surface characterization. Researchers have applied various acoustic microscopy techniques to polymeric materials and have been capable of imaging sub-surface defects beneath films, image different phases of mixed blend polymers, compute film thicknesses of polymer films non-destructively, identify nanoscale wear processes of polymer surfaces, and provide quantitative measurements of contact stiffness and elastic modulus of polymer films. The variety of material systems and techniques being used on polymers shows great promise in the use of acoustic techniques in the area of film characterization and for non-destructive evaluation for defects and film thickness.

## 16.7 Tip-Shape Models for Epoxy Characterization

The mechanical characteristics of the epoxy matrix found in filler-reinforced polymer composites are important for determining strength and performance. Locally, property variations in regions surrounding fillers can influence the overall macroscopic composite response to loading. Local nanomechanical stiffness of reinforced epoxy composites is investigated using AFAM. The effects of tip shape on the contact mechanics at the epoxy interface are found to influence the reported results significantly [44] and will be discussed in context of different tip models. The results have direct correlation to the effect of near-filler interphase regions and the long-term influence of environmental conditions on the polymer composites.

In polymer composites, the mechanical properties of the matrix surrounding the filler is critical to understand the composite performance. To measure this region, termed the interphase, which is on the scale of tens to hundreds of nanometers, a technique capable of providing high spatial resolution is needed. AFAM can determine quantitative mechanical properties [26, 28] and provides spatial resolution necessary for interphase measurements [17]. However, it has been shown for polymers when

using AFAM to measure elastic properties that the models utilized so far may be inadequate [38]. Hence, the study of geometry effects utilizing more appropriate contact mechanics are necessary to quantitatively determine the elastic modulus for polymers.

Quantitative determination of the elastic modulus by AFAM is shown to be influenced by a number of parameters, which are not fully understood [45, 46]. Passeri et al. [45] have studied the effects of blunted AFM tips and recommend the use of a flat punch model once a tip is used. Kopycinska-Müller et al. [46] investigated the effects of surface forces on the contact area, though for loads on the order of micronewtons the surface forces are a small fraction of the total applied load. Repeated use of AFM tips has been shown [45, 46] to alter the probe geometry significantly causing significant changes in the measured AFAM contact stiffness for subsequent tests. Changes in probe geometries were confirmed by SEM. To achieve accurate measurements with the technique it is an established necessity to perform quantitative analysis on reference materials with known mechanical properties. Reference materials with similar modulus to the sample materials are found to provide the most accurate results and are recommended. In this study [44], the contact stiffness is measured by three different AFAM probe geometries, designated as: *New*, *Flat*, and *Round* probes, for an Indium film and epoxy. Besides the Hertzian model, the AFAM probe tip geometry is modeled as a flat punch and a body of revolution model, which is proposed to better describe the actual tip geometry [34].

The reduced elastic modulus ( $E^*$ ) is related to the experimentally measured AFAM contact stiffness ( $k^*$ ) by,

$$E^* = k^*/2a \quad (16.9)$$

where the contact area is a circle with radius  $a$ , and  $E^*$  is calculated from (16.6). For a flat punch, the contact area remains constant regardless of applied normal load ( $F$ ). The Hertzian contact theory represents a spherical tip geometry contacting a flat surface, which has a contact area as a function of applied load, and is shown to follow the relation for  $k^*$  given in (16.7) [28].

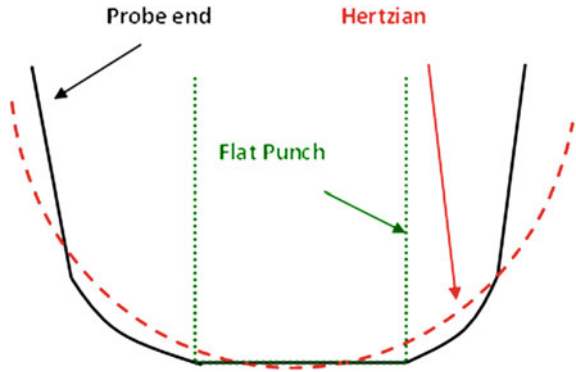
The punch and Hertz models represent two extremes of the actual probe end geometry, a flat and a sphere, respectively, but the probe end has been shown by SEM to be blunted in the center and rounded at the edges, schematically shown in Fig. 16.9. The actual geometry is better represented by a body of revolution model which allows higher order curvature and is in between the Hertzian and flat punch model geometries.

The proposed model is derived from a non-Hertzian surface contact relationship [33], where the tip end profile is defined as a power law,

$$h = \frac{1}{(2R)^{2n-1}} \cdot x^{2n}, \quad n \in 1, 2, \dots, n \quad (16.10)$$

and where,  $h$  and  $x$  are the depth and horizontal position of the tip end surface. The relationship between applied normal load and reduced elastic modulus for a power

**Fig. 16.9** Comparison of probe end geometry with flat punch and Hertzian geometry models (Reprinted with permission from Zhao et al. [44]. Copyright 2009 American Society of Mechanical Engineers)



law shape of order  $2n$  was developed by Steuermann (see [33] Chap. 5.3) and given as,

$$F_n = \frac{4E^* \cdot n \cdot a^{2n+1}}{(2n + 1) \cdot (2R)^{2n-1}} \cdot \frac{2 \cdot 4 \dots 2n}{1 \cdot 3 \dots (2n - 1)} \tag{16.11}$$

By taking  $n = 2$  and  $3$  (4th and 6th order power law shapes, respectively), (16.11) is rewritten as,

$$F_2 = \frac{8}{15} \cdot \frac{E^* a^5}{R^3} \quad \text{for } n = 2 \tag{16.12}$$

$$F_3 = \frac{6}{35} \cdot \frac{E^* a^7}{R^5} \quad \text{for } n = 3 \tag{16.13}$$

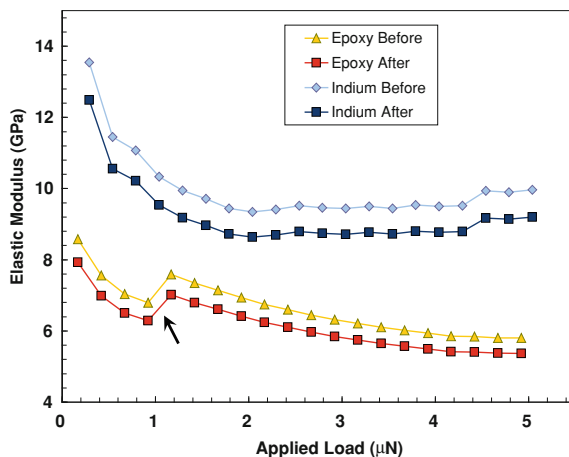
Combining (16.9) with (16.12) and (16.13), the measured contact stiffness can be related to the reduced modulus by,

$$E^* = \sqrt[4]{\frac{1}{60} \cdot \frac{k^{*5}}{R^3 F_n}} \quad \text{for } n = 2 \tag{16.14}$$

$$E^* = \frac{1}{2} \cdot \sqrt[6]{\frac{3}{35} \cdot \frac{k^{*7}}{R^5 F_n}} \quad \text{for } n = 3 \tag{16.15}$$

To determine the probe end geometry effects, three polysilicon ( $E_{Si} = 169$  GPa,  $\nu = 0.33$ ) AFM cantilevers with similar spring constant ( $k_c = 18\text{--}28$  N/m, determined by the thermal tuning method), but with distinctly different probe end geometries were used to perform quantitative measurements on Indium and Epon 862 epoxy. The known material properties of Indium ( $E_{In} = 12$  GPa,  $\nu = 0.3$ ) and the epoxy ( $E = 3\text{--}5$  GPa,  $\nu = 0.36$ ) are used to compare with the contact models. In the experiment, each probe measures both materials, in the sequence of Indium then epoxy, to a maximum load of  $5 \mu\text{N}$ . Probe end geometries are observed by SEM

**Fig. 16.10** Elastic modulus for Indium and Epon 862 samples analyzed using probe geometry measured before and after testing, using a body of revolution model ( $n = 2$ ) and the *round* probe. Probe geometry change location indicated by the arrow (Reprinted with permission from Zhao et al. [44]. Copyright 2009 American Society of Mechanical Engineers)



before and after the measurement. The probe micrographs are analyzed by digital imaging software, and 4th and 6th order power law curves are fit through a curve fitting algorithm to determine the radii of curvature.

The power law shaped body of revolution model is shown to have a good approximation of the real probe end geometry, and is best described as a *rounded punch* (see Fig. 16.9). Experiments showed that the probes which began with a large, flat end tended to become rounded after measurements.

Likewise, new AFM tips were found to blunt after usage. Both of these phenomena are attributed to the high local contact stress in the Si causing fracturing and damage of the probes at local stress concentrations, such as edges and apexes. As seen by others [45], the geometry variation from before and after AFAM measurements affects the quantitative results. Elastic modulus values are calculated for the measured contact stiffness values with (16.14) and (16.15). The location of the probe geometry change can be determined from contact stiffness and calculated elastic modulus values. The moment when significant probe geometry change occurs can be observed in Fig. 16.10 (indicated by arrow) and is believed to be caused by tip fracture at that test condition. Since the measured contact stiffness increases for an increase in contact area, the elastic modulus is overestimated since the model utilizes a smaller radius of curvature. Calculation of the elastic modulus with the before and after geometries leads to a shift in the result curves shown in Fig. 16.10. Since the Indium was measured prior to the fracture event, it is best represented by the before geometry, where modulus values are found to be larger and consistent with expected values ( $\sim 10\text{GPa}$ ). The epoxy is best represented by the post measurement geometry for values after the fracture event, leading to an elastic modulus value of  $\sim 5\text{GPa}$  at higher loads, which is consistent with measured bulk values. Prior to the fracture event, epoxy modulus values when analyzed with the pre-fracture geometry are more appropriate, where it is interesting to note that values before and after the fracture event are nearly continuous (see Fig. 16.10, loads of 1 and  $1.2\mu\text{N}$ ) when analyzed

with the pre- and post-fracture geometries, respectively. For the entire load range, the elastic modulus is expected to remain constant, and the body of revolution model provides a more consistent quantitative elastic modulus result than the Hertzian and flat punch models (not shown) which vary significantly with load, as expected. Similar results were obtained for all the probes tested. The application of nonlinear constitutive models and time-dependent material response to the analysis of contact resonance frequencies is an ongoing area of research. Yuya et al. [47] have modeled the viscoelastic response of polystyrene and polypropylene contact stiffness with a spring and dashpot model, combined with the quality (Q) factor of the cantilever contact modes. The model allows correct extraction of the damping coefficient for the polymers and shows an observed frequency dependence of the damping for both materials.

## 16.8 Conclusions

Polymers and soft materials are increasingly important in future applications and technology development. The ability to observe macromolecular behavior and microstructural features of polymeric materials and composites is paramount to new materials and application specific formulations. Acoustic force microscopy is a unique technique which combines the high spatial resolution of SPMs with the ability to quantitatively measure mechanical properties of materials. The application of acoustic microscopy techniques to polymer-based materials has been demonstrated for not only bulk solids, but also thin and thick polymer film surfaces, nanocomposites, and fibers of different geometries. The effects of probe geometries are an important aspect to proper measurements of polymers, though much work is still needed in the specific ability to combine nonlinear constitutive models to the analysis of contact response frequencies of materials. This should provide more accurate models of the mechanical properties and spatial mapping abilities. Although acoustic force microscopy techniques have proven to be a unique method for non-destructive evaluation of polymers that have undergone physical or chemical changes, or possess subsurface damage that is not visible using surface microscopy.

**Acknowledgments** The author is grateful for the support of the U.S. National Science Foundation award CMMI-0626025, and Drs. Yapa D.S. Rajapakse and Airan Perez of the U.S. Office of Naval Research for partially funding this work through grant #N0000141110816, and to Ms. Soshana Smith and Prof. Juan Hinestroza of Cornell University for the Islands-on-the-sea image.

## References

1. U. Rabe, S. Amelio, E. Kester, V. Scherer, S. Hirsekorn, W. Arnold, Quantitative determination of contact stiffness using atomic force acoustic microscopy. *Ultrasonics* **38**(1–8), 430–437 (2000)

2. G. Stan, R.F. Cook, Mapping the elastic properties of granular Au films by contact resonance atomic force microscopy. *Nanotechnology* **19**, 235701 (2008)
3. K. Yamanaka, S. Nakano, Ultrasonic atomic force microscopy with overtone excitation of cantilever. *Jpn. J. Appl. Phys.* **35**, 3787–3792 (1996)
4. K. Yamanaka, H. Ogiso, S. Nakano, Ultrasonic force microscopy for nanometer resolution subsurface imaging. *Appl. Phys. Lett.* **64**, 178–180 (1994)
5. S.A. Cantrell, J.H. Cantrell, P.T. Lillehei, Nanoscale subsurface imaging via resonant difference-frequency atomic force ultrasonic microscopy. *J. Appl. Phys.* **101**, 114324 (2007)
6. J. Le Rouzic, P. Vairac, B. Cretin, P. Delobelle, Sensitivity optimization of the scanning microdeformation microscope and application to mechanical characterization of soft materials. *Rev. Sci. Instrum.* **79**, 033707 (2008)
7. G.S. Shekhawat, V.P. Dravid, Nanoscale imaging of buried structures via scanning near-field ultrasound holography. *Science* **310**, 89–92 (2005)
8. O. Sahin, S. Magonov, C. Su, C.F. Quate, O. Solgaard, An atomic force microscope tip designed to measure time-varying nanomechanical forces. *Nat. Nanotechnol.* **2**, 507–514 (2007)
9. S. Hirsekorn, W. Arnold, High-resolution materials characterization by conventional and near-field acoustic microscopy. *Ultrasonics* **36**(1–5), 491–498 (1998)
10. W. Ngwa, W. Luo, A. Kamanyi, K.W. Fomba, W. Grill, Characterization of polymer thin films by phase-sensitive acoustic microscopy and atomic force microscopy: a comparative review. *J. Microsc.* **218**, 208–218 (2005)
11. U. Rabe, W. Arnold, Acoustic microscopy by atomic-force microscopy. *Appl. Phys. Lett.* **64**(12), 1493–1495 (1994)
12. E. Kester, U. Rabe, L. Presmanes, P. Tailhades, W. Arnold, Measurement of mechanical properties of nanoscaled ferrites using atomic force microscopy at ultrasonic frequencies. *Nanostruct. Mater.* **12**(5–8), 779–782 (1999)
13. D.C. Hurley, R.H. Geiss, M. Kopycinska-Muller, J. Muller, D.T. Read, J.E. Wright, N.M. Jennett, A.S. Maxwell, Anisotropic elastic properties of nanocrystalline nickel thin films. *J. Mater. Res.* **20**(5), 1186–1193 (2005)
14. V. Nalladega, S. Sathish, A.S. Brar, Characterization of defects in flexible circuits with ultrasonic atomic force microscopy. *Microelectr. Reliab.* **48**, 1683–1688 (2008)
15. Y. Liu, S. Chen, E. Zussman, C.S. Korach, W. Zhao, M.H. Rafailovich, Diameter-dependent modulus and melting point behavior in electrospun semi-crystalline polymer fibers. *Macromolecules* **44**(11), 4439–4444 (2011)
16. S. Ge, Y. Pu, W. Zhang, M. Rafailovich, J. Sokolov, C. Buenviaje, R. Buckmaster, R.M. Overney, *Phys. Rev. Lett.* **85**(11), 2340–2343 (2000)
17. W. Zhao, R.P. Singh, C.S. Korach, Near-fiber nanomechanical properties of environmentally degraded carbon fiber epoxy composites. *Compos. Part A* **40**, 675–678 (2009)
18. J.L. Hutter, J. Bechhoefer, Calibration of atomic-force microscope tips. *Rev. Sci. Instrum.* **64**(7), 1868–1873 (1993)
19. A. Arinstein, M. Burman, O. Gendelman, E. Zussman, *Nat. Nanotechnol.* **2**(1), 59–62 (2007)
20. T. Kikutani, J. Radhakrishnan, S. Arikawa, A. Takaku, N. Okui, X. Jin, F. Niwa, Y. Kudo, Highspeed melt spinning of bicomponent fibers: mechanism of fiber structure development in poly(ethylene terephthalate)/polypropylene system. *J. Appl. Polym. Sci.* **62**, 1913–1924 (1996)
21. K. Liao, C.R. Shultheisz, D.L. Hunston, L.K. Brinson, Long-term durability of fiber-reinforced polymer-matrix composite materials for infrastructure applications: a review. *SAMPE J. Adv. Mater.* **30**(4), 3–40 (1998)
22. F.R. Jones, Durability of Reinforced Plastics in Liquid Environments. in *Reinforced Plastics Durability*, ed. by G. Pritchard (Woodhead Publishing Company, Cambridge, 1999), pp. 70–110
23. G.S. Springer, *Environmental Effects on Composite Materials* (Technomic, Lancaster, 1984)
24. A. Hodzic, Z.H. Stachurski, J.K. Kim, Nano-indentation of polymer-glass interfaces Part I. Experimental and mechanical analysis. *Polymer* **41**(18), 6895–6905 (2000)
25. A. Hodzic, J.K. Kim, A.E. Lowe, Z.H. Stachurski, The effects of water aging on the interphase region and interlaminar fracture toughness in polymer-glass composites. *Compos. Sci. Technol.* **64**(13–14), 2185–2195 (2004)

26. D.C. Hurley, K. Shen, N.M. Jennett, J.A. Turner, Atomic force acoustic microscopy methods to determine thin-film elastic properties. *J. Appl. Phys.* **94**(4), 2347–2354 (2003)
27. L. Holliday, *Composite Materials* (Elsevier, Amsterdam, 1966)
28. U. Rabe, K. Janser, W. Arnold, Vibrations of free and surface-coupled atomic force microscope cantilevers: theory and experiment. *Rev. Sci. Instrum.* **67**(9), 3281–3293 (1996)
29. O.B. Wright, N. Nishiguchi, Vibrational dynamics of force microscopy: effect of tip dimensions. *Appl. Phys. Lett.* **71**(5), 626–628 (1997)
30. K. Yamanaka, S. Nakano, Quantitative elasticity evaluation by contact resonance in an atomic force microscope. *Appl. Phys. A Mater. Sci. Process.* **66**, S313–S317 (1998)
31. S. Hirsekorn, U. Rabe, W. Arnold, Theoretical description of the transfer of vibrations from a sample to the cantilever of an atomic force microscope. *Nanotechnology* **8**(2), 57–66 (1997)
32. U. Rabe, M. Kopycinska, S. Hirsekorn, J.M. Saldana, G.A. Schneider, W. Arnold, High-resolution characterization of piezoelectric ceramics by ultrasonic scanning force microscopy techniques. *J. Phys. D Appl. Phys.* **35**(20), 2621–2635 (2002)
33. K.L. Johnson, *Contact Mechanics* (Cambridge University Press, Cambridge, 1985)
34. W. Zhao, Quantitative measurement of nanomechanical properties in composite materials. Doctoral Dissertation, (State University of New York at Stony Brook, 2010)
35. P. Vaddadi, T. Nakamura, R.P. Singh, Inverse analysis to determine hygrothermal properties in fiber reinforced composites. *J. Compos. Mater.* **41**, 309–334 (2007)
36. S.-L. Gao, E. Mäder, Characterisation of interphase nanoscale property variations in glass fiber reinforced polypropylene and epoxy resin composites. *Compos. Part A* **33**, 559–576 (2002)
37. M. Preghenella, A. Pegoretti, C. Migliaresi, Atomic force acoustic microscopy analysis of epoxy-silica nanocomposites. *Polym. Test.* **25**, 443–451 (2006)
38. D. Passeri, M. Rossi, A. Alippi, A. Bettucci, M.L. Terranova, E. Tamburri, F. Toschi, Characterization of epoxy/single-walled carbon nanotubes composite samples via atomic force acoustic microscopy. *Physica E* **40**, 2419–2424 (2008)
39. J.P. Killgore, J.Y. Kelly, C.M. Stafford, M.J. Fasolka, D.C. Hurley, Quantitative subsurface contact resonance force microscopy of model polymer nanocomposites. *Nanotechnology* **22**, 175706 (2011)
40. K. Porfyarakis, H.E. Assender, I.M. Robinson, The interrelationship between processing conditions, microstructure and mechanical properties for injection moulded rubber-toughened poly(methyl methacrylate) (RTPMMA) samples. *Polymer* **43**, 4769–4781 (2002)
41. P. Vairac, B. Cretin, R. Boucenna, Imaging contrast in SMM: the mechanical approaches. *J. Phys. Conf. Ser.* **61**, 209–213 (2007)
42. F. Iwata, Y. Suzuki, Y. Moriki, S. Koike, A. Sasaki, Nanowearing property of a fatigued polycarbonate surface studied by atomic force microscopy. *J. Vac. Sci. Tech. B* **19**(3), 666–670 (2001)
43. P. Ihalainen, J. Järnström, A. Määttänen, J. Peltonen, Nano-scale mapping of mechanical and chemical surface properties of pigment coated surfaces by torsional harmonic atomic force microscopy. *Colloids Surf. A Physiochem. Eng. Aspects* **373**, 138–144 (2011)
44. W. Zhao, C.S. Korach, Measurement of epoxy stiffness by atomic force acoustic microscopy. in *Proceedings ASME 2009 International Mechanical Engineering Congress and Exposition*, vol. 12, Micro and Nano Systems, Part A and B, pp. 85–87 (2009)
45. D. Passeri, A. Bettucci, M. Germano, M. Rossi, A. Alippi, S. Orlanducci, M.L. Terranova, M. Ciavarella, Effect of tip geometry on local indentation modulus measurement via atomic force acoustic microscopy technique. *Rev. Sci. Instrum.* **76**, 093904 (2005)
46. M. Kopycinska-Müller, R.H. Geiss, D.C. Hurley, Contact mechanics and tip-shape in AFM-based nanomechanical measurements. *Ultramicroscopy* **106**, 466–474 (2006)
47. P.A. Yuya, D.C. Hurley, J.A. Turner, Relationship between Q-factor and sample damping for contact resonance atomic force microscope measurement of viscoelastic properties. *J. Appl. Phys.* **109**, 113528 (2011)



# Chapter 17

## Application of Acoustic Techniques for Characterization of Biological Samples

Bernhard R. Tittmann and Anne Ebert

**Abstract** The atomic force microscope (AFM) is emerging as a powerful tool in cell biology. Originally developed for high-resolution imaging purposes, the AFM also has unique capabilities as a nano-indenter to probe the dynamic viscoelastic material properties of living cells in culture. In particular, AFM elastography combines imaging and indentation modalities to map the spatial distribution of cell mechanical properties, which in turn reflect the structure and function of the underlying cytoskeleton. Such measurements have contributed to our understanding of cell mechanics and cell biology and appear to be sensitive to the presence of disease in individual cells. Examples of applications and considerations on the effective capability of ultrasonic AFM techniques on biological samples (both mammalian and plant) are reported in this chapter. Included in the discussion is scanning near-field ultrasound holography an acoustic technique which has been used to image structure and in particular nanoparticles inside cells. For illustration an example that is discussed in some detail is a technique for rapid in vitro single-cell elastography. The technique is based on atomic force acoustic microscopy (AFAM) but (1) requires only a few minutes of scan time, (2) can be used on live cells briefly removed from most of the nutrient fluid, (3) does negligible harm or damage to the cell, (4) provides semi-quantitative information on the distribution of modulus across the cell, and (5) yields data with 1–10 nm resolution. The technique is shown to enable rapid assessment of physical/biochemical signals on the cell modulus and contributes to current understanding of cell mechanics.

---

B. R. Tittmann (✉) · A. Ebert

Department of Engineering Science and Mechanics, The Pennsylvania State University,  
212 Earth-Engineering Sciences Building, University Park, PA 16802, USA  
e-mail: brt4@psu.edu

## 17.1 Survey of State of the Art

The study of biological samples is one of the most attractive innovative fields of application of ultrasonic based atomic force microscope (AFM) techniques. Examples of application and considerations on the effective capability of ultrasonic AFM techniques on biological sample are reported in this chapter.

The AFM is emerging as a powerful tool in cell biology. As pointed out by Costa [1], originally developed for high-resolution imaging purposes, the AFM also has unique capabilities as a nano-indenter to probe the dynamic viscoelastic material properties of living cells in culture. In particular, AFM elastography combines imaging and indentation modalities to map the spatial distribution of cell mechanical properties, which in turn reflect the structure and function of the underlying cytoskeleton. A case in point is the work of Elkin et al. [2] on the synopsis of mechanical heterogeneities of the rat hippocampus measured by atomic force microscopic indentation. Such measurements have contributed to our understanding of cell mechanics and cell biology and appear to be sensitive to the presence of disease in individual cells.

AFM has many valuable modifications oriented toward specific applications and two of these are ultrasonic atomic force microscopy (U-AFM) and atomic force acoustic microscopy (AFAM). These are well-established techniques primarily used to map the elastic modulus distribution of hard surfaces having variations in composition. This is accomplished by applying an ultrasonic frequency to either the tip (AFAM) or sample (U-AFM) while monitoring the cantilever response to sample stiffness [3, 4]. Typical modes of operation have the probe tip in contact, non-contact, or tapping (intermittent contact). The images are obtained by scanning the probe across the surface in a 2D raster pattern. The variation in modulus provides the contrast according to color or gray scale. Some examples include nano-crystalline materials, multi-domain piezoelectrics, polymeric composites, diamond-like carbon layers [3] on silicon, nano-scaled ferrites [5], thin films [6], Germanium islands grown on silicon substrates [7], carbon fiber composites, and atomic steps in gold [8]. The main objective of these studies was to obtain high-contrast images of these samples and in doing so, distinguish between different materials on the surface and gaining information about the compositional and elastic property heterogeneities across the sample [9]. Significant problems have been encountered, however, when trying to map thin layers of soft materials [10]. Among these are damage by the AFM tip to the soft specimen surface and the influence a stiff substrate exerts on the specimen modulus distribution.

Another application technique, due to its unique capability of visualizing buried structures in soft samples, scanning near-field ultrasound holography (SNFUH) has been used for studying structures and nanoparticles inside cells [11]. The technique synergistically integrates three disparate approaches: a unique combination of scanning probe microscope platform (which enjoys excellent lateral and vertical resolution) coupled to micro-scale ultrasound source and detection (which facilitates “looking” deeper into structures, section-by-section) and a novel holography approach (to enhance phase resolution and phase coupling in imaging).

By means of ultrasonic force microscopy and lateral force microscopy Szoszkievicz et al. [12], measured adhesion hysteresis, and friction on protein films of bovine serum albumin and concanavalin A at local scales. The investigations at different relative humidities (less than 5 % and at 50 % relative humidity) correspond to dehydrated and hydrated states of proteins. They demonstrate that a substantial increase of adhesion hysteresis with relative humidity is a sensitive measure of protein-water binding capacity at local scales. Cuberes [13] reports on the feasibility to implement ultrasonic atomic force microscopy techniques in liquid environments taking advantage of the mechanical diode effect. When using the mechanical diode mode, the inertia of the cantilever allows one to detect ultrasound without monitoring any particular cantilever resonance. It is shown that mechanical diode signals in liquids exhibit a similar dependence on the ultrasonic excitation amplitude and tip-sample normal force as in air. Moreover, ultrasonic force microscopy on samples of biological interest such as lipid bilayers yields to reasonable contrast. In some cases, apparent mechanical-diode signals are detected out-of-contact, with the cantilever far distant from the sample surface.

Among the major problems in using AFAM are damage by the AFM tip to the soft specimen surface and the influence a stiff substrate exerts on the specimen modulus distribution. We have developed a new approach to overcome these problems and recently have made preliminary short reports [14, 15]. Here, we present a more detailed description of the technique and describe results obtained on baby hamster kidney (BHK) cells, a commonly used eukaryotic cell type as a case study. We also present relevant finite element model (FEM) calculations providing guidance for the AFAM measurements. Finally, we present force–distance data obtained by what is considered the standard but lengthy and time-consuming way to map modulus. We use these data to verify the AFAM imaging results and to provide a gray-scale calibration.

## 17.2 Basic Background of Technical Approach

Forces are the fundamental component behind atomic force microscopy. The interaction between the tip and sample arises from different forces, as the tip is raster-scanned across the surface. The forces that are monitored and used for this study are mainly the attractive van der Waals forces and the repulsive electrostatic forces, in accordance with Pauli's exclusion principle [16, 17]. The operation of the AFM relies on the combination of these forces between the tip and sample and the operating mode determines the relative contribution of these forces. The forces felt between tips and samples are analogous to the bonding forces between two atoms. At the equilibrium separation distance,  $E_B$  represents the bonding energy or the energy required to separate the two atoms. In general the bonding energy can be described by the Lennard–Jones potential given by the following function,

$$E_B = 4\varepsilon \left[ \left( \frac{\sigma}{r} \right)^{12} - \left( \frac{\sigma}{r} \right)^6 \right] \quad (17.1)$$

where  $\varepsilon$  is the potential well depth and  $\sigma$  is the hard sphere radius. These parameters can be fitted to reproduce experimental data or deduced from results of accurate quantum chemistry calculations. This potential has an attractive tail at large  $r$ , it reaches a minimum around  $1.122\sigma$ , and it is strongly repulsive at shorter distance, passing through 0 at  $r = \sigma$  and increasing steeply as  $r$  is decreased further. The term  $1/r^{12}$ , dominating at short distance, models the repulsion between atoms when they are brought very close to each other. Its physical origin is related to the Pauli principle: when the electronic clouds surrounding the atoms start to overlap, the energy of the system increases abruptly. The exponent 12 was chosen exclusively on a practical basis: Eq. (17.1) is particularly easy to compute. In fact, on physical grounds an exponential behavior would be more appropriate. The term  $\sim 1/r^6$ , dominating at large distance, constitutes the attractive part. This is the term which gives cohesion to the system. A  $1/r^6$  attraction is originated by van der Waals dispersion forces, originated by dipole–dipole interactions in turn due to fluctuating dipoles. These are rather weak interactions, which, however, dominate the bonding character of closed-shell systems, that is, rare gases such as Ar or Kr. The total force the tip exerts on the sample is then the sum of the repulsive and attractive forces between the tip and sample during the contact mode AFM and is typically in the range of  $10^{-8}$ – $10^{-6}$  N [17].

### 17.2.1 Resonant Dipping Mode

Here, we report an apparently new variation of AFAM, which we have found successful in the in-vitro study of fragile biological cells. In contrast to most previously reported methods, this technique places the probe tip in shallow (few Å) contact with the cell (typically 1–10 μm tall) and executes a gentle resonant dipping motion, only 10–100 Å in depth, hence the name “resonant dipping” mode. The force of interaction during imaging is estimated at  $10^{-9}$  N and is at least an order of magnitude less than the force in the standard contact mode, thus minimizing any potential damage to the cell. The role of a thin layer of liquid during atomic force microscopy is not completely understood and has recently been given some attention in the literature. Lantz et al. [18] showed that in the presence of a liquid layer on a sample, when driven by direct application of a force to the tip, the microscope is stable over a wide range of operating frequencies. At low frequency they find that the interfacial stiffness extracted from approach curves is found to be of the order of 1 N/m on first contact, which is indicative of imaging via a compressed liquid layer. Measurements of the spectral response of the cantilever and numerical simulations confirm this and show that viscous damping at the surface also plays a small role. Overney et al. [19] reported force microscopy studies of friction and elastic compliance of phase-separated organic thin films and found that with increasing pH both the Young’s

modulus and friction force were found to decrease slightly. Our observations in the context of this work showed that repeated scanning produced negligible change in the modulus distribution. Given the various observations we conclude that the thin layer of nutrient fluid probably has a small effect on the modulus. On the other hand, the thin layer of nutrient fluid is most likely spread evenly over the cell surface so that a measurement of the change in modulus over the cell's surface is still meaningful on a semi-quantitative basis. The weak force interaction and the shallow penetration play a key role in the increase in scanning speed.

### ***17.2.2 Hardware Configuration***

The AFM can simultaneously collect information about topography and material properties. The topography image relies on the tip feeling the differences in height as it is raster-scanned across the surface, whereas U-AFM relies on the amplitude change of the cantilever in response to surface elasticity differences. The Autoprobe M5<sup>1</sup> was used for this study; a schematic of the configuration can be seen in Fig. 17.1. This figure shows the hardware and electrical signal configuration that allows for the simultaneous collection of topography and amplitude images. A key feature seen in the diagram is that the amplitude and phase are detected with a phase sensitive detector. Figure 17.2a, b shows scanning electron micrographs of a typical AFM tip and cantilever, respectively. The tip is in contact with the sample surface operating at a constant force vibrating at a specific frequency. The frequency of the cantilever is on the order of tens of kHz, where the feedback loop operates around 1 Hz, permitting both topography and force modulation signals to be obtained concurrently. The driving signal is supplied by the sine wave generator resulting in the piezoelectric tube movement that drives the cantilever oscillation. As the tip scans the surface, the cantilever deflects to changes in topography and the oscillation amplitude changes with elasticity differences. The cantilever deflection is captured by the use of a laser spot collected by the position sensitive photodetector (PSPD). The detection system monitors cantilever deflection measuring the position and intensity of the laser spot in the four quadrants. The output from the PSPD is an A-B signal, which has a DC and an AC component. When operating in contact mode, the feedback loop uses the DC cantilever deflection signal to maintain a constant force between the tip and sample as well as to generate a topographic image. The AC component is sent to the root mean square (RMS) detector that records changes in cantilever amplitude to produce the amplitude image. In general, scanning probe microscopy is most commonly used for imaging sample surfaces. But they also have the capability to be used as quantitative tools measuring material properties at single points on the sample surface. The scanning tunneling microscope can be used as a spectroscopic tool by measuring the electronic properties of the surface. By comparison, the AFM can be

---

<sup>1</sup> Autoprobe M5 from Park Scientific Instruments, 1996.

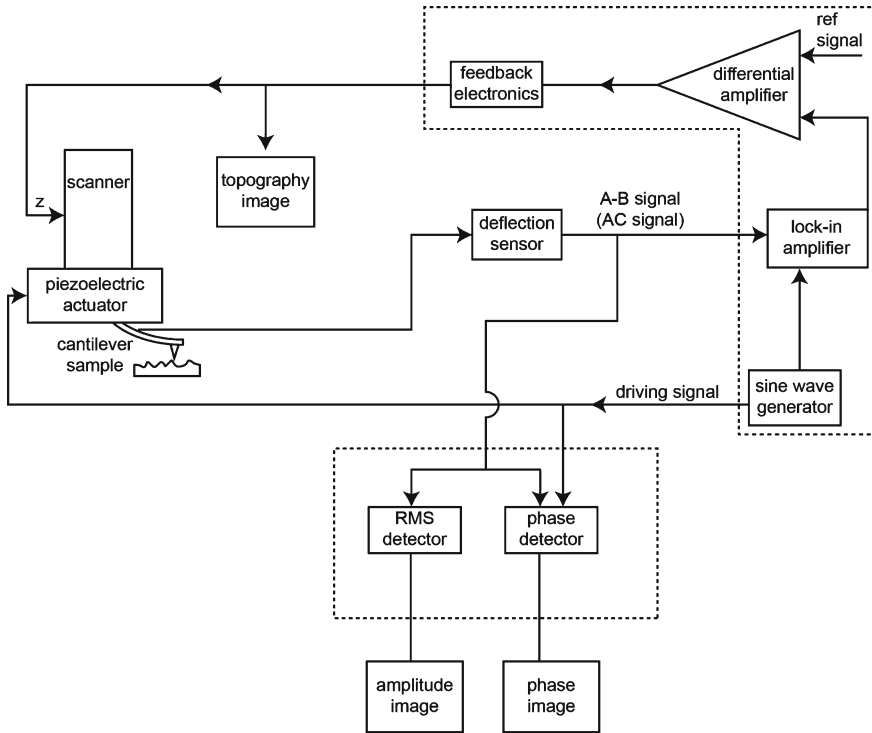


**Fig. 17.1** Schematic of the Autoprobe M5 AFM

used to measure force–distance curves that provide quantitative information about the local elastic properties of the surface [16]. In this study, force–distance curves were utilized for semi-quantitative analysis of the local elastic properties of BHK cells and the theory and operation of the force–distance curves will be discussed in the following section.

### 17.2.3 AFAM Imaging Technique

The AFAM imaging is possible through the special hardware and electrical configuration of the AFM. Our AFM used for imaging the BHK cells was the Veeco Autoprobe M5. The resonant dipping mode used has the ability to simultaneously collect topography and AFAM images. A set point force between 5 and 8 nN was used with a scan rate of 0.6–1.0 Hz in air. The maximum scan rate of the system is about 5 Hz. The glass substrates were removed from the growth media. The glass substrates were mounted on aluminum metal stubs with double-sided carbon tape. The aluminum stub was screwed into the AFM stage for stability. With practice this

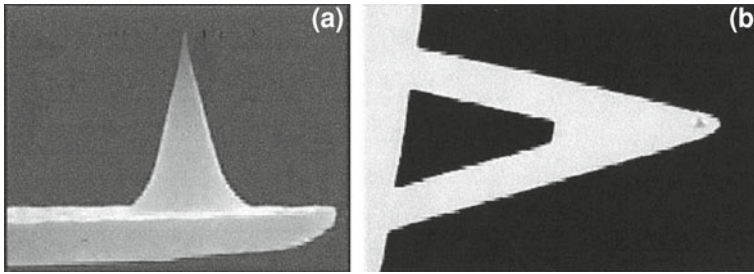


**Fig. 17.2** **a** A scanning electron micrograph of an AFM tip. Source: Veeco Metrology Group; **b** a scanning electron micrograph of an AFM tip mounted on the end of a “V” shaped cantilever. Source: Veeco Metrology Group

process took about 1 min. Desiccation was a main problem, as well as change in pH to an alkaline condition, in part due to lack of  $\text{CO}_2$  normally supplied to the culture atmosphere. Although cell death can be delayed up to 8 min under special conditions our mounting plus scan time was kept typically under 4–5 min. AFAM imaging was performed with an ultralever A cantilever and tip composed of silicon. The tip properties are listed in Table 17.1 [20]. The ultralever was originally chosen because of user experience with the tip and image quality achieved. The ultralever tips were manufactured with a 1,000 Å diamond coating to prolong the life of the tip. The backside of the cantilever was gold coated for high reflectivity to maximize the laser signal output. Tip A was used because of its relatively low spring constant compared to the other ultralever tips. This allowed for high sensitivity imaging while exerting the smallest force possible on the cell in the resonance dipping mode. The free resonant frequency of the cantilever was used, i.e., before the tip was in contact with the sample. The optimum operating frequency was selected as follows (1) locate the main resonance peak; this is done by sweeping a frequency range from 1 to 500 kHz. (2) Narrow the frequency range within 10 kHz of the main peak to verify uniform peak shape; (3) select a frequency to the right of the main peak where the phase curve has some slope. A typical frequency was to the right of the 36 kHz main resonance peak. Typical tip vibration amplitudes of 45–90 nm were used for this study. The quality of the image was the ultimate factor determining the operating frequency and drive amplitude.

### 17.3 Analyzes, Modeling, and Simulation

The interaction between the cells and the AFM tip plus cantilever was modeled using our modification of the well-known Hertz model. The model is important in the analysis associated with the force–distance curves. Using the model applied to the force–distance curves we obtained the elastic moduli for various locations on the cells. With these we were able to calibrate the AFAM images and assign modulus

**Table 17.1** Ultralever tip and cantilever characteristics

Ultralever tip A features	
Height	7 $\mu\text{m}$
Radius of curvature	10 nm
Cantilever features	
Length	180 $\mu\text{m}$
Width	25 $\mu\text{m}$
Thickness	1 $\mu\text{m}$
Force constant	0.26 N/m
Resonant frequency	40 kHz

Information supplied by Veeco Metrology Group

values based on image contrast. Live mammalian cells are typically very similar in structure, e.g., a nucleoid in the center of a cytoskeleton with cytoplasm at the edge [21]. Therefore, with some exceptions, the calibration results with force–distance curve measurements should apply to a wide variety of cells. If there is an anomalous modulus caused, for example, by melanoma or excessive waste products, this is an important finding and more attention should be exerted with additional force–distance data. The real benefit of the technique lies in enabling rapid assays which typically require many measurements to make the results statistically meaningful.

The material of the cantilever and tip influences the spring constant and therefore the resonant frequency used for operation, while also affecting sensitivity. We used diamond coated silicon tips for the imaging [17]. Cantilever deflection is directly related to the force applied to the tip with the use of Hooke's Law ( $F = k_c d$ ), where the spring constant,  $k_c$ , of the cantilever is known, where  $d$  is the cantilever deflection, and  $F$  is the force applied to the tip. This conversion leads to the force versus distance ( $f$ – $d$ ) curves (described in detail in a later section). The determination of the elastic modulus from the  $f$ – $d$  curve requires the use of a model. For this study, a nonlinear Hertz model was used. The Hertz model comes from continuum mechanics of contacts where tip shape can be modeled with parabolic geometry leading to the relation in Eq. (17.2),

$$F = \frac{4}{3} E^* R^{\frac{1}{2}} \delta^{\frac{3}{2}} \quad (17.2)$$

and where,  $F$  is the force applied to the tip,  $E^* = E/(1 - \nu^2)$  is the effective elastic modulus of the sample,  $R$  is the radius of curvature of the tip,  $\delta$  is the indentation depth into the sample,  $E$  is the actual elastic modulus of the sample, and  $\nu$  is the Poisson's ratio. The model is fitted to the graph of force versus distance to obtain the elastic modulus. The indentation depth,  $\delta$ , is found through a conversion of the tip-sample distance, discussed in more detail later.

This resonant dipping mode and the interaction between tip and sample were modeled and simulated by a finite element method. The simulation results provided good understanding of and gave guidance to the operation of the new mode. They also showed semi-quantitative agreement with the experimental observations. In



**Table 17.2** Material property information for silicon used in cantilever model

Material properties	
Elastic modulus	169 GPa
Poisson's ratio	0.21
Density	2.33 g/ml

Information supplied by Veeco Metrology Group

the work reported here, the feasibility of using resonant dipping to image delicate biological cells was applied to BHK cells. The interest is in describing the contrast rendered by elasticity differences across the BHK cell and to evaluate this technique for the study of other biological specimen. The FEM was constructed representing the cantilever and tip-sample interaction associated with resonant dipping. The computer model allowed for the cantilever vibration amplitude and resonant frequency to be theoretically determined when imaging soft materials. The range of forces for the BHK cell found in parallel force-distance work was 10–70 KPa.

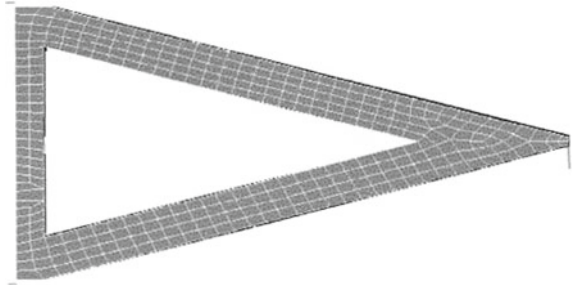
Specifically, Ansys Classic version 7.11C1 was used to develop a finite element model of the cantilever and tip-sample interaction during U-AFM operation. There are two main parts to the model: the cantilever and spring. The cantilever was modeled as a shell, named shell63. Shell63 has both bending and membrane capabilities. Both in-plane and normal loads are permitted. Each node has six degrees of freedom: translations in  $x$ ,  $y$ , and  $z$  directions and rotations about  $x$ ,  $y$ , and  $z$  axes. An element is defined by four nodes, four thicknesses, and the density, elastic modulus, and Poisson's ratio of the material. The cantilever was modeled after the ultralever used in U-AFM imaging with dimensions of 180  $\mu\text{m}$  long, 25  $\mu\text{m}$  wide, and 1  $\mu\text{m}$  thick. The material properties of the cantilever were modeled after silicon seen in Table 17.2, which is the composition of the ultralever.

The tip and sample were modeled by a nonlinear spring attached to the end of the cantilever. The nonlinear spring was defined as combin39. Combin39 is a unidirectional element with nonlinear force-deflection capability. Each node has up to three degrees of freedom: translations in the nodal  $x$ ,  $y$ , and  $z$  directions. The element is defined by two node points and a force-deflection curve. The points on this curve represent force versus relative translation for structural analyzes. The spring length was defined as 10  $\mu\text{m}$ .

The mesh size was defined by Ansys as smartsiz 4 for area meshing, defining 318 elements for the shell. The area of one element is between 28.8 and 39.9  $\mu\text{m}^2$ . The mesh shape is quad, defining four corners to each element. The spring is made of one element composed of two nodes. Figure 17.3 is an example of the mesh of the cantilever with a nonlinear spring attached to the end. The nonlinear spring is represented by Eq. (17.2).

The simulations consist of applying a harmonic pre-load force of  $0.5 \times 10^{-5}$  N in the  $z$  direction along the back of the cantilever section; all other directions, translational  $x$ ,  $y$ , rotational  $x$ ,  $y$ , and  $z$  are fixed. Also all points are fixed at node 688 at the end of the spring. The input data is indentation depth,  $\delta$ , as a function of force,  $F$ , at node

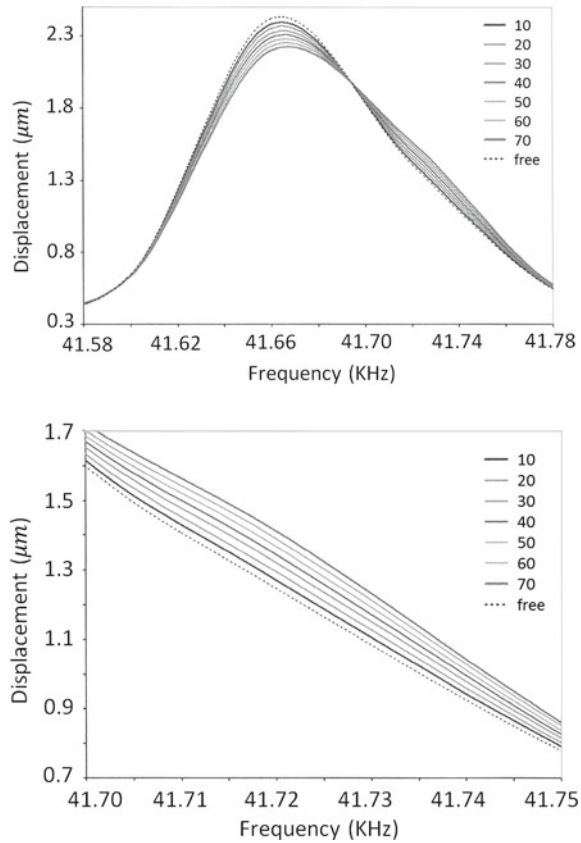
**Fig. 17.3** A picture of the finite element mesh of the cantilever with a nonlinear spring attached to the end representing the interaction between the tip and sample [14]. Reprinted with permission of Elsevier



687, which is the other end of the spring. Forces between 1 and 20 nN were applied at node 687 in the  $z$  direction only. The indentation depth,  $\delta$ , was calculated using Eq. (17.2) as a function of force for the elastic moduli range of 10–70 kPa, representing the stiffness of the BHK cell. A sweep frequency between 10 and 80 kHz was applied to the cantilever system, where the vibration response was measured at node 687. The frequency range was reduced to 20–50 kHz to obtain more accurate results with the maximum of 500 steps. The output data is given as displacement or amplitude versus frequency representing the response of the cantilever.

The simulation took into account the composition and dimensions of the cantilever, tip, elastic modulus of sample, and force applied to the sample. A frequency range between 20 and 50 kHz shows the theoretical resonant frequency peak of the cantilever. This is similar to the experimental resonant frequency of 36 kHz. Diamond coated silicon tips were used for the imaging [22–24]. The free cantilever vibration is plotted showing the resonant frequency of the cantilever when the tip is far from the sample surface. The free cantilever vibration is important since this is the procedure for choosing the operating frequency during imaging. The displacement amplitude versus frequency was plotted for each elastic modulus in the range of 10–70 KPa, as seen in Fig. 17.4a. It can be seen that the amplitude changes with varying elastic modulus. This shows the dependence of cantilever amplitude to the tip–sample interaction. When focusing on the right-hand side of the main resonance peak, the amplitude of the cantilever increases as the elastic modulus increases, see Fig. 17.4b. Experimentally, the right-hand side of the resonant peak was used in all our AFAM imaging. When the computer simulation is applied to the AFAM image, considering the right-hand side, stiffer materials produce higher amplitude of cantilever deflection, which leads to the conclusion that the stiffer materials appear brighter in the image. This agrees with the original hypothesis that the outer edge of the cell is stiffer and is represented by the brighter areas in the amplitude images. Another important feature of the computer simulation is that the indentation calculated from the modified Hertz model, demonstrates that the stiffer materials result in less indentation from the tip during imaging. This results in a larger cantilever deflection since the stiffer materials resist the interaction with the tip more than compliant materials. There was about a 10% difference between the computer simulated resonance frequency, around 41 kHz, and the experimental resonance frequency, around 36 kHz.

**Fig. 17.4** **a** Resonance curve,  
**b** magnified image



The discrepancy could stem from experimental deviations from the ideal assumed in the simulations, such as the mass loading of gold and diamond coatings on the tip and cantilever, respectively. Another possible reason is the presence of the thin layer of viscous fluid on the sample. The current FEM model does not take these into account explicitly. Refinement is necessary and is planned for a more accurate simulation but the current trends are in good semi-quantitative agreement. In summary, the computer model showed the cantilever response amplitude as a function of the elastic properties of the sample. The simulation described the contrast in the amplitude images where stiffer materials have a stronger interaction with the tip, resulting in brighter areas in the image, where more compliant materials are represented by relatively darker shades.

## 17.4 Sample Preparation

BHK cells, an immortal cell line grown in culture, were used as a model system for development of the resonant dipping AFAM technique. The BHK cells adhere and proliferate on glass thus eliminating any need for immobilization. Mammalian cells are characterized as eukaryotes as they possess a membrane-delimited nucleus as well as membranes surrounding and playing a significant part in the structure of many organelles [25]. The cytoplasm, which is the liquid substance that suspends the organelles, contains an array of fibrous proteins collectively called the cytoskeleton. The most abundant and significant cytoskeletal proteins are the microfilament, microtubule, and intermediate filaments. These proteins become attached to the cell membrane, to each other, and even to the cell nucleus thereby forming a 3D internal scaffold. This scaffold is documented to add strength and rigidity to the structure of the cell. The scaffold is a dynamic structure; it changes its assembly/disassembly character during its normal physiology [24–27].

### 17.4.1 Sample Characterization

For the purpose of characterizing the BHK cells by standard methods we first image them with the scanning electron microscope (SEM) and the laser scanning confocal microscope (LSCM). For the SEM the cells were grown on glass substrates and then fixed with glutaraldehyde, a cell rigidifier, and gold-coated, as both are required for SEM imaging. It is important to note that the cells for AFAM imaging were not fixed or gold-coated. The SEM used was a JEOL JSM 5400 model A. Typical SEM image is shown in Fig. 17.5 and is useful in exhibiting the shape, size, and exterior structure of the cells at high magnification. The image clearly shows the nucleoid of the cells in the center surrounded by cytoskeletal filaments. The scale is displayed in the image.

The LSCM used was an Olympus with Fluo-View FV1000 software. The cells were stained to exhibit the structure, which can be seen in Fig. 17.6. The lower image is a superposition of two different versions (shown above) of the same cell cluster. The upper left hand image is produced by green fluorescence with Phalloidin and emphasizes the actin cortical cytoskeleton, whereas the upper right hand image was obtained by staining with mitotracker red a fluorescent dye to emphasize the mitochondrial network. These are typical fluorescence images and show the distribution of cytoskeletal filaments which surround the periphery of the cells. The images show that the cell diameter is around 10–40  $\mu\text{m}$ , with some as long as 70  $\mu\text{m}$ . The cells appear to be stretched out on the surface, apparently making connections to other cells. The surfaces of the cells appear relatively rough within these sets of images, which was expected due to their highly heterogeneous surface. The topographic data were obtained by standard AFM. Figure 17.7 exhibits a cross-sectional image along a line through the region connecting two cells. These images show that the cells are

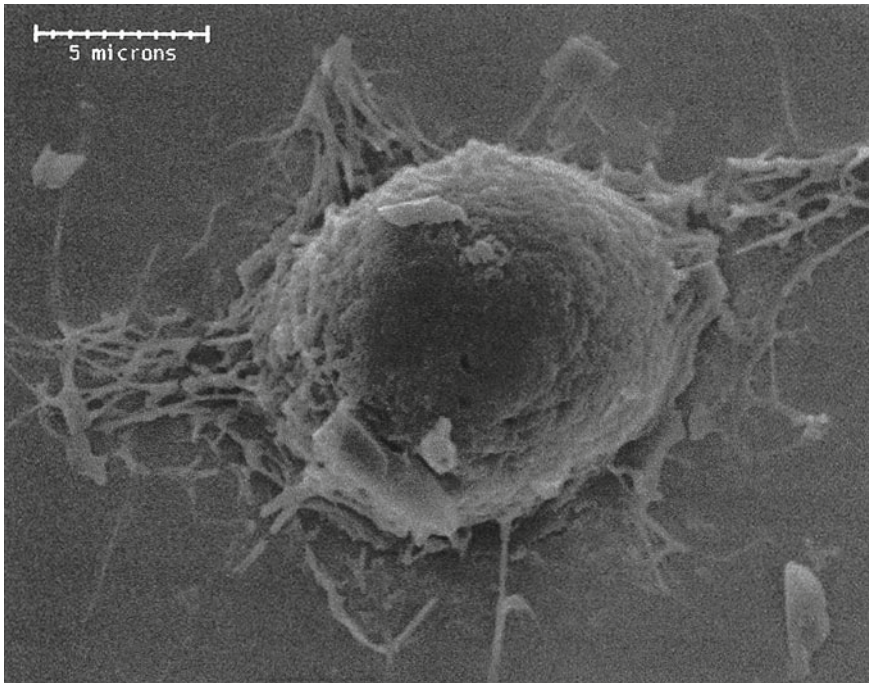


**Fig. 17.5** SEM micrograph of BHK cell fixed on glass surface at a magnification of 5000x [14]. Reprinted with permission of Elsevier

about 3–5  $\mu$  thick at the center in the region of the nucleus and 1–2  $\mu$  thick at the edges, where the cytoplasm predominates.

#### ***17.4.2 BHK Cell Viability Under Conditions of Drying***

When cells are removed from their culture liquid they have a short survival rate for up to about 5–10 min depending on the environmental conditions. The cells typically have some culture liquid adhering to their surfaces. We have imaged cells as a function of time after removal from the culture medium and report on their change in condition. Thus, when we imaged the cells by AFAM, when just removed from the culture medium we placed a limit of 5 min on the useful imaging operation. The images obtained in this manner with AFAM are maps of the relative elastic modulus across the cell and typically take only a few minutes of scan time. The modulus distributions were verified by force–distance curves carried out within the culture medium. The force–distance curves are the results of a well-established technique, which, however, is very time-consuming and cumbersome taking typically 1 h or

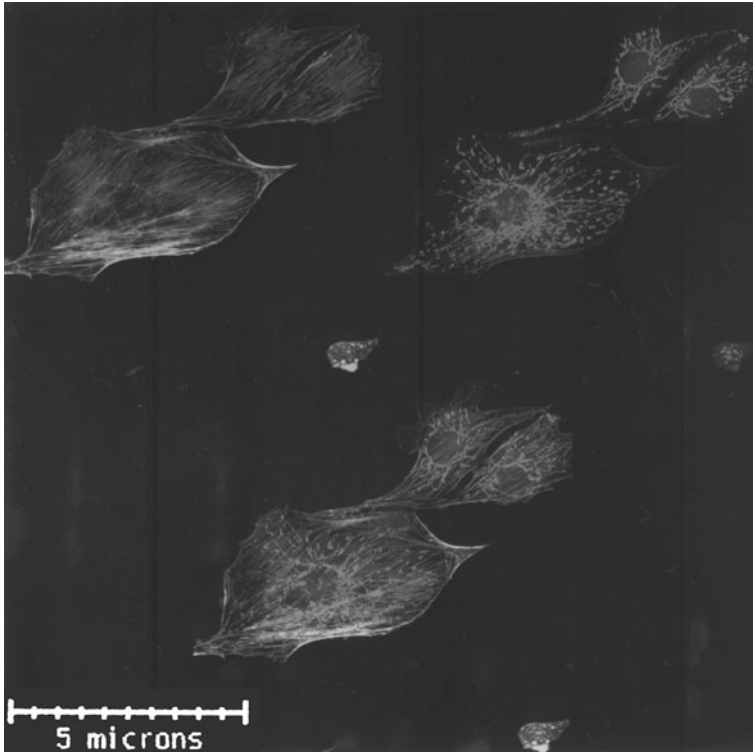
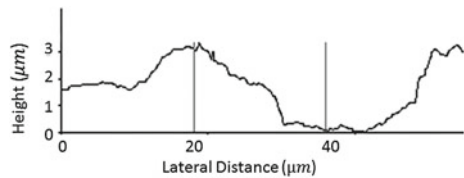


**Fig. 17.6** Fluorescence image verifying the distribution of cytoskeletal filaments (magnification of 5000x) [14]. Reprinted with permission of Elsevier

**Fig. 17.7** Height profile



more of scan time, while the cells are submerged in the nutrient fluid. The resolution is consistent with typical AFM performance and is estimated at 1–10 nm.

BHK cells were cultured in Lab-Tek Chamber Slides (Nunc Inc.) at a cell density of  $10^5$  cells per  $4\text{ cm}^2$  chamber. The cells were allowed to adhere in the chambers for 24 h prior to testing. As the procedure requires a minimal fluid environment for the cells it was first necessary to test the effect of a near dryness state on cell viability. This test was accomplished by decanting the growth medium from 4 chambers, and removing the chamber walls, leaving the BHK monolayers exposed on the slide, moistened only with residual growth medium that formed a thin layer of fluid over the cells. The slides were kept in a horizontal position and allowed to begin the drying process at ambient

**Table 17.3** Experiment results of cell viability change with time

Time (min)	Live/dead cells counts				Average survival percent (%)
0	56/0	48/0	52/1	39/2	98.3
5	42/0	47/4	50/7	36/11	89.1
10	0/48	0/40	0/49	0/46	0
15	0/40	0/39	0/39	0/47	0

The survival percent of the cells are acceptable (about 90%) within up to a 5 min interval

conditions; room temperature (21 °C), unknown humidity. The slides were observed for a 15 min drying period over the course of the trial. Immediately, and at 5, 10, and 15 min after removal of the culture medium, individual slides were immersed for 10s in 0.1% trypan blue solution prepared in Hank's balanced salt solution (HBSS), and then were washed by dipping several times in HBSS. Cell counts were done on the slides immediately, both to determine the total cells adhering, as well as the percentage of viable cells. Four fields were counted subsequently for each time point and the results averaged. As is seen in Table 17.3, under these conditions we observed that the cell monolayer appeared dried in some areas after about 6 min, and completely dried in about 8 min. As summarized in Table 17.3, under the conditions of this trial, cells attached to a glass slide dried to completeness in 6–8 min. However, it is apparent that cell death as measured by inclusion of trypan blue dye, corresponded directly with the drying process. Under conditions of this trial, cell monolayers with growth medium removed remained viable for approximately 5–6 min.

## 17.5 Results

### 17.5.1 Force–Distance Measurements

The force–distance curves for this study were collected with a special AFM (Bioscope<sup>TM</sup>), which has a liquid container to ensure cell viability over a long period of time, although it has no capability for either U-AFM or AFAM. Microlever cantilevers (see Table 17.4) of 0.01 N/m were used and were replaced after each experiment. The liquid environment and use of microlever cantilevers allowed the direct comparison to other published data. The locations probed on the cell were generalized as center or edge since the exact location can be determined only approximately with the built-in optical microscope. The tip was moved from the original position to probe multiple cells in one experiment; therefore it is inaccurate to compare indentation depths since each curve had a new starting position. The experimental cantilever deflection versus tip–sample distance plots were transformed into force versus indentation depth curves using the calibration data. Figure 17.8 shows an example of cantilever deflection versus tip–sample distance measured on glass (upper line) and

**Fig. 17.8** Example of cantilever deflection versus tip-sample distance curves

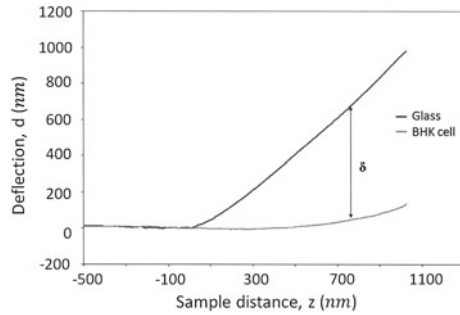


**Table 17.4** Microlever tip and cantilever characteristics

Microlever tip C features	
Height	3 μm
Radius of curvature	<50 nm
Cantilever features	
Length	320 μm
Width	22 μm
Thickness	0.6 μm
Force constant	0.01 N/m
Resonant frequency	7 kHz

Information supplied by Veeco Metrology Group

BHK cell (lower line). The difference,  $\delta$ , between the curves equals the tip indentation depth.

Figure 17.9 shows typical force versus indentation depth curves for three different locations on the surface of a BHK cell. The solid lines through each curve are derived from the modified Hertz model using the information from Table 17.2. The curves were then fitted with the nonlinear Hertzian model described by Eq. (17.2) to determine the elastic modulus. Three separate force-distance experiments were performed collecting a total of 50 curves, where 28 were from center positions and 22 were from outer edge positions of the cell. Tables 17.5 and 17.6 show the results of all force-distance curves providing data on the difference between cell center and edge. The results are summarized in Table 17.7. From a statistical point of view it is noted that there are two sizes to the elastic moduli in both the edge and center distribution. As will be seen in the imaging results (for example see Fig. 17.10, this observation is confirmed for the cell edge. For the cell center the two sizes could be a result of measurements in the nucleoid where both the soft nucleus and the harder skeleton are present as shown in Fig. 17.5.



**Fig. 17.9** Force versus indentation depth

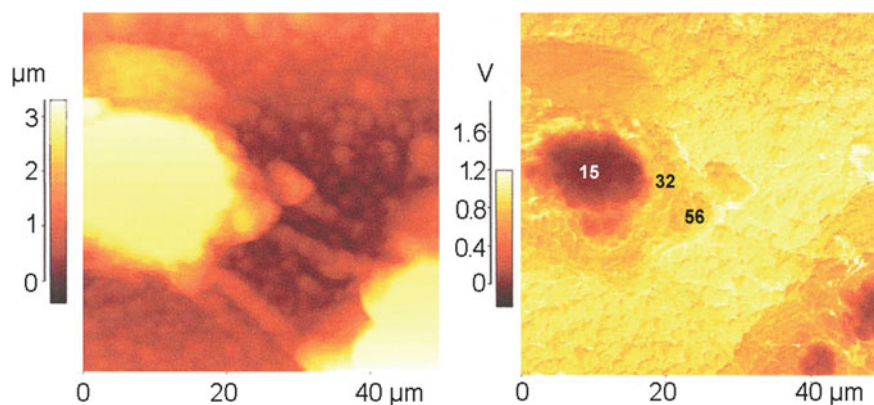
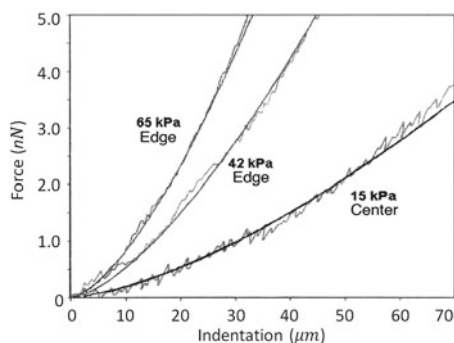


**Fig. 17.10** Topography on *left* and AFAM image of BHK cell on *right*. A scan size of  $50\mu\text{m}$  and a frequency of  $36\text{kHz}$  were used. The basic outline of the BHK cells can be distinguished in the topographic image but it lacks surface detail. In contrast, the AFAM image on the *right* shows several distinct regions of contrast [14]. Reprinted with permission of Elsevier

**Table 17.5** Young's modulus measured at the center of the cells (KPa)

Experiment values							Average value
16.2	15.7	29.4	39.8	15.3	12.3	12.7	19.6
8.7	11.4	11.4	15.1	18.3	44.5	14.5	
12.3	14.1	13.9	16.5	15.7	39.4	12.3	
14.8	10.1	40.3	17.6	18.4	16.7	41.2	

### 17.5.2 Imaging Results

In this section the resonance dipping AFAM images are displayed and for comparison some topographical images collected simultaneously. An ultralever A tip was used to collect the following images. The topography image maps differences in height across the surface, whereas the AFAM image maps differences in elasticity across

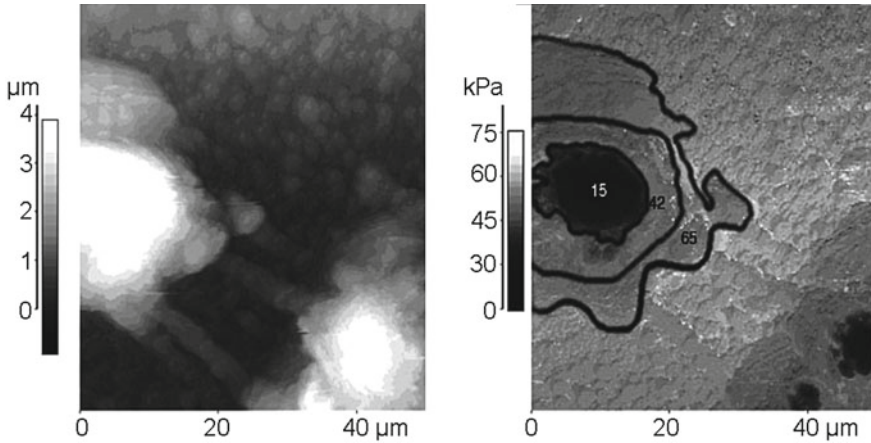


**Fig. 17.11** Three different force–distance curve experiments were performed on the BHK cells to quantitatively determine the elastic modulus at different locations on the cell surface, generalized as edge or center. By assuming parabolic tip geometry the Hertz model was applied to the data to obtain the elastic modulus as a function of cell position. The average  $E$  for the edge of the cell was determined to be 46.7 kPa, which was twice as stiff as the center of the cell, with an average of 19.1 kPa. The elastic moduli range for the BHK cell was determined to be 10–70 kPa. The force–distance work showed the same trend observed in the AFAM images with elasticity differences between the edge and center of the cell. The set of  $f$ – $d$  curves also provided the elastic modulus range used in the computer simulation [14]. Reprinted with permission of Elsevier

**Table 17.6** Young’s modulus measured at the edge of the cells (KPa)

Experiment value											Average value
36.6	48.0	28.0	18.0	22.0	25.5	26.5	22.5	22.5	45.9	54.0	46.7
23.4	75.0	84.9	66.0	34.9	60.0	68.1	60.0	64.9	54.9	85.0	

**Table 17.7** Average elastic moduli for BHK cell

Location	Avg. E and St. Dev. (kPa)
Edge of cell	46.7 ± 21.8
Center of cell	19.6 ± 10.9
Whole cell	31.3 ± 21.2

The elastic modulus is substantially higher in the center of the cell as obtained from AFM force–distance data with a fit to modified Hertz model [14]. Reprinted with permission of Elsevier

the surface. In Fig. 17.10, a scan size of 50 μm and a frequency of 36 kHz were used. The basic outline of the BHK cells can be distinguished in the topographical image but lacks surface detail. Height differences are mainly between the cell and the underlying glass substrate but virtually no detail is seen on the cell surface. The cell in the left hand corner appears to be attached to another cell in the bottom corner through a string-like feature present in the image. The corresponding amplitude or

AFAM image is on the right and shows two distinct areas of contrast. There are bright and dark regions present within the cell boundaries. The darker shades are present within the center of the cell, where the outer edges and boundaries of the cell appear much brighter. Also, there appear to be two cells in the bottom corner, which are not distinguishable in the topographical image. This alludes to elasticity differences across the cell. When the scan size is decreased to  $20\ \mu\text{m}$ , in the amplitude image, there is distinct contrast seen across the cell; the center of the cell appears darker than the outer edge. This amplitude image shows circular regions within the dark area. There also appears to be additional contrast around the center of the cell, where there are scattered bright features in this area. In addition, there is contrast between the outer boundary of the cell and the underlying glass substrate. Another cell was imaged under identical conditions using an ultralever A tip at a frequency of  $36\ \text{kHz}$  at a scan size of  $22\ \mu\text{m}$ . The matching amplitude image showed high contrast across the cell surface. The center of the cell appeared darker than the other areas of the cell. There were also brighter areas surrounding the center of the cell.

### ***17.5.3 Interpretation***

A total of six sets of topography and amplitude images were obtained (not all shown here) and the same phenomena were seen. The topography images lacked surface detail, where very little surface roughness or height differences were seen across the cell. The lack of surface detail present in the topography images is attributed to the BHK cell surface roughness.

Although the topography images lacked surface detail, the outline of the cell could be easily distinguished from the glass substrate. In some of the topography images, the glass substrate appeared rough. This could be a result of cellular secretions or outer membrane disruption. The BHK cells grow in monolayers, so as they grow and move, it is possible that residues (glycoprotein) were deposited across the glass surface, so that no area of the glass surface was pure glass. In comparison, the amplitude images showed high contrast between different regions of the BHK cells. Different surface and cellular features were distinguishable that were not present in the topography images. The contrast in the amplitude images generally differed from the center to the edge of the cell, suggesting elasticity heterogeneities across the cell surface. In characterizing the dark and bright regions in the images, it is suggested that the center of the cell is less stiff than the outer areas. This agrees with the common theory [28–31], in which the outer region of the cell contains larger amounts of fibrous proteins. The proteins in the cytoskeleton produce 3D networks in which larger quantities are believed to reside in the outer regions of the cell, providing strength and cellular movement. The cytoskeleton of the cell is within the plasma membrane, which leads to the belief that it senses both the outer membrane and the internal components of the cell. It is therefore suggested that the darker regions are areas of less stiffness; corresponding to the area where the tip is either interacting with the outer membrane or internal organelles of the cell, such as the nucleus.

In summary, the interaction between the tip and sample gives rise to contrast in the images. In this study it is suggested that the darker regions present in the amplitude images, prevalent in the center, represent lower stiffness when compared to the brighter regions concentrated at the outer edge. This would correspond to a stiffer material producing a larger cantilever deflection than a less stiff area.

It is important to note that there was no apparent cell damage during imaging, which is often a concern when imaging in contact mode. The same area was scanned repeatedly to confirm that the cell was not damaged. Cell stability, in this case, is attributed to the sample itself. Sample damage varies among different biological cells and different AFM systems.

## 17.6 Discussion and Summary

The elastic properties of BHK cells were evaluated with a new adaptation of AFAM. Both qualitative and quantitative information were collected with the new AFAM technique.

In contrast to most previously reported methods, the new technique places the probe tip in shallow (few Å) contact with the cell (typically 1–10 μm tall) and executes a gentle resonant dipping motion, only 10–100 Å in depth, hence the name “resonant dipping” mode. The force of interaction during imaging is estimated at  $10^{-9}$  N and is at least an order of magnitude less than the force in the standard contact mode, thus minimizing any potential damage to the cell. The presence of a thin layer of nutrient fluid on the surfaces of the cell has been considered. This role is not completely understood but has been the topic of interest in the literature. It has been shown that in the presence of a liquid layer on a sample, when driven by direct application of a force to the tip, the microscope is stable over a wide range of operating frequencies. At low frequency it is found that the interfacial stiffness extracted from approach curves is found to be of the order of 1 N/m on first contact, which is indicative of imaging via a compressed liquid layer. Measurements of the spectral response of the cantilever and numerical simulations confirm this and show that viscous damping at the surface also plays a role. On phase-separated organic thin films it was found that with increasing pH both the Young’s modulus and friction force were found to decrease. Our observations in the context of this work showed that repeated scanning produced negligible change in the modulus distribution. Given the various observations we conclude that the thin layer of nutrient fluid probably has a small effect on the modulus but little or no effect on the relative modulus distribution. The weak force interaction and the shallow penetration play a key role in the increase in scanning speed. This is confirmed by the observations that repeated scanning produces negligible change in the cell surfaces. The weak force interaction and the shallow penetration play a key role in the increase in scanning speed.

The new approach overcomes the limitations of customary atomic force acoustic microscopy. This approach (1) does not harm or damage the cell, (2) provides semi-quantitative information on the distribution of modulus across the cell, (3) gives

1–10 nm resolution, (4) requires less than 5 min scan time, and (5) can be used on cells briefly removed from the nutrient fluid. We describe the new approach, apply it to BHK cells and verify/calibrate the images obtained with force–distance measurements. AFAM and topographical images were simultaneously acquired at a cantilever modulation frequency of about 36 kHz. The scan sizes ranged from 50 to 14  $\mu\text{m}$ , where the AFAM images showed higher contrast in comparison to the conventional topography images; the topography images lacked surface detail and resolution. The main advantage of the amplitude images was the depiction of the elasticity differences across the cell surface. By using AFAM, the topography or roughness of the cell was not a factor in the image, resulting in high contrast and resolution images based on the elastic properties of the cell. The AFAM amplitude images showed the highest contrast between the e.g., which was bright, and center, which was dark, of the cell.

A series of force–distance curve experiments were performed on the BHK cells to quantitatively determine the elastic modulus at different locations on the cell surface, generalized as edge or center. By assuming parabolic tip geometry the Hertz model was applied to the data to obtain the elastic modulus as a function of cell position. The average  $E$  for the edge of the cell was determined to be 46.7 kPa, which was twice as stiff as the center of the cell, with an average of 19.1 kPa. The elastic moduli range for the BHK cell was determined to be 10–70 kPa (see Fig. 17.11). The force–distance work showed the same trend observed in the AFAM images with elasticity differences between the edge and center of the cell. The set of  $f$ – $d$  curves also provided the elastic modulus range used in the computer simulation.

The computer model described the contrast in the AFAM images. A finite element model was constructed using Ansys software of the cantilever and tip–sample interaction. The cantilever was modeled after the ultralever cantilever used in AFAM imaging, where the tip–sample interaction was represented by a nonlinear spring described by the nonlinear Hertz model. The results of the simulations showed that when operating at a frequency on the right side of the main resonance peak, the cantilever response amplitude increased as elastic modulus of the sample increased. This confirmed that the edge of the cell, which was brighter in the AFAM image, was stiffer than the center. The simulation also confirmed that the brighter color in the image was a result of the tip having a stronger interaction with stiff materials.

In conclusion, resonant dipping is a powerful technique with the ability to describe the elastic property heterogeneities across soft biological cells. The amplitude images obtained were of higher contrast and resolution than the corresponding topographical images. The elasticity differences seen in the images were confirmed by the force–distance curve techniques resulting in a twofold edge to center elastic modulus difference. The elastic moduli range was determined to be 10–70 kPa for the BHK cell where the average was determined to be 31.3 kPa. The computer model was able to describe the contrast of the AFAM images in agreement with the force–distance work. The technique should have many uses as a diagnostic tool for characterizing cells and will enable rapid assessment of the effects of physical and chemical signals on cells to obtain statistically meaningful data.

**Acknowledgments** B.R.T. was partially supported as part of the Center for Lignocellulose Structure and Formation (CLSF) an Energy Frontier Research Center funded by the U.S. Department of Energy, Office of Science, Office of Basic Energy Sciences under Award Number DE-SC0001090.

## References

1. K.D. Costa, Single-cell elastography: probing for disease with the atomic force microscope. *J. Dis. Markers* (ed. by N. Simpson) **19**, 139–154 (2004)
2. B.S. Elkin et al., Mechanical heterogeneity of the rat hippocampus measured by atomic force microscope indentation (Synopsis). *J. Neurot.* **24**(5), 812–822 (2007)
3. S. Amelio, A.V. Goldade, U. Rabe, V. Scherer, B. Bhushan, W. Arnold, Measurements of elastic properties of ultra-thin diamond-like carbon coating using atomic force microscopy. *Thin Solid Films* **72**, 75–84 (2001)
4. M.G. Heaton, C.B. Prater, P. Maivald, *Force Modulation Imaging: Application Note*. Veeco Metrology Group, Digital Instruments, 2001
5. E. Kester, U. Rabe, L. Presmanes, Ph Tailhades, W. Arnold, Measurement of Yong's modulus of nanocrystalline ferrites with spinel structures by atomic force acoustic microscopy. *J. Phys. Chem. Solid.* **61**, 1275–1284 (2000)
6. M. Kopycinska-Mueller, R.H. Geiss, J. Mueller, D.C. Hurley, Elastic property measurements of ultrathin films using atomic force acoustic microscopy. *Nanotechnology* **16**, 7033–709 (2005)
7. O.V. Kolosov, M.R. Castell, C.D. Marsh, G. Andrew, D. Briggs, Imaging the elastic nanostructure of Ge islands by ultrasonic force microscopy. *Phys. Rev. Lett.* **8**, 1046–1049 (1998)
8. P. Maivald, H.J. Butt, S.A.C. Gould, C.B. Prater, B. Drake, J.A. Gurley, V.B. Elings, P.K. Hansma, Using force modulation to image surface elasticities with the atomic force microscope. *Nanotechnology*, **2**, 103–106 (1991)
9. K. Yamanaka, H. Ogiso, O. Kolosov, Analysis of subsurface imaging and effect of contact elasticity in the ultrasonic force microscope. *Japanese J. Appl. Phys.* **33**, 3197–3203 (1994)
10. E.K. Dimitriadis, F. Horkay, J. Maresca, B. Kachar, R.S. Chadwick, Determination of elastic moduli of thin layers of soft material using the atomic force microscope. *Biophys. J.* **82**, 2798–2810 (2002)
11. G. Shekhawat, S. Avasthy, A. Srivastava, S.-H. Tark, V. Dravid, Probing buried defects in extreme ultraviolet multilayer blanks using ultrasound holography. *IEEE Trnas. Nanaotechnol.* **9**(6), 671–674 (2010)
12. R. Szoszkiewicz, A. Kulik, G. Gremaud, M. Lekka, Probing local water contents of in vitro protein films by ultrasonic force microscopy. *Appl. Phys. Lett.* **86**, 123901 (2005)
13. J. Cuberes, Mechanical diode mode ultrasonic friction force microscopy. *J. Phys. Conf. Series* **100**, 052014 (2008)
14. A. Ebert, B.R. Tittmann, J. Du, W. Scheuchenzuber, Technique for rapid in vitro single-cell elastography. *J. Ultrasound Med. Biol.* **32**(11), 1687–1702 (2006)
15. C. Miyasaka, B.R. Tittmann, Ultrasonic atomic force microscopy on spray dried ceramic powder. In: *Acoustic Imaging*, vol. 27, ed. by W. Arnold, S. Hirsekorn (Kluwer Academic, Dordrecht, 2004), pp. 715–720
16. R. Howland, L. Benatar, *A Practical Guide to Scanning Probe Microscopy*, vol. 74 (Park Scientific Instruments, Sunnyvale, 1996)
17. J.H. Kinney, M. Balooch, S.J. Marshall, G.W. Marshall, Atomic force microscope measurements of the hardness and elasticity of peritubular and intertubular human dentin. *J. Biomech. Eng.* **118**, 133–135 (1996)
18. M. Lantz, Y.Z. Liu, X.D. Cui, H. Tokumoto, S.M. Lindsay, Dynamic force microscopy fluids. *Surf. Interface Anal.* **27**(5–6), 354–360 (1999)
19. R.M. Overney, E. Meyer, J. Frommer, H.-J. Guentherrodt, M. Fujihara, H. Takano, Y. Gotch, Force microscopy study of friction and elastic compliance of phase-separated organic thin films. *Langmuir* **10**, 1282–1286 (1994)

20. D. Stamenovic, D.E. Ingber, Models of cytoskeletal mechanics of adherent cells. *Biomech. Model Mechanobiol.* **1**(1), 95–108 (2002)
21. A. Stevens, J.L. Lowe, *Human Histology* (Mosby, London, 1997)
22. K.N. Wadu-Mesthrige, A.A. Amro, A.S. Garno, A.A. Amro, S. Cruchon-Dupeyrat, G.Y. Liu, Contact resonance imaging—a simple approach to improve the resolution of AFM for biological and polymeric materials. *Appl. Surf. Sci.* **175–176**, 391–398 (2001)
23. M. Nagayama, H. Haga, Y. Tanaka, Y. Hirai, K. Kabuto, K. Kawabata, Improvement of force modulation mode with scanning probe microscopy for imaging viscoelasticity of living cells. *Jpn. J. Appl. Phys.* **44**, 952–955 (2002)
24. E. Al-Hassan, W.F. Heinz, M.D. Antonik, N.P. D’Costa, S. Nageswaran, C.A. Schoeneberger, J.H. Hoh, Relative microelastic mapping of living cells by atomic force microscopy. *Biophys. J.* **74**, 1564–1578 (1998)
25. J.H. Darnell, D. Lodish, D. Baltimore, *Molecular Cell Biology*, 2nd edn. (Scientific American Books, New York, 1990)
26. M. Radmacher, C.M. Kacher, J.P. Cleveland, P.K. Hansma, Measuring the viscoelastic properties of human platelets with the atomic force microscope. *Biophys. J.* **70**, 556–567 (1996)
27. R.I. Freshney, *Culture of Animal Cells: Manual of Basic Technologies* (Wiley, New York, 2000)
28. R. Nowakowski, P. Lucklam, Imaging the surface details of red blood cells with atomic force microscopy. *Surf. Interface Anal.* **33**, 118–121 (2002)
29. D.E. Ingber, I. Tensegrity, Cell structure and hierarchical systems biology. *J. Cell Sci.* **116**, 1157–1173 (2003a)
30. D.E. Ingber, Tensegrity II. How structural networks influence cellular information processing networks. *J. Cell Sci.* **116**, 1397–1408 (2003b)
31. A. Vinckier, G. Semenza, Measuring elasticity of biological materials by atomic force microscopy. *FEBS Lett.* **430**, 12–16 (1998)

# Index

3-D FEA, 427, 431

## A

Abbe's criterion, 2

Abbe's principle, 124, 295

Accuracy, 137

Acoustic

coupler, 267

force microscopy, 458

impedance, 297

noise, 297

scattering, 297

wave, 41, 303

Adhesion, 14, 25, 33, 37, 165, 344, 410, 425

Adhesion energy, 30, 270

Adhesive, 394

contact, 30

forces, 370

interaction forces, 445

Aging time, 258

Air damping, 109, 128, 161

Air damping matrix, 109

Amplitude, 58, 81, 124, 203, 465

bifurcation, 58, 85

modulation frequency, 266

modulation-atomic force microscope, 78

modulation-atomic force microscopy, 48

Amylin fibres, 275

Anelasticity, 407

Angular

deflection, 334

frequency, 286

spring constant, 210

Anti-resonance, 112

Apex radius, 212

Apparent force, 117

Apparent, 117

Area moment of inertia, 126

Array of MOSFET cantilevers, 310

Artifacts, 2, 13, 159, 276, 336

Atomic force acoustic microscope, 48, 77,  
124, 231, 352

Atomic force acoustic microscopy (AFAM), 7,  
48, 77, 124, 190, 263, 280, 295, 376,  
381, 391, 392, 413, 462, 480

Atomic force microscope, 262, 462

Atomic force microscopy (AFM), 1, 262, 316,  
391, 462

Atomistic modelling, 270

Attenuation coefficient, 67

Auger electron spectroscopy, 369

Axisymmetric FEA, 426

## B

Bandwidth, 324

Beam

equation, 54

shape, 117

vibration theory, 193

Bending momentum, 323

Berkovich hardnesses, 256

Berkovich, 358

Berkovich's indentations, 248

Berkovich's tip, 249

Best fitting line, 380

BHK monolayers, 474

Bicomponent polymer fibers, 442

Bifurcation, 63, 84



**B (cont.)**

Biological, 298  
 cells, 464, 469  
 composite materials, 286  
 samples, 462  
 tissues, 358  
 Bi-stability, 85  
 Blind tip reconstruction, 386  
 Bonding forces, 463  
 Borosilicate glass, 143  
 Boundary conditions, 395  
 Bow distortion, 381  
 Bright and dark regions, 479  
 Brillouin light scattering, 363  
 Bulk acoustic waves, 298  
 Buried  
 defects, 305  
 microcracks, 302  
 structures, 462

**C**  
 Calibration, 12, 139, 397  
 Calibration curve, 216  
 Cantilever, 4, 103, 126, 353, 354, 392, 393, 446  
 arrays, 310  
 chip, 175  
 deflection, 4  
 displacement amplitude, 78  
 driving force, 52  
 dynamics, 50  
 geometry, 236  
 holder, 113, 175  
 model, 10  
 stiffness, 53  
 vibration spectra, 148  
 Cantilever-tip-sample system's, 249  
 Capillary, 27  
 Carbon fiber reinforced plastics, 178  
 Carbon nanotube, 184, 450  
 Carbon-fiber-reinforced epoxy composite, 443  
 Cell boundaries, 479  
 Cells, 466  
 Ceramic fiber, 269  
 Characteristic equation, 130  
 Clamped-free beam, 127  
 Clamping plate, 175  
 Co-Cr-alloy layer, 218  
 Cohesive zone, 43  
 Complex modulus, 13  
 Compliant materials, 470  
 Concentrated-mass, 190, 193  
 Conservative forces, 59

**Contact**

area, 13, 22  
 damping, 129, 409  
 edge, 43  
 force, 23, 393  
 mechanics, 10, 139, 365  
 mode, 136, 298  
 model, 428  
 point, 381  
 radius, 23, 25, 232, 433  
 resonance, 298  
 stiffness, 6, 25, 137, 170, 235, 257, 271, 301, 362, 387, 392, 395, 397, 401, 418, 446  
 stresses, 23  
 Contact resonance  
 force microscopy, 352  
 frequency, 101, 131, 354  
 frequency images, 139  
 spectra, 135, 213  
 spectroscopy, 352, 353, 391  
 Contact resonance-AFM, 437  
 Contact stiffness  
 algorithm, 424  
 image, 144  
 simulations, 429  
 Continuous stiffness measurement, 231  
 Continuous waves, 66  
 Contrast, 101  
 Convolution, 2, 383  
 Copper, 304  
 Copper lines, 139  
 Counterpropagating, 362  
 Coupled independent systems, 50, 65  
 Crack, 14, 166, 280  
 Critical stress, 406  
 Cross-sectional acoustic imaging, 294  
 Cross-talk, 326  
 Cut-off frequency, 4  
 Cylindrical cavities, 434  
 Cylindrical inclusions, 432  
 Cytotoxicity, 308

**D**  
 Damascene process, 273  
 Damping, 329, 397, 400, 401  
 Damping coefficient, 58, 64, 109, 224  
 Damping factor, 53  
 Data leveling, 378  
 Data processing, 338, 376  
 Deconvolution, 384  
 Deflection, 4  
 amplitudes, 196

- signal, 465
- Deflectometer, 243
- Degraded composites, 447
- Delamination, 14, 166, 168, 280, 302, 424
- Delay, 339
- Delay phase angle, 196
- Depth, 369
- Depth sensing, 395, 451
- Derjaguin approximation, 26
- Derjaguin-Muller-Toporov (DMT) model, 11, 28, 319
- Desiccation, 467
- Diamond coated silicon tips, 468
- Diamond like carbon, 142
- Diamond-coated, 398
- Diamond-like carbon (DLC) films, 11, 218
- Difference-frequency contact resonance, 74
- Difference-frequency signal, 73
- Differential UFM, 362
- Diffraction, 297
- Dilation, 384
- Direct force modulation, 204
- Discontinuities, 269
- Dislocations, 166, 403, 407
- Dispersive flexural waves, 233
- Displacement, 54
- Dissipated energy, 407, 410
- Dissipation, 41, 42
- Dissipation force, 53
- Dissipative forces, 59
- Distortions, 377
- Distributed mass, 204
- Domain boundary, 179
- DRIE process, 242
- Drift distortions, 379
- Driving force, 321
- Duffing equation, 86, 166
- Dugdale-Barrenblat, 34
- Dupré adhesion energy, 195
- Duralumin, 230
- Dynamic
  - atomic force microscopy, 48
  - force microscope, 228
  - indentation, 5, 13
  - loading, 248
  - mechanical analysis, 229, 247, 370, 453
  - rigidity of the cantilever, 266
- Dynamical mechanical analysis, 13
- E**
- Effective
  - damping coefficient, 60
  - interaction force gradient, 58
  - spring constant, 64, 264
  - spring stiffness constant, 58
  - stiffness constant, 60
  - Young's modulus, 195, 219
- Eigenfunctions, 65
- Eigenmode, 296
- Eigenvalues, 234
- Elastic
  - axisymmetric bodies, 418
  - constant, 68
  - contact, 22
  - inhomogeneity, 282
  - isotropy, 367
  - modulus, 5, 352, 455, 468
  - properties, 311
  - regime, 393
- Elasticity, 268, 397, 413
  - mapping, 214
  - measurements, 392
- Elastography, 462
- Elastomers, 42
- Electric force microscopy (EFM), 15
- Electrode, 168
- Electron
  - backscatter diffraction, 369
  - beam, 298
  - beam microscopy, 294
- Electrospun polymer fibers, 439
- Electrostatic force, 115
- Electrostatic pressure, 115
- Embedded nanoparticle, 451
- Energy dissipation, 331
- Energy loss, 407
- Enhanced sensitivity, 370
- Epon 862, 457
- Equation of motion, 193
- Erosion, 384
- Erythrocytes, 309
- Euler-Bernoulli equation, 126
- Evanescent waves, 5
- Excitation mode, 113
- Excitation signals, 289
- Exfoliated graphene, 346
- Expansion coefficients, 55, 57
- Experimental contact spectra, 199
- F**
- Fabry-Perot interferometer, 360
- Fast fourier transform (FFT), 328, 335
- Fast scan direction, 377
- Feedback loop, 264
- Feedback system, 300
- FEM simulations, 244

**F** (*cont.*)

Ferroelectric domain, 179  
 Fiber-matrix interphase, 443  
 Film, 248, 368  
 Film thickness, 431  
 Filtering, 327, 378  
 Finite element  
   analysis, 423  
   method, 102, 451  
   model, 133, 463, 469, 481  
   modeling, 418, 424  
 First  
   contact mode, 239  
   harmonic, 340  
   mode approximation, 402  
   order (nonlinear) solution, 70  
 Flat punch model, 455  
 Flat tip, 217  
 Flexural, 13, 125, 244  
   deflection, 299  
   modes, 51  
   response, 322  
   sensitivity, 237  
   vibration, 101, 230  
   wave numbers, 51  
 Floquet indices, 89  
 Floquet solutions, 88  
 Fluorescence confocal microscopy, 307  
 Fluorescence images, 472  
 Force  
   curve, 145  
   gradient, 190  
   jump, 265  
   microscopy, 285  
   modulation, 393, 467  
   modulation microscopy, 5, 48, 77, 228, 316  
   spectroscopy, 316, 317, 328, 330, 332  
   volume Microscopy, 316  
 Forced vibration, 192, 202  
 Force–distance, 467  
   (F-D) method, 362  
   curve, 295, 300, 466  
   Measurements, 475  
 Fourier-space green function, 92  
 Four-quadrant photodiode, 325  
 Fractional harmonics, 50  
 Free energy, 405  
 Free resonance, 401  
 Frequency, 77, 340  
   modulation, 59  
   range, 356  
   shifts, 241  
 Frequency-dependent terms, 203  
 Friction, 39, 124, 183, 278, 392, 408, 409, 412

force, 267  
   force microscopy, 323, 412  
   damping, 193  
 Fumed silica-epoxy nanocomposites, 450  
 Function generator, 354  
 Fundamental resonant frequency, 189, 201, 205  
 Fused silica, 135

**G**

Gasb-inas superlattice, 273  
 Geometrical artifacts, 216  
 Geometrical distortions, 378  
 Glass  
   fibers, 380  
   surface, 198  
   transition, 344  
   transition temperature, 441  
 Gold nanoparticles, 450  
 Grain, 215  
 Grain sizes, 368  
 Graphene, 346  
 Graphene “nano-domes”, 282  
 Graphite, 170  
 Green function, 92  
 Grid measurements, 138

**H**

Hamaker constant, 27  
 Hamster kidney cells (BHK), 480  
 Hank’s balanced salt solution (HBSS), 475  
 Hard contact, 78, 79  
 Hardening nonlinearity, 145  
 Harmonic, 63, 85  
   balance method, 194, 197  
   forces, 321  
   generation, 61  
   motion, 299  
 Hertz, 23  
   analysis, 445  
   contact, 235, 250  
   model, 10, 24, 468, 476  
 Hertzian  
   contact, 284, 358, 396, 427  
   model, 418, 433  
   theory, 404  
 Hertzian contact  
   mechanics, 363  
   model, 213  
   repulsion, 195  
   theory, 455  
 Hertz’s theory, 235

Heterodyne force microscopy (HFM), 15, 48, 73, 286, 296  
 Heterodyne interferometer, 230  
 High frequency actuators, 310  
 High frequency oscillators, 309  
 High oriented pyrolytic graphite (HOPG), 8, 167, 271  
 High-purity oriented graphite (HPOG), 404  
 Homogeneous specimen, 67  
 Hooke's law, 468  
 Hybrid approaches, 358  
 Hybrid sensor, 230  
 Hygrothermal degraded, 449  
 Hyperelastic material, 253  
 Hysteresis, 42  
 Hysteretic effects, 270

**I**

Image contrast, 59, 80, 81  
 Imaging, 477  
 Indentation, 4  
   depth, 263, 469  
   moduli, 430  
   modulus, 13, 140, 397, 400, 420  
 Indium, 457  
 Induced lubricity, 279  
 Inertial effects, 41  
 Inertial stiffness, 268  
 Inhomogeneity, 255  
 Instability, 43  
 Installation slope, 381  
 Instantaneous, 255  
 Instrumented (nano-) indentation, 357, 366, 367, 369  
 Instrumented-indentation, 437  
 Interaction  
   force, 48, 52, 53  
   potential, 26, 28  
   stresses, 27  
 Interfaces, 14  
 Interfacial stiffness, 480  
 Intermittent contact heterodyne force microscopy, 296  
 Intermittent contact mode, 78, 318  
 Internal friction, 126, 161, 407, 408  
 Internal organelles, 479  
 Interphase, 449  
 Intracellular features, 307  
 Isotropic, 356, 396  
 Isotropic reduced elastic modulus, 140

**J**

Johnson-Kendall-Roberts, 11, 32  
 Jumping mode scanning force microscopy, 316

**K**

Kendall-Roberts (JKR) model, 270  
 Kinematic parameters, 103  
 Kinetic energy of the tip, 110

**L**

Langmuir-Blodgett film, 277  
 Laser acoustic surface wave, 409  
 Laser scanning confocal microscope, 472  
 Laser-ultrasonic SAW, 359  
 Lateral, 125

  contact damping, 129  
   contact stiffness, 129, 206, 241  
   deflection signal, 266  
   force microscopy, 241, 323, 463  
   force modulation, 183  
   motion of the contact point, 206  
   resolution, 295  
   vibration, 410

Layered materials, 418  
 Lead zirconate titanate, 179  
 Lennard-Jones potential, 6, 463  
 Line tension, 405  
 Linear

  contact vibration, 224  
   detection regime, 78  
   spectra, 7, 8, 163  
   springs, 144  
   tip-sample interaction, 199

Linearization, 328  
 Liquid, 463, 464, 473  
 Liquid meniscus, 28  
 Liquid-vapor interfacial energy, 320  
 Lock-in amplifier, 265, 297, 318, 339  
 Long tip, 119  
 Longitudinal acoustic waves, 444  
 Lorentz transmission electron microscopy, 302  
 Lorentzian, 403  
   Loss modulus, 13, 156, 254, 401  
 Low frequency generator, 230  
 Low megahertz range, 74  
 Low-density polyethylene, 439

**M**

Macroscopically-homogeneous stiff-samples, 205

**M (cont.)**

Magnetic force, 114  
 Magnetic force microscopy (MFM), 15  
 Magnetic force modulation microscopy, 191  
 Magnetic resonance force microscopy, 191  
 Malaria, 308  
 Mass Matrix, 105  
 Mass of the cantilever, 190  
 Mass-loaded cantilever, 191  
 Mass-spring system, 300  
 Mathieu's equation, 88  
 Maugis, 28  
 Maximum nonlinearity regime, 74  
 Mechanical
 

- diode, 164
- map, 386
- model, 395
- properties, 125, 341
- reactance, 200

 Mesh, 107  
 Metallic glass, 400  
 Michelson interferometer, 360  
 Microdeformation
 

- image, 232
- microscopy, 376
- volume, 230

 Microlever, 279  
 Microlever cantilevers, 475  
 Micromachined cantilever, 323  
 Microscopy dynamic indentation, 5  
 Minimum defect size, 431  
 Mode coupling, 55  
 Mode function, 207  
 Model, 110, 129  
 Model of vibrations of the CM cantilevers, 208  
 Molybdenum disulfide, 271  
 MOSFET embedded cantilevers, 310  
 Multi-asperities contact, 14, 159  
 Multilayer graphene, 283  
 Multi-phase materials, 443

**N**

Nanocomposites, 345  
 Nanocrystalline face-centered cubic (fcc-) metals, 406  
 Nanocrystalline materials, 368  
 Nanoindentation, 44, 229, 248, 254, 345, 346, 396, 453  
 Nanomechanical mapping, 370  
 Nanoswing, 347  
 Natural
 

- environment, 280
- flexural vibrations, 207

frequencies, 209  
 resonant frequency, 264  
 vibrational modes, 51  
 Near field, 124  
 Near field acoustic waves, 5  
 Near-field
 

- microscopes, 228
- scanning optical microscopy, 294
- ultrasound holography, 299

 Ni single crystal, 399, 408  
 Nickel, 135  
 Niobium, 143  
 Noise, 328  
 Non linearities, 245  
 Non-destructive evaluation, 423  
 Nondestructive, 304, 365, 421, 434  
 Non-Hertzian surface contact, 455  
 Nonlinear, 6
 

- force-deflection, 469
- force-separation interaction, 76
- mixing, 70
- spectra, 8, 162
- tip-sample interaction force, 54
- vibration model, 196

 Non-linear regime, 295  
 Nonlinearity, 6, 62, 117, 145  
 Nonsliding contact, 117, 119  
 Normal
 

- cantilevers, 205
- contact stiffness, 129, 140
- stiffness, 103

 Normalized
 

- contact stiffness, 426
- first flexural mode sensitivity, 237
- interactive force, 198
- resonant frequency, 203
- stiffness, 203, 205

 Nucleation, 406

**O**

One-freedom model, 209  
 Optical
 

- detection, 325
- glass slide, 214
- heterodyne force microscopy, 288

 Optimization, 338  
 Oriented domains, 180  
 Oscillation amplitude, 56, 78, 328  
 Oscillator, 406  
 Oscillatory solution, 69  
 Outer membrane, 479  
 Oxide particles, 280

**P**

Parasite infection, 308  
 Peak force, 331  
 Peak frequency shifting, 85  
 Peak-peak distances, 343  
 Penetration, 23  
   depth, 4, 397, 429  
   speed, 249  
 Perturbative procedure, 61, 68  
 Phase, 58, 124  
   contrast, 60, 303  
   delay, 203  
   factor, 65  
   image, 300  
   image contrast, 81  
   imaging, 74, 318, 342  
   sensitive acoustic microscopy, 452  
   signal, 299  
   velocity, 66, 360  
 Phase-locked loop, 177  
 Photodetector, 299  
 Photoresist, 247  
 Piezoelectric  
   element, 212  
   stiffening, 182  
   transducer, 230  
 Piezoplate, 267  
 Piezo-transducer, 298  
 Pixels, 337  
 Plane strain modulus, 356  
 Plasma-enhanced vapor deposition, 368  
 Plastic deformation, 157  
 Plasticity, 404  
 Platinum, 217  
 Point force, 466  
 Point-mass models, 200  
 Poisson ratio, 13, 126, 172, 255  
 Polished glass, 215  
 Poly-(ethylene-co-vinyl acetate), 439  
 Poly(methyl methacrylate) (PMMA), 275, 385, 450  
 Polyacrylonitrile, 444  
 Polyamide, 442  
 Polycarbonate, 453  
 Polycrystalline, 404  
 Polydimethylsiloxane (PDMS), 44, 236  
 Polydimethylsiloxane, 247  
 Polyester, 442  
 Polyethylene terephthalate, 280  
 Polyimide, 450  
 Polymer, 252, 358, 392, 428  
   binder, 280  
   blend, 386, 454  
   cross-links, 447

  film, 317, 452  
   matrix, 447  
   nanocomposite, 449  
 Polynomial expansions, 55  
 Polypropylene, 380, 458  
 Polysilicon, 456  
 Polystyrene, 170, 451  
 Polyurethane, 120  
 Probe geometry, 457  
 Pull-off point, 277  
 Pull-out force, 32  
 Pulsed electrodeposition, 368  
 Pulsed laser, 298  
 Pulse-echo ultrasonics, 354, 356

**Q**

Q factor, 156, 161, 403  
 Q factor mapping, 177  
 Quality factor, 224  
 Quantitative measurement, 228  
 Quantitative mechanical characterization, 387  
 Quantum dots, 284  
 Quartz glass, 398, 399, 411, 412  
 Quiescent separation distance, 54  
 Q-values, 128, 393

**R**

Radius of curvature, 387  
 Rayleigh criterion, 5  
 Rayleigh waves, 5  
 Reactance relative, 201  
 Real  
   force, 117  
   normal force, 117  
   tangential, 117  
 Rebound, 40, 43  
 Rectangular cantilever, 118, 171, 211  
 Rectangular, 102  
 Red blood cells, 307  
 Reduced elastic modulus, 455  
 Reduced modulus, 22  
 Reduced Young's modulus, 140  
 Reference materials, 455  
 Reference sample, 141  
 Regions of stability, 89  
 Relaxation time, 252, 286  
 Relaxed moduli, 257  
 Renormalization, 90  
   methods, 56  
   scale, 90  
 Resolution, 273, 364, 391  
 Resonance, 60, 112

- R** (*cont.*)
- angular frequency, 249
  - curve, 7, 245, 401
  - frequency tracking, 177
  - frequency, 64, 156, 392
  - spectra, 397
- Resonance-tracking, 156
- Resonant
- difference-frequency atomic force ultrasonic microscope, 73
  - difference-frequency atomic force ultrasonic microscopy, 9, 48, 296, 451
  - dipping, 481
  - frequency peak, 470
  - frequency, 124, 321
- Restoring force, 53
- Rod-like CM cantilever, 208
- Roughness, 38, 216, 272, 385, 398, 410, 481
- Rubber, 345
- S**
- Saint Vernant's principle, 284
- Sample
- elasticity, 204
  - holder, 114
  - stiffness, 80
  - tilt, 173
- Sampling ratio, 335
- SAW-assisted SPM, 364
- Scanning acoustic force microscopy, 124
- Scanning acoustic microscope, 294, 295, 366
- Scanning acoustic microscopy, 4, 5, 363–365, 452
- Scanning capacitance microscopy (SCM), 15
- Scanning electron micrographs, 465
- Scanning electron microscope, 472
- Scanning electron microscopy, 302, 409, 440
- Scanning force microscopy, 262
- Scanning Kelvin probe microscopy (SKPM), 15
- Scanning local-acceleration microscopy, 263
- Scanning microdeformation microscope, 228
- Scanning microdeformation microscopy, 7, 124, 190, 437–438
- Scanning near field ultrasonic holography, 9, 48, 73
- Scanning near-field optic microscopy, 6
- Scanning near-field ultrasound holography, 9, 376, 438, 462
- Scanning nonlinear dielectric microscopy, 179
- Scanning probe microscope, 462
- Scanning probe microscopy (SPM), 1, 382
- Scanning tunneling microscopy, 465
- Scanning tunneling microscopy, 262
- Scanning tunnelling microscope, 273
- Scattered waves, 297
- Scattering, 297
- Segmentation, 385
- Self calibration, 144
- Semicrystalline polymers, 442
- Sensitivity, 204, 257, 370
- Sensitivity optimization, 236
- Setpoint, 328
- Shear elasticity, 183
- Shear force, 207, 395
- Shear modulation force microscopy, 441
- Shear moduli, 172
- Shear stress, 405
- Shift, 64
- Shift frequency difference, 240
- Short tip, 119
- Si substrate, 256
- Signal processing, 331, 337
- Signal-to-noise ratio, 286
- Silica, 240
- Silica particles, 451
- Silicon, 143, 379
- carbide fibre, 208
  - dioxide (SiO<sub>2</sub>), 379
  - sample, 236
  - substrate, 440, 425
- Silicon-based viscoelastic polymer, 239
- Simulation, 198, 272, 404, 470
- Single-crystal, 396
- Single-walled carbon nanotube, 450
- Single walled carbon nanohorns, 308
- Sliding contact, 117, 119
- Slope detection, 212
- Sneddon relation, 357
- Soda-lime glass, 170
- Soft
- contact, 79
  - film, 431
  - samples, 205
- Softening nonlinear spring, 166
- Softening nonlinearity, 145
- Sound velocity, 41
- Spatial eigenfunctions, 51
- Spectroscopic AFAM, 404
- Spectrum, 244
- Spiral-spring constant, 211
- Spiral-spring model, 210
- Spreading resistance microscopy (SRM), 16
- Spring, 401
- Spring constant, 446
- Spurious resonances, 7
- Spurious vibration, 156, 175

- Stacked layers, 454
  - Static
    - deflections, 243
    - force, 245
    - load, 137
    - solution, 69
  - Steady-state solution, 68
  - Stick & slip, 241
  - Stiff
    - cantilevers, 205
    - film, 431
    - samples, 201
  - Stiffening nonlinear spring, 166
  - Stiffness, 22, 36, 55, 296, 338, 340, 394, 464, 470
    - atomic force microscope, 298
    - matrix, 106, 107
    - of the cantilever, 257
    - ratio, 210
  - Storage modulus, 13, 254, 401
  - Strain field, 255, 295
  - Stress field, 14
  - Structures, 74
  - Styrene butadiene styrene (SBS), 385
  - SU8 resin, 247
  - Subcellular structures, 306
  - Subharmonic, 50, 63, 86
    - components, 194
    - stability, 86
  - Substrate effects, 219
  - Subsurface, 74, 230
    - defects, 418, 421, 428
    - features, 66, 295
    - grooves, 230
    - imaging, 14, 302
    - properties, 295
    - resolution, 422
    - stress, 442
    - structures, 434
  - Superlubricity, 275
  - Surface
    - acoustic wave, 286, 361
    - acoustic wave spectroscopy, 366, 367, 369
    - drive amplitude, 77
    - dynamics, 55
    - elastic contrast, 303
    - roughness, 479
  - Symmetric, 244
  - Synchronization, 335
- T**
- Tabor parameter, 35
  - Tangential stiffness, 103
  - Tapping mode, 78, 391
  - Taylor series, 56
  - Test sample, 341
  - Test structure, 333
  - Thermal contrast, 280
  - Thin film, 36, 334, 400, 421, 429
  - Thin layer, 471
  - Thin-film polymers, 439
  - Threshold amplitude, 265, 277
  - Ti sheet, 215
  - Ti-alloy layer, 218
  - Time scale sensitivity, 289
  - Time'-space, 92
  - Time-force graphs, 321
  - Time-resolved waveforms, 319
  - Timoshenko, 129
  - Tip, 33, 36, 110, 269, 356, 382, 396, 409
    - geometry, 382
    - height, 119
    - material, 427
    - position, 132
    - radius, 420
    - shape, 21, 139, 212
    - wear, 365
  - Tip-sample, 301
    - interaction, 264
    - interaction force, 53, 318
    - separation, 48
  - Tip-shape models, 454
  - Tip-surface, 278
  - Titanium, 217, 426
  - Tomography, 310
  - Topography, 214, 270, 275, 303, 387, 410, 479
  - Torsional
    - bending, 347
    - contact resonance, 408
    - contact resonance frequencies, 13
    - friction, 410
    - harmonic atomic force microscopy, 9, 438
    - modes, 244
    - oscillation, 339
    - resonance frequency, 334
    - response, 322
    - stiffness, 183
    - vibration, 101, 125, 326
  - Transfer of energy, 58, 64
  - Transmission electron microscopy, 271, 302
  - Transparent silicon nitride tip, 286-287
  - Trench isolation, 306
  - Triangular, 126
    - beams, 102
    - cantilever, 118
    - shape, 117
  - T-shaped cantilevers, 9, 323



**T** (*cont.*)

Tungsten  
 powder, 212  
 wire, 230

**U**

Ultralever, 469  
 Ultrasonic, 68  
   atomic force microscopy AFM, 7, 48, 79,  
     124, 156, 190, 354, 418, 419, 421, 423,  
     424, 428, 437, 462, 463  
   force microscopy, 8, 48, 76, 124, 192, 231,  
     263, 264, 273, 295, 362, 376, 437, 463  
   frequency, 266  
   scanning pin microscope, 263  
   superlubricity, 280  
   velocity techniques, 217  
   vibration, 267  
   waves, 303  
 Ultrasonic-based AFM, 359  
 Ultrasound  
   holography, 303  
   lubrication, 413  
 Ultrathin films, 219  
 Uncertainty, 138, 365  
 Undegraded, 447

**V**

Van der Waals, 27  
 Velocity, 68  
 Vertical drift, 378  
 Vibration  
   amplitudes, 394, 467  
   analysis, 109  
   modes, 209, 211  
 Viscoelastic, 403, 441

  material, 13, 251  
   measurements, 370  
   properties, 247  
   relaxation, 269  
   response, 303, 305  
 Viscoelasticity, 80, 124, 358, 441  
 Viscosity, 164  
 Viscous damping, 193  
 Viscous constant, 41  
 Viscous fluid, 471  
 Void, 14, 306, 432  
 Voiding, 303  
 Von mises stress, 158

**W**

Waveforms, 360  
 Waveguide, 285  
 Wavevector, 282  
 Wear, 11, 142, 159, 331, 382  
 Working frequency, 253  
 W-shaped cantilevers, 243

**X**

X-ray imaging, 294

**Y**

Yield stress, 158  
 Young moduli, 320  
 Young modulus, 13, 68, 80, 126, 239, 329,  
   345, 356, 368

**Z**

Zeroth order solution, 69